ESA Support To Science Element (STSE)

SMOS Sea Ice Retrieval Study (SMOSIce)
Final Report

ESA ESTEC Contract No.: 4000101476/10/NL/CT

Lars Kaleschke, Xiangshan Tian-Kunze, Nina Maaß
Institute of Oceanography, KlimaCampus,University of Hamburg

Georg Heygster, Markus Huntemann, Huan Wang
Institute of Environmental Physics, University of Bremen

Stefan Hendricks, Thomas Krumpen
Alfred-Wegener-Institute, Bremerhaven

Rasmus Tonboe
Danish Meteorological Institute

Marko Mäkynen
Finnish Meteorological Institute

Christian Haas
York University, Toronto

ESA Technical Officer: Matthias Drusch

December 6, 2013

ESA STUDY CONTRACT REPORT – SPECIMEN

ESA Contract No: 4000101476/10/NL/CT	SUBJECT: STSE-SMOS Sea Ice Retrieval Study (SMOSIce)	CONTRACTOR: Universtity of Hamburg, Institute of Oceanography
ESA CR( )No:	No. of Volumes: 1	CONTRACTOR'S REFERENCE: LK-ESA-2010-01

ABSTRACT: (short summary, see Final Report for the complete abstract)

The aim of the SMOSIce study was to develop, improve and validate algorithms for sea ice thickness retrieval from the 1.4 GHz (L-band) data of the European Space Agency's (ESA) Soil Moisture and Ocean Salinity (SMOS) mission. The potential to derive the ice thickness from L-band radiometry mainly depends on sea ice temperature and salinity. Several different sea ice emissivity models and retrieval algorithms have been developed and assessed using independent ice thickness estimates. The assessment has shown a clear advantage of a retrieval method that accounts for variations in ice temperature and ice salinity. This retrieval method determines the maximum thickness that can be retrieved. Sensitivity studies as well as comparisons with MODIS ice thickness revealed significantly better performance of the retrieval based on the brightness temperature near nadir in comparison to the difference of vertically and horizonally polarised brightness temperatures in the higher incidence angle range. A sea ice thickness product including three winter (October 15 to April 15) seasons has been derived from SMOS Level 1C brigthness temperature and is distributed via the Integrated Climate Data Center at the University of Hamburg, available at https://icdc.zmaw.de. The approximate uncertainties of the SMOS ice thickness retrieval are about 20% for ice thickness less than 30 cm and 100% for ice thickness more than half a meter with an ill-constrained upper limit. To determine changes of the total sea ice thickness and volume we recommend to use SMOS and CryoSat-2 data together because of their complementary error characteristics. There is the need for more validation measurements in both hemispheres to further improve the retrieval algorithm.

The work described in this report was done under ESA Contract. Responsibility for the contents resides in the author or organisation that prepared it.

Names of authors: Lars Kaleschke, Xiangshan Tian-Kunze, Nina Maaß, Georg Heygster, Markus Huntemann, Huan Wang, Stefan Hendricks, Thomas Krumpen, Rasmus Tonboe, Marko Mäkynen, Christian Haas

NAME OF ESA STUDY MANAGER:	ESA BUDGET HEADING:

Revision history

Date	Author	Comments
Mar 15, 2013	L. Kaleschke	Initial outline
Apr 4, 2013	N. Maaß	Radiative transfer models and sensitivity study
May 28, 2013	X. Tian-Kunze	ATBD update
Aug 5, 2013	L. Kaleschke	Summary report
Sept 19, 2013	X. Tian-Kunze	ATBD update
Oct 13, 2013	L. Kaleschke	Summary report
Nov 4, 2013	L. Kaleschke	Final revision with comments from ESA (submitted)
Dec 6, 2013	L. Kaleschke	Layout, new refs in Tab. 1

CONTENTS

Part I

SMOSIce Summary Report

Lars Kaleschke (Editor) with contributions from the SMOSIce team.

Preface

Spaceborne passive microwave radiometry at 1.4 GHz (L-band) is a novel technique. Only a limited dataset of airborne L-band brightness temperatures over Baltic sea ice was available before the launch of SMOS. Concepts for the retrieval of sea ice thickness have been developed based on that data and on different emissivity models. The dependency of the brightness temperature on sea ice thickness under cold conditions was demonstrated when the first real SMOS data became available after the commissioning phase. Hence, it became clear that SMOS can be used to gain information about sea ice thickness, a parameter that is urgently required for climate sciences and other applications. SMOS provides novel and useful informations about the cryosphere and fills an important gap in the global earth observing system of systems.

However, the way to understand the microwave signal is not straightforward because of the complex nature of sea ice. Sea ice is a complex multiphase system consisting of solid ice and precipitated salts, liquid brine, and gas bubbles. Young sea ice is often covered with a brine layer and frost flowers. Furthermore, natural sea ice occurs not as a homogenous layer with one single thickness but is steadily deformed (e.g. through rafting and ridging). A physical model for the emissivity of such a complex medium requires many simplifications. Even more assumptions have to be made for solving the inverse problem for the retrieval of geophysical parameters, i.e. the sea ice thickness. The approach for the assessment of the assumptions is often heuristic depending on sparsely available validation data.

Although the first passive microwave satellite sensors were launched more than 40 years ago there is still no concensus about the best retrieval algorithm. Moreover, most sea ice concentration data products are still provided without uncertainties. This example demonstrates the scientific challenge and the time scales until a satellite retrieval technique becomes accepted as well validated and mature. With the launch of SMOS and the first availability of 1.4 GHz brightness temperatures we are only at the very beginning to gain its full potential for sea ice remote sensing. Thus, this report can be considered only as a snapshot of ongoing work. Some parts of this report have been previously published and other parts have been submitted and are under review. Because of this ongoing work there are likely some inconsistencies between different publications and this report.

0.1 Abstract

The aim of the SMOSIce study was to develop, improve and validate algorithms for sea ice thickness retrieval from the 1.4 GHz (L-band) data of the European Space Agency's (ESA) Soil Moisture and Ocean Salinity (SMOS) mission. SMOS payload is the Microwave Imaging Radiometer by Aperture Synthesis (MIRAS) measuring for the first time globally the L-band brightness temperature at a range of incidence angles and at different polarizations. Electromagnetic radiation at L-band wavelengths (about 21 cm) emerge from deep inside the sea ice layer. The attenuation mainly depends on the relative brine volume which is a function of ice bulk salinity and temperature. The penetration depth is up to 1.5 m for cold low-salinity sea ice and reduces to a few centimeters for saline sea ice at high temperatures. The potential to derive the ice thickness from L-band radiometry mainly depends on sea ice temperature and salinity.

Several different sea ice emissivity models and retrieval algorithms have been developed and assessed using independent ice thickness estimates. The independent ice thickness estimates include electromagnetic induction (EM) measurements, NASA's Operation IceBridge data, MODIS thermal infrared imagery, as well as model simulations. The models used are of different complexity and range from empirical freezing degree-day ice growth parameterisations over one- and two-dimensional thermodynamic sea ice models to advanced coupled dynamic-thermodynamic ocean-ice assimilation systems.

The assessment has shown a clear advantage of a retrieval method that accounts for variations in ice temperature and ice salinity. This retrieval method determines the maximum thickness that can be retrieved. Sensitivity studies as well as comparisons with MODIS ice thickness revealed significantly better performance of the retrieval based on the brightness temperature near nadir in comparison to the difference of vertically and horizonally polarised brightness temperatures in the higher incidence angle range.

For the production of a sea ice thickness data product we select an algorithm based on a forward model that includes a sea ice thermodynamic model and a three layer radiation model. During the iterative retrieval ice temperature and salinity are estimated from surface air temperature reanalysis and a weekly climatology of sea surface salinity. The retrieval model accounts for the thermodynamic effect of a snow layer parameterised as a function of ice thickness. The resulting sea ice thickness is corrected for the statistical influence of the thickness distribution function.

A sea ice thickness product including three winter (October 15 to April 15) seasons has been derived from SMOS Level 1C brigthness temperature and is distributed via the Integrated Climate Data Center at the University of Hamburg. The daily updated data products are available at `https://icdc.zmaw.de/`. The approximate uncertainties of the SMOS ice thickness retrieval are about 20% for ice thickness less than 30 cm and 100% for ice thickness more than half a meter with an ill-constrained upper limit. To determine changes of the total sea ice thickness and volume we recommend to use SMOS and CryoSat-2 data together because of their complementary error characteristics. We expect the greatest benefit of the SMOS data alone during the cold freeze-up periods when extensive areas of thin sea ice control the ocean-atmosphere heat exchange, which is important for weather and climate, as well as for operational marine applications. There is the need for more validation measurements in both hemispheres to further improve the retrieval algorithm.

0.2 Introduction

In preparation for the SMOS mission the potential to measure sea ice thickness was investigated in the project "L-band Radiometry for Sea-Ice Applications Study" (ESA ESTEC Contract 21130/08/NL/EL, 2007-2009), the precursor study of the project "SMOS Sea Ice Retrieval Study SMOSIce" (ESA ESTEC Contract No.: 4000101476/10/NL/CT, 2010-2013), in the following shortly referred to as "SMOSIce project", which is described in this report. The results of the precursor study are described in the final report (Heygster et al., 2009) and in three publications (Kaleschke et al., 2010; Mills and Heygster, 2011b,a). The precursor study merely has shown indications for the potential to obtain sea ice thickness from SMOS radiometry based on L-band radiometric data and nearly coincident thickness measurements from an airborne field campaign in the Bay of Bothnia in March 2007 (Kaleschke et al., 2010). At that time clear empirical evidence was missing due to limitations of the airborne dataset. However, different sea ice emissivity models suggested the sensitivity of SMOS brightness temperatures to sea ice thickness (Heygster et al., 2009).

The specified goals of the SMOSIce call for proposals were the development of at least two algorithms for the retrieval of sea ice thickness from SMOS, their validation and error assessment, and the production of a SMOS-based sea ice thickness data product. The SMOSIce consortium included two partners, the Alfred-Wegener-Institute (AWI), and the Finnish Meteorological Institute (FMI) which provided validation data, two Universities, University of Hamburg (UHH), and University of Bremen (UB) which developed and validated their different retrieval algorithms, and one partner, the Danish Meteorological Institute (DMI) which contributed sea ice thermodynamic and emissivity simulations. Two key areas were selected for validation: 1) the Baltic Sea due to the availability of suitable electromagnetic induction (EM) measurements, and 2) the Kara Sea for which ice thickness maps were derived from MODIS thermal infrared imagery. Simulations from the HIGHTSI thermodynamic model are available for both areas. In addition, results from other Arctic-wide sea ice models and assimilations systems, i.e. TOPAZ and PIOMAS, which are available to the public have been used for comparison. In order to achieve a suitable retrieval concept a variety of radiative transfer models as well as purely empirical methods have been investigated. The SMOS retrieval validation was accompanied by a comprehensive sensitvity and error analysis. This summary describes the selected procedures for SMOS sea ice thickness retrieval, discusses the main findings, and closes with conclusions and recommendations for fucture activities.

0.3 Sea ice emissivity models and retrieval concepts

The brightness temperature of an ice-covered ocean surface can be described as

$$T_{\mathrm{obs}}(p,\theta) = [(1-C)e_{\mathrm{sea}}T_{\mathrm{sea}} + Ce_{\mathrm{ice}}T_{\mathrm{ice}}]e^{\tau} + T_{\mathrm{other}} \quad (1)$$

with ice concentration C, emissivity $e_{\mathrm{ice/sea}}$ and temperature $T_{\mathrm{ice/sea}}$ of ice/water, atmospheric opacity τ and other contributions. The atmospheric attenuation is relatively small at 1.4 GHz and does not cause any difficulties for the retrieval (Section 1). The "other" term includes all contributions from space as well as from anthropogenic sources. In this study we have mostly neglected the potential impact of the other contributions except for the anthropogenic Radio Frequency Interference (RFI) which has a strong influence on the data quality (Section 5). The sea ice emissivity $e_{\mathrm{ice}}(p,\theta,..)$ is a function of polarization p, incidence angle θ and other parameters like the ice and snow thickness, their density and surface

roughness, ice temperature and salinity. In order to reduce the complexity and to constrain the retrieval problem one has to make several simplifications, for example to assume a semi-infinite plane-parallel geometry. A minimal physical emissivity model requires at least one ice layer of a variable thickness with reflecting boundaries. The ice medium is described by a permittivity $\epsilon_{\mathrm{ice}}(V_b)$ that depends on the relative brine volume $V_b(T_{\mathrm{ice}}, S_{\mathrm{ice}}, \rho_{\mathrm{ice}})$ as a function of sea ice temperature T_{ice}, salinity S_{ice} and density ρ_{ice}. A major simplifaction arises from the fact that volume scattering can be neglected at 1.4 GHz. The corresponding wavelength of 21 cm is large compared to the major ice impurities such as brine pockets or air bubbles. Thus, the radiative transfer calculation has only to account for absorption/emission and for reflections at the boundaries. However, there are still many possible approaches for the solution. An overview of the emissivity models and different retrieval concepts used for this and the precursor study is given in Table 1.

The models can roughly be categorized in coherent and incoherent approaches and the number of vertical layers. Oszillations occur as a function of ice thickness due to constructive and destructive interference when the phase relation is taken into account in coherent calculations. Thus, the coherent approach is not feasible for retrieval because of the ambiguities. In contrast, the incoherent radiative transfer method does not exhibit interference but is not well suited to treat discontinuities in the permittivity. Thus, the addition of an infinitely thin ice layer on the ocean or an infinitely thin snow layer on top of the sea ice causes a jump in the emissivity when treated with the radiative transfer method (Section 2). A reasonable combination of both methods is achieved when using the coherent/incoherent approach as described in Menashi et al. (1993). We use this coherent/incoherent model as the main tool for the ice thickness retrieval as described in Section 7. However, the coherent/incoherent formulation is valid only for one ice layer without an additional snow layer and limits our ability to account for the radiative effect of snow as well as for other effects like surface roughness. All limitations of the models have to be carefully taken into account for the interpretation of the results. This summary aims to provide a synthesis of the results from the variety of models and to highlight the conclusions that are robust irrespective of the individual model limitations.

Figure 1 provides a perspective on the sea ice and the ocean surface emissivity at a range of frequencies commonly used for spaceborne microwave radiometry. The monotonic increase of the ocean surface emissivity with frequency can be explained with the Debye equation and the frequency-dependent change of the real part of the permittivity. In constrast, the real part of the permittivity of pure ice $\epsilon \approx 3.17$ is constant in the microwave range. The permittivity of sea ice mainly depends on the relative brine volume. The decrease of the multi-year ice emissivity with frequency can be explained by volume scattering in the ice and snow medium. First-year ice is a strong absorber due to its high salinity and we can explain the relatively flat emissivity mainly with surface scattering. Two main characteristics of the emissivity at 1.4 GHz in comparison with the higher microwave frequencies can be depicted from Fig. 1:

- the largest range between an ice free ocean and thick ice,
- a unique order as a function of thickness.

The latter point is a prerequisite for the retrieval of sea ice thickness and not given for the other commonly used frequencies. The first point underlines the unique sensitivity at 1.4 GHz for sea ice applications in general.

The difference between the vertically and the horizontally polarized brightness temperature is called polarisation difference in the following. The brightness temperature intensity is

Table 1: Forward and retrieval models applicable for 1.4 GHz brightness temperature over sea ice

Method	Used by	Short description
Ulaby et al. (1981)	UHH	Coherent $N-$layer model Used in this study for sensitivity analysis.
Menashi et al. (1993)	UHH	Coherent/incoherent $3-$layer (air/ice/water) model
Burke et al. (1979)	UHH	Incoherent $N-$layer model; Used in this study for sensitivity analysis;
Maaß (2013a) (this report/PhD thesis)	UHH	Various models (listed above) used for senstivity studies and retrieval
Maaß et al. (2013b) (this report/PhD thesis)	UHH	Snow thickness retrieval
Kaleschke et al. (2010)	UHH	Based on Menashi et al. (1993);
Kaleschke et al. (2012) "Algorithm I"	UHH	Based on Kaleschke et al. (2010); Retrieval model with constant parameters
Tian-Kunze et al. (2013) "Algorithm II" (this report)	UHH	Based on Kaleschke et al. (2010); Accounts for ice salinity and temperature.
Tonboe (2005-11)	DMI	MEMLS sea ice emission model fed with profiles from thermodynamic sea ice model; Used in this study for sensitivity analysis;
Mills and Heygster (2011b)	UB	Monte Carlo raytracing ice ridge model; Not used in this study.
Mills and Heygster (2011a)	UB	$3-$layer (air/ice/water) model; Not used in this study.
Huntemann et al. (2013) (this report)	UB	Algorithm for high incident angles; Empirical method.

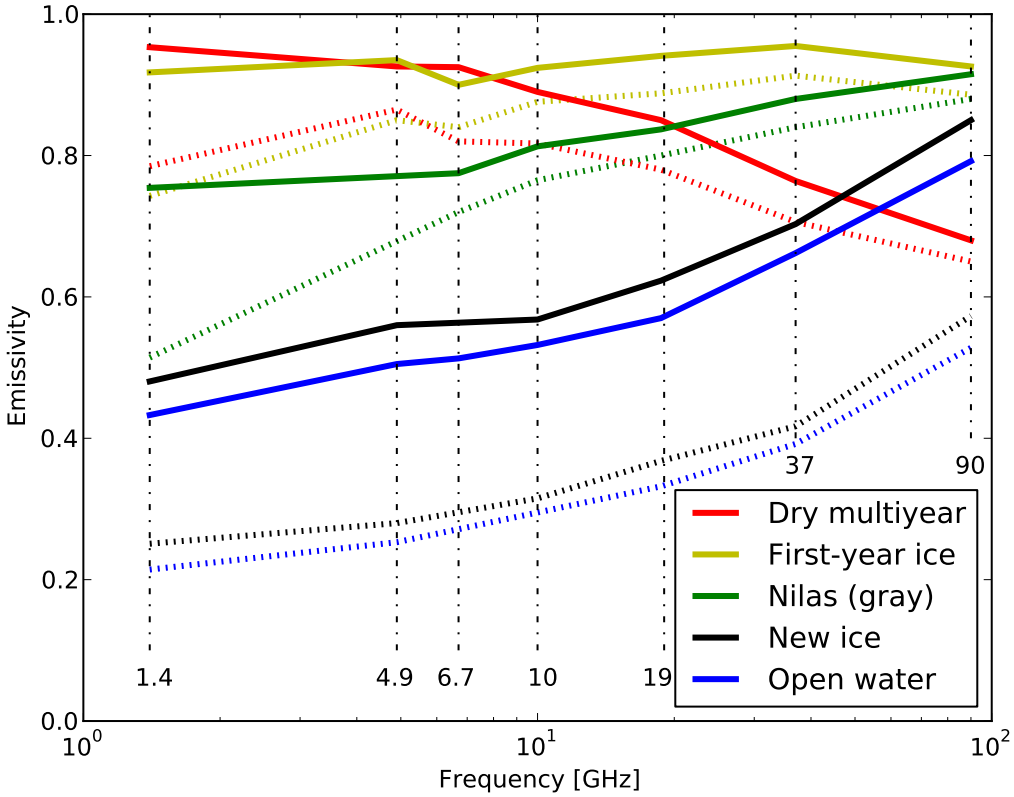

Figure 1: Sea ice emissivity at $\Theta = 50°$ from model simulations at 1.4 GHz and from radiometric measurements for the other frequencies (Eppler et al., 2013). The vertical and horizontal polarisation is displayed by the solid and dotted line, respectively. For the model simulations we assumed $d_{\mathrm{ice}} = 1$ cm and $T_{\mathrm{ice}} = -2°$C for new ice, 7 cm and -4°C for gray nilas, 1 m and -7°C for first year ice, and 3 m and -10°C for multi-year ice.

defined as the sum of both polarisations. We followed two main approaches for the development of retrieval algorithms. The first one is based on the measurement of the intensity, the second approach also takes the polarisation difference into account. It was hypothesized that the second approach could enable to derive more than one independent parameters, i.e. the ice thickness and the ice concentration simultaneously. At higher microwave frequencies, i.e. the 19 GHz, 37 GHz, and 85 GHz channels of SSM/I like sensors, the polarisation is widely used to estimate the sea ice concentration because of the large contrast between open water and sea ice (Cavalieri et al., 1984; Kaleschke et al., 2001). One problem for adapting this approach to 1.4 GHz arises from the fact that the polarisation difference of the sea ice emissivity increases for decreasing frequency at least for first year ice and nilas. For example, Fig. 1 shows that the polarisation difference at 1.4 GHz is similar for open water and nilas which is not the case at 90 GHz. This example demonstrates the difficulty of using the polarisation difference at 1.4 GHz to distinguish between a consolidated thin ice cover (nilas) and open water. Nevertheless, an attempt to derive ice thickness and concentration simultaneously was encouraging but the empirical algorithm needs further improvement (Section 8).

0.4 Results of sensitivity studies

0.4.1 Radiative transfer simulations using a thermodynamic sea ice model

A sea ice version of microwave emission model for layered snow-packs (MEMLS) fed with detailed profiles from a thermodynamic sea ice model has been used for simulating the sea ice brightness temperature, emissivity and effective temperature at frequencies between 1.4 and 89 GHz (Section 4). The advantage of using the combined thermodynamic and emission models for simulating the 1.4 GHz brightness temperature sensitivity to physical snow and sea ice parameters is that the thermodynamical model is providing realistic distribution of non-uniform input parameters to the emission model including the salinity and temperature profile. It logs all possible parameters and it is possible to derive parameters such as effective temperature and emissivity (Fig. 2). These parameters and this level of detail are virtually impossible to achieve in the field. The disadvantage is that the thermodynamic model is not capturing all physical processes especially those affecting the variability on a horizontal scale: deformation, redistribution of the snow cover, and sea ice concentration variability. These additional processes make it difficult to compare the simulated brightness temperatures to measured brightness temperatures. Using these simulated profiles as input to the emissivity model it has been found that:

- New ice is optically thin at 1.4 GHz but not at frequencies from 6 GHz to 89 GHz.
- The emissivity at horizontal polarisation is sensitive to the air-snow interface reflection.
- The deep penetration and the thermodynamic control of the snow cover constrain the 1.4 GHz effective temperature to a relatively narrow range of values. For optically thin new-ice the effective temperature is between approximately 269 K and 271 K.
- The deep penetration of the 1.4 GHz radiation compared to the frequencies between 6 GHz and 89 GHz makes the 1.4 GHz effective temperature different from effective temperatures between 6 GHz and 89 GHz and the physical temperature at the snow surface and the snow-ice interface.
- The salinity of the surface ice is important for the penetration depth and thin ice thickness estimation.

0.4.2 Influence of ice temperature and salinity on the brightness temperature

In order to compare the impact of ice temperature, salinity, and thickness on the brightness temperatures under realistic conditions, we examine an example case of freezing sea ice in the Laptev Sea (Section 7). For the considered case, we find that the increasing ice thickness causes the brightness temperature signal to increase by 143 K, while the estimated ice temperature and salinity variations cause the brightness temperature to vary only by 31 K (21%) and 16 K (11%), respectively. Thus, it can be stated that the ice thickness is the main contributor to the increasing brightness temperatures. The analysis for the intensity has been published in Kaleschke et al. (2012). Furthermore, we analysed the sensitivity of the brightness temperature polarisation difference. For that parameter the relative contributions of ice temperature and salinity variations as compared to the contribution of ice thickness variation were higher than for the brightness temperature intensity (Fig. 3). Thus, we conclude:

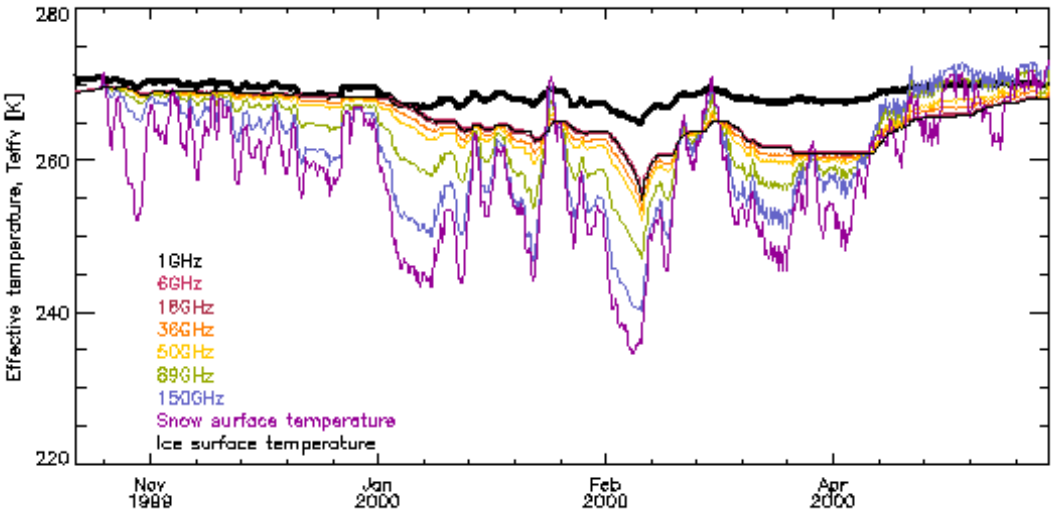

Figure 2: The effective and physical temperatures in the Kara Sea.

- The brightness temperature intensity of thin ice mainly depends on its thickness and is less influenced by changes of ice salinity and temperature compared to the polarisation difference.
- The influence of ice salinity on the brightness temperature is smaller compared to the influence of ice temperature for the conditions encountered during the Arctic freeze-up period.

Moreover, the sensitivity study suggest that the polarisation difference is not a monotonic function of the ice thickness and exhibits a maximum at about 3-4 centimeter.

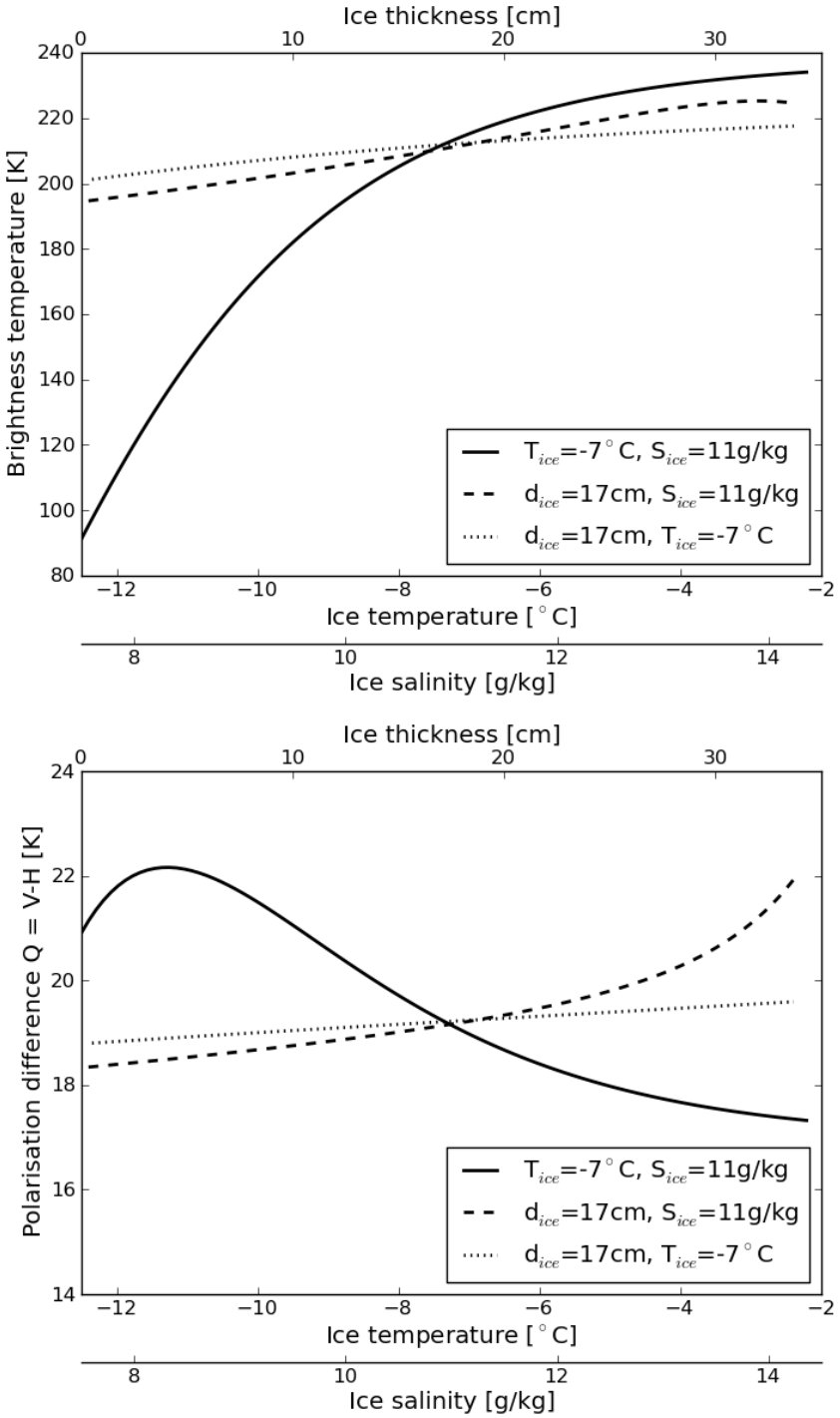

Figure 3: Change of brightness temperature intensity (top) and polarisation difference (bottom) at an incidence angle θ= 40° as a function of ice thickness, bulk ice temperature, and bulk ice salinity simulated with the incoherent Menashi model with one ice layer. In each case, two parameters are kept constant at an average value (see figure legend), while the remaining third parameter varies within the estimated range of values (see x-axis) for the situation in the Laptev Sea during 22nd October and 15th November, 2010.

0.5 Retrieval Algorithm I,II,II*

The selected algorithm is based on a forward model that includes a sea ice thermodynamic model and a three layer (ocean-ice-atmosphere) radiation model. The algorithm accounts for variations of ice temperature and ice salinity which determine to what maximum the thickness can be retrieved. Ice temperature and salinity are estimated during the iterative retrieval from surface air temperature reanalysis and a weekly climatology of sea surface salinity. The semi-empirical SMOS ice thickness retrieval algorithm applied previously in (Kaleschke et al., 2012) (called Algorithm I) does not account for variations of ice temperature and salinity.

Ice temperature and ice salinity measurements are rare and they are not continuously available on a daily basis. An alternative solution is therefore to derive these two parameters from auxiliary data during the sea ice thickness retrieval. Under the assumption of thermal equilibrium, the ice surface temperature can be estimated from the surface air temperature. Therefore, we use a heat flux balance equation and use the surface air temperature from atmospheric reanalysis data as a boundary condition. Ice salinity can be estimated from the underlying sea surface salinity (SSS) with an empirical function (Ryvlin, 1974). With these two parameters the brightness temperature is calculated with the sea ice radiation model (Menashi et al., 1993). However, both ice temperature and ice salinity are in turn functions of ice thickness. Thus, we need to apply a linear approximation method to simultaneously retrieve ice thickness and estimate suitable ice temperature and salinity values. This algorithm is called Algorithm II hereinafter (Fig. 4).

The sea ice thickness is corrected for the influence of the thickness distribution function to account for the invalid assumption of a uniform plane ice layer. The latter statistical correction leads to an apparent deeper penetration depth than previously reported. The correction of ice thickness retrieved from Algorithm II using this function is called Algorithm II*.

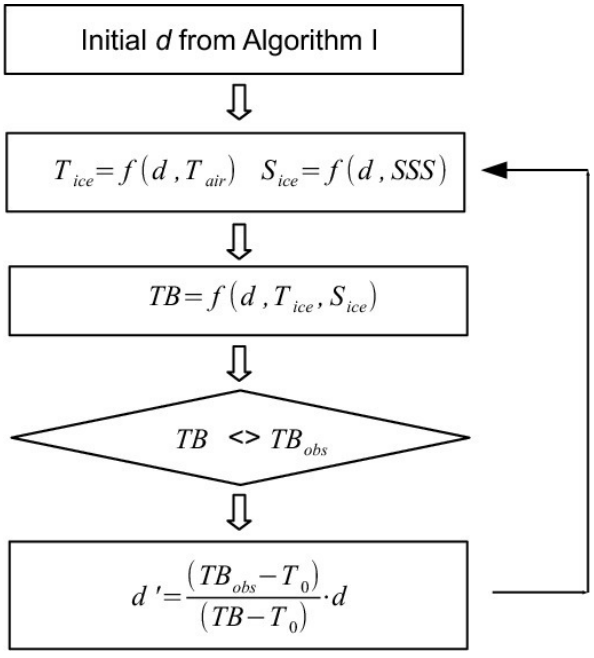

Figure 4: Schematic flow chart of the retrieval steps (Algorithm II). d and d' are the sea ice thicknesses from the consecutive steps, TB and TB_{obs} are calculated and observed brightness temperatures, T_0 is the brightness temperature of ice free sea water.

0.5.1 Maximal retrievable ice thickness

We define the maximum depth of the retrieval d_{max} for the plane-parallel geometry. The maximal depth d_{max} depends on the attenuation of the electromagnetic waves in the ice medium and the incidence angle. A minimum of the pathlength through the ice is obtained for nadir geometry. The pathlength increases with the secans (1/cos) of the incidence angle θ, e.g. with a factor two for $\theta = 60°$. The absorption coefficient depends on the sea ice temperature T_{ice}, ice salinity S_{ice} and ice density ρ_{ice}, whereas the ice temperature is the most variable factor on a day-to-day timescale. Figure 5 shows the maximum depth of the retrieval d_{max} at nadir for different ice temperatures and salinities.

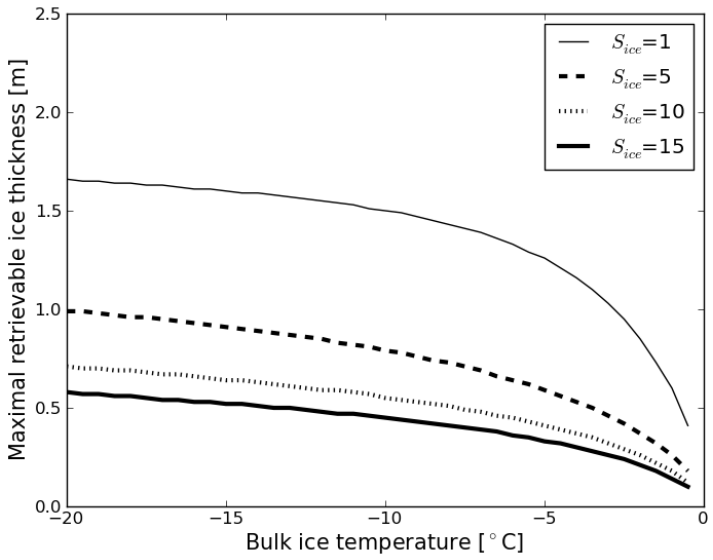

Figure 5: Maximal retrievable ice thickness d_{max} as a function of bulk ice temperature and salinity S_{ice} [g kg^{-1}].

0.5.2 Surface temperature

A byproduct of the iterative retrieval (Algorithm II) is the sea ice surface temperature. The surface temperature is used to calculate the bulk ice temperature, which is a variable parameter in the radiation model to calculate the emissivity of the ice layer. The surface temperature is estimated using a simple thermodynamic model based on Maykut (1986), with a simple parameterisation of the snow thickness, as well as with boundary conditions from JRA reanalysis data. Figure 9.2 shows the surface temperature as the result of the SMOS retrieval using Algorithm II (Section 7) compared to the independent estimate from MODIS infrared temperature (Section 12). We can draw the following conclusions:

- The SMOS-derived surface temperature is in general good agreement with the independent estimate from MODIS.
- The agreement demonstrates the consistency of the method and is a secondary way of validation.
- Discrepancies exist in the marginal ice zone and in the Ob estuary where the low salinities are not well represented. In the marginal ice zone with lower ice concentrations,

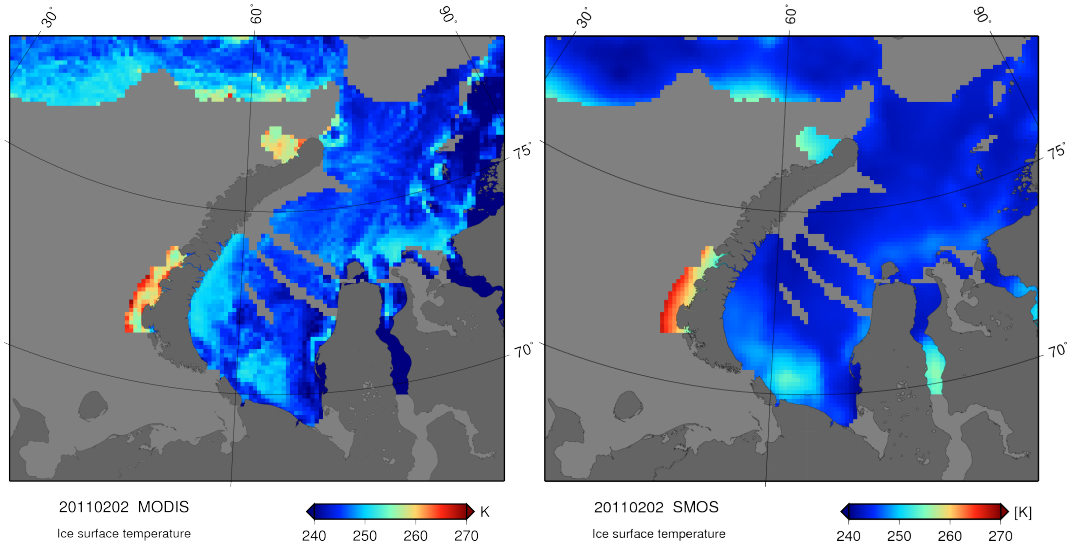

Figure 6: MODIS- (left) and SMOS-based (right) snow/ice surface temperature [K] in the Kara Sea on 2 February 2011.

the ice thickness is underestimated, which leads to too warm surface temperatures.

0.5.3 Thickness distribution

Empirical analysis of the SMOS brightness temperature revealed that the sensitivity for the sea ice thickness is larger than the maximum thickness d_{max} of $d \approx 0.5$m as reported in Kaleschke et al. (2012). An explanation for this apparent deeper penetration depth involves the subpixel scale heterogeneity of the sea ice cover. Natural sea ice is usually not a uniform layer of level ice with a plane geometry, as it was assumed in the emissivity model, but behaves fractal on a wide range of scales. The inherent skewness and exponential tail of the thickness distribution results in a considerable underestimation of sea ice thickness when the retrieval model is based on a plane sea ice layer.

Airborne sea ice thickness measurements have been used in order to investigate the effect of the subpixel-scale heterogeneity on the thickness retrieval. NASA's Operation IceBridge (OIB) airborne campaigns obtained large scale profiles of sea ice thickness derived from a laser altimeter system (Kurtz et al., 2013). In addition, we used helicopter-borne ice thickness measurements made with an electromagnetic (EM)-device in the Laptev Sea during the Transdrift XX campaign in April 2012.

We assume that the sea ice thickness follows a lognormal distribution with the two parameters logmean μ and logsigma σ. Furthermore, we assume a constant logsigma value $\sigma$to approximate the thickness distribution function with only one independent variable. From the analysis of the airborne thickness data we obtained an average value of $\sigma = 0.6 \pm 0.1$ for chunks of about 50 km length. Figure 7.7 (left panel) demonstrates that a constant σ yields a reasonable good approximation of the thickness distribution for a wide range of mean thicknesses including grey ice, first-year ice, as well as multi-year ice. Figure 7.7 (right panel) shows the impact of the thickness distribution on the brightness temperature. The integral transform of the brightness temperature weighted with the thickness distribution suggests a sensitivity to ice thicknesses much greater than the maximal retrievable ice thickness d_{max} of a uniform layer of level ice.

We conclude:

- The overall effect can be explained as an apparent deeper penetration depth caused by leading edge of thickness distribution. The real thickness is strongly underestimated if the retrieval does not account for the thickness distribution.
- The implementation of a radiative transfer model that includes this effect is straightforward but computational expensive because of the integration. A post-processing look-up table for the single-layer model has been developed to estimate an approximate correction factor (Section 7).
- A main uncertainty is the shape of the thickness distribution. The lognormal distribution seems to be a reasonable representation of the airborne thickness data. However, the data in the important thin ice range is only sparse. More field data are required to further analyse the thicknesss distribution for thin ice on different scales and conditions.

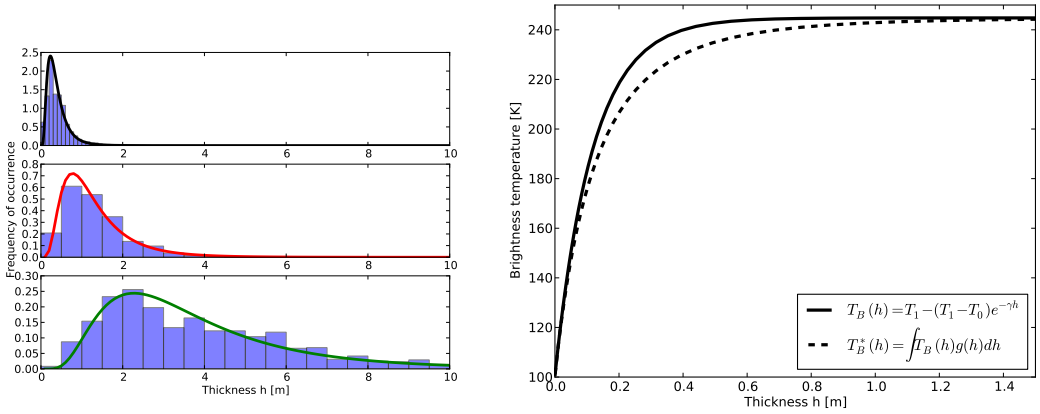

Figure 7: Left: Example sea ice thickness distribution functions $g(h, \sigma = 0.6)$ derived from EM-measurements over the Laptev Sea polynya (top graph, data of Thomas Krumpen, AWI) and selected chunks of NASA's Operation IceBridge data (center and bottom). Right: Effect of thickness distribution function $g(h)$ on the SMOS brightness temperature (dashed line) in comparison to the result for a layer of uniform ice thickness (solid line)

0.6 Validation and algorithm comparison

0.6.1 Ice thickness derived from MODIS night-time imagery

120 ice thickness charts of the Kara Sea and the eastern part of the Barents Sea covering two winters (Nov. to Apr.) in 2009-2011 derived from MODIS night-time thermal images have been used for validation (Sections 9, 8, 12). The derivation of the ice thickness and the uncertainty estimation are described in detail in Maekynen et al. (2013). The typical maximum reliable ice thickness (max 50% uncertainty) was estimated to be 35-50 cm under typical weather conditions (air temperature T_a < -20°C, wind speed V_a < 5 ms^{-1}) for the MODIS data.

Figure 9.3 shows a comparison of SMOS (Algorithm I and II) and MODIS derived ice thickness for a selected day (2 February 2011), on which a sufficient amount of pixels with valid MODIS data is available. Similarly to Algorithm I and Algorithm II, the MODIS sea ice thickness retrieval assumes a planar ice layer. Therefore, by spatial averaging of MODIS data to a grid resolution of 12.5 km we use the modal mean of the MODIS ice thickness instead of the arithmetic mean. For the comparison we use the plane layer SMOS ice thickness,

not the ice thickness of Algorithm II* that accounts for the lognormal thickness distribution function.

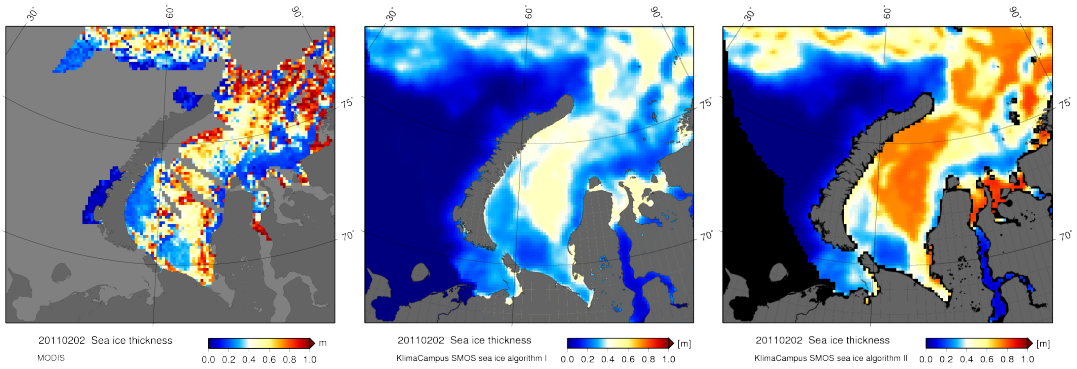

Figure 8: MODIS (left) and SMOS ice thicknesses retrieved from Algorithm I (center) and Algorithm II (left) in the Kara Sea on 2 February 2011.

Both SMOS and MODIS show similar patterns of thin and thick ice distributions, whereas SMOS ice thickness from Algorithm I is considerably lower than the other two in the thicker ice range. Large areas of thin ice can be observed from SMOS and MODIS near the Kara Sea Strait and in the estuaries. In both regions polynyas appear frequently due to the strong wind forcing. Under cold air temperatures, the polynyas are soon covered by thin ice. Both SMOS and MODIS show ice thicknesses in the range of 20-40 cm in the polynyas with similar distribution patterns. Ice concentration is normally higher than 90 %, except for the marginal ice zone. Surface air temperature in the Kara Sea is as low as -30°C, providing favorable conditions for both SMOS and MODIS ice thickness retrievals (Kaleschke et al., 2010; Yu and Rothrock, 1996). In total 4016 pixels have valid MODIS data. The mean ice thickness of SMOS Algorithm I, SMOS Algorithm II, and MODIS for the pixels are 33 cm, 50 cm, and 47 cm, respectively. The correlation coefficient and RMSD between the SMOS Algorithm II and MODIS are 0.61 and 21 cm, whereas between SMOS Algorithm I and MODIS they are 0.59 and 26 cm, respectively. The mean surface tempertures from MODIS and SMOS are 246 K and 245 K, with a RMSD of 4 K.

In total 33 and 87 days of MODIS validation data are available for the winter seasons of 2009-2010 and 2010-2011, respectively. However, many of them have only small areas with usable MODIS data due to cloud coverage. Therefore, we selected 30 days of particular good data coverage. Altogether 81350 pixels are available in 12.5 km resolution. Because of the much larger footprint of SMOS (∼40 km) compared to MODIS (1 km) we aggregate the MODIS retrievals on the SMOS grid by taking the modal mean. The different integration times (SMOS: daily averages versus MODIS: single overpasses) introduce additional uncertainties. Nevertheless, the ice thickness retrieved from SMOS and MODIS are very similar, with a considerably better agreement between SMOS Algorithm II and MODIS. The correlation coefficient R between SMOS and MODIS data is about 0.6 for both Algorithm I and Algorithm II. We conclude:

- The overall validation (30 days, 81350 data points) reveals better performance of SMOS Algorithm II as compared to SMOS Algorithm I.

Different SMOS sea ice thickness retrieval algorithms have been developed by University of Hamburg (UHH) and University of Bremen (UB). Whereas the UHH algorithms take advantage of the first Stokes component of brightness temperatures (intensity) averaged over

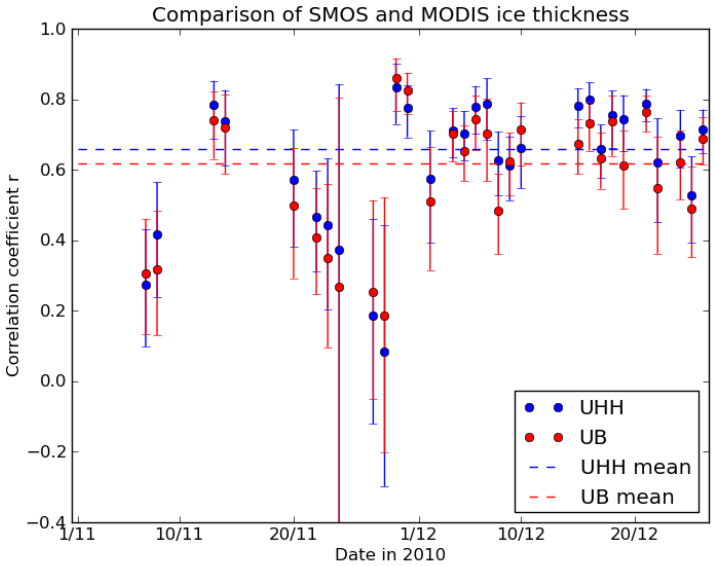

Figure 9: Correlation coefficients between SMOS and MODIS sea ice thickness (<0.5m) for the period Oct. 01 to Dec. 26, 2010. The error bars indicate the uncertainty at a 99.9% level of significance.

the incidence angle range of 0°-40°, UB uses the difference of horizonally and vertically polarised brightness temperatures in the higher incidence angle range. An algorithm comparison has been carried out with the MODIS-based sea ice thickness in the Kara Sea for the Period Oct. 01 to Dec. 26, 2010. The average correlation coefficient R is about 0.66 and 0.62 for UHH and UB, respectively (Figure 9). Furthermore, the UHH algorithm (Algorithm I) shows a smaller RMSD compared to the UB retrieval. We conclude:

- The algorithm comparison shows better results of the near nadir method (UHH Algorithm I) as compared to the retrieval based on the difference of horizonally and vertically polarised brightness temperatures in the higher incidence angle range (UB retrieval).

0.6.2 Validation with electromagnetic induction (EM) measurements of ice thickness

For the validation of SMOS ice thicknesses, we use ice thicknesses measured during an EU SafeWin project's winter field campaign in the northern Baltic Sea (Section 11). Between 2 and 7 March 2011 a helicopter-towed EM device measured the ice thickness in the Bay of Bothnia and the northern Sea of Bothnia. A comparison of ice thicknesses within 12 circular areas, which were representatively covered by both SMOS and EM measurements, revealed a root mean square deviation of 9.3 cm and a difference of 1.7 cm for the mean ice thicknesses (Fig. 10). The corresponding mean ice thicknesses were 40.0 $\pm$ 8.0 cm for the EM measurements and 41.7 $\pm$ 8.8 cm for the SMOS retrieval.

Additional sea ice thickness measurements were performed in the Laptev Sea during the Transdrift XX campaign on 20 April 2012. The survey flight made on 20 April has a length of about 200 km and covers mostly thin ice being formed in the West New Siberian polynya and the Anabar-Lena polynya. A period of strong and consistent offshore winds led to the development of an extensive thin ice zone extending several hundred kilometres offshore.

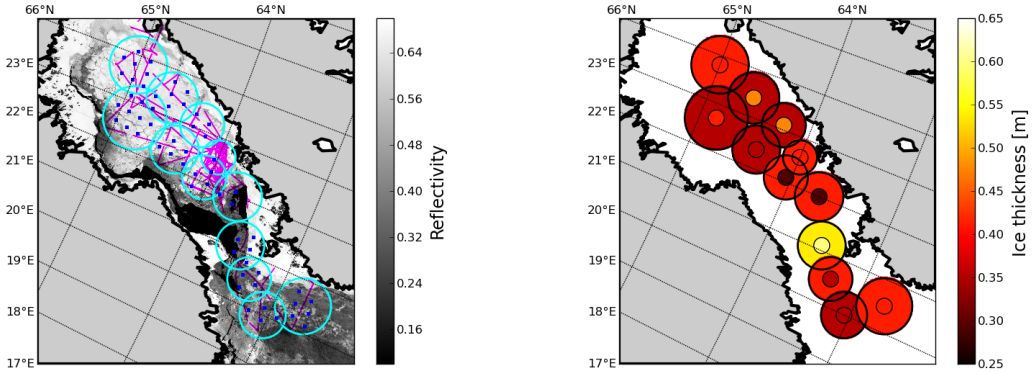

Figure 10: Distribution of EM and SMOS measurements in the Bay and Sea of Bothnia and the 12 circular areas we choose for comparison of ice thicknesses. The pink lines indicate EM Bird flight tracks, the blue dots indicate the positions of SMOS measurements. These are overlaid on a MODIS image showing the reflectivities in band 1 (wavelength 620 – 670 nm) on 3rd March, 2011; Total ice thicknesses as measured by the EM Bird and as retrieved from vertically polarised SMOS brightness temperatures. The inner circles depict ice thicknesses as retrieved from SMOS, the outer circles depict the modal values of all ice thicknesses measured within the validation circles by the EM Bird.

The EM measurement reveals that the ice thickness was about 43$\pm$33 cm in good agreement with the ice thickness from SMOS Algorithm II* (Fig. 11). We found:

- Good agreement between SMOS and EM ice thicknesses.
- SMOS provides information on ice thickness in a challenging[1] region like the Baltic Sea.

[1] Because of coastal spillover and RFI.

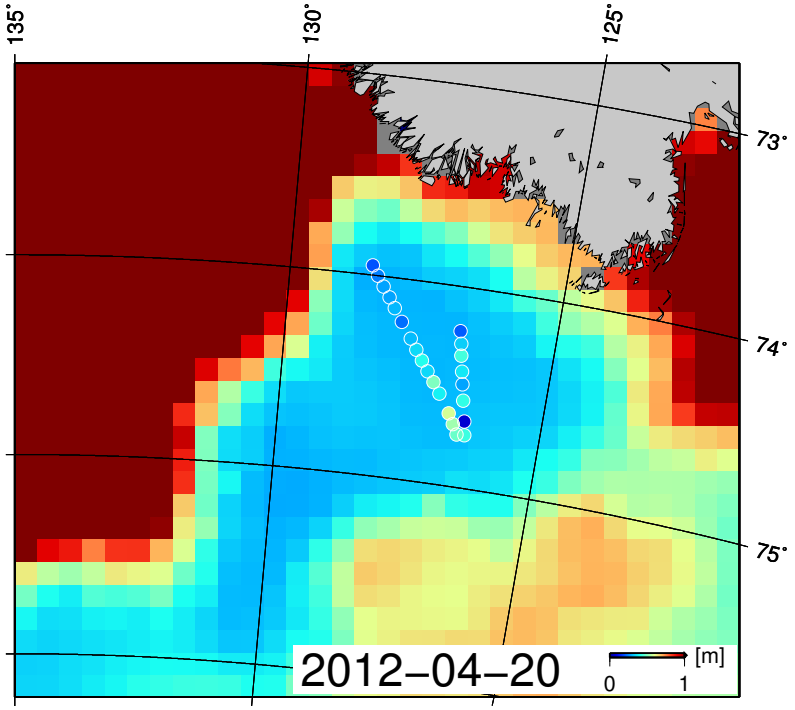

Figure 11: EM- and SMOS-based ice thickness (Algorithm II*) in the Laptev Sea on 20 April 2012. The EM-thickness is represented by the 50th percentile for each 2000 single measurements.

0.6.3 Comparison with results from assimilation systems

TOPAZ and PIOMAS are state-of-the-art data assimilation system that are based on ocean-ice models and use observations like the sea surface temperature, sea ice concentration, sea ice drift, in-situ temperature and salinity profiles, as well as atmospheric reanalysis fields (Bertino and Lisæter, 2008; Zhang and Rothrock, 2003). The results of the assimilation, e.g. the sea ice volume, agrees well with altimeter-based observations (Laxon et al., 2013). Thus, it is mandatory to compare our SMOS retrievals with the results of assimilation systems in order to analyse the temporal development of the sea ice thickness. Figure 12 shows the result of a time series located in the center of the EM measurement in the Laptev Sea polynya. From the analysis of this and other time series we conclude:

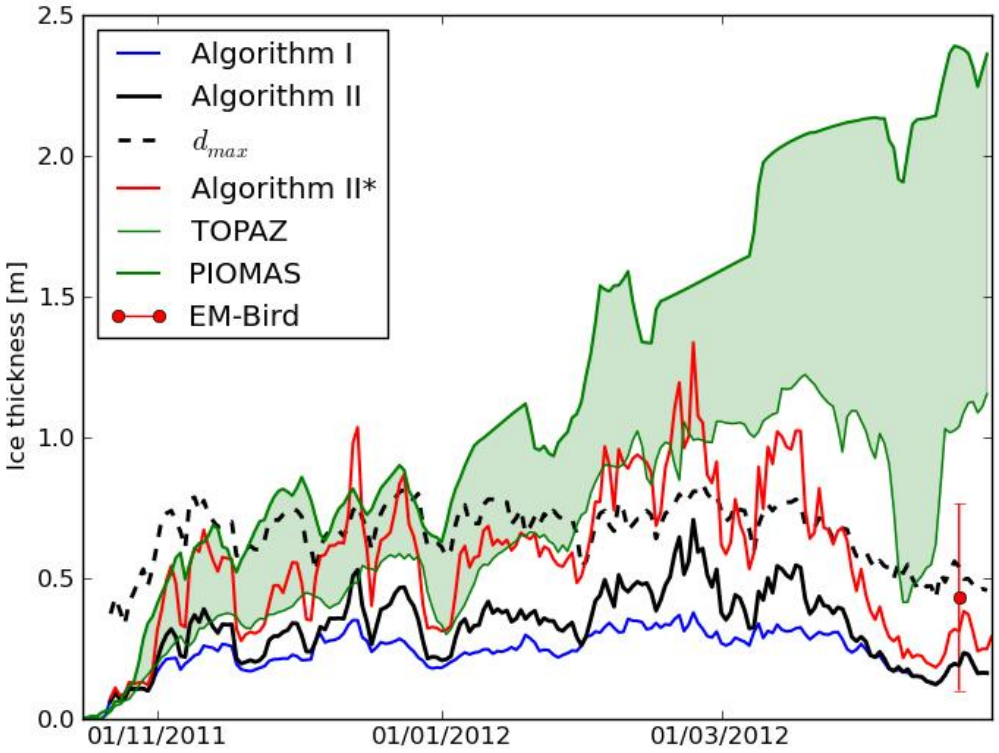

Figure 12: Time series of ice thicknesses derived from Algorithm I, II, and II*, together with d_{max} and simulated ice thicknesses from TOPAZ and PIOMAS at a position in the Laptev Sea Polynya (74.5°N, 127.0°E).

- The average thickness and its variability derived with SMOS Algorithm II* usually agrees well with TOPAZ and PIOMAS in the three months after the first ice growth.
- From March to April TOPAZ and PIOMAS exhibit much thicker ice compared to the SMOS retrieval. The discrepancy goes along with the onset of surface warming and indicates a possible shortcoming of our retrieval method.
- SMOS and EM ice thicknesses agree well whereas TOPAZ and PIOMAS overestimate the ice thickness by 0.5-2 m.

0.7 Outlook

0.7.1 Snow thickness

The impact of snow on the brightness temperature is twofold. We distinguish between a direct radiative and an indirect thermodynamic effect. Model simulations have shown (Section 10.1) that the direct effect seems to be negligible over thick sea ice while the indirect effect amounts to a signal of up to about 20 K depending on the surface air temperature. The model results have been confirmed using OIB airborne measurements (Figure 13) and demonstrate the potential of using SMOS data for the retrieval of the snow thickness over thick Arctic sea ice (Maaß et al., 2013b). This unexpected finding could fill a gap in the observational system. Traditional passive microwave methods for the retrieval of snow thickness use a spectral gradient ratio GR(19 GHz, 37 GHz) and fail over thick multi-year ice because of its frequency-dependent emissivity (Figure 1). SMOS delivers unique information about the snow thickness which could be of great importance for the thermodynamics of sea ice, diagnostics of the hydrological cycle, as well as for improving the retrieval of the ice thickness by using altimeter systems. However, a problem for our ability to properly simulate the effect of snow on thin ice is evident by the fact that the presence of an infinitesimal thin snow layer appears as a sudden increase of brightness temperature (Maaß et al., 2013b). We conclude:

- SMOS brightness temperatures observed over snow-covered thick Arctic sea ice increased with increasing snow thickness. This is explained by the thermal insulation effect of snow.
- The emissivity model fails to describe the transition from no snow to a very thin snow cover.
- More work is necessary to improve the emissivity model and to develop an operational snow thickness retrieval method.

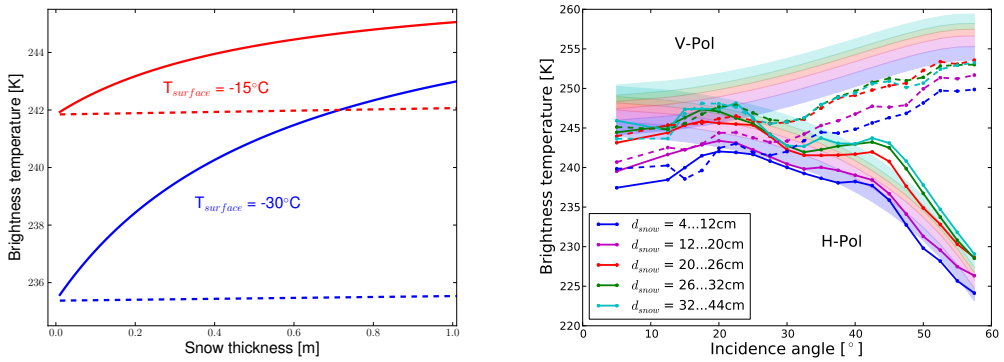

Figure 13: Left: Brightness temperature of 4m thick snow-covered ice as a function of snow thickness at horizontal polarisation at an incidence angle $\theta = 45°$ (solid line) for an ice surface temperature of -30°C (blue) and of -15°CC (red). The dashed line indicates the brightness temperature of snow-covered ice, when the thermal insulation by snow is neglected; Right: Brightness temperatures as simulated and as measured by SMOS for the snow thickness classes 1-5 as given in the figure legend. The shaded areas indicate the brightness temperature simulations, the lines indicate the averaged brightness temperature measurements. The solid lines indicate horizontal polarisation, the dashed lines indicate vertical polarisation. (Maaß et al., 2013b)

0.7.2 Synergy with CryoSat-2

The complementarity of SMOS and CryoSat-2 sea ice thickness measurements has been pointed out previously (Kaleschke et al., 2010). A first CryoSat-2 data level 3 product has become available only very recently. A preliminary analysis confirmed the complementary relationship (Kaleschke and Rickert, 2013). The shape of the lines in Figure 14 are very similar to the Figure 8 as published in Kaleschke et al. (2010). However, the previous analysis was based on model assumptions before the launch of SMOS and CryoSat-2. Figure 14 now includes actual measurements and their uncertainties as provided in the preliminary SMOS and CryoSat-2 data products. Figure 15 shows a comparison with NASA's IceBridge quicklook data (Kurtz et al., 2013). The synergy of CryoSat-2 and SMOS agrees better with the validation data than the single products which is obvious for the thin ice area north of Barrow and Bank Island. We conclude:

- A synergy of SMOS and CryoSat-2 provides improved estimates of sea ice thickness.
- The synergy allows to constrain the upper value of the sea ice thickness uncertainty which can not be estimated with SMOS alone.
- More work is necessary to develop and validate more advanced techniques for an optimal synergy of SMOS and CryoSat-2.

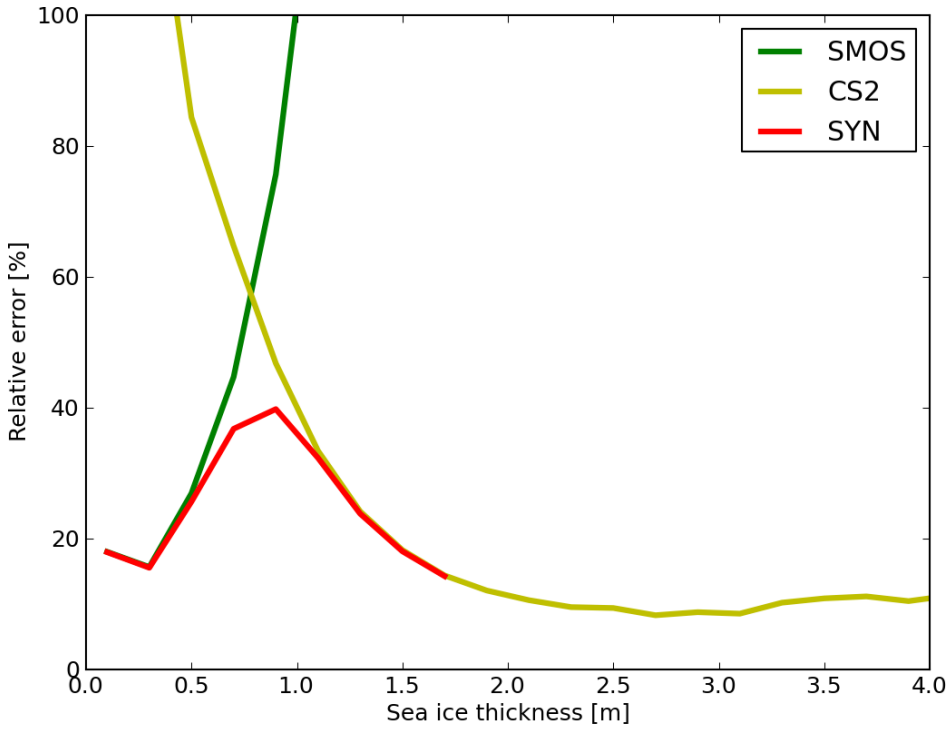

Figure 14: Relative error of CryoSat-2 and SMOS sea ice thickness and their weighted average (SYN).

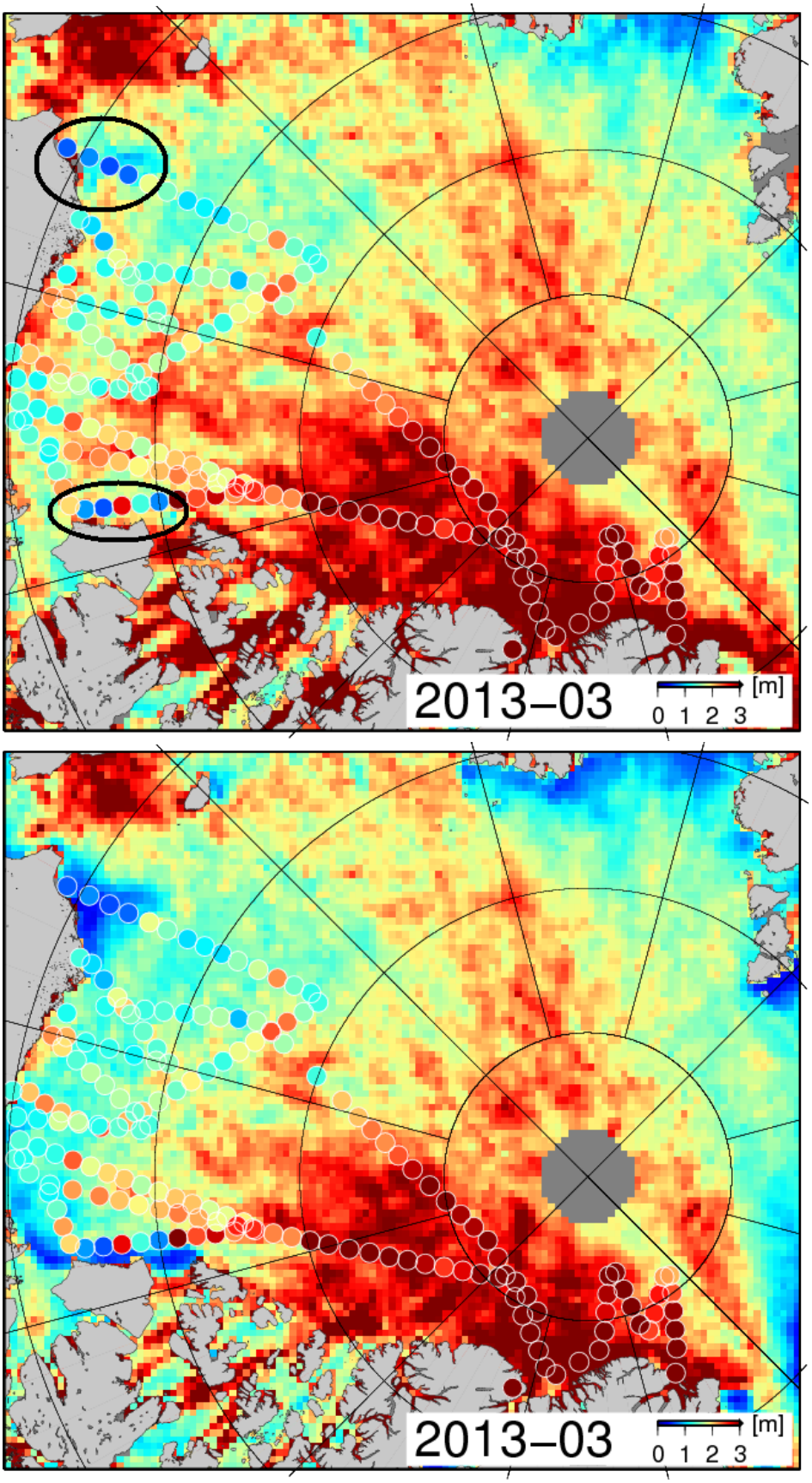

Figure 15: CryoSat-2 (top) and CryoSat-2+SMOS synergy (bottom) together with sea ice thickness from NASA's IceBridge quicklook data averaged over ∼70km lags (colored circles). The black ellipse shows thin ice areas where SMOS considerably improves the thickness retrieval. Monthly averages March 2013.

0.8 Recommendations

The competetive development of different retrieval algorithms has shown clear advantages of the methods that are based on radiative transfer models. The radiative processes that have to be taken into account at 1.4 GHz are far less complex than those scattering mechanisms that have to be considered at higher frequencies. Thus, it is manageable to include just a few basic physical parameters that influence the emissivity such as ice thickness, salinity, temperature, snow thickness, and ice concentration. This situation is differerent at higher frequency because of the complex scattering mechanisms which are controlled by additional not well-constrained parameters like the snow grain size. Therefore, the availability of SMOS data considerably increased the importance of physical sea ice emissivity models which have only seldomly used before for the retrieval of geophysical sea ice parameters. This can be regarded as a change of paradigm because hitherto empirical methods dominated the scene for passive microwave remote sensing of sea ice. Thus, it is important to *further improve and validate sea ice emissivity models* as the core of the retrieval. The emissivity model used for the thickness retrieval does not correctly account for vertical gradients of temperature and salinity. The invalid assumption of a vertically homogeneous ice layer introduces significant uncertainties because the relative brine volume and thus the permittivity depends on ice temperature and salinity. The effects of a vertically structured sea ice cover have to be taken into account for an improvement of the retrieval model. Furthermore, the effect of surface roughness has to be investigated and maybe taken into account. The largest uncertainty so far is introduced by changes of the ice concentration. Thus, it is necessary to take these changes into account which is not yet done so far. Another major uncertainty is the sub-pixel scale heterogeneity of ice thickness. *There is the clear need for more validation data* in thin ice areas for both hemispheres. The scarcity of ice thickness measurements in the marginal ice zone is the major limitation for further validation. Thus, we recommend that *more ice thickness measurements should be carried out in particular during the cold seasons.* Further work has to be done to validate the auxiliary data, in particular the surface air or the ice surface temperature. Methods for the synergy of SMOS and CryoSat-2 also have to be validated and to be improved. The development and validation of techniques for snow thickness retrieval can help to further improve the retrieval of the ice thickness with CryoSat-2. The use of SMOS sea ice thickness data for ocean-ice-atmospheric model initialisation requires a major effort. It is worthwile to study and advance the assimilation of SMOS brightness temperatures in ocean-ice model systems. A well-validated sea ice emissivity model would be the most important ingredient for such an application. Finally, the quality of the brightness temperature shall be refined by using advanced RFI-filter or -mitigation techniques.

0.9 Acknowledgements

The work presented in the report was mainly funded through ESA Support to Science Element programme under contract 4000101476, through the International Max Planck Research School on Earth System Modelling (Nina Maaß), and through the Cluster of Excellence CliSAP (EXC177), University of Hamburg, funded through the German Science Foundation (DFG). The implementation of the processing chain for the continuous generation of the ice thickness product has been funded through the SMOS mission. The Baltic EM thickness campaign and analysis was conducted within the EU-funded project “Safety of winter navigation in dynamic ice” (contract SCP8-GA-2009-233884 - SAFEWIN). The partners in this project are Aalto University, Arctic and Antarctic Research Institute, Finnish Meteorological Institute, Finnish Transport Agency, ILS Oy, Stena Rederi AB, Swedish Maritime Administration, Swedish Meteorological and Hydrological Institute, Tallinn University of Technology and AS Tallink Group.

Part II

Radiative transfer models and sensitivity studies

Nina Maaß

1 BRIGHTNESS TEMPERATURE AS SEEN BY SMOS

Nina Maaß

The brightness temperature $T_{B,TOA}$ as observed from a radiometer like the MIRAS instrument on-board the SMOS satellite originates from radiation emitted from the Earth's surface itself $T_{B,terr}$, from radiation that is emitted by extraterrestrial sources and then reflected at the Earth's surface $(1 - e_{terr})T_{B,extra}$, and from radiation emitted on the path between the Earth's surface and the radiometer $T_{B,atm}$:

$$T_{B,TOA} = T_{B,terr,TOA} + (1 - e_{terr})T_{B,extra,TOA} + T_{B,atm,TOA} \ , \tag{1.1}$$

where e_{terr} is the emissivity of the Earth's surface, and correspondingly $(1 - e_{terr})$ is the reflectivity of the Earth's surface, and the subscript TOA denotes that the considered contributions are influenced by the atmospheric particles on their way to the TOA. For the retrieval of geophysical parameters at the Earth's surface, $(1 - e_{terr})T_{B,extra,TOA}$ and $T_{B,atm,TOA}$ represent perturbing additional contributions. The SMOS Level 1C brightness temperatures used in this study are brightness temperatures at the TOA. The three main sources of additional contributions to these TOA brightness temperatures are sky radiation, sun glint, and atmospheric absorption and emission (Zine et al., 2008), which are considered in the following.

1.1 Sky radiation

The downwelling sky radiation that is scattered by the Earth's surface is called sky glitter. In L-band, sky radiation originates from the uniform cosmic microwave background, the line emission from hydrogen, and a continuum background (Le Vine and Abraham, 2004; Le Vine et al., 2005). The sky glitter contribution is expected to be geographically and seasonally variable and to vary from about 2 K to more than 7 K over sea surfaces (Zine et al., 2008). Due to the higher reflectivity of sea water as compared to sea ice, we expect the sky glitter contribution for sea ice to be smaller. Therefore, and because the correction for sky glitter is quite complex, we do not apply a correction for the sky glitter. Here, we only take into account the uniform and constant cosmic microwave background radiation $T_{B,cosm}$ of about 2.7 K that is reflected by the Earth's surface: $T_{B,extra}$= $T_{B,cosm}$= 2.7 K.

1.2 Sun glint

The sun is a very strong source of radiation in L-band. The solar radiation depends on the solar activity, and is thus time-dependent. The solar radiation reflected at the Earth's surface contributes to the TOA brightness temperature. However, the fraction of affected measurements is expected to be small. Thus, brightness temperatures are usually not corrected for sun glint; instead, affected measurements are flagged and discarded. (Zine et al., 2008)

1.3 Atmospheric absorption and emission

The TOA brightness temperatures $T_{B,TOA}$ are influenced by the atmosphere due to attenuation and to atmospheric self-emission. Because these two effects have opposite consequences on the TOA brightness temperature, the overall effect can be negative or positive. On the one hand, radiation originating from the Earth's surface is attenuated on its way through the atmosphere, i.e. the brightness temperature observed at the TOA is lower than the brightness temperature observed at the Earth's surface. On the other hand, atmospheric particles emit radiation themselves. This self-emission is added to the radiation of the Earth's surface. The TOA brightness temperature $T_{B,TOA}$ can thus be described by:

$$T_{B,TOA} = (T_{B,terr} + (1 - e_{terr})T_{B,extra})\mathrm{e}^{-\tau_{atm}} + T_{B,up} + (1 - e_{terr})T_{B,down}\mathrm{e}^{-\tau_{atm}} \quad , \quad (1.2)$$

where τ_{atm} is the optical thickness of the atmosphere, $T_{B,terr}$ is the upwelling brightness temperature from the Earth's surface, $T_{B,up}$ is the brightness temperature that is self-emitted by the atmosphere upward and attenuated along the upward path to the TOA, $T_{B,down}$ is the brightness temperature that is self-emitted by the atmosphere downward and attenuated along the downward path to the Earth's surface. Equation (1.2) describes how $T_{B,terr}$ is attenuated on its path upward to the TOA, and how the downwelling radiation $T_{B,down}$ is reflected by the Earth's surface, which has the reflectivity $1 - e_{terr}$, and is then again attenuated along the upward path to the TOA.
Numerical simulations with the Liebe model (Liebe et al., 1993) indicate that the main contribution to both $T_{B,up}$ and $T_{B,down}$ is emission from a thin layer near the Earth's surface. Thus, their radiative contributions are almost equal. Because the difference is less than 0.01 K, they can be represented by a single value $T_{B,ud} = T_{B,up} = T_{B,down}$. (Zine et al., 2008)
The constituents of the atmosphere that have to be considered for an atmospheric correction are the dry atmosphere, water vapour, clouds, and rain. In L-band, the radiative contribution by clouds and rain is negligible, except for very deep cumulus clouds and heavy precipitation events. The by far largest radiative contribution from the dry atmosphere is assigned to molecular oxygen. Water vapour has rotational absorption lines in the microwave region. Thus, the atmospheric contributions to brightness temperatures measured at the TOA mainly originate from atmospheric oxygen and water vapour. (Zine et al., 2008)
In order to account for atmospheric absorption and emission, we calculate the total atmospheric contribution $\Delta T_{B,atm}$ for different scenarios and use the pre-calculated values of the total atmospheric contribution $\Delta T_{B,atm}$ as correction terms for simulated brightness temperatures. We calculate the correction terms $\Delta T_{B,atm}$ for different terrain brightness temperatures, terrain emissivities, incidence angles and states of the atmosphere. Thus, using equations (1.1) and (1.2), the brightness temperature at the TOA is expressed as

$$T_{B,TOA} = T_{B,terr} + (1 - e_{terr})T_{B,extra} + \Delta T_{B,atm} \quad , \quad (1.3)$$

with

$$\Delta T_{B,atm} = T_{B,TOA} - (T_{B,terr} + (1 - e_{terr})T_{B,extra}) \quad (1.4)$$

$$= (T_{B,terr} + (1 - e_{terr})T_{B,extra})(\mathrm{e}^{-\tau_{atm}} - 1) + T_{B,ud}(1 + (1 - e_{terr})\mathrm{e}^{-\tau_{atm}}) \quad . \quad (1.5)$$

The optical thickness of the atmosphere τ_{atm} is defined as

$$\tau_{atm} = \frac{1}{\cos\theta} \int_{z=0}^{\infty} \kappa(z) dz \ , \tag{1.6}$$

where $\kappa(z)$ is the atmospheric absorption coefficient at height z, and θ is the incidence angle. For frequencies below 10 GHz, scattering effects may be ignored for most atmospheric weather conditions and we may use the expression of the brightness temperature that represents the upwelling and downwelling atmospheric radiation for a non-scattering atmosphere:

$$T_{B,ud} = \frac{1}{\cos\theta} \int_{z=0}^{\infty} \kappa(z) T(z) \mathrm{e}^{-\tau_{atm}} dz \ , \tag{1.7}$$

where $T(z)$ is the air temperature at height z. (Ulaby et al., 1981)

Calculation of the atmospheric absorption coefficient
In this study, we calculate the absorption coefficients of water vapour $\kappa_{wv}(p)$, oxygen $\kappa_{O_2}(p)$ and nitrogen $\kappa_{N_2}(p)$ as functions of pressure p using the atmospheric absorption model developed by Rosenkranz (1998). Because it is part of the atmospheric absorption model, we here also include the radiative contribution by nitrogen, even if it is much smaller than the contributions by water vapour and oxygen. The atmospheric absorption coefficient is the sum of the contributions by water vapour, oxygen, and nitrogen:

$$\kappa(p) = \kappa_{wv}(p) + \kappa_{O_2}(p) + \kappa_{N_2}(p) \ . \tag{1.8}$$

The atmospheric absorption model calculates the absorption coefficients $\kappa_{wv}(p)$, $\kappa_{O_2}(p)$ and $\kappa_{N_2}(p)$ at frequency f from 1. the pressure profile, 2. the temperature profile, and 3. the water vapour density profile in the atmosphere. Here, we use the following approach to derive these three profiles:

1. We use a logarithmic pressure profile with 100 pressure levels between 1013 hPa and 13 hPa described by
$$p[\text{hPa}] = 1013 - 1000 \cdot \log_{10}(k) \ , \tag{1.9}$$
where k takes values between 1 and 10.

2. The temperature profile $T(p)$ is based on the monthly mean air temperatures from the National Centers for Environmental Prediction (NCEP) Reanalysis temperature data derived by the Climate Diagnostics Center (CDC). The monthly mean air temperatures have been averaged over the time period from 1948 to 2011 and are provided for 17 pressure levels ranging between 1000 and 10 hPa. We use only the data for polar latitudes $\phi > 70°$. We linearly interpolate the temperatures, which are given for the NCEP pressure profile, to match the pressure profile as defined in equation (1.9).

3. The water vapour density profile is derived from the relative humidity profile. We use the monthly mean relative humidities from NCEP reanalysis data averaged from 1948 to 2011 for 8 pressure levels ranging between 1000 and 300 hPa. We use only the data for polar latitudes $\phi > 70°$. As for the temperature profile, we linearly interpolate the relative humidities given for 8 pressure levels to the pressure profile given in equation

(1.9). To derive the water vapour density profile from the relative humidity profile, we first use the ideal gas law to relate the water vapour density $\rho_{wv}(p)$ to the water vapour pressure $p_{wv}(p)$:

$$\rho_{wv}(p) = \frac{p_{wv}(p) M_{wv}}{R \cdot T(p)} \quad , \tag{1.10}$$

where M_{wv}= 18.016 $\cdot 10^{-3}$ $\frac{\text{kg}}{\text{mol}}$ is the molar mass of water vapour, and R= 8.3144 $\frac{\text{J}}{\text{mol K}}$ is the gas constant. The water vapour pressure $p_{wv}(p)$ is

$$p_{wv}(p) = \phi(p) p_{sat}(p) \quad , \tag{1.11}$$

where $\phi(p)$ is the relative humidity and $p_{sat}(p)$ is the water vapour saturation pressure. The water vapour saturation pressure can be calculated using the relationship by Murray (1967):

$$p_{sat}(p)[\text{hPa}] = 100 \cdot 6.1078 \cdot e^{\frac{a(T(p) - 273.16\ \text{K})}{T(p) - b}} \quad , \tag{1.12}$$

with a= 17.2693882 and b= 35.86 K.

With the input profiles from 1. to 3., we calculate the atmospheric absorption coefficient profile $\kappa(p)$ as a function of pressure p. However, equation (1.7) requires the atmospheric absorption coefficient profile $\kappa(z)$ and the temperature profile $T(z)$ with regard to the geometric height z. Therefore, we use the barometric formula to convert pressure p to height z. The barometric formula for a constant temperature gradient $\gamma = -\frac{\partial T}{\partial z}$ in the atmosphere is

$$p = p_0 \left(\frac{T_0 - \gamma z}{T_0 - \gamma z_0} \right)^{\frac{g}{\gamma R_d}} \quad , \tag{1.13}$$

where p_0 is the pressure and T_0 is the temperature at height z_0, g= 9.81 m/s^2 is the Earth's gravitational acceleration, and R_d= 287 J/(kgK) is the gas constant of dry air. For p_0, T_0, and z_0, we here use the values p_0= 1000 hPa, the corresponding temperature T_0= $T(p = p_0)$ from the NCEP temperature profile, and z_0= 111 m from the U.S. standard atmosphere (NOAA and Force, 1976). For the temperature gradient we use the value γ= 0.65 K/100 m, as assigned to the lowest 11 km of the U.S. standard atmosphere (NOAA and Force, 1976). Reorganizing equation (1.13) gives the height z as a function of pressure p:

$$z = \frac{1}{\gamma} (T_0 - \left(\frac{p}{p_0} \right)^{\frac{\gamma R_d}{g}} (T_0 - \gamma z_0)) \quad . \tag{1.14}$$

Atmospheric correction of brightness temperatures

The atmospheric contributions $\Delta T_{B,atm}$ for different terrain brightness temperatures $T_{B,terr}$, terrain emissivities e_{terr}, and incidence angles, as calculated with the described approach, are given in the appendix of Maaß (2013a). We perform the calculations for emissivities ranging between 0.3 and 1.0. For each emissivity, we choose representative brightness temperatures, as they would be observed at realistic physical temperatures for ice and water. The incidence angles considered here are 0°, 20°, 40° and 60°. We perform the calculations for three different months. We use the monthly means of the NCEP temperature and humidity profiles for January, April and October. The values of the atmospheric contributions $\Delta T_{B,atm}$ are used as correction terms for the brightness temperature simulations in this study.

According to our calculations, the atmospheric contribution $\Delta T_{B,atm}$ to the brightness tem-

perature as observed at the TOA ranges between -0.36 K and +5.67 K, i.e. in most cases the effect of the atmospheric self-emittance dominates over the attenuation of radiation from the Earth's surface. Note that due to the definition of $\Delta T_{B,atm}$ as a correction term that accounts for the overall effect of the atmosphere on the brightness temperature of the Earth's surface, we sometimes obtain negative values for $\Delta T_{B,atm}$, even if the brightness temperature itself can of course never be negative.
We find the following relationships regarding the different scenarios with 1. different emissivities, 2. different brightness temperatures (and thus different physical temperatures), 3. different incidence angles, and 4. different states of the atmosphere (represented here by the month of the year):

1. The atmospheric contribution decreases with increasing emissivity. The higher the emissivity e_{terr}, the lower is the reflectivity $1 - e_{terr}$. Thus, the fraction of $T_{B,down}$ that is reflected at the Earth's surface is lower and contributes less to the brightness temperature measured at the TOA. For emissivities e_{terr} higher than about 0.95 the atmospheric contribution $\Delta T_{B,atm}$ can reach negative values, i.e. the brightness temperature observed at the TOA is lower than the brightness temperature observed at the Earth's surface.

2. The atmospheric contribution $\Delta T_{B,atm}$ decreases with increasing brightness temperature of the Earth's surface, i.e. with increasing physical temperature. The higher the brightness temperature of the Earth's surface, the more radiation is attenuated by atmospheric particles on the path through the atmosphere.

3. The absolute value of the atmospheric contribution $\Delta T_{B,atm}$ increases with increasing incidence angle of the brightness temperature observation. For higher incidence angles, the path through the atmosphere is longer than for lower incidence angles. Thus, if the self-emittance of the atmosphere dominates over the attenuation of the atmosphere, the atmospheric contribution is higher for higher incidence angles. Whereas, if the attenuation of the atmosphere dominates over the self-emittance of the atmosphere, the atmospheric contribution has higher negative values for higher incidence angles.

4. The atmospheric contributions $\Delta T_{B,atm}$ for the mean atmospheric profiles of air temperature and humidity in January, April and October are very similar. Averaged over all considered emissivities, brightness temperatures, and incidence angles, the atmospheric contributions $\Delta T_{B,atm}$ for the October values are 2.6% higher than the atmospheric contributions for the April values, and 5.9% higher than the January values, respectively.

1.4 The TOA brightness temperature

For sea ice applications, the terrain brightness temperature consists of the brightness temperature of sea water and the brightness temperature of sea ice. Thus, the brightness temperature at the TOA is

$$T_{B,TOA} = (1-c)(T_{B,water} + (1-e_{water})T_{B,cosm}) + c(T_{B,ice} + (1-e_{ice})T_{B,cosm}) + \Delta T_{B,atm} \quad , \tag{1.15}$$

where c is ice concentration, e_{water} is the emissivity and $T_{B,water}$ the brightness temperature of water, e_{ice} is the emissivity and $T_{B,ice}$ the brightness temperature of the ice layer.

The calculation of the brightness temperature of an ice layer $T_{B,ice}$ is described in section 2. The brightness temperature of sea water $T_{B,water}$ is

$$T_{B,water} = e_{water} T_{water} \quad , \tag{1.16}$$

where T_{water} is the physical temperature of water. We calculate the emissivity of water e_{water} from the Fresnel equations for a specular surface (e.g. Ulaby et al., 1981):

$$e_{water}(p = H) = 1 - \left| \frac{\cos\theta - \sqrt{\epsilon_{water} - \sin^2\theta}}{\cos\theta + \sqrt{\epsilon_{water} - \sin^2\theta}} \right|^2 \tag{1.17}$$

$$e_{water}(p = V) = 1 - \left| \frac{\epsilon_{water}\cos\theta - \sqrt{\epsilon_{water} - \sin^2\theta}}{\epsilon_{water}\cos\theta + \sqrt{\epsilon_{water} - \sin^2\theta}} \right|^2 \quad , \tag{1.18}$$

where θ is the incidence angle and ϵ_{water} is the permittivity of water. Here, the permittivity of water is calculated from empirical equations (Klein and Swift, 1977).
As mentioned before, we assume $T_{B,cosm}$= 2.7 K for the cosmic background radiation in this study and use a look-up table to determine the atmospheric contribution $\Delta T_{B,atm}$ for given brightness temperatures, emissivities, and incidence angles, respectively.

2 MODEL DESCRIPTIONS

Nina Maaß

In this section, we focus on the brightness temperature as observed over sea ice ($T_{B,ice}$). In order to retrieve ice thickness from SMOS brightness temperatures, we have to set up a model that describes brightness temperature as a function of ice thickness.
In previous studies (Kaleschke et al., 2010, 2012), the ice brightness temperature was determined with a radiation model based on the approach described in Menashi et al. (1993). The approach is valid for a dielectric slab of ice that is bordered by the underlying water and the air above the slab of ice. However, here we want to investigate the impact of a temperature gradient within the ice as compared to a bulk ice temperature, and the impact of a snow layer on brightness temperatures above sea ice. Thus, we need radiation models that are capable of treating multiple layers of ice, and an ice layer that is covered by a snow layer.
In general, there are two approaches to consider radiometric emission from layered media; they are called the coherent and the incoherent approach. A coherent model is based on the solutions for the Maxwell equations and accounts for both the magnitudes and the phases of the electromagnetic fields that are reflected within the layered structure of the medium. An incoherent model is an approximation of the radiometric emission. The approximation is applicable, if the coherence of the radiation is reduced as a result of irregular boundaries, finite receiver bandwith, or antenna beam width (Menashi et al., 1993).
For sea ice applications in L-band, a coherent model describes sea ice emissivity as a periodic function of sea ice thickness. If the root mean square ice thickness within the illuminated footprint varies by at least a quarter of the considered wavelength λ (for SMOS: $\lambda = 21$ cm), the periodicity averages out. Instead of a coherent signal, we then observe an incoherent signal, and sea ice emissivity can be described as a unique function of ice thickness. This incoherent behaviour is the prerequisite for the retrieval of ice thickness from L-band measurements.
Here, we use an incoherent radiation model for multiple layers as described in Burke et al. (1979). This model is referred to as the incoherent Burke model throughout the thesis. Because the Burke model makes some simplifying assumptions, we also use a coherent multiple-layer model as described in Ulaby et al. (1981) and compare the results from both models. The coherent model is referred to as the coherent Ulaby model throughout the thesis. These two models, which are used for the following analyses, are presented in the following two sections. The main differences between these two models and the model after Menashi et al. (1993), which was used in previous studies, are summarised in Table 2.1.

2.1 The coherent Ulaby model

In order to consider the coherent emissivity of electromagnetic radiation in a medium that consists of multiple layers, we here use a method described in Ulaby et al. (1981) that follows Kong (1975). This method gives the reflection and the transmission coefficients for a N-layer

Table 2.1: Radiation models used for the calculation of L-band brightness temperatures above sea ice.

	Ulaby et al. (1981)	**Menashi et al. (1993)**	**Burke et al. (1979)**
approach	coherent	coherent/incoherent	incoherent
number of layers in medium	$N \in \mathbb{N}$	1	$N \in \mathbb{N}$
reduces to water emissivity for $d_{ice} \to 0$	yes	yes	no
based on	Maxwell equations	Fourier series expansion of coherent expression + integral over ice thickness variation	radiative transfer equation
neglects reflection terms of order > 1	no	partly	yes

medium with plane boundaries. A sketch of a N-layer medium as it is considered here is depicted in Figure 2.1. For our sea ice applications, the semi-infinite layer on top consists of air, and the semi-infinite layer at the bottom is the sea water underneath the ice layer. The approach of this method is that the wave equation's solutions for the electric and the

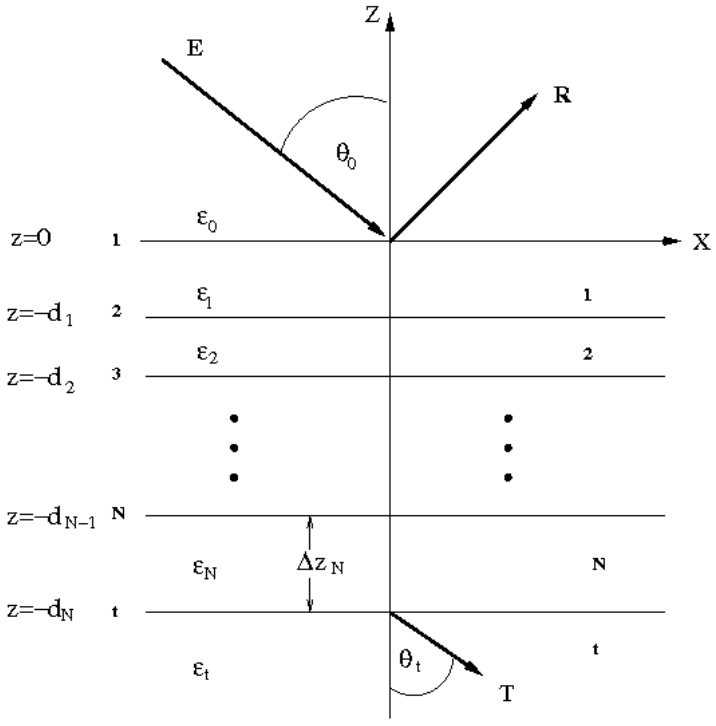

Figure 2.1: Reflection and transmission for a N-layer medium with the notations as used in the coherent model after Ulaby et al. (1981), as well as in the incoherent model after Burke et al. (1979).

magnetic fields in the mth layer can be expressed as functions of the field amplitudes A_m and C_m of the mth layer, the depth z, the incidence angle on the first interface θ_0, and the

z-component of the wave number in the mth layer k_{zm}, which can be expressed by

$$k_{zm} = \frac{\omega}{c_0}\sqrt{\epsilon_m - \sin^2\theta_0} \ , \tag{2.1}$$

where ω is the frequency in radians per second, c_0 is the speed of light (in vacuum), and ϵ_m is the permittivity of the mth layer.
The wave equations for the mth and the $(m+1)$th layer are related to each other by the boundary conditions at z= -d_m. From the continuity of the tangential electric and magnetic fields we obtain two equations. In matrix form these two equations can be combined to one. Here, we consider the matrix for a horizontally polarised incident field:

$$\begin{pmatrix} A_m e^{-ik_{zm}d_m} \\ C_m e^{ik_{zm}d_m} \end{pmatrix} = B_{m(m+1)} \begin{pmatrix} A_{m+1} e^{-ik_{z(m+1)}d_{m+1}} \\ C_{m+1} e^{ik_{z(m+1)}d_{m+1}} \end{pmatrix} \ , \tag{2.2}$$

where

$$B_{m(m+1)} = \frac{1}{2}(1 + \frac{\mu_m k_{z(m+1)}}{\mu_{m+1} k_{zm}}) \begin{pmatrix} e^{i\gamma} & R_{m(m+1)} e^{-i\gamma} \\ R_{m(m+1)} e^{i\gamma} & e^{-i\gamma} \end{pmatrix} \ ,$$

$$\text{with } \gamma = k_{z(m+1)}(d_{m+1} - d_m) \ ,$$

$$R_{m(m+1)} = \frac{\mu_{m+1} k_{zm} - \mu_m k_{z(m+1)}}{\mu_{m+1} k_{zm} + \mu_m k_{z(m+1)}} \ .$$

$B_{m(m+1)}$ is called the backward propagation matrix, and $R_{m(m+1)}$ is the Fresnel reflection coefficient for horizontal polarisation at the boundary z= -d_m within the medium that is characterised by the permittivity ϵ_m.
The amplitudes for the incident and the reflected fields can be related to those in the first layer by B_{01}, and to those in the second layer by $B_{01}B_{12}$, etc. In the semi-infinite medium below layer N, there is only a transmitted field amplitude. The value for d_t in equation (2.2) can be an arbitrary finite number, because the d_t in the transmitted field will cancel with that in B_{Nt}. Hence, the incident and the reflected field amplitudes are related to the transmitted field amplitudes by

$$\begin{pmatrix} 1 \\ R \end{pmatrix} = B_{01}B_{12}\cdots B_{Nt} \begin{pmatrix} Te^{-ik_{zt}d_t} \\ 0 \end{pmatrix} \ , \tag{2.3}$$

where R is the reflection coefficient and T the transmission coefficient for the N-layer medium. Equation (2.3) represents two equations with two unknowns R and T. Inserting the expression for T from the first equation into the second equation gives

$$R = \frac{B[2,1]}{B[1,1]} \ , \tag{2.4}$$

where $B[m,n]$ is the entry of the matrix $B = B_{01}B_{12}\cdots B_{Nt}$ in the mth row and the nth column. The emissivity of the N-layer medium is then

$$e = 1 - \left|R^2\right| \ . \tag{2.5}$$

The above described approach covers the horizontally polarised case. The solution for vertical polarisation is obtained by replacing ϵ by μ, and μ by ϵ in all equations. (Ulaby et al., 1981)
The brightness temperature at polarisation p (p= H for horizontal and p= V for vertical polarisation) of the N-layer medium is then the emissivity of the medium at polarisation p times the medium's physical temperature T_g:

$$T_{B,p} = e_p T_g \quad . \tag{2.6}$$

Here, we take the mean temperature of the considered ice and snow layers for T_g.

2.2 The incoherent Burke model

In order to consider the incoherent emissivity of electromagnetic radiation in a medium that consists of multiple layers, we here use a method described in Burke et al. (1979). The emission model is based on the radiative transfer equation and was originally developed for soil moisture applications of X- and L-band radiometer measurements. The model describes the radiation emitted from a stratified bare soil with N layers. The dielectric properties are assumed to be constant across the layers. A sketch of a N-layer medium as considered here is depicted in Figure 2.1. For our sea ice applications, the semi-infinite layer on top consists of air, and the semi-infinite layer at the bottom is the sea water underneath the ice layer.
The radiative transfer equation for the first layer can be written as

$$\frac{dT_p}{d(\gamma_1 z)} = -T_p + T_1 \quad , \tag{2.7}$$

where T_p is the brightness temperature at polarisation p, γ_1 is the absorption coefficient of the first layer, z is the path length, and T_1 is the physical temperature of the first layer. Equation (2.7) can be integrated from a point just below the surface to a point just above the interface between the first and the second layers. The resulting expression has two components. One accounts for the radiation emitted upward in the first layer and heading towards the surface, the other describes the upwelling radiation at the bottom of the first layer. The upwelling radiation in turn also has two components. Firstly, radiation emitted downward in the first layer that is reflected at the interface between the first and the second layers, and secondly, radiation transmitted from lower layers. The radiation field just above the surface is the radiation field just below multiplied by the transmittance of the interface.
The radiative transfer equation can then be integrated again from just below the first layer to a point just above the interface between the second and the third layer. If this procedure is repeated for N layers, we obtain the brightness temperature above the layered medium:

$$T_p(\theta_0) = \sum_{i=1}^{N} T_i (1 - e^{-\gamma_i(\theta_0)\Delta z_i})(1 + R_{p,i+1}(\theta_0) e^{-\gamma_i(\theta_0)\Delta z_i}) \cdot \prod_{j=1}^{i} (1 - R_{p,j}(\theta_0)) e^{-\sum_{j=2}^{i} \gamma_{j-1}(\theta_0)\Delta z_{j-1}} \quad , \tag{2.8}$$

where θ_0 is the angle of incidence at the first layer, T_i is the physical temperature of the ith layer, and Δz_i is the ith layer's thickness. The absorption coefficient γ_i can be expressed as

$$\gamma_i = 2\frac{\omega\alpha_{zi}(\theta_0)}{c_0} \quad , \tag{2.9}$$

where ω is the frequency in radians per second, c_0 is the speed of light (in vacuum), and

$$\alpha_{zi}(\theta_0) = \frac{\epsilon_{Ii}}{2\beta_{zi}(\theta_0)} \quad , \tag{2.10}$$

$$\beta_{zi}(\theta_0) = \sqrt{\frac{1}{2}(\epsilon_{Ri} - \sin^2\theta_0)(1 + \sqrt{1 + \frac{\epsilon_{Ii}^2}{(\epsilon_{Ri} - \sin^2\theta_0)^2}})} \quad , \tag{2.11}$$

where ϵ_{Ri} and ϵ_{Ii} are the real and the imaginary parts of the ith layer's complex permittivity, respectively.
$R_{p,i}$ is the absolute value squared of the Fresnel coefficient $\rho_{p,i}$ in the ith layer for the p polarisation:

$$\rho_{H,i} = \frac{k_{zi} - k_{z(i-1)}}{k_{zi} + k_{z(i-1)}} \quad , \tag{2.12}$$

$$\rho_{V,i} = \frac{\epsilon_{j-1}k_{zi} - \epsilon_j k_{z(i-1)}}{\epsilon_{j-1}k_{zi} + \epsilon_j k_{z(i-1)}} \quad , \tag{2.13}$$

where $k_{zi} = \beta_{zi}(\theta_0) + i\alpha_{zi}(\theta_0)$ and $\epsilon_j = \epsilon_{Ri} + i\epsilon_{Ii}$. (Burke et al., 1979)

2.3 Model assumptions for sea ice applications

The dielectric properties of the layers considered in the coherent Ulaby model and the incoherent Burke model are described by the permittivities of the layers. In order to calculate the brightness temperature over sea ice, we consider one or more layers of sea ice that are bounded by an infinitely thick layer of air and an infinitely thick layer of sea water. As already done in Kaleschke et al. (2010), we here use the following expressions for the corresponding permittivities.
The permittivity of air is assumed to be ϵ_{air}=1, which is the value for vacuum. For the permittivity of sea water, we use the empirical relationship by Klein and Swift (1977).
For the permittivity of sea ice we use an empirical relationship that describes the ice permittivity ϵ_{ice} as a function of brine volume fraction V_b within the ice (Vant et al., 1978):

$$\epsilon_{ice} = a_1 + a_2 V_b + i(a_3 + a_4 V_b) \quad , \tag{2.14}$$

where V_b is given in %■, and a_1, a_2, a_3, and a_4 are frequency-dependent coefficients. The empirical relationship is valid for $V_b < 70$ %■. For the SMOS frequency of f= 1.4 GHz, we linearly interpolate the coefficients a_1, a_2, a_3, and a_4 for 1 and 2 GHz, as introduced by Vant et al. (1978) for first-year ice and multi-year ice conditions (Table 2.2). The brine volume fraction V_b can be expressed as a function of the bulk values for the ice salinity S_{ice}, the ice density ρ_{ice}, the density of the brine ρ_{brine}, and the ice temperature T_{ice}. For ice temperatures lower than -2°C, we use the equations given in Cox and Weeks (1983), and for higher ice temperatures (as can be encountered particularly in low-salinity sea ice), we use

Table 2.2: Coefficients used here for the calculation of sea ice permittivity according to equation (2.14) as interpolated for f= 1.4 GHz from the values for 1 and 2 GHz (Vant et al., 1978).

	a_1	a_2	a_3	a_4
first-year ice	3.10	0.0084	0.037	0.00445
multi-year ice	3.10	0.0084	0.003	0.00435

the equations given in Leppäranta and Manninen (1988). For the ice density ρ_{ice}, we use an expression that relates ice density to ice temperature T_{ice} (Pounder, 1965):

$$\rho_{ice} = 0.917 - 1.403 \cdot 10^{-4} T_{ice} \quad , \tag{2.15}$$

where T_{ice} is given in °C. For the brine density, we use an expression that depends on brine salinity S_{brine} (Cox and Weeks, 1983):

$$\rho_{brine} = 1 + 0.0008 S_{brine} \quad , \tag{2.16}$$

where S_{brine} is inserted in %■. We obtain the brine salinity S_{brine} from polynomial approximations for the dependency between brine salinity and ice temperature (Vant et al., 1978).

3 SENSITIVITIES

Nina Maaß

3.1 Impact of ice temperature

In order to investigate the effect of ice temperature variability on brightness temperature simulations, we set up the following investigations: In section 3.1.1, we use a simple heat conduction model to identify the conditions under which the temperature gradient within ice can be assumed to be linear. In section 3.1.2, we compare brightness temperatures as simulated for a linear temperature gradient within the ice with brightness temperatures as simulated for a bulk ice temperature. In section 3.1.3, we calculate how sensitive simulated brightness temperatures are to ice temperature changes and how this sensitivity impacts the retrieval of ice thickness from brightness temperatures. Thus, we can estimate both, the influence of changing temperature conditions on the retrieval and the retrieval error introduced by the uncertainty of the ice temperature estimation.

3.1.1 Conditions for a linear temperature gradient

The radiation models used to retrieve ice thickness from SMOS data require information on the ice temperature. A possible approach is to use ice surface temperatures obtained from MODIS thermal imagery, for example. In the absence of any temperature information for the ice, ice temperature could also be estimated from air temperature, which is globally available on short terms from reanalysis data sets, for example. If only one ice layer is considered in the radiation model, a bulk ice temperature is required, whereas the models with multiple layers within the ice can be applied to an ice temperature profile. However, note that in the coherent Ulaby model the ice temperature profile is only taken into account via the permittivity profile and the permittivity's dependence on ice temperature, while for the ice temperature the mean value of the profile is used. In contrast, the Burke model contains both the temperature profile and the permittivity profile.
In order to estimate the required bulk ice temperature or ice temperature profile from the ice surface temperature, we have to make some assumptions regarding the temperature distribution within ice. If the temperature gradient within ice can be assumed to be linear, the temperature in the ice increases linearly from the surface temperature to the freezing temperature of the water underneath the ice. In order to investigate under which conditions this assumption is applicable for the retrieval of ice thickness from SMOS data, we set up a heat conduction model and simulate abrupt temperature changes at the ice surface. Thus, we can roughly estimate how long it takes for the ice system to re-establish a linear temperature gradient within ice.
The heat equation for a function $u(x, y, z, t)$ with the spatial variables x, y, z and the time variable t is

$$\frac{du}{dt} - \alpha \Delta u = 0 \ , \tag{3.1}$$

where α is the thermal diffusivity, and Δ is the Laplace operator. For a homogeneous ice column, in which the ice temperature is assumed to vary only with depth, equation (3.1) can be written in the form

$$\rho_{ice} c_{p,ice} \frac{dT}{dt} = \kappa_{ice} \frac{d^2T}{dz^2} \quad , \tag{3.2}$$

where ρ_{ice} is the density of ice, $c_{p,ice}$ is the specific heat capacity of ice, and κ_{ice} is the heat conductivity of ice. Because we here only need to roughly estimate the time scales, we neglect the temperature dependence of the heat capacity and heat conductivity and use typical values for the above parameters: ρ_{ice}= 910 kg/m^3, $c_{p,ice}$= 2113 J/(kgK), and κ_{ice}= 2.1 W/(Km) (as used for example in Tonboe et al. (2011)).
We perform our calculations for an ice thickness d_{ice}= 50 cm and an ice thickness d_{ice}= 100 cm, respectively. These thicknesses are at and above the maximum ice thickness that is retrievable from SMOS measurements in the Arctic. The ice column is uniformly divided into 11 layers, corresponding to a vertical resolution of about 4.5 cm for the ice with d_{ice}= 50 cm, and 9.1 cm for the ice with d_{ice}= 100 cm, respectively. The initial temperature profile is set to be at a constant temperature of -2°C for all ice layers, i.e. near the freezing temperature of Arctic water. We simulate three abrupt temperature changes at the ice surface. First, the ice surface temperature drops down from the initial value of -2°C to -10°C, followed by a further sudden drop to -30°C, and a final abrupt increase back to -2°C. In our simulations, the abrupt changes occur each after one day for the ice with d_{ice}= 50 cm, and after two days for the ice with d_{ice}= 100 cm, respectively. The bottommost layer is kept near the freezing temperature of water at -2°C throughout the simulations. The temperatures of the remaining ice layers are calculated from equation (3.2) using forward in time and central in space finite differences with a time step of 10 minutes. The simulations (Figures 3.1 to 3.4) yield that in the chosen example cases with quite large temperature changes on the ice surface, an almost linear temperature gradient within ice is established within time scales of hours.

Impact on brightness temperature
We use the coherent Ulaby model to simulate brightness temperatures for sea ice with ice temperature profiles as they occur during the simulated temperature changes (Figure 3.5). In addition, we simulate brightness temperatures for an assumed linear temperature gradient between the surface temperature and the bottom temperature at the water freezing point, and compare the resulting brightness temperatures.
We perform the simulations for the 50 cm thick ice. For the bulk ice and water salinity and the water temperature we assume typical Arctic values: S_{ice}= 8 g/kg, S_{water}= 30 g/kg, T_{water}= -1.8°C. In order to get a representative brightness temperature for 50 cm thick ice from the oscillating coherent model, we calculate the average brightness temperature for one oscillation around the ice thickness of 50 cm. At nadir, the period of the coherent oscillation is half the electromagnetic wavelength in the medium. Here, we model L-band brightness temperatures for a wavelength in vacuum of about λ_0= 21 cm. The wavelength in ice is λ_{ice}= $\frac{\lambda_0}{\sqrt{\epsilon_{ice}}}$. Thus, we perform the simulations for d_{ice}= 50 cm $\pm\frac{1}{2}\frac{\lambda_{ice}}{2}$ (e.g. for $d_{ice} \approx$ 50 cm $\pm$ 2.9 cm for ϵ_{ice}= 3.2).
On the first day, the ice surface temperature of the temperature simulations is at -10°C, while the remaining ice layers first have a constant temperature of -2°C and then gradually adjust their temperature until a linear temperature gradient between the ice surface and the ice bottom temperature is formed. The resulting average brightness temperature from the coherent Ulaby model is 231.5 K, while the resulting average brightness temperature is 229.9 K for ice that is assumed to have a linear temperature gradient over the 11 layers with temperatures

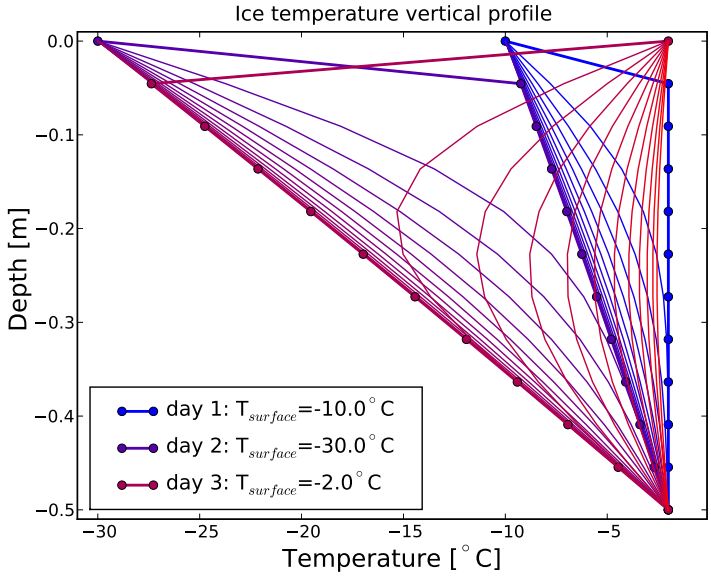

Figure 3.1: Vertical ice temperature profile for a 50 cm thick ice column with simulated abrupt temperature changes of the uppermost surface ice layer, as described in section 3.1.1. The lines with dots show the temperature profiles at the beginning of each day. The remaining lines show the temperature profiles every two hours, gradually changing their color with time from blue at the beginning of day 1, to violet at the beginning of day 2, to magenta at the beginning of day 3, and red at the end of day 3.

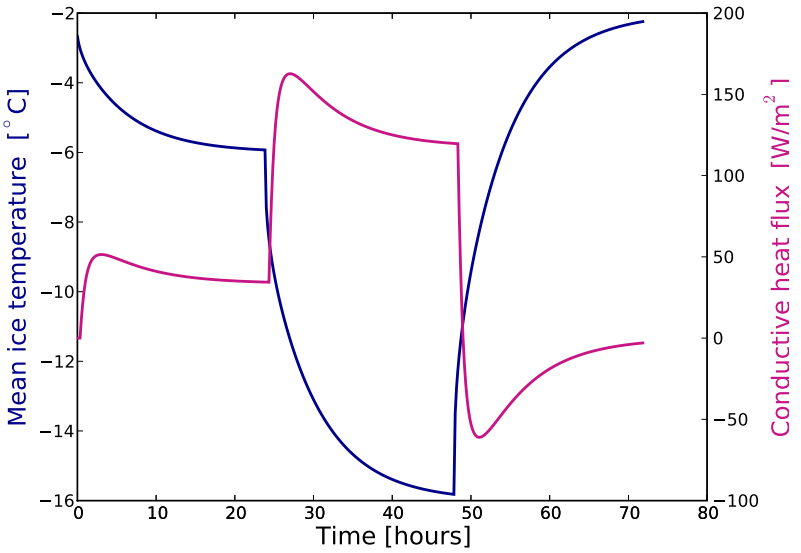

Figure 3.2: Temporal development of the mean ice temperature and the conductive heat flux within a 50 cm thick ice column with simulated abrupt temperature changes of the uppermost surface ice layer, as described in section 3.1.1.

ranging from -10°C at the surface to -2°C at the bottom. Thus, the difference between ice with a surface temperature of -10°C and a non-linear temperature gradient and ice with a surface temperature of -10°C and a linear temperature gradient is 1.6 K. However, already two hours after the change in ice surface temperature, the difference to the ice with a linear temperature gradient is only 0.5 K, and 0.3 K after four hours. On the second day with a surface temperature jump to -30°C, the brightness temperature at the end of the day, when

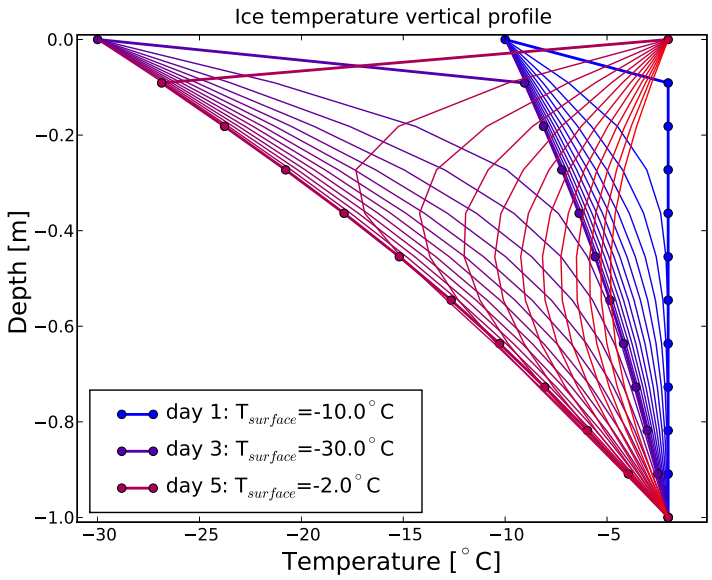

Figure 3.3: Vertical ice temperature profile for a 100 cm thick ice column with simulated abrupt temperature changes of the uppermost surface ice layer, as described in section 3.1.1. The lines with dots show the temperature profiles at the beginning of day 1, 3 and 5. The remaining lines show the temperature profiles every four hours, gradually changing their color with time from blue at the beginning of day 1, to violet at the beginning of day 3, to magenta at the beginning of day 5, and finally to red at the end of day 6.

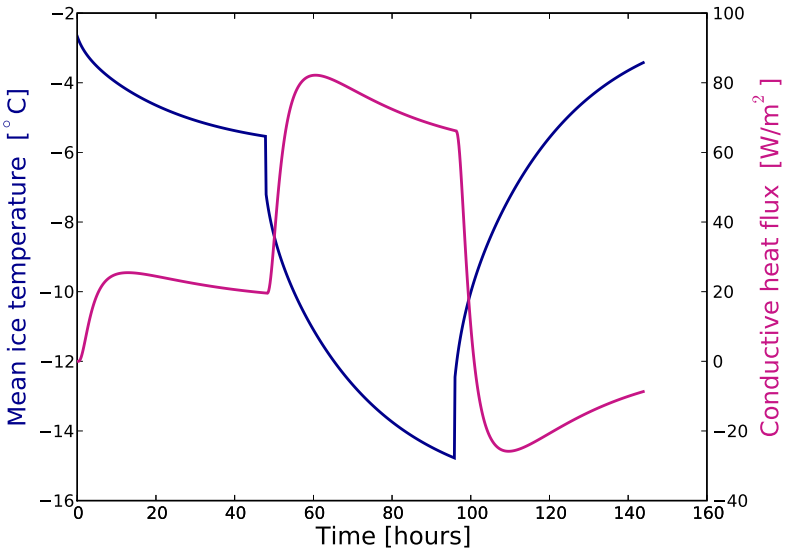

Figure 3.4: Temporal development of the mean ice temperature and the conductive heat flux within a 100 cm thick ice column with simulated abrupt temperature changes of the uppermost surface ice layer, as described in section 3.1.1.

the temperature gradient is almost linear, is 221.9 K, while the brightness temperature of the first temperature profile, when the temperature gradient is highly non-linear, is 228.5 K. The difference thus being 6.6 K, but again the difference reduces to 4.3 K two hours after the surface temperature change, and to 3.1 K after four hours. After more than about eight hours, the brightness temperature difference is less than 0.5 K. For the last day, when the surface temperature abruptly increases back to -2°C, the brightness temperature of ice with a linear

temperature gradient is 232.1 K, as compared to 225.3 K for the non-linear temperature gradient in the ice at the beginning of the day. The corresponding difference in the brightness temperature is 6.8 K, and 2.9 K two hours after the ice surface temperature has changed, and 1.3 K after four hours.

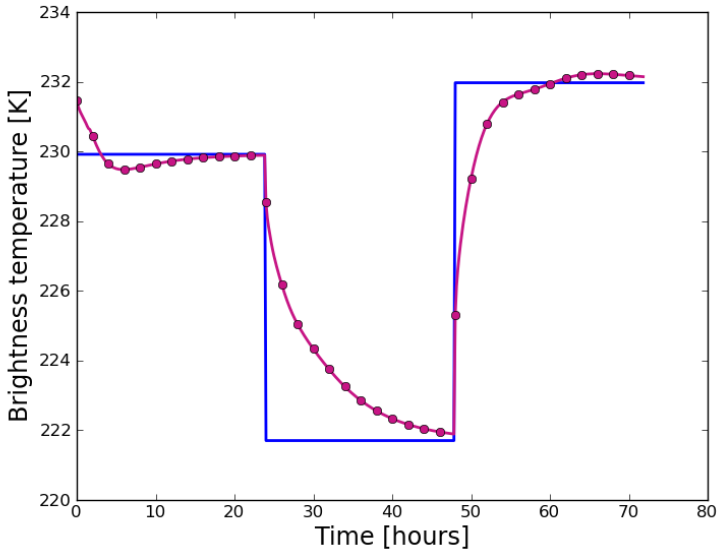

Figure 3.5: Brightness temperature at nadir view for the ice temperature profiles as calculated for Figure 3.1 (pink) and as calculated for an assumed linear temperature gradient between the temperature at the surface and at the bottom of the ice column (blue). The given brightness temperatures are simulated with the coherent Ulaby model and represent the average values for one oscillation around an ice thickness of 50 cm. The dots indicate the brightness temperature every two hours.

3.1.2 Bulk ice temperature vs. temperature gradient

In the previous section, we investigated under which conditions a linear temperature gradient within ice is a reasonable assumption. Here, we investigate how the assumption of a bulk ice temperature impacts the modelled brightness temperature as compared to a model that contains multiple layers and a temperature gradient within ice.

Multiple layers in the Burke model

As a first test of the incoherent Burke model with multiple ice layers, we assume a constant temperature for the entire ice column and gradually increase the number of layers within the ice from 1 to 100. For these isothermal conditions, we expect the brightness temperature as a function of ice thickness to be independent of the number of layers. For the coherent Ulaby model, this expected behaviour is confirmed (not shown here). However, for the incoherent Burke model, we find that the modelled brightness temperature decreases considerably with an increasing number of ice layers (Figure 3.6). The largest difference occurs when moving from the consideration of one ice layer to the consideration of two ice layers. The more layers we add, the less any additional ice layer impacts the brightness temperature. Thus, the brightness temperature curves for 20 and 100 layers are almost identical.

Multiple layers in the Ulaby model

For the test case of an isothermal temperature profile in ice, brightness temperatures as mod-

elled with the coherent Ulaby model are independent of the number of layers in ice (not shown here). Due to the Burke model's dependence on the number of considered layers in ice, we use the coherent Ulaby model to estimate the error that is introduced to the brightness temperature simulation by considering only one ice layer with a bulk ice temperature instead of multiple ice layers with a temperature gradient in the ice. The example case for typical Arctic first-year ice conditions shows that the brightness temperatures for the model with one ice layer are somewhat lower than for the model with multiple layers (Figure 3.7). When averaged over the ice thickness range considered here, the mean brightness temperature for one ice layer is 224.9 K, whereas the mean brightness temperature for 100 layers in the ice is 229.7 K.

We hypothesise, that one reason for the difference between the model with one ice layer and a bulk ice temperature and the model with multiple ice layers and a linear temperature gradient is the following. Ice permittivity in our models is a function of brine volume fraction (Vant et al., 1978), which is a non-linear function of ice temperature and ice salinity (Cox and Weeks, 1983). If only one ice layer is considered, the model's input value for ice temperature is the average value of the ice surface temperature and the ice bottom temperature (= the water freezing temperature). However, due to the non-linear relation between permittivity and ice temperature, the permittivity associated with the average ice temperature is not equal to the average value of the permittivity profile associated with the ice temperature profile (Figure 3.8). A possible approach to deal with this non-linearity could be to use

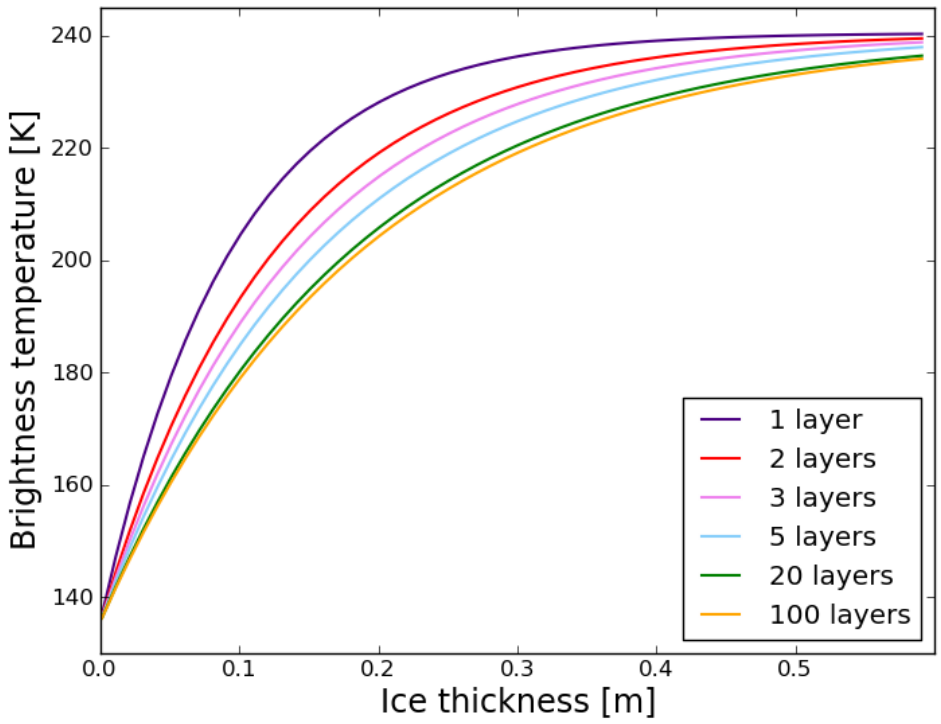

Figure 3.6: Nadir brightness temperature as a function of ice thickness as simulated with the incoherent Burke model for typical Arctic conditions (S_{water}= 30 g/kg, S_{ice}= 8 g/kg, T_{water}= -1.8°C, $T_{surface}$= -10°C). The temperature within ice is assumed to be constant for the whole ice column, i.e. the ice temperature is equal to the ice surface temperature for all ice layers. The colors indicate the number of ice layers used in the model.

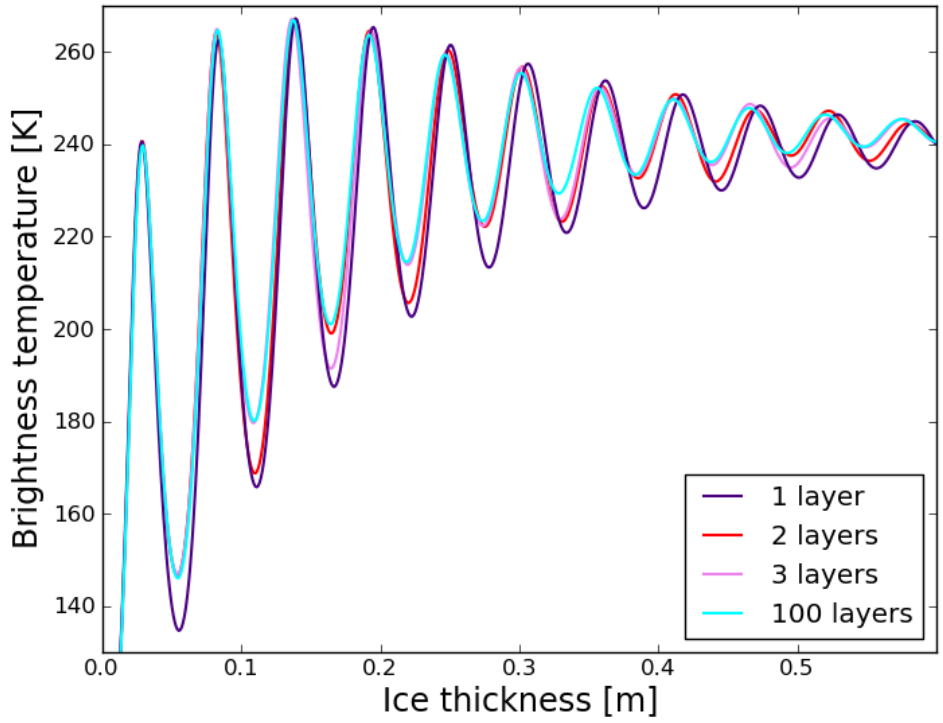

Figure 3.7: Nadir brightness temperature as a function of ice thickness as simulated with the coherent Ulaby model for typical Arctic conditions (S_{water}= 30 g/kg, S_{ice}= 8 g/kg, T_{water}= -1.8°C, $T_{surface}$= -10°C). The temperature within ice is assumed to increase linearly from the ice surface temperature to the ice bottom temperature, which is at the freezing point of sea water (here: -1.8°C). The colors indicate the number of ice layers used in the model.

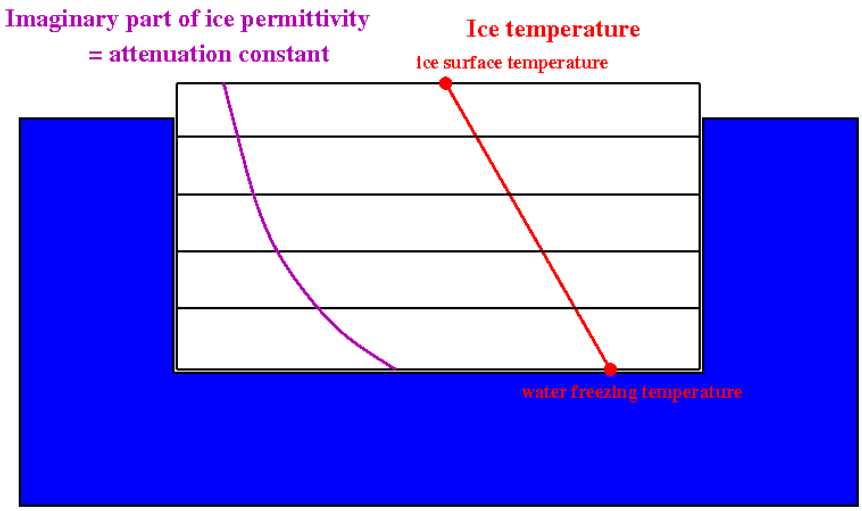

Figure 3.8: Sketch of the ice temperature profile and the related profile of the imaginary part of the ice permittivity (= attenuation constant).

the average permittivity of the permittivity profile as input to the radiation model, instead of the permittivity associated with the average ice temperature. However, ice emissivity is a non-linear function of ice permittivity, and the ice emissivity of the average ice permittivity is not equal to the ice emissivity associated with the ice permittivity profile. Thus, because it

would be convenient to apply only the model with one ice layer for the retrieval of ice thickness, we here try to find one representative value for the ice permittivity. Because the ice permittivity in the coherent Ulaby model mainly occurs within the exponential function, we here take the logarithm of the average value of the exponentiated ice permittivity as value for the ice permittivity. We find that the effectivity of this procedure depends on ice temperature (Figure 3.9). For an ice surface temperature of T_{surf}= -5°C, the model with one ice layer and the new ice permittivity value is not very representative for the brightness temperatures of the model with 100 ice layers, whereas for an ice surface temperature of T_{surf}= -15°C, the model with one ice layer and the new ice permittivity value represents better the brightness temperature curve of the time-consuming model with 100 ice layers.

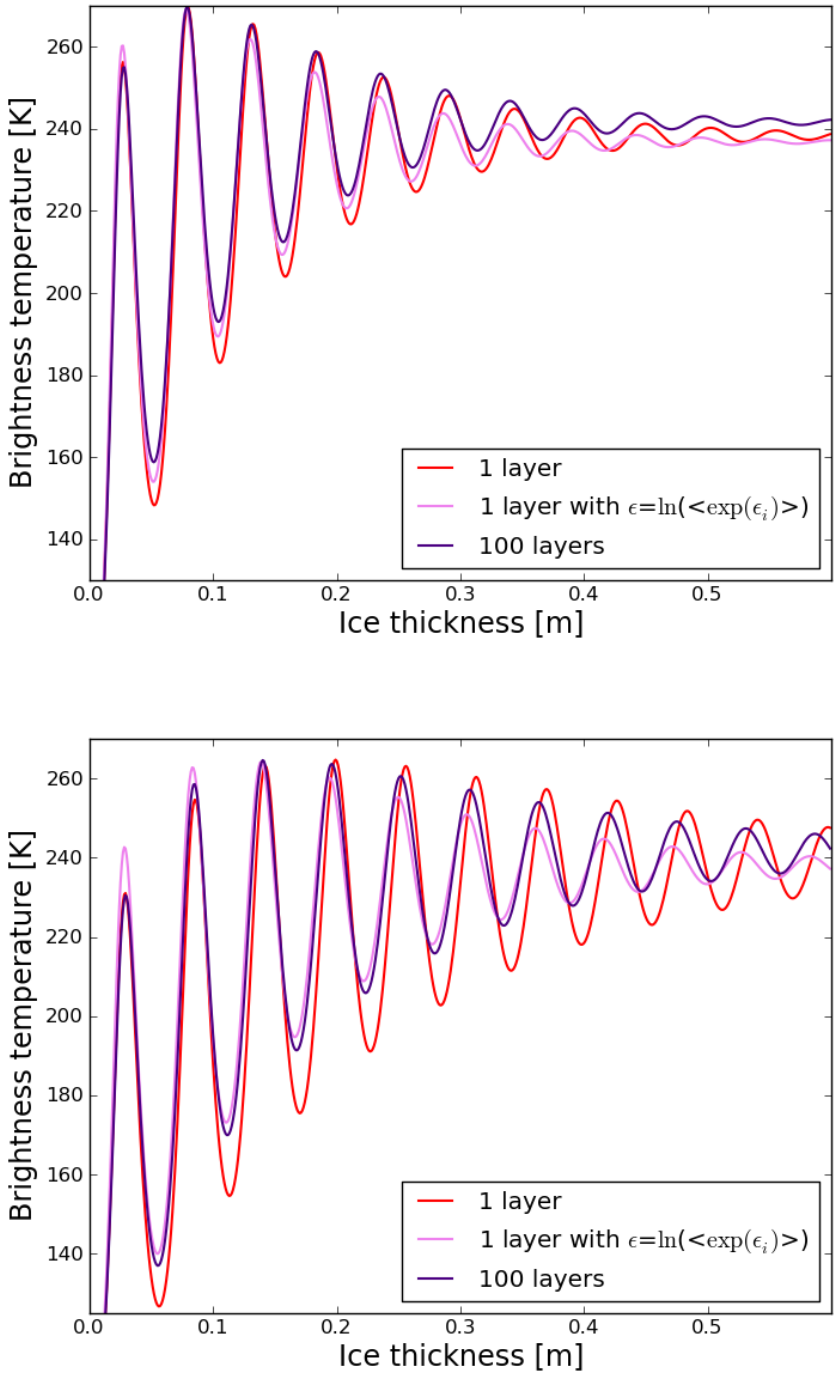

Figure 3.9: Nadir brightness temperature as a function of ice thickness as simulated with the coherent Ulaby model for typical Arctic conditions (S_{water}= 30 g/kg, S_{ice}= 8 g/kg, T_{water}= -1.8°C). The upper figure shows the results for T_{surf}= -5°C, the lower figure for T_{surf}= -15°C. Temperature within ice is assumed to increase linearly from the ice surface temperature to the ice bottom temperature, which is at the freezing point of sea water (here: -1.8°C). The red and the violet lines show the results for 1 and 100 ice layers, respectively. The pink line shows the result that is obtained, when the one-ice-layer-model is applied with a representative value for the ice permittivity (as described in section 3.1.2).

3.1.3 Sensitivity to bulk ice temperature

Here, we investigate how the bulk ice temperature and its variability impact brightness temperature simulations. We use the incoherent Burke model with one ice layer. The calculations are performed for four different ice thicknesses and three incidence angles. For ice and water salinities, we choose typical values for Arctic and for Baltic conditions. For the Arctic, water and bulk ice salinity are set to S_{water}= 30 g/kg and S_{ice}= 8 g/kg, respectively. For the Baltic, water and bulk ice salinity are set to S_{water}= 6 g/kg and S_{ice}= 1 g/kg, respectively. Water is assumed to be at the freezing point, i.e. T_{water}= -1.8°C for Arctic and T_{water}= -0.3°C for Baltic conditions, respectively. Bulk ice temperature is assumed to be the average value of the ice surface temperature and the water temperature.

Brightness temperature derivative with respect to ice temperature
First, we describe brightness temperature TB as a function of ice surface temperature T_{surf} (Figures 3.10 and 3.14). We then numerically differentiate the brightness temperature function with respect to ice surface temperature (Figures 3.11 and 3.15). The derivative $\frac{\partial TB}{\partial T_{surf}}$ is also a function of ice surface temperature and describes the change of the observed brightness temperature with a changing ice surface temperature. For $\frac{\partial TB}{\partial T_{surf}} > 0$, brightness temperatures increase with increasing ice temperature, whereas they decrease with increasing ice temperature for $\frac{\partial TB}{\partial T_{surf}} < 0$. The derivative $\frac{\partial TB}{\partial T_{surf}}$ can be used to estimate the error of the brightness temperature simulation caused by the uncertainty of the ice surface temperature estimation.
According to our model, brightness temperatures increase with increasing ice temperatures for cold conditions until a reversal point is reached, where $\frac{\partial TB}{\partial T_{surf}} = 0$. For ice temperatures higher than this reversal point, brightness temperatures decrease with further increasing ice temperatures. The ice temperature of this reversal point depends on ice thickness. For thinner ice, the reversal occurs at higher temperatures than for thicker ice. For thin ice, brightness temperatures increase with increasing ice temperature, except for very high ice temperatures. For thick ice, brightness temperatures increase only slightly with ice temperature for ice surface temperatures below -10°C, start to decrease with ice temperature for ice surface temperatures above -10°C, and decrease more strongly for warm temperatures. With thin or thick ice we here refer to ice that is thin or thick compared to the maximum retrievable ice thickness, which is about 50 cm for Arctic conditions and about 1 m for Baltic conditions.

Brightness temperature derivative with respect to ice thickness
When we differentiate the brightness temperature function with respect to ice thickness (Figures 3.12 and 3.16), the calculated derivatives $\frac{\partial TB}{\partial d_{ice}}$ clearly show how the potential for retrieving ice thickness from L-band brightness temperatures declines for increasing ice thickness. Furthermore, brightness temperature sensitivity to ice thickness decreases with increasing ice temperature for all ice thicknesses. The only exception is found for thin ice under Baltic conditions (Figures 3.16). In this case, the brightness temperature sensitivity increases with increasing ice temperature up to a surface ice temperature of about -5°C. For further increasing temperature the sensitivity then reduces rapidly.
The derivative $\frac{\partial TB}{\partial d_{ice}}$ can be used to estimate the ice thickness retrieval's uncertainty for different ice temperature and ice thickness conditions. For example, if radiometric uncertainty is considered to be 2 K, and we require an ice thickness accuracy of 5 cm, we should apply the ice thickness retrieval only in the regime with $\frac{\partial TB}{\partial d_{ice}} > 2$ K/5 cm= 0.4 K/cm. For the Arctic conditions, this requirement is fulfilled for all ice surface temperatures, if the ice is 15 cm

thick, and for ice surface temperatures below about -9°C, if the ice is 30 cm thick, for example. For the Baltic conditions, this requirement is fulfilled for ice surface temperatures below about -0.5°C, -3°C, and -10°C, if the ice thickness is 25 cm, 50 cm, and 75 cm, respectively.

Impact of the ice temperature on the retrieval
The derivatives $\frac{\partial TB}{\partial T_{surf}}$ and $\frac{\partial TB}{\partial d_{ice}}$ can be used to estimate the impact of ice temperature variability on the ice thickness retrieval:

$$\frac{\partial d_{ice}}{\partial T_{surf}} = \frac{\partial TB}{\partial T_{surf}} \left(\frac{\partial TB}{\partial d_{ice}} \right)^{-1} . \tag{3.3}$$

For both Arctic and Baltic conditions, the ice thickness retrieval for thin ice is only very slightly affected by ice surface temperature (Figures 3.13 and 3.17). The thicker the ice is, the more the ice thickness retrieval is influenced by ice temperature. The ice thickness retrieval's sensitivity to ice surface temperature has a positive sign for cold conditions, that is we would retrieve too high ice thicknesses, if we assumed too high values for the ice surface temperature. The ice thickness retrieval's sensitivity to ice temperature then increases with increasing ice surface temperature until a reversal point. At this reversal point, $\frac{\partial d_{ice}}{\partial T_{surf}}$ shows a deep drop and reaches very high negative values for further increasing ice temperatures, that is we would retrieve too small ice thicknesses, if we assumed too high values for the ice surface temperature. This reversal point originates from the change of sign for $\frac{\partial TB}{\partial T_{surf}}$ at a certain ice surface temperature. The temperature of this reversal point is at higher temperatures for thinner ice than for thicker ice, and the reversal generally occurs at higher temperatures for the Baltic than for the Arctic ice conditions. For example, for the Arctic conditions at nadir view, the reversal point occurs at T_{surf}= -2.8°C for an ice thickness of 15 cm, and at T_{surf}= -9.6°C for an ice thickness of 60 cm, respectively. Below this reversal point, the ice thickness retrieval's sensitivity to ice temperature is about 1 – 2 cm per 1 K of ice temperature change for ice thicknesses up to 30 cm, about 1 – 3 cm per 1 K of ice temperature change for ice thicknesses of 45 cm, and about 2 – 10 cm per 1 K of ice temperature change for ice thicknesses of 60 cm for the Arctic conditions.

3.2 Impact of ice salinity

Similarly to the approach for investigating the effect of temperature variability on brightness temperature simulations, we here investigate how ice salinity and its variability impact brightness temperature simulations. We again use the incoherent Burke model with one ice layer. As for the analysis of temperature sensitivity, the calculations are performed for four different ice thicknesses and three incidence angles. For Arctic conditions water salinity is assumed to be S_{water}= 30 g/kg, and the bulk ice temperature is assumed to be T_{ice}= -7°C; for Baltic conditions we assume S_{water}= 6 g/kg and T_{ice}= -3°C. Water is assumed to be at the freezing point, i.e. T_{water}= -1.8°C for Arctic and T_{water}= -0.3°C for Baltic conditions, respectively.

Brightness temperature derivative with respect to ice salinity
First, we describe brightness temperature as a function of ice salinity (Figure 3.18 and 3.22). We then numerically differentiate the brightness temperature function with respect to ice salinity (Figure 3.19 and 3.23). The derivative $\frac{\partial TB}{\partial S_{ice}}$ is also a function of ice salinity and

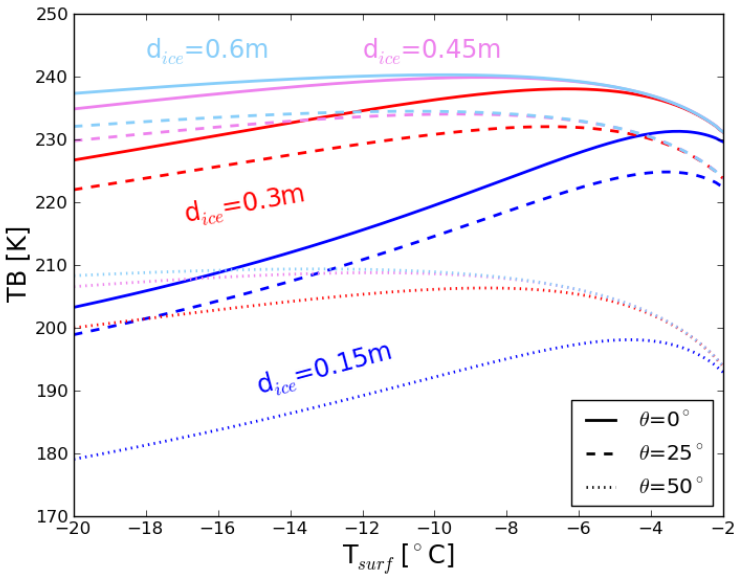

Figure 3.10: Horizontally polarised brightness temperature TB as a function of ice surface temperature T_{surf} according to the incoherent Burke model for one ice layer. The ice is assumed to be at typical Arctic conditions (S_{water}= 30 g/kg, S_{ice}= 8 g/kg, T_{water}= -1.8°C). The four colors indicate the different ice thicknesses, the line styles indicate the incidence angles.

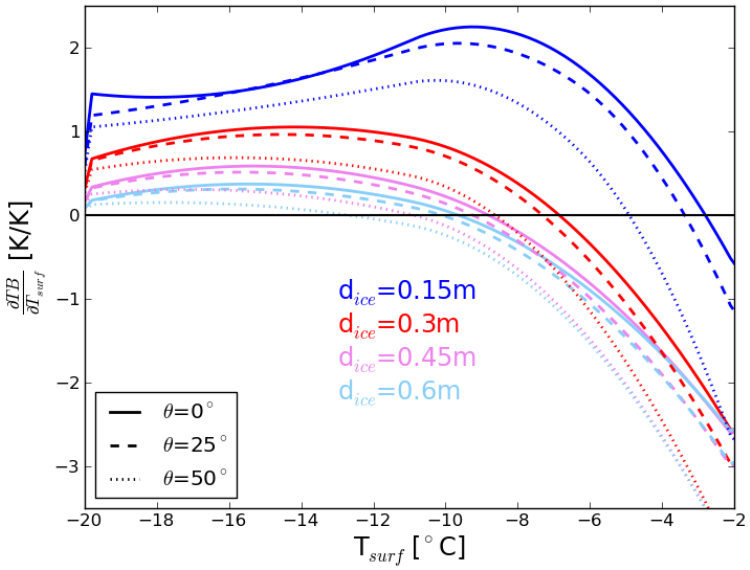

Figure 3.11: Derivative of horizontally polarised brightness temperature TB with respect to ice surface temperature T_{surf} as a function of T_{surf} according to the incoherent Burke model for one ice layer. For the assumed ice conditions and the explanation of the lines see caption of Figure 3.10.

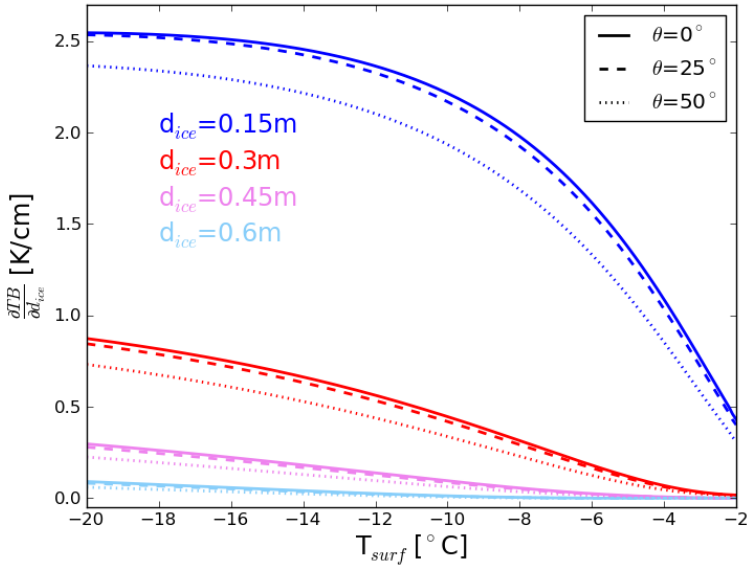

Figure 3.12: Derivative of horizontally polarised brightness temperature TB with respect to ice thickness d_{ice} as a function of ice surface temperature T_{surf} according to the incoherent Burke model for one ice layer. For the assumed ice conditions and the explanation of the lines see caption of Figure 3.10.

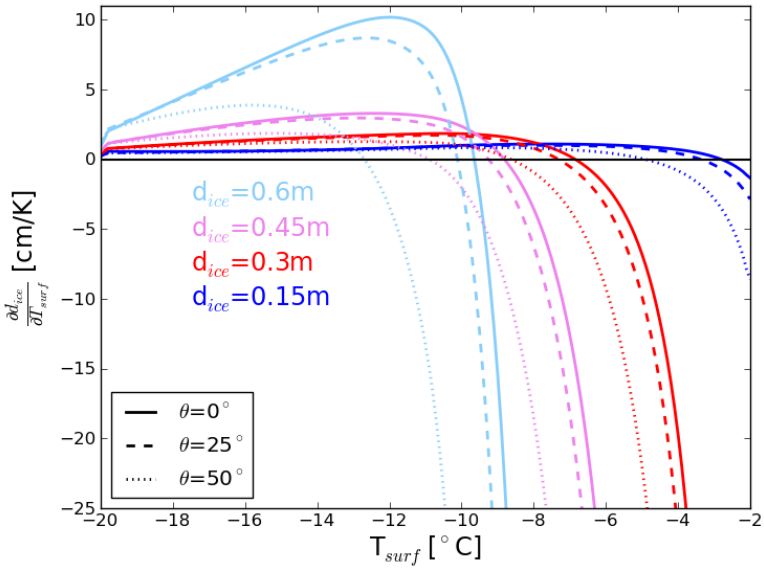

Figure 3.13: Derivative of ice thickness d_{ice} with respect to ice surface temperature T_{surf} as a function of T_{surf}, when the horizontally polarised brightness temperature is described as a function of ice thickness following the incoherent Burke model for one ice layer. For the assumed ice conditions and the explanation of the lines see caption of Figure 3.10.

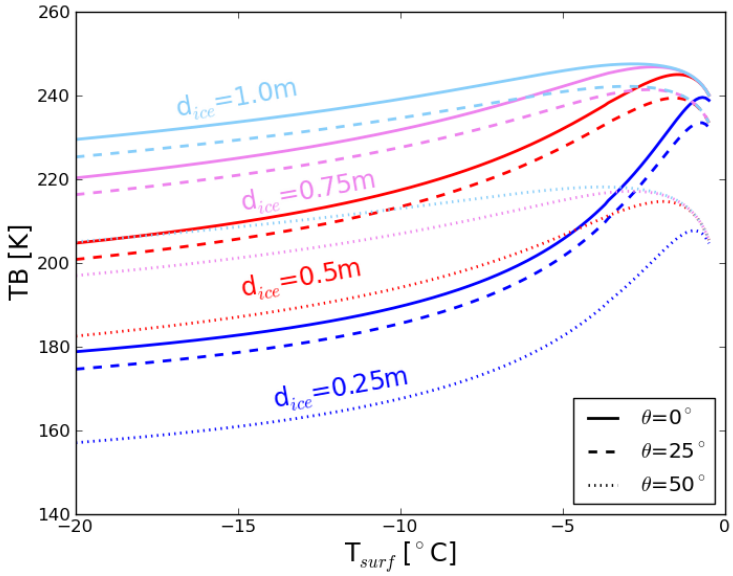

Figure 3.14: Horizontally polarised brightness temperature TB as a function of ice surface temperature T_{surf} according to the incoherent Burke model for one ice layer. The ice is assumed to be at typical Baltic conditions (S_{water}= 6 g/kg, S_{ice}= 1 g/kg, T_{water}= -0.3°C). The four colors indicate the different ice thicknesses, the line styles indicate the incidence angles.

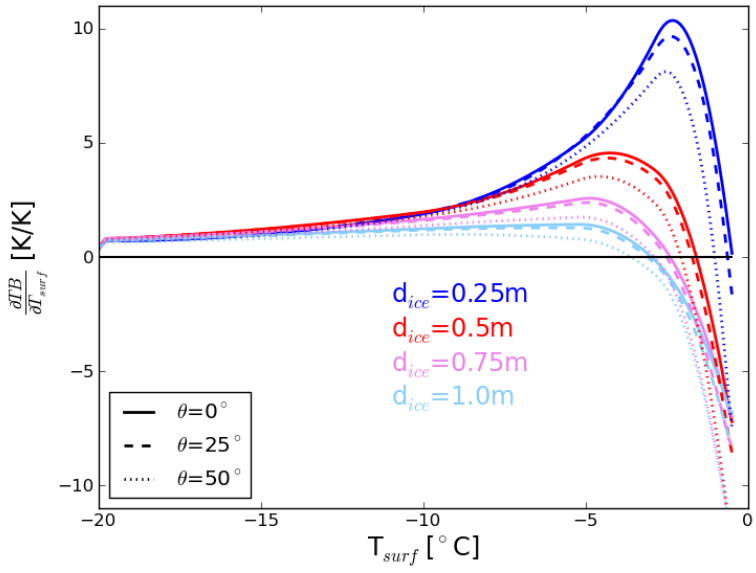

Figure 3.15: Derivative of horizontally polarised brightness temperature TB with respect to ice surface temperature T_{surf} as a function of T_{surf} according to the incoherent Burke model for one ice layer. For the assumed ice conditions and the explanation of the lines see caption of Figure 3.14.

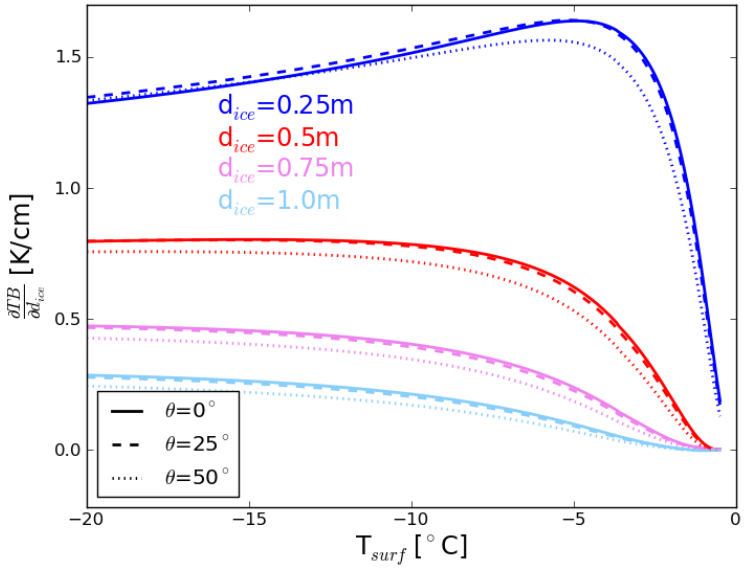

Figure 3.16: Derivative of horizontally polarised brightness temperature TB with respect to ice thickness d_{ice} as a function of ice surface temperature T_{surf} according to the incoherent Burke model for one ice layer. For the assumed ice conditions and the explanation of the lines see caption of Figure 3.14.

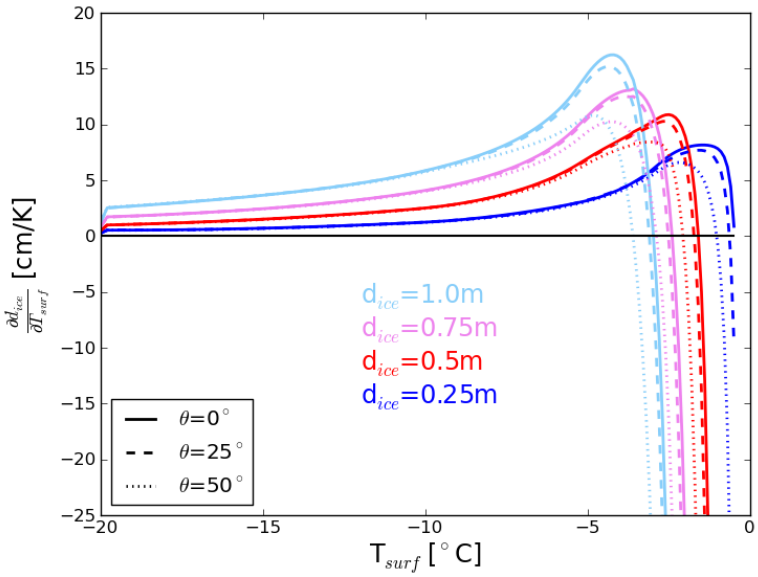

Figure 3.17: Derivative of ice thickness d_{ice} with respect to ice surface temperature T_{surf} as a function of T_{surf}, when the horizontally polarised brightness temperature is described as a function of ice thickness following the incoherent Burke model for one ice layer. For the assumed ice conditions and the explanation of the lines see caption of Figure 3.14.

describes the change of the observed brightness temperature with a changing salinity. For $\frac{\partial TB}{\partial S_{ice}} > 0$, brightness temperatures increase with increasing ice salinity, whereas they decrease with increasing ice salinity for $\frac{\partial TB}{\partial S_{ice}} < 0$. The derivative $\frac{\partial TB}{\partial S_{ice}}$ can be used to estimate the error of the brightness temperature simulation caused by the uncertainty of the ice salinity estimation.
According to our model, under Arctic conditions the brightness temperature for ice salinities $S_{ice} > 5$ g/kg and ice thicknesses $d_{ice} \geq 45$ cm is only very slightly sensitive to ice salinity changes; for thinner ice, the sensitivity is somewhat higher. In contrast, brightness temperature sensitivity to ice salinity is very high for all ice thicknesses, if ice salinity is low. For the Arctic conditions and ice salinities $S_{ice} < 5$ g/kg, brightness temperatures vary by up to more than 20 K for ice salinity variations of 1 g/kg. However, ice salinities $S_{ice} < 5$ g/kg are seldom found in Arctic sea ice with ice thicknesses below 60 cm, which are the retrievable thicknesses. According to an empirical relationship between ice salinity and ice thickness in the Arctic (Cox and Weeks, 1974), sea ice with a thickness ranging from 15 cm to 60 cm has typically ice salinities ranging from S_{ice}= 11.3 g/kg to S_{ice}= 6.9 g/kg.
Compared to the Arctic conditions, brightness temperatures under the Baltic conditions are even more sensitive to ice salinity for low ice salinities. For an ice salinity S_{ice}= 1 g/kg, which is a value often used for Baltic applications, an ice salinity variation of 1 g/kg causes a brightness temperature variation of about 8 K for an ice thickness d_{ice}= 100 cm, and even 26 K for an ice thickness d_{ice}= 25 cm.

Brightness temperature derivative with respect to ice thickness
When we differentiate the brightness temperature function with respect to ice thickness (Figure 3.20 and 3.24), the calculated derivatives $\frac{\partial TB}{\partial d_{ice}}$ again clearly show how the potential for retrieving ice thickness from L-band brightness temperatures declines with increasing ice thickness. The brightness temperature's sensitivity to ice thickness first increases with increasing salinity, reaches a maximum value, and then decreases with further increasing ice salinity. The salinity value associated with the maximum sensitivity to ice thickness depends on ice thickness and ranges from S_{ice}= 0 g/kg for d_{ice}= 60 cm to S_{ice}= 4.5 g/kg for d_{ice}= 15 cm under Arctic conditions, and from S_{ice}= 0 g/kg for d_{ice}= 100 cm to S_{ice}= 1 g/kg for d_{ice}= 25 cm under Baltic conditions.
The derivative $\frac{\partial TB}{\partial d_{ice}}$ can also be used to estimate the ice thickness retrieval's uncertainty for different ice salinity and ice thickness conditions. For example, if the radiometric uncertainty is assumed to be 2 K, and we require an ice thickness accuracy of 5 cm, we should consider the ice thickness retrieval only in the regime with $\frac{\partial TB}{\partial d_{ice}} > 2$ K/5 cm= 0.4 K/cm. For the Arctic conditions, this requirement is fulfilled for all ice salinities considered here, if the ice is 15 cm thick, and for ice salinities below about 9 g/kg, if the ice is 30 cm thick, for example. For the Baltic conditions, this requirement is fulfilled for all ice salinities considered here, if the ice is 25 cm thick and for ice salinities $S_{ice} < 2$ g/kg, if the ice is 50 cm thick, for example.

Impact of ice salinity on the retrieval
The derivatives $\frac{\partial TB}{\partial S_{ice}}$ and $\frac{\partial TB}{\partial d_{ice}}$ can be used to estimate the impact of ice salinity variability on the ice thickness retrieval:

$$\frac{\partial d_{ice}}{\partial S_{ice}} = \frac{\partial TB}{\partial S_{ice}} \left(\frac{\partial TB}{\partial d_{ice}} \right)^{-1} \quad . \tag{3.4}$$

For the Arctic conditions, the ice thickness retrieval for thin ice (d_{ice}= 15 cm) is only slightly affected by ice salinity (Figure 3.21).
Based on the empirical relationship between ice salinity and ice thickness (Cox and Weeks, 1974), we can state the following for Arctic conditions. For the range of salinities that is generally associated with a certain ice thickness, the sensitivity of the retrieved ice thickness is always below 10 cm thickness variation per ice salinity variation of 1 g/kg. For example, according to the empirical relationship, ice with a thickness of d_{ice}= 45 cm has an ice salinity of roughly S_{ice}= 7 g/kg. Our sensitivity study predicts $\left|\frac{\partial d_{ice}}{\partial S_{ice}}\right| < 10 \frac{\text{cm}}{\text{g/kg}}$ to be valid for d_{ice}= 45 cm, if the salinity is 3 g/kg$< S_{ice} <$ 12 g/kg. Thus, this statement is true for our example of ice with a thickness of d_{ice}= 45 cm. Accordingly, the statement $\left|\frac{\partial d_{ice}}{\partial S_{ice}}\right| < 10 \frac{\text{cm}}{\text{g/kg}}$ is valid for the ice thicknesses considered here, if we assume that the corresponding ice salinities are close to the ice salinities related to the considered ice thickness via the empirical relationship by Cox and Weeks (1974). For typical Arctic conditions, an ice salinity change of 1 g/kg mostly has the same impact on brightness temperature as an ice thickness change of 0.5 – 6 cm, depending on the ice thickness. For the Baltic conditions, the ice thickness retrieval's sensitivity to ice salinity is considerably higher.

3.3 Comparison of the impact by ice temperature, salinity, and thickness

Here, we consider an example case of freezing sea ice in the Laptev Sea to investigate how observed SMOS brightness temperature changes are related to estimated changes of ice temperature, salinity, and thickness. Thus, we aim to compare the contributions of these three ice parameters to the brightness temperature under realistic conditions.

Freezing sea ice in the Laptev Sea
We examine sea ice that is forming and gradually growing in October and November, 2010 in the Laptev Sea. We here consider the SMOS grid point at 77.5°N and 137.5°E, which is the grid point analysed in Kaleschke et al. (2012). They estimate the variability of the ice parameters that influence the observed brightness temperatures from the surface air temperature time series from NCEP reanalysis data (Kalnay et al., 1996) and from ice concentration data from AMSR-E observations (Cavalieri et al., 2004). The ice concentration time series indicates that the considered area is ice-free until the 20th October, and that on the 20th October ice is formed, and that the ice cover is almost closed after two days and stays closed for the following weeks. Kaleschke et al. (2012) use the Lebedev sea ice thickness parameterisation to estimate ice thickness from observed surface air temperatures (Maykut, 1986). The Lebedev parameterisation of sea ice thickness is based on cumulative freezing degree days: d_{ice}= $1.33\Theta^{0.58}$ [cm], where $\Theta = \int (T_f - T_a) dt$ are the cumulative freezing degree days, and T_a and T_f are the surface air temperature and the freezing point of sea water (here: T_f= -1.9 °C), respectively. For the examined case, the Lebedev parameterisation describes the sea ice growth reasonably; the ice thicknesses calculated from the freezing degree days and the ice thicknesses as retrieved from SMOS agree well (Kaleschke et al., 2012).
Here, we consider the situation in the Laptev Sea from 22nd October to 15th November, 2010, because this is the main ice growth period. According to the Lebedev parameterisation, the ice thickness increases from 0 to about 34 cm during this time period. In order to estimate the ice salinity variability associated with this ice thickness increase, we use an empirical relationship between ice salinity and ice thickness for Arctic first-year ice (Cox

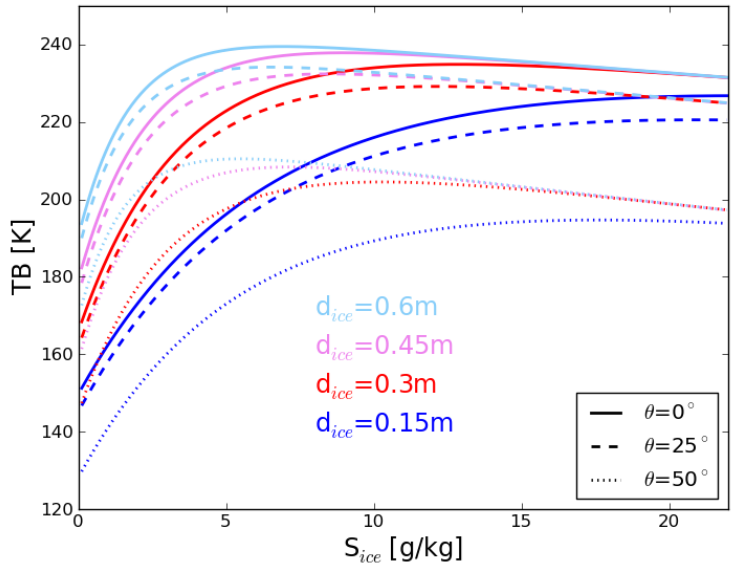

Figure 3.18: Horizontally polarised brightness temperature TB as a function of ice salinity S_{ice} according to the Burke model for one ice layer. The ice is assumed to be at typical Arctic conditions (S_{water}= 30 g/kg, $T_{surface}$= -15°C, T_{water}= -1.8°C). The four colors indicate the different ice thicknesses, the line styles indicate the incidence angles.

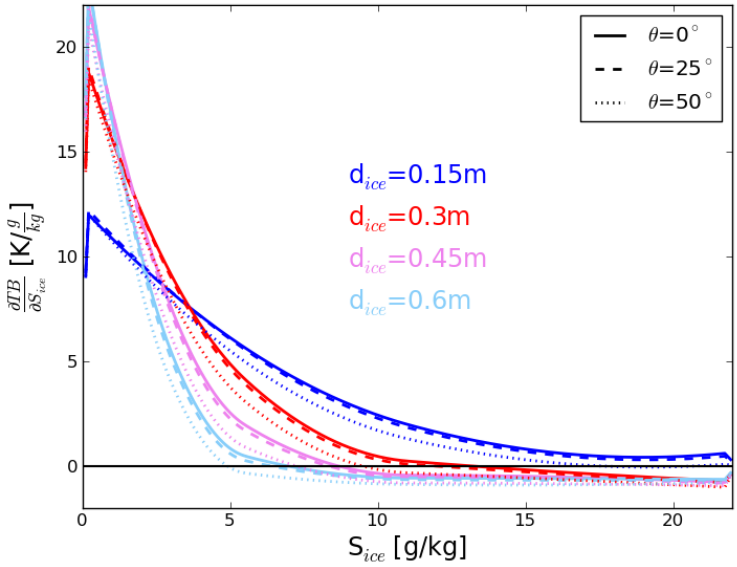

Figure 3.19: Derivative of horizontally polarised brightness temperature TB with respect to ice salinity S_{ice} as a function of S_{ice} according to the Burke model for one ice layer. For the assumed ice conditions and the explanation of the lines see caption of Figure 3.18.

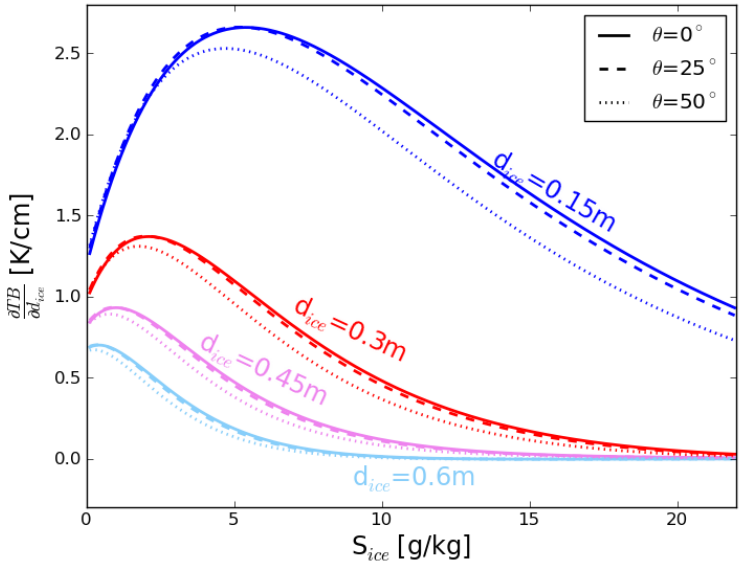

Figure 3.20: Derivative of horizontally polarised brightness temperature TB with respect to ice thickness d_{ice} as a function of ice salinity S_{ice} according to the Burke model for one ice layer. For the assumed ice conditions and the explanation of the lines see caption of Figure 3.18.

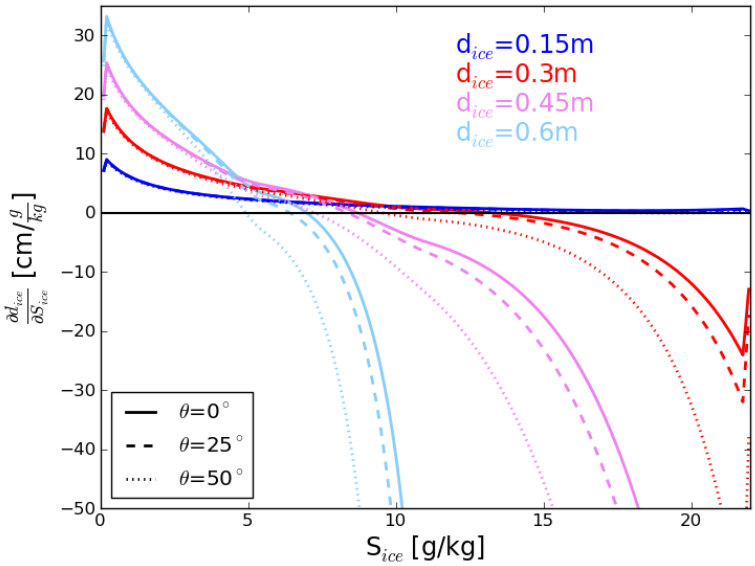

Figure 3.21: Derivative of ice thickness d_{ice} with respect to ice salinity S_{ice} as a function of S_{ice}, when the horizontally polarised brightness temperature is described as a function of ice thickness following the Burke model for one ice layer. For the assumed ice conditions and the explanation of the lines see caption of Figure 3.18.

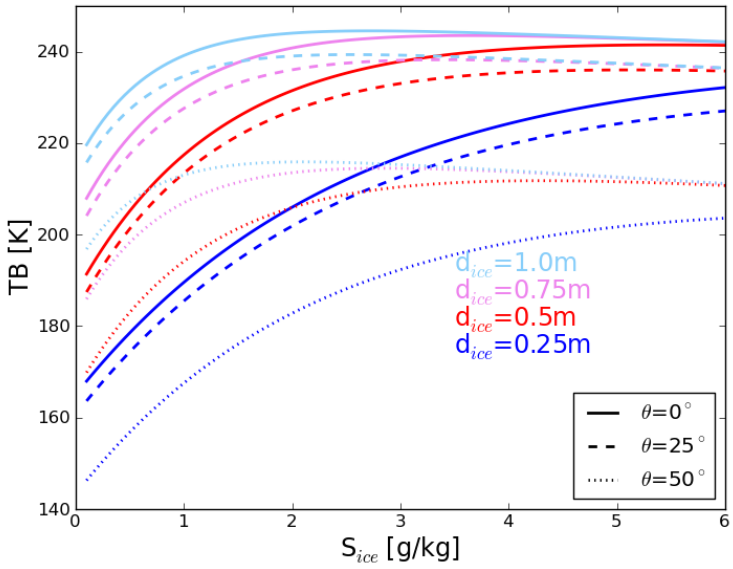

Figure 3.22: Horizontally polarised brightness temperature TB as a function of ice salinity S_{ice} according to the Burke model for one ice layer. The ice is assumed to be at typical Baltic conditions (S_{water}= 6 g/kg, $T_{surface}$= -10°C, T_{water}= -0.3°C). The four colors indicate the different ice thicknesses, the line styles indicate the incidence angles.

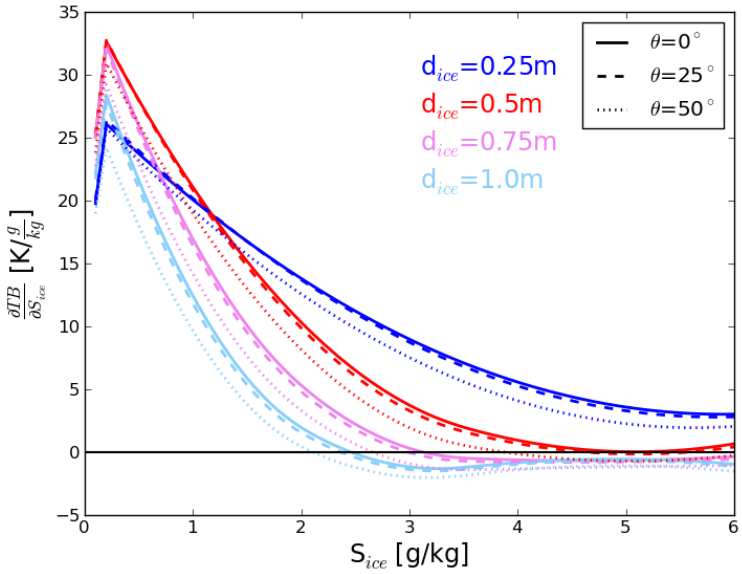

Figure 3.23: Derivative of horizontally polarised brightness temperature TB with respect to ice salinity S_{ice} as a function of S_{ice} according to the Burke model for one ice layer. For the assumed ice conditions and the explanation of the lines see caption of Figure 3.22.

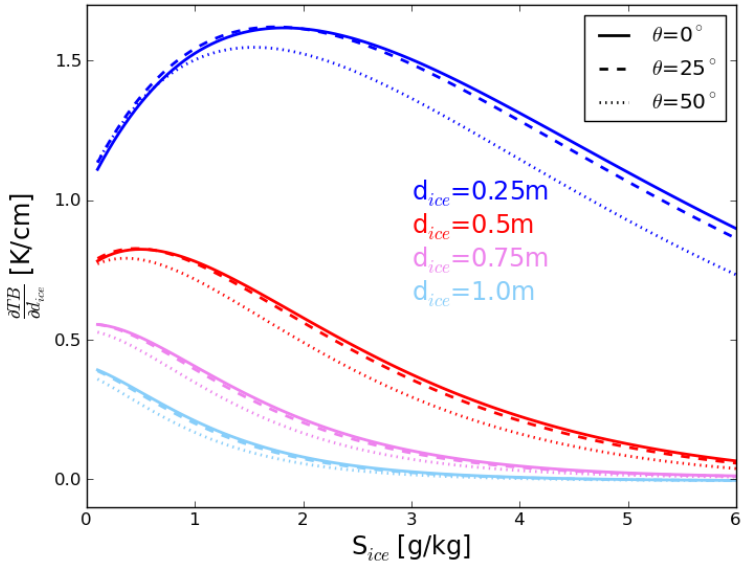

Figure 3.24: Derivative of horizontally polarised brightness temperature TB with respect to ice thickness d_{ice} as a function of ice salinity S_{ice} according to the Burke model for one ice layer. For the assumed ice conditions and the explanation of the lines see caption of Figure 3.22.

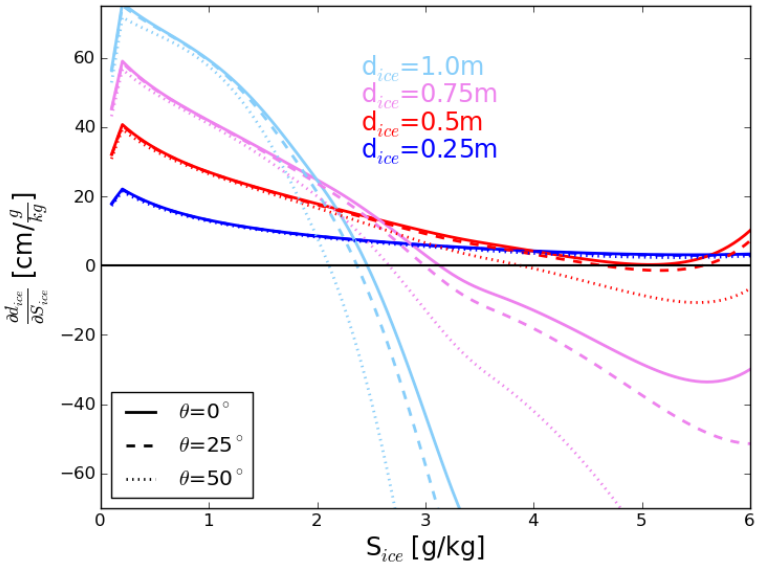

Figure 3.25: Derivative of ice thickness d_{ice} with respect to ice salinity S_{ice} as a function of S_{ice}, when the horizontally polarised brightness temperature is described as a function of ice thickness following the Burke model for one ice layer. For the assumed ice conditions and the explanation of the lines see caption of Figure 3.22.

and Weeks, 1974). The ice salinities that correspond to the estimated ice thickness range of 0 – 34 cm are between 14.2 and 7.6 g/kg. Assuming that the ice temperature is the average value of the air surface temperature and the water temperature at freezing point, we estimate the variability of ice temperature from NCEP reanalysis data. The ice temperature for the considered time period from 22nd October to 15th November takes values between -12.4 and -2.4°C.

Variability of the intensity

Ice thickness in Kaleschke et al. (2012) is retrieved using an approach for the radiation model that is based on Menashi et al. (1993). Thus, we here also use the incoherent radiation model based on Menashi et al. (1993) to simulate how the variability of ice thickness, ice temperature, and ice salinity impact brightness temperature (Figure 3.26). As the ice thickness increases from 0 to 34 cm, the brightness temperature increases by 143 K, whereas the brightness temperature increases only by 31 K for the ice temperature increasing from -12.4 to -2.4°C, and by 16 K for the ice salinity increasing from 7.6 to 14.2 g/kg. The brightness temperature change caused by the variability of the temperature corresponds to about 21%, and the brightness temperature change caused by the variability of salinity corresponds to about 11% of the brightness temperature change associated with the variability of ice thickness. Hence, according to the radiation model, the ice thickness change is the main contributor to the temporal development of the brightness temperature signal.

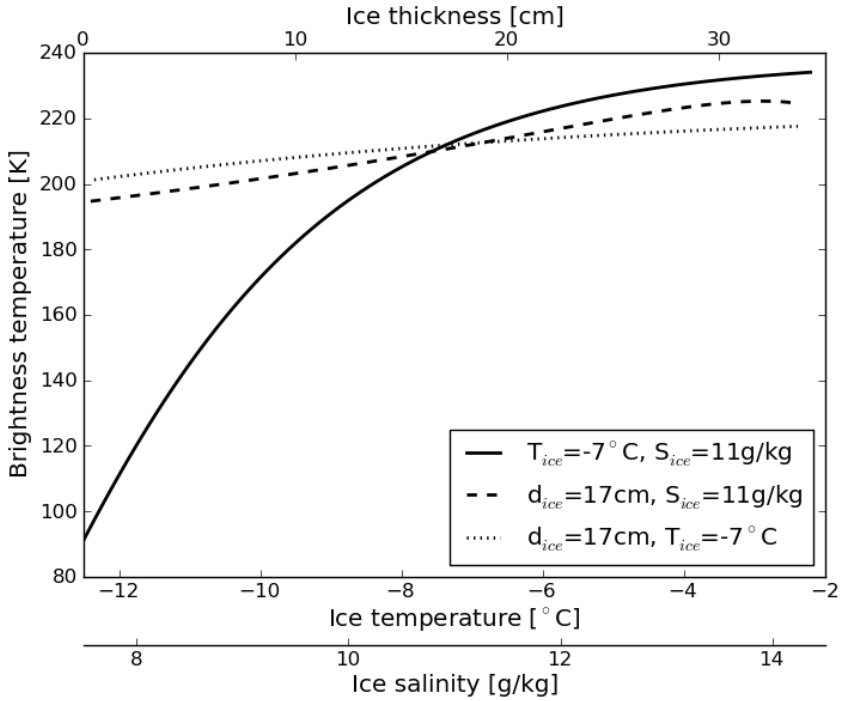

Figure 3.26: Change of brightness temperature intensity at an incidence angle θ= 30° as a function of ice thickness, bulk ice temperature, and bulk ice salinity simulated with the radiation model for one ice layer based on Menashi et al. (1993). In each case, two parameters are kept constant at an average value (see figure legend), while the remaining third parameter varies within the estimated range of values (see x-axis) for the situation in the Laptev Sea during 22nd October and 15th November, 2010.

Variability of the polarisation difference

There are attempts to retrieve ice thickness from SMOS brightness temperatures using the polarisation difference $TB_V - TB_H$ (Heygster et al., 2012). Thus, we here perform the

above described analysis also for the polarisation difference at an incidence angle θ= 30° (Figure 3.27). As the ice thickness increases from 0 to 4 cm, the polarisation difference first increases and then decreases with a further increasing ice thickness from 4 to 34 cm. Thus, the polarisation difference between about 0 and 10 cm ice thickness is not a unique function of ice thickness. The overall variability of the polarisation difference related to the change of ice thickness is 4.8 K, whereas the variabilities related to the ice temperature and salinity changes are about 3.6 K and 0.8 K, respectively. Thus, the brightness temperature changes caused by the variabilities of temperature and salinity correspond to about 74% and 16% of the brightness temperature change caused by the variability of ice thickness. The polarisation difference is hence considerably more affected by ice temperature variations than the intensity.

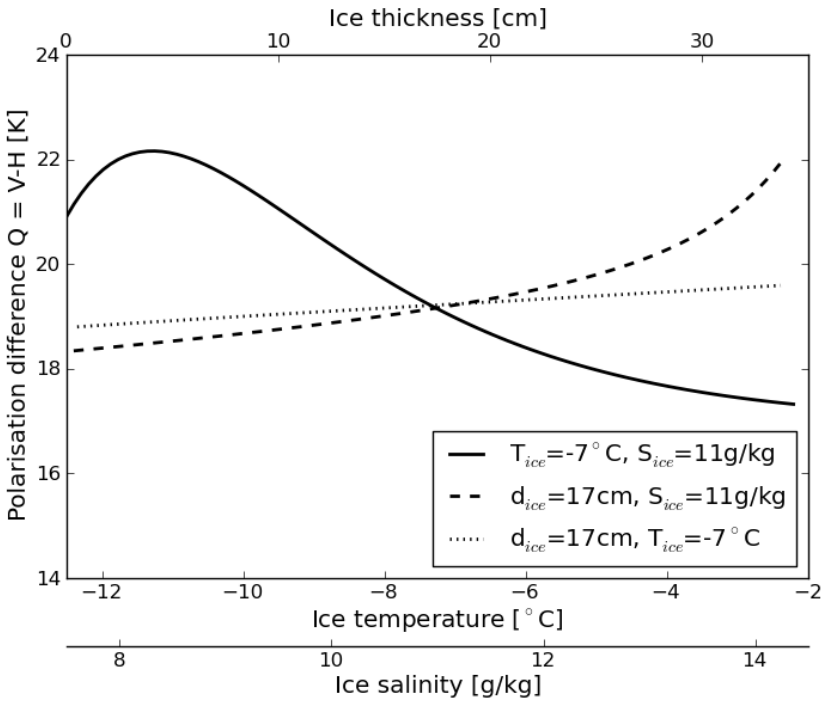

Figure 3.27: Change of brightness temperature polarisation difference at an incidence angle θ= 30° as a function of ice thickness, bulk ice temperature, and bulk ice salinity simulated with the incoherent Menashi model with one ice layer. In each case, two parameters are kept constant at an average value (see figure legend), while the remaining third parameter varies within the estimated range of values (see x-axis) for the situation in the Laptev Sea during 22nd October and 15th November, 2010.

3.4 Impact of snow

Here, we investigate the impact of a potential snow cover on brightness temperatures above sea ice. In contrast to the coherent Ulaby model, the incoherent Burke model neglects higher order reflection terms. This simplification particularly affects the modelled brightness temperatures, when the attenuation of the considered medium is low, or when the layers are thin. Dry snow is assumed to be almost transparent in L-band (e.g. Rott and Mätzler, 1987; Hall, 1996), i.e. the attenuation of dry snow is low. Thus, we need to investigate whether neglecting the higher order reflection terms is applicable, when a snow layer is considered. Therefore, we here use both the coherent Ulaby model and the incoherent Burke model to investigate the impact of snow on the modelled brightness temperatures.

In section 3.4.1, we shortly introduce the properties of snow that are important for the simulation of brightness temperatures in L-band. In section 3.4.2, we investigate the impact of the dielectric properties of snow on brightness temperatures above sea ice. First, we add a snow layer of constant thickness on top of the sea ice. Subsequently, we investigate whether the brightness temperature of snow-covered sea ice depends on the thickness of the snow layer. In section 3.4.3, we investigate how the modelled brightness temperatures above sea ice are influenced, when the ice is covered by a snow layer of typical thickness, as observed in the Arctic and in the Baltic Sea. Snow has two different effects on brightness temperatures over sea ice. Firstly, the impact by the dielectric properties of snow. Secondly, the impact by the thermal insulation of a snow cover and the resulting higher ice temperatures. We investigate these two effects of snow separately and compare their contributions with each other. In section 10.1, we compare our brightness temperatures modelled for snow-covered sea ice with brightness temperatures measured by SMOS. Finally, we investigate the potential for a retrieval of snow thickness from SMOS brightness temperatures observed over thick Arctic sea ice.

3.4.1 Properties of snow

The implementation of an additional layer in our radiation models requires information on the permittivity, the thickness, and the physical temperature of this layer. We present the empirical model we use for the snow permittivity (section 3.4.1.1), the empirical formulas we use to estimate snow thickness (section 3.4.1.2), and a simple heat conduction model that allows us to calculate the bulk temperatures of the snow layer and the snow-covered ice layer (section 3.4.1.3).

3.4.1.1 Permittivity of snow in L-band

For the snow permittivity, we use a polynomial fit obtained for snow permittivity measurements at microwave frequencies ranging between 840 MHz and 12.6 GHz. Based on these measurements, it is suggested that the permittivity of snow mainly depends on snow density and snow wetness and that the permittivity is practically independent of the structure of snow. For dry snow with a density ρ_d, the real and the imaginary part of the snow permittivity are

$$\epsilon_{R,d} = 1. + 1.7\rho_d + 0.7\rho_d^2 \tag{3.5}$$

$$\epsilon_{I,d} = 1.59 \cdot 10^6 (0.52\rho_d + 0.62\rho_d^2)(\frac{1}{f} + 1.23 \cdot 10^{-14}\sqrt{f})e^{0.036(T-273.15)} \quad , \tag{3.6}$$

where f is the frequency of the electromagnetic radiation, T is the temperature of snow in °C, and ρ_d is given in g/cm^3. (Tiuri et al., 1984)
The frequency dependence of the permittivity of wet snow is the same as that for water. Thus, the polynomial fit for the permittivity of wet snow contains the permittivity of pure water ϵ_{water}. For wet snow with a wetness by volume W_v, the real and the imaginary part of the snow permittivity are

$$\epsilon_{R,w} = \epsilon_{R,d} + (0.1W_v + 0.8W_v^2)\,\mathrm{Re}\{\epsilon_{water}\} \tag{3.7}$$

$$\epsilon_{I,w} = -(0.1W_v + 0.8W_v^2)\,\mathrm{Im}\{\epsilon_{water}\} \quad , \tag{3.8}$$

where $\mathrm{Re}\{\epsilon_{water}\}$ and $\mathrm{Im}\{\epsilon_{water}\}$ denote the real and the imaginary part of the permittivity of pure water, respectively. (Tiuri et al., 1984)
For the permittivity of pure water, we use the same equations as for the permittivity of sea water (Klein and Swift, 1977) and assume a salinity of S_{water}=0 g/kg.

3.4.1.2 Snow thickness

The snow thickness for Arctic applications is estimated from an empirical relationship between ice thickness d_{ice} and snow thickness d_{snow} (Doronin, 1971):

$$d_{snow} = 0 \text{ cm} \qquad \text{for } d_{ice} < 5 \text{ cm} \tag{3.9}$$
$$d_{snow} = 0.05 d_{ice} \qquad \text{for } 5 \text{ cm} \leq d_{ice} \leq 20 \text{ cm} \tag{3.10}$$
$$d_{snow} = 0.10 d_{ice} \qquad \text{for } d_{ice} > 20 \text{ cm}. \tag{3.11}$$

For the Baltic Sea, we use an empirical relationship based on Finnish ice breaker thickness measurements from 2006 to 2010 (Mäkynen, 2012):

$$d_{snow} = 0 \text{ cm} \qquad \text{for } d_{ice} < 6 \text{ cm} \tag{3.12}$$
$$d_{snow} = 0.22 d_{ice} - 1.3 \text{ cm} \qquad \text{for } d_{ice} \geq 6 \text{ cm}. \tag{3.13}$$

3.4.1.3 Snow temperature

Snow has a thermal insulation effect on ice. The bulk ice temperature of snow-covered sea ice is generally higher than the bulk ice temperature of bare sea ice. In order to include the effect of thermal insulation by snow, we here assume a balance of heat fluxes at the snow-ice-interface. We account for the different thermal conductivities of ice and snow to calculate the bulk temperature of the snow layer and the snow-covered ice layer. We assume that the temperature at the bottom of the ice is at the freezing point of water (i.e. T_{bottom}= T_{water}= -1.8°C for Arctic and T_{bottom}= T_{water}= -0.3°C for Baltic conditions), and that the temperature gradients within ice and snow are linear. We assume that at the snow-ice-interface the ice temperature equals the snow temperature: $T_{ice}(z = d_{ice})$= $T_{snow}(z = d_{ice})$= T_{si} with T_{si} being the snow-ice-interface temperature, and d_{ice} being the ice thickness. Here, z denotes the vertical distance from the ice-water-interface. Thus, z is z= 0 at the ice-water-interface, $z = d_{ice}$ at the snow-ice-interface, and $z = d_{ice} + d_{snow}$ at the snow surface. We assume that thermal conduction is continuous through the snow-ice-interface (Maykut and Untersteiner, 1971):

$$k_{ice}\gamma_{ice}(z = d_{ice}) = k_{snow}\gamma_{snow}(z = d_{ice}) \ , \tag{3.14}$$

where

$$\gamma_{ice}(z^*) = \left.\frac{\partial T_{ice}(z)}{\partial z}\right|_{z=z^*} \tag{3.15}$$
$$\gamma_{snow}(z^*) = \left.\frac{\partial T_{snow}(z)}{\partial z}\right|_{z=z^*} \ , \tag{3.16}$$

and k_{ice} and k_{snow} are the thermal conductivities of ice and snow, respectively. Because we assume linear temperature gradients within the ice and the snow layer, $\gamma_{ice}(z) = \gamma_{ice}$ and $\gamma_{snow}(z) = \gamma_{snow}$ are constant values. The surface temperature T_{surf} and the snow-ice-

interface temperature T_{si} are then described by

$$T_{surf} = T_{si} + \gamma_{snow} d_{snow} \tag{3.17}$$
$$T_{si} = T_{water} + \gamma_{ice} d_{ice} \quad . \tag{3.18}$$

If we know the surface temperature T_{surf}, we can solve this system of equations with the three equations (3.14), (3.17), and (3.18) and the three unknowns γ_{ice}, γ_{snow}, and T_{si}. The bulk ice and snow temperatures T_{ice} and T_{snow} are then

$$T_{ice} = 0.5(T_{si} + T_{water}) \tag{3.19}$$
$$T_{snow} = 0.5(T_{si} + T_{surf}) \quad . \tag{3.20}$$

For the thermal conductivity of snow we use a constant climatological value of k_{snow}= 0.31 $\frac{\mathrm{W}}{\mathrm{mK}}$ (Yu and Rothrock, 1996), and for the thermal conductivity of ice we use a parameterisation accounting for ice temperature and salinity (Untersteiner, 1964):

$$k_{ice} = 2.034 \frac{\mathrm{W}}{\mathrm{Km}} + 0.13 \frac{\mathrm{W}}{\mathrm{kgm^2}} \frac{S_{ice}}{T_{ice} - 273.} \quad . \tag{3.21}$$

To simplify the calculations we use the mean temperature of the snow and ice column T_{mean}=0.5(T_{surf}+T_{water}) instead of the ice temperature T_{ice} in equation (3.21).
From equations (3.14), (3.17), and (3.18) we get the following expressions for the ice and snow temperatures:

$$T_{ice} = T_{water} + \frac{1}{2} K (T_{surf} - T_{water}) k_{snow} d_{ice} \tag{3.22}$$
$$T_{snow} = \frac{1}{2} (T_{water} + T_{surf} + K (T_{surf} - T_{water}) k_{snow} d_{ice}) \tag{3.23}$$

where $K = (k_{ice} d_{snow} + k_{snow} d_{ice})^{-1}$.

3.4.2 Impact of dielectric properties of snow

As a first test, we implement a very thin and a rather thick snow layer on top of the sea ice in our radiation models. Thereafter, we investigate how the thickness of the snow layer impacts the modelled brightness temperatures. Here, we account only for the dielectric properties of the snow layer and use equations (3.5) – (3.8) to calculate the snow permittivity.

3.4.2.1 Impact of a snow layer with constant thickness

We compare the effect of a 1 mm and a 50 cm thick snow layer on the brightness temperatures as modelled with the incoherent Burke model and as modelled with the coherent Ulaby model. Regarding the coherent Ulaby model, we have to take into account that the coherent brightness temperature signal oscillates with the thickness of the considered layers. When we add a snow layer on top of the ice layer, these oscillations occur for both the variation of the ice layer thickness and the variation of the snow layer thickness. If we add a snow layer with a fixed thickness on top of the sea ice, the resulting brightness temperature represents the brightness temperature at a certain phase of this coherent oscillation. The resulting brightness temperature thus corresponds to the brightness temperature caused by the considered specific combination of the snow layer and the ice layer thickness, but the brightness temperature is not necessarily representative for snow layers with similar thicknesses. Thus,

when modelling a 50 cm thick snow layer with the coherent Ulaby model, we perform the simulation for each ice thickness for a range of snow thicknesses around 50 cm and take the average brightness temperature as a representative value. At nadir, the period of the coherent oscillation is half the electromagnetic wavelength in the medium. We model L-band brightness temperatures for a wavelength in vacuum of about λ_0= 21 cm. The wavelength in snow is λ_{snow}= $\frac{\lambda_0}{\sqrt{\epsilon_{snow}}}$. Thus, we perform the simulations for d_{snow}= 50 cm $\pm$ $\frac{1}{2}\frac{\lambda_{snow}}{2}$ (i.e. for $d_{snow} \approx$ 50 cm $\pm$ 4.05 cm).
We do the simulations for typical Arctic sea ice conditions. Water salinity is assumed to be S_{water}= 30 g/kg, and water temperature is at the corresponding freezing temperature T_{water}= -1.8°C. Bulk ice salinity is assumed to be S_{ice}= 8 g/kg, and the surface temperature is T_{surf}= -15°C.

Results for dry snow
Here, we consider a layer of dry snow with a density of ρ_{snow}= 350 kg/m^3 and a wetness of W_v= 0%. According to the coherent Ulaby model, the very thin layer of dry snow (d_{snow}= 1 mm) has a negligible effect on brightness temperatures above sea ice at nadir view, as well as for both horizontal and vertical polarisation at an incidence angle θ= 50° (Figures 3.28 to 3.30). For the 50 cm thick snow layer of dry snow, brightness temperatures increase at nadir view, and at an incidence angle θ= 50° at horizontal polarisation, whereas the brightness temperatures at θ= 50° at vertical polarisation are unaffected by the snow layer.
According to the incoherent Burke model, brightness temperatures at nadir view and at θ= 50° at horizontal polarisation increase already for a snow layer of 1 mm thickness. For snow layer thicknesses of dry snow as considered here (d_{snow}= 1 mm and d_{snow}= 50 cm), the brightness temperatures modelled with the incoherent Burke model are independent of snow layer thickness. In accordance with the coherent Ulaby model, brightness temperatures at vertical polarisation are not influenced by a snow layer, neither for d_{snow}= 1 mm, nor for d_{snow}= 50 cm.
For both models, the brightness temperature increase at nadir view and at θ=50° at horizontal polarisation is higher for thicker ice than for thinner ice. Thus, the snow layer impacts the maximum brightness temperature that is reached, when the brightness temperature signal saturates for thick ice. In both models, for d_{snow}= 50 cm the maximum brightness temperature (averaged over the oscillations) increases by about 10 K at nadir view and by 25 K at θ= 50° at horizontal polarisation as compared to snow-free ice.
For comparison, at nadir view, the brightness temperature of an infinitely thick layer of ice would be about 240 K, while the brightness temperature of an infinitely thick layer of snow would be about 260 K. The corresponding snow-covered thick ice here has a brightness temperature of 250 K (for both models). At an incidence angle θ= 50° at horizontal polarisation, the brightness temperature of an infinitely thick layer of ice would be about 210 K, while the brightness temperature of an infinitely thick layer of snow would be about 250 K. The corresponding snow-covered thick ice here has a brightness temperature of 235 K (for both models). At vertical polarisation, the brightness temperature of an infinitely thick layer of ice would be about 260 K, and 265 K for an infinitely thick layer of snow. Thus, brightness temperatures modelled for snow-covered sea ice at nadir view and at horizontal polarisation take approximately the average value of the brightness temperatures over infinitely thick bare sea ice and over infinitely thick dry snow. At vertical polarisation, these two values are very similar and our models show no impact on brightness temperatures, when we add a layer of dry snow of up to 50 cm thickness.

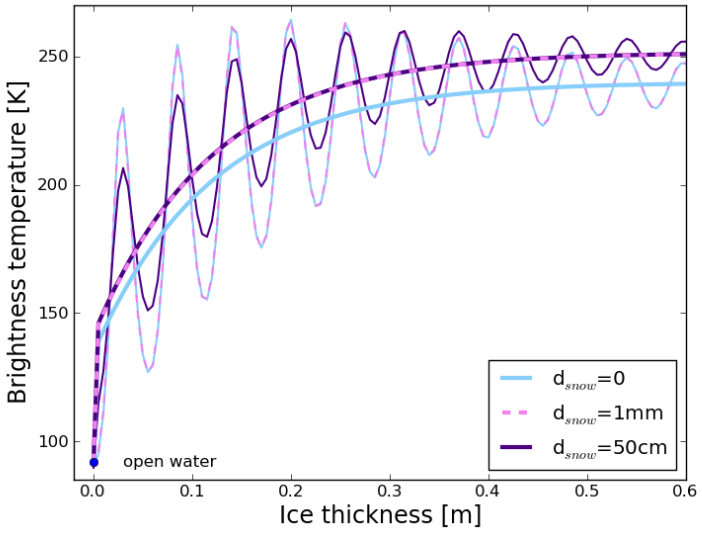

Figure 3.28: Brightness temperature at nadir view as a function of ice thickness according to the incoherent Burke model (thick lines) and the coherent Ulaby model (thin lines) for three different scenarios with dry snow (ρ_{snow}= 350 kg/m^3, W_v= 0%): 1) The light blue curves show the brightness temperatures as modelled for snow-free sea ice, 2) the pink dashed curves show the brightness temperatures as modelled for sea ice covered with a 1 mm thick snow layer, and 3) the purple curves show the brightness temperatures as modelled for sea ice covered with a 50 cm thick snow layer (average over d_{snow}= 50 cm $\pm$ 4.05 cm). The model assumptions are: S_{water}= 30 g/kg, S_{ice}= 8 g/kg, T_{surf}= -15°C, T_{water}= -1.8°C.

Results for wet snow

For comparison, we here consider a snow layer with a higher density than in the previous case (here: ρ_{snow}= 500 kg/m^3) and a volumetric fraction of 5% of liquid water (W_v= 5%), called wet snow in our study. We show only the results for brightness temperatures at nadir view (Figure 3.31). According to the coherent Ulaby model, a very thin layer (d_{snow}= 1 mm) of wet snow has a negligible effect on brightness temperatures at nadir view. For the incoherent Burke model, brightness temperatures increase, when we add a 1 mm thick layer of wet snow on top of the ice. The resulting brightness temperatures for the 1 mm thick layer of wet snow are very similar to the brightness temperatures we obtained for dry snow. For the 50 cm thick layer of wet snow brightness temperatures increase considerably in both models. The brightness temperatures reach quite quickly the maximum brightness temperature value of 250 K, which corresponds to the brightness temperature of an infinitely thick layer of wet snow.

3.4.2.2 Impact of an increasing snow thickness

In the previous section, we found that brightness temperatures of snow-covered sea ice with different ice thicknesses and a layer of dry snow of constant thickness are not affected by an increase of the snow layer thickness from 1 mm to 50 cm, when modelled with the incoherent Burke model. We investigate whether brightness temperatures over sea ice with a constant ice thickness depend on the thickness of the snow layer. We use the coherent Ulaby and the incoherent Burke model to simulate brightness temperatures above an ice layer with thickness d_{ice}= 4 m that is covered by a snow layer whose thickness increases from 0 to 1 m

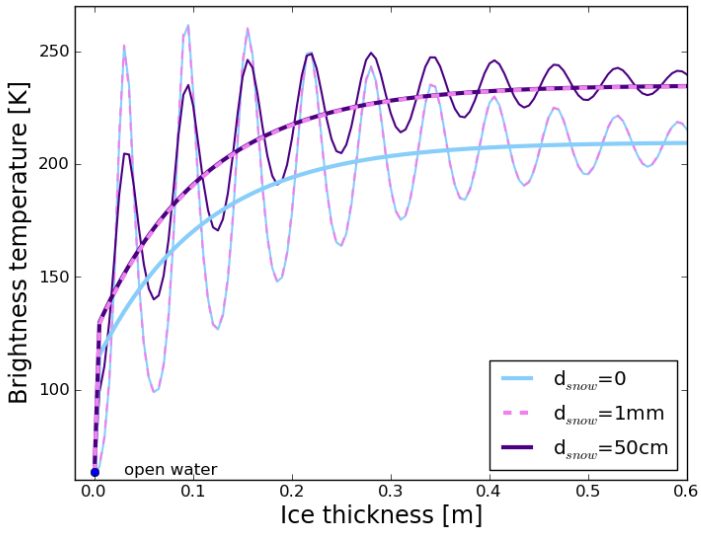

Figure 3.29: For figure description see caption of Figure 3.28, but here we show the results for horizontally polarised brightness temperatures at an incidence angle θ= 50°.

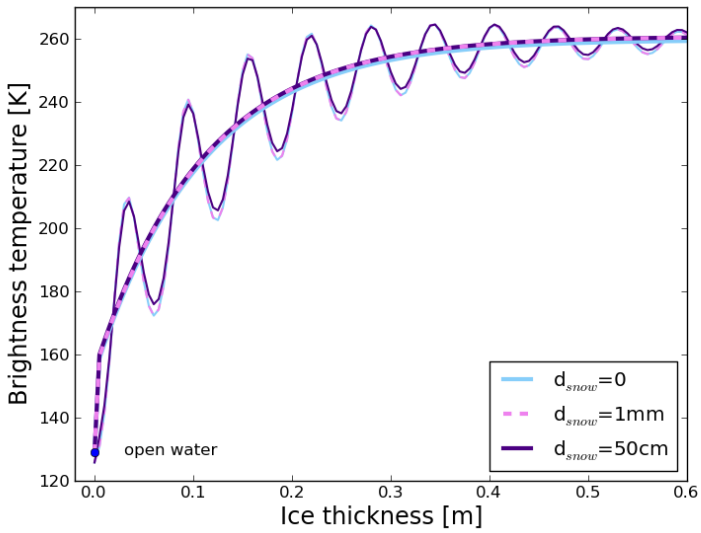

Figure 3.30: For figure description see caption of Figure 3.28, but here we show the results for vertically polarised brightness temperatures at an incidence angle θ= 50°.

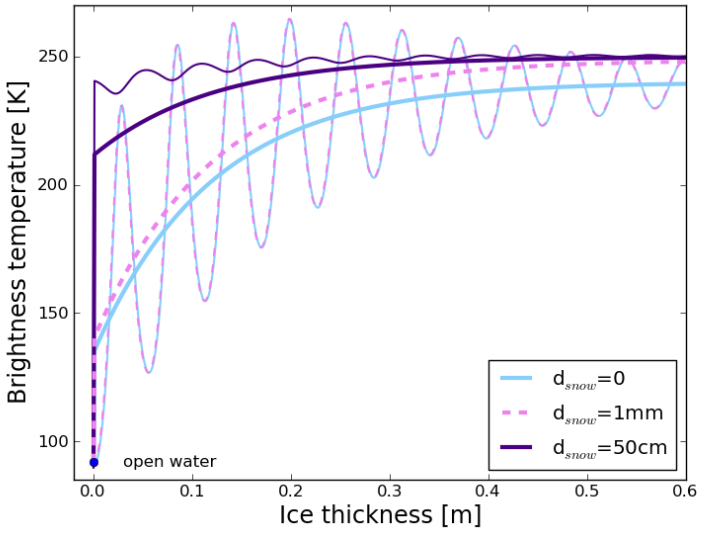

Figure 3.31: For figure description see caption of Figure 3.28, but here we show the results for wet snow (ρ_{snow}= 500 kg/m^3, W_v= 5%).

for wet snow and from 0 to 100 m for dry snow, respectively. As in the previous section, we here perform the simulations for every snow thickness for a range of ice thicknesses around the chosen constant value of d_{ice}= 4 m (here: average over d_{ice}= 4 m $\pm$ 2.625 cm). We simulate brightness temperatures for nadir view and for an incidence angle θ= 50° at horizontal and at vertical polarisation. The model assumptions are the same as in the previous section.

Results

For dry snow conditions, the incoherent brightness temperature and the average value of the coherent brightness temperature depend only very slightly on snow thickness for all incidence angles and polarisations (Figure 3.32(a)). The corresponding brightness temperatures of infinitely thick ice are 260 K at nadir view, 250 K at θ= 50° at horizontal polarisation, and 265 K at θ= 50° at vertical polarisation. With increasing snow thickness the incoherent brightness temperatures and the average values of the coherent brightness temperatures increase towards these values. However, the slope is very flat; for an increase of snow thickness from 0 to 10 m, the brightness temperatures increase only by 1.3 K, 2.7 K, and 0.7 K at nadir view, horizontal polarisation at θ= 50°, and vertical polarisation at θ= 50°, respectively. For wet snow conditions, brightness temperatures of infinitely thick ice are already reached for thinner snow layers than under dry snow conditions (Figure 3.32(b)). Thus, the brightness temperature increase is slightly higher for smaller snow thicknesses. For an increase of snow thickness from 0 to 1 m, brightness temperatures increase by 1.4 K, 1.9 K, and 0.8 K at nadir view, horizontal polarisation at θ= 50°, and vertical polarisation at θ= 50°, respectively. However, the dependence of brightness temperature on snow thickness is still very small.

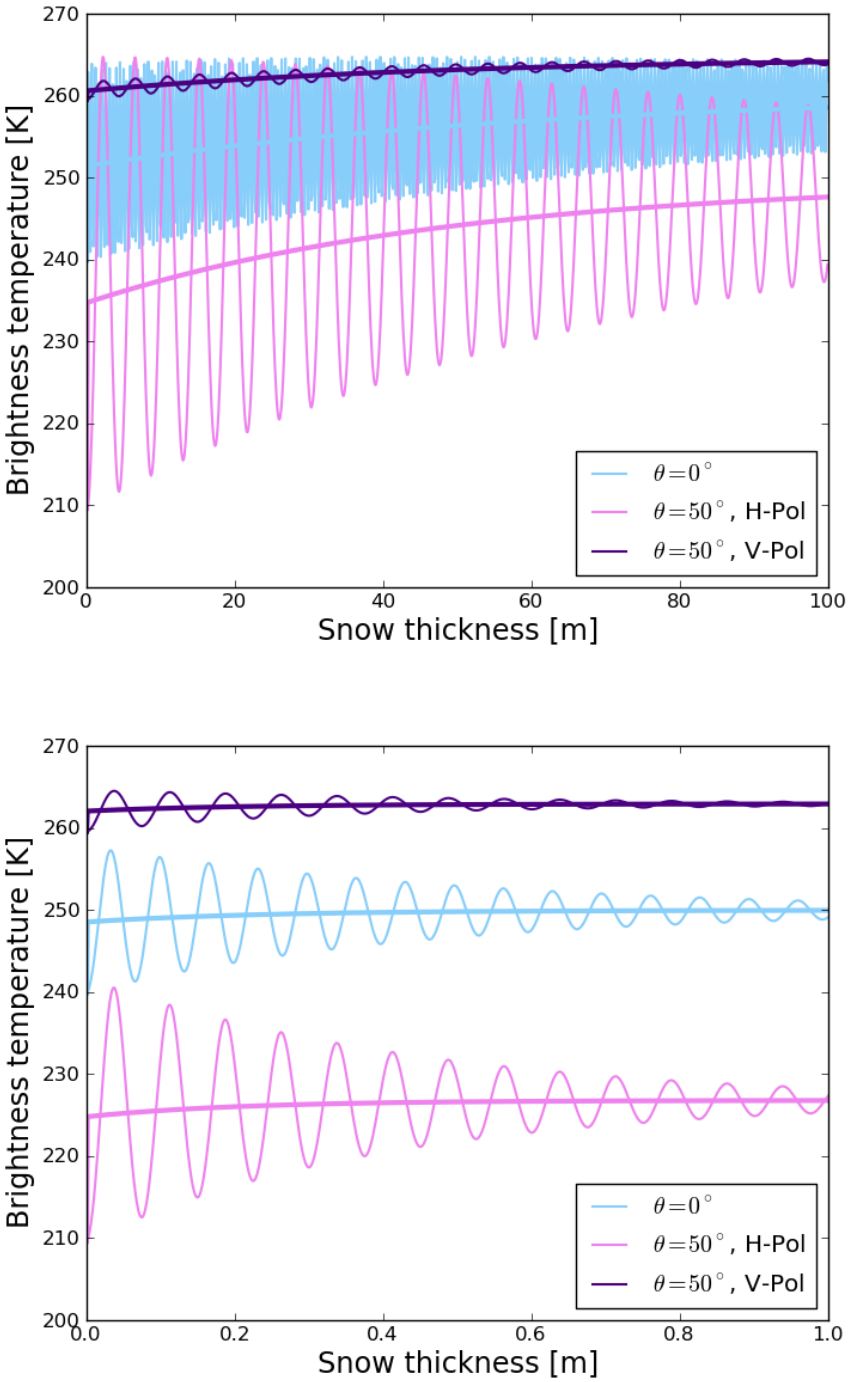

Figure 3.32: Brightness temperature over a constant ice thickness d_{ice}= 4 m (average over d_{ice}= 4 m $\pm$ 2.625 cm) as a function of snow thickness according to the coherent Ulaby (thin line) and the incoherent Burke model (thick line). We show the results for nadir view, and for horizontal and vertical polarisation at an incidence angle θ= 50°. The upper figure shows the results for dry snow (ρ_{snow}= 350 kg/m^3, W_v= 0%), and the lower figure for wet snow (ρ_{snow}= 500 kg/m^3, W_v= 5%). Note the different range of snow thicknesses at the x-axes. The model assumptions are: S_{water}= 30 g/kg, S_{ice}= 8 g/kg, T_{surf}= -15°C, T_{water}= -1.8°C.

3.4.3 Comparison of the impact by thermal insulation and by dielectric properties of snow

We investigate the impact of a snow layer with a realistic thickness on brightness temperatures over sea ice. We simulate brightness temperatures for typical snow thicknesses as observed in the Arctic and in the Baltic Sea (see section 3.4.1.2). For Arctic conditions water salinity is assumed to be S_{water}= 30 g/kg and the surface temperature is assumed to be T_{surf}= -15°C; for Baltic conditions we assume S_{water}= 6 g/kg and T_{surf}= -10°C. Water is again assumed to be at freezing temperature, thus T_{water}= -1.8°C for Arctic and T_{water}= -0.3°C for Baltic conditions, respectively. Simulations are performed for brightness temperatures at nadir view and at an incidence angle θ= 50° at horizontal and at vertical polarisation. In order to investigate the impact of the snow cover on the brightness temperatures due to the dielectric properties of snow separately from the impact due to the thermal insulation effect of snow, we compare three different scenarios for the brightness temperature as a function of ice thickness:

1. Bare sea ice without a snow cover.

2. Sea ice covered with snow, where snow thickness is an empirical function of ice thickness, as given in the equations (3.9) – (3.13). Bulk snow and ice temperatures are as calculated from equations (3.23) and (3.22), respectively.

3. Bare sea ice without a snow cover, but a bulk ice temperature as if the thermal insulation effect of snow was present. To calculate the bulk ice temperature, we use equation (3.22), the snow thickness being the same as in 2.

Results

The results of our investigations for a dry snow layer with a density of ρ_d= 350 kg/m^3 and a wetness W_v= 0% are shown in Figures 3.33 to 3.35. Due to the steps in the equations that relate snow thickness and ice thickness (given in section 3.4.1.2), we observe jumps in the incoherent brightness temperature signal, while the coherent brightness temperature oscillations for snow-covered sea ice consist of two oscillations that are superimposed. One oscillation is caused by variation of ice thickness, while the other is caused by snow thickness variation. Because snow and ice thickness are related via an empirical relationship, we obtain two oscillations that appear to have two different periods in terms of the ice thickness. At nadir, the oscillations have a period of half the wavelength of the electromagnetic radiation in the medium. Here, we consider L-band radiation with a wavelength in vacuum of about λ_0= 21 cm. The wavelength in sea ice is λ_{ice}= $\frac{\lambda_0}{\sqrt{\epsilon_{ice}}}$. Thus, at nadir view, the maximum amplitudes of the oscillations caused by increasing ice thickness occur about every $\frac{\lambda_{ice}}{2} \approx$ 5.25 cm of ice thickness increase for typical Arctic conditions. The period of the additional oscillations caused by the snow layer at nadir view is also half the wavelength within the medium. The wavelength in snow is λ_{snow}= $\frac{\lambda_0}{\sqrt{\epsilon_{snow}}}$. Thus, the oscillation period in snow is about 8.1 cm at nadir view for typical Arctic conditions. However, the snow thickness is only about 10% of the ice thickness for Arctic conditions, and about 20% of the ice thickness for Baltic conditions. The brightness temperatures here are shown as a function of ice thickness. Thus, at nadir view, the maximum amplitudes of the superimposed oscillations caused by the increasing snow layer thickness occur only about every 10 × 8.1 cm= 81.0 cm (Arctic conditions), or about every 5 × 8.1 cm= 40.05 cm (Baltic conditions) of ice thickness increase. We state that, although the incoherent Burke model neglects higher order reflection terms,

the modelled brightness temperatures represent the average values of the coherent oscillations as modelled with the coherent Ulaby model. For all considered cases (Arctic and Baltic conditions, nadir view, and θ= 50° at horizontal and at vertical polarisation) a snow layer causes the modelled brightness temperatures to increase. Under Baltic conditions, the higher ice temperatures caused by the thermal insulation effect of snow contribute more to this brightness temperature increase than under Arctic conditions. The main reason for this is that, according to the empirical relationship used here, the snow layer on Baltic sea ice is thicker than the snow layer on Arctic sea ice. The thickness of the snow thus has an impact on brightness temperatures, although in the previous section, we found that the thickness of the snow layer does not impact brightness temperatures, if we consider only the dielectric properties of snow. However, a thicker snow layer has a higher insulation effect and thus the bulk ice temperature under a thick snow layer is higher than under a thin snow layer.
At nadir view, the thermal insulation effect contributes to approximately half of the brightness temperature increase under Baltic conditions (Figure 3.33(b)). The temperature contribution is higher for small ice thicknesses and declines with increasing ice thickness. Under Baltic conditions, at horizontal polarisation (θ= 50°) the relative contribution of the increased ice temperature to the overall brightness temperature increase is smaller than at nadir view (Figure 3.35(a)). At vertical polarisation, the increased ice temperature under the snow cover is solely responsible for the brightness temperature increase (Figure 3.35(b)). For Arctic conditions, our models give very similar results. However, as mentioned before, the impact by thermal insulation and thus the overall impact is smaller than under Baltic conditions (Figures 3.33(a) and 3.34). We do not show the results for wet snow (ρ_d= 500 kg/m^3 and W_v= 5%) here. However, they are very similar to the presented results for dry snow.

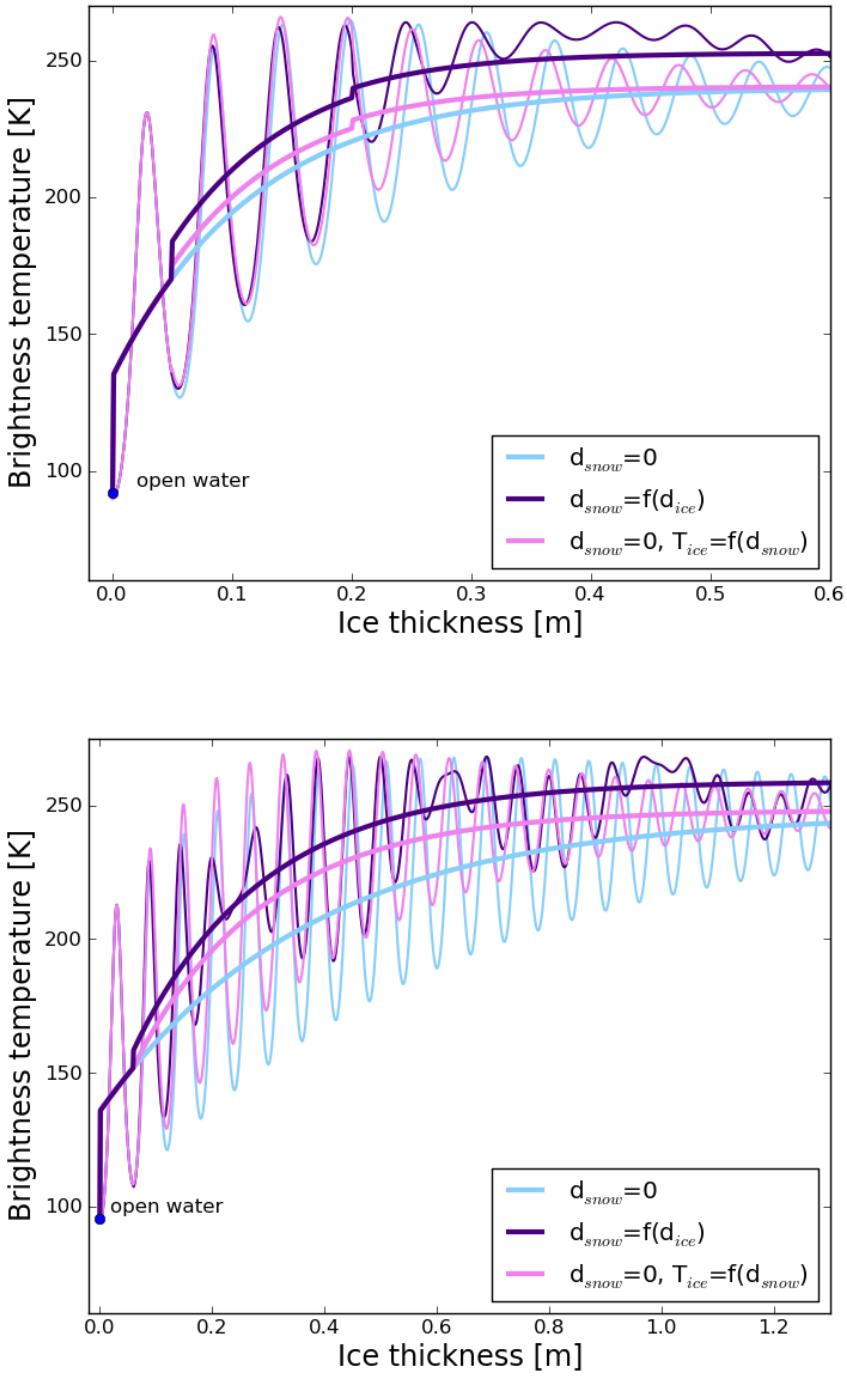

Figure 3.33: Brightness temperature at nadir view as a function of ice thickness according to the incoherent Burke model (thick lines) and the coherent Ulaby model (thin lines) for three different scenarios with dry snow (ρ_{snow}= 350 kg/m^3, W_v= 0%): 1) The light blue curves show brightness temperatures as modelled for snow-free sea ice, 2) the purple curves show brightness temperatures as modelled for snow-covered sea ice, and 3) the pink curves show brightness temperatures as modelled for snow-free sea ice with ice temperatures, as if the snow cover was present (see section 3.4.3). The upper figure shows the results for Arctic conditions (S_{water}= 30 g/kg, S_{ice}= 8 g/kg, T_{surf}= -15°C, T_{water}= -1.8°C), the lower figure for Baltic conditions (S_{water}= 6 g/kg, S_{ice}= 1 g/kg, T_{surf}= -10°C, T_{water}= -0.3°C).

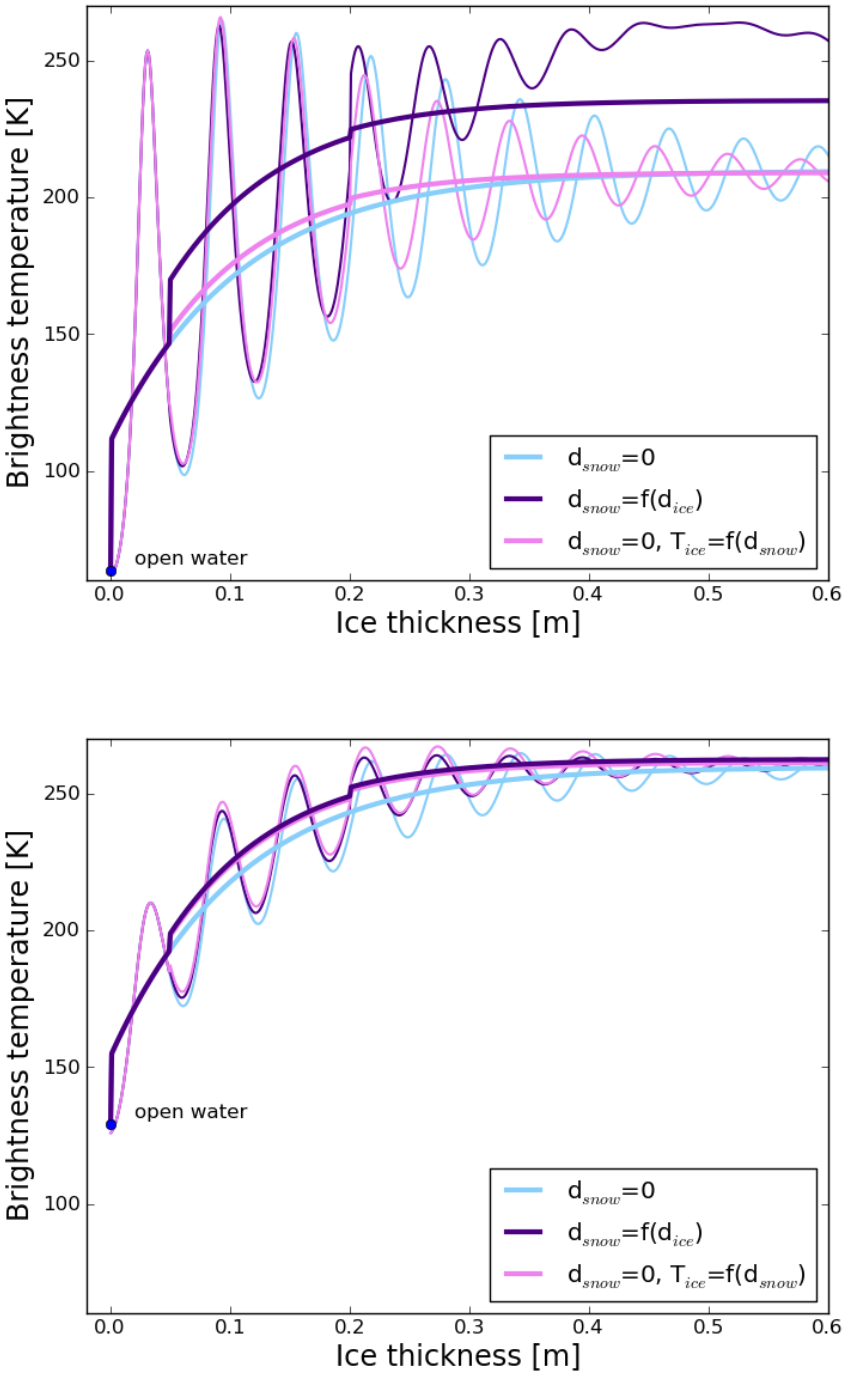

Figure 3.34: Horizontally polarised (upper figure) and vertically polarised (lower figure) brightness temperature at an incidence angle θ= 50° as a function of ice thickness according to the incoherent Burke model (thick lines) and the coherent Ulaby model (thin lines) for three different scenarios with dry snow (ρ_{snow}= 350 kg/m^3, W_v= 0%): 1) The light blue curves show brightness temperatures as modelled for snow-free sea ice, 2) the purple curves show brightness temperatures as modelled for snow-covered sea ice, and 3) the pink curves show brightness temperatures as modelled for snow-free sea ice with ice temperatures, as if the snow cover was present (see section 3.4.3). Here, we show the results for Arctic conditions (S_{water}= 30 g/kg, S_{ice}= 8 g/kg, T_{surf}= -15°C, T_{water}= -1.8°C).

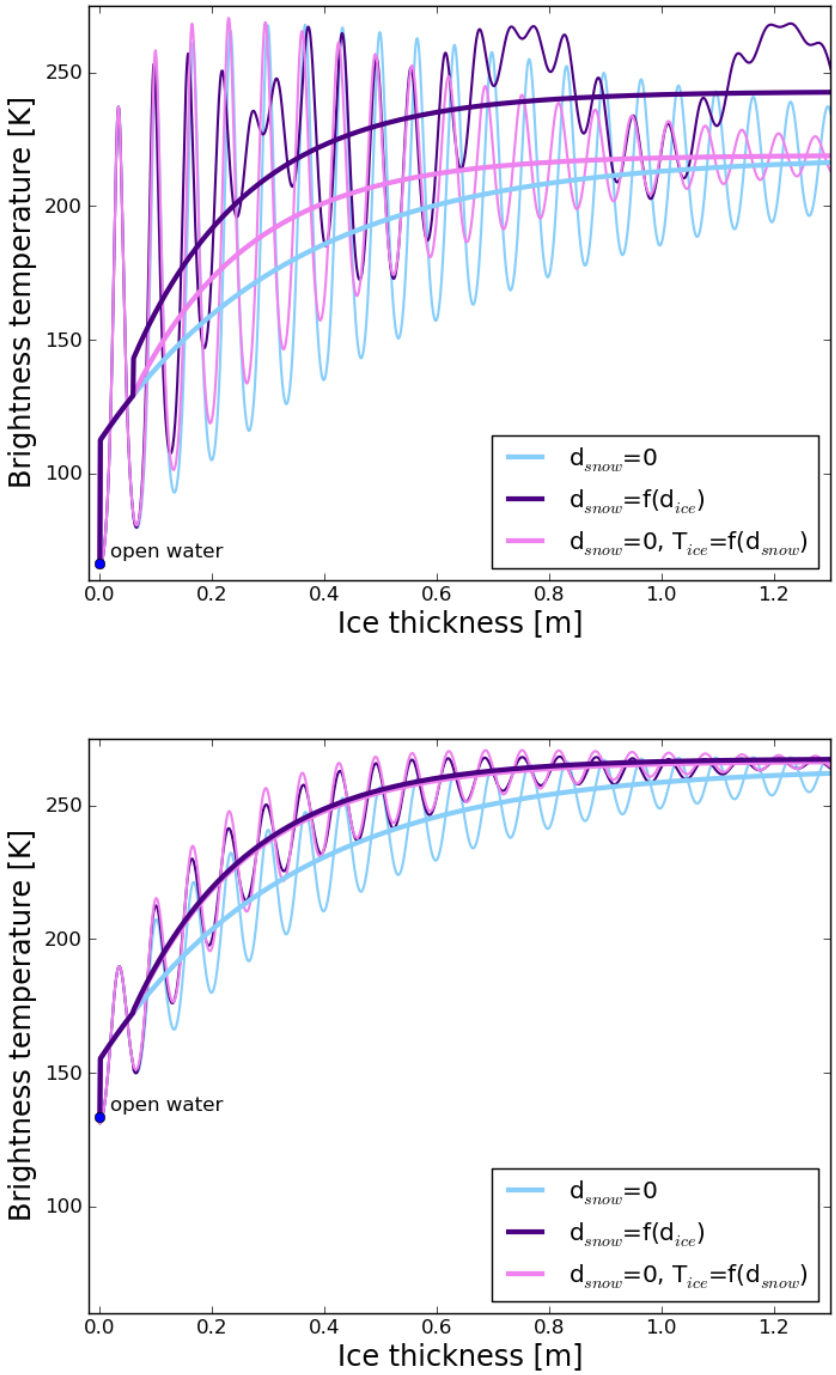

Figure 3.35: For figure description see caption of Figure 3.34, but here we show the results for Baltic conditions (S_{water}= 6 g/kg, S_{ice}= 1 g/kg, T_{surf}= -10°C, T_{water}= -0.3°C).

3.5 Summary and Discussion

Conditions for a linear temperature gradient
We used a simple heat conduction model and simulated temperature changes at the ice surface. The surface temperature took values between -2 and -30°. We found that even for sudden large changes of the ice surface temperature, the temperature distribution within ice adjusted to the new situation within a time scale of hours for ice thicknesses of 50 cm and 1 m. Sudden large changes of the ice surface temperature caused temperature gradients in ice to be highly non-linear. The brightness temperatures over 50 cm thick ice with such non-linear temperature gradients differed by up to 6.8 K from the corresponding brightness temperatures over linear temperature gradients, if the ice surface temperature was assumed to be equal in both cases. However, according to our simple heat conduction model, ice temperatures within the 50 cm thick ice adjusted quite quickly to the new temperature conditions. Two hours after the surface temperature change, brightness temperature differences were below 4.3 K, and two more hours later below 3.1 K for all cases considered here. After more than about eight hours, brightness temperature differences were less than 0.5 K.
These results reflect maximum deviations, because the ice considered here is 50 cm thick, and thus represents the maximum retrievable ice thickness for Arctic conditions; for thinner ice a linear temperature gradient would be achieved even more rapidly after changes of the ice surface temperature. Furthermore, the temperature changes considered here were quite large and are probably less pronounced in most cases observed in nature, particularly for ice covered by an insulating snow layer.
For an ice column of 50 cm thickness, the temperature gradient within ice can reasonably well be assumed to be linear for our purposes, because the time the ice temperature needs to adjust to changing conditions at the surface is in the same order of magnitude as the expected temporal deviation between SMOS measurements and possibly available surface temperature information.

Bulk ice temperature vs. linear temperature gradient
As a first test, we simulated brightness temperatures for an increasing number of layers within an isothermal ice column. For a constant ice temperature in all layers, we expected brightness temperatures to be independent of the number of layers within ice. This expectation was confirmed by the coherent Ulaby model. However, brightness temperatures as simulated with the incoherent Burke model decreased with an increasing number of layers in ice. The reason for this obviously unphysical behaviour of the incoherent Burke model is that this model is calculated from the solution of the radiative transfer equation and neglects higher order reflection terms. Thus, every additional layer within the ice leads to the disregard of that part of the radiation that is associated with multiple reflections and refractions at the different layer boundaries. The Burke model has been widely used for soil moisture applications with multiple layers in the past (e.g. Jackson and O'Neill, 1986; Goodberlet and Mead, 2012). There are mainly two reasons why neglecting the higher order reflection terms is more applicable for describing radiation in soils than in sea ice: 1) Both the real and the imaginary part of the permittivity can take higher values in soils as compared to sea ice. Higher values of the permittivity's imaginary part indicate higher attenuation within the medium, and after multiple reflections only a small fraction of the radiation's original energy is preserved. Higher values of the permittivity's real part also reduce the impact of the higher order reflection terms. 2) The range of permittivities that is associated with different soil types, soil temperatures, and moisture contents is broader than the range of values sea ice

takes for different ice conditions. The reflectivity between two media whose permittivities differ distinctly is higher than the reflectivity between two media with similar permittivities. The higher reflectivity results in a higher fraction of the original radiation to be reflected at the first interface between two layers. This reflection at the first interface is described by the first-order reflection term. Thus, neglecting higher order reflection terms influences modelled brightness temperatures less, if the considered layers differ more in their dielectric properties, i.e. in their permittivities. Furthermore, the more the dielectric properties within the considered medium differ from each other, the more important it is to account for the different properties of the layers, instead of reducing the number of layers in order to minimize the impact of neglecting the higher order reflection terms. Thus, the Burke model is more suitable for modelling radiation in and above soil layers than in and above sea ice. For sea ice applications, the Burke model can be unsuitable, if more than one layer within the ice is considered.

Thus, we used the coherent Ulaby model for the further investigations regarding the difference between the implementation of a temperature gradient and of a bulk ice temperature in the model. According to the coherent Ulaby model, brightness temperatures for multiple ice layers and a linear temperature gradient in the ice were on average about 5 K higher than brightness temperatures for one ice layer and a bulk ice temperature. We showed that one reason for this is the non-linear relationship between ice temperature and ice permittivity, because the ice permittivity that is related to the average ice temperature (= the bulk ice temperature for the one-ice-layer-model) is not equal to the average ice permittivity of the temperature profile. Thus, we introduced a value for the ice permittivity that was obtained from the ice permittivity profile associated with the considered temperature profile. Using this value in the model with one ice layer and a bulk ice temperature improved the model performance towards the results for the multiple layer model and a temperature gradient, if the ice surface temperature was T_{surf}= -15°C, but not if the ice surface temperature was T_{surf}= -5°C.

Thus, this approach was a first step towards an improvement of a radiation model that uses only one ice layer. Due to the more time-consuming calculations associated with a model with multiple layers, a model with only one ice layer would be preferred for an ice thickness retrieval using SMOS data. However, here we did not take into account the salinity variations within the ice column; ice salinity was assumed to be constant over the ice column. Various forms of salinity profiles in ice have been observed (e.g. Weeks and Lee, 1962; Cox and Weeks, 1974), often for example a C-shaped salinity profile with higher ice salinities near the surface and near the bottom of the ice column, and lower salinities in the middle parts of the ice column. The ice permittivity, as calculated here, depends on the brine volume fraction, which depends on ice temperature and salinity. Thus, even if we introduced an ice permittivity value for the one-ice-layer-model that is more representative with regard to ice temperature variation within ice, we would not account for ice salinity variation in ice. Furthermore, the coherent Ulaby model accounts for different ice permittivities due to different temperatures in the ice layers. However, the temperature of the ice column is assumed to be constant over the considered ice layers (see equation (2.6)), and we used the average ice temperature for the calculations, thus introducing a probably small but not determined uncertainty to the investigations. Hence, we suggest that further investigations towards the determination of a representative value for the ice permittivity are needed, in order to improve the performance of a radiation model with one ice layer and bulk values for ice temperature and salinity.

Sensitivity to ice temperature and salinity

In order to investigate the sensitivity of brightness temperature to ice temperature and salinity, we here differentiated the brightness temperature function as obtained from the incoherent Burke model with respect to ice temperature, ice salinity, and ice thickness. We considered the corresponding derivatives for four different ice thicknesses and three different incidence angles. For the remaining parameters we assumed typical values.

We found that for all ice temperatures and all ice salinities, brightness temperatures increase with increasing ice thickness. Thus, if ice temperature and salinity are known, brightness temperature is a unique function of ice thickness, and we can retrieve the ice thickness from the observed brightness temperature for all ice temperatures and salinities. As expected, brightness temperature sensitivity to ice thickness was higher for thinner ice than for thicker ice.

Regarding the sensitivity of brightness temperature to ice temperature, we found that the sensitivity is higher for thinner ice than for thicker ice. According to our calculations, brightness temperatures first increased with increasing ice temperature, but started to decrease with a further increasing ice temperature, when a certain ice temperature was reached. This critical ice temperature depended on ice thickness and was higher for thinner ice than for thicker ice. For Arctic conditions at nadir view, the reversal point occurred at T_{surf}= -2.8°C for an ice thickness of 15 cm, and at T_{surf}= -9.6°C for an ice thickness of 60 cm, respectively.

A possible reason why we observed this reversal point is that the brightness temperature, which is defined as the physical temperature times the emissivity, is dominated by temperature for lower ice temperatures and by emissivity for higher ice temperatures. For colder conditions, the increasing ice temperature dominates and causes the brightness temperature to increase, while, for warmer ice conditions, the decreasing ice emissivity dominates and causes the brightness temperature to decrease. For warmer conditions, the brine volume fraction within ice increases more rapidly with increasing ice temperature than for colder conditions. Thus, an increasing ice temperature under warm conditions modifies the permittivity of ice more strongly by increasing both the phase constant and the attenuation constant.

Regarding the brightness temperature sensitivity to ice salinity, we found that for low ice salinities, brightness temperatures strongly increased with increasing ice salinity. The rate of increase reduced rapidly with further increasing salinity until it reached very low values. For thicker ice this value was even slightly negative, i.e. brightness temperatures decreased with increasing ice salinity. Except for ice salinities $S_{ice} < 4$ g/kg, the sensitivity to ice salinity was higher for thinner ice than for thicker ice (for T_{ice}= -7°C, θ= 0°). Thus, thinner ice is more sensitive to both, ice salinity and ice temperature.

For the retrieval of ice thickness from SMOS data, it is important to know whether the main brightness temperature variability over sea ice originates from the variability of ice thickness or from variations of the other ice parameters, e.g. temperature and salinity. For the investigated case with S_{ice}= 8 g/kg, an ice temperature change of 1 K caused approximately the same change in the brightness temperature signal as the one caused by an ice thickness change of about 1 – 3 cm for ice thicknesses up to 45 cm and ice surface temperatures colder than -8°C. Regarding the impact by ice salinity, we observed roughly three different regimes (for T_{ice}= -7°C). For low ice salinities ($S_{ice} < 5$ g/kg), the brightness temperature sensitivity to salinity changes was very high. However, thin first-year ice in the Arctic usually has higher salinity values. For salinities 5 g/kg$< S_{ice} <$ 10 g/kg, an ice salinity change of 1 g/kg caused approximately the same change in the brightness temperature signal as the one caused by an ice thickness change of about 3 – 6 cm, depending on ice thickness. For higher ice salinities ($S_{ice} > 10$ g/kg), brightness temperature was almost independent of ice thickness

for ice thicker than 30 cm. Thus, if the ice salinity is $S_{ice} > 10$ g/kg, a retrieval would only be possible for ice thinner than 30 cm. In contrast, at 15 cm ice thickness and $S_{ice} > 10$ g/kg, an ice salinity change of 1 g/kg corresponded to a brightness temperature change as caused by an ice thickness change of only about 0.5 cm.
Here, we showed the results of our sensitivity studies for brightness temperatures at nadir view and at two incidence angles at horizontal polarisation. The brightness temperatures at vertical and at horizontal polarisation show a very similar behaviour. The main differences are that brightness temperature sensitivity to ice temperature is somewhat higher at vertical polarisation, and thus ice temperature has a slightly higher impact on ice thickness retrieval. At vertical polarisation, the reversal points occur at higher ice temperatures than at horizontal polarisation. Furthermore, the range of salinities, for which the impact of ice salinity on the ice thickness retrieval is low, is somewhat broader at vertical than at horizontal polarisation. According to our sensitivity studies, for ice thickness retrieval applications, L-band brightness temperatures over thin Arctic ice are sensitive enough to ice thickness variations, when compared to ice temperature and salinity variations. The brightness temperature supplies information on ice thickness within a certain accuracy, which can be specified using our model and assumptions about the ice temperature and salinity and their expected variations.

Comparison of the impact by ice temperature, salinity, and thickness
In order to compare the impact of ice temperature, salinity, and thickness on the brightness temperatures under realistic conditions, we examined an example case of freezing sea ice in the Laptev Sea. For the considered case, we found that the increasing ice thickness caused the brightness temperature signal above sea ice to increase by 143 K, while the estimated ice temperature and salinity variations caused the brightness temperature to vary only by 31 K (21%) and 16 K (11%), respectively. Thus, the ice thickness was the main contributor to the increasing brightness temperatures, as they were observed by SMOS. The analysis also showed that for the polarisation difference, the relative contributions of ice temperature and salinity variations as compared to the contribution of ice thickness variation were higher than for the brightness temperature intensity.

Dielectric properties of snow
First, we added a snow layer on top of a layer of sea ice in both the coherent Ulaby and the incoherent Burke model. A very thin layer of snow (d_{snow}= 1 mm) had an impact on brightness temperatures as modelled with the incoherent Burke model, but not on brightness temperatures as modelled with the coherent Ulaby model. For a rather thick snow layer of 50 cm thickness, we obtained consistent results from both models. The incoherent Burke model represented the average brightness temperatures of the oscillating signal in the coherent Ulaby model. We observed this consistency of the models also when we increased the thickness of the snow layer on top of an ice layer of constant thickness. One of our aims was to investigate whether the incoherent Burke model, which is based on the radiative transfer equation, is suitable for the implementation of a snow layer on ice, although the Burke model neglects higher order reflection terms. We expected this negligence to have a higher impact for thin layers and for media with low attenuation. However, our model comparison showed that the incoherent Burke model represents well the average brightness temperatures of snow-covered sea ice as modelled with the coherent Ulaby model, which accounts for higher order reflection terms. As for the transition from open water to a very thin ice layer, the incoherent Burke model does not reduce to the value of snow-free ice for very thin snow layers. Thus, the incoherent Burke model is not suitable for modelling very thin ice (approx-

imately below 1 – 2 cm), and, as was confirmed in this study, not for very thin snow layers on ice.
In L-band frequencies, dry snow is almost transparent. Thus, snow modifies only very slightly the brightness temperature of the underlying sea ice that would be observed, if the snow layer was not present. Nevertheless, the presence of a snow layer modifies brightness temperatures above sea ice, because the snow layer emits radiation itself. In L-band, the emissivity of snow is generally higher than the emissivity of sea ice. In accordance with these considerations, our brightness temperatures modelled for snow-covered sea ice were higher than brightness temperatures of snow-free sea ice. For our model assumptions and negligence of the thermal insulation by snow, the presence of a snow layer on ice caused brightness temperatures to increase by 10 K at nadir view. At horizontal polarisation, the brightness temperature increase caused by snow increased with increasing incidence angle and reached 25 K at θ= 50°. In contrast, at vertical polarisation, the increase of brightness temperatures due to the presence of a snow cover decreased with increasing incidence angle. At θ= 50°, the vertically polarised brightness temperatures of snow-covered and snow-free sea ice were almost identical. The resulting brightness temperatures were similar for dry and wet snow, if the snow thickness had values typically observed on thin sea ice. For thick layers of wet snow (here: d_{snow}= 50 cm), brightness temperatures were almost independent of ice thickness and took the values for an infinitely thick layer of wet snow.
When we considered only the dielectric properties of snow, brightness temperatures as modelled with both radiation models were almost independent of snow thickness. With increasing snow thickness, brightness temperatures converged to the brightness temperatures of an infinitely thick snow layer. However, this increase was very small. The brightness temperatures of sea ice covered by dry snow increased only by 0.7 to 2.7 K for an increase of snow thickness by 10 m for the incidence angles and polarisations considered here. For wet snow, the brightness temperatures that would be observed over an infinitely thick layer of snow were reached already for thinner snow layers. However, the dependence on snow thickness was still very small, and brightness temperatures increased by 0.8 to 1.9 K for an increase of snow thickness by 1 m.

Thermal insulation by snow
Additionally to its dielectric properties, a snow layer modifies brightness temperatures above sea ice due to the thermal insulation effect of snow. The bulk ice temperature of snow-covered ice is usually higher than the bulk ice temperature of bare sea ice. In order to investigate the effect of thermal insulation by snow on brightness temperatures, we assumed snow thicknesses as they have been observed during field campaigns and used a simple heat conduction model to estimate the snow and ice temperatures. The thickness of the snow layer was assumed to be about 10% of the ice thickness for the Arctic, and 20% for the Baltic Sea. To calculate the bulk snow and ice temperatures from the snow surface temperature, we assumed the snow-ice-column to be in thermal equilibrium and used typical values for the thermal conductivities of ice and snow.
We found that, for all considered cases, the increased ice temperatures due to thermal insulation by snow increased the modelled brightness temperatures. At higher incidence angles at vertical polarisation, only the thermal insulation effect of snow caused an increase of brightness temperatures, while the presence of a snow cover had almost no impact, when the temperature effect was neglected. At lower incidence angles and at horizontal polarisation, the brightness temperature increase caused by the higher ice temperatures due to thermal insulation of snow added on the increase by the dielectric properties of snow. The contribution

to the brightness temperature increase by the dielectric properties was higher than the contribution by thermal insulation. Due to the higher snow thicknesses assumed for Baltic Sea ice, the brightness temperature increase due to thermal insulation was higher for the Baltic than for the Arctic sea ice.
Regarding the observed increase of brightness temperatures due to thermal insulation of snow, we have to pay regard to the ice temperature assumed for our model simulations. According to our sensitivity studies in section 3.1.3, brightness temperatures increase with increasing ice temperatures for ice temperatures up to a reversal point. The ice temperature of this reversal point depends on ice salinity and ice thickness. The ice salinities in the investigations in section 3.1.3 and in the snow-related investigations here were equal (S_{ice}= 8 g/kg). For this ice salinity, the reversal point occured at an ice surface temperature of about -3°C for an ice thickness of 15 cm, and at an ice surface temperature of about -10°C for an ice thickness of 60 cm. For ice surface temperatures higher than these values, brightness temperatures decreased for further increasing ice surface temperatures. Our brightness temperature simulations for the investigation of the snow impact were performed for an ice surface temperature of T_{surf}= -15°C. Thus, if we had considered a higher ice surface temperature, the thermal insulation effect of snow could have caused a decrease of brightness temperature. Because the contribution of the dielectric properties of snow was higher than the contribution by thermal insulation of snow, the overall effect of a snow layer would still be an increase of the brightness temperature of snow-covered ice compared to the brightness temperature of snow-free ice.
The coherent Ulaby model showed two superimposed oscillations in brightness temperature, one caused by variation of ice thickness, the other by variation of snow thickness. As for the model results in the first section, the incoherent Burke model represented well the average value of the oscillating brightness temperature modelled with the coherent Ulaby model.

4 SIMULATION TIMESERIES

Rasmus Tonboe

Simulations of the snow covered sea ice surface temperature and microwave effective temperature at L-Band

Rasmus T. Tonboe
Danish Meteorological Institute

November 7, 2012

1 Introduction

The thin ice L-band emission is investigated in this simulation study. In particular, the possibilities for deriving the effective temperature from auxiliary measurements are investigated. The complete description of the emission and physical characteristics is difficult to achieve in praxis from measurements therefore all data are simulated. The model relates the sea ice physical properties such as density, salinity, ice thickness and temperature to microwave attenuation, reflectivity, emissivity effective temperature and brightness temperature. The model is a sea ice version of Microwave Emission Model for Layered Snowpacks (MEMLS) (Wiesmann & Mätzler, 1999) described in Tonboe (2010) and Tonboe et al. (2006 and 2011) and hereafter called the emission model. The emission model is used for simulating the sea ice brightness temperature (T_b), at vertical and horizontal polarisation denoted by the subscript v and h respectively and at 50º incidence angle. Similarly for emissivity, e.g. e_v for the emissivity at vertical polarisation, the penetration depth and the effective thermometric temperature T_{eff}. SMOS is measuring the complete brightness temperature polarisation state described by the Stokes vector and for each of the resolution cells (about 50km). However, the model cannot simulate the last two Stokes parameters. The penetration depth is defined as the depth where the intensity above the surface has decreased beneath the surface to 1/e (0.37) of its initial value. This includes the transmission loss at the surface and at layer interfaces within the medium such as icy layers and the snow ice interface. This definition differs from Hallikainen & Winnebrenner (1992) where transmission loss is not included.

There is an ice thickness signal in L-band for thin ice because of penetration even in saline ice to near the ice water interface (Kaleschke et al., 2010). However, both the ice salinity and ice temperature are affecting the microwave penetration and thin ice transparency and therefore they have a similar effect on the emissivity as thickness does (Tonboe et al., 2006). This is a potential ambiguity for using the brightness temperature as an ice thickness proxy and this is why the sea ice concentration of thin ice should be derived separately using near 90GHz ice concentration algorithms. Near 90 GHz algorithms are least sensitive to the new-ice and mature ice emissivity differences. At the same time the near 90 GHz channels are sensitive to atmospheric emission.

In order to produce input to the emissivity model a one dimensional snow/ice thermodynamic model has been developed (Tonboe, 2005 and 2010). The thermodynamic model is fed with ECMWF ERA40 data input from Arctic and Antarctic grid points. In return the thermodynamic model produces detailed snow and ice profiles which are input to the emission model. The intension is to simulate significant emission processes and the brightness temperature variability in level sea ice even though the one dimensional thermodynamic model is not capturing the spatial variability of the sea ice cover (convergence/deformation, divergence/new-ice formation, wind redistribution with mechanical break-up of the snow cover). It does not have a hydrological module and cannot simulate melt processes in the snow and ice thus the simulations are restricted to the cold season which is about Sep. 1. to May 31. on the Northern Hemisphere and Mar. 1. to Dec. 31. on the southern hemisphere. The focus is on the freeze-up period approximately October - December and April - June. The simulated snow depths during winter are comparable to climatology in the Arctic (Warren et al., 1999).

The simulations begin with a 1 cm 22 psu layer and an underlying layer where the salinity is determined by the growth rate. For all profiles the salinity of additional layers (these are 2 cm thick) is determined by ice growth rate and ocean salinity (Nakawo & Sinha, 1981). Snow precipitation is accumulated on top according to the meteorological input. New-snow density is a function of air temperature and wind speed and deposited snow layers later compact to higher density as part of the snow metamorphosis. Two grid points are selected on each hemisphere in the Kara Sea (80 N, 60 E) and in the Weddell Sea (75 S, 320 E).

It is the intension with this report to analyse the L-band brightness temperature. In particular to find

proxies for the emissivity and the effective temperature and investigate if it is meaningful to constrain these variables or to simplify the snow and ice system description and the radiative transfer equation.

2 Microwave emission from sea ice

The microwave brightness temperature of a lossy half-space such as snow and sea ice is the product of the effective temperature and the emissivity. The effective temperature is the integrated emitting layer thermometric temperature. Usually during winter when the atmosphere is colder than the ocean the surface temperature is also lower than the effective temperature. The emissivity at a certain polarisation, frequency and incidence angle is a function of subsurface extinction and reflections between layers with different permittivity. The microwave penetration for frequencies higher than 89 GHz is usually confined to the snow cover due to significant extinction in the snow. The ice is saline which leads to a high absorption coefficient thus limiting penetration into the ice. The effective permittivity used in the model for a background medium with freely arranged random needles. The background consists of pure (non-saline) ice and the inclusions are the liquid brine pockets. The permittivity of the brine is computed using the set of equations in Ulaby et al. (1986) appendix E5. The brine volume V_b is a function of temperature T (C) and ice salinity S (psu) (Ulaby et al., 1986):

$$V_b = 10^{-3}\left(\frac{-49.185S}{T} + 0.532\right)$$

(1).

Eppler *et al.* (1992) noted that during winter at frequencies around 19 GHz, the level first-year ice microwave signatures change primarily due to snow cover related processes. At these relatively high frequencies compared to L-band snow cover is very important for the signature variability of all sea ice types including multiyear ice and new/ young ice (Eppler et al., 1992). Snow cover does also affect the emission at L-band mostly by moderating the impedance at the surface and the incidence angle in particular at horizontal polarisation. This effect is seen in cases with or without snow cover and during precipitation events. Snow with its low thermal conductivity is also important for the snow and ice temperature profile thus the effective temperature. Scattering from snow grains, brine pockets and air bubbles is insignificant at L-band but is

included in the computation anyway.

4 The combined thermodynamic and emission model

Combined thermodynamic and emissivity models have the potential to build long snow/sea ice/microwave time-series that can be used for statistical analysis of radiometer sea ice data sensitivities (Mätzler et al., 2006). However, Wiesmann et al. (2000) show that 1-D thermodynamic models for snow and frozen ground including microphysical parameters and a vertical stack of layers, e.g. SNTHERM (Jordan, 1991) and Crocus (Brun et al., 1989), underestimate the formation of thin crusts or weak layers in the snow pack. Comparison to snow pit measurements showed that the density of thin layers is underestimated in Crocus and thin layers are not represented properly in SNTHERM. Further, when the thermodynamic model output is used as input to a microwave emission model this leads to underestimation of the simulated polarisation difference. These models were developed for other applications. The thermodynamic model used here treats layers from individual precipitation events and retains all layers even when thin (1 mm) in an attempt to alleviate earlier problems in microwave modelling applications. To ensure reasonable initial snow layer thickness precipitation events less than 1 kg/m^2 are retained and released only when the next precipitation event exceeds the threshold. While this may not be totally realistic it does produce simulated snow depths which are comparable to climatology (Warren et al., 1999). At L-band it is particularly important that the thermodynamic model can reproduce realistic temperature, ice salinity profiles and ice thickness. The thermodynamic model has the following prognostic parameters for each layer: thermometric temperature, density, thickness, snow grain size and type, ice salinity and snow liquid water content. Snow layering is very important for the microwave signatures therefore it treats snow layers related to individual precipitation events. For sea ice it has a growth rate dependent salinity profile. The sea ice salinity is a function of growth rate and water salinity (Nakawo & Sinha, 1981), i.e.

$$S = 0.12 S_w / \{0.12 + 0.88 \exp(-4.2 \times 10^4 u)\} \quad (2)$$

where S_w is the water salinity (here 32 psu for the Arctic surface waters) and u is the growth rate in cm/day.

The model is initialized with a 1cm ice layer the salinity of this layer is 22 psu and it is not changed during the simulation. The 22 psu were measured for thin during a freeze-up experiment in Qaanaaq in Greenland 2011.

6 Simulation results

Two simulations are selected and shown in the following. Each one of these is representative for the Arctic and the Antarctic: the Kara Sea at 80 N, 60 E and the Weddell Sea at 75 S, 320 E. Both places have snow precipitation throughout the winter and the ice grows to about 1 m in the Kara Sea and 1.2 m in the Weddell Sea.

The simulations in the Kara Sea begin on October 1. The snow depth and ice growth as a function of time is shown in figure 1 together with the penetration depth at frequencies between 1.4 and 89 GHz. Only 1.4 and 6 GHz are penetrating into the ice. Frequencies higher than 6 GHz are penetrating to the snow ice interface. In spite of the growing ice thickness the ice freeboard is near the water-line throughout the season because of the snow accumulation. The penetration depth at L-band is near but not to the ice water interface. The ice at the ice-water interface is relatively warm throughout the season. This means that penetration is limited even at L-band.

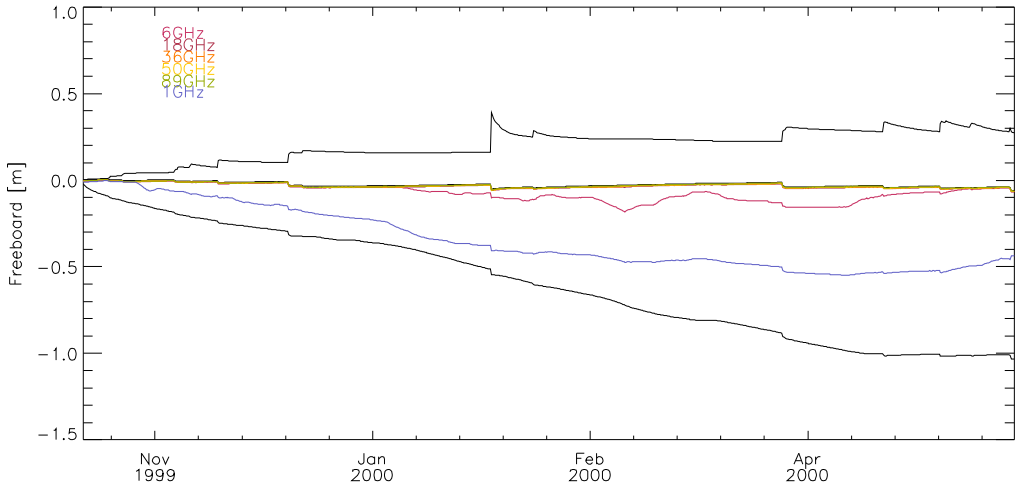

Figure 1. The Kara Sea ice growth and penetration depth.

The 1.4 GHz emissivity at vertical polarisation is shown in figure 2 together with the 6 to 89 GHz emissivity for the same floe as in figure 1. The 1.4 GHz emissivity variability is determined primarily by the ice thickness when the ice is thin. The emissivity at other frequencies is determined primarily by snow cover processes and not by the ice thickness. The 89 GHz is the lowest at a level around 0.9 after the initial freeze-up phase. The L-band emissivity is

near 0.94 after the initial freeze-up phase.

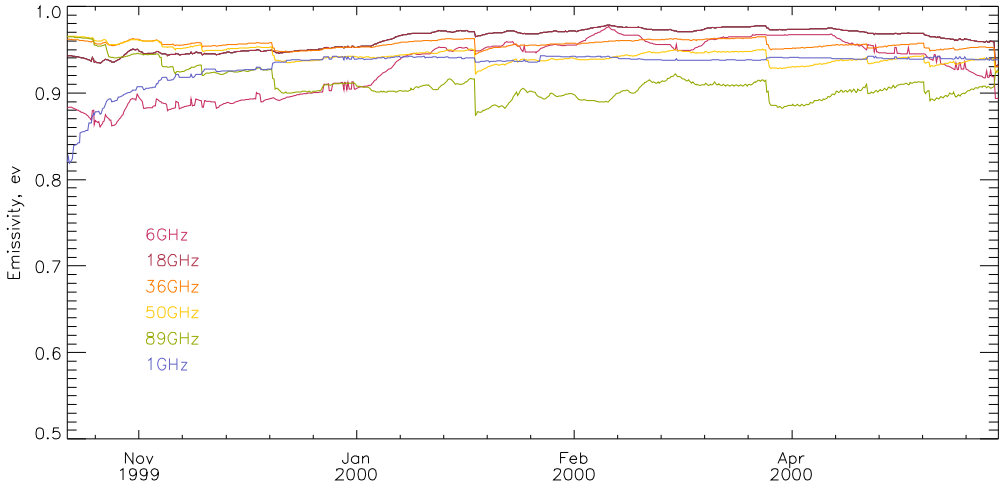

Figure 2. The Kara Sea emissivity (vertical polarisation). Same floe as in fig. 1.

The effective and physical temperatures for the Kara Sea profile is shown in figure 3. The warmest temperature is clearly the 1.4 GHz effective temperature because of its deep penetration. The 1.4 GHz effective temperature is different from effective temperatures at other frequencies even at 6 GHz and the physical temperatures at the snow surface and at the snow ice interface. The variability of the L-band effective temperature is lower than all the other temperature estimates. Even during mid winter it is constrained to a narrow range of temperatures from 265 to 271 K. It is noted that while the ice is optically thin the effective temperature is constrained within 2 K.

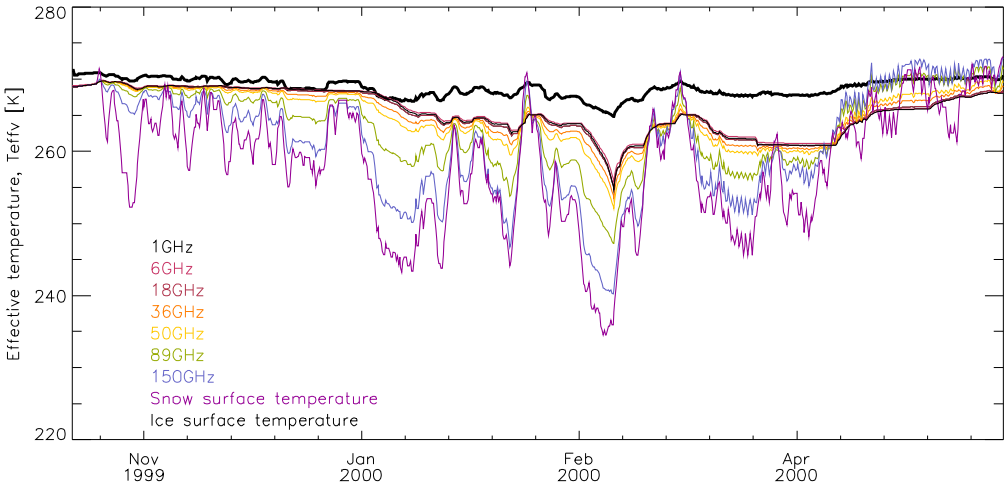

Figure 3. The effective and physical temperatures in the Kara Sea profile as in fig. 1.

Figure 4 shows ice growth and snow accumulation together with the penetration depth at frequencies between 1.4 and

89 GHz for the simulated floe at 75 S, 320 E in the Weddell Sea. Only 1.4 and 6 GHz penetrate into the ice. The intermediate frequencies at 18, 36 and 50 GHz penetrate to the snow ice interface. During spring the 89 GHz penetration depth is decreasing due to snow metamorphic processes. The ice growth and snow accumulation is greater than in the Arctic. Like in the Arctic the ice freeboard is near the water line throughout the season. The snow cover is thicker in Antarctica than in the Arctic and also the ice is thicker.

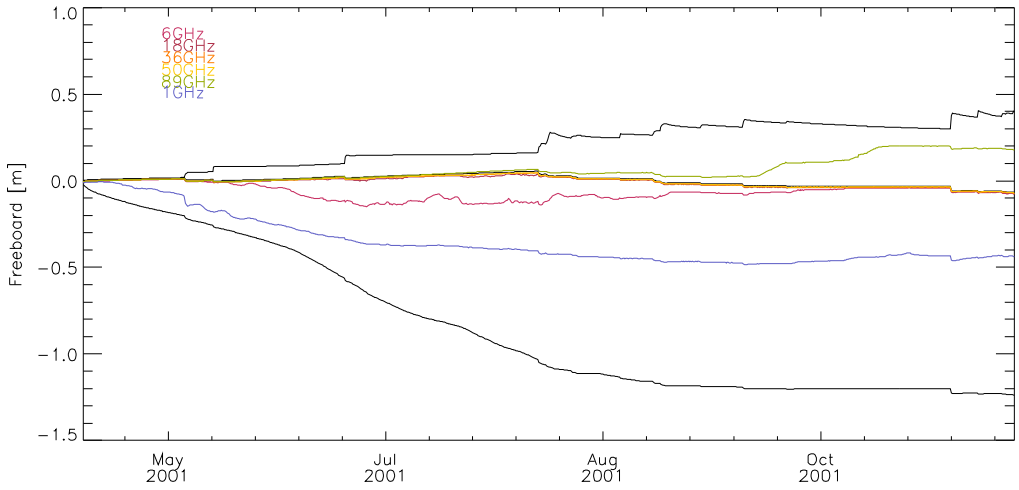

Figure 4. The ice floe thickness growth and penetration depth in the Weddell Sea.

Figure 5 show the simulated emissivity at frequencies between 1.4 and 89GHz for the Weddell Sea floe. The1.4 GHz emissivity variability is a function of ice thickness as long as the ice is semitransparent. The variability of the 18 to 89 GHz emissivity is dominated by snow cover processes. There are three categories of emissivity response to the evolving ice and snow conditions: 1) the L-band emissivity is affected by the ice/water interface emission while the ice is optically thin after that when the ice is thick then the emissivity is constrained to 0.92, 2) after the initial freeze-up period the 6 and 18 GHz emissivity is very high. In fact it is over 0.95. During the spring scattering processes in the snow is gradually decreasing the emissivity to around 0.9, and 3) The 36, 50 and 89 GHz are affected with increasing strength by snow cover processes in particular new snow precipitation events.

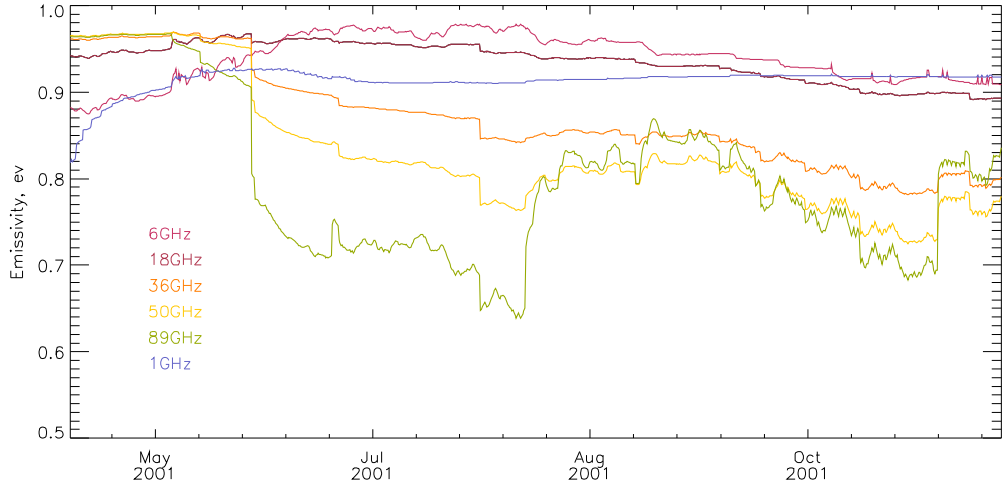

Figure 5. The emissivity in the Weddell Sea.

The simulated physical and effective temperatures for the Weddell Sea are shown in figure 6. The 1.4 GHz effective temperature variability is smaller than all other temperature estimates. The variability is dampened for the frequencies penetrating into the snow and ice. The largest variability and coldest temperatures is seen for the snow surface temperature with direct contact with the atmosphere.

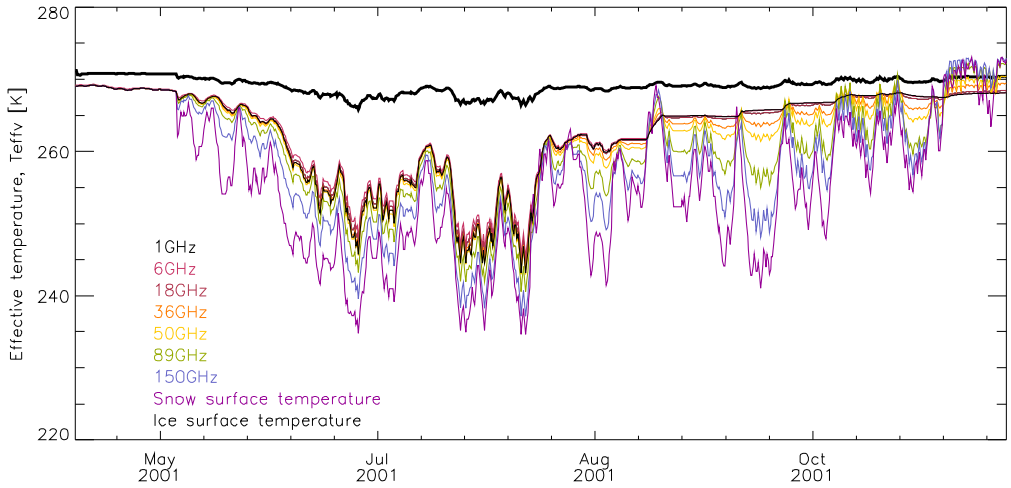

Figure 6. The effective and physical temperature in the Weddel Sea.

The 1.4 GHz emissivity as a function of the ice thickness is shown for the Kara Sea freeze-up in figure 7. A precipitation event with new and low density snow is affecting the horizontal polarisation much more than the vertical polarisation. The snow surface density changes from 283 kg/m^3 to 118 kg/m^3 during the snow fall. The emissivity variability at vertical polarisation is smaller when the ice is 30 cm or thicker, i.e. when the ice is optically thick. The optical thickness at L-band depends on

the ice salinity and its temperature. The temperature at the ice-water interface is constrained to the freezing point while the air snow interface temperature is determined by the radiation and energy balance. While the vertical polarization is affected primarily by the ice thickness, the horizontal polarisation is affected significantly by the surface reflectivity. This makes the horizontal polarisation and the polarisation ratio less suited than the vertical polarisation for ice thickness estimation. It further complicates the ice thickness estimation procedure because the polarisation state is affected by Faraday rotation. The initial salinity of the upper 1 cm is 22 psu. This salinity was estimated during a freeze-up experiment near Qaanaaq in Greenland in 2011. There are not many detailed surface sea ice salinity measurements available. Nevertheless the surface salinity is significantly affecting the L-band penetration and therefore the ice thickness estimation.

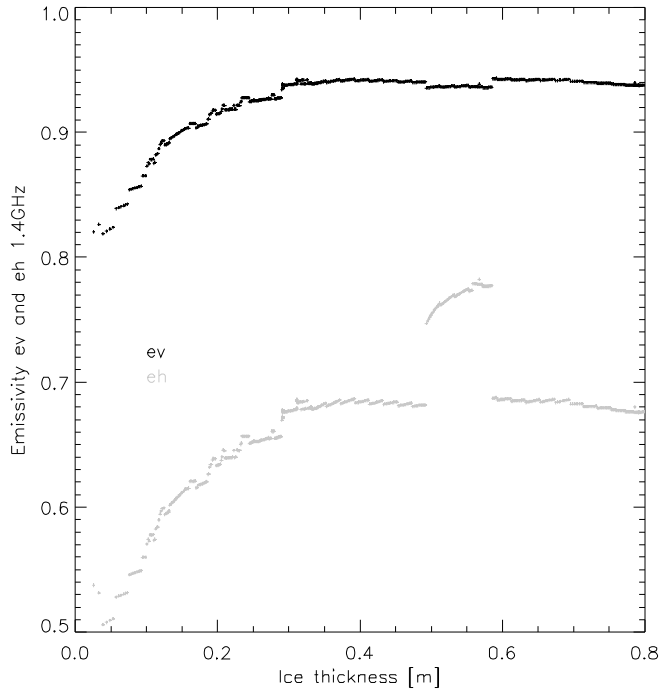

Figure 7. The emissivity as a function of ice thickness in the Kara Sea.

In the following we are looking for L-band brightness temperature proxies. The snow or ice surface physical temperature vs. the 1.4 GHz brightness temperature for the profile in the Kara Sea is shown in figure 8 and the Weddell Sea in figure 9. The 1:1 line and the 0ºC line is show in the plot. Clearly the temperature gradient in the snow and ice is very high in winter and there is little correlation between the physical snow surface temperature and the 1.4 GHz brightness temperature penetrating deep into the ice. The lowest brightness temperatures around 220

K are for thin ice. However while the surface temperature varies between 230 K and 270 K the brightness temperature is constrained to a narrow interval of a few Kelvin around 250 K during most of the winter at both hemispheres. The brightness temperature of mature ice is therefore well constrained and it is not correlated with the surface temperature of cold ice.

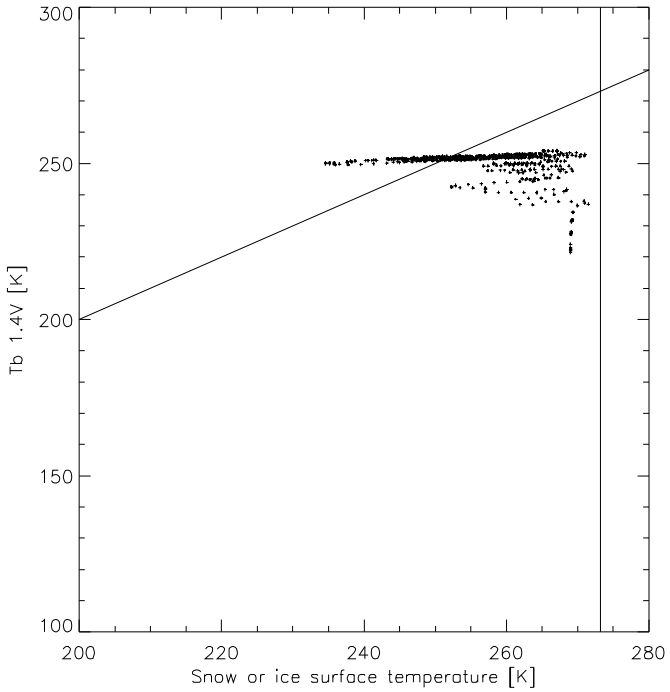

Figure 8. The snow or ice surface physical temperature vs. the 1.4GHz brightness temperature for the profile in the Kara Sea. The 1:1 line and the 0ºC line is show in the plot.

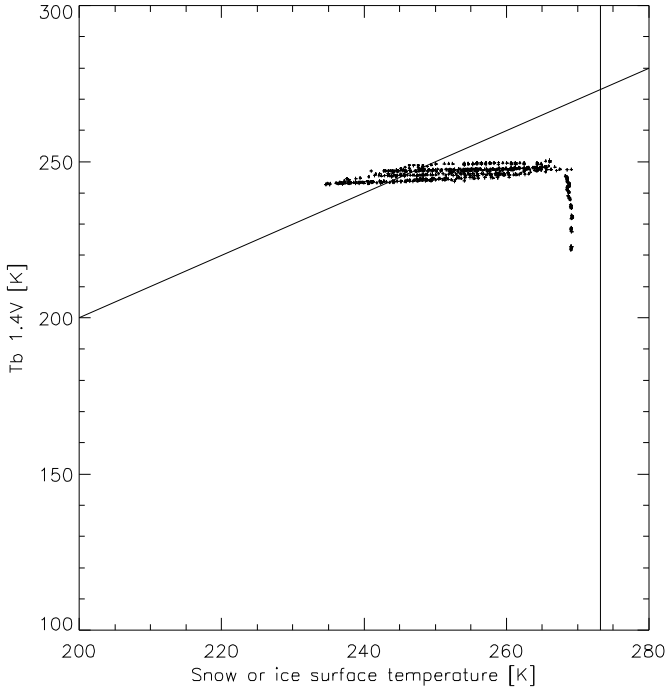

Figure 9. The snow or ice surface physical temperature vs. the 1.4GHz brightness temperature for the profile in the Weddell Sea. The 1:1 line and the 0ºC line is show in the plot.

While the surface temperature which may be measured by infrared radiometers is not a proxy for the L-band brightness temperature we look at the C-band (6 GHz) brightness temperature. C-band radiometers were part of the SMMR, the AMSR and now on the AMSR 2 satellite instruments. The C-band is used for e.g. sea surface temperature estimation. Like the L-band, C-band is penetrating into the ice and could potentially provide an independent estimate of the ice temperature which could be related to the L-band temperature. Figure 10 shows the brightness temperature at 1.4 GHz vs. the brightness temperature at 6 GHz for ice thicknesses between 2 cm and 50 cm for both the Kara and the Weddell Seas. The thinnest ice is colour-coded purple and the thickest ice is colour-coded red. Water is a cold target in terms of emissivity at both frequencies and the thin ice is more transparent at 1.4 GHz than at 6 GHz at the very beginning of the freeze-up. Later when a temperature gradient builds up, 6 GHz which is not penetrating as deep as 1.4 GHz, is colder in terms of effective temperature. The two brightness temperatures at L-band and at C-band do not have a 1:1 relation for thin ice. The emissivities at these two frequencies are significantly different.

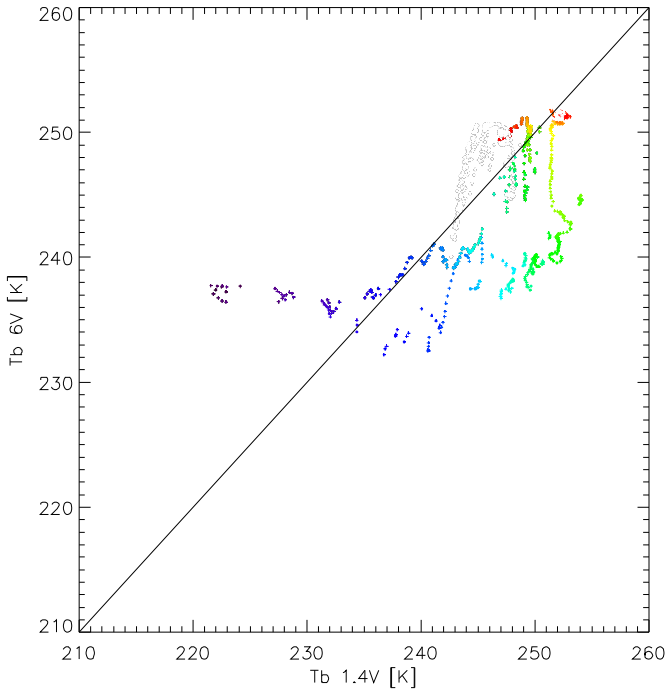

Figure 10 shows the brightness temperature at 1.4 GHz vs. the brightness temperature at 6 GHz for ice thicknesses between 2 cm and 50 cm for both the Kara and the Weddell Seas. The thinnest ice is colour-coded purple and the thickest ice is colour-coded red.

The snow surface temperature is most often colder than the snow-ice interface temperature. The low heat conduction rate in the snow has a strong moderating effect on the snow and sea ice thermodynamics and temperature profile. This means that even though ev at L-band is not sensitive to the snow cover the physical temperature may be sensitive to situations with or without snow cover and indirectly to snow thickness. Figure 11 shows the snow surface temperature vs. the snow-ice interface temperature for the Kara Sea profile and figure 12 shows the Weddell Sea profile. It is clear because of the strong temperature gradient in the snow that the snow surface temperature is not synonymous with the snow ice interface temperature and that there is no simple relation between the two physical temperatures.

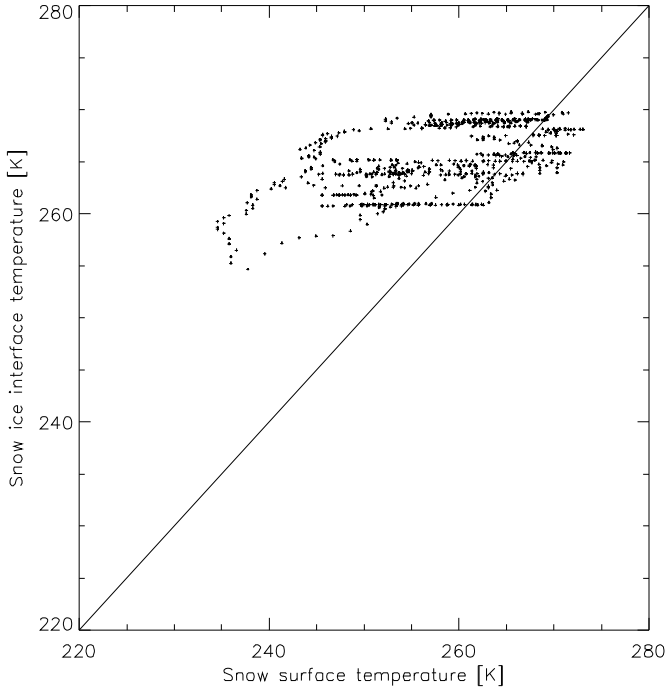

Figure 11. Shows the snow surface temperature vs. the snow-ice interface temperature for the Kara Sea profile.

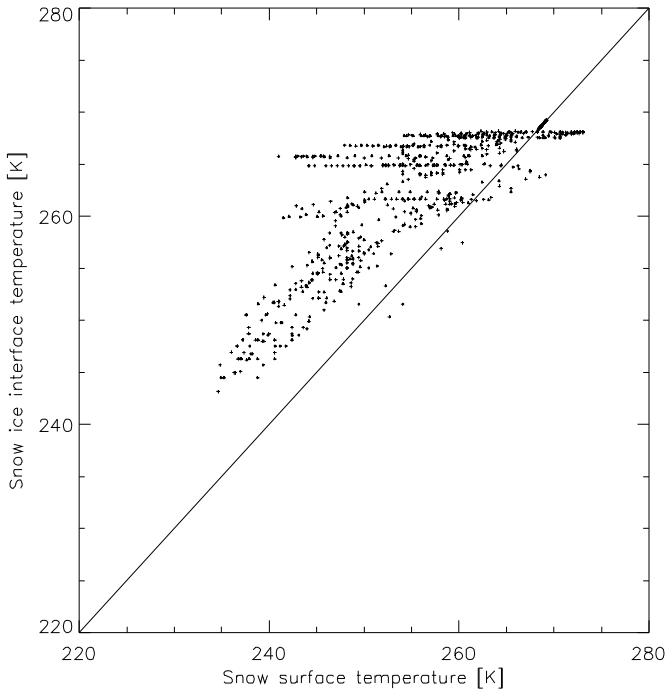

Figure 12. Shows the snow surface temperature vs. the snow-ice interface temperature for the Weddell Sea profile.

Optically thin ice in Kara Sea and the Weddell Sea profile simulation is ice up to about 20-30 cm. The 1.4 GHz effective temperature of optically thin ice is constrained to

a relatively narrow range of temperatures in the simulated data between 269 K and 271 K inversely proportional with ice thickness as shown in figure 13 for the Kara Sea profile and figure 14 for the Weddell Sea profile.

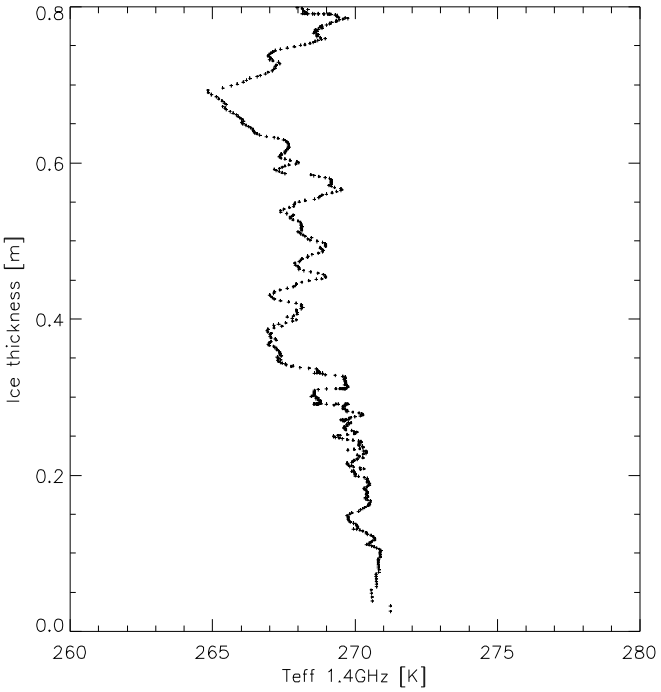

Figure 13 The 1.4GHz effective temperature vs. the ice thickness for relatively thin ice in the Kara Sea.

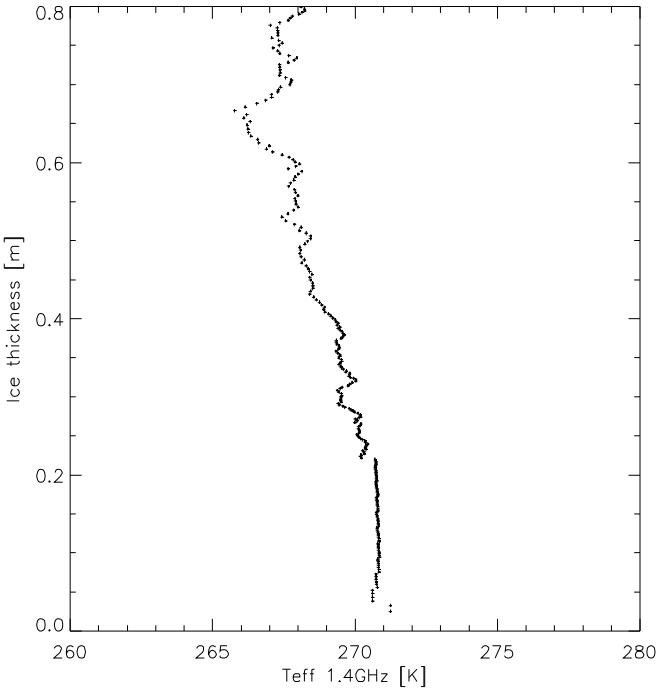

Figure 14. The 1.4GHz effective temperature vs. the ice thickness for relatively thin ice in the Weddell Sea.

7 Conclusions

A sea ice version of microwave emission model for layered snow-packs (MEMLS) fed with detailed profiles from a thermodynamic sea ice model has been used for simulating the sea ice brightness temperature, emissivity and effective temperature at frequencies between 1.4 and 89 GHz. The advantage of using the combined thermodynamic and emission models for simulating the 1.4 GHz brightness temperature sensitivity to physical snow and sea ice parameters is that the thermodynamical model is providing realistic distribution of non-uniform input parameters to the emission model including the salinity and temperature profile. It logs all possible parameters and it is possible to derive parameters such as effective temperature and emissivity. These parameters and this level of detail are virtually impossible to achieve in the field. The disadvantage is that the thermodynamic model is not capturing all physical processes especially those affecting the variability on a horizontal scale: deformation, redistribution of the snow cover, and sea ice concentration variability. These additional processes make it difficult to compare the simulated brightness temperatures to measured brightness temperatures. Using these simulated profiles as input to the emissivity model it has been found that:

1. That new ice is optically thin at 1.4 GHz but not at frequencies from 6 GHz to 89 GHz. This means that the sea ice concentration derived from brightness temperatures is affected less by new-ice and mature ice radiometric differences at near 90 GHz than at 1.4 GHz. Finding an independent estimate of the sea ice concentration in regions covered by new ice is a prerequisite for estimating the thin ice thickness. Because the near 90 GHz channels are least sensitive to new-ice mature ice differences these ought to be used for deriving the new-ice sea ice concentration. At the same time the near 90 GHz channels are quite sensitive to atmospheric emission and this may cause an unacceptably large uncertainty in the ice concentration estimate especially near the ice edge.
2. The emissivity at horizontal polarisation is sensitive to the air-snow interface reflection. The simulations show that the uncertainty is increased when using the L-band brightness temperature at horizontal polarisation for deriving the ice thickness of thin ice. The problem in praxis is that when only using the brightness temperature at vertical polarisation and not the sum of horizontal and vertical polarisation then a correction for the Faraday

rotation is required. This is complicated and requires auxiliary information.

3. The deep penetration and the thermodynamic control of the snow cover constrain the 1.4 GHz effective temperature to a relatively narrow range of values. For optically thin new-ice the effective temperature is between approximately 269 K and 271 K. It seems like a reasonable approximation to constrain the effective temperature to e.g. 270 K in simple radiative transfer models used for thin ice thickness estimation.
4. The deep penetration of the 1.4 GHz radiation compared to the frequencies between 6 GHz and 89 GHz makes the 1.4 GHz effective temperature different from effective temperatures between 6 GHz and 89 GHz and the physical temperature at the snow surface and the snow-ice interface. Therefore it seems difficult to find an independently measured proxy for sea ice effective temperature at L-band.
5. The salinity of the surface ice is important for the penetration depth and thin ice thickness estimation. A winter freeze-up experiment suggests that the salinity of the upper layer is high (22 psu) because of rapid freeze-up. However, several mechanisms may play a role during the initial freezing of ice and a more systematic investigation together with the dielectric properties of new-ice at L-band is needed. It is recommended to do a survey of new-ice salinities and dielectric properties at L-band. These two issues are not well constrained and they are important for the estimation of thin ice thickness.

References

Brun, E., E. Martin, V. Simon, C. Gendre, C. Coleou. An energy and mass model of snow cover suitable for operational avalanche forecasting. Journal of Glaciology 35(121), 333-342, 1989.

Eppler, D. T. and 14 others, “Passive microwave signatures of sea ice”, In: F. D. Carsey, Ed., *Microwave remote sensing of sea ice, geophysical monograph 68* (pp. 47-71). Washington DC: American Geophysical Union, 1992.

Hallikainen, M. and D. P. Winebrenner, “The physical basis for sea ice remote sensing”, In: F. D. Carsey, Ed., *Microwave remote sensing of sea ice, geophysical monograph 68* (pp. 29-46). Washington DC: American Geophysical Union, 1992.

Jordan, R. A one-dimensional temperature model for a

snow cover. CRREL SP 91-16, 1991.
Kaleschke, L., N. Maaß, C. Haas, S. Hendricks, G. Heygster, and R. T. Tonboe. A sea ice thickness retrieval model for 1.4 GHz radiometry and application to airborne measurements over low salinity sea ice. The Cryosphere 4, 583-592, 2010.
Mätzler, C. Autocorrelation functions of granular media with free arrangement of spheres, spherical shells or ellipsoids, J. Appl. Phys. 81(3), 1509-1516, 1997
Nakawo, M., N. K. Sinha. Growth rate and salinity profile of first-year sea ice in the high Arctic. Journal of Glaciology 27(96), 315-330, 1981.
Tonboe, R. T. A mass and thermodynamic model for sea ice. Danish Meteorological Institute SR05-10, p. 12, 2005.
Tonboe, R. T., G. Heygster, L. Toudal Pedersen & S. Andersen. Sea ice emission modelling. In Mätzler (Ed.), Thermal Microwave Radiation: Applications for remote sensing. IET Electromagnetic Wave series 52, 382-400, London, 2006.
Tonboe, R. T. The simulated sea ice thermal microwave emission at window and sounding frequencies. Tellus 62A, 333-3344, 2010.
Tonboe, R. T., G. Dybkjær, J. L. Høyer. Simulations of the snow covered sea ice surface temperature and microwave effective temperature. Tellus 63A, 1028-1037, 2011.
Mätzler, C. A. Wiesmann, J. Pulliainen, & M. Hallikainen. Microwave emission of snow. In Mätzler (Ed.), Thermal Microwave Radiation: Applications for remote sensing. IET Electromagnetic Wave series 52, 371-382, London, 2006.
Ulaby, F., R. K. Moore, A. K. Fung. 1986. Microwave remote sensing, active and passive, vol. III. Artech House, Norwood MA.
Warren, S. G., I. G. Rigor, N. Untersteiner, V. F. Radionov, N. N. Bryazgin, Y. I. Aleksandrov & R. Colony. Snow Depth on Arctic Sea Ice. *Journal of Climate 12*, 1814-1829, 1999.
Wiesmann, A. & C. Mätzler. Microwave emission model for layered snowpacks. Remote sensing of environment 70, 307-316, 1999.
Wiesmann, A., C. Fierz, C. Mätzler. Simulation of microwave emission from physically modelled snowpacks. Annals of Glaciology 31, 397-405, 2000.
Wiesmann, A., C. Mätzler, T. Weise. Radiometric and structural measurements of snow samples. Radio Science 33(2), 273-289, 1998.

Part III

Operational SMOS ice thickness algorithms

5 LEVEL 3 BRIGHTNESS TEMPERATURE PROCESSING

Xiangshan Tian-Kunze

5.1 SMOS L1C Data

The SMOS payload Microwave Imaging Radiometer using Aperture Synthesis (MIRAS) measures in L-band the brightness temperatures in full polarisation with incidence angles ranging from 0° to 65°. All four Stokes parameters are obtained. It has a global coverage every three days (Kerr et al., 2001), whereas daily coverage up to 85° can be expected in the polar regions. Brightness temperature is taken every 1.2 s by hexagon-like, two-dimensional snapshots which have a spatial dimension of about 1200 km across (Kerr et al., 2001). The geometric distribution of incidence angles and radiometric accuracy within the alias-free areas of a snapshot is shown in Figure 5.1. The footprint varies from about 35 km at nadir view to more than 50 km at incidence angles higher than 60°. Each snapshot measures one or two of the Stokes components in the antenna reference frame. Horizontally and vertically polarised brightness temperatures are measured by separate snapshots.

The brightness temperature is defined as

$$TB = e \times T, \tag{5.1}$$

where e is the emissivity, T is the physical temperature.

During the SMOS commissioning phase (from November 2009 to May 2010), the antenna's dual and full mode measurements are tested. Therefore, either dual or full mode L1C data were available in this period with missing data in some days. After the SMOS mission went to the operational phase, only full mode data have been available (about 9 GB per day for ocean product). Browse products with incidence angle 43° are delivered separately. L1C data are swath-based and include information about snapshot ID, polarisation, incidence angles, geometric and Faraday rotation angles. Ocean and land products are stored separately. For our purpose we use only ocean product. L1C data are downloaded from ESADPGSFTP server.

The SMOS L1C data are given on the Discrete Global Grid (DGG) system. The DGGs are fixed Earth grid coordinates of the ISEA 4-9 hexagonal grid centers which have a spatial distance of 15 km (Indra, 2010). Most of the pixels in the Arctic are covered by several overflights during one day.

The version number of L1C data has changed several times (Table 5.1). The first L1C reprocessing by ESA covers the period from 12 January to 26 December 2010. The reprocessed data and the operational data thereon have the version number 346. The version update from 346 to 503, followed by 504 soon thereafter, happened on Oct. 23, 2011. However, due to a software anomaly in the L1OP V5.03 and V5.04 processor, the L1C Sea Product contains some corrupted measurements. The grid points affected by this anomaly are all the pure sea pixels located in the polar region in an area above 72° latitude North and South (for more de-

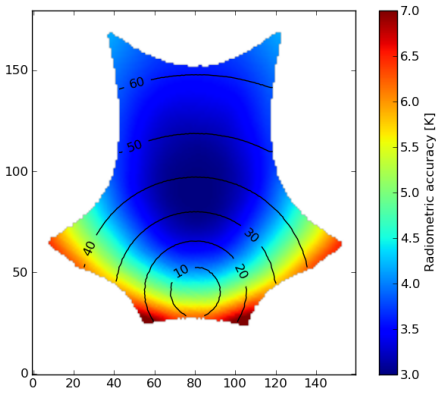

Figure 5.1: Distribution of radiometric accuracy within a typical snapshot with incidence angles ([degree]) as contour lines. The snapshot is gridded with 10 km spatial grid resolution.

Table 5.1: Overview of SMOS L1C data

Data version	Mode	Time period
v330	Dual	12 and 13 December 2009; 5 and 7 March 2010
v344	Full	19 July 2010 - 26 December 2010
v346	Dual, Full	12 January 2010- 23 May 2010
v346	Full	24 May 2010 - 23 October 2011
v503	Full	23 October 2011- November 2011
v504	Full	November 2011- 21 March 2012
v505	Full	12 January 2010-now

tail refer to Read-me-first note for the release of the SMOS Level 1 Brightness Temperature data products, ESA Earthnet Online, 21 March 2012). This problem was solved in version 505 in March 2012 and all L1C data are reprocessed to this version. The current daily mean level three brightness temperature is based on the reprocessed L1C data with the version number 505. Due to anomalies related to the temperature readings on one of the antenna segments of arm B, between 27 and 31 December 2010 no data are available.

5.2 Polarisation transformation

In full polarimetric mode a SMOS snapshot contains only one of the following four combination of polarization components in the *Antenna frame*: [XX], [XX, XY],[YY], [YY,YX]. To get full usage of polarization information we need to transform the data from *Antenna frame* into *Earth frame*. The Faraday and geometric rotation are considered by the transformation.

We describe the four Stokes components in *Antenna frame* and *Earth frame* as $TB_x, TB_y, T3, T4$ and $TB_h, TB_v, ST3, ST4$ respectively. The transformation matrix between the two frames can be written as follows (Camps et al., 2005):

$$\begin{bmatrix} TB_x \\ TB_y \\ T3 \\ T4 \end{bmatrix} = \begin{bmatrix} \cos^2(\alpha) & \sin^2(\alpha) & -\cos(\alpha)\sin(\alpha) & 0 \\ \sin^2(\alpha) & \cos^2(\alpha) & \cos(\alpha)\sin(\alpha) & 0 \\ \sin(2\alpha) & -\sin(2\alpha) & \cos(2\alpha) & 0 \\ 0 & 0 & 0 & 1 \end{bmatrix} \begin{bmatrix} TB_h \\ TB_v \\ ST3 \\ ST4 \end{bmatrix}$$

where $\alpha = \alpha_r + \omega_{F_a}$, α_r and ω_{F_a} are geometric and Faraday rotation angles.

The third and fourth Stokes components in *Antenna frame*, $T3$ and $T4$, can be derived from the real and imaginary parts of TB_{xy} and TB_{yx}. The real parts of TB_{xy} and TB_{yx} are the same while the imaginary parts of TB_{xy} and TB_{yx} have opposite signs (Camps et al., 2005). Therefore,

$$T3 = 2\Re(TB_{XY}) = 2\Re(TB_{YX}), \tag{5.2}$$

$$T4 = -2\Im(TB_{XY}) = 2\Im(TB_{YX}). \tag{5.3}$$

XX, YY, XY(or YX) components from the nearest snapshots whose acquisition time difference is less than 2.5 s are used for the transformation. This guarantees similar atmospheric and surface condictions for the measurements. The incidence angle of the consecutive snapshots at each grid point varies less than $0.5°$.

In the processing of L1C to L3, University of Hamburg (UHH) and Univeristy of Bremen (UB) apply different methods to combine the four Stokes components to carry out the polarisation transformation. Whereas UHH use the three polarisations from consecutive snapshots to get a complete combination of Stokes components, UB interpolates at each snapshot missing polarisation using neighboring snapshots before and after current snapshot. We use one example measurement which is listed in the Table 5.2 to explain the difference.

In Table 5.2, the DGG point has ten measurements with one of the four polarization combinations: [XX], [XX, XY], [YY], [YY, YX]. Since the XY or YX polarization is observed within the same snapshot as the XX or YY polarization, the ten measurements of this DGG distribute over seven snapshots. UB interpolates either one or three values (XY counts for two interpolations because it is complex) for each of the snapshots (see the last columm of Table 5.2). UHH selects XX, YY, XY(or YX) components from the nearest snapshots and neglect the differences in the incidence angle, as well as Faraday and georotation angles which vary very slowly in the neighboring snapshots. In this way a sequence of [XX, YY, XY (or YX)] datasets (this is named as series number in the Figures 3 and 4) can be obtained for the transformation. For example, from the measurements listed in Table 5.2 we get three sets [XX, YY, XY (or YX)]. We combine the measurements 1,3,4 as the first set, combine the measurements 2,5,6 as the second set and combine the measurements 7,9,10 as the third set. The difference of acquisition times inside one set is less than 2.5 s. Both UHH and UB methods guarantee that the incidence angle of the snapshots used in one dataset varies less than $0.5°$. In case of RFI or missing measurement both methods will have data loss.

Figure 5.2 and Figure 5.3 show the comparison of horizontally and vertically polarized brightness temperatures interpolated and transformed at UHH and UB. The first test grid point is located in the Arctic and the second one is located in the Antarctic. Only brightness temperatures measured in the incidence angles between 40° and 50° are considered. One SMOS swath in 13 October 2010 is used for the comparison.

Table 5.2: The first ten measurements at a selected DGG: 4102890, Date: 2010.10.13

Nr.	Polarization	Snapshot	Acquisition time (second)	Incidence angle (°)	Azimuth angle (°)	Values interpolated by UB
1	YY	49641343	5167.5	45.26	208.88	XX, XY
2	YY	49641344	5168.7	45.07	209.49	XX
3	YX					
4	XX	49641345	5169.9	44.89	210.11	YY, YX
5	XX	49641347	5171.1	44.70	210.75	YY
6	XY					
7	YY	49641348	5172.3	44.53	211.38	XX, XY
8	YY	49641349	5173.5	44.35	212.03	XX
9	YX					
10	XX	49641350	5174.7	44.18	212.68	YY, YX

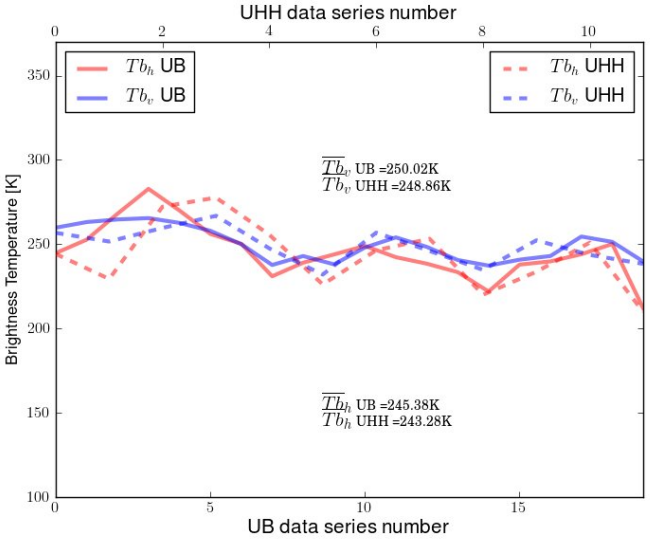

Figure 5.2: Comparison of the first two Stokes components at test point 1 (DGG Nr. 4102890, lat:83.65°, lon:37.97°) between UHH and UB in *Antenna frame* and *Earth frame*. This grid point is located in the Arctic. There are RFI signals which are not removed from the measurement data. Only incidence angle range between 40 and 50 degrees are used.

At the arctic test point 1 the measured brightness temperatures have values higher than 300 K which are probably contaminated by Radio Frequency Interference (RFI). More information about RFI and RFI filter will be given in Chapter 5.4. For the comparison we included these measurements to estimate the propagation of the extreme values via interpolation. At the antarctic test point 2 the signals are quite stable and no RFI contamination can be observed. The two different methods show very good agreement at test point 2 with brightness temperature differences less than 0.05 K in both polarizations. At test point 1 the difference in vertical and horizontal polarizations is as high as 3 K. This indicates that if the brightness temperatures have strong variability and include extreme values, the interpolation methods have different propagation. In contrast to the interpolation method of UB, UHH uses only the measured brightness temperatures from the consecutive measurements and combine them to carry out polarisation transforamtion. This can reduce the propagation of extreme values caused by the interpolation.

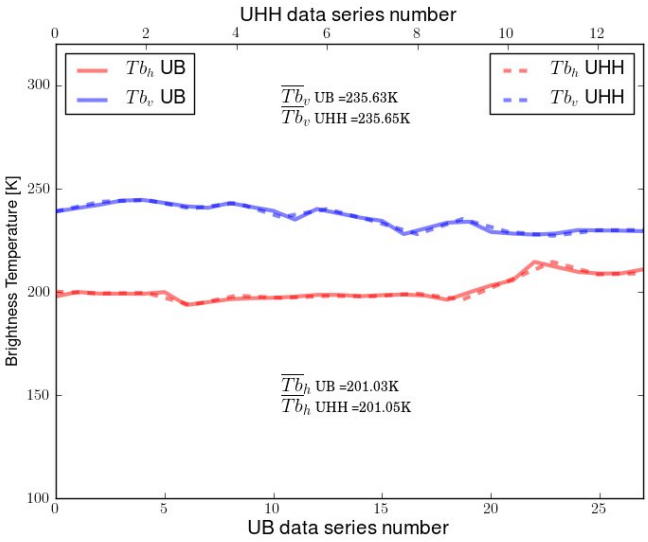

Figure 5.3: Comparison of first two Stokes components at test point 2 (DGG Nr. 7177702, lat:-79.66°, lon:164.66°) between UHH and UB in *Antenna frame* and *Earth frame*. This grid point is located in the Antarctic. There are no RFI signals. Only incidence angles between 40 and 50 degrees are used.

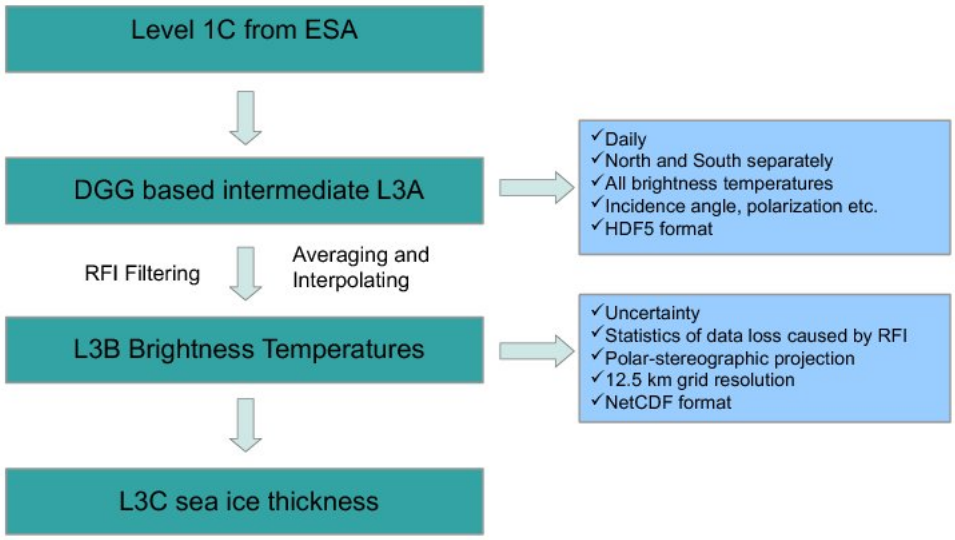

Figure 5.4: The flow chart of processing steps from SMOS L1C to L3

5.3 Operational L3B brightness temperature at University of Hamburg

5.3.1 Processing of SMOS L1C data to L3B brightness temperature

The processing steps from L1C to L3 are optimized in such to ease the reprocessing after possible revisions of the RFI filters and retrieval algorithms (Figure 5.4). For this purpose we produce an intermediate L3A product. The daily L3A data collects all orbital data for each 24-hour period at the respective DGG grid points. The daily L3A product is stored in north and south polar regions separately and contains not only all the daily available brightness temperature measurements but also incidence angle, polarization and flags, Snapshot ID, Faraday and geometric rotation information. The L3A product is stored in HDF format and can be read in a few seconds. L3B product which includes the first Stokes component, uncertainties of brightness temperature measurements, as well as the number of TB_h and TB_v pairs and the data loss percentage caused by RFI is derived from L3A product. The RFI filtering is done within the processing steps from L3A to L3B. L3B data is directly produced from L1C data. No single swath-based Level 2 dataset is produced in our processing chain.

Over sea ice the first Stokes parameter (intensity) is almost independent of incidence angle in the incidence angle range of 0°-40° (Figure 5.5). The intensity is the average of the horizontally and the vertically polarised brightness temperatures, i.e. it is equal to $0.5(TB_h + TB_v)$. The intensity is independent of both geometric and Faraday rotations and robust to instrumental and geophysical errors (Camps et al., 2005). We can avoid additional uncertainties caused by the transformation from the antenna reference frame to the Earth reference frame by using the intensity. Since each snapshot measures either horizontally or

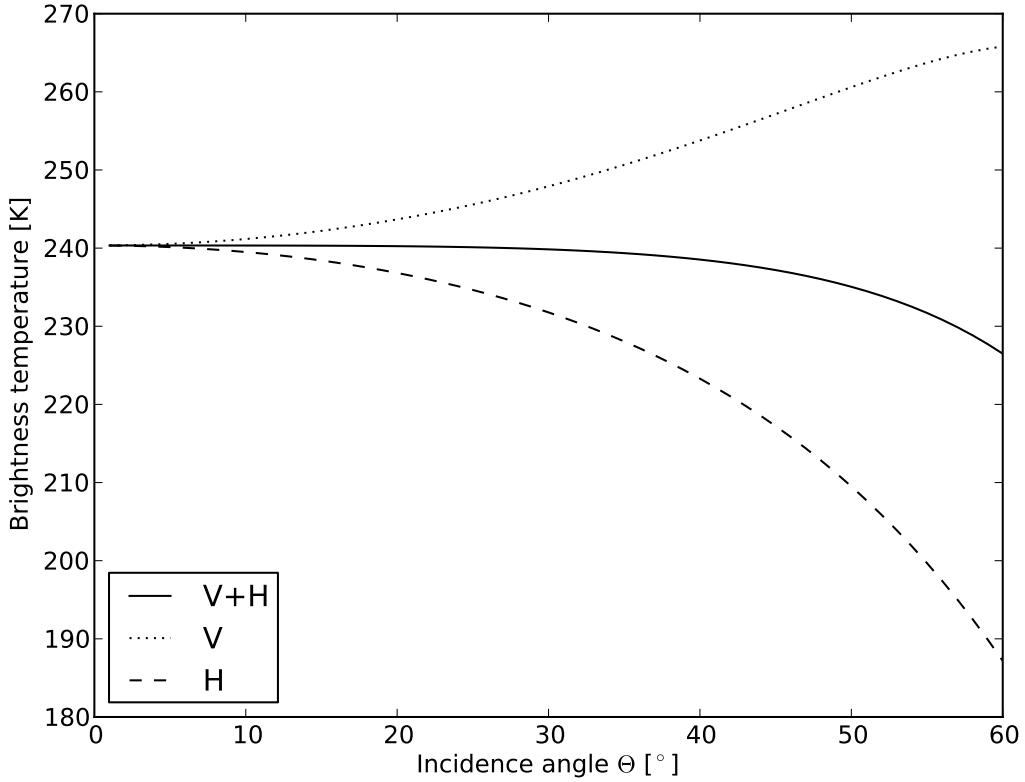

Figure 5.5: Vertically (V) and horizontally (H) polarised TBs and the first Stokes parameter as a function of incidence angle calculated using a three layer model for sea ice with a thickness of $d_{ice} = 1$m, a bulk salinity of $S_{ice} = 8$ g/kg, and a bulk ice temperature of $T_{ice} = -7°$C.

vertically polarised brightness temperature, we use consecutive snapshots with an acquisition time difference of less than 2.5 s to calculate the intensity. The advantage of using near nadir view measurements is the smaller footprint associated with low incidence angles. Furthermore, by using the whole incidence angle range of 0°-40° we get more than 100 brightness temperature measurements per day for most of the pixels in the Arctic, and by averaging over a lot of measurements we can significantly reduce the uncertainty of the retrieval. The daily averaged brightness temperature intensities in the Arctic and in the Antarctic are interpolated with nearest neighbor algorithm and gridded into the National Snow and Ice Data Center (NSIDC) polar stereographic projection with a grid resolution of 12.5 km. We use this grid resolution because other products that we use as auxiliary data in the retrieval are also given in this resolution. We call this product L3B brightness temperature. In the following we use TB to indicate the daily averaged brightness temperature intensity. The data have been available since January 2010. Data are processed with two days latency for both hemispheres. The L3B TBs are the basis of the sea ice thickness retrieval with Algorithm I and II from UHH which will be introduced in Chapter 6 and can be obtained from icdc.zmaw.de.

5.3.2 L3B brightness temperature over selected grid points

The stability and variability of L3B TB is estimated over open water, multiyear ice, first year ice in the Arctic from 1 October 2010 to 30 September 2011. The geographical positions of the selected grid points are marked with a star in Figure 5.6. During the one year period

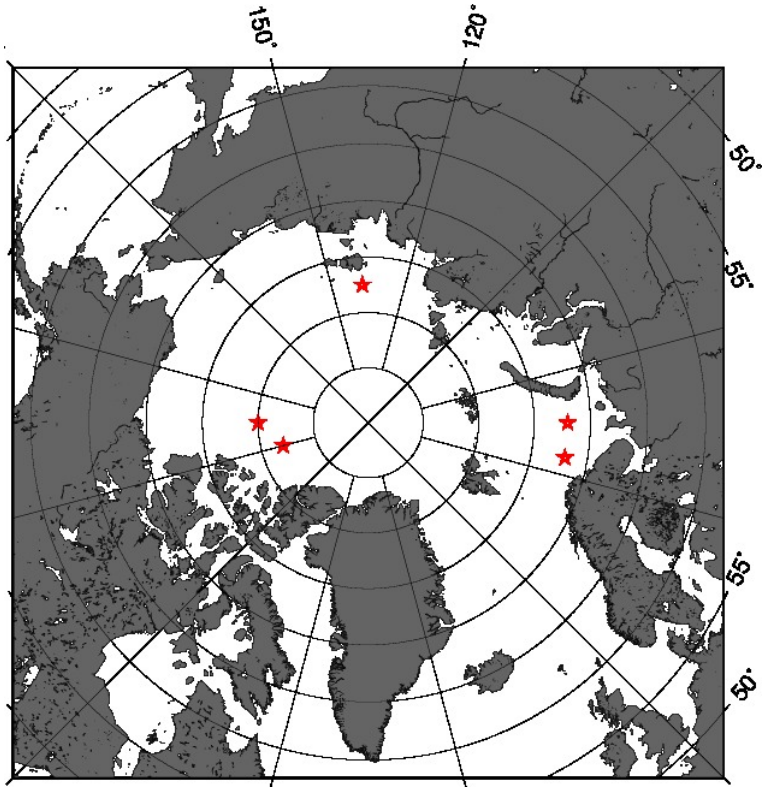

Figure 5.6: The geographical positions of the selected grid points over open water, multiyear ice, and first year ice.

TB over open water shows an average of about 100 K with a standard deviation of 2.4 K (Figure 5.7). This is close to the value of the first tie point T_0 (100.5 K) over open water used in the retrieval algorithm I from UHH. To verify the other tie point T_1 which is TB over thick ice, we selected out grid points over first year thick ice and multi year thick ice. Due to less salinity in multiyear ice, the brightness temperature from multiyear ice is about 2-3 K heigher than that over first year thick ice (Figure 5.7).

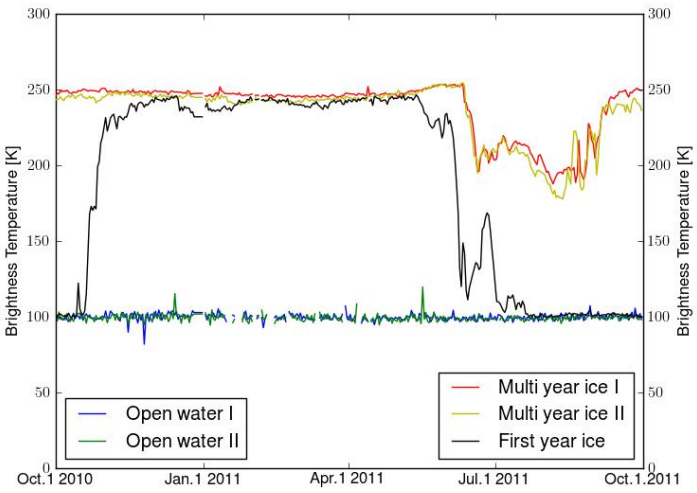

Figure 5.7: SMOS L3B brightness temperature over open water, multiyear ice, and first year ice from 1 October 2010 to 30 September 2011. Incidence angle: 0°-40°

5.3.3 L3B brightness temperature during freeze-up period in the Arctic and Antarctic

Weekly averaged L3B TB is shown for the freeze-up period of 2010 for the Arctic and 2011 for the Antarctic respectively (see Figure 5.8, Figure 5.9, Figure 5.10, Figure 5.11).

5.3.4 L3B brightness temperature uncertainties

A first estimation of TB uncertainties is provided at each grid point on daily basis in L3B TB data set. The TB uncertainties are caused not only by the radiometric accuracy of the instrument which is dependent on the incidence angles, but also the variability of the measurements from consecutive snapshots from different swaths. We define the TB uncertainty as one standard deviation of all TB measurements devided by the number of TBh and TBv pairs used for the calculation of mean intensity daily. An example of TB uncertainty is shown in Figure 5.12 for 15 November 2010.

5.3.5 Data variables and format Description

The variables TB, $TBuncertainty$, $nPair$, and $RFIratio$ have dimensions of (time,y,x), with (y=896 x=608) in Arctic and (y=664 x=632) in Antarctic. The time is the hours since 2010-01-01 00:00:00. Geolocations (latitude and longitude) are given at each grid cell. An overview of the variables is given in Table 5.3. Data files are offered on the THREDDS server. A quick look of daily data can be visualized with LAS. Data are available since 12 January 2010 daily in NetCDF format for the north and south polar regions.

The following example shows how to cite the use of this data set in a publication.

X. Tian-Kunze, L. Kaleschke, N. Maass (2012) SMOS Daily Polar Gridded Brightness Temperatures, [list dates of temporal coverage used]. ICDC, University of Hamburg, Germany, Digital media.

Table 5.3: Description of variables

variables	long name	data type	dimension	missing value	scale factor	unit
Latitude	latitude	32 bit float	(y,x)	-999	1.0	degree
Longitude	longitude	32 bit float	(y,x)	-999	1.0	degree
TB	brightness temperature intensity (TBh+TBv)/2	32 bit float	(time,y,x)	-999	1.0	K
TB uncertainty	brightness temperature uncertainty	32 bit float	(time,y,x)	-999	1.0	K
nPair	number of TBh and TBv pairs	16 bit integer	(time,y,x)	-999	1.0	
RFI ratio	percent of RFI-contaminated measurements in total measurements	32 bit float	(time,y,x)	-999	1.0	percent

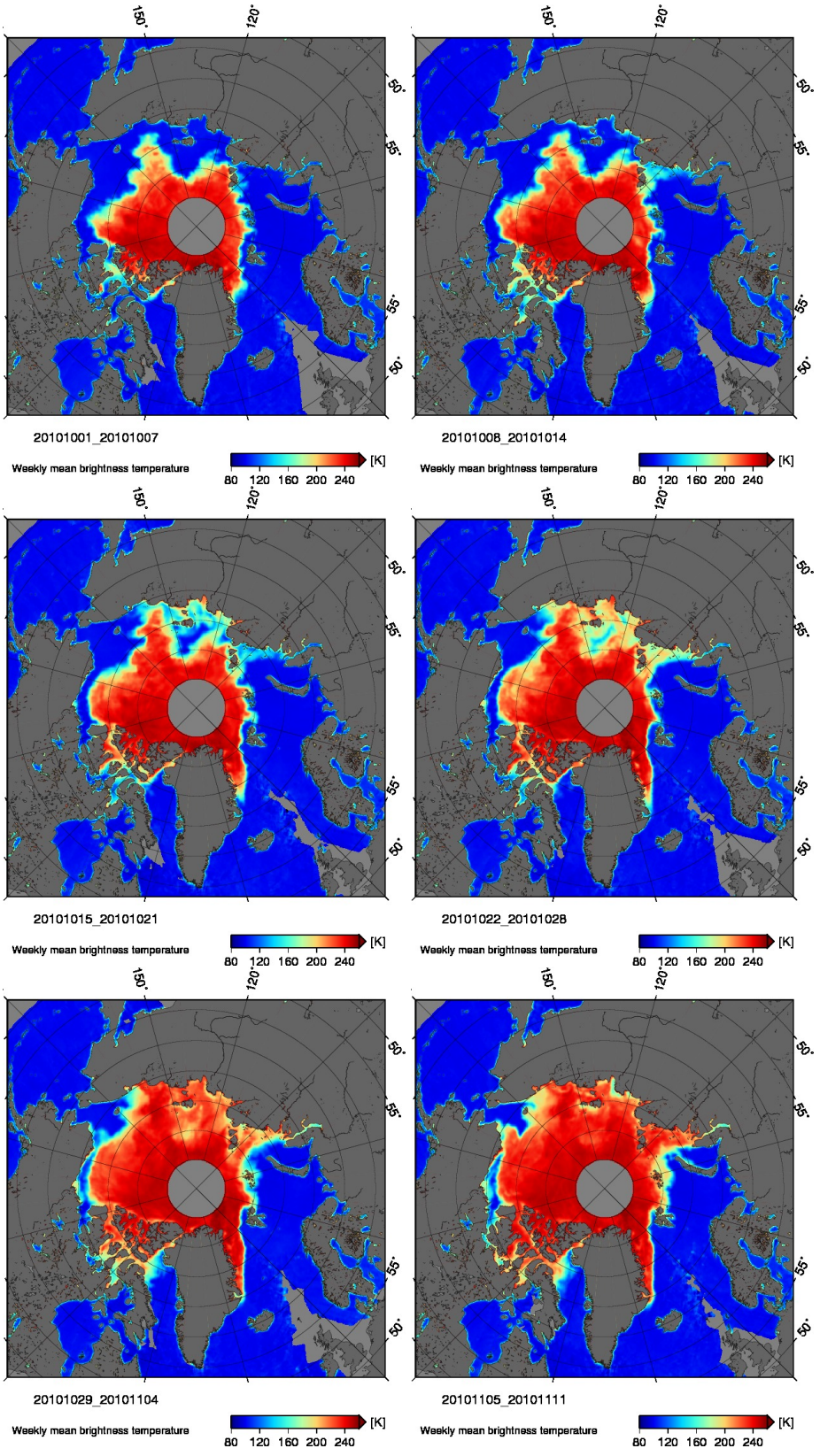

Figure 5.8: Weekly averaged TB in the freeze up period of 2010 in the Arctic

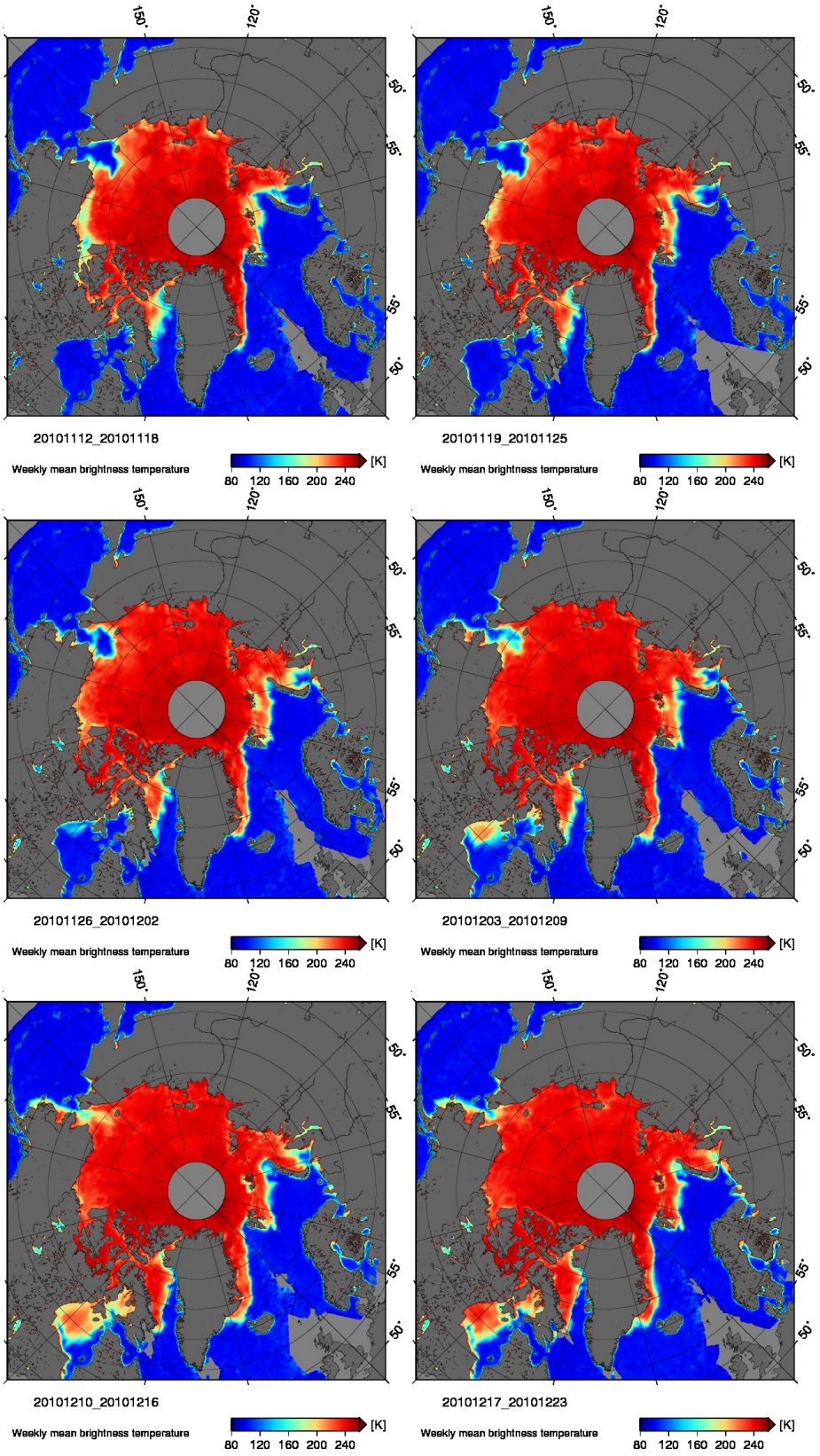

Figure 5.9: Weekly averaged TB in the freeze up period of 2010 in the Arctic

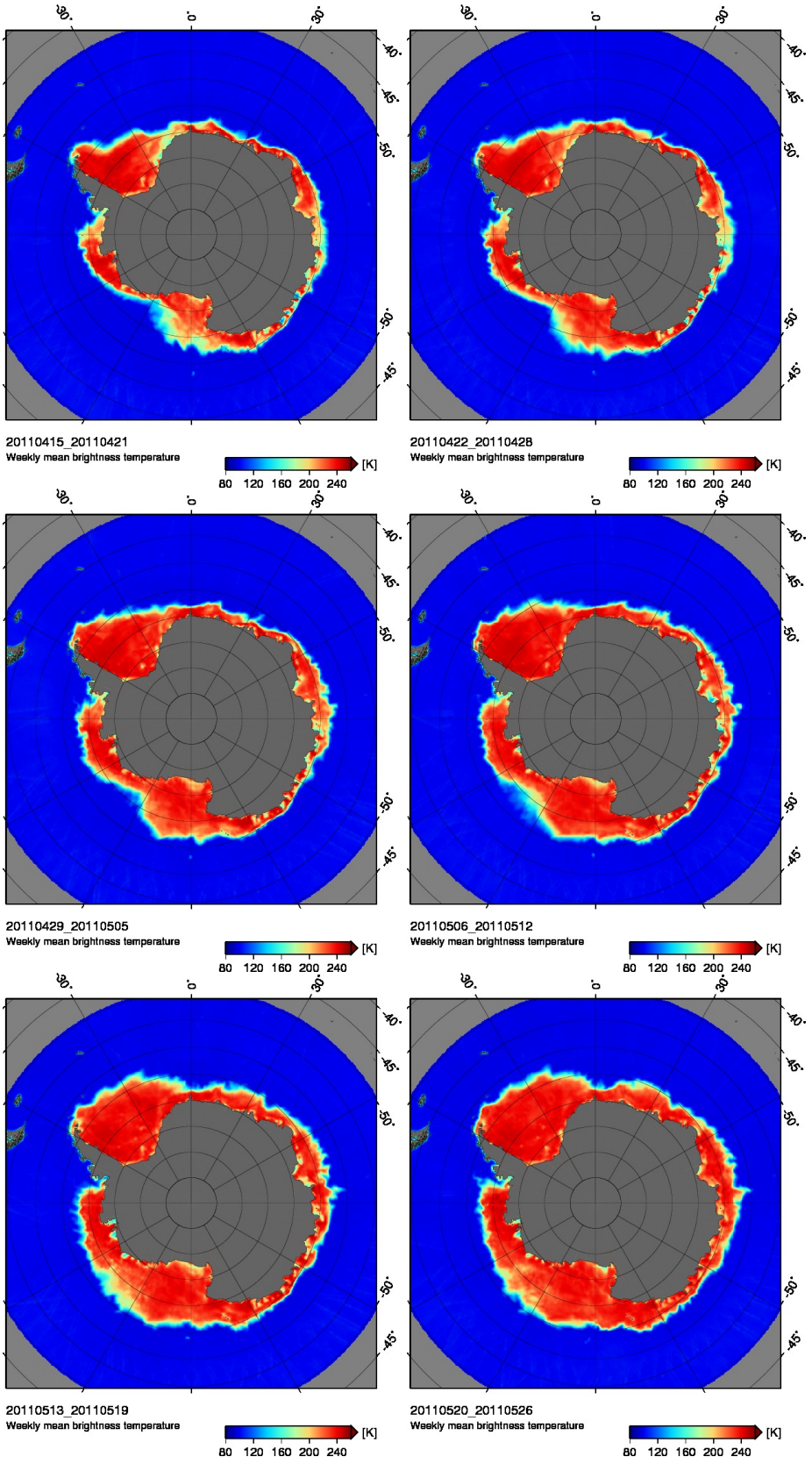

Figure 5.10: Weekly averaged TB in the freeze up period of 2011 in the Antarctic

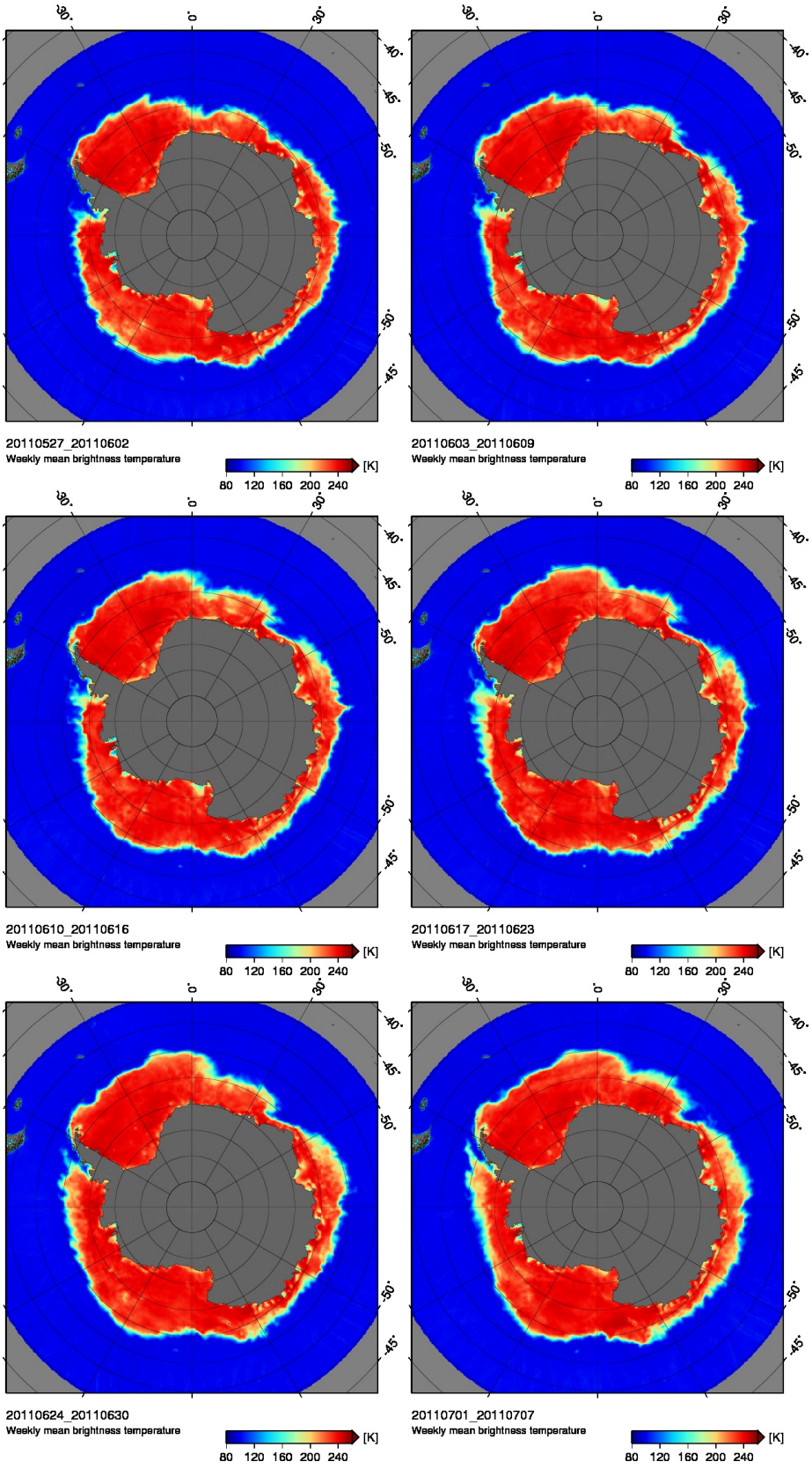

Figure 5.11: Weekly averaged TB in the freeze up period of 2011 in the Antarctic

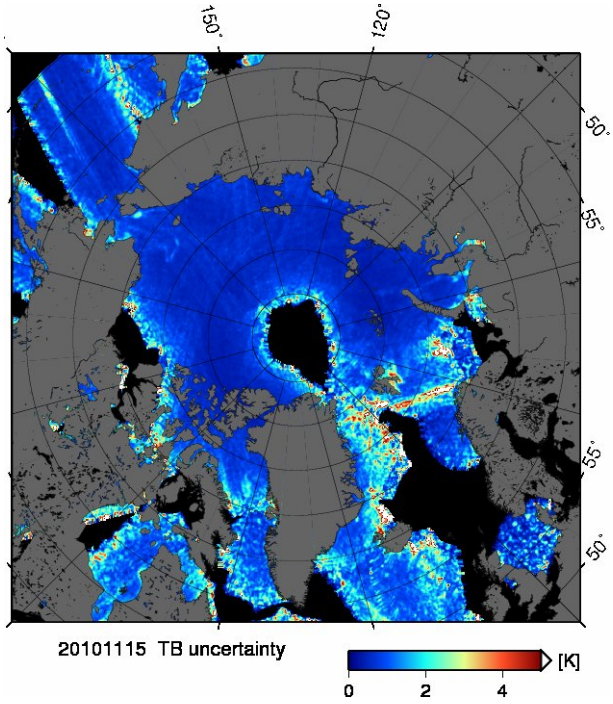

Figure 5.12: SMOS TB uncertainty distribution. Date: 15 November 2010

5.4 RFI and data loss due to RFI

SMOS measurements are partly influenced by Radio Frequency Interference (RFI) which comes from radars, TV and radio transmission (Mecklenburg et al., 2012). The detection of the RFI sources and the mitigation of RFI influence are critical steps for the further retrieval of geophysical parameters. The RFI influence depends on the incidence angle, polarisation, and ascending and descending modes of the satellite (Camps et al., 2010). A closer look into RFI contaminated snapshots shows that RFI can either completely or partly destroy a snapshot (Camps et al., 2010). Figure 5.13 and Figure 5.14 show the maximum brightness temperatures at each grid point either in horizontal or vertical polarisation in ascending and descending modes. Three days data (15-17 November 2010) are used for the analysis. RFI influence differs from region to region for horizontal and vertical polarisation. At nadir look RFI signals have less impact on the surrounding regions than at higher incidence angles (Figure 5.15, Figure 5.16). Especially at high incidence angles there is a strong RFI impact in the horizonally polarised brightness temperature around the central Arctic. We suspect that this is caused by remote RFI signals.

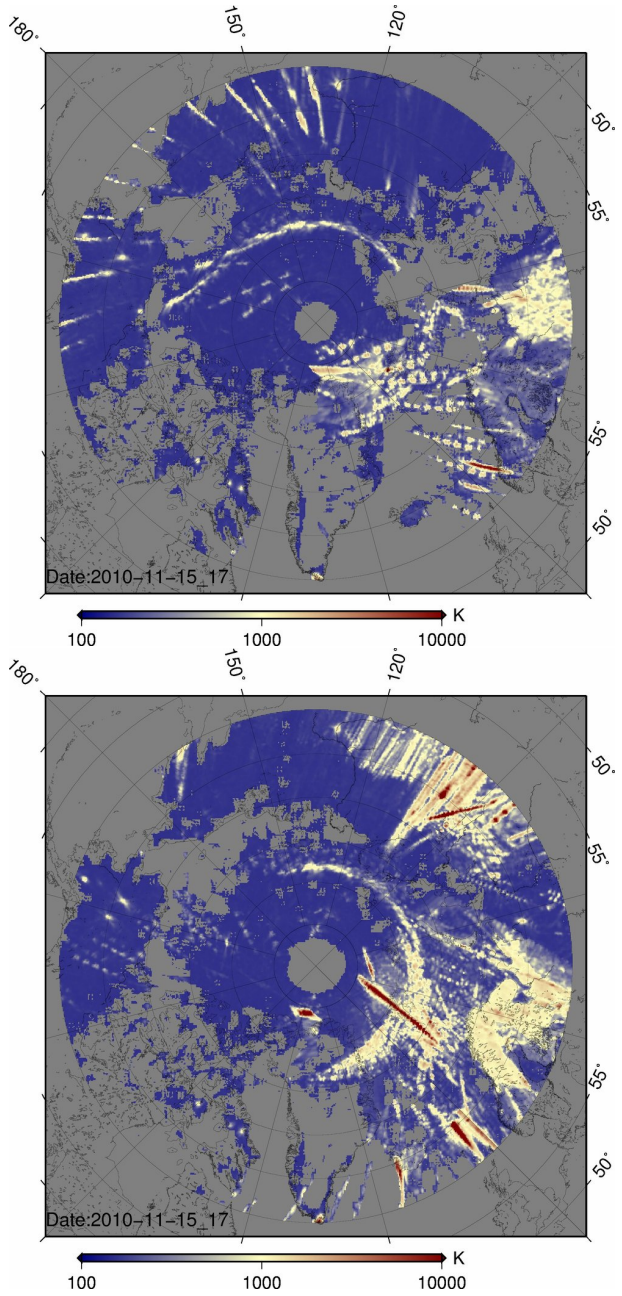

Figure 5.13: The maximum brightness temperatures at each grid point in XX polarization in Ascending (top) and Descending (bottom) modes.

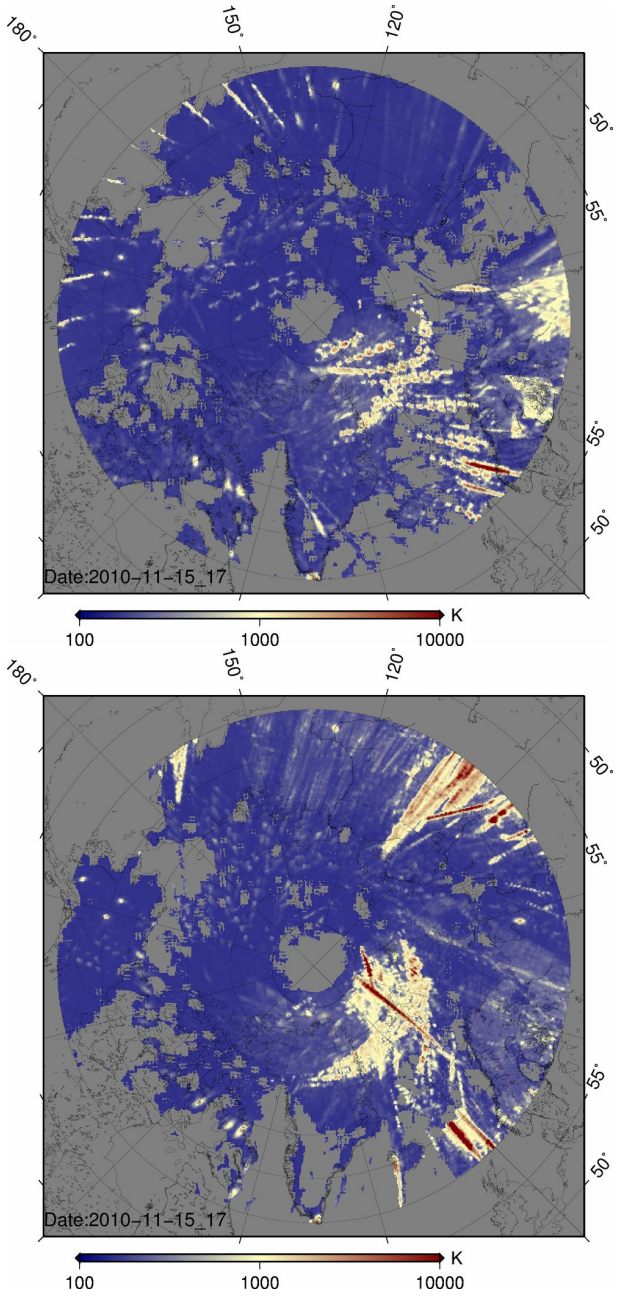

Figure 5.14: The maximum brightness temperatures at each grid point in YY polarization in Ascending (top) and Descending (bottom) modes.

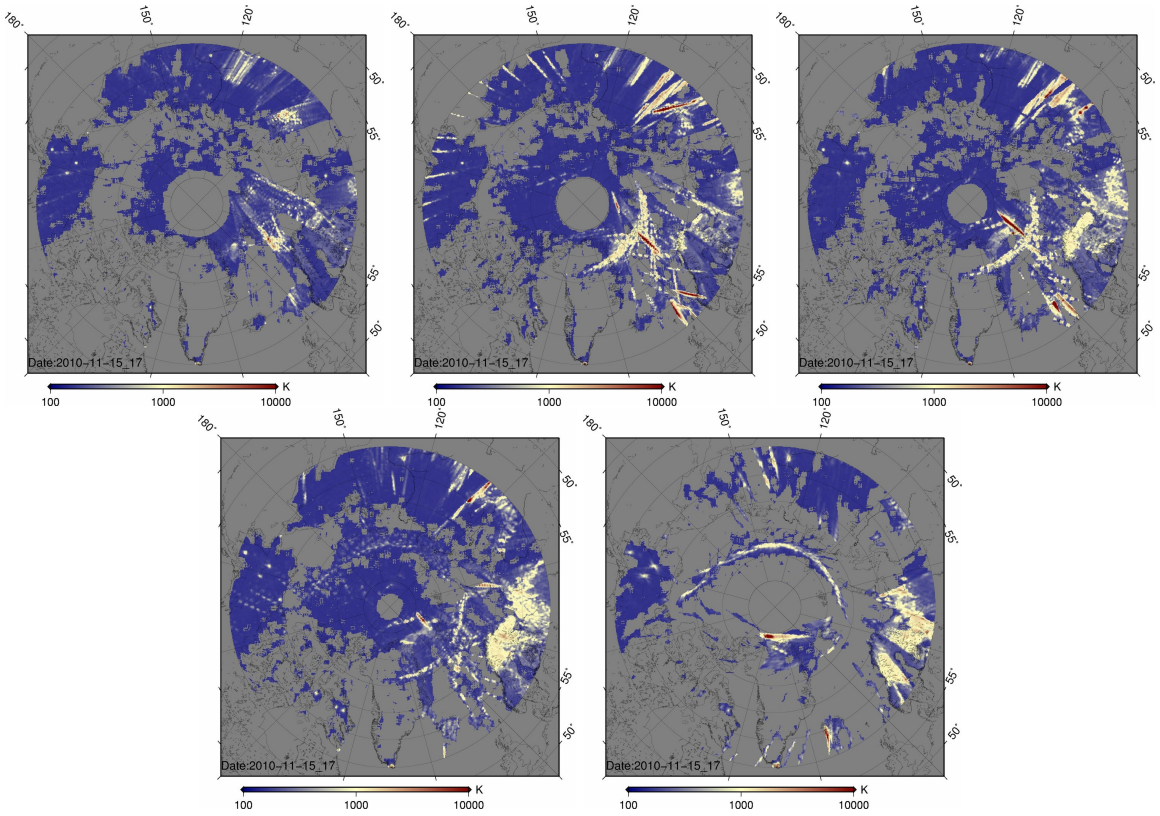

Figure 5.15: The maximum brightness temperatures at each grid point in XX polarizations in incidence angle ranges 0°-20° (upper left), 20°-30° (upper right), 30°-40° (middle left), 40°-50° (middle right), and 50°-70°(lower middle). Time period 2010.11.15-17

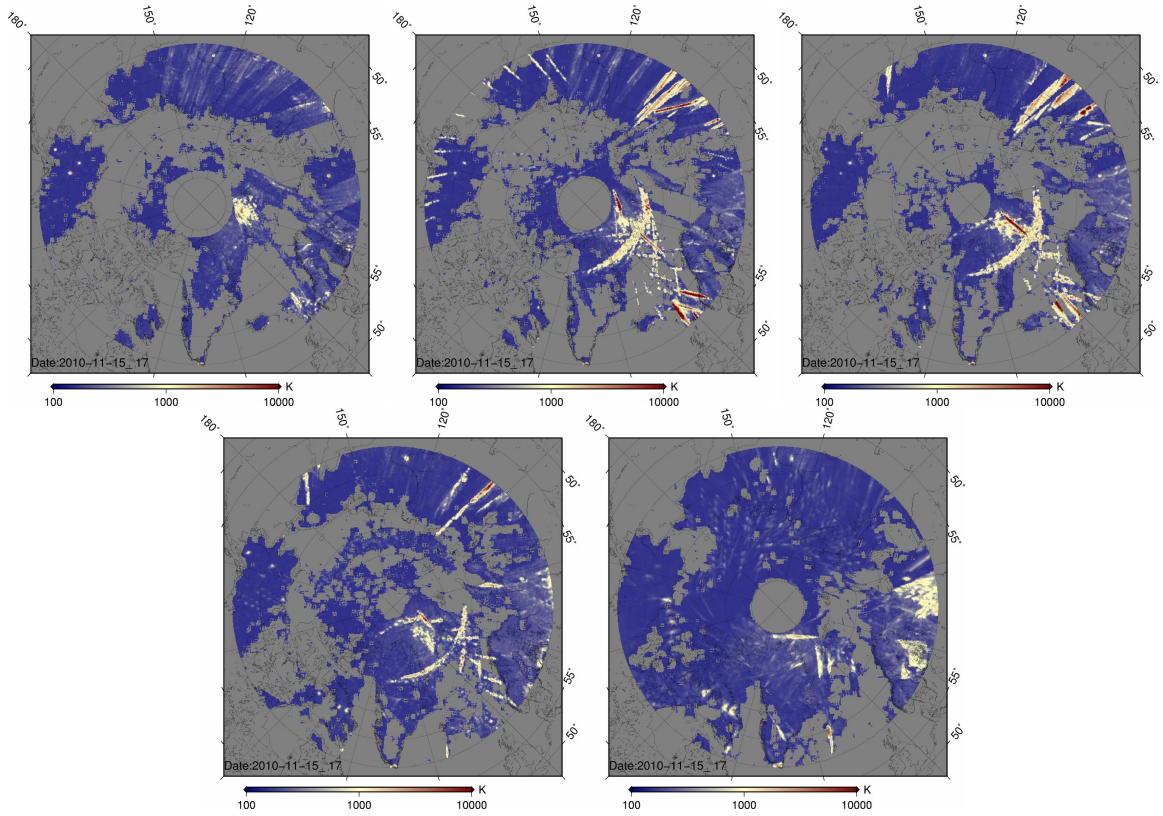

Figure 5.16: The maximum brightness temperatures at each grid point in YY polarizations in incidence angle ranges 0°-20° (upper left), 20°-30° (upper right), 30°-40° (middle left), 40°-50° (middle right), and 50°-70°(lower middle). Time period 2010.11.15-17

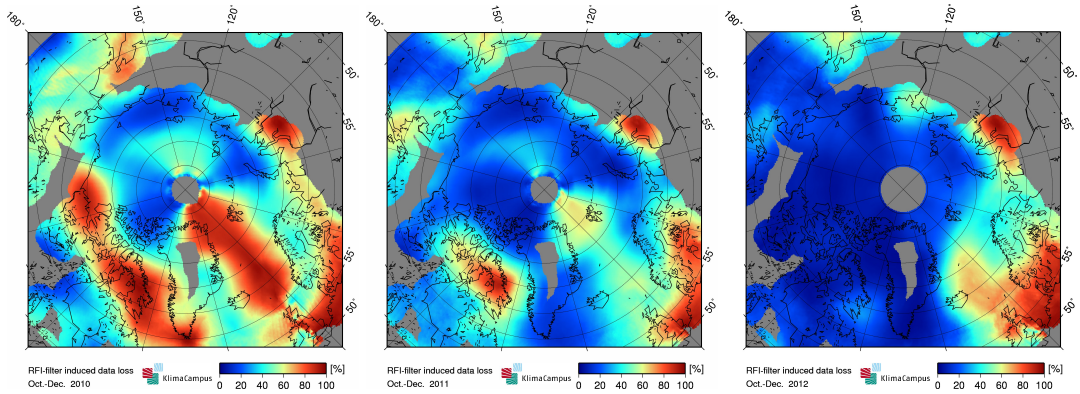

Figure 5.17: The improvement of RFI-induced data loss in the Arctic from 2010 to 2012.

For simplification we apply a treshold value for both horizontally and vertically polarised brightness temperatures. If either of them exceeds 300 K within one snapshot, this snapshot is considered as RFI contaminated. Brightness temperatures higher than 300 K can not be expected either in the Arctic or in the Antarctic. The RFI filtering is done within the processing steps from L3A to L3B. RFI influence is seldom observed in Antarctic. However, in the Arctic RFI contamination is widely and frequently detected. According to this RFI filter, strongly RFI affected regions are the region northeast of Greenland and parts of the Canadian Arctic Archipelago. Figure 5.17 shows the RFI-induced data loss based on our RFI filter. The data loss in the figure is defined as the ratio between the number of RFI contaminated measurements and the number of total measurements. As can be seen from Figure 5.17, RFI situation in the Arctic region has improved much since 2010.

6 ATBD1

Lars Kaleschke

6.1 Introduction

The ocean-atmosphere heat exchange is controlled by the ice thickness distribution in the polar oceans. Thin ice with a thickness of less than half a meter dominates the overall heat exchange and has thus potential impact on weather and climate.

The aim of the SMOSIce study is to develop, improve and validate algorithms for sea ice thickness retrieval from the 1.4 GHz (L-band) data of the European Space Agency's (ESA) Soil Moisture and Ocean Salinity (SMOS) mission. SMOS payload is the Microwave Imaging Radiometer by Aperture Synthesis (MIRAS) measuring the brightness temperature at a range of incidence angles and at different polarizations.

Electromagnetic radiation with wavelengths of 20 cm can emerge from deep inside the sea ice layer. The attenuation mainly depends on the relative brine volume which is a function of ice bulk salinity and temperature. The penetration depth is up to 1.5 m for cold low-salinity ice and reduces to a few centimeters for saline sea ice at high temperatures. The potential to derive the ice thickness from L-band radiometry thus depends on sea ice temperature and salinity.

A physical sea ice emissivity model is an integral part for the retrieval of ice thickness from SMOS measurements. The most simple setup consists of a three layer (ocean-ice-atmosphere) dielectric slab with plane-parallel specular surfaces. The dielectric properties are parameterized as a function of the bulk ice salinity and temperature. The sea ice bulk salinity and ice surface temperature has to be obtained either from auxilliary measurements or has to be parameterized.

One main objective of the SMOSIce study is to determine the best solution for SMOS sea ice thickness retrieval. This document describes the first version of the retrieval algorithm developed by the KlimaCampus team of the University of Hamburg, named *KlimaCampus SMOS sea ice algorithm I*. This first version of the algorithm is based on the semi-empiric retrieval model described in (Kaleschke et al., 2010). The semi-empiric model approximates the results of a physical three layer model. The meaning of the "I" in the algorithm's name is twofold. Firstly, it refers to the first element of the Stokes vector I, which is used for the retrieval, and secondly it refers to the version number one, which means that further improvements are likely.

Three parameters are necessary to empirically describe the development of the brightness temperature as a function of the sea ice thickness: two tie points for open water and thick ice, and an attenuation factor. The attenuation factor is a function of ice temperature and salinity. In the first version of the alorithm we assume the attenuation factor to be constant. With this assumption the three parameters can be obtained in three different ways. The first method is to calculate the parameters from the three-layer model with assumptions about a mean ice salinity and temperature. The second method is to obtain the parameters from SMOS

brightness temperatures in combination with reference ice thicknesses. The third method is a combination of both previous methods.

In order to keep the design of the algorithm as simple as possible and to avoid the usage of additional ice concentration data from other sensors we assume a complete 100% ice coverage for the retrieval. This assumption simplifies the implementation of the *algorithm I* in an operational SMOS processing chain. We further show that the retrieved ice thickness represents an effective ice thickness, i.e. the average thickness per unit area. Thus, the result can be interpreted as a measure of ice volume, the product of ice concentration and thickness.

6.2 Algorithm Description and Theoretical Basis

6.2.1 The radiative transfer model

The brightness temperature measured at the satellite level consists of four main contributions: i) the surface emission, ii) the up-welling atmospheric emission, iii) the down-welling atmospheric emission reflected at the surface, iv) sky background reflected by the surface.

At L-band, the atmospheric influence is small except for the ionosphere. The Faraday rotation depends on the ionospheric total electron content (TEC) and causes a rotation of the polarisation which has to be taken into account.

The sky background includes the isotropic cosmic background of 2.7 K, as well as the directional galactic and the solar source. The sky background can contribute significantly to the measured signal.

For the retrieval we assume two surface types, open water and ice with the fractional area coverage (total ice concentration) $1 - C$ and C, respectively. The observed brightness temperature depends on the temperatures of the sea T_{sea} and the ice T_{ice} and their emissivities e_{water} and e_{ice}. By neglecting the atmospheric attenuation we write the radiative contributions of the observed signal as following

$$T_{\text{obs}} = (1 - C)e_{\text{sea}}T_{\text{sea}} + Ce_{\text{ice}}T_{\text{ice}} + T_{\text{other}}. \tag{6.1}$$

The observed brightness temperature $T_{\text{obs}}(\theta, p)$ is a function of the incidence angle θ and the polarisation p. The latter term T_{other} represents all other contributions including the atmospheric contribution, the reflected sky background and RFI.

6.2.1.1 Ocean emissivity e_{sea}

The emissivity of the water surface e_{water} is calculated from the Fresnel equations (SWIFT, 1980) for the special case of a specular reflecting surface. The model of Klein and Swift (1977) is used to estimate the permittivity of sea water as a function of temperature and salinity.

The L-band emissivity of a flat sea as a function of viewing angle and polarisation is quite well understood. Several different theoretical formulations exist for the emission of a roughened surface. At present it can not be decided which model delivers the best representation (Font et al., 2010). It is expected that SMOS data will soon generate substantial scientific progress in this field. Until then we describe the ocean emissivity as a sum of the specular term e_{flatsea} and the increase due to surface roughness $\delta e_{\text{roughness}}$

$$e_{\text{sea}} = e_{\text{flatsea}} + \delta e_{\text{roughness}}. \tag{6.2}$$

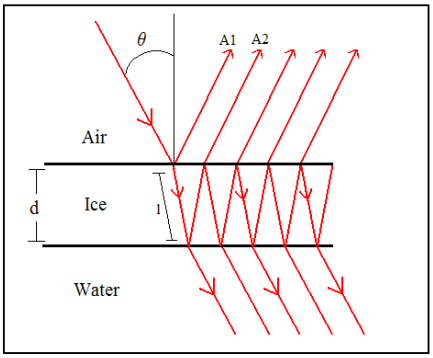

Figure 6.1: Three layer model for the emissivity of sea ice with thickness d. The optical pathlength l depends on the incidence angle θ, the thickness d, and the sea ice permittivity.

6.2.1.2 Sea ice emissivity e_{ice}

The most important parameters that influence the L-band emissivity of sea ice are the ice salinity and ice temperature. The brine volume and thus the permittivity are mainly a function of salinity and ice temperature. A snow layer changes the dielectric as well as the thermal properties of the underlying sea ice. Similar as for the ocean surface the influence of sea ice surface roughness on the emissivity is not yet well understood.

The model for the KlimaCampus SMOS sea ice algorithm I is based on the three-layer model of Kaleschke et al. (2010). In the following we repeat our assumptions and equations for completeness. A sketch of the model is shown in Fig. 6.1. The model does not take into account the effect of surface roughness, except for the assumption of a statistical thickness variation σ_d, that is necessary for the incoherent averaging.

We further neglect volume scattering due to brine pockets and air bubbles and treat the sea ice layer as a homogeneous medium. This is very likey a good approximation since the scatterering objects are small with respect to the L-band wavelength of 21 cm.

Another approximation is the assumption of a single bulk temperature of the sea ice layer. This assumption is not well justified since in general we do not have an isothermal medium but strong temperature gradients. In the first model version we neglect these effects. Also we do not account for the influence of an additional snow layer, except for its thermally insulating effect which increases the estimate of a bulk temperature from the surface air temperature.

The emissivity of ice e_{ice} follows from considering reflection at a dielectric slab of ice over water (Fig. 6.1). The reflection coefficient of an ice slab over an infinite half plane can be expressed as a function of the reflection coefficients R_1 and R_2, describing reflection at the upper and lower boundary of the slab (Ulaby et al., 1981):

$$R = \frac{R_1 + R_2 e^{-2ik_{i,z}d}}{1 + R_1 R_2 e^{-2ik_{i,z}d}}, \tag{6.3}$$

where d is ice thickness and $k_{i,z}$ is the z-component of the propagation vector in ice $\vec{k_i}$, with the z-axis perpendicular to the slab. The expression for $k_{i,z}$ can be separated into its real part β, which is called the phase constant, and its imaginary part α, which is referred to as the

attenuation coefficient: $k_{i,z} = \beta - i\alpha$. The expressions for α and β are

$$\alpha = \frac{\omega}{c_0} \cos\theta_i |Im\sqrt{\epsilon_i}| \quad (6.4)$$

$$\beta = \frac{\omega}{c_0} \cos\theta_i Re\sqrt{\epsilon_i}, \quad (6.5)$$

with the angle of refraction θ_i in the ice, the relative permittivity of ice ϵ_i, the angular frequency $\omega = 2\pi f$, and the speed of light c_0 in vacuum. The ice emissivity is calculated from $e_{ice} = 1 - r = 1 - R\overline{R}$, where r is reflectivity and $\overline{R}$ is the conjugate-complex of the reflection coefficient R. Assuming real power reflection coefficients the following expression for ice emissivity was derived (Menashi et al., 1993):

$$e_{ice} = \frac{(1 - r_i)(1 - Ar_w)}{1 + Ar_i r_w + 2\sqrt{Ar_i r_w}\cos(2\beta d)}, \quad (6.6)$$

where $A = \mathrm{e}^{-4\alpha \mathrm{d}}$. The reflectivity of air to ice r_i and the reflectivity of ice to water r_w are calculated from the Fresnel equations with the permittivity of ice provided in the next section.

The above equation is a coherent solution describing ice emissivity as a periodic function of ice thickness. If the rms thickness variation of the ice slab is sufficiently large, i.e. more than a quarter of the used electromagnetic wavelength over the illumination footprint, the periodicity averages out and an incoherent solution can be introduced instead. The emissivity of ice averaged over a variety of ice thicknesses was derived by Menashi et al. (1993) and can be expressed as follows:

$$e_{\mathrm{ice}} = \frac{(1 - r_i)(1 - Ar_w)}{1 - Ar_i r_w} \left[\frac{1 - \sqrt{Ar_i r_w}\mathrm{e}^{-\beta\sigma_\mathrm{d}}}{1 + \sqrt{Ar_i r_w}\mathrm{e}^{-\beta\sigma_\mathrm{d}}}\right], \quad (6.7)$$

where σ_d is rms thickness variation (roughness) and σ_l the optical pathlength. As proposed ad hoc in Kaleschke et al. (2010) we use $\sigma_d = 0.1\, d$ to parameterise σ_d in the first version of the algorithm I.

6.2.1.3 Sea ice permittivity ϵ_{ice}

Vant et al. (1978) proposed an empirical relationship for the permittivity of ice ϵ_{ice} depending on the relative brine volume (in ‰; valid for $V_b < 70‰$):

$$\epsilon_{\mathrm{ice}} = a_1 + a_2 V_b + i(a_3 + a_4 V_b), \quad (6.8)$$

A linear combination of the coefficients derived at 1 and 2 GHz (Table 6.1) is used as an approximate value for 1.4 GHz.

6.2.2 Sea ice physics for the radiative transfer model

6.2.2.1 Brine volume V_b

Leppäranta and Manninen (1988) derived equations for determining the relative brine volume of low-salinity ice for temperatures between -2°C and 0°C

$$V_b = \frac{\rho_i S_{\mathrm{ice}}}{F_1(T) - \rho_i S_{\mathrm{ice}} F_2(T)}. \quad (6.9)$$

Table 6.1: Coefficients for the calculation of the sea ice dielectric constant (Hallikainen and Winebrenner, 1992). The 1.4 GHz coefficients are linearly interpolated.

Frequency [GHz]	a_1	a_2	a_3	a_4
First year ice				
1.0	3.12	0.0090	0.039	0.00504
1.4	3.10	0.0084	0.037	0.00445
2.0	3.07	0.0076	0.034	0.00356
Multi year ice				
1.0	3.12	0.0090	−0.004	0.00436
1.4	3.10	0.0084	0.003	0.00435
2.0	3.07	0.0076	0.013	0.00435

Table 6.2: Polynomial coefficients for the calculation of the brine volume for sea ice of low salinity and high temperature (Leppäranta and Manninen, 1988).

	α_0	α_1	α_2	α_3
F_1	−0.041221	−18.407	0.58402	0.21454
F_2	0.090312	−0.016111	0.00012291	0.00013603

Table 6.2 gives the coefficients of the polynomials $F = \sum_{j=0}^{3} \alpha_j T^j$. The pure ice density ρ_i is 917 kg/m^3. Winter bulk ice salinity averaged over samples collected at landfast sea ice in the Gulf of Finland in 1999–2001 is $S_{\text{ice}} = 0.65 \pm 0.3$ g/kg (Granskog et al., 2004).

For saline Arctic and Antarctic conditions the equations of Cox and Weeks (1983) for determining the brine volume fraction in sea ice are applicable. For temperatures in the range of -2 to -22.9°C

$$V_b = \frac{\rho_i S_{\text{ice}}}{F(T)} \tag{6.10}$$

the brine volume is calculated from the polynomial $F(T)$ as given in Table 6.3.

6.2.2.2 Sea ice salinity S_{ice}

Sea ice is a complex poroes multi-phase system and the evolution of the vertical salt distribution is governed by several processes such as the initial salt entrapment, brine expulsion and diffusion, gravity drainange, and flushing with surface meltwater (Vancoppenolle et al., 2007; Notz and Worster, 2009). Common sea ice models do not adequately represent the evolution of salinity. Recently, progress has been made by including a salinity distribution function and a parameterization of brine entrapment and drainage in a large scale 3D model (Vancoppenolle et al., 2009b,a).

Cox and Weeks (1974) describe a relationship based on two linear equations for the average salinity as a function of the ice thickness from cold sea ice at the end of the growth

Table 6.3: Polynomial coefficients for the calculation of the brine volume for sea ice with temperatures of -2$\geq T \geq$ -22.9°C (Cox and Weeks, 1983).

	α_0	α_1	α_2	α_3
F	−4.732	−22.45	−0.6397	−0.01074

season. Such a relationship could in principle be used to constrain the retrieval problem. This however, inherently connects the emissivity of the sea ice surface to the thickness. The relation holds even for ice that is much thicker than the penetration depth of the electromagnetic waves. Therefore, one has to be very careful with the interpretation of the results.

We do not prescribe the salinity as a function of ice thickness for our retrieval algorithm I. The salinity is treated as an independent parameter prescribed a priori.

6.2.2.3 Sea ice temperature T_{ice}

The ice temperature depends on the surface air temperature and on the snow thickness. The retrieval algorithm I is based on a mean bulk ice temperature prescribed a priori.

6.2.2.4 Surface roughness

The prototype model assumes a plane surface. This assumption is probably not reasonable for a realistic representation of the polarisation and angular dependency. A rough surface scattering approach introduces additional independent parameters such as RMS-height and correlation length and further assumptions about the statistical characteristics (Tsang et al., 2000). Even more as for the oceanic application it is not clear which rough surface scattering theory is best suited for the representation of a rough sea ice surface. The influence of the surface roughness depends on the incidence angle and polarisation with a larger effect for large incidence angles. The algorithm I is not based on large incidence angles and thus minimises the effect of surface roughness.

6.3 Sea ice thickness retrieval method

6.3.1 Semi-empiric retrieval model

A semi-empiric formulation allows to directly calculate the sea ice thickness from the brightness temperature. An approximation of the emissivity model is given by the following expression (Kaleschke et al., 2010)

$$T_{\mathrm{obs}} = T_m - (T_m - T_0)\exp(-\gamma d), \tag{6.11}$$

with the brightness temperature of open water T_0 and an attenuation factor γ. The mixture brightness temperature T_m is defined as

$$T_m = CT_1 + (1 - C)T_0, \tag{6.12}$$

with the brightness temperature of infinitely thick ice T_1 and ice concentration C. The parameters T_0 and T_1 are called tie points in analogy to the denomination used for ice concentration algorithms.

Equation 7.1 can directly be inverted for the retrieval of ice thickness

$$d = -\frac{1}{\gamma}\ln(\frac{T_m - T_{\mathrm{obs}}}{T_m - T_0}). \tag{6.13}$$

The maximum ice thickness d_{max} that can be retrieved for a given observational error δ is defined by the condition

$$d_{\mathrm{max}} = -\frac{1}{\gamma}\ln(\frac{\delta}{T_1 - T_0}). \tag{6.14}$$

The observational error δ can be defined by the uncertainty for the determination of the tie points. Thus, it includes the measurement uncertainty as well as the geophysical uncertainty due to the variability of emissivity.

6.3.2 Retrieval design

The design of the retrieval scheme depends on the subset of SMOS data that is used for the retrieval. Since SMOS offers the capability of multi-angle multi-polarisation measurements a restriction to a range of certain incidence angles and polarisations has to be well justified. In the following we show the advantages for using the first Stokes parameter I

Our first design decision is based on the incidence angle. The choice of an incidence angle range determines not only the spatial resolution but also the sensitivity to thickness. If we limit the observations close to nadir the highest resolution can be obtained. There is a trade-off between the spatial resolution, the swath width, and the time needed to achieve a complete spatial coverage. The cost of higher resolution is a narrower swath width. Thus, more time is needed to achieve a complete spatial coverage of the polar regions. By taking into account the incidence angle up to $\theta < 40°$ a complete coverage of the polar region can be achieved almost daily while by restricting the incidence angle to $\theta < 20°$ an integration over three days is necessary.

Another advantage of using near nadir measurements is the reduced RFI influence as compared to off-nadir measurements (Tian-Kunze et al., 2011).

The atmospheric contribution due to the emission of water vapor is less than 1 K for nadir and about 50% larger for $\theta = 50°$.

There are two advantages for the useage of the first Stokes parameter I instead of the polarizations separately. Firstly, it avoids possible errors due to the Faraday rotation. Secondly, the angular dependency is reduced as compared to the polarised signals. The drawback of using only the first Stokes parameter I is the possible loss of information that could be obtained from the polarizations. However, our model does not suggest that there is any extra information.

Figures 6.2 and 6.3 justify our selected range of incidence angles and the useage of intensity. In Fig. 6.2 shows that the vertical and horizontal components vary considerably but sum up to the intensity I which is almost constant up to $\theta < 40°$. Fig. 6.3 demonstrates the advantage of near nadir measurements in comparison to $\theta = 60°$. For the latter case the retrievable maximum ice thickness is reduced by 10%.

We summarise the advantages of our retrieval design that uses the first Stokes parameter I for incidence angles $\theta < 40°$:

- large ice thickness sensitivity,
- fine spatial resolution,
- complete daily coverage,
- small angular dependency,
- small atmospheric and RFI influence,
- no influence of Faraday rotation.

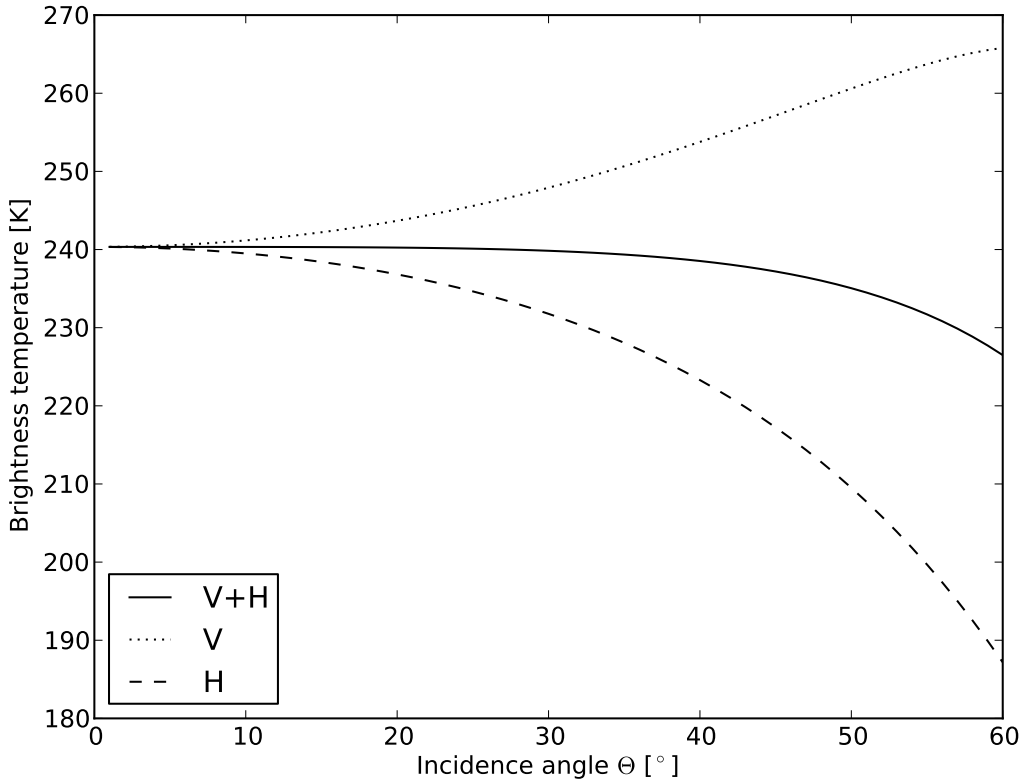

Figure 6.2: Vertically (V) and horizontally (H) polarized components of the brightness temperatures and the first Stokes parameter I as a function of incidence angle calculated using the three layer model for sea ice with a thickness of $d = 1$m, salinity $S = 8$ g/kg, and temperature $T = -7°$C.

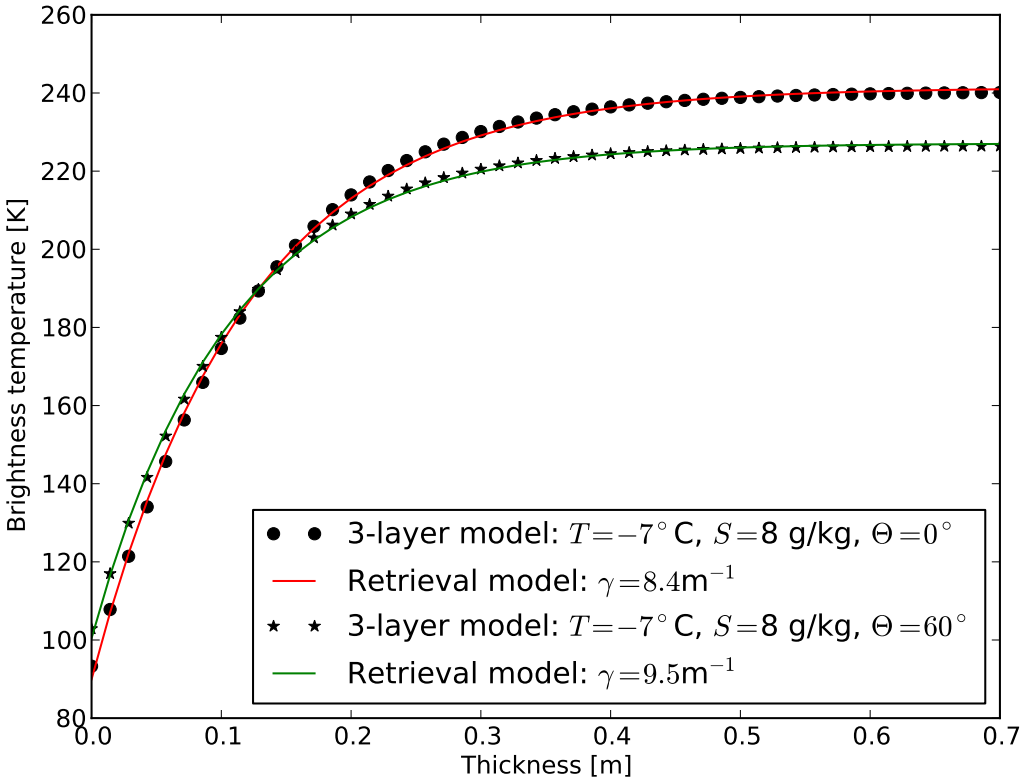

Figure 6.3: The first Stokes parameter I as a function of ice thickness for two different incidence angles $\theta = 0\,^\circ$ and $\theta = 60\,^\circ$ calculated using the three layer model for sea ice with a salinity $S = 8$ g/kg, and temperature $T = -7°$C. The marked data points represent the exact numbers calculated using the three layer model, the solid line is the retrieval approximation. The three parameters T_0, T_1, and γ have been obtained by fitting the retrieval model to the exact three layer model solution using least squares optimization. The resulting maximum thickness $d_{\max}$ for an uncertainty $\delta = 2$ K is 0.51 m for $\theta = 0\,^\circ$ and reduces to 0.45 m for $\theta = 60\,^\circ$, respectively.

6.3.3 Assumptions of the retrieval algorithm I

The retrieval *algorithm I* is based on several assumptions and simplifications. We consider the *algorithm I* as a simple baseline method that defines a standard product. Further algorithm versions could replace the simplifications with more accurate expressions. This will likely involve the useage of additional a priori informations like ice concentration or temperature that can not be retrieved from SMOS simulaneously with the thickness. The *algorithm I* needs only SMOS data for the sake of simplicity.

6.3.3.1 Level 1C processing

The first simplification is to neglect angular dependendy of the intensity (Fig. 6.2. The average of the first Stokes parameter I is calculated over the range of incidence angles θ from $0°$ to $40°$,

$$T_{\mathrm{obs}} =< I(\Theta = 0°..40°) > . \tag{6.15}$$

Using this assumption a level 3 brightness temperature product is derived from the SMOS level 1C data. After removing RFI contaminated snapshots the brightness temperature measurements are averaged and binned into a polar stereographic grid with 12.5 km resolution (see SMOSIce delivery D6 for more details). Examples of the level 3 brightness temperature are shown in Fig. 6.4.

6.3.3.2 Asymptotic tie points

We assume that asymptotic brightness temperature of open water T_0 and thick ice T_1 exist and that they do not vary much. This assumption can be validated by the analysis of brightness temperature time series as it is shown in section 6.3.4.

For the melting season the assumption of asymptotic brightness temperature is not valid any more. We can see from Fig. 6.5 that the thick ice tie point T_1 decreases significantly by about 20 K when the temperatures approach melting. The maximum retrievable ice thickness d_{max} decreases to about 0.15m because of the increase of the attenuation factor γ. Due to the depression of T_1 the ice thickness will be strongly underestimated for melting condidtions.

6.3.3.3 Ice concentration

We assume a spatially homogeneous ocean that is either ice free or 100% covered by sea ice (ice concentration $C = 1$). This assumption leads to an *effective ice thickness* as the results of the retrieval. The *effective ice thickness* is used in numerical dynamic-thermodynamic sea ice models and thus allows a direct comparison.

The brightness temperature can be interpreted as a measure of sea ice volume $T_b = f(V = C \cdot d)$. Fig. 6.6 shows that this assumption is reasonable for $d < 0.05$m. The almost linear relation between the brightness temperature and ice volume does not hold for thicker ice.

The 100% sea ice cover approximation is a reasonable assumption for the freeze-up period when the ocean mixed layer is already at the freezing point and large areas quickly change from 0% to 100%.

The relatively large uncertainty of sea ice concentration data from AMSR-E and SSM/I is one argument for the 100% assumption. The sea ice concentration from AMSR-E and SSM/I has the highest uncertainty for new and thin ice and low ice concentrations. Therefore, the possible advantage of using the ice concentration as auxilliary information for the

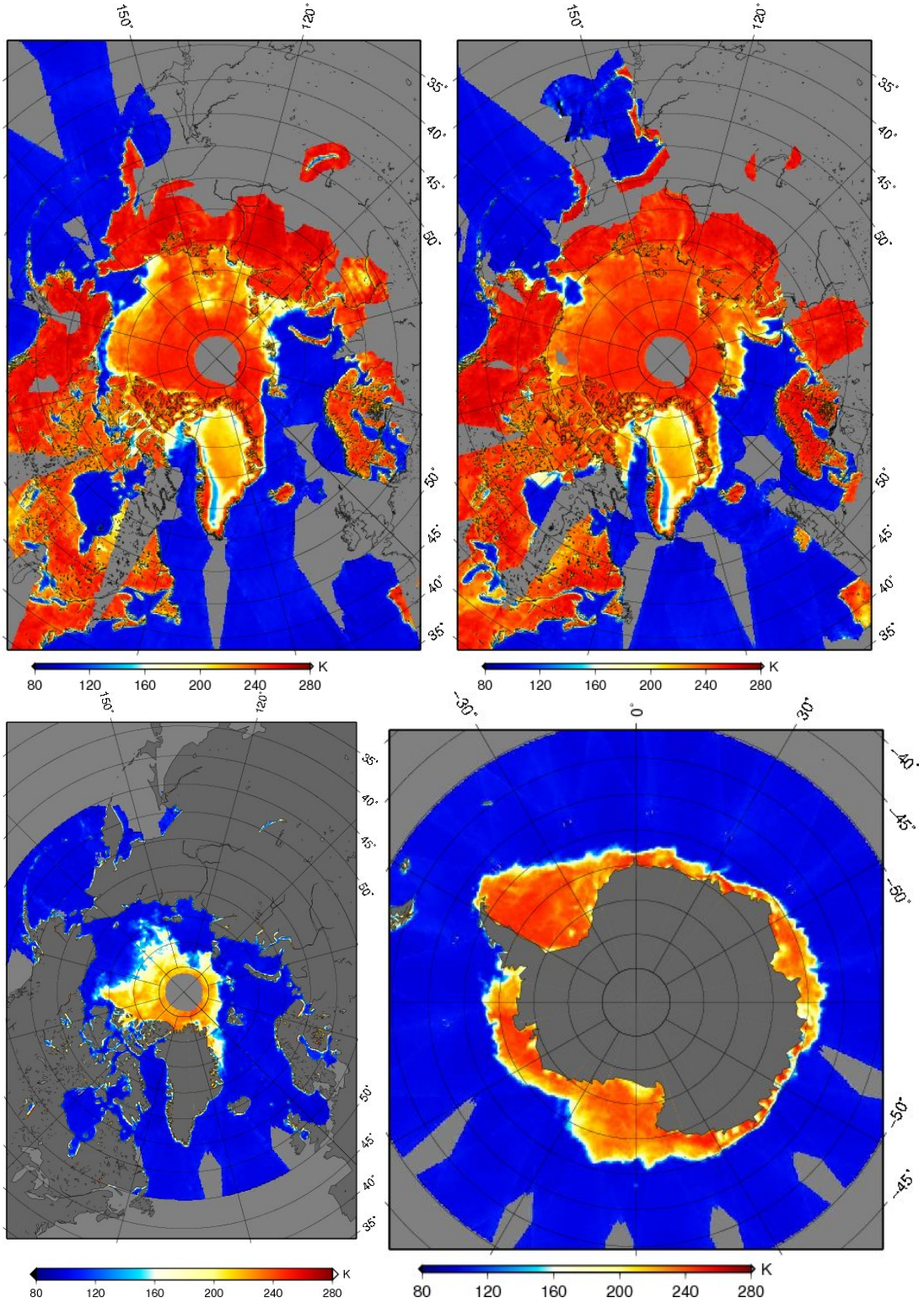

Figure 6.4: Brightness temperature of 1 November 2010 (upper left), 1 December 2010 (upper right), 1 September 2011 (lower left), and 1 May 2011 (Antarctic, lower right) in polar stereographic projection with 12.5 km grid spacing. The intensity has been averaged over $\Theta = 0°..40°$.

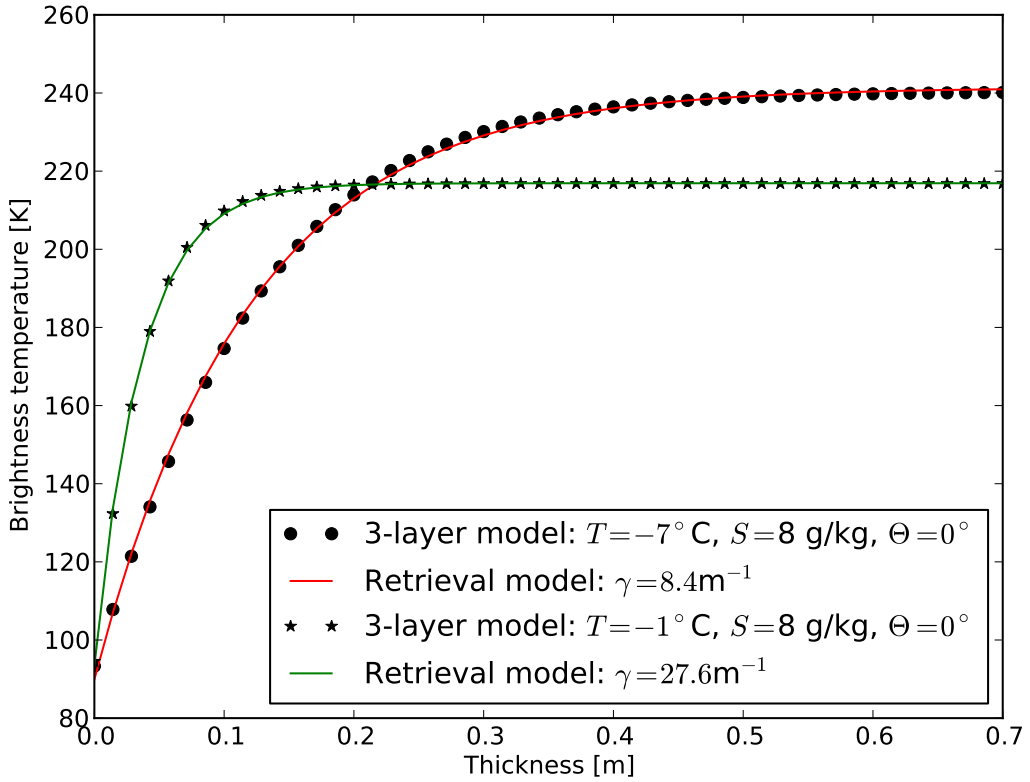

Figure 6.5: The first Stokes parameter I as a function of ice thickness for two different sea ice temperatures $T = -7°$C and $T = -1°$C calculated using the three layer model for sea ice with a salinity $S = 8$ g/kg, and nadir incidence. The marked data points represent the exact numbers calculated using the three layer model, the solid line is the retrieval approximation. The three parameters T_0, T_1, and γ have been obtained by fitting the retrieval model to the exact three layer model solution using least squares optimization. The resulting maximum thickness $d_{\max}$ for an uncertainty $\delta = 2$ K is 0.51 m for $T = -7°$C and reduces to 0.15 m for $T = -1°$C, respectively.

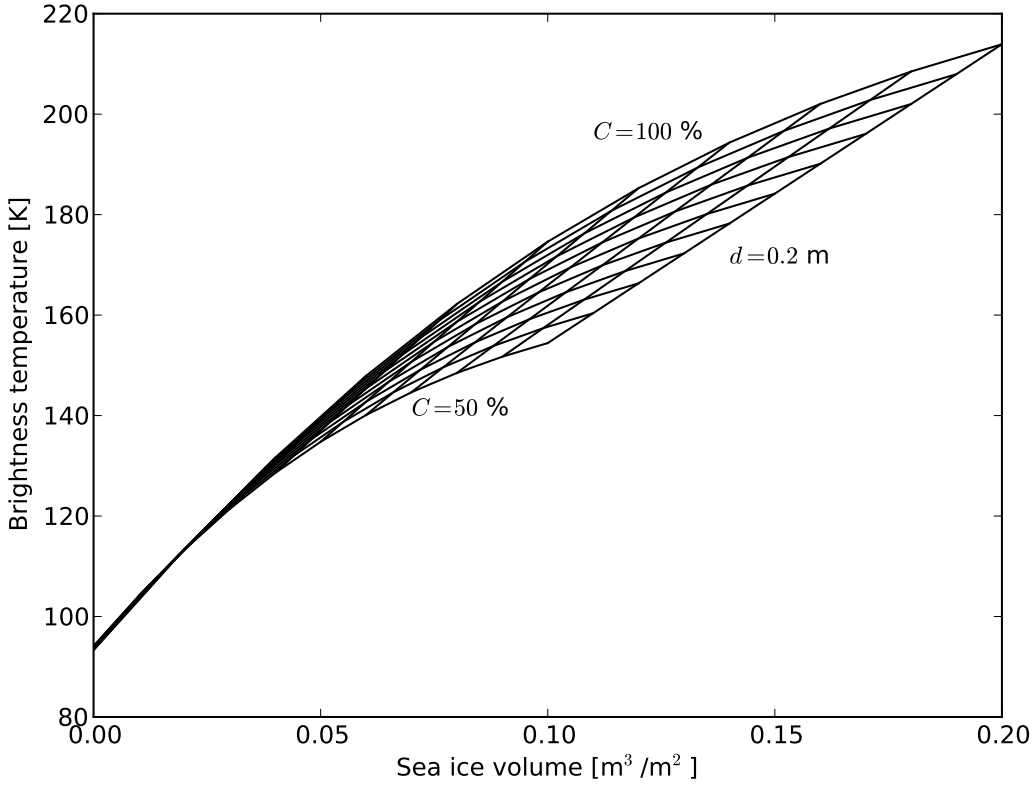

Figure 6.6: Brightness temperature as a function of sea ice volume $T_b = f(V = C \cdot d)$.

SMOS thickness retrieval could also be a drawback because it potentially increases the overall uncertainty. For the algorithm I the influence of ice concentration is therefore neglected. The uncertainties due to this assumption are described in section 6.3.6.

6.3.3.4 Constant attenuation factor

For the first version of the algorithm we assume a constant attenuation factor $\gamma(T_{ice}, S_{ice})$. The factor represents the average conditions. The retrieval is most useful during the freeze-up period, therefore γ shall be adjusted to represent such conditions. Furthermore, it is appropriate to select γ for an average thickness within the range of retrievable thickness, for example 20 cm. By doing so we minimize the error for ice thicknesses close to this value. The values for the brackish Baltic sea ice are likely different from that of Arctic sea ice. The differences between Arctic and Antarctic are probably relatively small as the salinity of the parent waters is similar.

Fig. 6.7 demonstrates that γ is only a weak function of ice temperature for temperatures well below the freezing point. This justifies the assumption at least for cold conditions.

By including auxilliary data such as the ice temperature from AMSR-E it could be possible to improve the retrieval by using a temperature dependent attenuation factor. We will further investigate if this approach is feasible. However, informations about ice salinity are difficult to obtain.

6.3.4 Methods for the estimation of parameters for the retrieval-model

The three parameters T_0, T_1, and γ are necessary to empirically describe the development of the brightness temperature as a function of the sea ice thickness. The attenuation factor γ is a function of ice temperature and salinity. In the first version of the alorithm I we assume the attenuation factor to be constant. With this assumption the three parameters can be obtained in three different ways:

- The first method is to calculate the parameters from the radiative transfer model with assumptions about a mean ice salinity and temperature. This approach is demonstrated in Fig. 6.3.
- The second method is to obtain the parameters from SMOS brightness temperatures in combination with reference ice thicknesses. For example, the ice thickness derived from a thermal infra-red image can be used to derive the three parameters by a least squares optimization.
- The third method is a combination of both previous methods. The two tie points are exctracted from SMOS data and the attenuation factor is estimated from the physical three layer-model.

The first method is suitable when the radiative transfer model reproduces the absolute values of the brightness temperature. This is not yet the case since our model for T_{other} in Eq. 6.1 is not complete. The second method represents a fit of the retrieval model function to reference data that are used as "calibration" of the method. With the third method we estimate the tie points from SMOS data with a priori assumptions about ice free and thick ice conditions. The attenuation factor γ and the corresponding maximum ice thickness are shown in Fig. 6.7 and Fig. 6.8.

6.3.5 Estimation of retrieval parameters for the Arctic freeze-up

We analyse the intensity of 1.4 GHz radiation in seasonally ice covered Arctic waters during the Autumn freeze-up from October to December 2010 (Fig. 6.9).

In order to get an estimate of the maximum ice thickness that can be retrieved from SMOS we calculate approximate sea ice thicknesses from the cumulative freezing degree days by using NCEP reanalysis data and compare this to the corresponding observed brightness temperature.

The ice thickness d is calculated from the freezing-degree days Θ, where

$$\Theta = \int_0^t (T_f - T_a) dt, \tag{6.16}$$

T_f is the freezing point of sea water and T_a the air temperature. Lebedev (1938) derived an empirical relation from 24 station years in the Russian Arctic as

$$d = 1.33\Theta^{0.58}, \tag{6.17}$$

with the resulting d in cm. Similar parameterizations have been proposed by Zubov (1943) and Anderson (1961) and have been compiled by Maykut (1986). In addition we use the growth parameterization of Maykut (1986) for ice with a snow layer of one and of two centimeters. Because these five different parameterizations represent a reasonable variety of

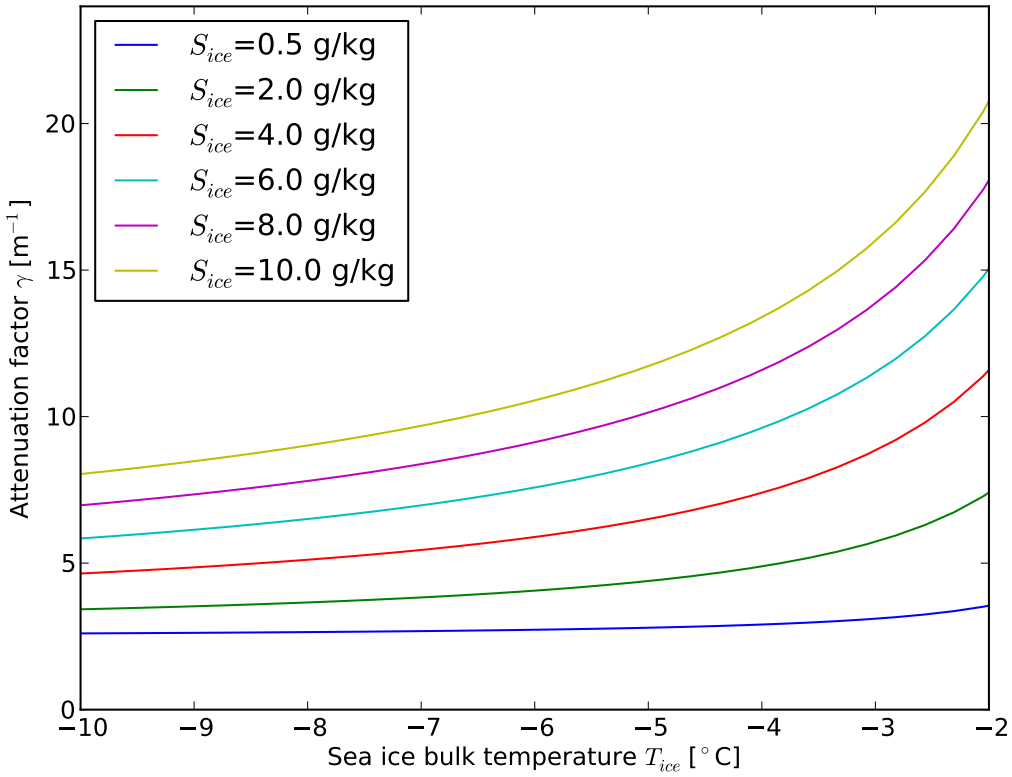

Figure 6.7: Attenuation factor γ obtained from the three layer model solution as a function of ice temperature and ice salinity.

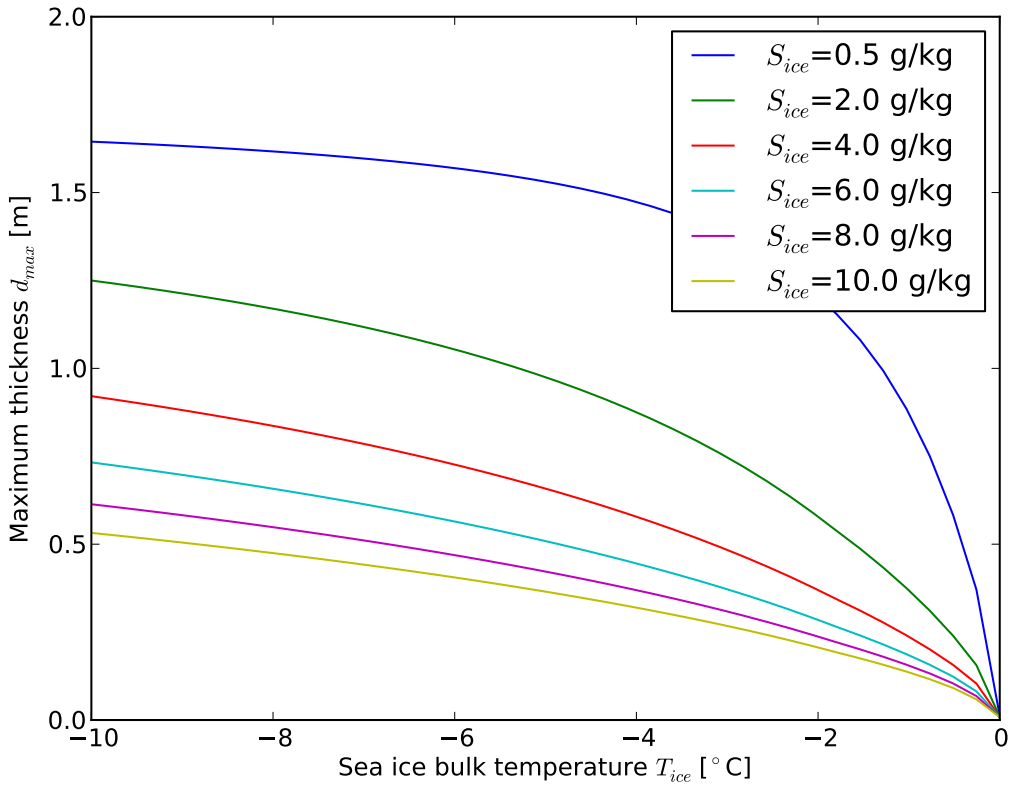

Figure 6.8: Maximum sea ice thickness $d_{\max}$ that can be retrieved obtained from the three layer model solution as a function of ice temperature and ice salinity for an uncertainty $\delta = 2$ K.

different conditions, we use the standard deviation of the ensemble as an estimate for the thickness uncertainty.

Since the sea ice development starts only when the complete oceanic mixed layer is at or slightly below the freezing point of sea water, we constrain the timing of the freezing-degree day integration by the first occurence of sea ice as detected in the corresponding AMSR-E ice concentration data.

The semi-empiric model is used to calculate the ice thickness. from the measured brightness temperature T_{obs} (also named as I in Figures) and the three parameters, with the brightness temperature of the ice free ocean at the freezing point T_0, the brightness temperature of thick ice T_1 and the attenuation factor γ.

6.3.6 Results

Figure 7.9 shows the time series of brightness temperature, ice concentration from AMSR-E, surface air temperature from NCEP reanalysis, and cumulative freezing-degree days thickness for the two positions that are indicated in Fig. 6.9.

Figure 7.10 shows the time series of observed and modeled brightness temperature for the Laptev Sea. This case is selected as one example where the assumption $C = 1$ approximates the real condition with a high accuracy because the time evolution of the ice concentration could be well decribed by the heavyside function: within only very few days the ice cover changes from 0% to 100% (see Fig. 7.9, red curve).

In contrast to the previous case, Fig. 7.11 represents an example where the assumption of a varying ice concentration C provides significantly improved results as compared to the assumption $C = 1$. The selected position is located at close to the sea ice edge in the Kara Sea. The ice situation is governed by atmospheric dynamics that strongly influence the ice concentration due to shifts of the ice edge position (see Fig. 7.9, black curve). This example is selected to discuss the uncertainties of the assumption $C = 1$. We learn from this example, that the information of ice concentration from AMSR-E leads to a better correspondence between the observered and simulated brightness temperature. However, the assumption of $C = 1$ still leads to a reasonable agreement of the modeled and observed brightness temperature. The corresponding deviations of the ice thickness are less than about five centimeters at maximum.

The scatterplot Fig. 6.13 shows the uncertainties of the retrieval for the two cases discussed previously. The uncertainty of freezing degree day thickness is defined as the standard deviation of the five different formulations. The corresponding root mean square (RMS) differences for four ice thickness intervals are given in table 6.4. Please note that this values represents only the two selected cases. The asymmetric nature of the uncertainty is not captured in the RMS value but can be seen in Fig. 6.13.

The analysis of the time series at the two positions allows the following conclusions:

1. Both intensities for the ice-free ocean $T_0 = 100.5 \pm 1\,\mathrm{K}$ and the thick (> 0.5m) ice cover $T_1 = 244.8 \pm 1.3\,\mathrm{K}$ exhibit little variability over several weeks (Fig. 7.10)

2. The intensity is monotonically increasing with the ice thickness as previously inferred from incoherent model simulations (Fig. 7.10). Thus, coherent effects seem to be negligible.

3. After the ice concentration has reached 100%, the 1.4 GHz intensity still increases for about three weeks (Fig. 7.9).

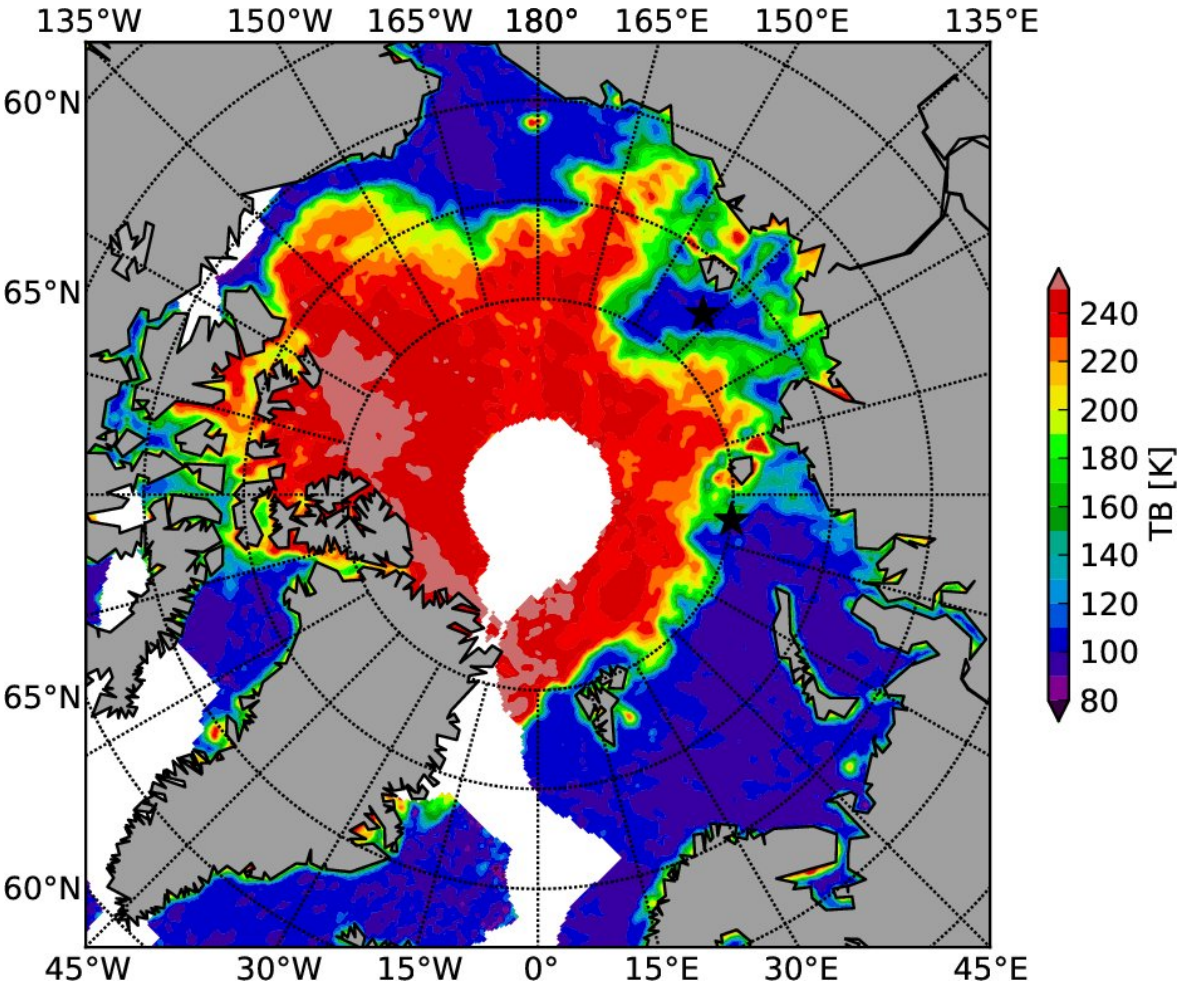

Figure 6.9: Brightness temperature of the Arctic ocean measured with SMOS on 16th October 2010. The black stars indicate the center coordinates of NCEP grid cells for which we conduct the time series analysis. The white areas indicate data gaps due to the limitations of the swath and due to the RFI filter.

4. At a maximum ice thickness of about 0.5 m the intensity reaches T_1 and further ice growth does not increase the brightness temperature (Fig. 7.9 and 7.10).

5. Ice concentration variations have an influence on ice thickness retrieval during the thin ice growth. The maximum deviation of the SMOS retrieval from the cumulative thickness is about 5 cm for the assumption of 100% ice coverage (Fig. 7.11).

6. A constant $\gamma \approx 8.5\text{m}^{-1}$ is a suitable first choice for operational sea ice thickness retrieval with SMOS without using any auxiliary data. This choice represents sea ice with a bulk ice temperature of $T = -7°\text{C}$ and a salinity of $S = 8$ g/kg which is a reasonable average for the Arctic freeze-up period in November.

6.4 Results and validation

6.4.1 Results

In this section we present some results of the ice thickness retrieval together with maps of the ice concentraiton derived with the ASI algorithm from AMSR-E (Spreen et al., 2008). In

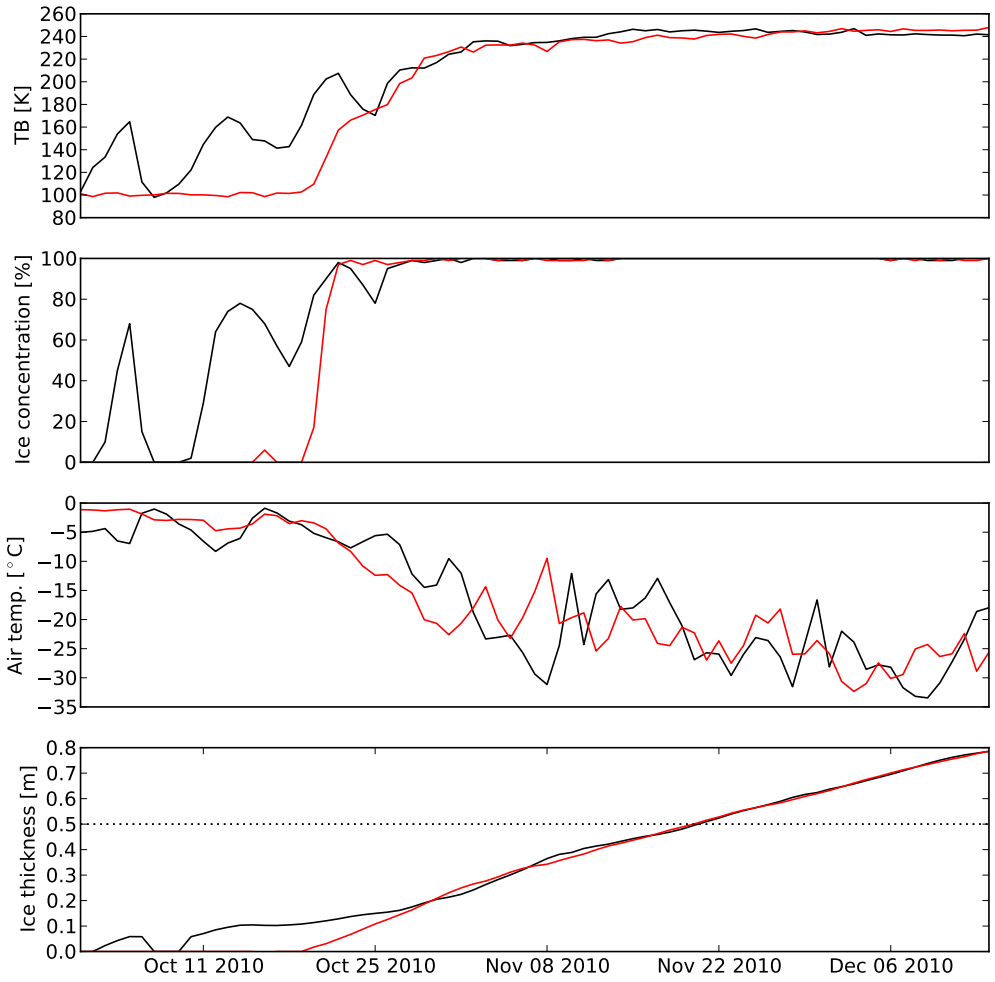

Figure 6.10: Time series of brightness temperature, ice concentration, surface air temperature from NCEP reanalysis, and cumulative freezing-degree days thickness. The two positions in the Kara Sea (black curve) and the Laptev Sea (red curve) are indicated in Fig. 6.9.

Table 6.4: Root mean square error (RMSE) between cumulative freezing degree days thickness and SMOS thickness.

Thickness range [cm]	RMSE [cm]
0-10	2
10-30	4
30-40	5
40-50	12

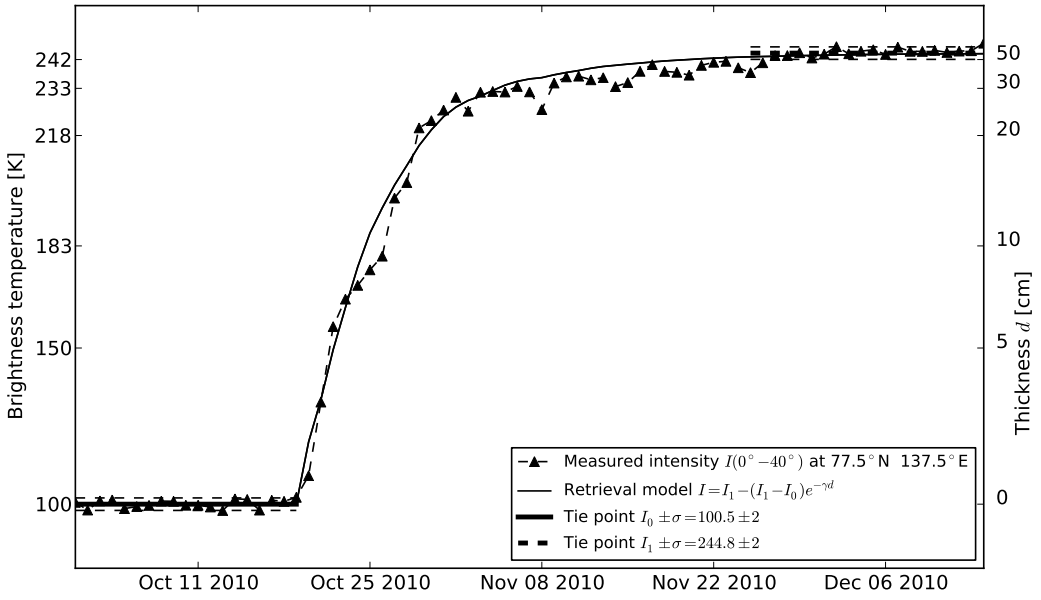

Figure 6.11: Time series of simulated and observed brightness temperature and corresponding ice thickness for the Laptev Sea (position indicated in Fig. 6.9). The simulated brightness temperature is based on the semi-empiric retrieval model with the assumption $C = 1$.

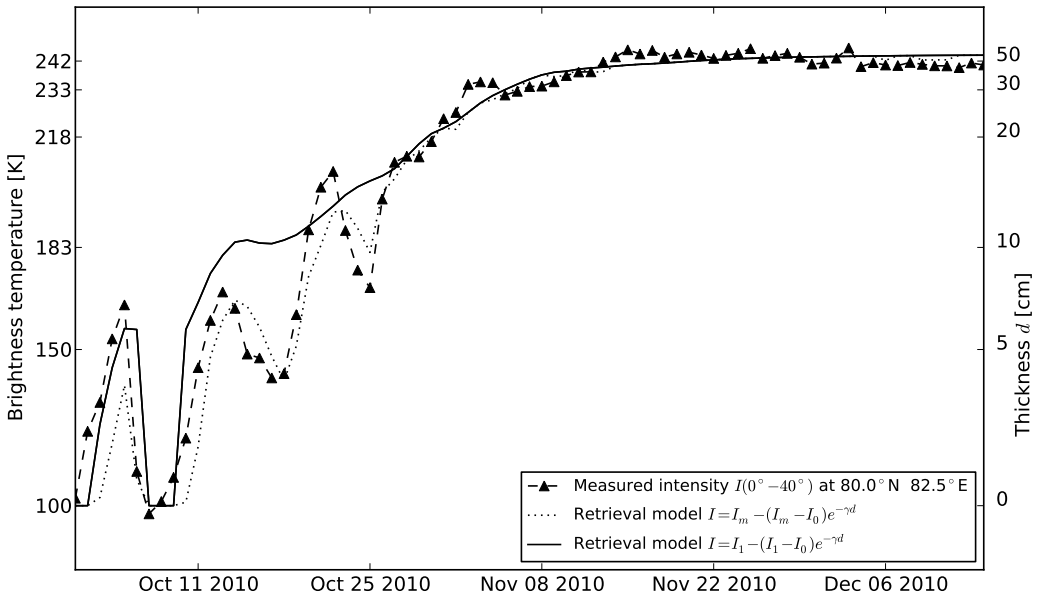

Figure 6.12: Time series of simulated and observed brightness temperature and corresponding ice thickness for the Kara Sea (position indicated in Fig. 6.9). The simulated brightness temperature are based on two versions of the semi-empiric retrieval model. The first version is based on the assumption $C = 1$ (solid line), the second version is based on ice concentrations C derived from AMSR-E data (dotted line).

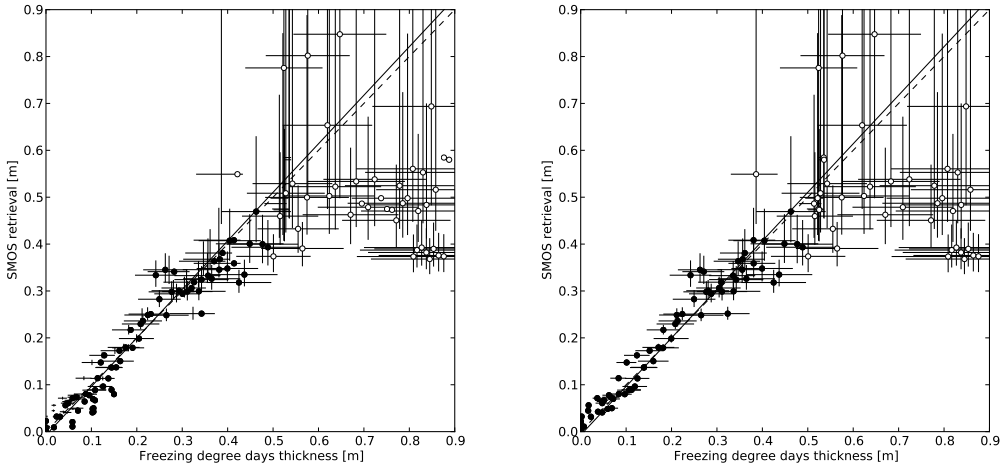

Figure 6.13: Ice thickness calculated from the cumulative freezing degree days and retrieved with two versions of the semi-empirical model: with the assumption $C = 1$ (left) and with C from AMSR-E (right).

Figs. 6.14- 6.17 the Arctic sea ice thickness and concentration is shown for the November 1, December 1 and 26 in 2010, and March 15, April 30 2011. Just by looking at the images we can already draw some conclusions about the novel ice thickness information, the resolution, the effectiveness of the RFI filter, and also about the severe limitations during the melting season.

6.4.1.1 New information about sea ice thickness

The SMOS ice thickness provides new insights that are not visible in the ice concentration maps: For example, the distinct border of thin and thick ice on November 1 (Fig. 6.14). On November 1 about one third of the Arctic ocean is covered with ice thinner than 0.5 m. The thin ice in the Laptev Sea at about 80°N corresponds to 100% ice concentration. The ice thickness seems to be very reasonable if we compare this with the time evolution of the ice concentration of the previous days (not shown here). On 15 March the polynya areas at the border of the fast ice zone in the Laptev Sea can easily be identified in the thickness but not in the ice concentration maps. Thus, we can conclude that the SMOS thickness provides useful, new information about the state of the sea ice cover. The ice thickness information is clearly complementary to the ice concentration.

6.4.1.2 Spatial resolution

The spatial resolution of SMOS is sufficient to map the sea ice thickness in the straits in the Canadian Archipelago. In contrast to other passive microwave imagers such as SSM/I, the SMOS brightness temperatures are already separated in coastal and oceanic fractions. Thus, there is a much reduced land spillover effect.

6.4.1.3 RFI filtering

Our relatively simple approach reduces the RFI sufficiently while a large fraction of valid data still remains. On December 1 (Fig. 6.14) the result of the snapshot based RFI filter is clearly visible. The hexagon-like shape of the footprint is RFI flagged (grey, missing value)

in the North Atlantik. We neglect the complete snapshot when a single measurement exceeds 300 K. This strict filtering avoids non-local RFI effects.

6.4.1.4 Limitations due to melting

The *algorithm I* provides reasonable results in the freeze-up period through October, November, and December but large errors are apparent at the onset of melt and during the melting season. Such an error is evident on April 30 in the Kara Sea. Because of temperatures close to melting the ice thickness is strongly underestimated. This effect is due to the decrease of the tie point T_1 for an increase of temperature (compare Fig. 6.5). The decrease of brightness temperature is evident in Fig. 6.4 for the Arctic sea ice of 1 September 2011. The temperature dropped from 245 K to about to 220 K. The *algorithm I* with its tie points adapted to the freeze-up period would yield extensive thin ice areas where the modal ice thickness was in fact 90 cm as reported from Polarstern based EM measurements.

Thus, we conclude that the present method is not reliable for melting conditions. The application of the *algorithm I* should therefore be restricted to the cold periods with ice temperatures well below -2°. During the melting phase the potential for ice thickness retrieval is strongly reduced. Therefore, it is not even possible to adapt the tie points.

6.4.1.5 Stripe artefacts

On March 15 and in several other images (not shown here), linear stripes of reduced ice thickness can be identified. This artefacts occur at the border of the swaths. It is not yet clear if this is a result of neglecting the angular dependency of the sea ice emissivity or if it is an artefact of the level 1C to level 3 gridding procedure. Clearly, this errors shall be removed in future versions of the processing software.

6.4.2 Validation

For the validation of the SMOS sea ice thickness algorithm the Finnish Meteorological Institute (FMI) provided data for the Baltic and Barents and Kara Sea areas (Mäkynen, 2012): The main remote sensing validation data is the MODIS ice surface temperature based thin ice thickness charts for both the Baltic and Kara Seas. In-situ data for the Baltic Sea includes coastal weather station data, snow and ice thickness measurements by Finnish icebreakers, and data from two field campaigns. For the Kara Sea only coastal weather data are available. Helicopter-borne EM-ice thickness data have been provided by AWI for two field campaigns in the Baltic Sea.

The validation will be described in a separate report. Here we show only one example in Fig. 6.18. This example demonstrates the general agreement but also the differences between the SMOS and MODIS thickness. In addition the SMOS sea ice results are compared to two different model simulations. In general, the SMOS ice thickness is lower in comparison to the three other results. As the other results also have their uncertainties we can not draw clear conclusion from only this single day.

6.5 Discussion and conclusion

The *KlimaCampus SMOS sea ice algorithm I* has been outlined in this document. This algorithm is a first version that will serve as a baseline reference for further possible improvements. As SMOS delivers the first ever L-band brightness temperatures and not much

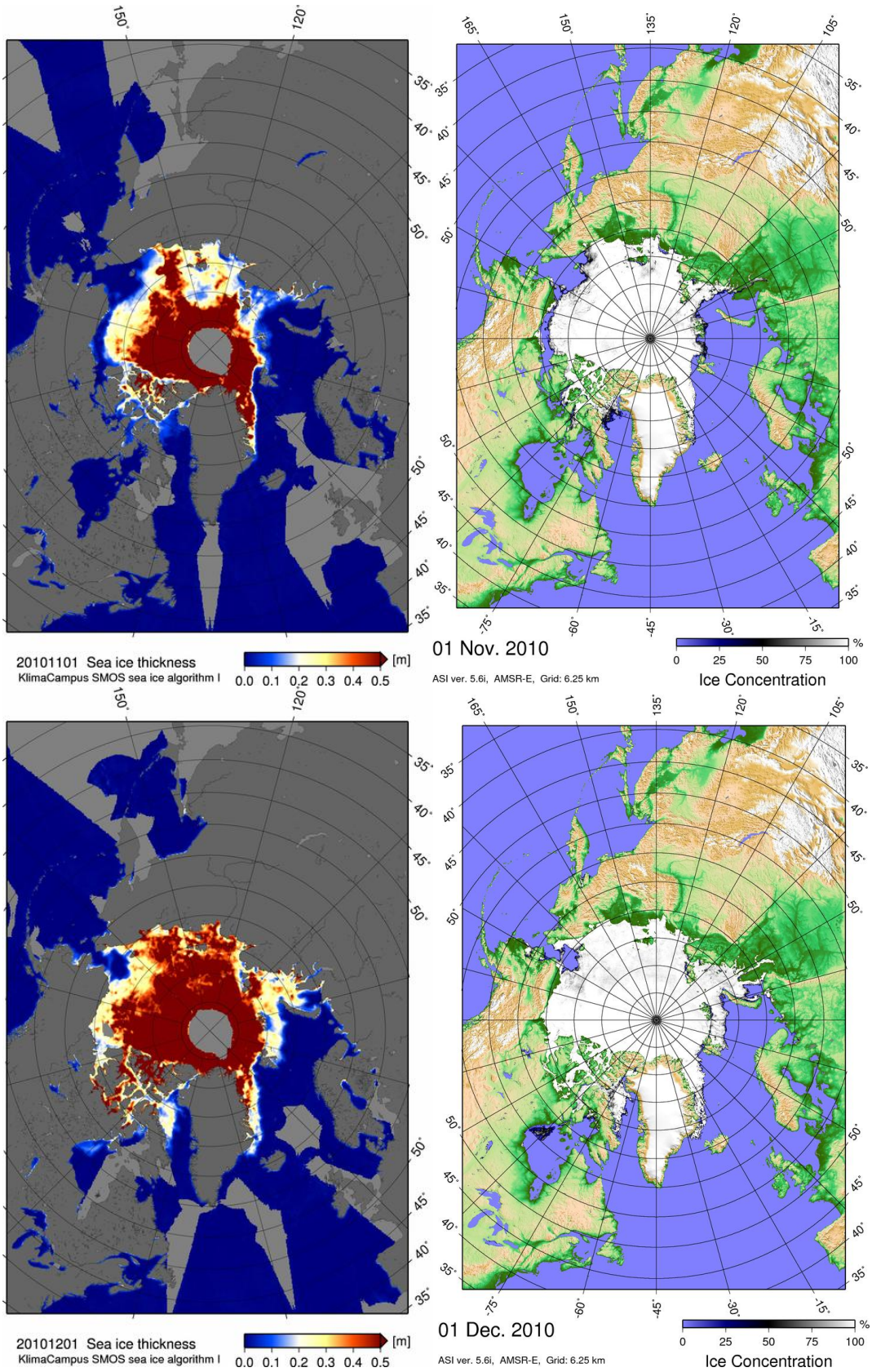

Figure 6.14: SMOS sea ice thickness (left column) and AMSR-E ice concentration (right column) of 1 November 2010 (upper row) and of 1 December 2010 (lower row).

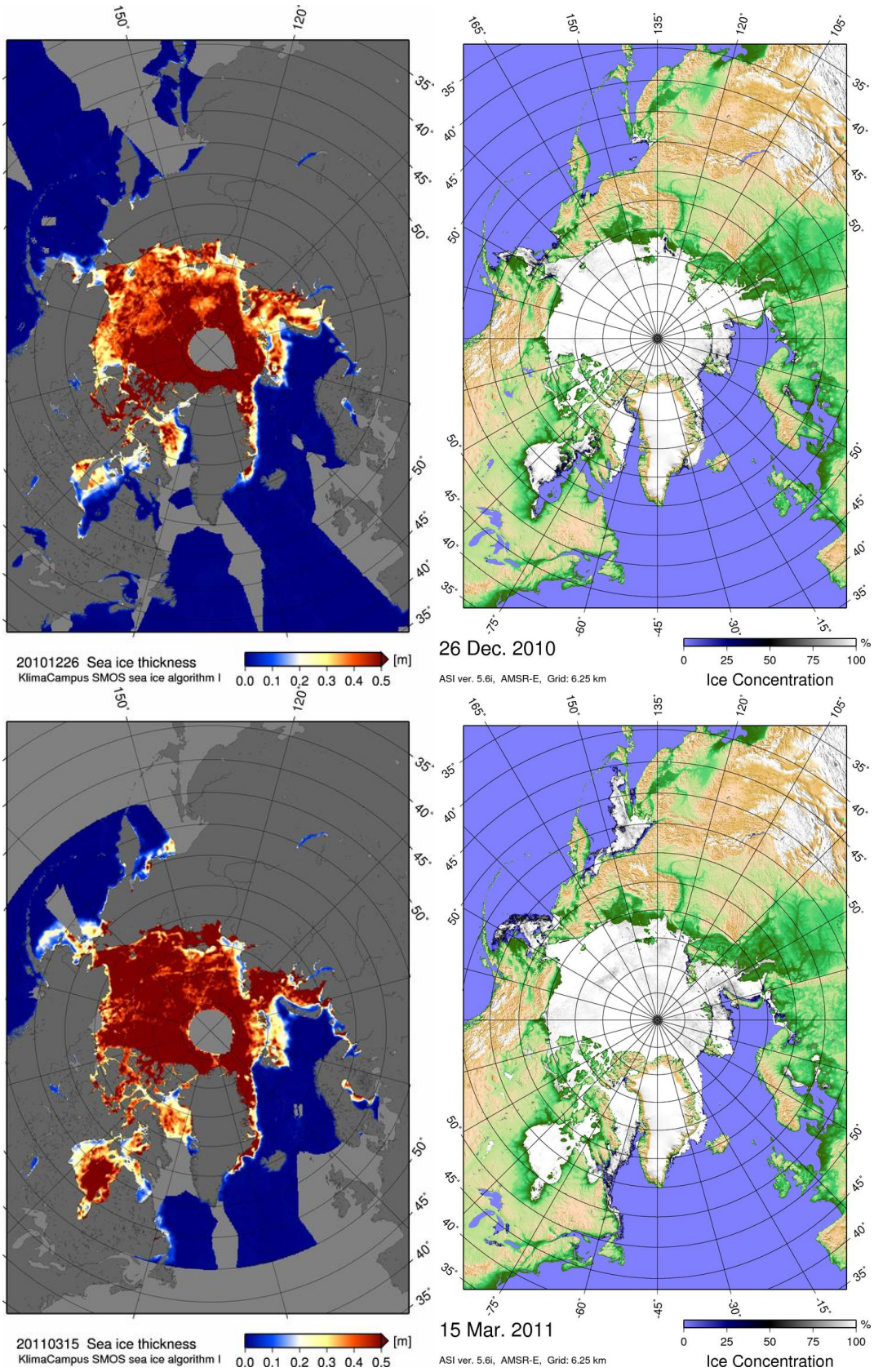

Figure 6.15: SMOS sea ice thickness (left column) and AMSR-E ice concentration (right column) of 26 December 2010 (upper row) and of 15 March 2011 (lower row).

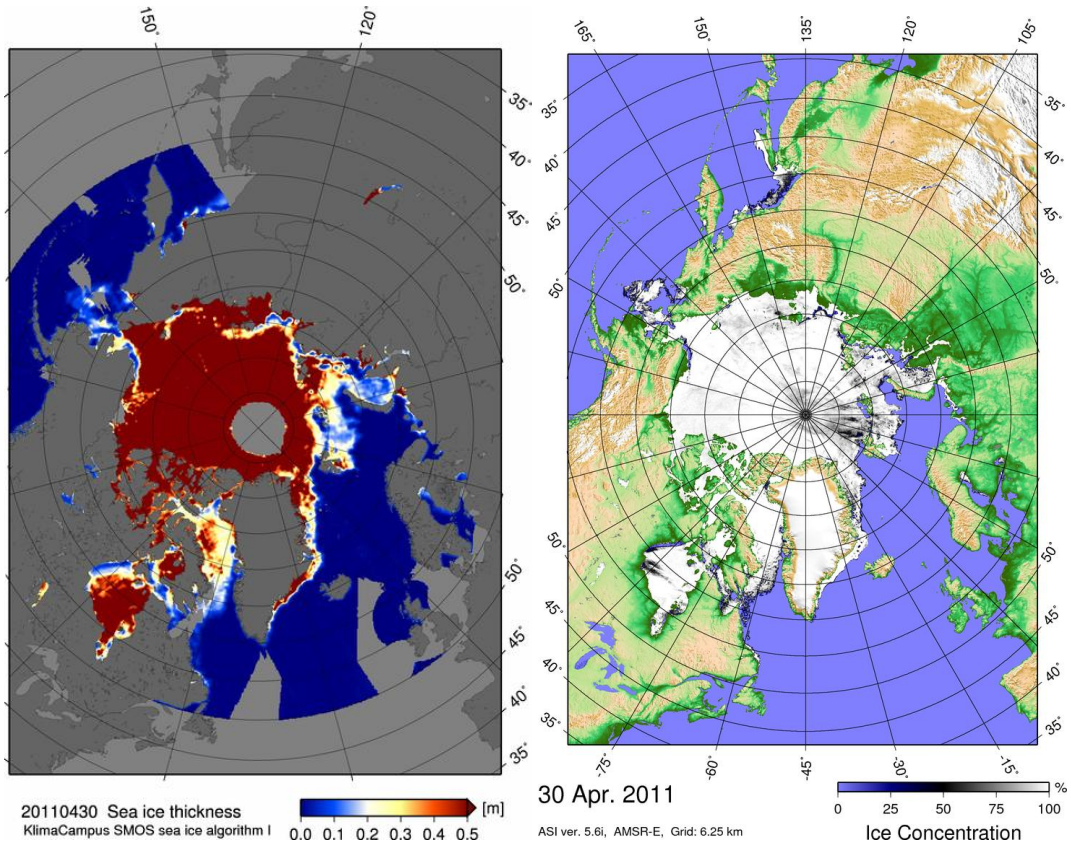

Figure 6.16: SMOS sea ice thickness (left) and AMSR-E ice concentration (right) of 30 April 2011. The SMOS thickness in the Kara sea is strongly underestimated due to the melting.

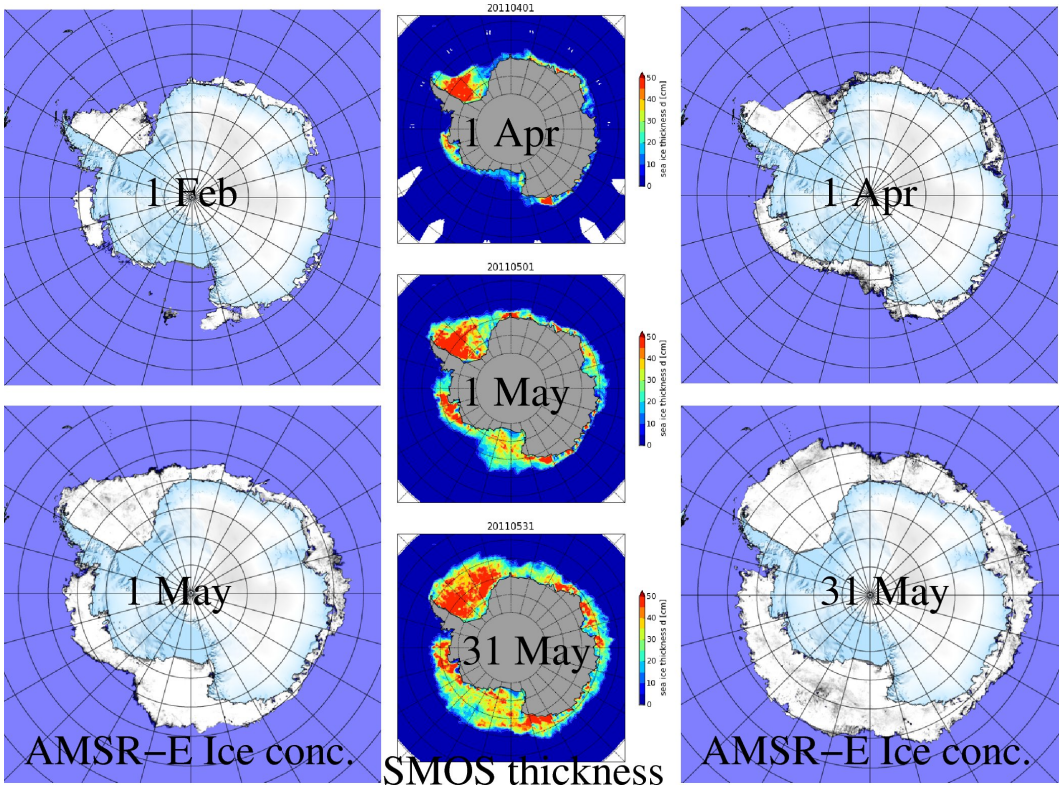

Figure 6.17: Antarctic SMOS sea ice thickness and AMSR-E ice concentration.

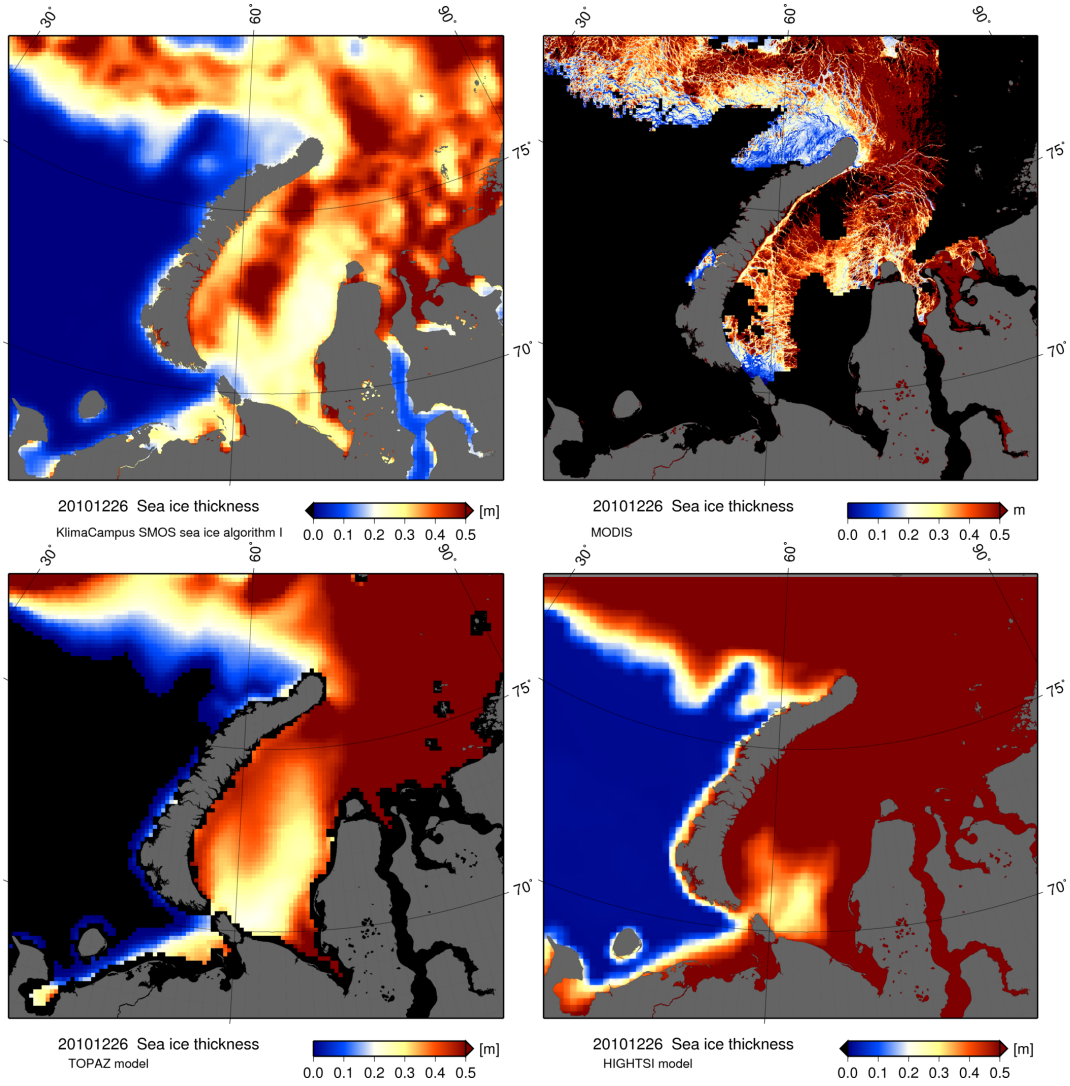

Figure 6.18: Ice thickness derived from SMOS (upper left) and MODIS IR (upper right) measurements and TOPAZ (lower left) and HIGHTSI (lower right) model simulations.

research has been conducted yet, it is to be expected that the retrieval method will further evolve and improve. The research on algorithms for the retrieval of sea ice concentration from passive microwave instruments has begun more than 40 years ago and still there is not final "best" algorithm.

The advantages of our retrieval design that uses the first Stokes parameter I for incidence angles $\theta < 40^\circ$ are a large ice thickness sensitivity, a relatively fine spatial resolution, a complete daily coverage, small atmospheric and RFI influence, and no influence of Faraday rotation.

For the sea ice algorithm I two major assumptions are made. The first is to assume a constant attenuation factor γ, the second is to neglect the influence of changing ice concentrations. Both assumptions can possibly be replaced by more accurate representations in the future. However, it was shown that even with this strong simplifications the retrieval results are still reasonable.

We have described a method to derive the three retrieval parameters by model simulations and analysis of brightness temperature time series. The first set of tie points for the *algorithm I* is valid for the freeze up periods in the Arctic and possibly also in the Antarctic:

$$\begin{aligned} T_0 &= 100.5 \text{ K} \\ T_1 &= 244.8 \text{ K} \\ \gamma &= 8.5 \text{ m}^{-1} \end{aligned}$$

The resulting maximum ice thickness $d_{\max}$ that can be retrieved for a given observational error $\delta \approx 2$ K is calculated from Eq. 6.14 as

$$d_{\max} = 0.5 \text{ m}$$

The resulting maximum ice thickness depends on the observational error. This includes the variations due to the geophysical variability of the emissivity, the errors due to atmospheric variability, RFI, as well as the measurement uncertainty. Since our level 1C to level 3 processor is not very sophisticated there is probably room for potential improvements to further reduce the measurement uncertainty. However, the largest uncertainties probably arise from the geophysical variability of the tie point T_1 and the attenuation factor γ as well as from the ice concentration.

We have demonstrated the clear potential for ice thickness retrieval during the important freeze-up period but we have also shown the strong limitations that are evident during the melting phase. In a pre-launch study Mills and Heygster (2011a) came to the conclusion "The results suggest that it may be possible to retrieve ice thickness simultaneously with ice concentration only at temperatures close to melting.". In contrast to the findings of Mills and Heygster (2011a), we do not see potential for sea ice thickness retrieval for ice temperatures close to melting. But we have confirmed that the thickness retrieval is well feasible for cold conditions and that the *algorithm I* is a suitable approach.

7 ATBD2

Xiangshan Tian-Kunze

7.1 Introduction

The semi-empirical SMOS ice thickness retrieval algorithm introduced in the previous section (hereinafter Algorithm I) can be described as

$$TB(d_{ice}) = T_1 - (T_1 - T_0)\exp(-\gamma d_{ice}), \tag{7.1}$$

where d_{ice} is the ice thickness, T_1 and T_0 are two constant tie points which were estimated from the observed SMOS TB over open water and thick first year ice during the freezing period of 2010 in the Arctic, and γ is a constant attenuation factor which was derived from a sea ice radiation model (Menashi et al., 1993) for a representative bulk ice temperature and bulk ice salinity in the Arctic.

The advantage of Algorithm I is the retrieval of ice thickness from TB without any auxiliary data set. However, the TB measured by L-band radiometer over sea ice depends on the dielectric properties of sea ice which are functions of ice temperature and ice salinity (Kaleschke et al., 2010). Although the change of TB caused by the sea ice thickness variation is much larger than that caused by the variation of ice temperature and ice salinity, the typical variabilities of these two parameters in the Arctic can induce up to 30 K difference in TB (Kaleschke et al., 2012). This means the assumption of constant retrieval parameters could cause considerable errors in the regions where these parameters strongly differ from the assumed constant values.

Ice temperature and ice salinity measurements are rare and they are not continuously available on a daily basis in the Arctic. An alternative solution is therefore to derive these two parameters from auxiliary data during the sea ice thickness retrieval. Under the assumption of thermal equilibrium, the ice surface temperature can be estimated from the surface air temperature. Therefore, we use a heat flux balance equation and use the surface air temperature from atmospheric reanalysis data as a boundary condition. Ice salinity can be estimated from the underlying sea surface salinity (SSS) with an empirical function (Ryvlin, 1974). With these two parameters we can calculate brightness temperature with the sea ice radiation model (Menashi et al., 1993). However, both ice temperature and ice salinity are in turn functions of ice thickness. Thus, we need to apply a linear approximation method to simultaneously retrieve ice thickness and estimate suitable ice temperature and salinity values. This algorithm is called Algorithm II hereinafter.

In the radiation model of Menashi et al. (1993) a plane ice layer is assumed. However, due to sea ice deformation in the natural sea ice, a broad scale of ice thicknesses occurs within one footprint of SMOS. The brightness temperature measured by SMOS at each footprint is a mixture of brightness temperatures from different ice thicknesses, and possibly open water. As SMOS brightness temperature is more sensitive to ice thicknesses less than 0.5 m

(Kaleschke et al., 2012), SMOS-derived ice thickness under the assumption of a plane ice layer tends to represent the lower end of the ice thickness distribution within the footprint. A possible solution for the corresponding underestimation of ice thickness is to correct the retrieved ice thickness using an ice thickness distribution function. The correction of ice thickness retrieved from Algorithm II using this function is called Algorithm II* in this study.

As in Algorithm I we continue to use the first Stokes parameter, which is $(TBh + TBv)/2$, averaged over the incidence angle range of 0°-40° for the retrieval of ice thickness.

Here we compare the three different SMOS ice thickness retrieval algorithms in the Arctic. The plane layer ice thicknesses retrieved from Algorithm I and II are compared with independent data to examine if the method that considers variable ice temperature and ice salinity considerably improves the accuracy of the ice thickness retrieval. Next, sea ice thickness uncertainty is estimated with the best algorithm on a daily basis. The growth of the sea ice cover as seen by SMOS during a freezing period in the Arctic is also discussed.

7.2 Data

Three different data sets are used for the retrieval of sea ice thickness in Algorithm II. The basis of the retrieval is the brightness temperature measured by SMOS L-band radiometer. This data set is described in Chapter 5. In the following we describe the surface air temperature (T_a) from Japanese 25-year ReAnalysis (JRA-25) data and the SSS climatology for the estimation of bulk ice temperature (T_{ice}) and bulk ice salinity (S_{ice}).

7.2.1 JRA-25 Reanalysis Data

For estimating the ice surface temperature, we extract the 2 m surface air temperature and the 10 m wind velocity data from JRA-25 atmospheric reanalysis data and interpolate them into the polar stereographic projection with 12.5 km grid resolution. JRA-25 reanalysis data provide various physical variables in 1.125 ° resolution every six hours. The data have been produced by the Japanese Meteorological Agency using the latest numerical analysis and prediction system. The data are available from 1979 to the present (Onogi et al., 2007). Various studies have been carried out to compare the JRA-25, ERA40 and NCEP data sets. Good agreements were found between JRA-25 and ERA40 (Onogi et al., 2007).

7.2.2 Sea Surface Salinity Climatology

The SSS information is needed to estimate the bulk ice salinity which is an input parameter of the radiation model of sea ice. There are global ocean salinity products derived from SMOS brightness temperatures. Ocean salinity is one of the two applications SMOS was originally designed for. However, SMOS-derived ocean salinity is not available for the ice covered regions in the Arctic. Thus, we use a SSS climatology based on the outputs of an ocean-sea ice model. SSS weekly climatology was computed based on the daily output from a high-resolution numerical simulation of the Atlantic and Arctic Oceans' circulations using the MIT general circulation ocean-sea ice coupled model (Marshall et al., 1997). The model was configured for the Atlantic Ocean north of 33°S, including all Atlantic marginal seas and the Arctic Ocean up to the Bering Strait, and was integrated at the eddy-resolving resolution of approximately 4 km. The vertical resolution of the model varies from 5 m in the upper ocean to 275 m in the deep (100 vertical levels were used). Bottom topography

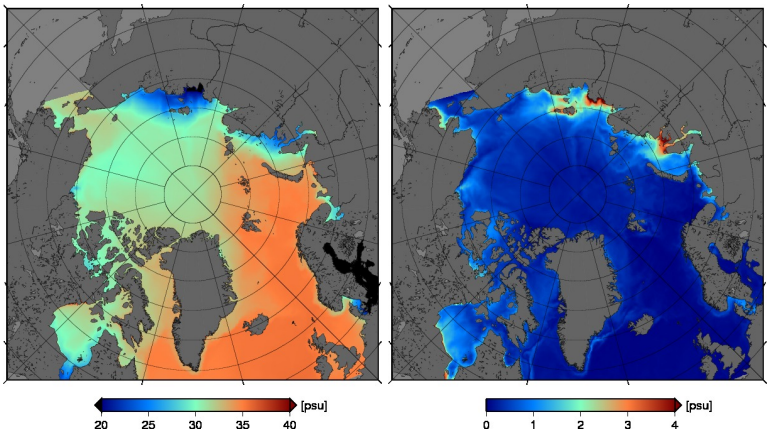

Figure 7.1: Mean and standard deviation of weekly sea surface salinity for the winter period from October to April, based on 8 years of daily model output.

was interpolated from the ETOPO2 database and initial temperature and salinity conditions from a 8-km resolution integration of the same model (to achieve a good degree of spin-up), which in turn started from the WOA09 climatology. The model is forced at the surface by fluxes of momentum, heat and freshwater computed internally in the model with the help of the 6-hourly atmospheric state from the ECMWF/ERA-interim Reanalysis (Dee et al., 2011) and bulk formulae. At the open northern (Bering Strait) and southern (33°S) boundaries, the model is forced by a 1° resolution global solution. The K-Profile Parameterisation(KPP) formulation is used for the parameterization of vertical mixing, with a background vertical viscosity coefficient of 1×10^{-4} m^2. The vertical diffusion employed amounts to 1×10^{-5} m^2 s^{-1}. Unresolved horizontal mixing uses a biharmonic diffusion/viscosity of 3×10^9 m^4 s^{-1}. The overall good performance of the above model configuration (integrated at 8km resolution), assessed through comparisons with in-situ measurements, can be found in Serra et al. (2010); Brath et al. (2010); Dmitrenko et al. (2012). We chose to use a model climatology and not Polar science center Hydrographic climatology (PHC) to make profit from the dynamical oceanographic structures realistically resolved in the model, which leads to spatial and seasonal variability of SSS.

Figure 7.1 shows the mean and standard deviation of weekly SSS from October to April, based on 8 years of daily model output. SSS in the Laptev Sea, parts of the Kara Sea, and the Baltic Sea is much lower than in the central Arctic due to the influence of river run-offs. On the contrary, in the Baffin Bay, the Greenland Sea, and the Barents Sea the SSS is higher than in the central Arctic. The mean weekly SSS in the Baltic sea varies in the range of 4-10 gkg^{-1} which agrees well with the observed climatology given in Janssen et al. (1999). As the ice salinity is correlated with SSS, the variability of SSS should be considered in the retrieval when we calculate Arctic-wide ice thickness distributions.

7.3 Sea ice thickness retrieval Algorithm II

7.3.1 The sea ice radiation model

The basis of the SMOS ice thickness retrievals Algorithm I and II is the sea ice radiation model adapted from Menashi et al. (1993). The sea ice radiation model is described in detail in Chapter 6. While for Algorithm I the radiation model is used to calculate the constant attenuation factor γ for a representative T_{ice} and S_{ice} in the Arctic, in Algorithm II it is used to calculate TB at variable T_{ice} and S_{ice}.

The sea ice radiation model consists of a plane ice layer bordered by the underlying sea water and air on the top. The model does not include a snow layer. The TB over sea ice depends on the dielectric properties of the ice layer which are a function of brine volume (Vant et al., 1978). The brine volume is a function of S_{ice} and T_{ice} (Cox and Weeks, 1983).

For a thin ice layer, the ice temperature gradient within the ice can be assumed to be linear (Maaß, 2013a). Assuming that the water under sea ice is at the freezing point, we can calculate T_{ice} with $0.5(T_{si} + T_w)$, where T_{si} is the snow-ice interface temperature and T_w is the freezing sea water temperature. The T_{si} is calculated with a thermodynamic model with T_a as boundary condition. The thermodynamic model is presented in the next section.

S_{ice} is estimated using the empirical function of Ryvlin (1974)

$$S_{ice} = S_w(1 - S_R)e^{-a\sqrt{d_{ice}}} + S_R S_w, \tag{7.2}$$

where S_w is the SSS, d_{ice} is the ice thickness (here in cm), S_R is the salinity ratio of the bulk ice salinity at the end of the ice growth season and the SSS, a is the growth rate coefficient which varies from 0.35 to 0.5. Ryvlin (1974) suggests to use 0.5 for a and 0.13 for S_R. However, Kovacs (1996) compared the Ryvlin empirical equation with observed data in the Arctic and suggests to use 0.175 for S_R instead of 0.13. In our model we use 0.175 for S_R which seems to fit better to the observation data in the Arctic. Cox and Weeks (1983) give another empirical relationship between S_{ice} and d_{ice} in the Central Arctic. The two empirical relationships have similar values for first year ice and a water salinity of S_w = 31 gkg^{-1} (Kovacs, 1996). The S_{ice} in Eq. (2) is a function of the underlying SSS, and can therefore be applied to regions outside the central Arctic where SSS is much lower.

The ice thickness retrieval with SMOS data is limited by the saturation of TB. We consider TB to reach saturation if the change of TB with d_{ice} is less than 0.1 K per cm. Thus, TB of an ice layer with a T_{ice} of -2°C and a salinity of 8 gkg^{-1} reaches its saturation for ice thicknesses of less than 20 cm, for example. This means that the maximal retrievable ice thickness d_{max} under warmer conditions can be as low as a few centimeter. On the contrary, under cold conditions and a low ice salinity, which is typical for coastal regions with river run-off, L-band TB emanates from a thicker ice layer. TB reaches its saturation much more slowly and d_{max} can be as high as 1.5 m (Figure 7.2 and Figure 7.3). Therefore, SMOS ice thickness retrieval is more suitable for cold conditions and low ice salinities. If the ice temperature varies between -5°C and -10°C, which is typical for the Arctic in winter, the difference of retrieved ice thicknesses can be as high as 20 cm. The influence of ice salinity on the ice thickness retrieval increases with decreasing ice salinity (Maaß, 2013a). d_{max} at 1 gkg^{-1} S_{ice} can be twice of that at 5 gkg^{-1} S_{ice}.

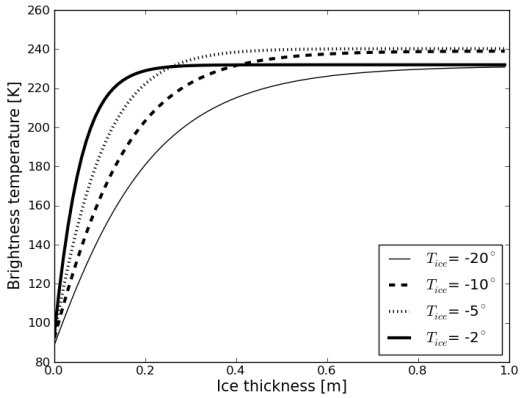

Figure 7.2: TB as function of d_{ice} under different T_{ice}, calculated with the sea ice radiation model with a S_{ice} of 8 gkg^{-1}

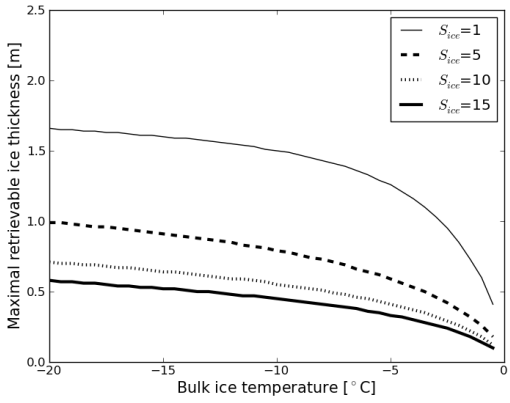

Figure 7.3: d_{max} under different T_{ice} ([K]) and S_{ice} ([gkg^{-1}]).

Table 7.1: Net shortwave radiation over various ice thickness categories (Maykut, 1986).

	Sep.	Oct.	Nov.	Dec.	Jan.	Feb.	Mar.	Apr.	May
open water	89	24	0	0	0	0	7	83	209
0.05 m	60	16	0	0	0	0	5	56	141
0.1 m	56	15	0	0	0	0	4	52	131
0.2 m	53	14	0	0	0	0	4	49	124
0.4 m	48	13	0	0	0	0	4	46	114
0.8 m	45	12	0	0	0	0	3	42	104
3.0 m	16	4	0	0	0	0	1	17	42

7.3.2 The thermodynamic model

In Algorithm II T_{ice} is estimated at each step from the d_{ice} and T_a. For this purpose thermal equilibrium is assumed at the surface of the ice layer and the heat fluxes are calculated with a thermodynamic model based on Maykut (1986). Although we neglect in the sea ice radiation model snow layer, we consider its thermal insulation effect in the thermodynamic model when we calculate the T_{ice}. It is shown in Maaß et al. (2013b) that the impact of a snow layer on the TB is partly caused by its insulation effect on the ice temperature. The insulation effect of a snow layer increases with snow thickness. Linear temperature gradient profiles are assumed for the ice and snow layers in the model.

The thickness of the snow layer is assumed to follow Doronin (1971):

$$\begin{aligned} h_s &= 0\text{m} && \text{for } d_{ice} < 0.05\text{m} \\ h_s &= 0.05 \times d_{ice} && \text{for } 0.05\text{m} \leq d_{ice} < 0.2\text{m} \\ h_s &= 0.1 \times d_{ice} && \text{for } d_{ice} \leq 0.2\text{m}, \end{aligned}$$

where h_s is the snow depth and d_{ice} is the ice thickness.

Under the assumption of thermal equilibrium, the incoming and outgoing heat fluxes compensate each other. During winter season, surface melting can be neglected. Therefore the heat balance at the surface of a slab ice layer with thickness d_{ice} and a layer of snow with thickness h_s on top can be described as

$$(1-\alpha)F_r - I_0 + F_{Lin} - F_{Lout} + F_s + F_e + F_c = 0 \tag{7.3}$$

where F_r is the incoming shortwave radiation, α is the albedo of the snow/ice layer, I_0 is the part of the incoming shortwave radiation that is transmitted into the ice, F_{Lin} is the incoming longwave radiation, F_{Lout} is the outgoing longwave radiation, F_s is the sensitive heat flux, F_e is the latent heat flux, and F_c is the conductive heat flux.

Incoming shortwave radiation F_r is negligible during the winter seasons. However, for the fall and spring periods we should consider this item. Most part of incoming shortwave radiation is reflected at the snow/ice surface due to the high albedo of snow covered ice layer. The downwelling shortwave radiation at the snow/ice surface is partly absorbed and partly transmitted into the ice (I_0) because ice is a translucent material. For the estimation of the net shortwave radiation ($(1-\alpha)F_r - I_0$) over various ice thickness categories we use the monthly averages over perennial Arctic ice given in Maykut (1986) (see Table 7.1) . The monthly averages are given for the beginning of each months. A linear interpolation is made for the days inbetween.

Longwave radiation depends on the air temperature T_a and water vapor in the atmosphere. We parameterize F_{Lin} with the following equations.

$$F_{Lin} = \epsilon^* \sigma {T_a}^4, \tag{7.4}$$

and

$$\epsilon^* = 0.7855(1 + 0.2232C^{2.75}), \tag{7.5}$$

where ϵ^* is the effective emissivity for the atmosphere, σ is the Stefan-Boltzmann constant, and C is the fractional cloud cover.

The outgoing longwave radiation F_{Lout} from the snow surface can be calculated with

$$F_{Lout} = \epsilon \sigma {T_s}^4 \tag{7.6}$$

where ϵ is the emissivity of snow ice layer which can be considered as 1 for the longwave. T_s is the snow surface temperature.

The sensible and latent heat fluxes F_s and F_e are calculated with

$$F_s = \rho c_p C_s u(T_a - T_s), \tag{7.7}$$

and

$$F_e = 0.622 \rho L C_e u \frac{r e_{sa} - e_{ss}}{P}, \tag{7.8}$$

where ρ is the density of the air, u is the wind velocity at 2 m over the surface, P is the surface pressure, r is the relative humidity, e_{sa} and e_{ss} are the saturated vapor pressure at 2 m over the surface and direct above the snow surface, L is the latent heat of vaporization, c_p is the specific heat of air, C_s and C_e are bulk transfer coefficients for sensible and latent heat.

The saturated vapor pressure e_s is shown empirically as

$$e_s = 6.11 \times 10^{\frac{aT}{b+T}} \tag{7.9}$$

where a is 9.5, b is 265.5 for the ice surface, and T is either the surface air temperature or the snow surface temperature.

The conductive heat flux F_c is given by

$$F_c = \frac{k_i k_s}{k_i h_s + k_s d_{ice}} (T_w - T_s) \tag{7.10}$$

where k_s is the thermal conductivity of snow, T_w is the freezing point of sea water. k_s is set to 0.31 $\mathrm{Wm^{-1}K^{-1}}$ according to Yu and Rothrock (1996). The thermal conductivity of ice k_i can be expressed as (Untersteiner, 1964)

$$k_i = 2.034 + 0.13 \frac{S_{ice}}{T_{ice} - 273}, \tag{7.11}$$

where S_{ice} is in $\mathrm{gkg^{-1}}$ and T_{ice} is in K. T_{ice} can be calculated with

$$T_{ice} = 0.5(T_{si} + T_w), \tag{7.12}$$

where T_{si} is the snow-ice interface temperature calculated with

$$T_{si} = \frac{T_s + \frac{k_i h_s}{k_s d_{ice}} T_w}{1 + \frac{k_i h_s}{k_s d_{ice}}}. \tag{7.13}$$

To calculate T_{si} we need to know k_i. However, k_i is in turn a function of T_{ice}. As an approximation we first calculate k_i with $0.5(T_s + T_w)$ instead of T_{ice} and use this k_i to calculate T_{ice} and T_{si}. T_s is estimated with leastsquare method for each d_{ice} under thermal equilbrium assumption.

For simplification we assume constant values for the cloud cover C, the relative humidity r, and the bulk transfer coefficients for sensible and latent heat flux C_s and C_e estimated from the reanalysis data. However, these parameters can be obtained from the auxiliary data that will be delivered with SMOS L1C data in the future.

Figure 7.4 shows the various fluxes at the snow surface with different ice thicknesses and corresponding snow thicknesses. For the calculation we assume an air temperature of 250 K, a surface wind speed of 10 ms^{-1}, a relative humidity of 0.8, a cloud coverage of 0.4, and a sea surface salinity of 30 gkg^{-1}. As can be seen in the figure latent heat flux is relatively small compared with other fluxes. The net heat flux through the thin ice increases exponentially with descreasing ice thicknesses as long as the ice thickness gets less than about 50 cm. This means that when more and more thick perennial ice is replaced by thin first year ice, the net heat loss from the underlying ocean to the atmosphere will increase dramatically.

Table 7.2: Overview of constants used in the thermodynamic model

Parameter	Value	Unit
Surface air Pressure P	1013	hPa
Cloud cover C	0.4	
Air density ρ	1.3	kgm^{-3}
Stefan-Boltzmann constant σ	5.67×10^{-8}	$\mathrm{Wm}^{-2}\mathrm{K}^{-4}$
Emissivity of snow ice layer ϵ	1	
Specific heat of air c_p	1005	$\mathrm{Jkg}^{-1}\mathrm{K}^{-1}$
bulk transfer coefficient for sensible heat C_s	3.0×10^{-3}	
bulk transfer coefficient for latent heat C_e	3.0×10^{-3}	
Relative humidity r	0.8	

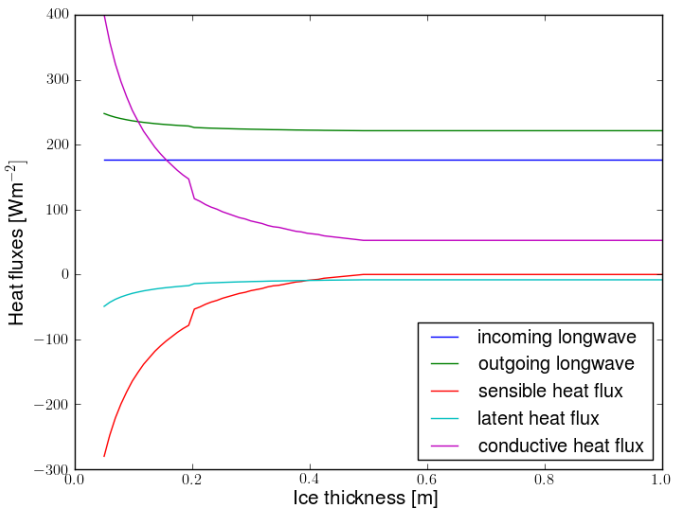

Figure 7.4: The various components affecting the surface heat balance according to Maykut (1986).

7.3.3 Retrieval steps

As discussed in Chapter 7.3.1, the challenge of using variable T_{ice} and S_{ice} in the Algorithm II is that both of them are in turn functions of d_{ice}. The algorithm is based on the forward model consisting of the radiation and thermodynamic model. Therefore, we approximate d_{ice} by repeating the radiation and the thermodynamic model until a convergence point is found for the solution (Figure 7.5). In this process, at each step T_{ice} and S_{ice} are calculated for the respective d_{ice} approximation. The starting point of the iteration is the d_{ice} retrieved with Algorithm I, which uses a constant T_{ice} of -7°C and S_{ice} of 8 gkg^{-1}. At each iteration step, we use d_{ice}, T_{ice}, and S_{ice} to calculate TB with the radiation model. The calculated TB is then compared with that observed by SMOS. To minimize the difference between the observed and the calculated TBs, the new d_{ice} is estimated with a linear approximation method. We define two stopping criteria for the iteration: a brightness temperature difference of less than 0.1 K, or an ice thickness difference of less than 1 cm. The first criteria represents half of the optimal accuracy of daily averaged measurements. We apply the first criteria if the ice is thicker than 30 cm and otherwise the second criteria. The d_{max} is determined with the same criteria for the saturation of TB, i.e. that the TB change is less than 0.1 K per 1 cm d_{ice}. We define a saturation factor

$$S_{TB} = d_{ice}/d_{max}. \tag{7.14}$$

If the saturation factor reaches 100 %, it indicates that the d_{max} can be considered as the minimum ice thickness of the pixel.

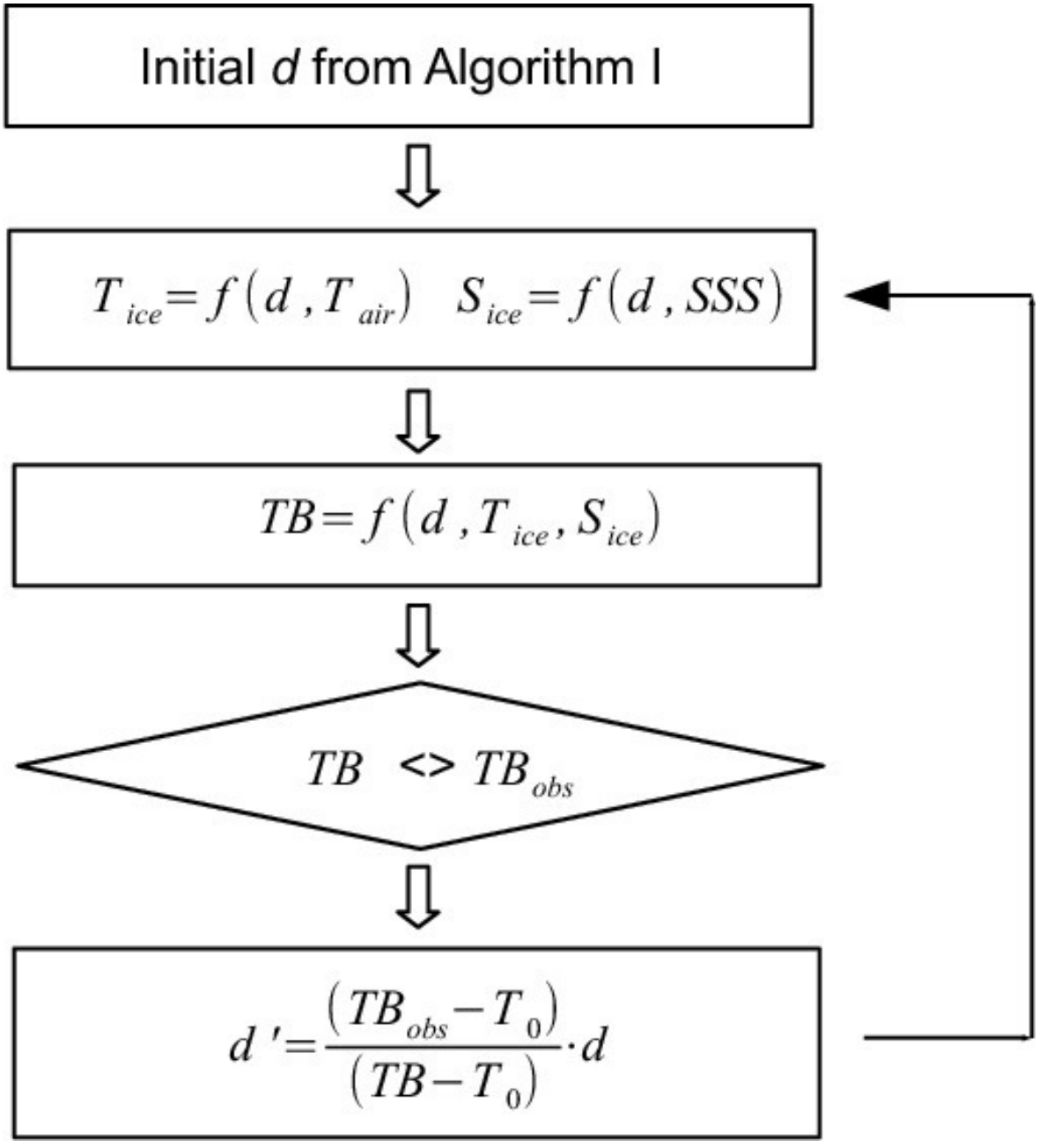

Figure 7.5: Schematic flow chart of the retrieval steps. d and d' are the sea ice thicknesses from the consecutive steps, TB and TB_{obs} are calculated and observed brightness temperatures, T_0 is the brightness temperature of sea water assumed to be 100.5 K.

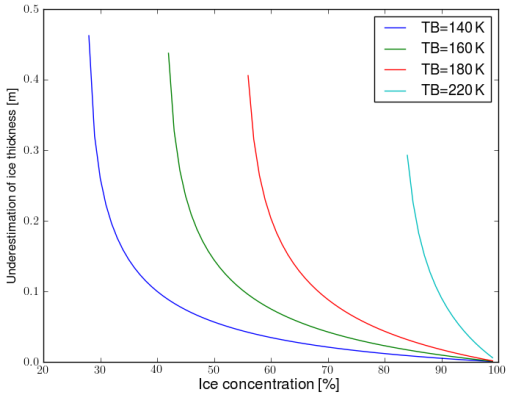

Figure 7.6: The underestimation of ice thickness caused by the 100 % ice coverage assumption.

7.4 Assessment of uncertainties

7.4.1 Systematic errors

In both algorithms we assume 100 % ice coverage for simplicity. TB over ice-sea water mixed areas can be described as

$$TB = TB_{water} \times (1 - IC) + TB_{ice} \times IC, \tag{7.15}$$

where IC is the ice concentration, TB_{water} and TB_{ice} are the TBs over sea water and ice, respectively.

SMOS TB_{water} shows a stable value of about 100.5 K with a standard deviation of about 1 K in the Arctic region. With this constant TB_{water}, we can calculate TB_{ice} using ice concentration charts from radiometer data. During the winter most of the ice covered area in the Arctic has IC higher than 90 % (Andersen et al., 2007). Radiometer IC charts have an uncertainty of 5 % in the winter time (Andersen et al., 2007). At high concentrations, correcting the retrieved ice thickness with IC data set with an uncertainty of 5 % can cause higher errors than the 100 % ice coverage assumption. Therefore, we assume in the retrievals a 100 % ice coverage. The possible underestimation of ice thickness due to this assumption is investigated with the simple semi-empirical function used in the Algorithm I. Figure 7.6 shows that the bias caused by this assumption increases exponentially with decreasing ice concentration. If we assume a SMOS TB of 220 K, the bias can be very high even for IC of more than 80 %. At lower brightness temperatures the bias caused by this assumption is less than a few centimeters.

Table 7.3: Estimated ice thickness uncertainties caused by std(TB), std(T_{ice}), and std(S_{ice}).

d_{ice}	std(TB) = 0.5 K	std(T_{ice}) = 1 K	std(S_{ice}) = 1 gkg^{-1}
0-10 cm	less than 1 cm	less than 1 cm	less than 1 cm
10-30 cm	less than 1 cm	1 cm-5 cm	1 cm-13 cm
30-50 cm	1 cm-4 cm	2 cm-10 cm	2 cm-22 cm
50 cm-	4 cm-more than 1 m	7 cm-more than 1 m	up to 40 cm

7.4.2 Sea ice thickness uncertainties

There are several factors that cause uncertainties in the sea ice thickness retrieval: the uncertainty of the SMOS TB; the uncertainties of the auxiliary data sets; the assumptions made for the radiation and thermodynamic models.

For our purpose we average TB over the incidence angle range of 0°-40°. Due to the large amount of measurements in one day this can significantly reduce the uncertainty of TB by deviding std(TB) with sqrt(number of measurements during one day) at each pixel. This uncertainty is less than 0.5 K in the Arctic except for the strongly RFI affected regions. The uncertainties of T_{ice} and S_{ice} depend on the uncertainties in the T_a and SSS. Both T_a and SSS are derived from model outputs. Due to the sparse observations in the polar regions T_a and SSS consist themselves large uncertainties.

A first estimation of SMOS retrieved ice thickness uncertainty is made with Algorithm II based on the std(TB), std(T_{ice}) and std(S_{ice}). The std(TB) is calculated at each pixel with standard deviation of all available TB measurements devided by the sqrt(number of TB measurements) for each day. The std(S_{ice}) is calculated based on the std(SSS) chart (see Figure 7.1) and d_{ice}. The estimation of std(T_{ice}) is rather difficult because it depends not only on the T_a but also the assumptions made in the thermodynamic model. As a first approximation we assume 1 K for the std(T_{ice}) which is an average value under the assumption of 10 K uncertainty in T_a. More investigations should be conducted to better estimate the uncertainty in T_{ice} in the future.

In Table 7.3 we show an example of estimated ice thickness uncertainties for conditions where T_{ice} varies from -10°C to -2°C and S_{ice} varies from 2 gkg^{-1} to 8 gkg^{-1}. We assume a standard deviation of 0.5 K, 1 K, and 1 gkg^{-1} for TB, T_{ice} and S_{ice}. The ice thickness uncertainty caused by std(TB) is rather small for thin ice less than 50 cm, and increases exponentially for thicker ice. The uncertainty caused by std(T_{ice}) is higher than that caused by std(TB) with an increasing trend with increasing ice thickness. S_{ice} uncertainty has little impact on the ice thickness retrieval for saline ice with a S_{ice} of more than 5 gkg^{-1}. However, for less saline ice, which is typical for example in the regions with river run-off, std(S_{ice}) has much more impact on the ice thickness uncertainty than the other two parameters for d_{ice} less than half a meter.

7.5 The effect of the subpixel-scale heterogeneity on the thickness retrieval (Algorithm II* postprocessing)

Natural sea ice is usually not a uniform layer of level ice with a plane geometry, as it was assumed in the emissivity model, but behaves fractal on a wide range of scales. Sea ice deformation patterns are often described using self-similar functions such as the lognormal distribution (Erlingsson, 1988; Key and McLaren, 1991; Tan et al., 2012). A theory of sea ice thickness distribution was developed by Thorndike et al. (1975). Models which include ice growth and deformation may be used to simulate the evolution of the thickness distribution (Thorndike, 1992; Godlovitch et al., 2012). A common feature of simulations and empirical observations is the exponential tail resulting from dynamic deformation processes. The inherent skewness of the thickness distribution results in a considerable underestimation of sea ice thickness when the retrieval model is based on a plane sea ice layer. In the following we use airborne sea ice thickness measurements in order to parameterise the thickness distribution function and to investigate the effect of the subpixel-scale heterogeneity on the thickness retrieval.

NASA's Operation IceBridge (OIB) airborne campaigns obtained large scale profiles of sea ice thickness derived from a laser altimeter system (Kurtz et al., 2013). The footprint size of a single laser beam is about 1 m and the vertical accuracy is given as 6.6 cm. The sea ice thickness is estimated from the freeboard by accounting for the snow thickness and assumption about the densities of ice and snow. The snow thickness is retrieved using a snow-depth radar simultaneously. The uncertainty of OIB sea ice thickness data is given as 0.4 m (Farrell et al., 2012). Here we use the OIB "quicklook" data as obtained from a NSIDC website.

We assume that the sea ice thickness follows a lognormal distribution

$$p(d_{ice}, \mu, \sigma) = \frac{1}{d_{ice}\sigma\sqrt{2\pi}} e^{-\frac{(log(d_{ice})-\mu)^2}{(2\sigma^2)}} \tag{7.16}$$

with the two parameters logmean μ and logsigma σ. Furthermore, we assume a constant logsigma value σ to approximate the thickness distribution function with only one independent variable. To test this assumption we split the 2012 and 2013 OIB Arctic sea ice thickness data in chunks of about 30 km length. We found that using constant values $\sigma = 0.6 \pm 0.1$ rejects less than 15% of the chunks tested with Kolmogorov-Smirnov statistics at a significance level of 95%. The parameter σ increases with increasing length of the chunks and converges to about 0.7 for the maximal number of samples. The parameter σ changed only slightly from 0.692 to 0.695 while the mean thickness decreased considerably from 3.1 m to 2.2 m when considering the entire datasets of the years 2012 and 2013, respectively (Fig. 7.7). One percent of the 2012 thickness data ($N_{1\%} = 3430$) are above 10 m, and one permil exceeds 16 m with a maximum thickness value as large as 27.4 m which justifies the exponential tail of the distribution function. The effect of the ice thickness distribution on TB is taken into account by the integration over the thickness range according to the superposition principle

$$TB^*(d_{ice}) = \int_0^{max(d_{ice})} TB(d_{ice}) g(d_{ice}) dd_{ice} \tag{7.17}$$

with the thickness distribution function $g(d_{ice})$ and the brightness temperature of a single/plane-layer model $TB(d_{ice})$. The brightness temperature weighted with the thickness distribution

TB^* suggests a sensitivity to ice thicknesses larger than d_{max}. Here d_{max} and d_{ice} both refer to the single-layer thickness. The real mean thickness denoted as H is strongly underestimated if the retrieval does not account for the thickness distribution. The overall effect can be explained as an apparent deeper penetration depth caused by leading edge of the thickness distribution. The implementation of a radiative transfer model that includes this effect is straightforward but computationally expensive because of the integration. A post-processing look-up table for the single-layer model has been generated to estimate an approximate correction factor. This method that converts the single-layer thickness d_{ice} to the mean thickness H is called Algorithm II* hereinafter. Figure 7.8 shows that the involved correction factor increases with increasing salinity and temperature.

A main uncertainty is the shape of the thickness distribution and its parameterisation with a constant σ. This seems to be a reasonable good representation of the IceBridge thickness data. However, the data in the important thin ice range is only sparse. More field data are required to further analyse the thickness distribution for thin ice on different scales.

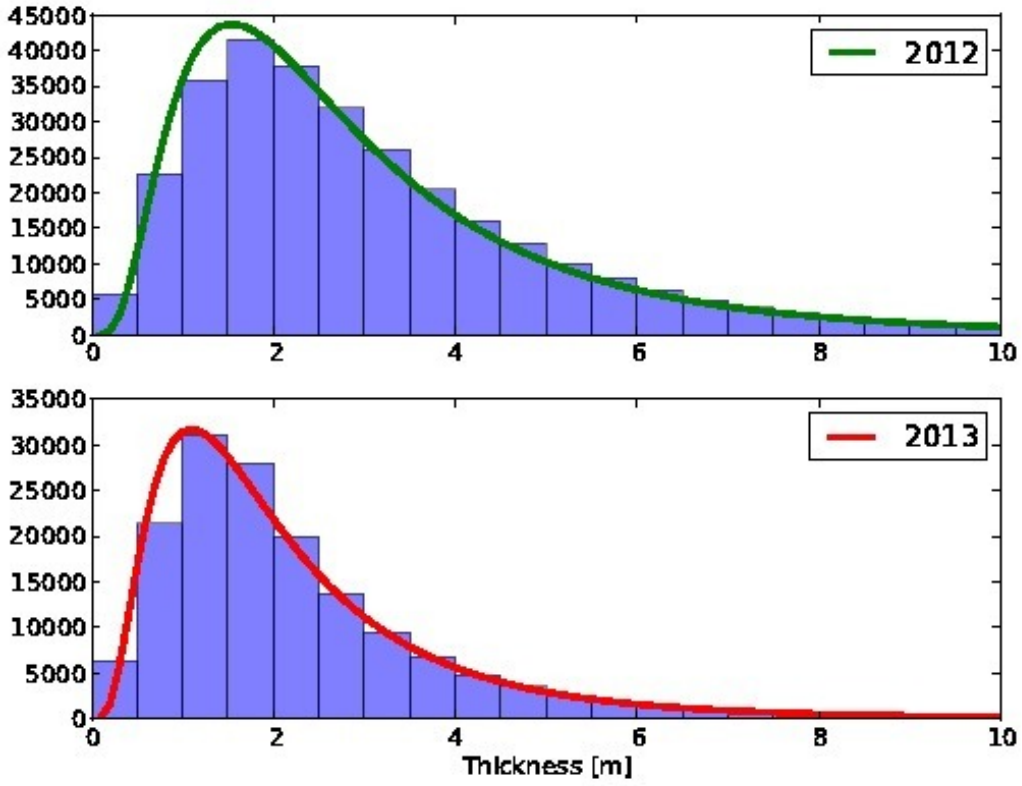

Figure 7.7: Sea ice thickness distribution derived from NASA's Operation IceBridge data of 2012 (upper, $\sigma = 0.692$) and 2013 (lower, $\sigma = 0.695$). The Y-axis is the number of occurrence.

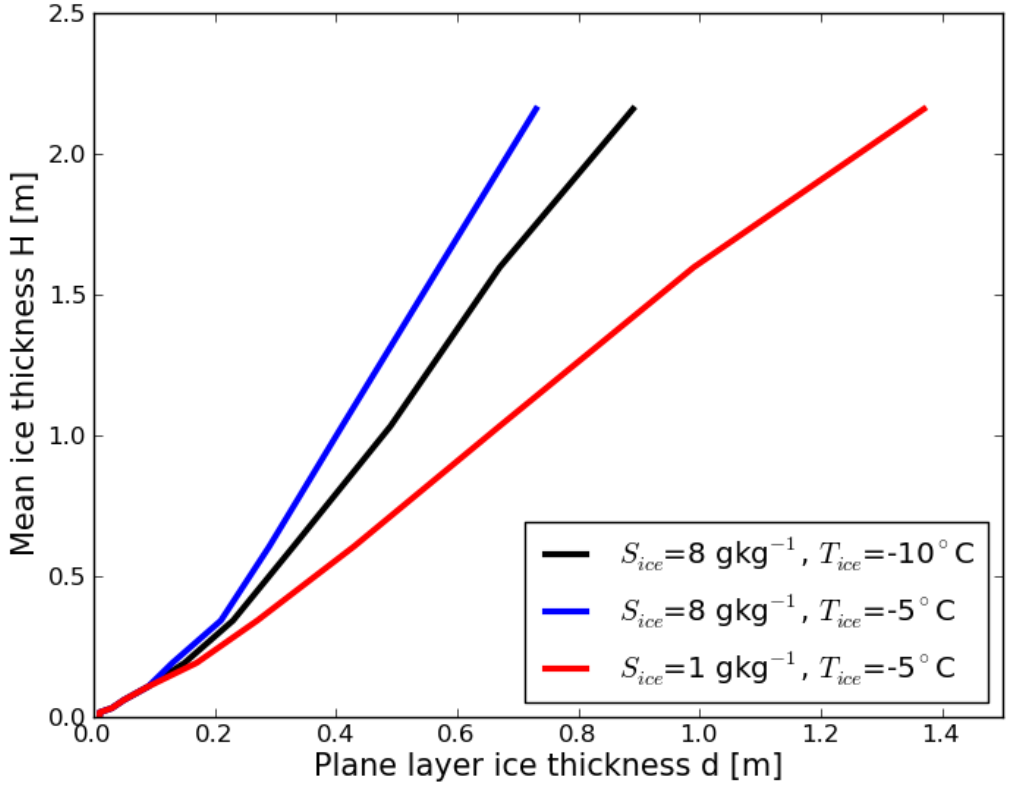

Figure 7.8: Relationship between the plane ice layer thickness d_{ice} and the mean inhomogeneous ice layer thickness H at different T_{ice} and S_{ice}.

7.6 Comparison of ice thicknesses retrieved with Algorithms I, II, and II*

In this section, we analyse the time series of ice thicknesses retrieved from the Algorithm I, II, and II* at single grid points in the Laptev Sea and the Beaufort Sea (Point 1: 77.5°N, 137.5°E, Point 2: 71.0°N, 165.0°W, Point 3: 74.5°N, 127.0°E). The time series begin on 15 October 2011. The time series of ice thickness extracted from two different sea ice assimilation systems are included for comparison. In addition, we show time series of SMOS TB together with ice concentration and derived snow/ice surface temperature.

One of the assimilation systems is the TOPAZ system. TOPAZ is an advanced data assimilation system, using the Ocean model HYbrid Coordinate Ocean Model(HYCOM) and Elastic-Viscous-Plastic(EVP) ice rheology (Bertino and Lisæter, 2008). TOPAZ has a resolution between 18 and 36 km with 22 isopycnal layers. The assimilated observations are satellite-observed Sea Level Anomaly (SLA), Sea Surface Temperature (SST), sea ice concentrations from AMSR-E, sea ice drift products from CERSAT, and Coriolis in-situ temperature and salinity profiles. The TOPAZ system has been in operation since 1 January 2003. The major outcomes in terms of products are weekly issued short term forecasts.

The other assimilation system is the Panarctic Ice Ocean Modeling and Assimilation System (PIOMAS) (Zhang and Rothrock, 2003). It is based on a coupled ocean-ice model forced with National Centers for Environmental Prediction Atmospheric Reanalysis data. PIOMAS assimilates satellite-observed sea ice concentration and sea surface temperature data.

At Point 1, which is located in the north of the Laptev Sea, in the first 30 days both algorithms show very similar d_{ice} ranging from 0 m to about 0.3 m (Figure 7.9). The TB increases from about 100 K to about 230 K. In this TB range, d_{ice} is the dominant factor of TB variation (Kaleschke et al., 2012). In the next 30 days, TB increases to about 240 K, whereas d_{ice} increases from about 0.3 m to about 0.4 m in Algorithm I and to more than 0.5 m in Algorithm II. From mid-December to the end of April, the TB shows little variability with mean value of 237.4 K and a standard deviation of 1.9 K. In this period, d_{ice} from Algorithm I shows a stable value around 0.35 m with a standard deviation of 3 cm, which results from the constant parameters assumed in Algorithm I. On the contrary, d_{ice} from Algorithm II shows an average value of 0.48 m with a standard deviation of 11 cm. The strong variability in d_{ice} is mainly caused by T_{ice}. A correlation coefficient R of -0.7 can be found between T_{ice} and d_{ice}. In the total time period of 200 days, the d_{ice} from Algorithm II is on average 10 cm thicker than that from Algorithm I. The ice thickness corrected with the thickness distribution function (Algorithm II*) is about two times that of Algorithm II.

Simulated ice thicknesses from TOPAZ and PIOMAS show continuous ice growth during the time period, however, with more than half a meter span between them (shaded area in the upper panel of Figure 7.9). The ice thicknesses retrieved with Algorithm II* correspond well with those from TOPAZ and PIOMAS in the first three months. However, from March to April TOPAZ and PIOMAS show further growth in the ice thickness, whereas SMOS shows rather constant or decreasing trends. The decreasing trend in d_{ice} corresponds to the decreasing d_{max} caused by the increasing T_s.

Point 2 is located in the Beaufort Sea, near Barrow. The first sea ice occurrence happens in mid-November, one month later than at Point 1. A few days after the first occurrence of sea ice, the ice concentration rapidly reaches nearly 100 % (Figure 7.10). In the following 80 days, the T_s decreases from about 270 K to 240 K, d_{ice} retrieved with Algorithm II* increases from a few centimeters to more than 1.5 m. In this period, the ice thickness growth

from SMOS Algorithm II* agrees well with that simulated by TOPAZ and PIOMAS. Just as at point 1, after the three months freeze-up period the SMOS retrieved d_{ice} reaches its maximum with a decreasing trend in April, which corresponds to the increasing T_s.

Point 3 is located north of the Lena Delta where frequent formation of polynyas can be observed. The area is characterised by large interannual variations, being the consequence of an enormous freshwater input from the Lena river and ice formation and salt rejection processes taking place in polynyas offshore the fast ice edge. Anticyclonic wind conditions force the riverine water northwards and result in a stronger density stratification in the eastern Laptev sea during winter. Cyclonic atmospheric circulation deflects the freshwater plume of the Lena river eastward towards the East Siberian Sea, thus causing higher salinity in the eastern Laptev Sea and the area around the West New Siberian (WNS) polynya.

The strong variability of ice thicknesses in SMOS and PIOMAS shows good correlation (Figure 7.11). The decrease and increase of ice thicknesses in SMOS and in the model outputs are very likely caused by the drift of thick ice due to wind forcing and thin ice formation in the polynya areas. From March to April, there is a large discrepancy between the model outputs and the SMOS-derived ice thickness. While PIOMAS shows an ice thickness of more than 2 m in April, SMOS-derived ice thickness is less than half a meter.

Sea ice thickness measurements were carried out in this area during helicopter-borne ice thickness surveys performed in the Laptev Sea during the Transdrift (TD) XX campaign in April 2012. The helicopter-borne ice thickness measurements were made with an electromagnetic (EM)-Bird that utilizes the contrast of electrical conductivity between sea water and ice to determine the distance to the ice-water interface (Haas et al., 2009). An additional laser altimeter yields the distance to the uppermost reflecting surface. Hence, the obtained ice thickness is the ice- plus snow thickness from the difference between the laser range and the EM-derived distance. The accuracy over level sea ice is in the order of 10 cm (Pfaffling et al., 2007). Uncertainties in the ice thickness measurements may arise from the assumption that sea ice is a non-conductive medium. Over thin ice, this assumption may be invalid because the conductivity of saline young ice can be significantly higher than that of older first-year or multi-year ice. This can lead to an underestimation of ice thickness.

The survey flight made on 20 April has a length of about 200 km and covers mostly thin ice being formed in the WNS polynya and the Anabar-Lena polynya. A period of strong and consistent offshore winds led to the development of an extensive thin ice zone extending several hundred kilometre offshore. Point 3 is located in the middle of the flight track. Therefore, we use the EM-bird measurements to validate the SMOS derived ice thickness. During the flights, the EM-Bird recorded a total of 46386 measurements with a mean value of 43 cm and a standard deviation of 33 cm. This agrees well with the 31 cm ice thickness from SMOS Algorithm II*, considering that the EM-Bird derived ice thickness is the sum of the thicknesses of the ice layer and the snow layer on top of it. The comparison shows that in the polynya area SMOS estimates the ice thickness better than TOPAZ or PIOMAS.

After the time series comparison at single points, we compare the daily ice thickness distribution from the three algorithms in the Arctic on 1 February 2013. As can be seen in Figure 7.12, the mean ice thickness considerably increases from Algorithm I to Algorithm II*. In the central Arctic covered with thick multi-year ice, the TB reaches its saturation. Therefore, none of the algorithms can deliver reliable ice thickness information in the thick multi-year ice area. If we consider only the pixels where TB has not reached its saturation, ice thickness from Algorithm II* is on average 0.82 m, which is about 40 cm thicker than that from Algorithm II and 55 cm thicker than that from Algorithm I. However, the increase of ice thickness varies from region to region, depending on SSS and weather conditions. For

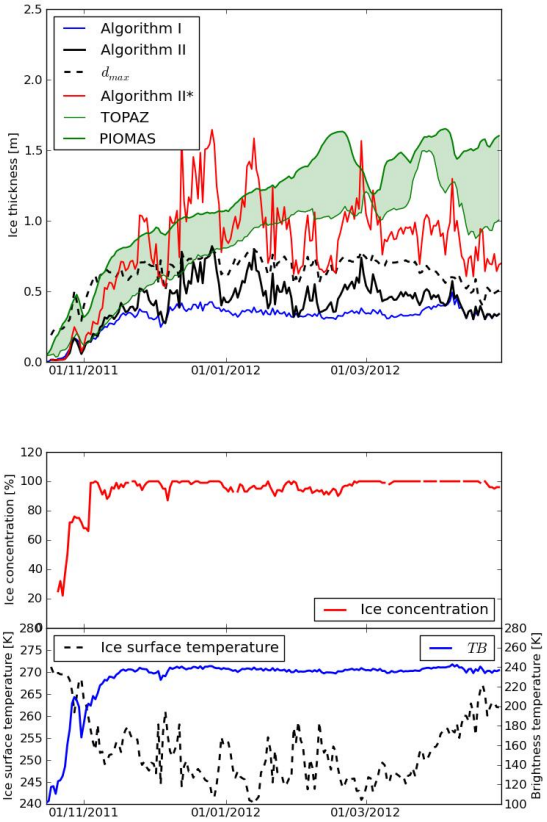

Figure 7.9: Time series of ice thickness derived from Algorithm I, II, and II*, together with d_{max} and simulated ice thicknesses from TOPAZ and PIOMAS (upper panel) and time series of ice concentration, snow (or ice in case of bare ice) surface temperature and SMOS TB (lower panel) at Point 1 (77.5°N, 137.5°E).

example, in the Laptev Sea where the SSS is much lower than that in the central Arctic, the difference between Algorithm II and Algorithm I is as large as half a meter. On the contrary, in parts of the Kara Sea and north of the Barents Sea little change can be observed between Algorithm I and II. The increase of ice thickness in Algorithm II compared to Algorithm I is caused by the deviation of estimated T_{ice} and S_{ice} from the constant values assumed in Algorithm I. To investigate the contribution of T_{ice} and S_{ice} in the thickness retrieval separately we carried out two tests with the data of 1 February 2013. In the first test S_{ice} is assumed to be 8 gkg^{-1} as in Algorithm I and we vary only T_{ice}. In the second test T_{ice} is assumed to be -7°C as in Algorithm I and S_{ice} is calculated from SSS. In both tests we assume planar ice layer. If we only consider the pixels where TB has not reached its saturation, the change of ice thickness caused by T_{ice} in Test 1 varies from -10 cm to more than 50 cm, with an average of 11 cm. Larger change is found where cold air temperature prevails. The ice thickness change caused by S_{ice} from Test 2 is in average 3 cm. However, up to 20 cm and 60 cm difference can be found in the Laptev Sea and in the Baltic Sea.

The comparisons show that Algorithm II* has a considerably better agreement with the model outputs and the EM-Bird validation data than Algorithm I and II. Taking into account the variability of ice temperature and ice salinity delivers better information about the Arctic-wide ice thickness distribution. Therefore, we use Algorithm II* to retrieve ice thickness in our operational data processing.

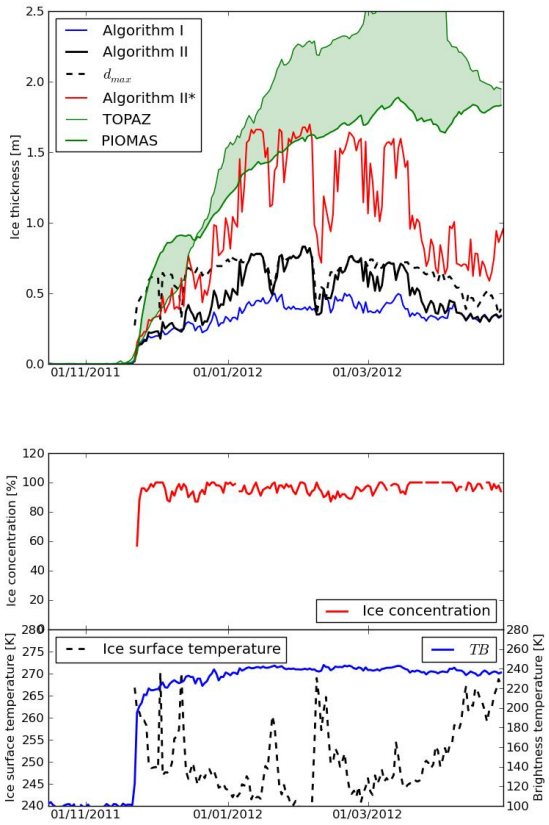

Figure 7.10: Time series of ice thicknesses derived from Algorithm I, II, and II*, together with d_{max} and simulated ice thicknesses from TOPAZ and PIOMAS (upper panel) and time series of ice concentration, snow (or ice in case of bare ice) and SMOS TB (lower panel) at Point 2 (71.0°N, 165.0°W).

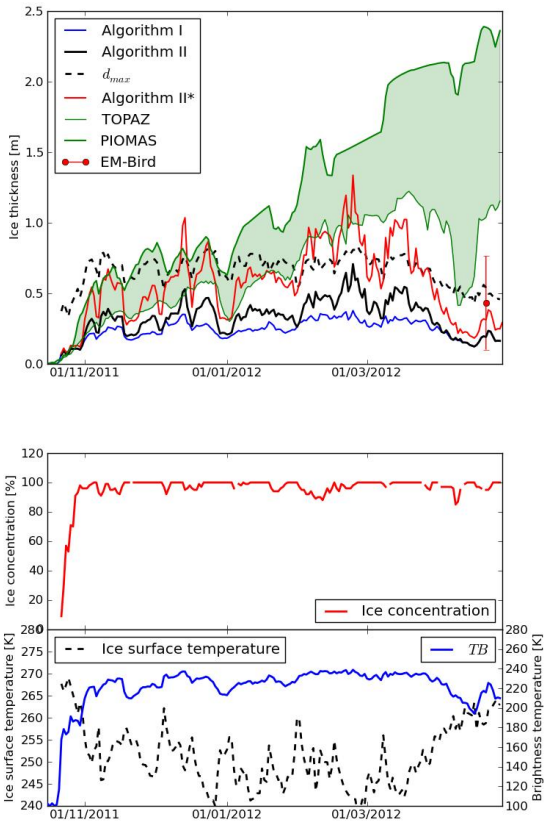

Figure 7.11: Time series of ice thicknesses derived from Algorithm I, II, and II*, together with d_{max} and simulated ice thicknesses from TOPAZ and PIOMAS (upper panel) and time series of ice concentration, snow (or ice in case of bare ice) and SMOS brightness temperature (lower panel) at Point 3 (74.5°N, 127.0°E).

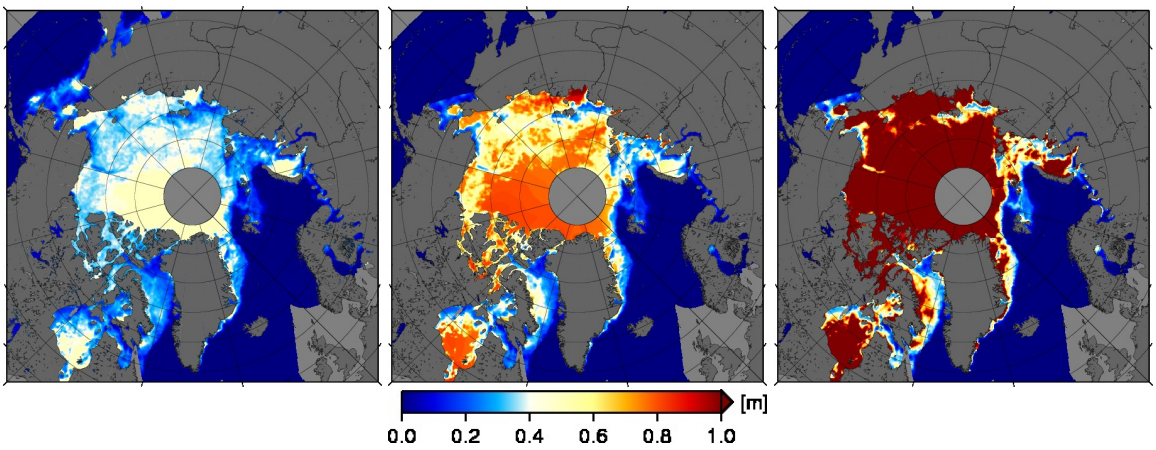

Figure 7.12: SMOS ice thickness derived from retrieval algorithm I, II, and II* in the Arctic on 1 February 2013.

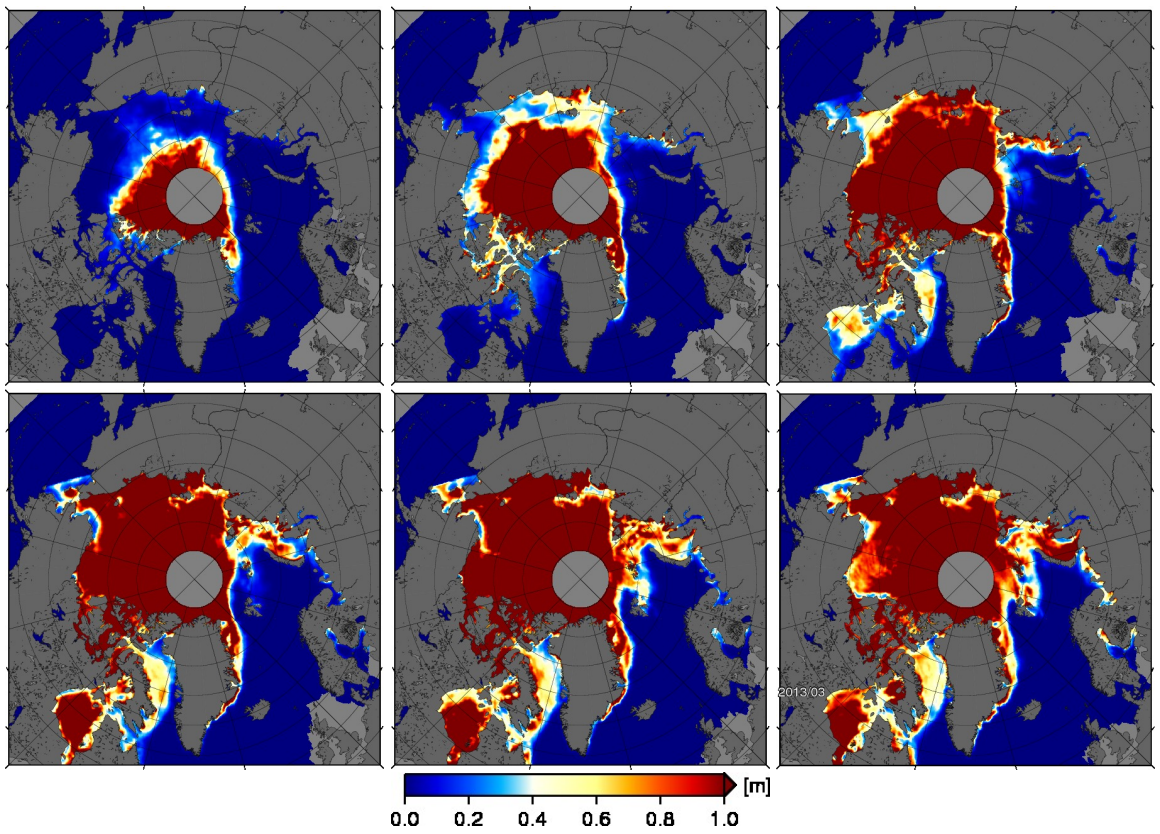

Figure 7.13: Monthly sea ice thickness derived from Algorithm II* during the freeze-up period of October 2012 to March 2013 (from upper left to lower right) in the Arctic.

7.7 Ice thickness growth and distribution as seen by SMOS during the freeze-up period

SMOS-derived ice thickness shows continuous growth and expansion of first year ice in the Arctic during the freeze-up period. Figure 7.13 shows the monthly mean sea ice thickness from October 2012 to March 2013 retrieved with Algorithm II*. From October to November, thin first-year ice extends to most areas of the East Siberian Sea, the Laptev Sea, and the Beaufort Sea. In addition to the area expansion, also an increase of ice thickness due to the thermodynamic growth can be observed. In December, first-year ice reaches a thickness of more than 1 m in the Laptev Sea and the Beaufort Sea. In March 2013 large areas of thin ice with a thickness less than 40 cm is observed in the Beaufort Sea which is caused by the opening of leads and polynyas in this period.

7.8 Conclusions

In this chapter we introduce a new SMOS sea ice thickness retrieval algorithm (denoted as Algorithm II) in which we take into account variations of ice temperature T_{ice} and salinity S_{ice}. T_{ice} and S_{ice} are estimated during the ice thickness retrieval from the surface air temperature T_a of atmospheric reanalysis data and a model-based SSS climatology as boundary conditions. Ice thicknesses retrieved from Algorithm II are compared with that from an earlier semi-empirical algorithm (Kaleschke et al., 2012)(Algorithm I) in which a constant T_{ice} (-7°C) and S_{ice} (8 gkg^{-1}) are assumed. The new algorithm allows to retrieve considerably higher thickness for cold conditions and less saline ice. The maximal retrievable ice thickness d_{max} can be estimated based on the T_{ice} and S_{ice} at each pixel. In contrast, we estimated d_{max} at about 0.5 m as a constant upper limit for the ice thickness retrieval with Algorithm I. In Algorithm II d_{max} varies from a few centimeters to about 1 m depending on the T_{ice} and S_{ice}. A TB saturation factor is defined as the ratio of d_{ice} to d_{max} for each pixel. A saturation ratio close to 100 % indicates that the retrieved ice thickness has to be considered as a minimum ice thickness and that the upper bounds of uncertainty can not be constrained by the SMOS measurement alone.

Natural sea ice exhibits a broad scale of ice thicknesses within one SMOS footprint due to ice deformation. Algorithm II is based on an emissivity model including a plane layer geometry which is not an adequate assumption for natural sea ice. Therefore, Algorithm II is statistically corrected assuming that the thickness of natural sea ice follows a lognormal distribution. This version of the retrieval is denoted as Algorithm II*. The statistical correction factor depends on T_{ice} and S_{ice}. For warm saline ice the correction factor is higher than for cold less saline ice. The corrected ice thickness is on average about twice as large compared to the plane layer assumption which is similar as the general relation between modal and mean ice thickness.

The ice thickness from Algorithm II* agrees well with those from assimilation systems TOPAZ and PIOMAS in the three months after the first occurence of sea ice. However from March to April TOPAZ and PIOMAS exhibit much higher ice thickness compared to the SMOS retrieval. The discrepancy goes along with the onset of surface warming and indicates a possible shortcoming of our retrieval method. We observe a strong impact of T_{ice} on the ice thickness retrieval when TB approaches saturation. The emissivity model used here does not correctly account for vertical gradients of temperature and salinity. The invalid assumption of a vertically homogeneous ice layer introduces significant uncertainties because the relative brine volume and thus the permittivity depends on ice temperature and salinity (Maaß, 2013a). More work has to be done to develop and test parameterisations that could account for the effects of a vertically structured sea ice cover to further improve the emissivity model. However, a validation with EM-Bird measurements in the polynya areas of the Laptev Sea in April 2012 shows very good agreement between EM-Bird and SMOS ice thicknesses whereas TOPAZ and PIOMAS overestimate the ice thickness by 0.5-2 m.

The retrieval uncertainty is dominated by inaccurate assumptions and boundary conditions obtained from auxiliary data whereas the radiometric accuracy is well constrained and sufficient except for RFI-affected areas. Factors that affect the ice thickness retrieval include the ice concentration, ice salinity, ice temperature, snow thickness as well as the statistical thickness distribution function. Sea ice concentration data available from passive microwave sensors like the Special Sensor Microwave Imager/Sounder (SSMIS) and the Advanced Microwave Scanning Radiometer 2 (AMSR2) have an inherent uncertainty of about 2.5-5 % over high-concentration ice in winter, and even more difficult, have strong limitations in

new-ice areas (Andersen et al., 2007; Ezraty, 2002). Thus, we do not correct for varying ice concentration because this would considerably increase the noise and raise so far unresolved problems in regions where new ice is not detected with traditional methods but with SMOS. The variability of the parent water salinity contributes only little to the overall uncertainty except for low-salinity areas. By neglecting the growth-rate dependend salt inclusion in Ryvlin's parameterization we introduce additional errors that can not be quantified without the use of more advanced sea ice thermodynamic models (Notz and Worster, 2009; Vancoppenolle et al., 2006). The radiation model used in this study is adapted from Menashi et al. (1993) which is a simple one layer model without a snow layer. Although we consider the insulation effect of snow, the radiative contribution of the snow layer to the overall brightness temperature is neglected. This effect is investigated in Maaß et al. (2013b) with another radiation model based on Burke et al. (1979).

A distinct advantage of the SMOS sea ice thickness retrieval is the daily coverage independent of clouds and the large sensitvity for thin ice. Thus, our SMOS product is complementary to the sea ice thickness derived from CryoSAT-2 and feasible for operational useage. However, the thickness retrieval is strictly limited to cold periods and not applicable during late Spring and Summer. Daily SMOS ice thickness charts from Oct. 15 to Apr. 15 since 2010 are available via `http://icdc.zmaw.de`.

8 ATBD3

Georg Heygster, Marcus Huntemann, Huan Wang

STSE SMOSICE

Algorithm Theoretical Basis Document (ATBD) for the University of Bremen

Polarization-based SMOS sea ice thickness retrieval algorithm (Algorithm II)

Georg Heygster, Marcus Huntemann and Huan Wang
Institute of Environmental Physics, University of Bremen

May 11, 2012

Contents

Revision history

Date	Author	Comments
JAN 16, 2012	MH	Initial outline
MAR 6, 2012	MH, GH	Version 0.9
MAY 11, 2012	GH, MH, LK, PM	Version 0.95, Sections 5 and 6 extended, and detail corrections

1 Introduction

Geophysical information is not only included in the total radiances (intensities) observed by spaceborne microwave sensors, but also in the polarization. While most spaceborne microwave radiometers observe only the the vertically and horizontally polarized radiation (first two components of the Stokes vector), SMOS in addition measures the third and fourth ('higher') Stokes components. The only other spaceborne sensor capable of detecting all four components of the Stokes vector is WindSat launched in 2003. However, WindSat observes only at 10.7, 18.8 and 37 GHz which are considerably higher frequencies than the 1.4 GHz frequency of SMOS. Here, the information content over sea ice of L-band polarized radioactivity is investigated.

Many parts of this report build upon a previous ESA study [1], especially the first two sections of Chapter 2 and the basic idea of the sea ice concentration retrieval of Chapter 5, which is also published in [2].

2 Calculation of Stokes components

In order to use the polarization observing capabilities of SMOS, the Stokes components of the SMOS brightness temperatures must be correctly determined. This step involves a transformation from the (X, Y) coordinate system of the sensor to the (V, H) coordinate system. As the (X, Y) is relative to the sensor, its polarizations vary over the swath if considered in the earth-oriented (V, H) coordinate system. The SMOS L1C data are distributed in the (X, Y) system.

2.1 Transformation from the (X, Y) instrument reference frame to (V, H) earth reference frame

At full polarization, the transformation from the (X, Y) to the (V, H) system is done for each SMOS snapshot, according to the transformation matrix [3]:

$$\begin{bmatrix} A_1 \\ A_2 \\ A_3 \\ A_4 \end{bmatrix} = \begin{bmatrix} \cos^2(\alpha) & \sin^2(\alpha) & -\cos(\alpha)\sin(\alpha) & 0 \\ \sin^2(\alpha) & \cos^2(\alpha) & \cos(\alpha)\sin(\alpha) & 0 \\ \sin(2\alpha) & -\sin(2\alpha) & \cos(2\alpha) & 0 \\ 0 & 0 & 0 & 1 \end{bmatrix} \begin{bmatrix} TB_H \\ TB_V \\ TB_3 \\ TB_4 \end{bmatrix}$$

with $A_1 = real(TB_{XX})$, $A_2 = real(TB_{YY})$, $A_3 = 2real(TB_{XY})$, $A_4 = -2imag(TB_{XY})$

$\alpha = \alpha_r + \omega_{F_a}$, where α_r and ω_{F_a} are geometric rotation angle and the Faraday rotation angle respectively, which are supplied in the SMOS L1C data.

The transformation needs for each snapshot brightness temperatures at three polarizations: XX, YY and XY. However, only one (either XX or YY) or two (either (XX, XY) or (YY, XY)) are measured at one observation time. For example, in Table 1, this DGG (Discrete Global Grid) has ten observations,

Table 1: The observation informations in one example DGG 4102890

Observation	Polarization	Snapshot	Acquisition time(second)	Values to be interpolated
1	YY	49641343	5167.5	XX, XY
2	YY	49641344	5168.7	XX
3	XY			
4	XX	49641345	5169.9	YY, XY
5	XX	49641347	5171.1	YY
6	XY			
7	YY	49641348	5172.3	XX, XY
8	YY	49641349	5173.5	XX
9	XY			
10	XX	49641350	5174.7	YY, XY

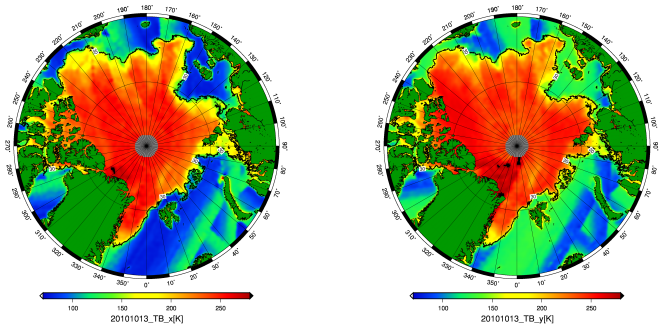

(a) TB_x (b) TB_y

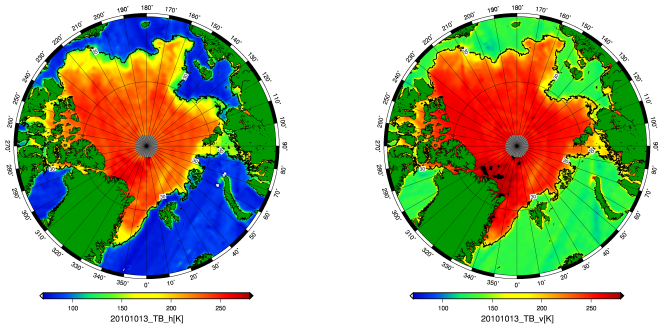

(c) TB_h (d) TB_v

Figure 1: SMOS full polarization data of 13 October 2010 for incidence angle range $40° - 50°$. (a)X-pol brightness temperature; (b)Y-pol brightness temperature; (c)H-pol brightness temperature; (d)V-pol brightness temperature; The contour lines are the 30% ice concentration from ASI algorithm.

whose polarizations are given as (YY, YY, XY, XX, XX,.....). Since the XY polarization is observed at the same time as the one before, we have for this DGG measurements over seven snapshots. Now the interpolation has to be done for each of the snapshots, see the last column of Table 1. That means, we have to interpolate either one or three values. Here for the interpolation, we use the SMOS observations measured in acquisition time, and only the data acquired within ± 2.5 seconds before or after our time of interest are used (SMOS measures at every 1.2 second). This time limitation of 2.5 second is to makes sure that the data for interpolation is temporally not too far from the one to be interpolated, which means, they are measured at similar atmosphere and surface conditions. If no suitable values for interpolation are found within ± 2.5 second, this observation is discarded from the transformation and data analysis. In addition, the incidence angle may vary less than $0.5°$, which also insures the accuracy of the interpolation.

2.2 Results

The SMOS full polarization brightness temperatures have been read using the Python routine read_L1C.py, a version based on the routine with the same name provided by L. Kaleschke and colleagues of the University of Hamburg, but with a much decreased processing time. Moreover, a fast Python code has been built to transform the X-pol and Y-pol brightness temperatures into H-pol and V-pol brightness temperatures, based on the algorithm described in the Soil Moisture Algorithm Theoretical Basis Document [3], pages 71-72. The third and fourth Stokes components have been produced as well.

Figure 1 shows the SMOS full polarization brightness temperatures for the whole Arctic for 13 October 2010, using a grid size of $0.1°$ and the incidence angle range of $40° - 50°$. Figures 1a and 1b are the brightness temperatures at X and Y polarization relative to the antenna reference frame. They fit very well with the ASI sea ice concentrations (the black contour line of 30% ice concentration). However, there are some extremely large values (higher than 280K) which are unphysical (the black area north of

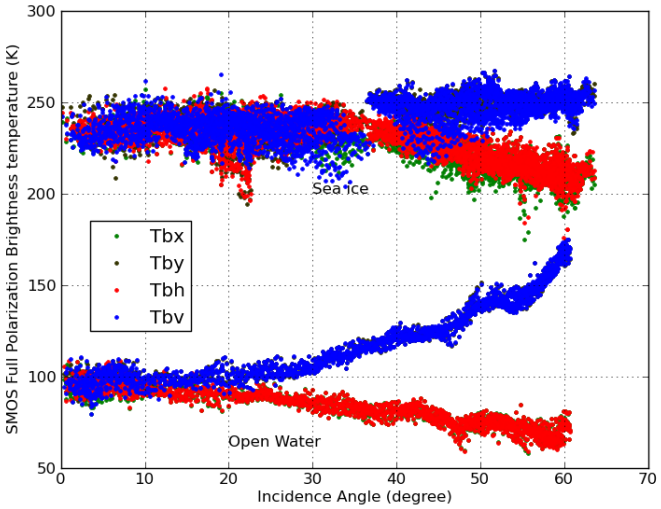

Figure 2: SMOS full polarization brightness temperatures at different incidence angles for the sea ice region $79° - 82°$N, $111° - 112°$E and the open water region $79° - 80°$N, $74° - 75°$E.

Greenland). In addition, there are some stripes in the open water region. They are caused by the different incidence angles on which the TBx and TBy values in the antenna frame depend. Figures 1c and 1d are the transformed brightness temperatures at H and V polarization relative to the surface reference frame. They also show some unphysically high values. In the 3rd and 4th Stokes components (Figs. **??** and **??**) the swathes strongly shine through, indicating a strong dependence of these components on the incidence angle. Also, the retrieved values in the 3rd and 4th components are clearly different from that expected from the fully polarized radiometer WindSat observing at 10 GHz [4] which were all below 3K. These results require further investigation in order to find out if the unexpectedly high signals are due to sensor physics or geophysics.

Two regions for sea ice ($79° - 82°$N, $111° - 112°$E) and open water ($79° - 80°$N, $74° - 75°$E) are chosen to show the brightness temperature at different incidence angles (Fig. 2). Sea ice and open water are easily separated. For open water, the brightness temperature depends much on incidence angles, especially at incidence angles higher than 20°. V-pol and Y-pol brightness temperatures increase with incidence angles while H-pol and X-pol decrease. On the other hand, the variation for sea ice is not as strong as that for open water. The brightness temperature increases (V-pol and Y-pol) and decreases (H-pol and X-pol) mainly at incidence angle higher than 40°, at lower incidence angles they are nearly constant and identical.

In Figure 1 we found similar stripes in most of the sub-figures which look like different SMOS swathes. In order to check this hypothesis, one single swath has been plotted for the same day (13th, October, 2010) and the same incidence angle range ($40° - 50°$). Figure 3a shows the H-pol brightness temperatures, in which we see different values in the open water region (high in the border and low in the center). The difference in one swath can also be seen in other polarizations, which is not shown here. For example, at vertical polarization, brightness temperatures are high in the center and low in the border over open water. This is not physical since the brightness temperatures should be nearly homogeneous over the region with similar surface type and same atmospheric conditions. This difference is probably caused by the incidence angles, see the stripes in Figure 3b which show similar patterns. In order to avoid this problem, smaller incidence angle range is recommended in the future work.

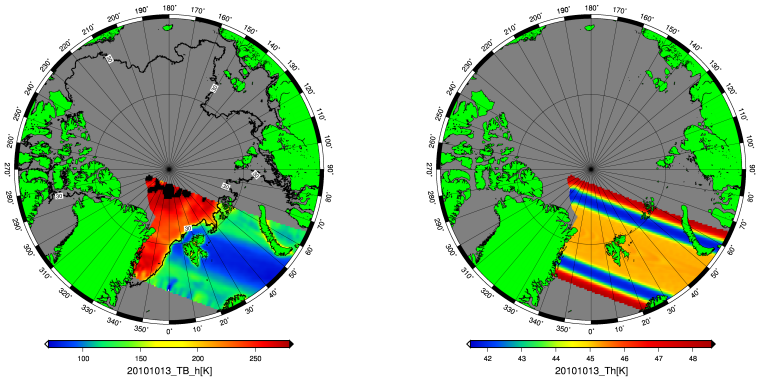

(a) TB_h (b) Incidence angle

Figure 3: (a) SMOS H-pol brightness temperatures and (b) mean incidence angles for the incidence angle range $40° - 50°$ on 13th, October 2010.

3 Concept of algorithm, channel selection

3.1 Brightness temperature dependence on sea ice thickness

Generally, there are few in situ measurements of thin sea ice: one can not walk on it, and campaigns observing sea ice thickness tend to focus on thicker ice. At the beginning of the project, the sea ice concentration difference between two maps taken with one week of distance in time were used to detect region of recently grown ice which therefore should be thin. In late summer, sea ice in the Arctic starts growing quickly, as shown in Figure 4a, which is the ASI ice concentration difference between 13. 10. 2010 (the date of our SMOS data used here) and 06. 10. 2010 (one week before). The red parts are the new grown ice. We presume that sea ice is getting thicker from the new ice edge towards the Central Arctic. Since it shows large area of new ice north Alaska in Figure 4a, in total six transects are chosen in this area, with a width of 1° each, along the meridians 145°W, 150°W, 155°W, 160°W, 165°W and 170°W, respectively. The corresponding profiles of SMOS brightness temperatures (incidence angle: $40° - 50°$) are shown in Figure 5. The first four transects in the subfigures (a)-(b) give at the beginning high values (land), then decrease to constant low values (open water), then again increase sharply (thin ice), finally reach constant high values (thick ice). Subfigures (e) and (f) show similar findings, but without land. This proves the dependence of brightness temperatures on thin ice thickness, and what we are interested in is the physical process causing the sharp increase of brightness temperature when ice forms (thin ice).

3.2 First L-band characterization of open water, thin ice and thick ice

Since we initially only had SMOS data of one day available, we could not investigate how the SMOS Tb changes in time with ice thickness quantitatively. However, we could find out the Tb characteristics of the different surface types, thick ice (larger than 2-3 m), thin ice (<20 cm) and open water. As a criterion for thin ice we take the condition to be grown during the last week, determined from two ice concentration map as described above (see Figure 4a, and chose one region ($75° - 76°$N, $152° - 154°$W) in the red area which is the new formed ice with small thickness. Choosing thick ice and open water region is relatively easy, we define regions fully ice covered ($80° - 82°$N, $120° - 130°$W) and fully ice free ($75° - 76°$N, $152° - 154°$W) through the whole year to be investigated. Figure 6 shows a brightness temperature (Tbh) map pf the Arctic with the three regions marked.

Then the SMOS brightness temperatures are extracted over these regions, the result is shown in the scatter plot of (Tbv, Q), with $Q = Tbv - Tbh$ the polarization difference, see Figure 7. Here we see that the three surface types are clearly distinguished. In addition, for the same incidence angle, thick ice region has the highest Tbv, open water lowest, and thin ice in between. The incidence angle also plays a important role, see the different triangles which connect the three tie points. Our idea is to retrieve ice thickness from each of the triangles. Although the clear separation of the three surface types makes us

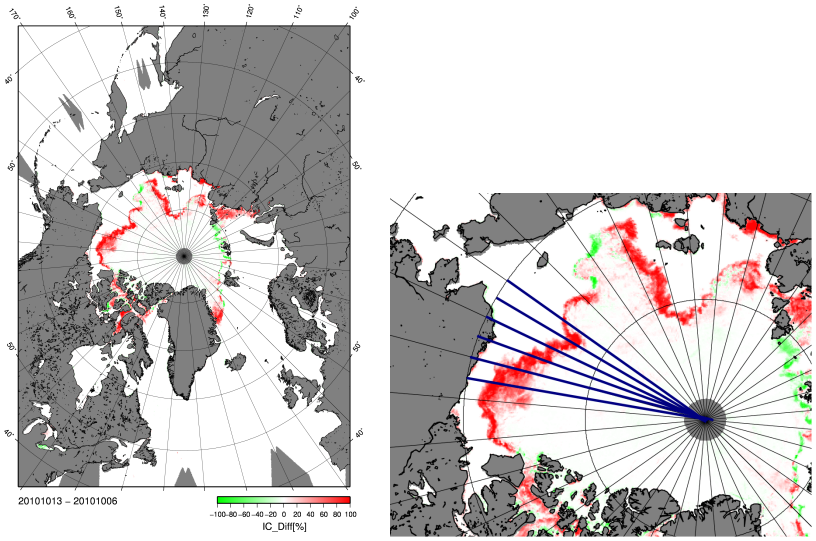

(a) (b)

Figure 4: (a) ASI ice concentration difference between 13. 10. 2010 and 06. 10. 2010. Red means higher ice concentration at 13. 10. 2010 and green means less. (b) six transects for Figure 5.

optimistic to separate them based on the observations, we still lack accurate ice thickness information. Figure 6 only shows the three different types, but what is the ice thickness in the thin ice region? How does the brightness temperature change when ice forms and grows? Answering these questions requires brightness temperature observations with attached sea ice thickness values. This will be done in the next section.

3.3 Cumulative freezing degree days ice thickness

According to a suggestion of Kaleschke [5] we use the close relation between sea ice thickness and Cumulative Freezing Degree Days (CFDD) [6],

$$\theta = \int_0^t (T_f - T_a)\,\mathrm{d}t \tag{3.1}$$

to estimate thickness values

$$d = 1.33\theta^{0.58} \tag{3.2}$$

for thin sea ice, see Figure 8. From equations (3.1) and (3.2), the ice thickness can be defined.

θ: CFDD; T_f: sea water freezing temperature; T_a: air temperature; d: ice thickness in cm.

For the calculation of CFDD, the NCEP reanalysis air temperatures at surface level are used. This data set represents the daily average with a resolution of 2.5°.

Also the selection of the proper starting point in the integral is important. Initially we looked into the time series of air temperature for each of the four NCEP grid points, and chose as starting point the date after which the air temperature is always below the sea water freezing point. However, this turned out to be not very reasonable since sea ice does not start forming immediately when air temperature drops below the freezing point, but first needs to be cooled to the freezing temperature. The results obtained from different points in the Arctic (next section) are more consistent if we start the integral (3.1) at the time when the ASI sea ice concentration algorithm indicates sea ice for the first time in this season.

3.4 First version of algorithm

The following work is based on the four NCEP grid cells located at (80°N, 147.5°E), (80°N, 85°E), (75°N, 67.5°E), (72.5°N, 190°E), see Figure 9. These four grid cells have been chosen by Kaleschke et

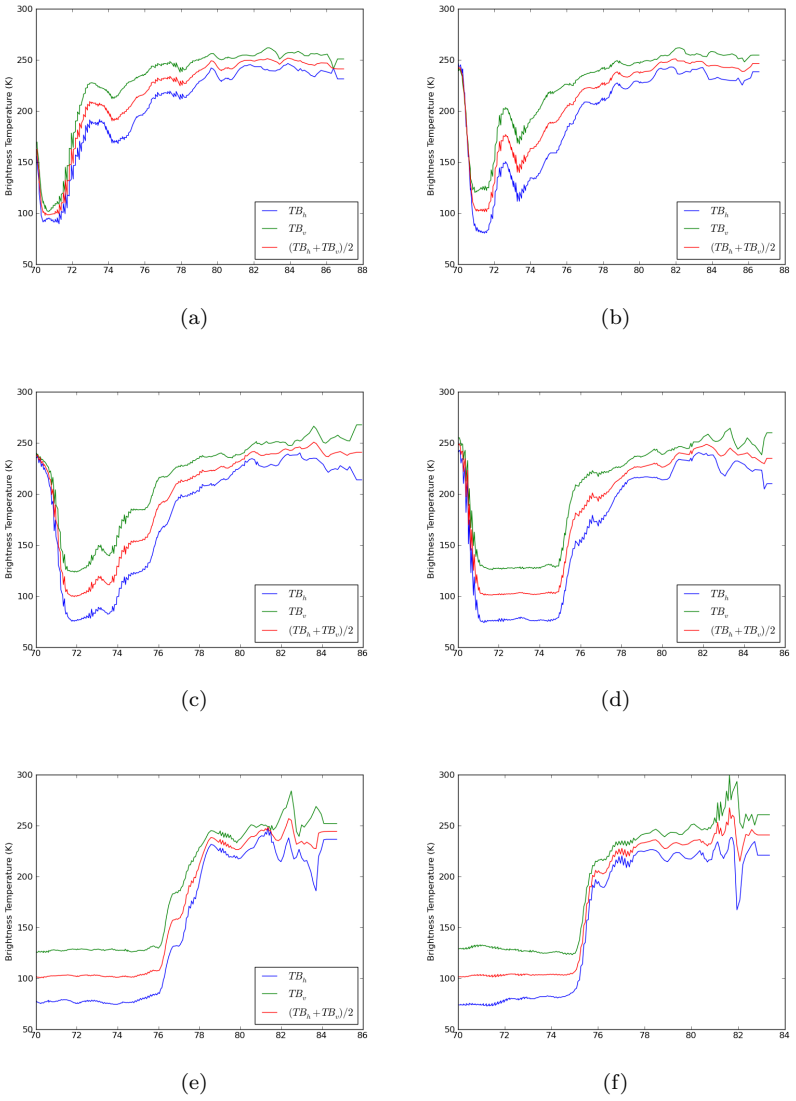

Figure 5: SMOS brightness temperatures from 70°N to 90°N, along a 1° wide transect with the middle of (a)145°W, (b)150°W, (c)155°W, (d)160°W, (e)165°W, (f)170°W.

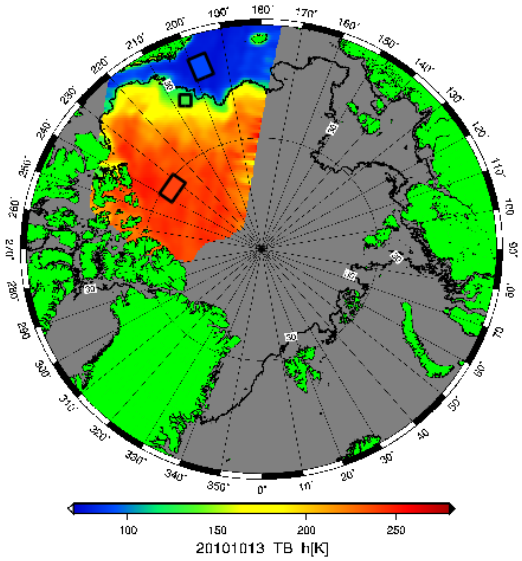

Figure 6: The test region of thick ice, thin ice and open water on the one swath data of Tbh on 13. 10. 2010, shown as squares.

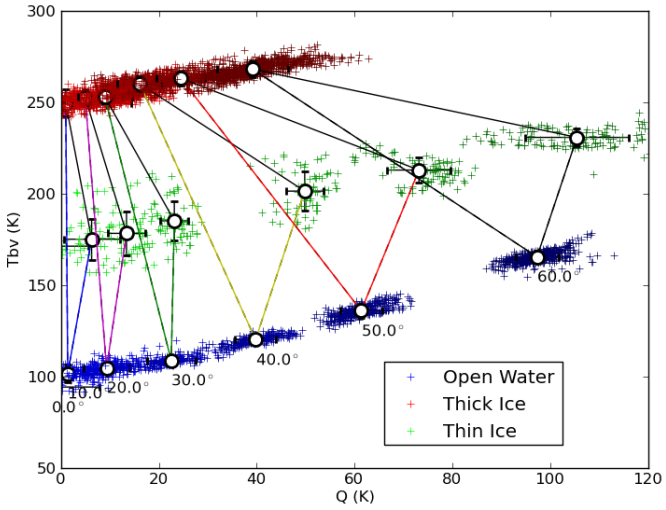

Figure 7: Vertically polarized brightness temperature Tbv vs. polarization difference Q based on the three test regions in Figure 6. The numbers below the open water points denote the incidence angles. The range 10° means the data within 9.5° and 10.5° and similarly for other incidence angles. The white-faced circles are the average values, with standard deviations indicated by error bars. The triangles connect average values of the same incidence angle range.

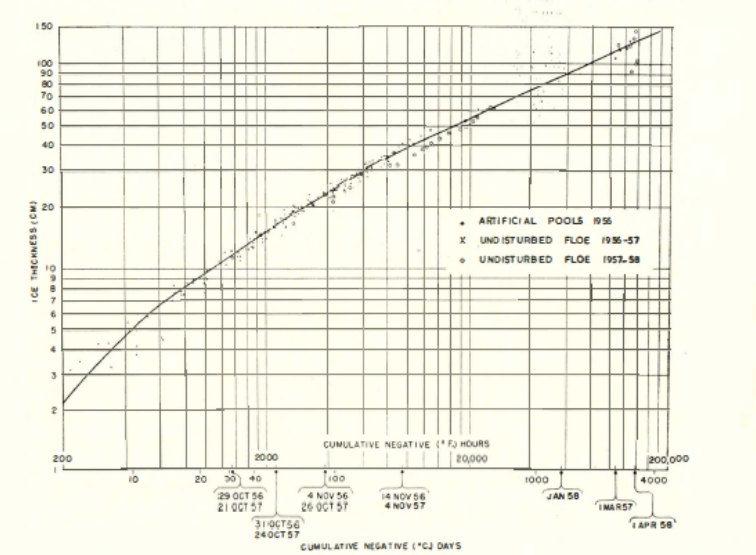

Figure 8: Sea ice thickness as function of CFDDs, data taken in Thule, Greenland. Figure from [6].

al., and we use the same grid cells in order to compare with his results. In addition, we got the SMOS data observed over these four cells for the months October to December 2010.

Figure 10 shows the time series of NCEP air temperatures, CFDD, ASI ice concentration, SMOS V-pol brightness temperatures and SMOS polarisation difference in each of the four NCEP grid cells for the period of October - December 2010. The last two SMOS quantities are given for each 10° incidence angle interval. We see that SMOS Tbv increases and Q decreases when ice forms, as indicated by the ASI ice concentrations and CFDD. Using Equation (3.2), we expect to find a relation between ice thickness and SMOS brightness temperatures, at different incidence angles. We first focus on the incidence angle range 40°-50°, and combine the data for all the four NCEP grids into one scatterplot of Tbv vs. CFDD ice thickness (Figure 11a) and one of Q vs. CFDD ice thickness (Figure 11b). We clearly see that Tbv increases and Q decreases with CFDD ice thickness up to 30-40 cm, afterwards they remain rather constant with some overlaid noise. To describe the variations quantitatively, two functions in the forms

$$y = \frac{b-a}{1+\exp(-x/c)} + a \tag{3.3}$$

$$y = (b-a)\cdot \exp\left(-(x/c)^d\right) + a \tag{3.4}$$

are suggested, and the unknown parameters are determined using the least root mean squares method. The forms of the two equations have been selcted ad hoc so that Equation (3.3) for fitting the Tbv observations starts linearly at $x = 0$ and tends exponentially towards $-b$ if x approaches infinity, while Equation (3.4) for fitting the Q observations starts at $x = 0$ with slope 0 and decreases exponentially towards a if x goes to infinity.

The results of the fitting procedure are for Tbv: a = 19.36, b = 249.28, c = 9.14, and for Q: a = 13.26, b = 54.51, c = 30.56, d = 2.61, the corresponding curves are indicated as black lines in Figures 11a and 11b.

Equations (3.3) and (3.4) are empirical forward models to predict Tbv and Q from the sea ice thickness. The statistical rms errors are 7.8K for Tbv and 6.4K for Q, containing contributions from various error sources:

- error of CFDD model relation between CFDD and ice thickness
- error of NCEP near surface air temperatures
- setting the brightness temperature value of the NCEP grid cells to be that of the nearest SMOS grid cell

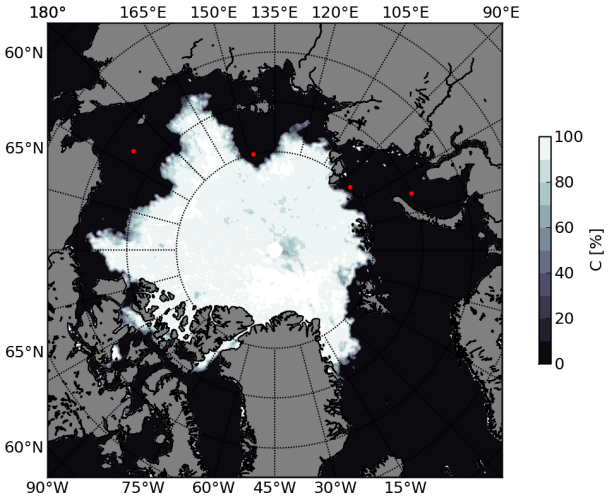

Figure 9: The location of the four NCEP grid points on which we have the SMOS data for October, November and December 2010 (Kaleschke, 2010)

.

- daily averaging of the SMOS brightness temperatures over the DGG (15km)
- errors in the SMOS L1C brightness temperatures in the instrument reference frame
- error introduced by the convention of the SMOS brightness temperatures from the SMOS instrument reference frame to the earth reference frame which requires combination of observations taken at different time (section 1.2)
- error by averaging over incidence angle bins of 10°

The next step is to derive the ice thickness for any given SMOS grid cell using the relations (3.3) and (3.4). As we have fitting functions for Tbv and Q seperately, we may use them separately to detect the ice thickness from Tbv or Q individually by simply inverting the Equations (3.3) and (3.4). However, the results are expected to be noisy, and for cases where the brightness temperature is outside the values covered by the fit function, an inversion is not possible.

Therefore, we propose a more stable way to detect ice thickness from the combination of Tbv and Q. First, a lookup table of Tbv and Q values at every 1 cm ice thickness is built using the equations (3.3) and (3.4). Second, for any given SMOS Tbv and Q measurements, its thickness is determined to be that of the closest point of the function resulting from combining the fit functions (3.3) and (3.4) in the (Tbv, Q) plane. Figure 12 illustrates the procedure for the incidence angle range 40°-50°. Technically, the procedure is realized by selecting the nearest sea ice thickness in the sense of Euklidian distance in the (Tbv, Q) plane in a table containing Tbv and Q values in steps of 1 cm thickness, see the black dots in the retrieved curve in Figure 12. The sensitivity of the retrieval curve decreases with increasing thickness. Between 0 cm (when ice forms) and 40 cm ice, the microwave signals change a lot in Tbv (about 100 K) and in Q (about 37 K). However, between 40 cm and 90 cm ice, the change is only 5 K in Tbv and 6 K in Q, which indicates that ice thickness larger than 40 cm cannot be retrieved.

3.5 Retrieval for 40°-50° incidence angles

The first result of retrieved ice thickness from SMOS is shown in Figure 13, for the same time period as before, based on the incidence angle range 40°-50°, the other ranges will be shown later. The figure contains three types of retrieval: from Tbv only (red), from Q only (blue) and from both Tbv and Q together (black). In general, these results are similar. The red and black lines agree very well at small ice thickness (0-30 cm). However, the Q based retrieval (blue) shows more noise at low thicknesses because

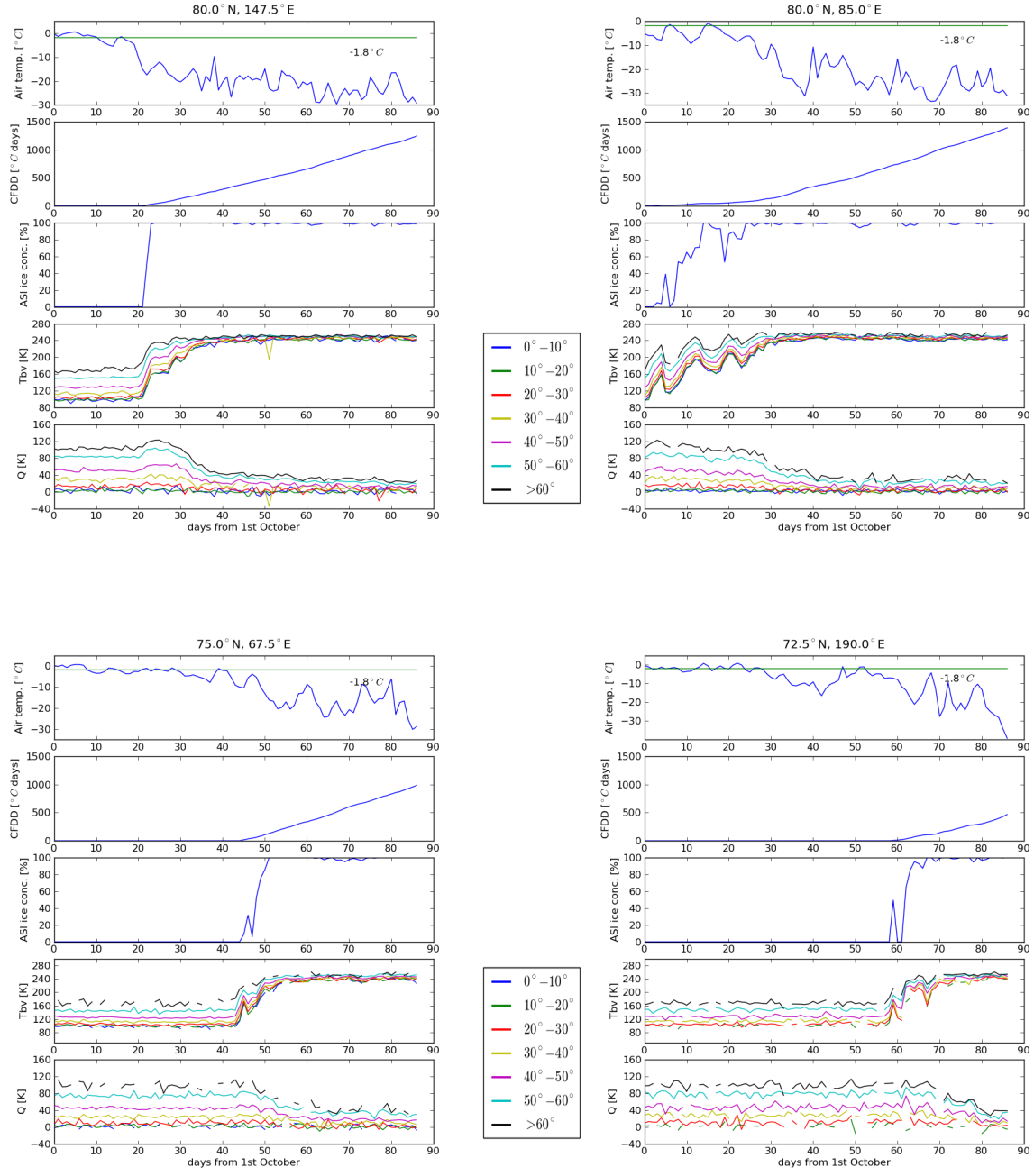

Figure 10: Time series of different parameters in the four SMOS DGGs for the months October to December 2010. For each of the subplots, from top to bottom: air temperature from NCEP (the green line is the sea water freezing temperature $-1.8°C$), cumulative freezing degree days, ASI ice concentration, V-pol brightness temperature Tbv and polarization difference Q. The colorbar shows the 10° average values of incidence angles for SMOS Tbv and Q.

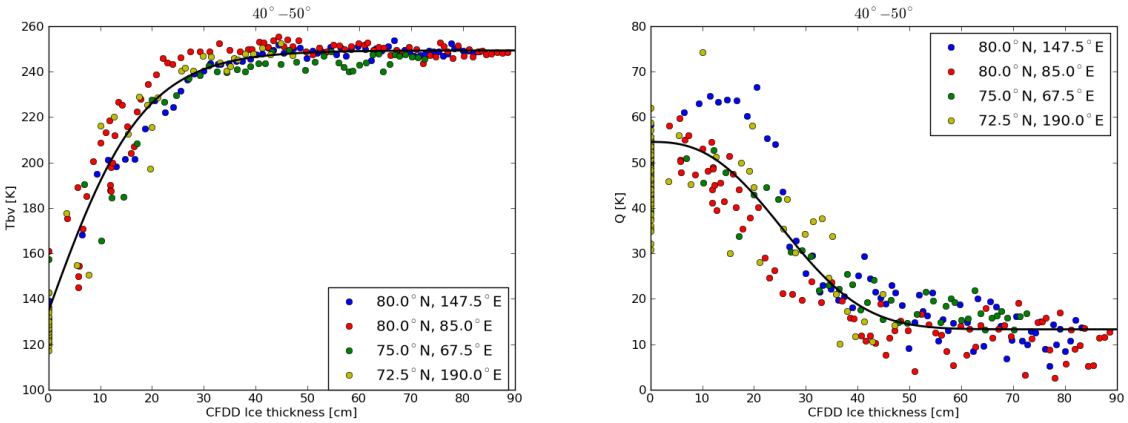

(a) (b)

Figure 11: Scatterplot of CFDD ice thickness and (a) SMOS Tbv (b) SMOS Q, in incidence angle range 40°-50°. Dots of different color represent different NCEP grid cells, and the black lines are the fitted line in the format of equation (3.3) and (3.4).

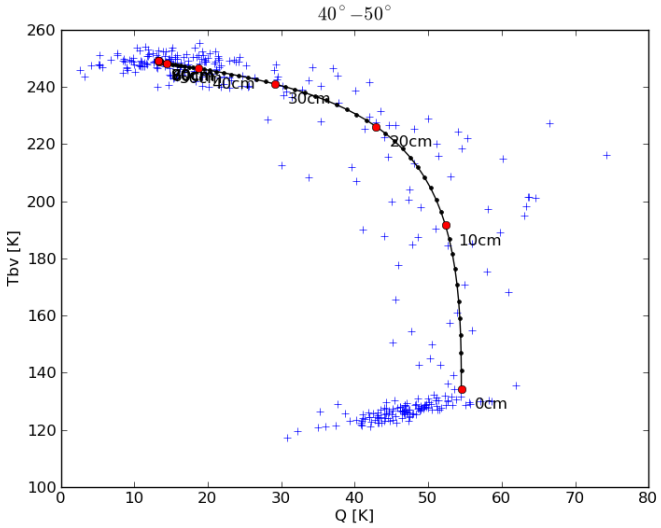

Figure 12: Retrieval curve of ice thickness from SMOS Tbv and Q for incidence angle of 40°-50°. The blue crosses are the SMOS measurements over those four NCEP grids cell for October to December 2010. Each black dot represents each 1 cm ice thickness, and red dots every 10 cm.

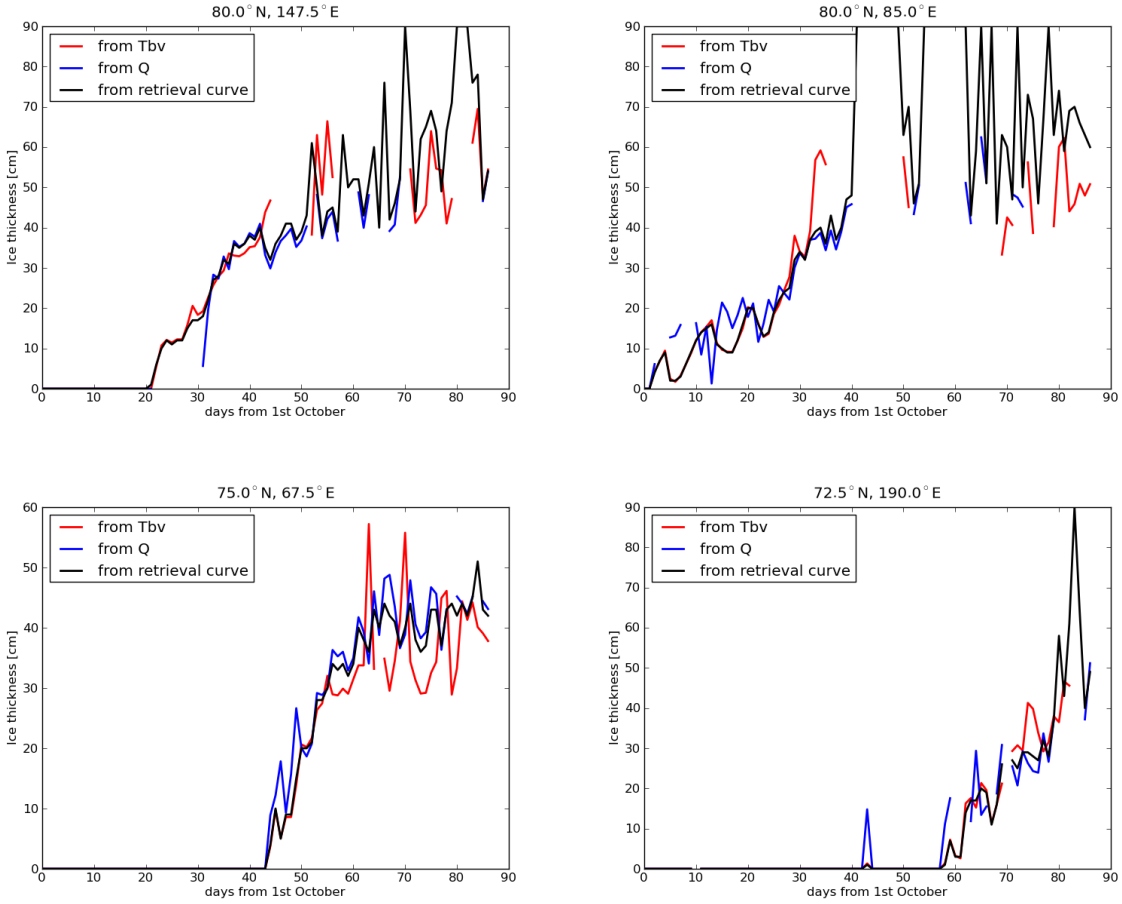

Figure 13: Retrieved daily ice thickness from SMOS measurements in the 40°-50° incidence angle range for the time period of October to December 2011. The red and blue lines are the results from Tbv and Q individually, black are from both Tbv and Q using the lookup table.

the signal on thin ice is relatively independent of Q which can be seen in Figure 12. All three results are more noisy at higher ice thickness because the sensitivity of both brightness temperature decreases with thickness (Figure 12). Considering that the retrieval from Tbv and Q seperately is discontinuous since the inverse function is unsolvable at many cases, we suggest to use both parameters in combination for the retrieval.

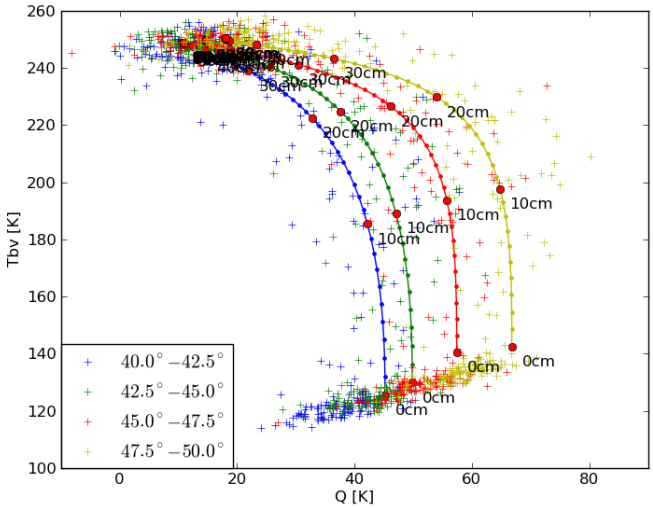

Figure 14: Retrieval curve of ice thickness from SMOS Tbv and Q, averaged for 2.5° incidence angles. The crosses are SMOS measurements averaged for every 2.5° in incidence angle of 40°-50°. Small dots along the curves represent every 1 cm ice thickness, and big red dots represent every 10 cm.

3.6 Incidence angle dependence

3.6.1 Retrieval for smaller incidence angle bins

Until now, we have only considered brightness temperatures averaged over the incidence angle range of 40°-50°. In order to characterize the error introduced by this approach, we calculate the 2.5° averaged SMOS brightness temperatures for the intervals 40°-42.5°, 42.5°-45°, 45°-47.5°, 47.5°-50° seperately, see the retrieval curves in Figure 14 which are similar to Figure 12, and the corresponding retrieved results in Figure 15. We see that although the fit functions in Figure 14 differ up to 10 K, the differences among the retrieved ice thickness are quite small, especially for thinner ice than 40 cm. In addition, the results from the 10° averages of incidence angles are less noisy than those from the 2.5° averages because less observations enter the average. Moreover, the rms errors of the retrieval using 10° and 2.5° intervals are calculated for every 10 cm ice thickness, see Table 2. The rms errors are smallest (1 cm) for 0-10 cm ice and can reach 30 cm for ice thicker than 40 cm. The retrieval from higher incidence angles give in general lower rms errors. If retrieving only the sea ice thickness, we do not see the advantage of using 2.5° interval since the rms errors do not show big difference from that using 10° intervals. However, the subject will have to be re-examined in the context of the two-paramter retrieval (Section 5).

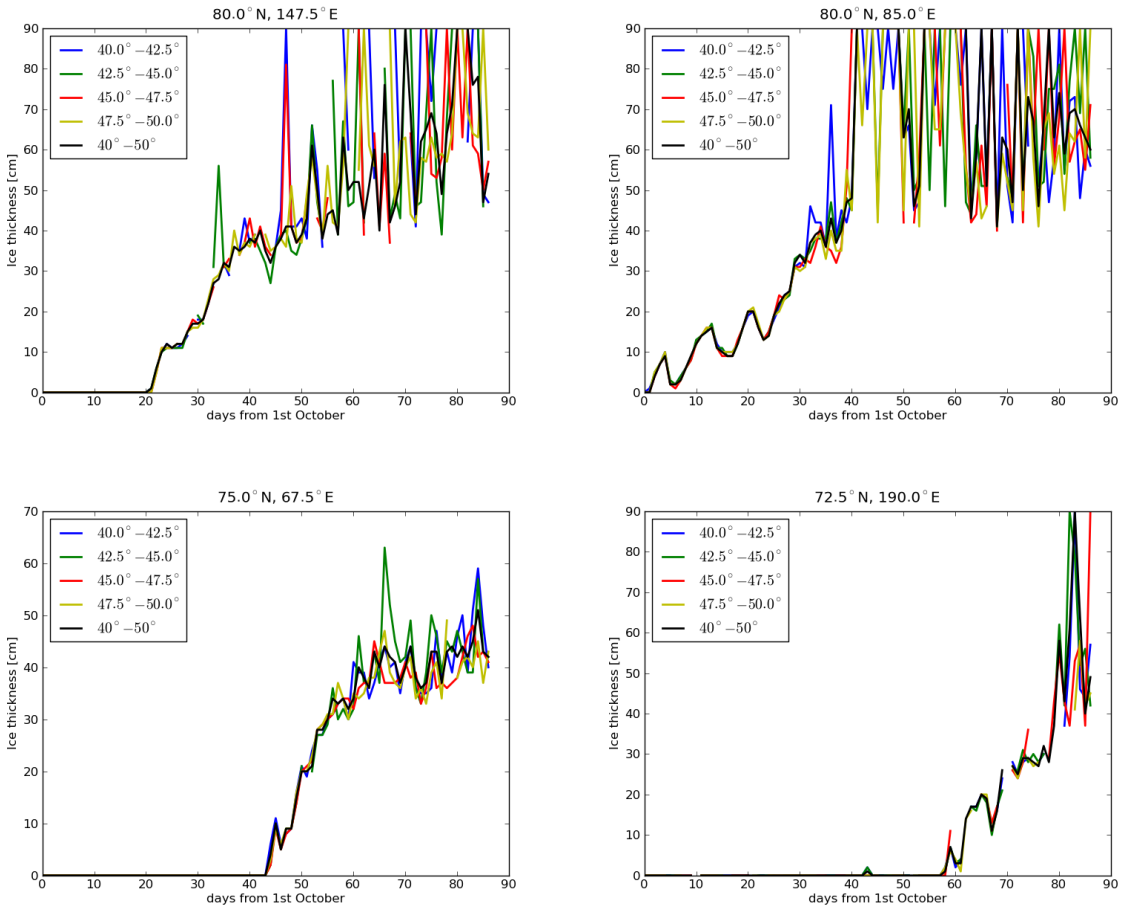

Figure 15: Retrieved ice thickness time series from SMOS measurements Tbv and Q averaged for 2.5° incidence angles. Each subplot is for each of the four NCEP grids cells. The colored lines are from the 2.5° averages while the black lines are from 10° averages.

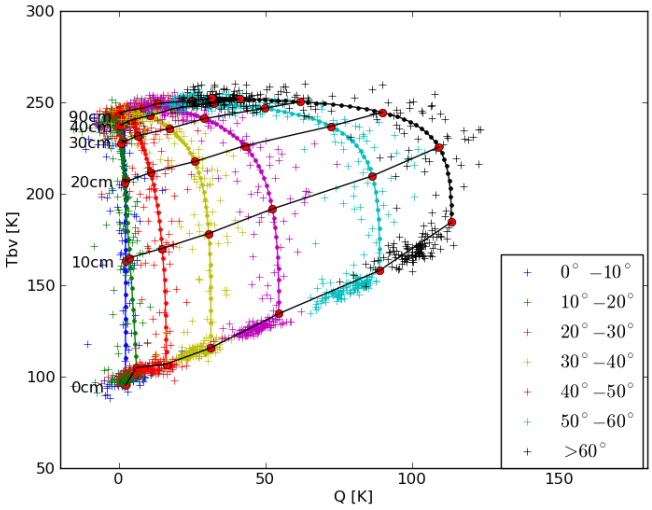

Figure 16: Retrieval curves of ice thickness from SMOS Tbv and Q, for every 10° incidence angles (shown by different colors). The crosses are the SMOS measurements over those four NCEP grids cells for October to December 2010. Each small dot represents each 1 cm ice thickness, and big red dots are every 10 cm ice. These dots are calculated from the fitting functions between SMOS Tbv (Q) and CFDD ice thickness.

3.6.2 Retrieval at other incidence angles

We have investigated the retrieval using SMOS data of 40°-50°, now the retrieval using other incidence angles is investigated, see Figure 16 for the resulting empirical forwards models and Figure 17 for the retrieval results. The retrievals from different incidence angles show quite good agreement up to 40 cm. Again, the ice thickness map on 13. 10. 2010 is calculated using the retrieval (Figure 18) at 40° to 50° incidence angle.

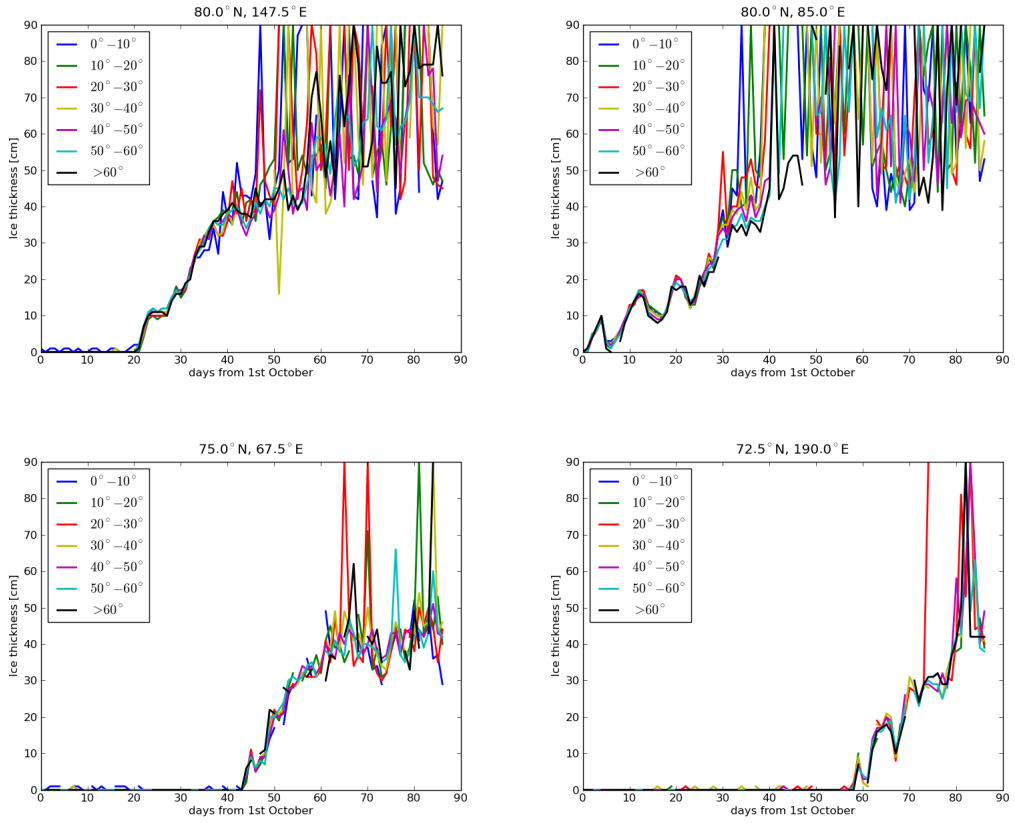

Figure 17: Retrieved ice thickness from SMOS measurements Tbv and Q averaged for every 10° incidence angles, for the time period October to December 2010.

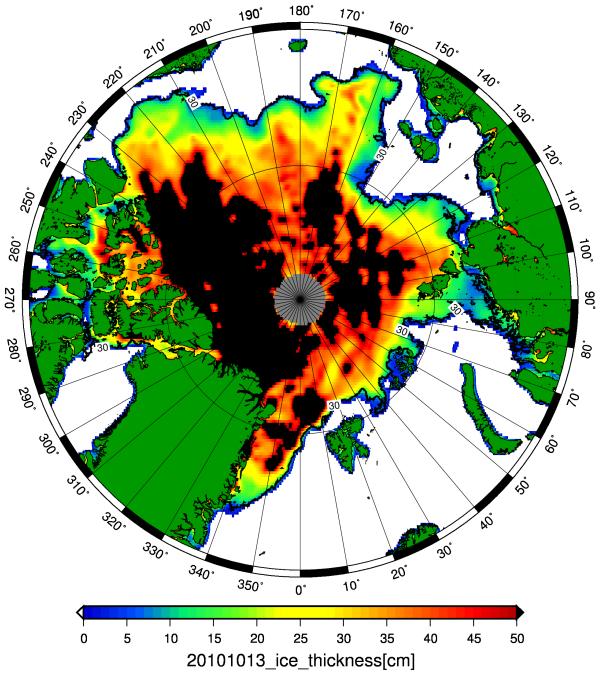

Figure 18: Retrieved ice thickness for Arctic on 13.Oct.2010, based on retrieval curve in Figure 12 for the SMOS Tbv and Q values with incidence angles between 40° and 50°. Open water and ice thicker than 50cm are shown in white and black, respectively. The contour line is 30% ASI ice concentration.

Table 2: Rms errors in cm of retrievals at different incidence angle (vertically) and ice thickness (horizontally)

	0-10 cm	10-20 cm	20-30 cm	30-40 cm	40-50 cm	50-60 cm	60-70 cm	70-80 cm	80-90 cm
0°-10°	1.26	3.81	9.59	20.41	34.02	25.7	22.78	23.83	23.26
10°-20°	1.12	4.23	8.88	18.28	27.03	19.19	20.95	20.67	24.24
20°-30°	1.24	4.04	10.01	14.19	29.6	21.69	22.79	20.68	27.29
30°-40°	1.27	3.91	6.69	15.42	28.48	22.36	18.39	17.93	19.86
40°-50°	1.08	3.68	6.46	7.76	26.16	19.73	20.8	17.57	18.65
50°-60°	1.05	3.46	5.04	10.66	25.42	17.75	19.26	16.8	13.68
60°-70°	1.37	3.43	4.47	18.3	25.62	17.04	18.35	19.03	19.99
40.0°-42.5°	1.31	3.77	7.54	13.42	29.19	21.95	20.39	20.42	24.64
42.5°-45.0°	1.02	3.63	7.77	12.74	27.41	21.42	22.22	20.47	20.44
45.0°-47.5°	1.14	3.46	6.04	12.33	28.19	21.14	22.84	19.48	17.65
47.5°-50.0°	1.07	3.55	5.89	7.63	26.29	22.69	20.85	18.56	15.19

3.7 Retrieval from other SMOS channel combinations

In order to optimize the retrieval, we have also investigated other combinations of SMOS measurements: intensity and Q, Tbh and Q, Tbh and Tbv, see Figure 19. Obviously, any of these combinations is suitable to retrieve ice thickness. However, considering that polarisation Q can cancel a constant calibration error by taking the difference of H-pol and V-pol brightness temperatures, also that intensity decreases the error by taking the mean value of these two terms, it is supposed that the combination of intensity and Q could give more accurate ice thickness. The corresponding results are calculated and shown in Figure 20.

In order to assess the quality of the different retrievals quantitatively, we have compared the rms errors (Figures 21 and 22) of each of the four retrievals at different ice thickness and incidence angles. As the retrieval is not reliable for thick ice, it can be seen from Figure 21 that the rms error for all the four retrievals increases with ice thickness up to 40 cm (less than 10 cm for ice of 0-10 cm, larger than 30 cm for ice of 40-50 cm). The decrease of the rms error beyond 40 cm thickness in the channel combinations (I, Q), (Tbh, Q), and (Tbv, Q) is probably due to the small number of samples and not considered to be generally valid. There is not a clear trend about how the retrieval error changes with incidence angle, so that at this stage we can not say which level of incidence angles is the best for the retrieval. But what we can see is that the results from SMOS intensity and Q are stablest in both of the two figures. Until here, we can propose that using I and Q can give better result than the other retrievals, and the error is smaller at smaller ice thickness.

3.8 Conclusion

Based on the retrieval quality assessments in Figures 21 and 22, we suggest for the retrieval of sea ice thickness the procedure described in Section 3.4, using the two parameters intensity and polarisation difference of the incidence angle interval $40° - 50°$. The flexibility and stability of the retrieval procedure is demonstrated by applying it to the whole Arctic, see Figure 18. However, we can not assess the quality of the retrieval since we do not have in-situ ice thickness data for validation yet.

Therefore, it is suggested to repeat the determination of the retrieval parameters (Section 3.3) with SMOS observations of regions where more reliable validation values are available, e.g. from EM-bird observations or from sea ice thermodynamic or thermodynamic/dynamic models. It will be best to have several independent informations about the sea ice thickness in order to assess their reliability.

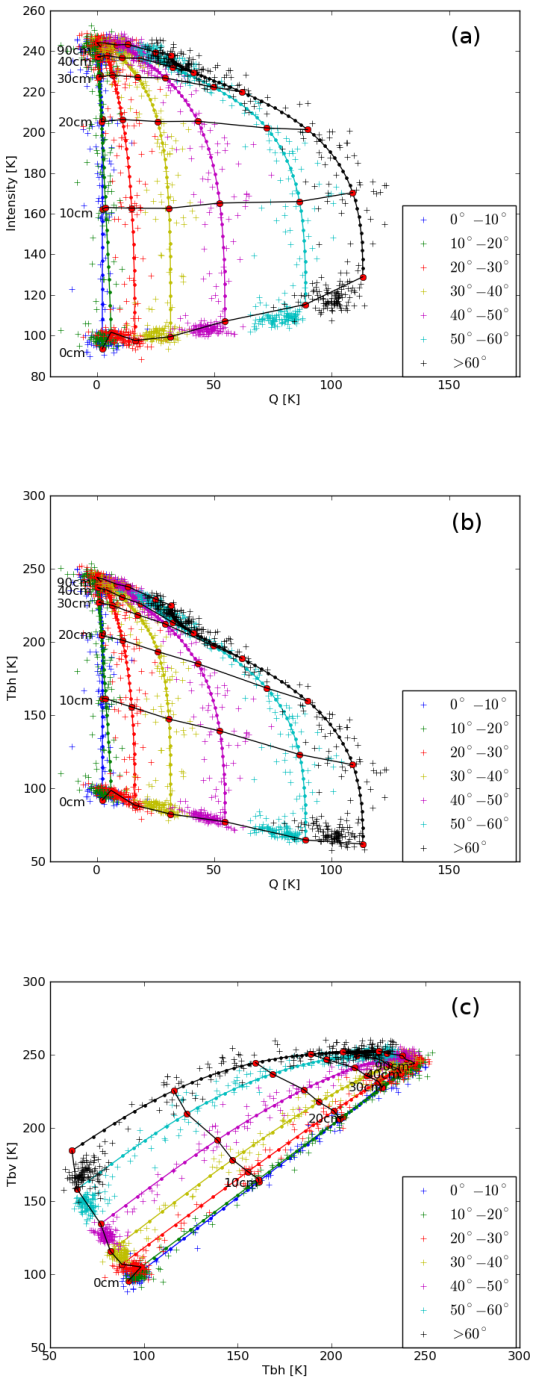

Figure 19: SMOS data on 13. 10. 2010 in the frames of (a) Intensity and Q, (b) Tbh and Q, (c) Tbv and Tbh. Colors represent incidence angle intervals of 10°. Each dot represent each 1cm ice, and red dots are every 10cm ice.

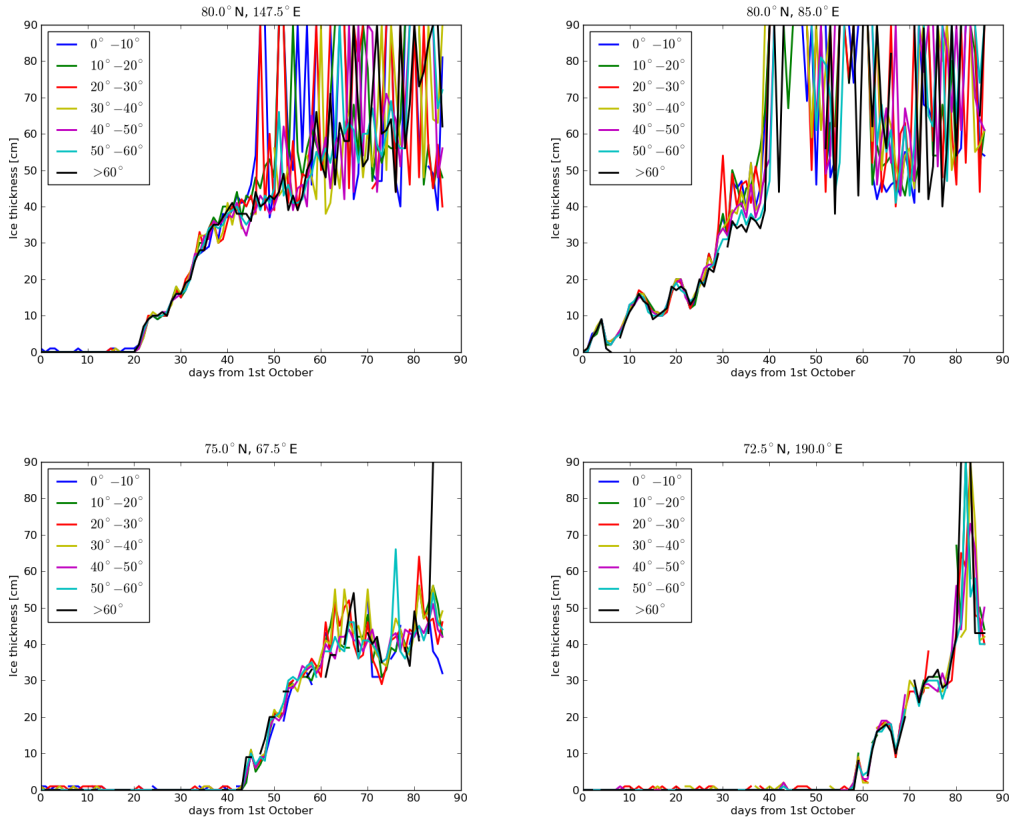

Figure 20: Retrieved ice thickness from SMOS intensity and Q, for every 10° incidence angles, on the four DGGs for the time period October to December 2010.

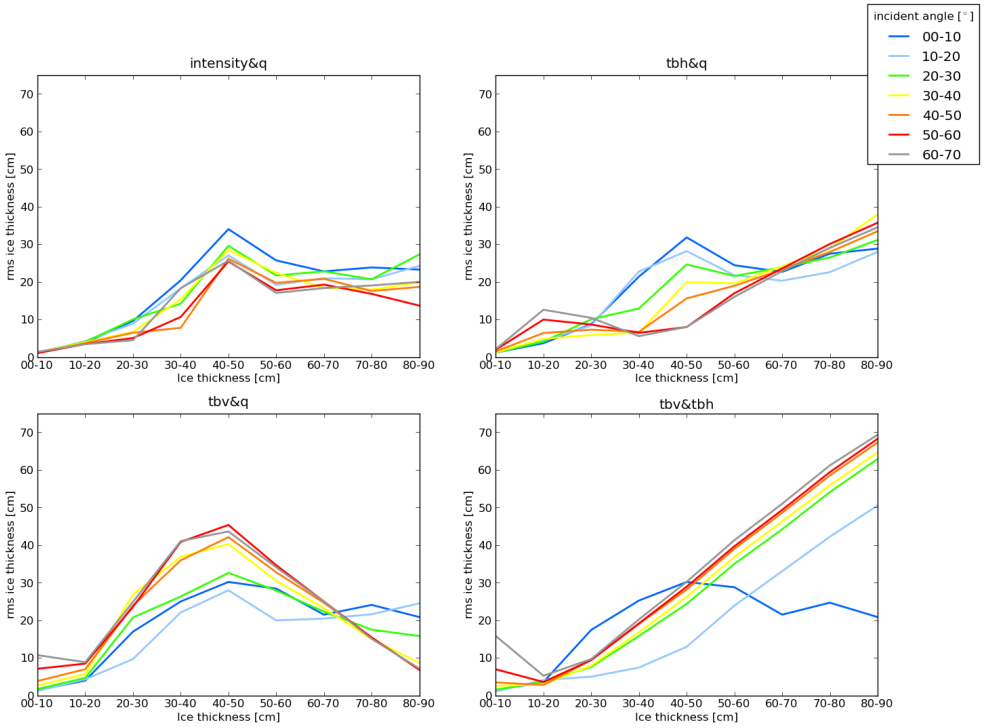

Figure 21: Rms error of the retrievals in cm as a function of retrieved ice thickness. Each subplot is retrieval using different SMOS measurements. Different colors show results of every 10° incidence angles.

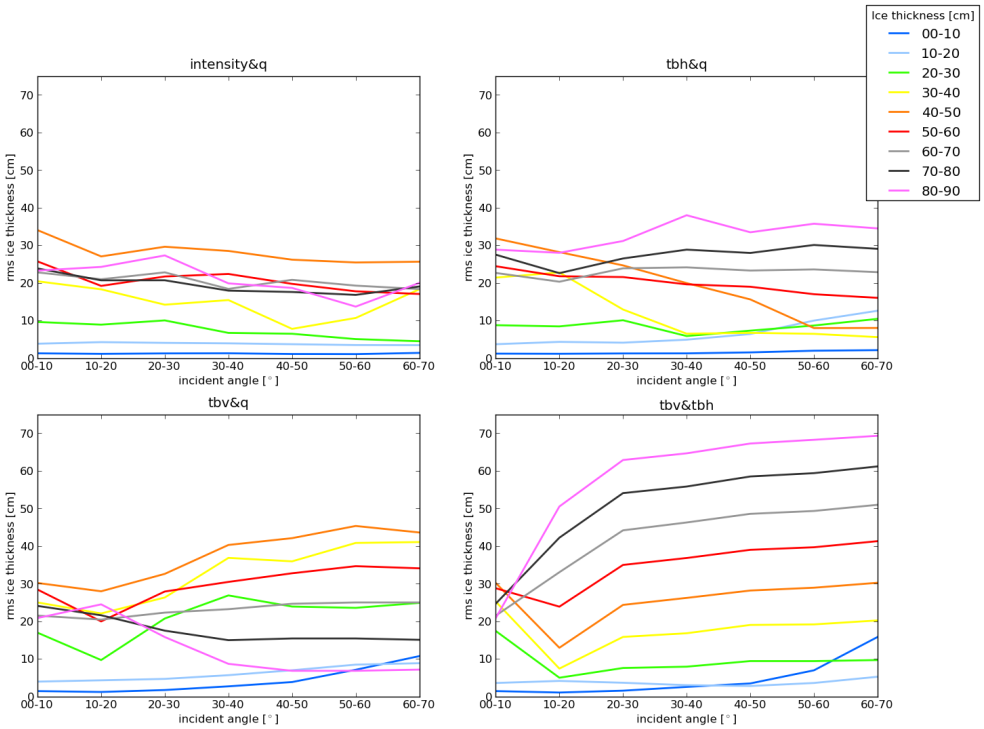

Figure 22: Rms error of the retrievals as a function of incidence angles. Each subplot is retrieval using different SMOS measurements. Different colors show different ice thickness.

4 Deriving the sea ice thickness algorithm

4.1 Test area selection and available sea ice thickness data

As a region and period with more information about sea ice thickness available,the Kara Sea in the months October to December 2010 was selected. Here, 10 points (Figure 23 and Table 3) located far enough from the coast lines were selected according to a suggestion by Mäkynen. For each of them, sea ice thickness from the following sources are used:

HIGHTSI model data: This thermodynamic sea ice model is based on [7]. For details see description in Deliverable 6b 'SMOSIce-Dat user manual for the validatation data' of this ESA project [8].

TOPAZ: Sea ice model developed at the Nansen Environmental and Remote Sensing Center, Bergen, Norway, and exploited operationally at met.no [9]. d

CFDD from NCEP and ECMWF: For all of the 10 points, temperatures from the lowest air level (ECMWF) respecively of the surface (NCEP) were extracted from the NCEP and ECMWF numerical weather prediction models, and the CFDDs calculated (Section 3.3) using the regression of [6].

MODIS derived thickness: Estimated from the surface temperature, which in turn is estimated from IR channels of MODIS according the the method of [10]. The method works under cloud-free conditions only, a condition which strongly reduces the number of retrievable pixels. For details see [8].

MODIS and ENVISAT WSM SAR derived thickness: In order to extend the aerial coverage of the MODIS derived thicknesses, radiances of the required MODIS channels are estimated from a combination of MODIS and ENVISAR SAR images in regions where the SAR image has similar characteristics as in neighbouring cloud-free regions. See [8] for details.

Table 3: Coordinates of the 10 areass selected to derive the algorithm.

Area	lat	lon
1	76.8N	42.5E
2	78.3N	47.4E
3	78.7N	57.4E
4	78.3N	66.6E
5	78.3N	74.8E
6	77.3N	81.7E
7	75.8N	79.5E
8	74.8N	69.2E
9	73.1N	61.7E
10	71.8N	60.7E

4.2 SMOS L1C input data and RFI filtering

For this study, the SMOS L1C data are used, organized in swath layout. For every swath the corresponding DGG points of the overflight is saved. Since the synthetic aperture takes snapshots instead of lines, one DGG point is observed at the same overflight from different zenith (incidence) and azimuth angles at different times. The L1C product contains a flag to indicate if a measurement is contaminated by RFI but this flag is not used in the example product version 346 we examined.

The criteria of the RFI filter is whenever a single brightness temperature in a snapshots exceeds 300 K, the whole snapshot is discarded from the ananalysis.This criterion may appear quite restrictive, but in the Arctic not that many RFIs occur. Due to the overlap of the swathes from different overflights, even after applying this filter the coverage is still quite good in the Arctic. The structure of the L1C

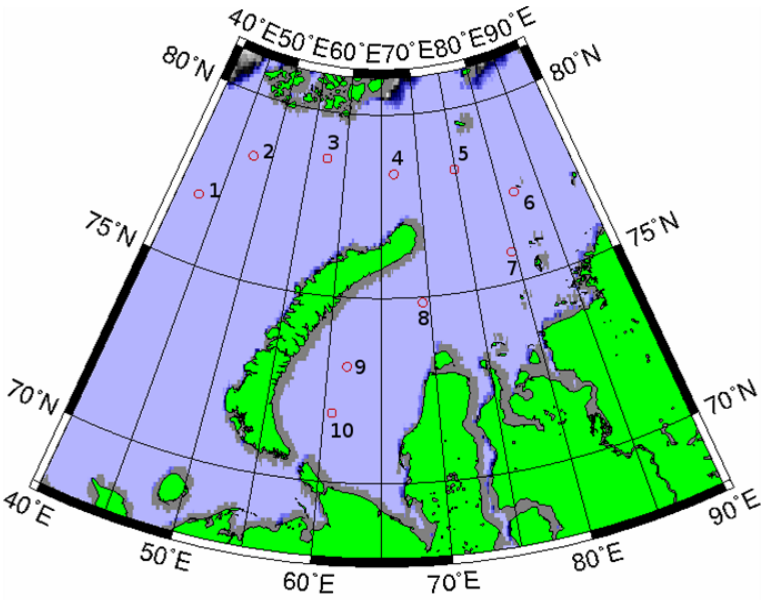

Figure 23: The 10 areas in the Kara Sea selected to derive the retrieval algorithm.

files requires searching for RFI also in neighbouring swaths, since the snapshots at the beginning and at the end of a swath file may extend over two consecutive files. Restricting the RFI filtering to single files would remove the RFI infected snapshots only incompletely.

Another source of potentially incomplete RFI filtering is the use of the 'ocean only' SMOS SLSF1C files which contain of the land only a stripe of few hundred km along the coastline, so that snapshots with RFI cases occurring in the inner land will not be excluded.

4.3 Analysis of time series at 10 points in Kara Sea

The results for all 10 areas are shown in Figure 24. The detailed analysis of the time series reveals that by far not all regions may be used for the training of the retrieval algorithm:

Area 1: Area is quite far out in the Barents sea, so that it comes to late freezing and sea ice is present only at the end of the time series. Therefore this area is not used for training the algorithm.

Area 2: Freezing starts on day 50. After day 70 there is a longer break in the sea ice concentration, likely because of sea ice drift not reflected in HIGHTSI. Therefore use of data later than day 70 is questionable. As only a few days would remain, the whole area is excluded.

Area 3: Early start of freezing on day 30. There is a short drop in sea ice concentration around day 45. This area has been selected.

Area 4: Freezing starts on day 50. A longer and deep drop in sea ice concentration after day 75 indicates a drift event and restricts the usability of this area for training the retrieval algorithm. Not selected.

Area 5: Early freezing on day 30, followed by a drop in sea ice concentration on day 38. After the reduction in sea ice concentration, the sea ice thickness in Area 5 cannot be taken as thermodynamically grown. Area not selected.

Area 6: Very early freeze up on day 20. Long time of high sea ice concentration with no indication reducition of sea ice cover due to drift. Later on day 70, there is an unexplained drop of TBh and TBv which we do not expect to occur at higher sea ice thicknesses. Days 70 and later excluded from training.

Area 7: Very early freeze up on day 20. Early short reduction of sea ice concentration. Since the sea ice is quite thin before the break in ice concentration the time after this event is included in retrieval training.

Area 8: Freeze up on day 40 with a longer reduction in sea ice concentration after day 70. Days 40 to 70 seem usable but appear to be constant in thickness after 20 cm thickness are reached although sea ice freezing conditions continue. Reason of stopped growth unknown, area excluded from training.

Area 9: Freeze up on day 50, not taken because of late freeze up and unstable Q at high sea ice concentration.

Area 10: Very late freeze up and unstable freezing condition make Area excluded from training.

The sea ice thickness time series from the three used data sources all increase monotonically in all 10 regions of Figure 24, and their spread varies between 10 cm (Area 7) and about 25 cm (Areas 2 and 4). Comparing the different sea ice thickness proxies shows that those based on CFDD/ECMWF (red) and TOPAZ (green) belong to the lowest values, the CFDD/NCEP based thicknesses (green) are the highest ones in Regions 2, 4 and 5, and the HIGHTSI thicknesses (blue) are highest in Regions 8 and 9. The HIGHTSI and CDFF/NCEP thicknesses are similar in Regions 2, 4 and 5. Among the sea ice thickness time series in Figure 24, those from TOPAZ show the most variable behaviour.

4.4 Retrieval

We select for the learning phase of the retrieval algorithm the not grey shaded parts of the time series of Areas 3, 6, and 7 where the thicknesses appear most reliable to us. Including the additional Areas 8 and 9 changes the result only slightly so that we stay for the retrieval with Areas 3, 6, and 7. As sea ice thickness values those from CFDD/NCEP were used in order to keep the retrieval independent of HIRLAM which also goes into the HIGHTSI thicknesses.

The resulting values for the parameters in the numerical fits equation 3.3 and 3.4 are: a=19.4, b=51.0, c=31.8, d=1.65, and a=−20.6, b=232.3, c=8.8, respectively. Figure 25 shows the corresponding retrieval curve. The retrieval procedure is described in the last paragraph of Section 3.4.

For learning, only the CFDD/NCEP thickness values are used so that the HIRLAM driven MODIS observations may serve in the next section as independent validation data. Since HIGHTSI is also driven by HIRLAM, HIGHTSI data is not used for training of the retrieval.

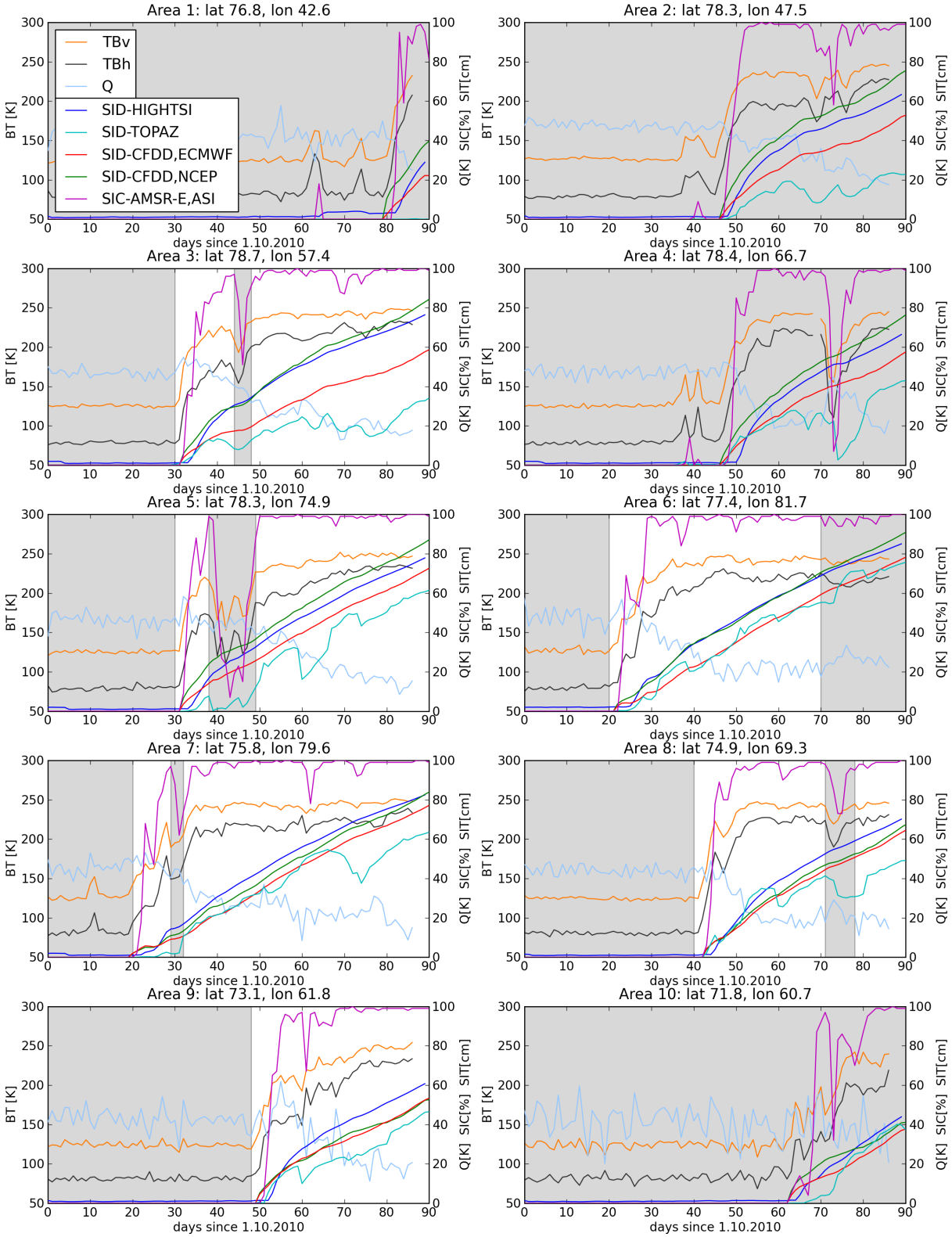

Figure 24: Time series of for the 10 areas in the Kara Sea selected to derive the retrieval algorithm. Grey shaded areas are excluded from the retrieval algorithm training.

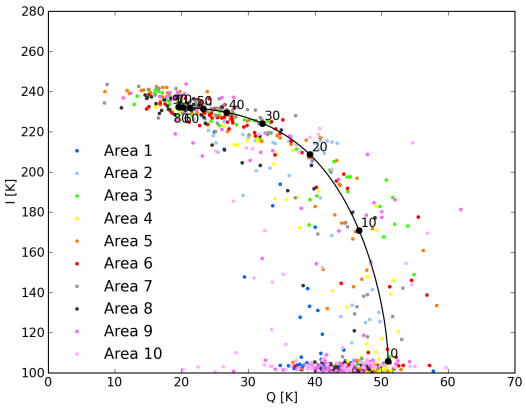

Figure 25: Retrieval curve resulting from 10 points in Kara Sea, used for validation study.

Table 4: RMS error for retrieval learning areas 3,6,7 and for all 10 areas.

NCEP-CFDD ith	RMS from areas 3,6,7 [cm]	RMS from all areas [cm]
00 - 10 cm	2.35	3.37
10 - 20 cm	5.72	7.33
20 - 30 cm	8.70	9.05
30 - 40 cm	9.70	13.75
40 - 50 cm	7.05	15.78

4.5 Error considerations

The errors of this retrieval procedures are obtained from the differences from the ice thickness from NCEP-CFDD and the retrieved ice thicknesses from this method from SMOS. In Table 4 the RMS of this method is shown for the 3 learning areas and for all areas. The lower RMS on 40-50 cm than on 20-30 cm and 30-50 cm can be explained by the small number of data points. Therefore the RMS from all areas seem more realistic and representative. However, since the NCEP data, where we obtained the CFDD from, is in 1.5 degree geographical grid. So the grid might be to coarse for algorithm training and error estimation.

4.6 Results and validation

4.6.1 Comparison to the MODIS thicknesses

The MODIS sea ice thickness product is available for many days during the winter 2010/2011 when SMOS was operational. Figure 26 shows as an example the result for Oct. 25, 2010. Cloudy areas are removed from the retrieval, so that the image appears patchy and only in a small fraction of pixels thickness retrievals are available.

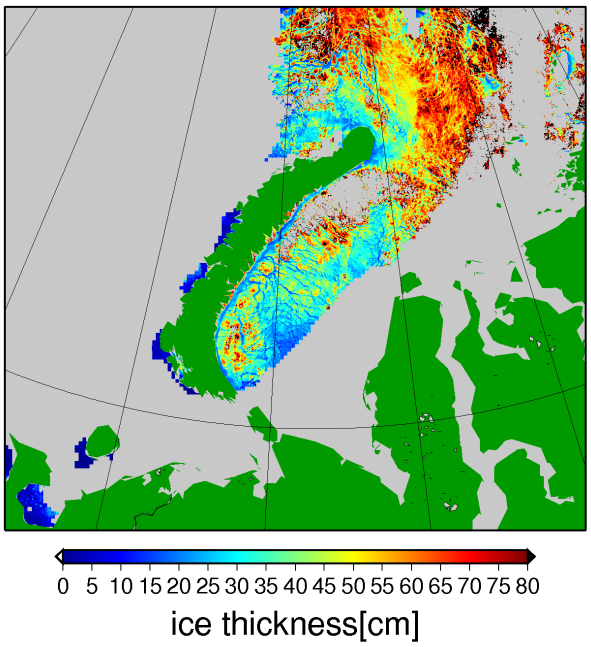

Figure 26: MODIS sea ice thickness as of Oct. 25, 2010 in original high resolution of 1km (data by Mäkynen).

A difficulty when comparing these with the retrievals from SMOS is the difference in horizontal resolution between both sensors, 1 km for MODIS and about 30 km for SMOS. Before the comparison,

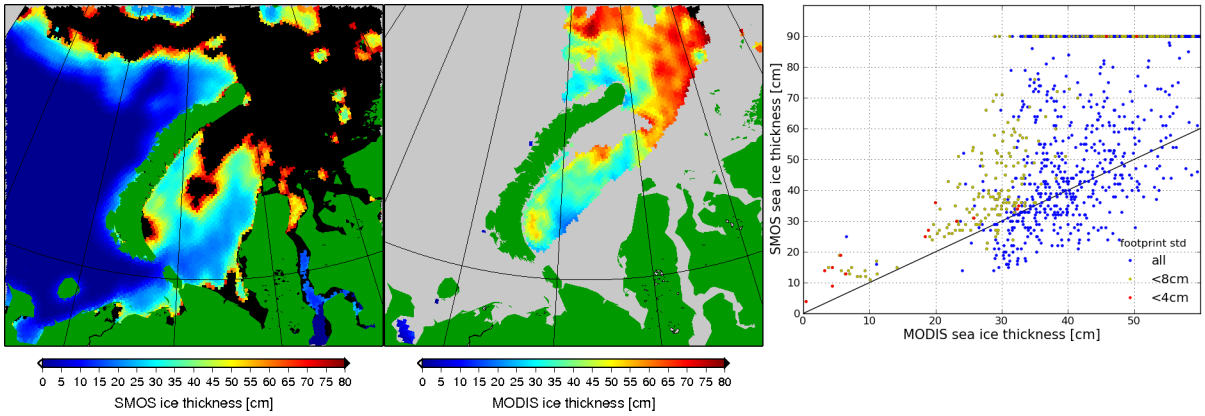

Figure 27: Left: Ice thickness retrieved from SMOS, center: ice thickness from MODIS averaged over SMOS footprint size of 40 km, right: scatter plot of SMOS vs. MODIS. Different Colors indicates the standard deviation of MODIS values over the footprint area of SMOS of about 40 km. Data of Oct. 25, 2010.

the MODIS based data are brought to the resolution of the SMOS retrieval by generating maps of the MODIS based retrieval at the desired SMOS resolution by calculating at the centers of each SMOS DGG averages of the MODIS thicknesses over a circle of 40 km diameter. This is a simple approach to simulate the footprint size of SMOS at the incident angle of 40° to 50° which is an ellipse of about $25 \times 40\,\mathrm{km}^2$. Note that the averaging diameter of 40 km is clearly larger than the size of the DGGs of about 15×15 km: The footprints of neighbouring DGGs overlap.

The retrieval on the SMOS data is applied on the averaged brightness temperatures of all overflights of this day. All subsequent results and comparisons are based on these averages.

The comparison of SMOS and MODIS retrievals in Figure 27 left and center shows a qualitatively good agreement and the much higher coverage of the image with SMOS retrievals compared to MODIS retrievals. The scatterplot Figure 27 right confirms the correlation. The scatter between the two retrievals increases with thickness, and SMOS finds slightly higher values than MODIS. The color of the points indicates the standard deviation of MODIS retrievals involved in the average for this SMOS pixel. We interpret the standard deviation as an indicator for the homogeneity of the ice thickness within the SMOS footprint. The standard deviation tends to increase with retrieval value. A number of points in the scatterplot has SMOS thicknesses exceeding 90 cm. They correspond to the black points in the SMOS retrievals Figure 27 left.

Figure 28 shows a similar comparison for Dec. 04, 2010. On this day, the range of low ice thicknesses (up to 25 cm) is better covered, and there is a high correlation of SMOS and MODIS for this range.

For sea ice thicker than 20-30 cm as detected by MODIS, SMOS tends to overestimate the sea ice thickness. Also the correlation of the two retrievals decreases with thickness.

The blue points, indicating more inhomogeneous ice thickness (standard deviation > 8 cm) within one SMOS footprint area, are located closer to the one-to-one line than the areas with more homogeneous ice thicknesses denoted in green and red, most likely caused by the fact that they belong to different disconnected regions of MODIS retrievals (Fig. 27 center). For one of these regions, east of Nowaja Semlja, we can recognize from Figure 26 the high horizontal variability of the MODIS based retrievals.

One aspect explaining at least in part the scatter in the scatterplot may be differenct physical regimes in the disjunct regions of MODIS retrievals in Figure 27, potentially connected to varying salinity, temperature of surface roughness of the sea ice.

The collinearly arranged set of dots at 90 cm SMOS ice thickness can be explained by the fact that in the retrieval curve, the Q value for 90 cm thickness is higher than the Q values of the actual observations. Since there are only few training values for higher thicknesses than about 50 cm, and the sensitivity in Q and I at these thicknesses are quite small, we cut off the retrieval at 50 cm ice thickness.

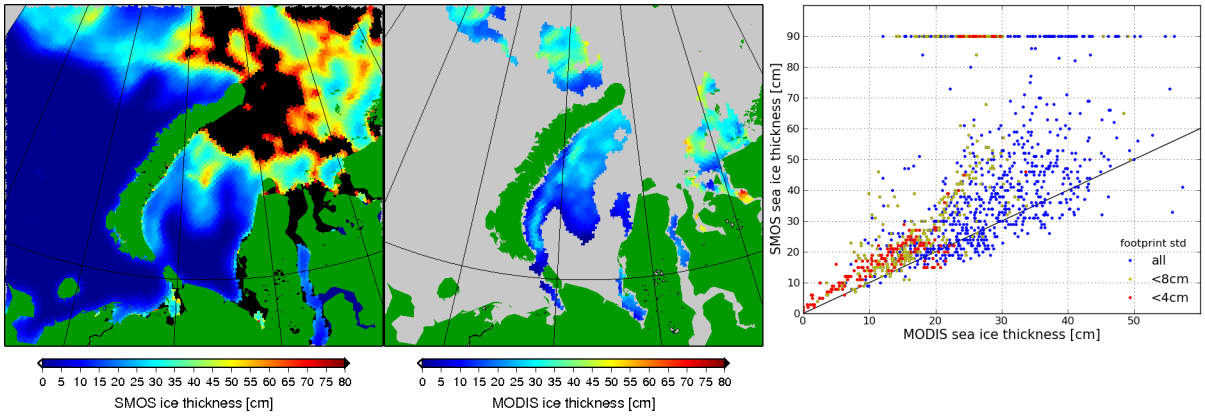

Figure 28: Same as Fig. 27, but of Dec. 4, 2010.

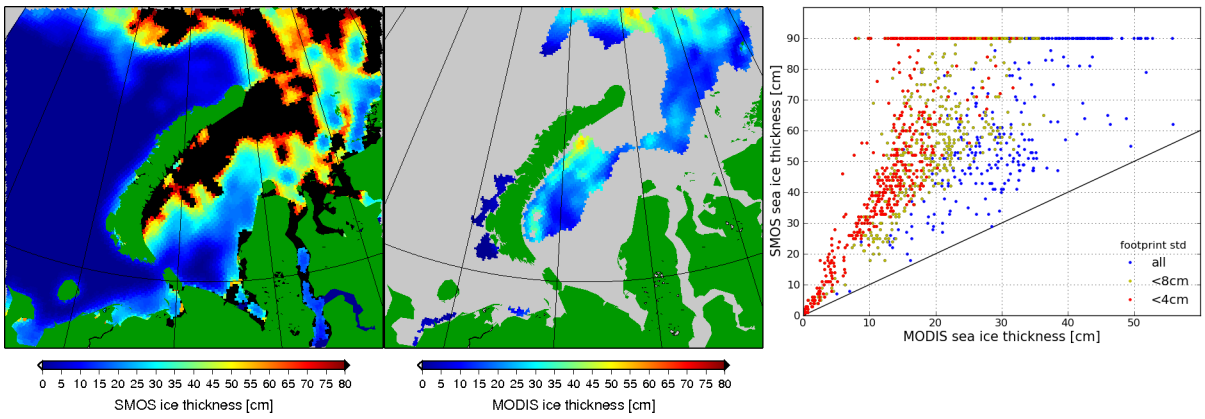

Figure 29: Same as Fig. 27, but of Dec. 17, 2010.

Figure 29 shows the results of Dec. 17, 2010. The area covered with valid SMOS retrievals (center) is slightly different, covering an extended region northeast of Novaya Zemlya which was not covered on Oct. 10 (Fig. 28 center). The only area the retrievals of both days have in common is a fraction of the Kara Sea east of Novaya Zemlya around 74°N, 60°E.
On the day and region of Figure 29, the algorithm overestimate the ice thicknesses below 20 cm by about three times compared to the MODIS thickness, however the correlation is quite high. Here again the agreement between both retrievals is better for more inhomogeneous (blue points in scatterplot) ice thicknesses of MODIS on the scale of a SMOS footprint, i.e., they do not overestimate sea ice thickness as much and therefore are closer to the one-to-one line than areas with more homogeneous ice thicknesses.

In the upper right part of Figure 29 an elliptical structure can be recongnized, in the SMOS retrieval (left) of turquoise color with a local thickness minimum in the center (blue), while in the MODIS retrieval (center) the same region appears dark blue with a local maximum thickness (light blue), which is in addition shifted a bit eastward. The shift may be cause by the discrepancy in the overflight times of the two satellites, which represent an additional source of discrepancy between the two retrievals.

4.6.2 Comparison to the MODIS/SAR thicknesses

Mäkynen [8] also provided a MODIS/SAR product in the resolution of 400 m. For comparison, Fig. 30 shows the results in a similar scheme as Figure 27 does for the MODIS retrievals of the same day. According to the intention of this data product, the aerial coverage of the MODIS/SAR retrievals (center) is much more complete. However, the agreement between the two retrievals is much less, as to be seen by comparing the two images left and center as well as from the scatterplot (right). Therefore, for evaluating the SMOS sea ice thickness retrieval we only use the MODIS thicknesses.

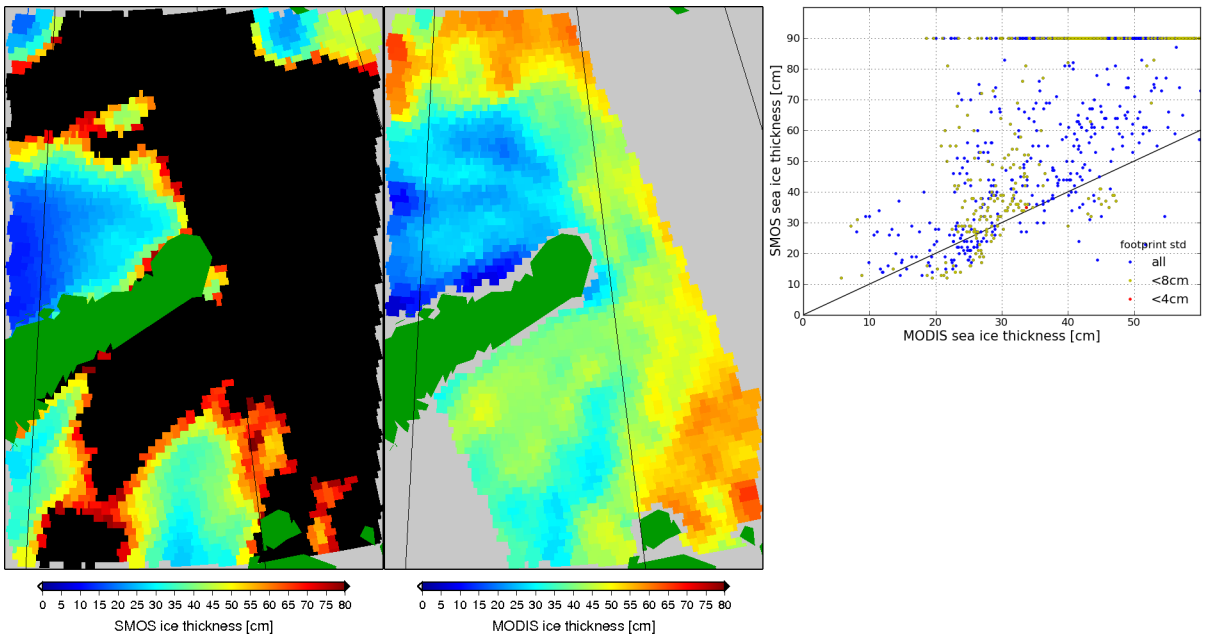

Figure 30: Same as Fig. 27, but taking in center the MODIS/SAR retrievals as reference. Right the corresponding scatterplot.

5 Deriving simultaneously sea ice thickness and concentration

The potential to retrieve sea ice concentration and thickness simultaneously from SMOS observations has first been suggested by [2]. As two parameters, the intensity I and polarization difference Q enter the retrieval, it is an compelling idea to attempt retrieving two parameters from the SMOS polarization data. That is the subject of this section.

5.1 Concept and algorithm of two-parameter retrieval

As an introductory example, consider the sketch of Figure 31: An observation (Q, I) (the blue dot in Fig. 31), taken under 50°...60° incidence angle, can be interpreted as a linear combination of the brightness temperatures of, in this example, about 60% open water and 40% of 30 cm thick ice. The retrieval of both paramters is posssible because the retrieval line is curved. If it would be linear, as it is the case for low incidence angles (see retrieval lines alsin Fig. 16), we could not distinguish in the diagram between the influence of sea ice thickness and concentration.

Figure 32 shows the retrieval lines for different ice concentrations at the incidence angle range 40°...50°. Observations outside the area encompassed by the retrieval lines would correspont to ice concentrations $> 100\,\%$ and thickness $d > 50\,\mathrm{cm}$, see marked regions in Figure 33. Inserting the observations of one day of the whole Arctic shows that in fact many observations fall outside the retrieval area (Fig. 33). Especially observations at ice concentration $0\,\%$ (pink) cover a broad range of Q values, due to some uncontrolled parameters, among them in order of assumed importance, the incidence angle (see Figure 2), sea ice temperature and salinity. Therefore, the retrieval of all observations with $I < 115\,\mathrm{K}$ are set to open water.

As both of the parameters sea ice thickness and concentration influence the observed brightness temperatures, a two-parameter retrieval has to be considered more appropriate in principle than a one-parameter retrieval. However, stability and noise in the retrieval results have also to be taken into account during the decision about the algorithm.

Two more insights can be gained from Figure 32:

- In Figure 14, at thicknesses 30 cm a change of 5° incidence angle corresponds to a change in Q of about 12 K which from Figure 32 translates to a change in thickness from 30 to 38 cm, but the influence on the sea ice concentration is low. As a consequence, at higher thicknesses, the bin size of the incidence angle of 10° represents a considerable error contribution to the thickness retrieval, but not to the concentration. At lower ice concentrations (Fig. 32), the sea ice signal reduces linearly, making the retrieval of both thickness and concentration more vulnerable to noise.

- Therefore, at lower thicknesses, e.g. between 10 cm and 20 cm, the influence of a similar error in Q will influence both ice concentration and thickness considerably. Consider as an in Figure 32 the point of 10 cm thickness and 100% concentration. A reduction of Q by 10 K will change the result to about 40 cm thickness and 50% concentration. This is intuitively understandable: As the influence of the sea ice in the brightness temperature signals reduces with decreasing thickness, a retrieval will become more uncertain in such cases.

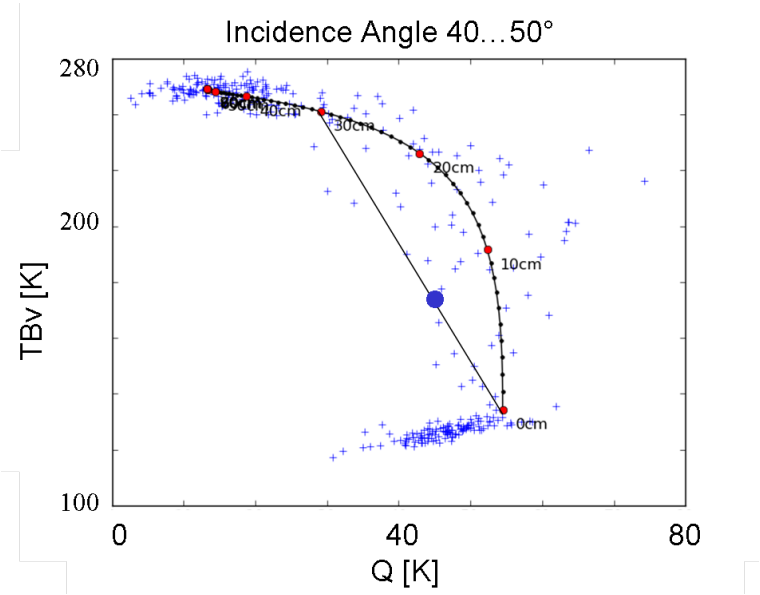

Figure 31: Retrieval line as derived from the learning data in the Kara Sea data set. Blut dot: mixed signature of about 60 % open water and 40 % of 30 cm thick ice.

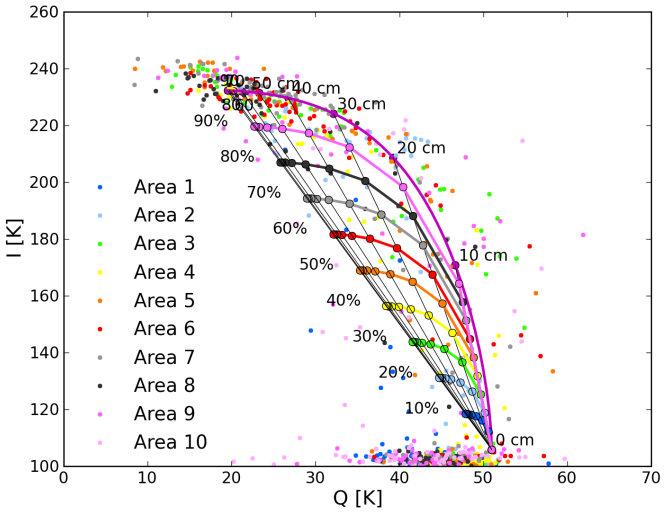

Figure 32: Retrieval lines for various sea ice concentrations with points from learning data set from the Kara Sea.

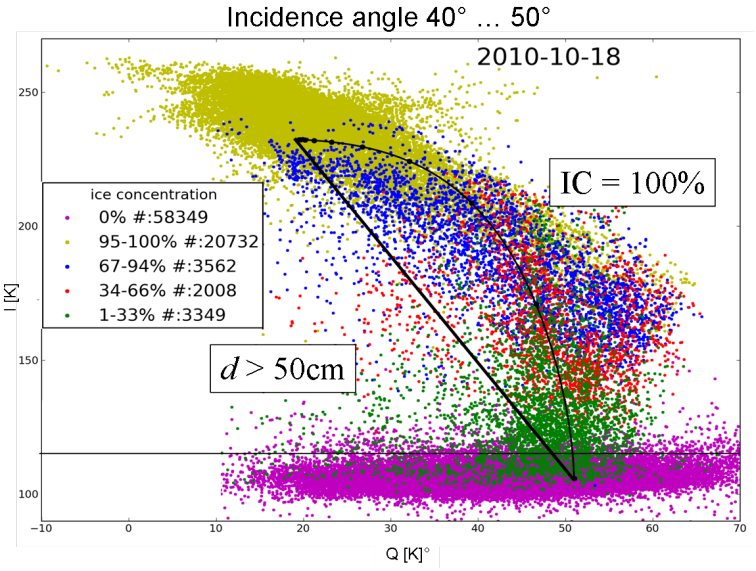

Figure 33: Retrieval lines for 100 % ice concentration, ice thickness > 50 cm and all observations of Oct 18, 2010. The color of the dots represents the AMSR-E/ASI sea ice concentration of the same day. The color of the dots represents the sea ice concentration as determined from AMSR-E/ASI observations of the same day. Retrievals of all observations below I =115 K are set to open water.

5.2 Results

Figures 34 and 35 compare the sea ice thicknesses and concentrations from the different retrievals, respectively. The one-parameter retrieval of the thickness in the left column shows overall plausible values with decreasing thickness towards the sea ice edge, and exended fields of thin sea ice in the Beaufort, Chukchi and East Siberia Seas. This is also in agreement with the results of the sea ice thickness model TOPAZ in the rightmost column. Columns 2 and 3 with the two-parameter retrieval and two-paramter retrievals with additional threshold, respecively, show an unphysical increase of the ice thickness toward the ice edge, understandable from Figure 32: at low sea ice thickness values, a small variation in I or Q will have a strong influence on the retrieved thickness. Also the ad hoc introduced threshold $I > 115$ K obviously does not improve the situation.

Figure 34 shows from left to right the sea ice concentration retrieval from the AMSR-E/ASI algorithm for comparison, from the 2-paramter retrieval based on SMOS data, and with additional threshold at I =115 K. The SMOS-based retrieval are in good agreement with the AMSR-E/ASI ones, except a smoother transision from high ice concentrations to open water at the ice edge, due to the much lower horizontal resolution of SMOS (about 40 km) at high incedence angles, compared to AMSR-E/ASI (6 km).

The scatterplot Figure 36 compares the SMOS retrieved sea ice concentrations of Oct. 18, 2000 of the whole Arctic to those of the AMSR-E ASI [11] based ones. Prior to the comparison, the ASI sea ice concentration, available in a 6 km grid, have been resolution adapted to the larger SMOS footprint of about 50 km diameter in the considered incidence angle range. For stability reasons, the SMOS ice concentrations are retrieved in 10% steps only. The high correlation of 0.93 between both ice concentrations is obvious in the scatter plot. The SMOS based ice concentrations are slightly higher than those from ASI (average bias 7% ice concentration). However, the plot shows that the agrement much better for ice concentrations up to 60%. The bias is highest at 70% ice concentration, and then decreasing to about 6% at 100% ice concentration. The RMS is highest at 70% ice concentration, lowest at ice concentrations of 0, 10 and 100 %, and 13% on average. As a result, the SMOS ice concentrations are well suited to obtain an overview of the Arctic sea ice distribution, but for detailed and and precise estimates the sea ice concetrations maps from higher frequency sensors (AMSR-E, SSMI/S) and algorithms (ASI, Bootstrap, NASA Team) are preferred.

The numbers near the top of the plot give for each 10% bin the number of SMOS pixels (DGGs) involvedin the comparison. When calculating correlation, bias and standard deviation, the pixels with 0% ice concentration have been discarded.

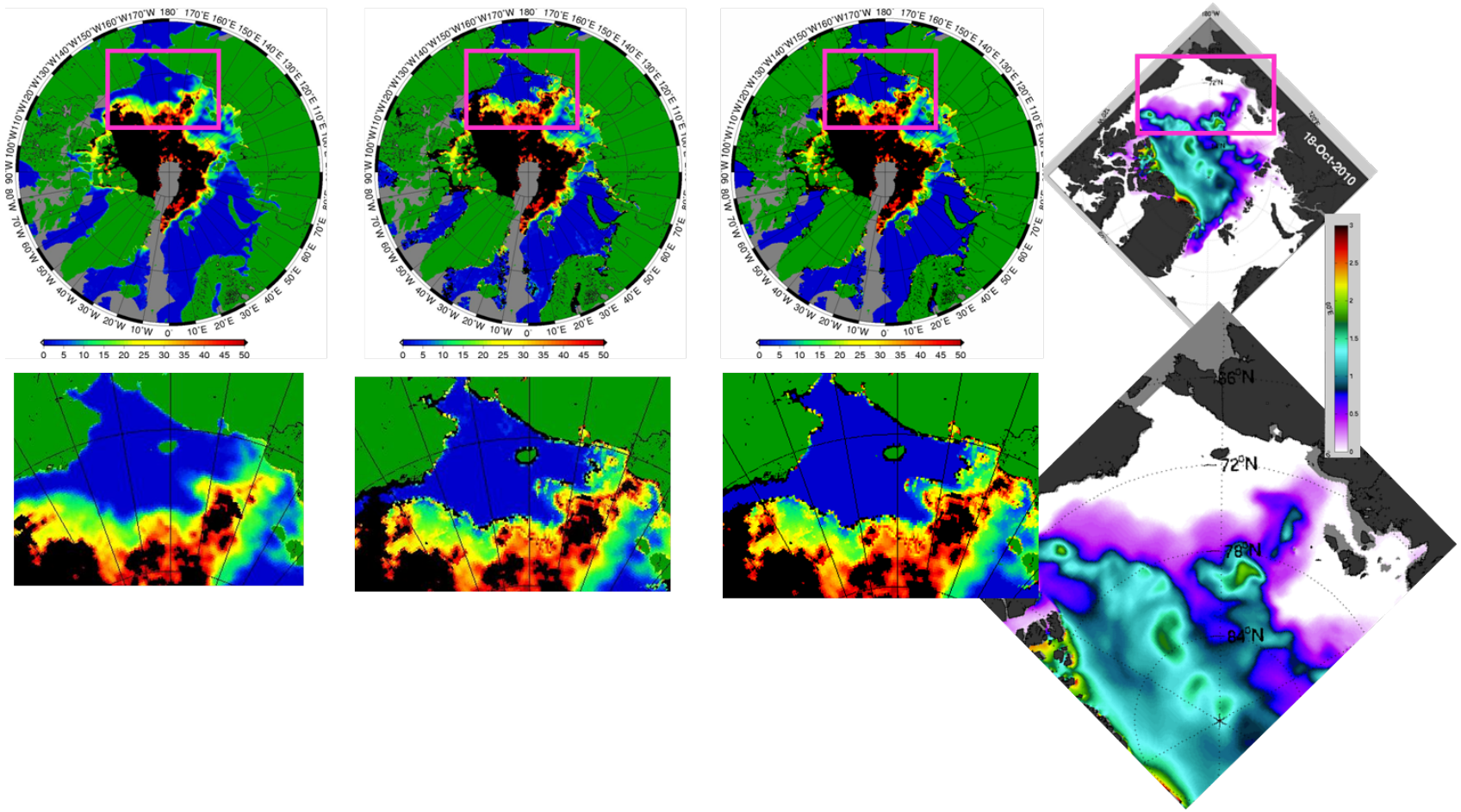

Figure 34: Results of sea ice thickness retrieval as of Oct 18, 2010. Top row: whole Arctic, bottom row: zoom of marked region in top row. Columns from left to right: retrieval of SID ony (Section 4), two-parameter retrieval, and two-parameter retrieval with additional theshold for intensities $> 115\,\mathrm{K}$, sea ice model TOPAZ.

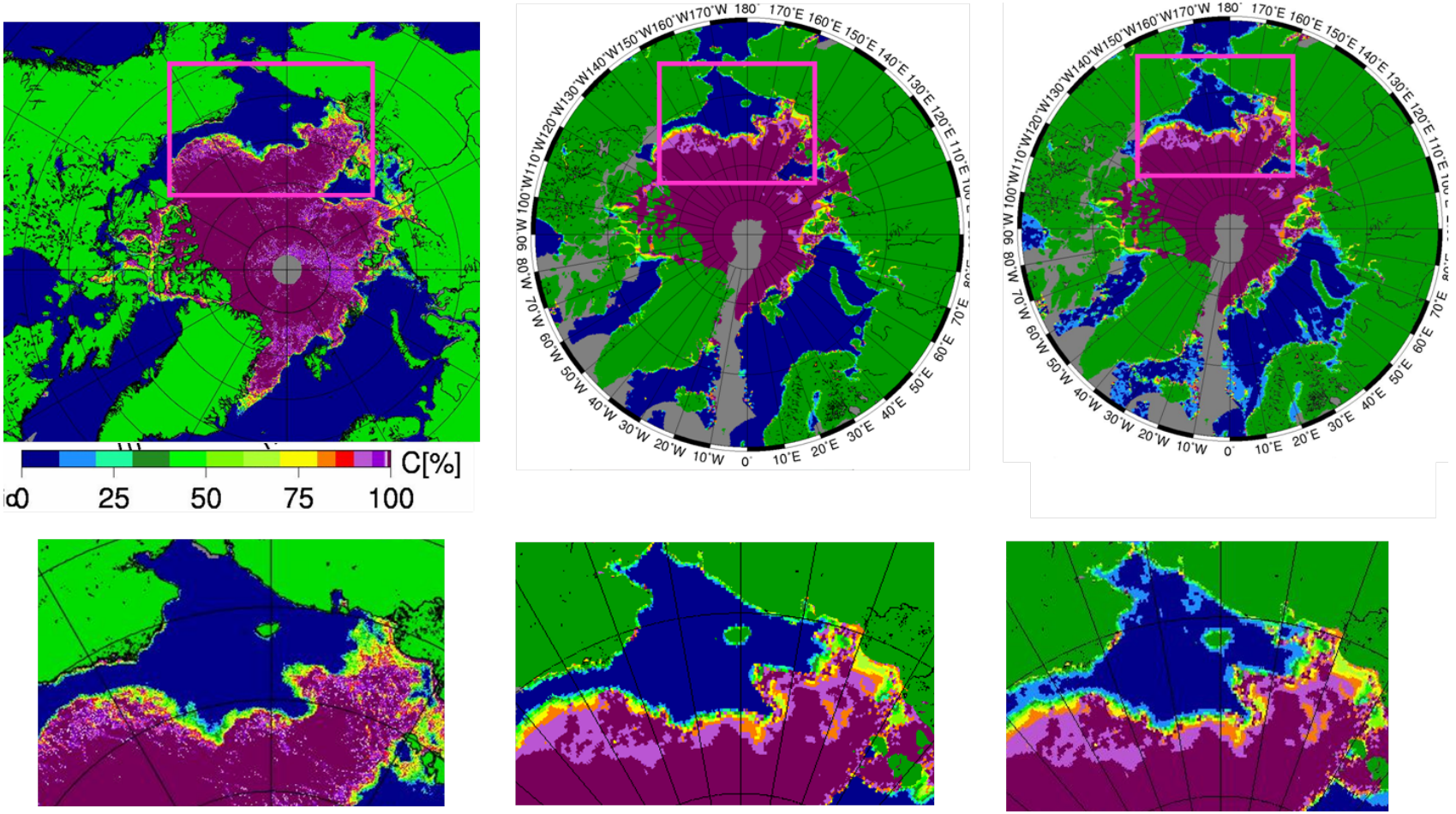

Figure 35: Results of sea ice concentration retrievals as of Oct 18, 2010. Top row: whole Arctic, bottom row: zoom of marked region in top row. Columns from left to right: retrieval of SID ony (Section **??**), two-parameter retrieval, and two-parameter retrieval with additional theshold for intensities $> 115\,\mathrm{K}$.

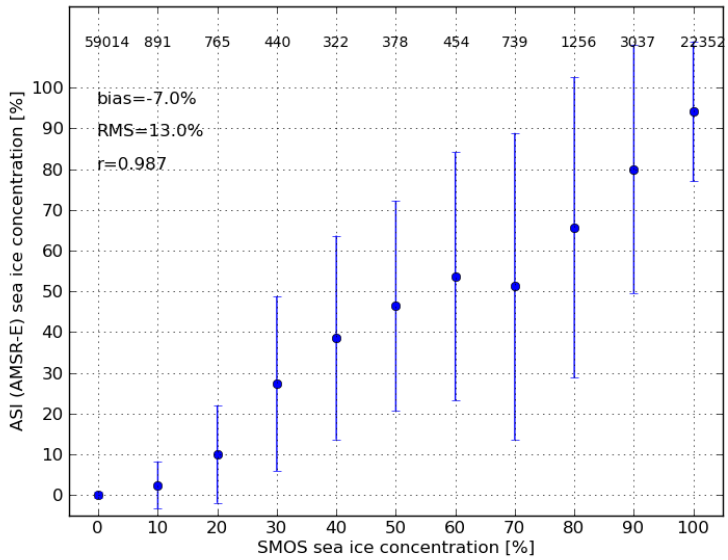

Figure 36: Scatterplot of AMSR-E ASI sea ice concetrations vs. SMOS retrieved sea ice concentrations over the whole Arctic for the Oct. 18, 2010. SMOS ice concentrations are retrieved in steps of 10%. The error bars give the standard deviations of the ASI sea ice concentrations within the SMOS footprints. The numbers at the top of the plot give the numbers of SMOS pixels with this sea ice concentration. When calculating RMS, correlation and bias, the SMOS pixels with ice concentration 0 have been excluded.

6 Conclusions

A method for retrieval of the thickness of thin sea ice from SMOS polarization data at incidence angles between 40° and 50° has been developed. A first study using a sea ice thickness proxy based on Cumulative Freezing Degree Days shows a sensitivity of the SMOS signal to sea ice thickness up to about 40 cm to 50 cm. Sample applications to a test region in the Kara Sea with sea ice thickness values obtained from MODIS satellite observations of higher horizontal resolution have been presented. The MODIS thickness values have been used for validation. A correlation of both thickness retrievals is found, where the SMOS retrievals tend to show higher thickness values than those from MODIS. An important advantage of the SMOS thickness retrieval is that is can, in contrast to MODIS, also be applied in cloudy and (polar) night conditions.

As both sea ice thickness and concentration influence the SMOS brightness temperatures, a retrieval should in principle cover both parameters. An appropriate procedure has been developed based on SMOS observed intensities and polarization differences. While the procedure works correctly in principle, the quantitative results for sea ice thickness are better if retrieving thickness only. The retrieved sea ice concentrations show a high correlation (0.93) with those retrieved with the ASI algorithm from AMSR-E 89 GHz observations. But the SMOS based concentrations are systematically higher, show an RMS difference of 13% to the ASI results and have a horizontal resolution of about 6 km in contrast to 50 km of the SMOS observations.

Both suggested types of retrieval are based on SMOS observations between 40° and 50° incidence angle and do not take the incidence angle explicitly into account. It has turned out during the validation study that the large incidence angle range of 10 ° is a considerable source of error in the retrieval. It can be eliminated by explicitly taking the incidence angle into account during the retrieval, e.g. by interpolating the retrieval curve to the incidence angle at hand. On the other hand, in such a retrieval no more daily averages of SMOS brightness tempertures could be used. Instead, the retrieval results can be averaged.

Concluding, it appears most promising to further develop the sea thickness retrieval. The next steps should be to optimize the incidence angle range, and to take into account the dependence of the SMOS brightness tempertures on the temperature and salinity of the sea ice and surrounding water.

It will be appealing to combine the intensity-based retrieval developed in this project with the polarization-oriented retrieval of this document in order to allow the most complete use of SMOS data for sea ice thickness retrieval.

References

[1] G. Heygster, S. Hedricks, L. Kaleschke, N. Maass, P. Mills, D. Stammer, R. T. Tonboe, and C. Haass, "L-Band Radiometry for Sea-Ice Applications," Institute of Environmental Physics, University of Bremen, Bremen, Germany, IUP Technical Report, 2009.

[2] P. Mills and G. Heygster, "Retrieving ice concentration from smos," *IEEE Geoscience and Remote Sensing Letters*, no. 99, pp. 283–287, 2011.

[3] "Soil moisture algorithm theoretical basis document," Tech. Rep., 2010. [Online]. Available: http://www.cesbio.ups-tlse.fr/fr/smos/smos_atbd.html

[4] P. Narvekar, G. Heygster, R. Tonboe, and T. Jackson, "Analysis of windsat data over arctic sea ice," *IEEE Trans. Geosci. and Remote Sensing*, vol. 49, no. 5, pp. 369–372, 2008.

[5] L. Kaleschke, X. Tian-Kunze, N. Maaß, M. Mäkynen, and M. Drusch, "Sea ice thickness retrieval from SMOS brightness temperatures during the Arctic freeze-up period," *Geophysical Research Letters*, vol. 39, no. 5, Mar. 2012. [Online]. Available: http://www.agu.org/pubs/crossref/2012/2012GL050916.shtml

[6] G. Maykut, *The surface heat and mass balance. In: The geophysics of sea ice (pp.395-464). NATO ASI Series*, N.Untersteiner, Ed. Plenum Press, 1986.

[7] J. Launiainen and B. Cheng, "Modelling of ice thermodynamics in natural water bodies," *Cold Reg.Sci. Technol.*, vol. 27, no. 3, pp. 153–178, 1998.

[8] M. Makynen, "STSE-SMOS Sea Ice Retrieval Study SMOSIce WP 3 Assembly of the SMOSIce Data Base SMOSIce-DAT. User manual for the validation data Deliverable D-6b Draft EUROPEAN SPACE AGENCY STUDY CONTRACT REPORT Under ESTEC Contract No. 4000101476/10/NL/CT," Finnish Meteorological Institute, Tech. Rep., 2011.

[9] D. Dumont, K. Lisaeter, and L. Bertino, "Sea ice modelling of the marginal ice zone july 2007 - june 2010," NERSC, Bergen, Norway, Technical Report of NERSC, June 2010.

[10] Y. Yu and D. Rothrock, "Thin ice thickness from satellite thermal imagery," *JOURNAL OF GEOPHYSICAL RESEARCH-OCEANS*, vol. 101, no. C11, pp. 25 753–25 766, NOV 15 1996.

[11] G. Spreen, L. Kaleschke, and G. Heygster, "Sea ice remote sensing using AMSR-E 89-GHz channels," *JOURNAL OF GEOPHYSICAL RESEARCH-OCEANS*, vol. 113, no. C2, JAN 17 2008.

Part IV

Validation

Xiangshan Tian-Kunze, Nina Maaß

9 MODIS

Xiangshan Tian-Kunze

9.1 MODIS Ice Thickness Charts

MODIS ice thickness charts covering an area of 1500 km x 1350 km over the Kara Sea and the eastern part of the Barents Sea have been calculated by Finnish Meteorological Institute (FMI). The derivation of the charts and their uncertainty estimation are described in detail in Maekynen et al. (2013) and Chapter 14. MODIS ice thickness is estimated based on the ice surface temperature (T_s) together with atmospheric forcing data through ice surface heat balance equation (Yu and Rothrock, 1996; Maekynen et al., 2013). The major drawback with the T_s based thickness retrieval is the requirement for cloud-free conditions, and thus, there may be long temporal gaps in the thickness chart coverage over a region of interest. In addition, discriminating clear-sky from clouds is difficult in winter night-time conditions (Frey et al., 2008). The total number of the charts is 120 and they cover two winters (Nov. to Apr.) in 2009-2011. The spatial resolution of the charts is 1 km and they show ice thickness from 0 to 99 cm. The external forcing data for solving the ice thickness from the surface heat balance equation came from a numerical weather prediction (NWP) model HIRLAM (HIgh-Resolution Limited Area Model) (Kaellen, 1996; Unden, 2002). Only night-time MODIS data was employed. Thus, the uncertainties related to the effects of solar shortwave radiation and surface albedo were excluded. For the cloud masking of the MODIS data, in addition to the different cloud tests (Frey et al., 2008), also manual methods were used in order to improve the detection of thin clouds and ice fog. The cloud masking was conducted with 10 km x 10 km blocks to identify larger cloud-free areas and to reduce errors due to the MODIS sensor striping effect. In the ice thickness chart calculation an average snow thickness (h_s) vs. ice thickness (h_i) relationship was used. The thickness of the snow layer is assumed to be:

$$
\begin{aligned}
h_s &= 0\text{m} && \text{for } d_{ice} < 0.05\text{m} \\
h_s &= 0.05 \times d_{ice} && \text{for } 0.05\text{m} \leq d_{ice} < 0.2\text{m} \\
h_s &= 0.09 \times d_{ice} && \text{for } d_{ice} \geq 0.2\text{m}
\end{aligned}
$$

This relationship was based on Doronin (1971) and the Soviet Union's Sever expeditions data (NSIDC, 2004). The typical maximum reliable ice thickness (max 50% uncertainty) was estimated to be 35-50 cm under typical weather conditions (air temperature T_a < -20°C, wind speed V_a < 5 ms^{-1}) for the MODIS data. The accuracy is the best for the 15-30 cm thickness range, around 38%. These figures are based on Monte Carlo method using estimated or guessed standard deviations and covariances of the input variables to the thickness retrieval. No in-situ data were available for the thickness accuracy estimation.

9.2 Comparison of SMOS-based and MODIS-based ice thicknesses in the Kara Sea

For the initial verification of SMOS-retrieved sea ice thickness we use MODIS ice thickness charts for the Kara Sea. The area is suitable for SMOS ice thickness validation because even in the winter time this area is frequently covered by thin first-year ice, which SMOS can best detect. To compare SMOS and MODIS ice thicknesses, we reduce the 1 km spatial resolution of the MODIS thickness charts to the NSIDC grid resolution of 12.5 km by spatial averaging.

In this section we only compare the ice thicknesses derived from the algorithms developed in UHH with the MODIS data. We first compare ice thickness distributions from SMOS and MODIS for two selected days (26 December 2010 and 2 February 2011), on which a sufficient amount of pixels with valid MODIS data is available. After that, we collect all pixels with valid MODIS data from 30 days during the two winter seasons 2009-2010 and 2010-2011 and carry out a pixel to pixel comparison. The 30 days are selected manually. MODIS ice charts with strong cloud limitation are excluded. Similarly to Algorithm I and II, the MODIS sea ice thickness retrieval assumes a planar ice layer. Therefore, by spatial averaging of MODIS data to a grid resolution of 12.5 km we use the modal mean of the MODIS ice thickness instead of the arithmetic mean. For the comparison we use the plane layer SMOS ice thickness, not the inhomogeneous mean ice thickness of Algorithm II*.

9.2.1 Daily comparison

Figure 9.1 shows the averaged MODIS ice thickness in a 12.5 km grid resolution, the SMOS ice thicknesses retrieved from Algorithm I and II, and the histogram of the three ice thickness data in the Kara Sea on 26 December 2010. Ice concentration from the same day (Figure 9.2) shows near 100 % ice coverage in the ice-covered area except for the marginal ice zone. We use here the ice concentration maps derived from SSM/I with the ARTIST Sea Ice(ASI) algorithm. Both SMOS and MODIS show similar patterns of thin and thick ice distributions, whereas SMOS ice thickness from Algorithm I is considerably lower than the other two in the thicker ice range. Surface air temperature over the ice covered area varies from -30°C to -20°C (Figure 9.2), providing favorable conditions for both SMOS and MODIS ice thickness retrievals (Kaleschke et al., 2010; Yu and Rothrock, 1996).

The insulation effect of snow is considered in the SMOS algorithm II and in the MODIS ice thickness retrieval, but not in the SMOS Algorithm I. Surface temperature and ice thickness are retrieved simultaneously in Algorithm II with the surface air temperature as a boundary condition. The SMOS-derived snow surface temperature is in good agreement with that from the MODIS snow/ice surface temperature product (Hall et al., 2004) (Figure 9.2). The mean surface temperatures from MODIS and SMOS are both 247 K, and the root mean square deviation (RMSD) is 4 K. Discrepancies can be seen in the marginal ice zone and in the Ob estuary where the low salinities are not well represented by the ocean model. In the marginal ice zone with lower ice concentrations, SMOS strongly underestimates ice thickness, which leads to too warm surface temperatures. The surface temperature is used in SMOS Algorithm II to calculate the bulk ice temperature, which is a variable parameter in the radiation model to calculate the emissivity of an ice layer.

In total there are 4167 pixels in 12.5 km grids with valid MODIS ice thicknesses. For these pixels MODIS has a mean thickness of 44 cm, whereas SMOS has an average of 32 cm and 47 cm from Algorithm I and II, respectively. The correlation coefficient R and RMSD

between the SMOS Algorithm II and MODIS are 0.60 and 20 cm, whereas for SMOS Algorithm I and MODIS they are 0.57 and 23 cm, respectively. If we only consider the 2679 pixels with a MODIS ice thickness less than 50 cm, mean ice thicknesses of SMOS Algorithm I, SMOS Algorithm II and MODIS are 29 cm, 40 cm, and 29 cm respectively. That means in the thin ice range Algorithm II overestimates ice thickness compared to MODIS. The bulk ice temperature derived from the surface temperature in Algorithm II is on average 263.6 K, which is 2.5 K lower than that assumed in SMOS Algorithm I. This can partly explain the ice thickness difference between Algorithm I and II. The SMOS-derived ice thickness decreases with increasing ice temperature when the ice temperature is less than -5°C (Maaß, 2013a).

Similar results can be derived from another comparison on 2 February 2011 (see Figure 9.3, Figure 9.4). On this day, large areas of thin ice can be observed from SMOS and MODIS near the Kara Sea strait and in the estuaries. In both regions polynyas appear frequently due to the strong wind forcing. Under cold air temperatures, the polynyas are soon covered by thin ice. Both SMOS and MODIS show ice thicknesses in the range of 20-40 cm in the polynyas with similar distribution patterns. Ice concentration is normally higher than 90 %, except for the marginal ice zone. Like on 26 December 2010, surface air temperature in the Kara Sea is as low as -30°C. In total 4016 pixels have valid MODIS data. The mean ice thickness of SMOS Algorithm I, SMOS Algorithm II, and MODIS for the pixels are 33 cm, 50 cm, and 47 cm, respectively. The correlation coefficient and RMSD between the SMOS Algorithm II and MODIS are 0.61 and 21 cm, whereas between SMOS Algorithm I and MODIS they are 0.59 and 26 cm, respectively. The mean surface tempertures from MODIS and SMOS are 246 K and 245 K, with a RMSD of 4 K.

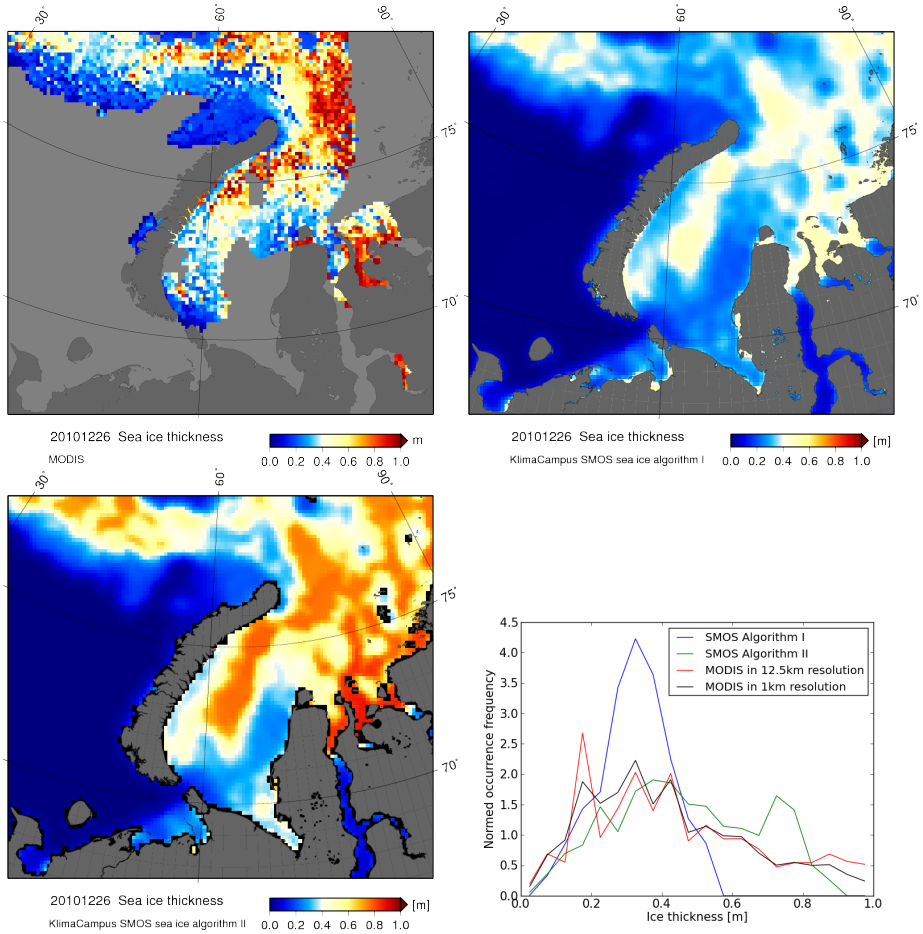

Figure 9.1: The averaged MODIS ice thickness in 12.5 km grid resolution (upper left), SMOS ice thicknesses retrieved from Algorithm I (upper right) and II (lower left), and the histogram of the three ice thickness data (lower right) in the Kara Sea on 26 December 2010.

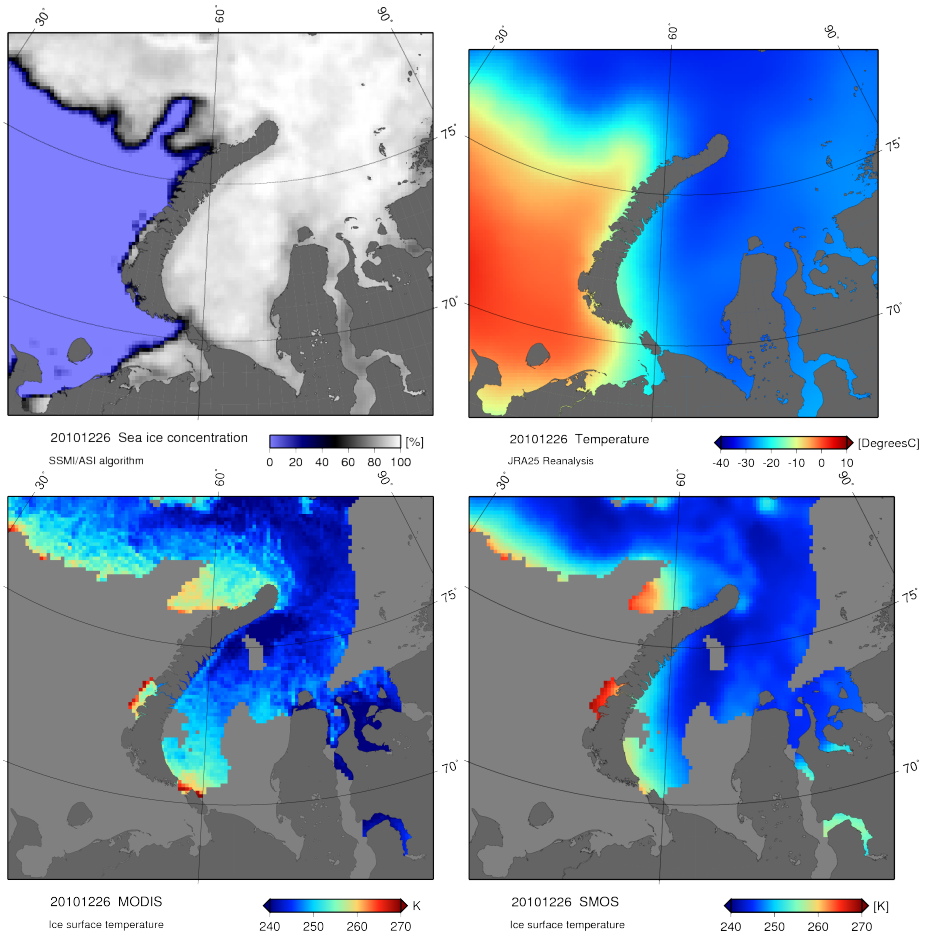

Figure 9.2: AMSR-E ice concentration [%] (upper left), JRA-25 surface air temperature [K] (upper right), MODIS- and SMOS-based snow/ice surface temperature [K] (lower left and lower right) in the Kara Sea on 26 December 2010.

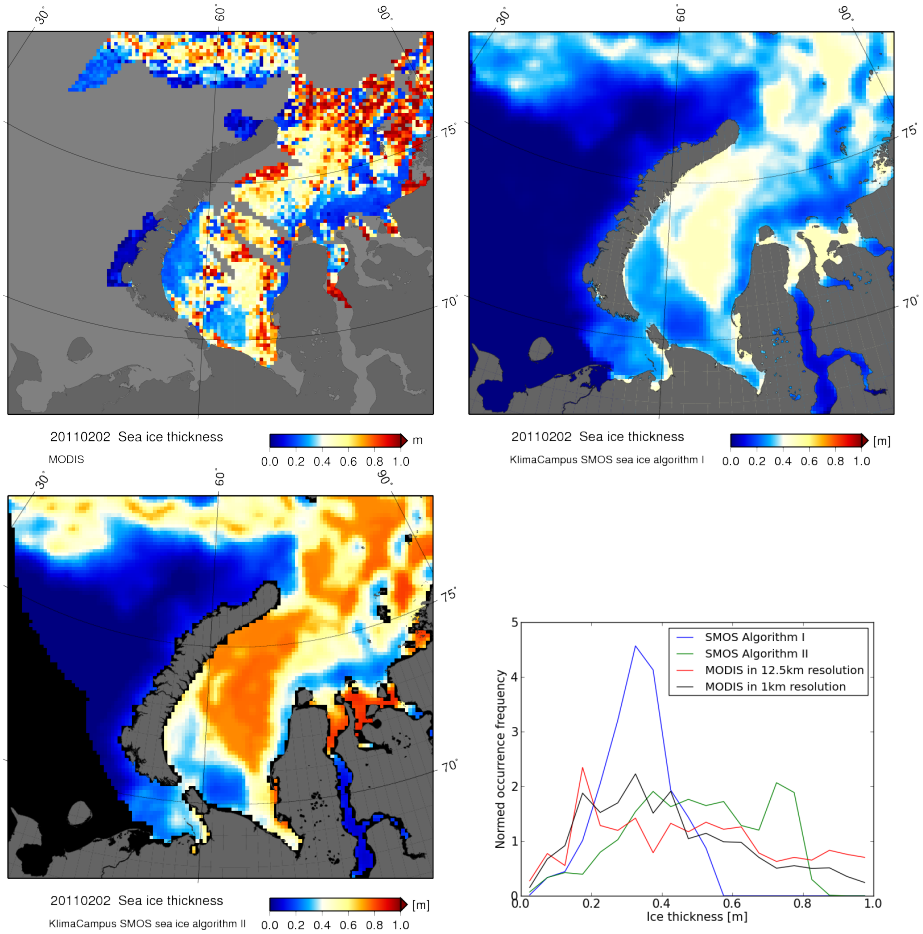

Figure 9.3: The averaged MODIS ice thickness in 12.5 km grid resolution (upper left), SMOS ice thicknesses retrieved from Algorithm I (upper right) and II (lower left), and the histogram of the three ice thickness data (lower right) in the Kara Sea on 2 February 2011.

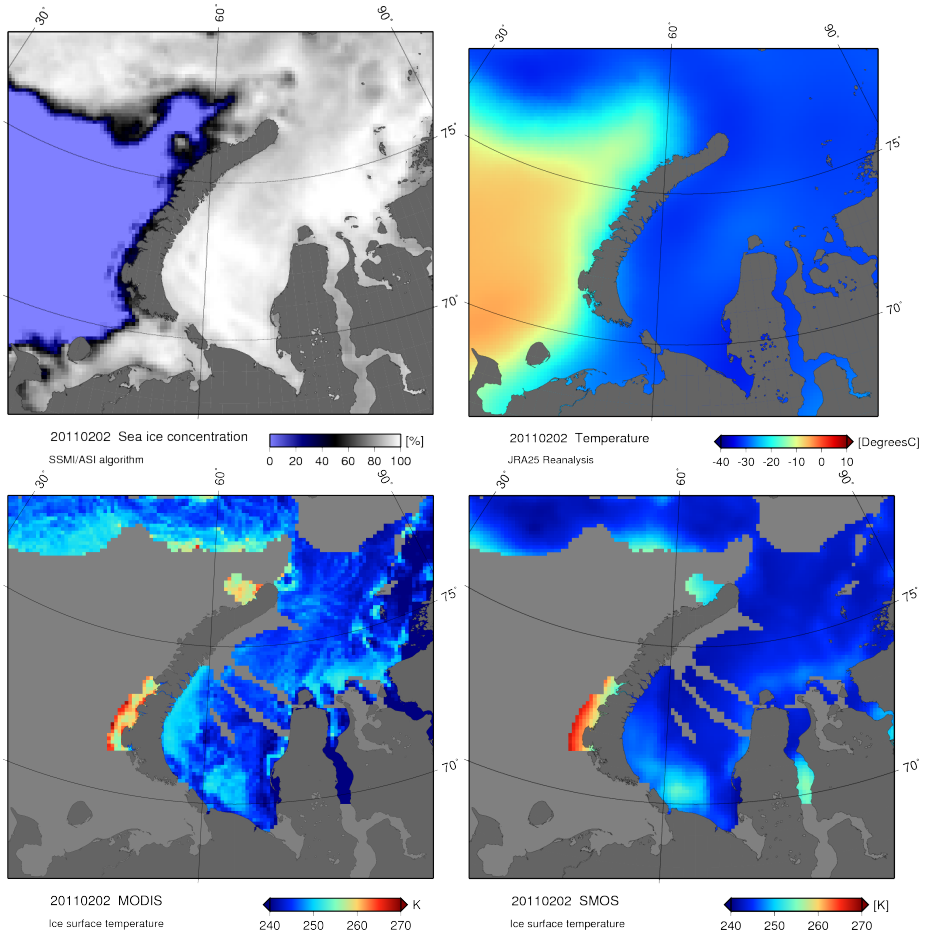

Figure 9.4: AMSR-E ice concentration [%] (upper left), JRA-25 surface air temperature [K] (upper right), MODIS- and SMOS-based snow/ice surface temperature [K] (lower left and lower right) in the Kara Sea on 2 February 2011.

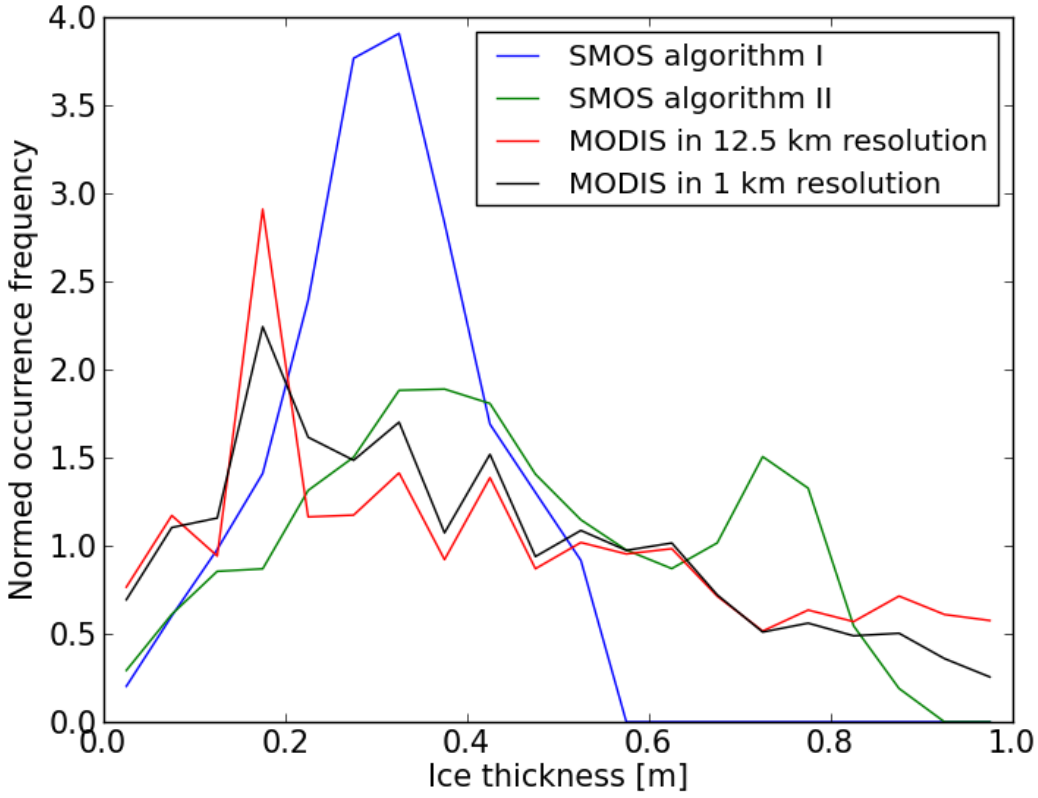

Figure 9.5: Histogram of ice thicknesses from all pixels of the 30 days.

9.2.2 Comparison with 30 days data from the two winter seasons

In total 33 and 87 days of MODIS validation data are available for the winter seasons of 2009-2010 and 2010-2011. However, many of them have only small areas with usable MODIS data. Therefore, we selected out 30 days on that the data are not badly affected by cloud coverage. Altogether 81350 pixels are available in 12.5 km resolution. The histogram of the ice thicknesses (Figure 9.5) shows better agreement between SMOS Algorithm II and MODIS than between SMOS Algorithm I and MODIS for these pixels. The mean ice thicknesses derived from SMOS Algorithm II and MODIS are of the same order, 44 cm and 42 cm, respectively, whereas SMOS Algorithm I shows on average 31 cm. If we restrict the comparison to the pixels with MODIS ice thicknesses less than 50 cm, the mean ice thickness from SMOS Algorithm II is about 13 cm higher than the MODIS mean value (see Table 9.1). Because of the much larger footprint of SMOS ($\sim$40 km) compared to MODIS (1 km) we aggregate the MODIS retrievals on the SMOS grid by taking the modal mean. The different integration times (SMOS: daily averages versus MODIS: single overpasses) introduce additional uncertainties. Nevertheless, the ice thickness retrieved from SMOS and MODIS are very similar, with a considerably better agreement between SMOS Algorithm II and MODIS. The correlation coefficient R between SMOS and MODIS data is about 0.6 for both Algorithm I and II.

Table 9.1: Comparison of SMOS and MODIS based ice thicknesses in the Kara Sea during the 30 days selected from the two winter seasons of 2009-2010 and 2010-2011.

		pixels with MODIS ice thickness < 0.5 m	all pixels
Number of pixels		51716	81350
mean	MODIS	0.24 m	0.42 m
	SMOS I	0.27 m	0.31 m
	SMOS II	0.37 m	0.44 m
R	SMOS I	0.64	0.61
	SMOS II	0.63	0.62
RMSD	SMOS I	0.11 m	0.25 m
	SMOS II	0.19 m	0.22 m

9.3 Algorithm comparison between University of Hamburg and University of Bremen

9.3.1 Comparison with MODIS-based sea ice thickness during the freeze-up period of 2010

Within the scope of SMOSIce project, seperate SMOS sea ice thickness retrieval algorithms are developed by University of Hamburg (UHH) and University of Bremen (UB). Whereas UHH algorithm focuses on the first Stokes component of brightness temperatures averaged in the incidence angle range of 0°-40°, UB uses polarisation difference of horizonally and vertically polarized brightness temperatures in the higher incidence angle ranges. The algorithm comparison is carried out comparing with the MODIS-based sea ice thickness in the Kara Sea. UHH ice thickness retrieval is based on the latest reprocessed L1C brightness termpature data with version number 505, but UB retrieval is based on the reprocessed L1C data with version number 346. There are slight differences between the two version L1C data. In version 505 pattern correction is carried out to remove apparent bias caused by sun glint and RFI. Unreliable measurments at the borders of a snapshot are also removed. This can cause several Kalvin difference in L1C brightness temperature at some pixels. However for the following comparison we neglect this difference.

The freeze-up period from October to December 2010 is selected for the algorithm comparison. In this period we have altogether 30 days of MODIS sea ice thickness data. We compare the correlation coefficient as well as the root-mean-square deviation (RMSD) between SMOS-based and MODIS-based sea ice thickness for both algorithms. Pixel-to-Pixel, day-to-day comparison has been carried out. The average correlation coefficient R is about 0.66 and 0.62 for UHH and UB respectively if we only consider MODIS pixels with ice thickness less than 0.5 m. This correlation coefficient reduces to 0.61 and 0.58 if we include the MODIS pixels with ice thickness more than 0.5 m. Overall UHH algorithm shows much less RMSD than that of UB in the Kara Sea (see Table 9.2).

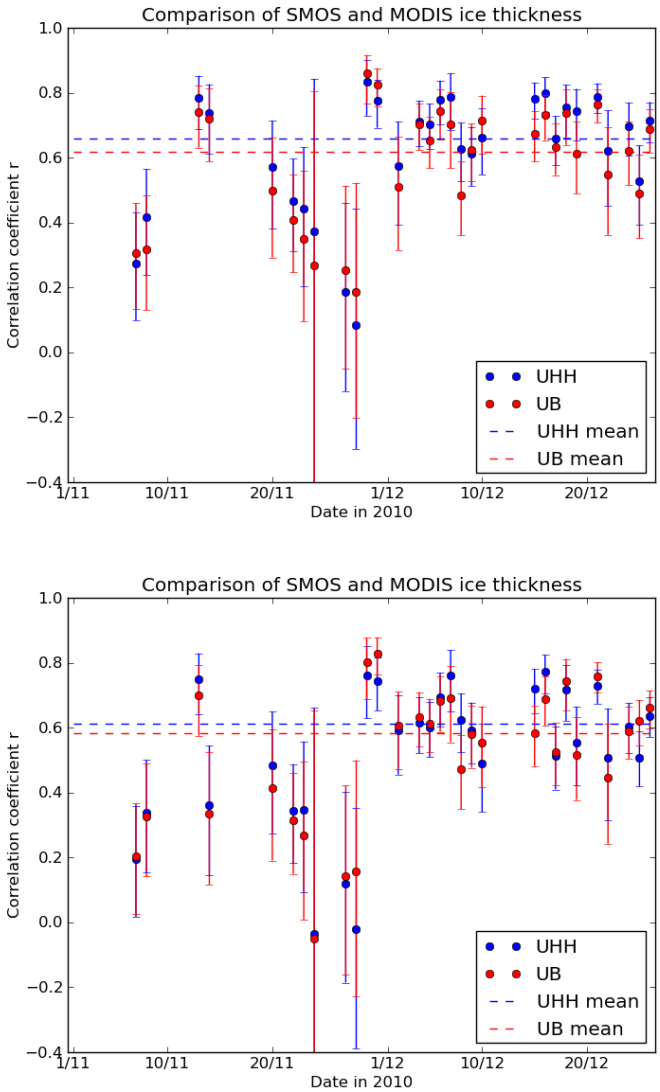

Figure 9.6: Correlation coefficient between SMOS and MODIS sea ice thickness with significance variance. The significance level is more than 99.9 %. Top: MODIS pixel <0.5m Bottom: MODIS pixel<=0.5 Period: Oct. 01 - Dec. 26, 2010

Table 9.2: Correlation coefficient and RMSE between SMOS and MODIS based ice thickness in Kara Sea in Nov. and Dec. 2010.

pixels used		UHH Algorithm I	UB
d<=0.5 m	R	0.61	0.58
	RMSE	0.13 m	0.18 m
	MODIS mean	0.28 m	
	SMOS mean	0.28 m	0.39 m
d<0.5 m	R	0.66	0.62
	RMSE	0.11 m	0.20 m
	MODIS mean	0.21 m	
	SMOS mean	0.26 m	0.37 m

(Figure 9.6, Figure 9.7, Figure 9.8, Figure 9.9, Figure 9.10) show day-to-day comparison of UHH and UB SMOS ice thickness with that from MODIS.

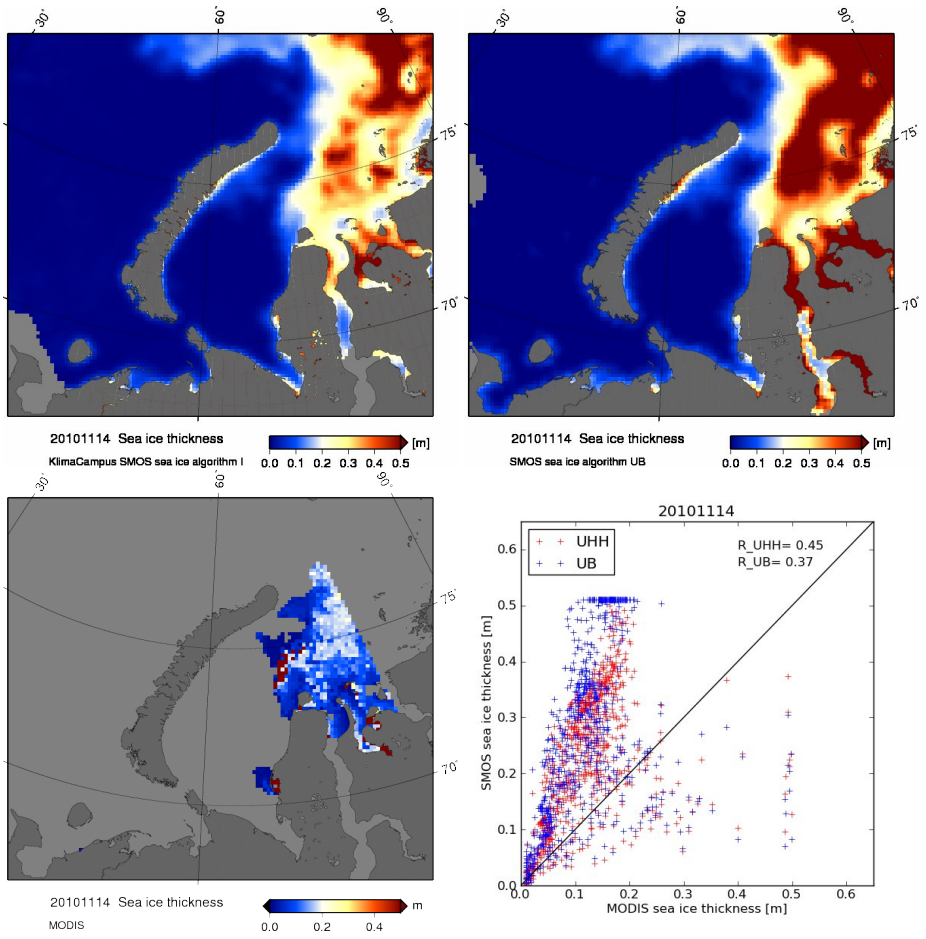

Figure 9.7: Comarison of SMOS and MODIS sea ice thickness. Date: 2010.11.14

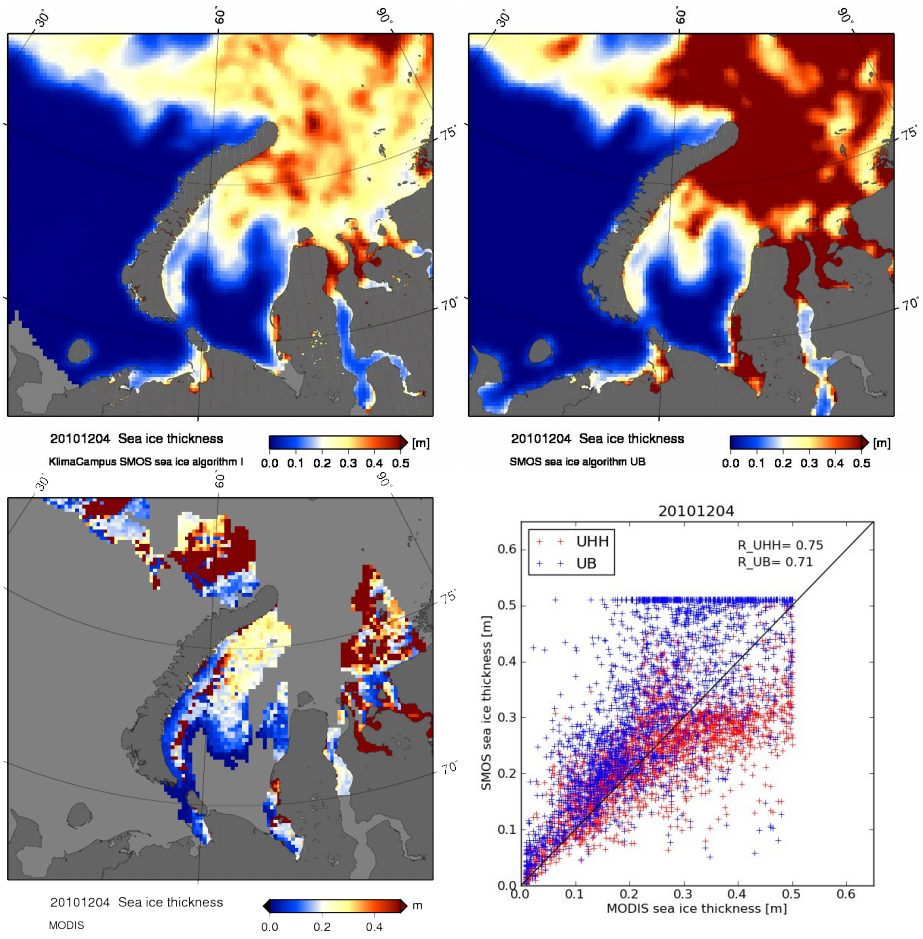

Figure 9.8: Comarison of SMOS and MODIS sea ice thickness. Date: 2010.12.04

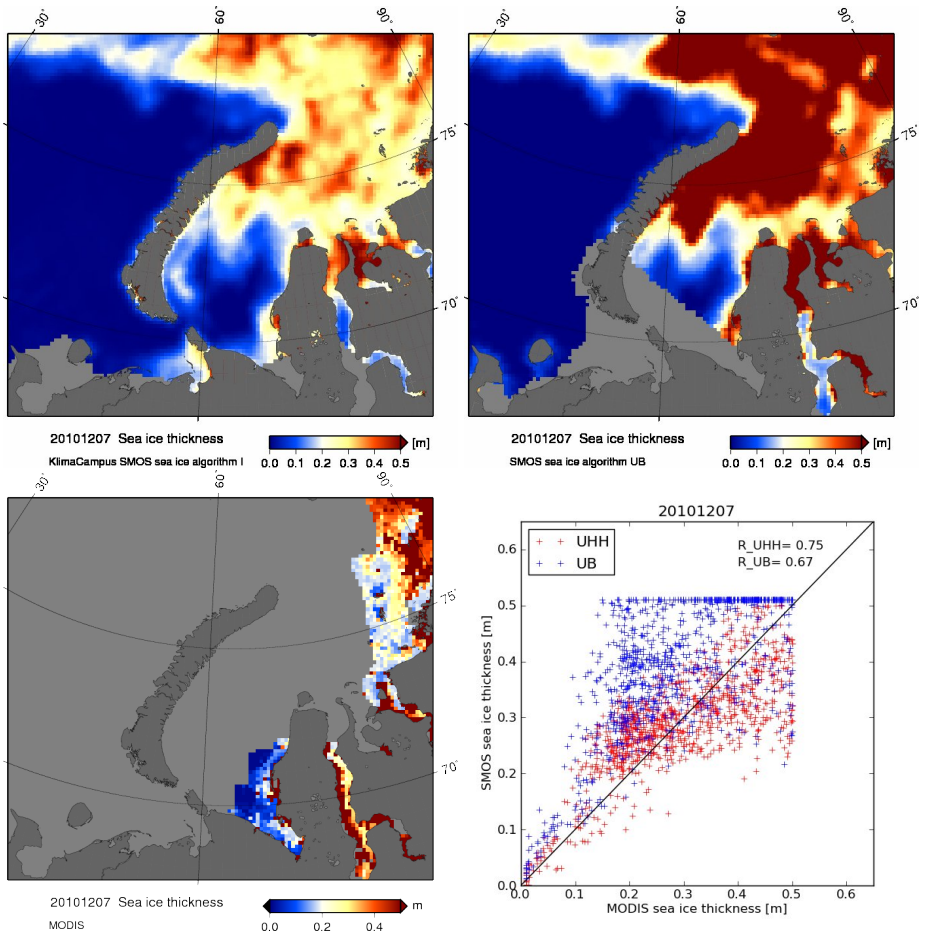

Figure 9.9: Comarison of SMOS and MODIS sea ice thickness. Date: 2010.12.07

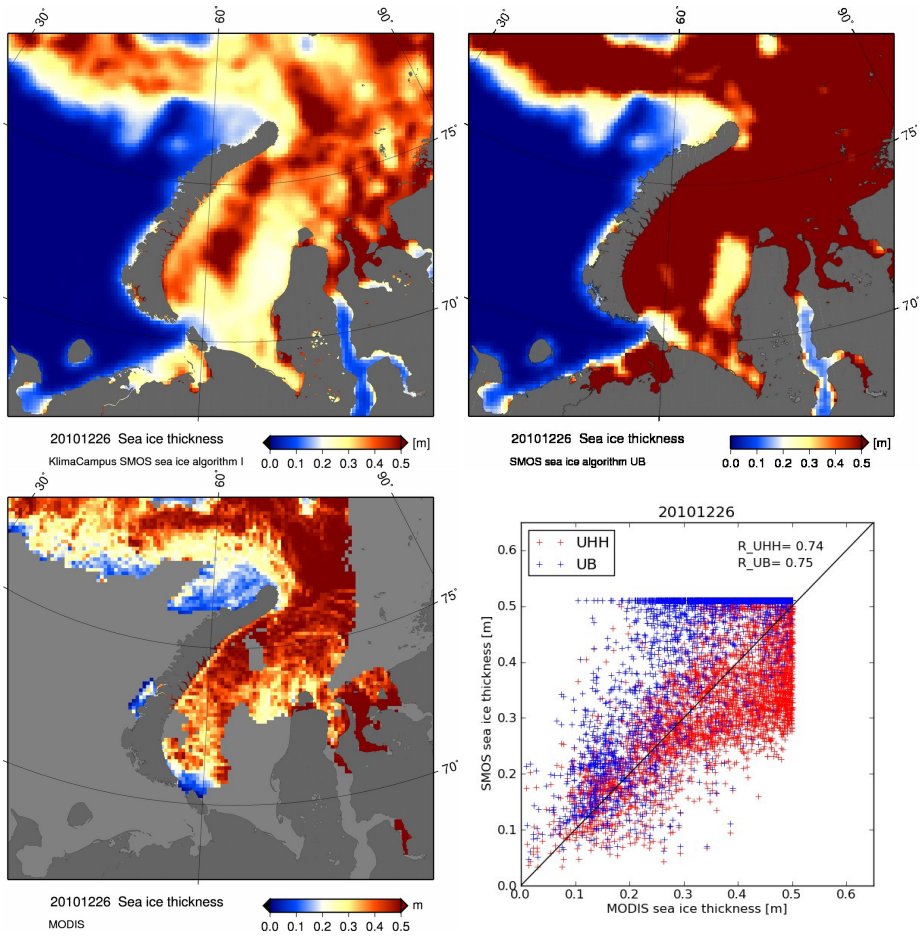

Figure 9.10: Comarison of SMOS and MODIS sea ice thickness. Date: 2010.12.26

9.3.2 Algorithm comparison in the Antarctic

Further comparison of two algorithms has been carried out in Antarctic on 25 June, 2011. To avoid the possible difference caused by different interpolation and transformation steps by UHH and UB, we use the same DGG based mean brightness temperatures from UB to calculate sea ice thickness with UHH and UB algorithms. Overall UB algorithm shows thicker ice than UHH algorithm (Figure 9.11). The maximum ice thickness difference is as high as 35 cm and average ice thickness difference is about 5.7 cm (Figure 9.12).

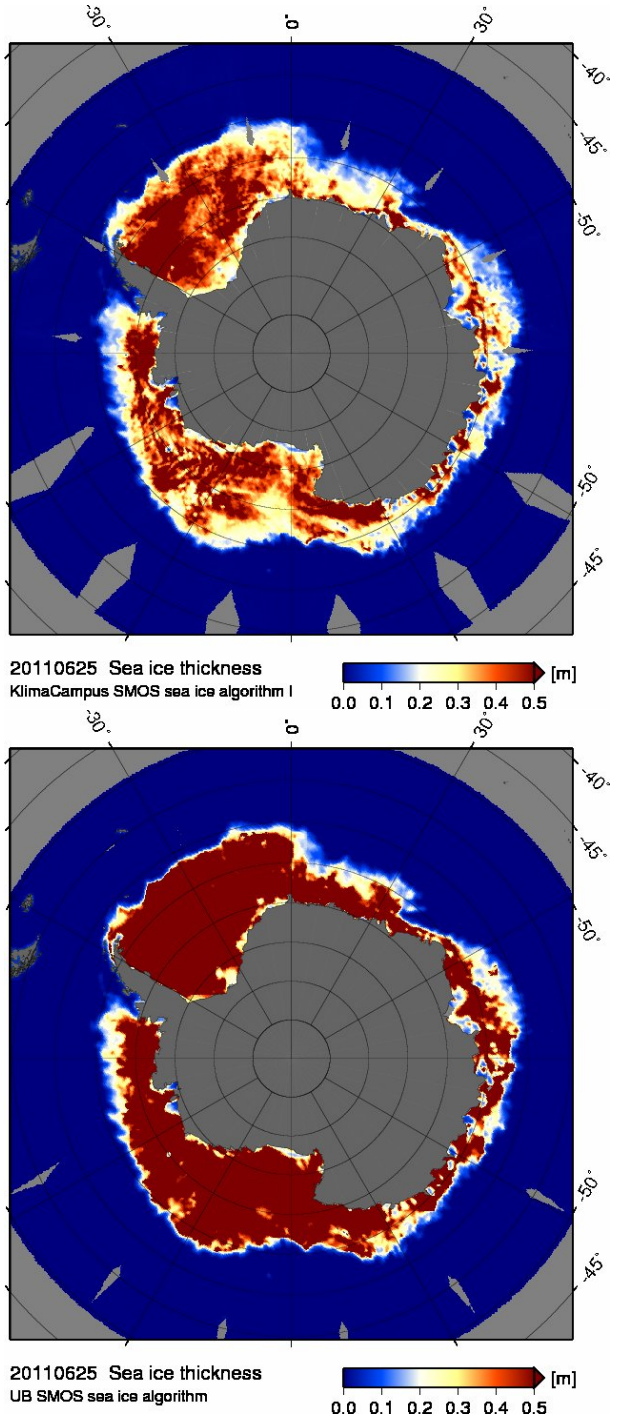

Figure 9.11: SMOS sea ice thickness in Antarctic from UHH and UB. Date: 2011.06.25

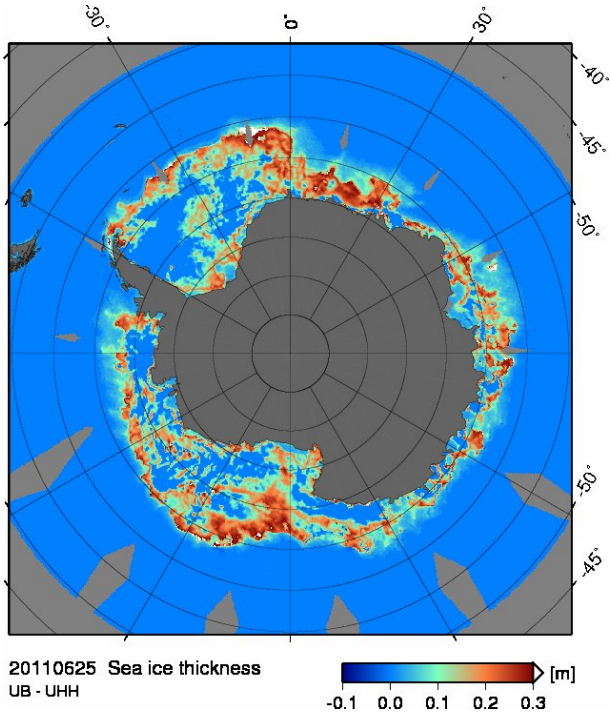

Figure 9.12: SMOS sea ice thickness difference in Antarctic between UB and UHH. Date: 2011.06.25

10 ICEBRIDGE

Nina Maaß

10.1 Comparison with observations

In order to test the validity of our theoretical considerations, we use the incoherent Burke model to simulate brightness temperatures over snow-covered sea ice, and compare these brightness temperature simulations with SMOS brightness temperature measurements. Additionally, we investigate whether brightness temperatures as observed by SMOS over thick Arctic sea ice depend on snow thickness and whether there is a potential for retrieving snow thickness from SMOS observations.

10.2 The IceBridge flight campaign

For simulation of brightness temperatures we use ice and snow thicknesses measured during the NASA Operation IceBridge mission (Kurtz et al., 2012). We use the data from the flight campaign that took place from 14th March to 2nd April, 2012 in the Arctic. The NASA IceBridge Sea Ice Freeboard, Snow Depth, and Thickness (IDCSI2) data set contains derived geophysical data products including sea ice thickness retrieved from the Airborne Topographic Mapper (ATM) laser altimeter, and snow depth retrieved from the IceBridge snow radar. Simultaneously, the ice surface temperature was measured by a KT19.85 infrared pyrometer alongside the ATM instrument. The IceBridge flight tracks and the measured ice and snow thicknesses are depicted in Figure 10.1.

IceBridge sea ice thickness

The footprint size of the ATM laser altimeter is about 1 m $\times$ 268 m. In spring 2009, airborne ATM laser altimeter measurements and temporally and spatially coincident in-situ sea ice thickness measurements were conducted on sea ice north of Greenland (GreenArc campaign). The mean sea ice thickness retrieved from laser altimeter data and the mean in-situ sea ice thickness agreed within 5 cm, while the modal values agreed within 10 cm. From this analysis, the uncertainty associated with IceBridge sea ice thickness estimates is assumed to be 40 cm. (Farrell et al., 2012)

The average ice thickness of all IceBridge ice thickness measurements obtained between 14th March and 2nd April, 2012 is about 4 m, and the flight tracks were mainly located over multi-year ice. Only a very small fraction of the measurements was carried out over ice thicknesses below 1 m ice thickness. Thus, the IceBridge measurements are not suitable for a validation of ice thickness retrieval from SMOS brightness temperatures. However, we here use the IceBridge measurements to examine whether we can use our radiation model to realistically simulate L-band brightness temperatures over snow-covered thick sea ice.

IceBridge snow thickness

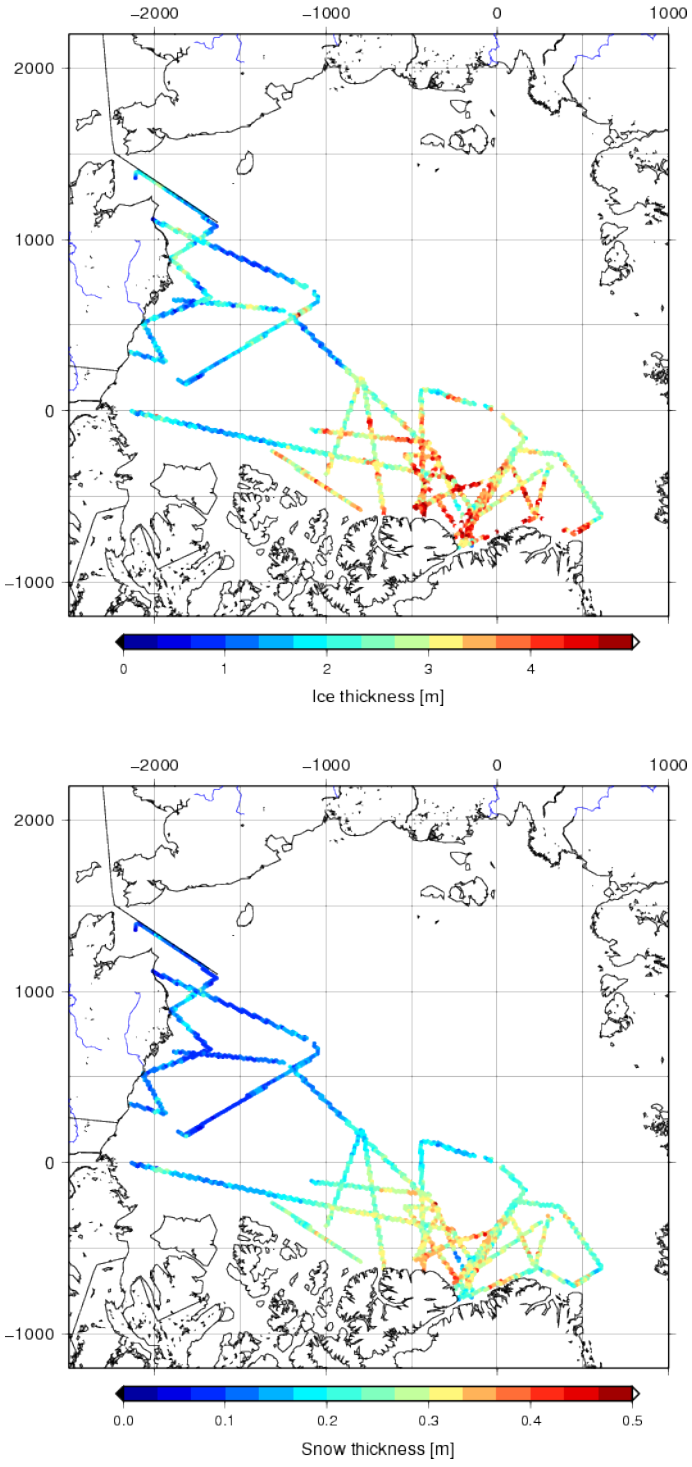

Figure 10.1: Ice thicknesses (upper figure) and snow thicknesses (lower figure) as measured during the IceBridge flight campaign in the Arctic from 14 March to 2 April, 2012. The thicknesses shown here are the average values of all thickness measurements located within a SMOS grid cell. The map is given in polar stereographic projection.

The footprint size of the IceBridge snow radar is about 15 m $\times$ 16 m. The GreenArc campaign served also as a validation for the IceBridge snow thicknesses. The mean snow thickness retrieved from radar data and the mean in-situ snow thickness agreed within 1 cm,

while the modal values agreed within 2 cm (Farrell et al., 2012). The correlation coefficient between the snow thicknesses was r= 0.7, i.e. r^2= 0.49 (Farrell et al., 2012). The agreement between airborne and in-situ measurements was very good over level ice, while the observed differences were larger over multi-year ice, particularly at pressure ridges. In these regions, snow thicknesses differed by up to 20–60 cm (Farrell et al., 2012). A comparison of GreenArc snow thicknesses with climatological snow thicknesses (Warren et al., 1999) revealed a difference of 0.3 cm for the mean values (Kurtz and Farrell, 2011).

IceBridge ice surface temperature
The footprint size of the KT19.85 infrared pyrometer is about 40 m (Kurtz, 2012). Here, we use the KT19.85 temperature data (Krabill, 2012) to estimate the surface temperature of (snow-covered) sea ice. However, the uncertainty of the surface temperature data is unknown (Kurtz, 2012).

10.3 Brightness temperature simulations

General model assumptions
We compare two different brightness temperature simulations with brightness temperatures measured by SMOS. One simulation is performed with the incoherent Burke model with one ice layer and the ice thickness information from IceBridge measurements. In this simulation we neglect a potential snow cover. The other simulation is performed with the incoherent Burke model with one ice layer that is covered by one layer of snow; the ice and snow layer thicknesses are taken from the IceBridge measurements.
We simulate brightness temperatures for every SMOS grid cell that contains at least 50 single IceBridge measurements. For the simulations, we use the mean values of all IceBridge ice and snow thickness measurements that are located within the SMOS grid cell as model input for ice and snow thickness. Ice salinity is estimated from ice thickness using an empirical relationship between ice salinity and ice thickness in the Arctic (Cox and Weeks, 1974):

$$S_{ice}[\text{g/kg}] = 14.24 - 19.39 d_{ice}[\text{m}] \quad \text{for } d_{ice} \leq 0.4 \text{ m} \tag{10.1}$$

$$S_{ice}[\text{g/kg}] = 7.88 - 1.59 d_{ice}[\text{m}] \quad \text{for } d_{ice} > 0.4 \text{ m}. \tag{10.2}$$

This empirical relationship was determined for ice thicknesses up to d_{ice}= 4 m. For thicker ice we use the value for d_{ice}= 4 m, which is S_{ice}= 1.52 g/kg. Water salinity is assumed to be S_{water}= 33 g/kg. Water temperature is assumed to be at the freezing temperature of Arctic sea water, i.e. T_{water}= -1.8°C. Ice and snow temperatures are estimated from the KT19 ice surface temperatures measured during the IceBridge flight campaign. For the snow-free simulations, we use the mean value between the KT19 ice surface temperature and the water temperature as model input for the ice temperature. For the simulations that include a snow layer, we use equations (3.22) and (3.23) to calculate ice and snow temperatures for the model from KT19 ice surface temperatures. As model input for ice concentration, we use ice concentrations that have been retrieved from the 85 GHz channel of SSMIS using the ARTIST Sea Ice (ASI) algorithm (Kaleschke et al., 2001; Spreen et al., 2008). The ice concentration data are given on a polar stereographic grid with 12.5 km grid resolution. The data are 5-day median filtered in order to mitigate unrealistic short-term sea ice concentration variations due to weather effects. For snow density we assume a value of ρ_{snow}= 260 kg/m^3, which is the mean snow density determined from in-situ measurements during the GreenArc campaign (Farrell et al., 2012). According to the IceBridge surface temperatures, we had

freezing conditions during the campaign. Thus, we expect the ice to be covered by dry snow and assume a snow wetness of W= 0% in the model. For the calculation of ice permittivity, we use the equations for multi-year ice (Table 2.2).

Modifications
Additionally to the above described approach for the simulation of brightness temperatures, we do two simulations with the following constraints and changes. Ice concentration has a large impact on the modelled brightness temperatures. The difference between the brightness temperature of thick ice (for our purposes: $d_{ice} > 0.5$ m in the Arctic) and water is typically in the order of 100 K. An error of only 5% in the ice concentration would thus cause an error in the brightness temperature of about 0.05 $\times$ 100 K= 5 K. The uncertainty of ASI ice concentrations is higher for low ice concentrations than for high ice concentrations. The theoretically expected standard deviation of ice concentration is about 25% for ice concentrations around c_{ice}= 0%, about 13% for c_{ice}= 50%, and about 6% for c_{ice}= 100% (Spreen et al., 2008). A comparison with in-situ data and high-resolution satellite data revealed a standard deviation of almost 5% for ice concentrations $c_{ice} > 90\%$ (Andersen et al., 2007). Thus, we also consider simulations that are constrained to pixels that have an almost closed ice cover. For these simulations we use only pixels with ice concentrations $c_{ice} \geq 95\%$, and set the ice concentration in the model to c_{ice}= 100%.
Furthermore, the pixels included in our analysis are constrained with respect to the ice surface temperature. Because we do not know how reliable the KT19 surface temperature information is, we also perform simulations for a fixed surface temperature. Therefore, we calculate the average surface temperature from all KT19 measurements that are included in our analysis. As model input for the surface temperature we then use this average value and include only pixels with surface temperatures that are within one standard deviation of the average surface temperature. The average surface temperature for all pixels with ice concentrations $c_{ice} \geq 95\%$ is $< T_{surf} >$= -32.8°C, and the standard deviation is $\sigma_{T_{surf}}$= 4.5°C.
Thus, we here compare SMOS brightness temperatures with brightness temperature simulations that neglect and that include a snow layer
1) for all ice concentrations and surface temperatures; ice concentration and surface temperature are variable,
2) only for almost completely ice-covered cases ($c_{ice} \geq 95\%$), but for all surface temperatures; the ice concentration is set to c_{ice}= 100%, surface temperature is variable, and
3) only for almost completely ice-covered cases ($c_{ice} \geq 95\%$) and only for surface temperatures within one standard deviation of the average surface temperature (-37.3°C$< T_{surf} <$ -28.3°C); the ice concentration is set to c_{ice}= 100%, the surface temperature is set to the average value T_{surf}= -32.8°C.

10.4 Comparison of modelled and observed brightness temperatures

For the comparison with simulated brightness temperatures, we use all SMOS brightness temperatures with incidence angles θ between 0 and 60°. For each SMOS pixel we average the measured brightness temperatures θ= 0° – 10°, for the remaining incidence angles we average the brightness temperatures over 5° incidence angle intervals, i.e. for 10° – 15°, 12.5° – 17.5°, 15° – 20°, ..., 55° – 60°. The simulations are calculated for the corresponding mean incidence angles θ= 5°, 12.5°, 15°, 17.5°, ..., 57.5°.
The results for 1) all ice concentrations and all ice surface temperatures are shown in the Figures 10.2 to 10.5, and the results for 3) the pixels constrained to closed ice cover cases

and a surface temperature within one standard deviation of the average value are shown in the Figures 10.6 to 10.9. The root mean square deviations, the mean deviations, and the correlation coefficients between the simulated and the measured brightness temperatures, as well as the corresponding numbers of compared data points for all simulation scenarios 1) – 3) are given in Table 10.1.

1) Results for all ice concentrations and ice surface temperatures
For this simulation scenario, the simulations that neglect and that include a snow layer differ considerably for horizontal polarisation, while the impact of a snow layer is smaller for the simulations at vertical polarisation. For both polarisations, the modelled brightness temperatures increase, when a snow layer is added. Contemporaneously, the range of brightness temperatures decreases, when a snow layer is added.
At horizontal polarisation, brightness temperatures at low incidence angles ($\theta < 15°$) increase by about 13 K, when a snow layer is added, while brightness temperatures at high incidence angles ($\theta > 50°$) increase by about 26 K, when a snow layer is added. The range of brightness temperatures for different incidence angles decreases from about 60 K, when neglecting the snow cover, to about 47 K, when including the snow cover.
In contrast to the results at horizontal polarisation, including a snow layer causes the simulated brightness temperatures at vertical polarisation to increase more for lower incidence angles than for higher incidence angles. At vertical polarisation, brightness temperatures at low incidence angles ($\theta < 15°$) increase by about 10 K, when a snow layer is added, while brightness temperatures at high incidence angles ($\theta > 50°$) increase only by about 3 K, when a snow layer is added. The range of values decreases from about 35 K, when neglecting the snow cover, to about 28 K, when including the snow cover.
At horizontal polarisation, including the snow layer considerably reduces the deviations between simulated and measured brightness temperatures (Table 10.1). When neglecting the snow layer, the simulations underestimate the measured brightness temperatures on average by 22.9 K, as compared to an average underestimation by 4.4 K, when the snow layer is included. The root mean square deviation decreases from 24.6 K for the simulations without a snow cover to 7.8 K, when including the snow layer. The correlation coefficients are rather similar, being r^2= 0.44, when the snow is neglected, and r^2= 0.38, when the snow layer is included.
At vertical polarisation, the simulations that neglect the snow cover on average underestimate the measured brightness temperatures by 5.8 K, while the measured brightness temperatures are overestimated by 2.1 K for the simulations that include the snow cover. The root mean square deviation of the brightness temperatures reduces from 8.6 K, when snow is neglected, to 5.6 K, when snow is included. The correlation coefficient is relatively low for both scenarios, r^2= 0.25, when snow is neglected, and r^2= 0.19, when snow is included.

2) Results for the closed ice cover cases and all surface temperatures
When we consider only the pixels that are almost completely ice-covered ($c_{ice} \geq 95\%$), the number of data points for the comparison reduces from N= 22798 to N= 17756. Compared to the scenario 1) simulations, the mean deviations and the root mean square deviations decrease, and the correlation coefficients increase for scenario 2), except for the mean deviation and the root mean square deviation for the simulations with snow at vertical polarisation, which increase slightly (Table 10.1).

3) Results for the closed ice cover cases and a fixed surface temperature

Table 10.1: Root mean square deviations RMSD, mean deviations MD, and correlation coefficients r^2 for simulated brightness temperatures and brightness temperatures as measured by SMOS for horizontal and vertical polarisation. The columns f(c_{ice}), f(T_{surf}) and $c_{ice} \geq 95\%$, f(T_{surf}) and $c_{ice} \geq 95\%$, $\Delta T_{surf} < 1\sigma_{T_{surf}}$ give the results for the simulation scenarios that are described in section 10.3 and indicated with 1) and 2) and 3), respectively.

			f(c_{ice}), f(T_{surf})	$c_{ice} \geq 95\%$, f(T_{surf})	$c_{ice} \geq 95\%$, $\Delta T_{surf} < 1\sigma_{T_{surf}}$
H-Pol	RMSD [K]	no snow	24.6	20.1	20.0
		snow	7.8	5.2	4.4
	MD [K]	no snow	22.9	18.3	18.5
		snow	4.4	-1.1	-0.9
	r^2	no snow	0.44	0.49	0.58
		snow	0.38	0.50	0.61
V-Pol	RMSD [K]	no snow	8.6	5.8	5.2
		snow	5.6	7.9	7.4
	MD [K]	no snow	5.8	1.8	2.0
		snow	-2.1	-6.7	-6.5
	r^2	no snow	0.25	0.28	0.39
		snow	0.19	0.26	0.39
Data points N			22798	17756	12084

Here, we consider only the pixels that are both, almost completely ice-covered and have a surface temperature that is within one standard deviation of the average surface temperature, i.e. pixels with -37.3°C< T_{surf} <-28.3°C. These conditions are fulfilled by N= 12084 data points. Compared to scenarios 1) and 2), the root mean square deviations for scenario 3) decrease, and the correlation coefficients increase.
At horizontal polarisation, the root mean square deviation between simulated and measured brightness temperatures is 20.0 K, when the snow layer is neglected, and decreases to 4.4 K, when the snow layer is included. The correlation coefficient is r^2= 0.58 without snow, and r^2= 0.61 with snow.
At vertical polarisation, the correlation coefficient is r^2= 0.39 for both the simulations without snow and the simulations with snow. The corresponding root mean square deviations are 5.2 K for the simulations without snow, and 7.4 K for the simulations with snow.

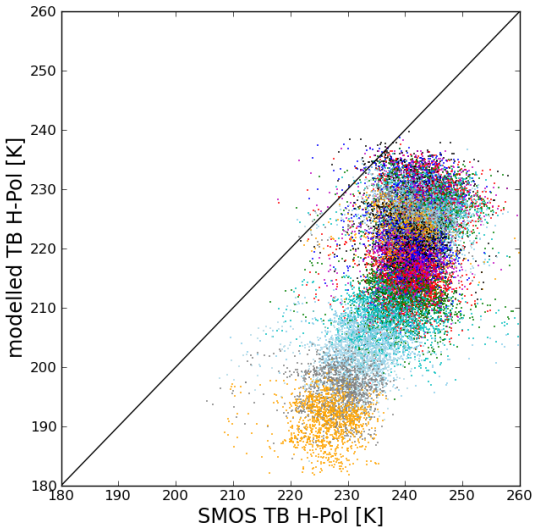

Figure 10.2: Horizontally polarised brightness temperatures as measured by SMOS and as modelled for IceBridge **ice thicknesses** using the model for **one ice layer**. The colors indicate the incidence angle increasing from 0° at the upper right corner to 60° at the lower left corner of the data cloud. The root mean square deviation between the brightness temperatures is 24.6 K, the correlation coefficient is r^2= 0.44 (for N= 22798).

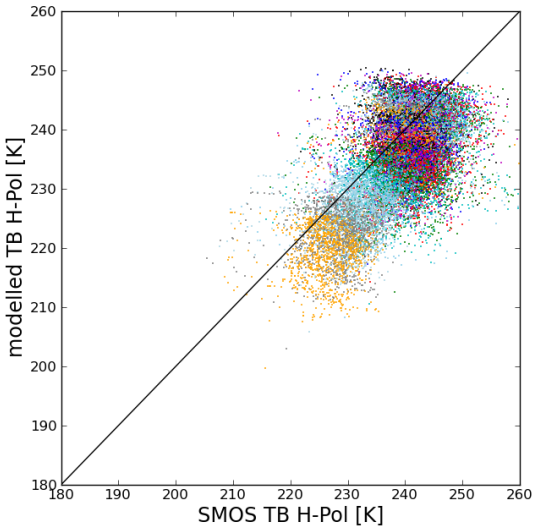

Figure 10.3: Horizontally polarised brightness temperatures as measured by SMOS and as modelled for IceBridge **ice and snow thicknesses** using the model for **one ice and one snow layer**. The colors indicate the incidence angle increasing from 0° at the upper right corner to 60° at the lower left corner of the data cloud. The root mean square deviation between the brightness temperatures is 7.8 K, the correlation coefficient is r^2= 0.38 (for N= 22798).

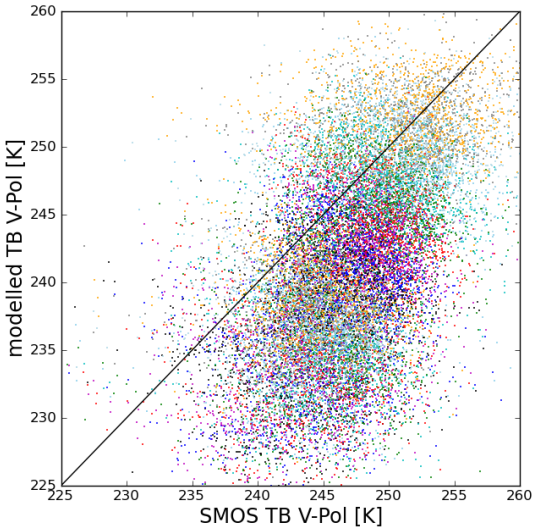

Figure 10.4: Vertically polarised brightness temperatures as measured by SMOS and as modelled for IceBridge **ice thicknesses** using the model for **one ice layer**. The colors indicate the incidence angle increasing from 0° at the lower left corner to 60° at the upper right corner of the data cloud. The root mean square deviation between the brightness temperatures is 8.6 K, the correlation coefficient is r^2= 0.25 (for N= 22798).

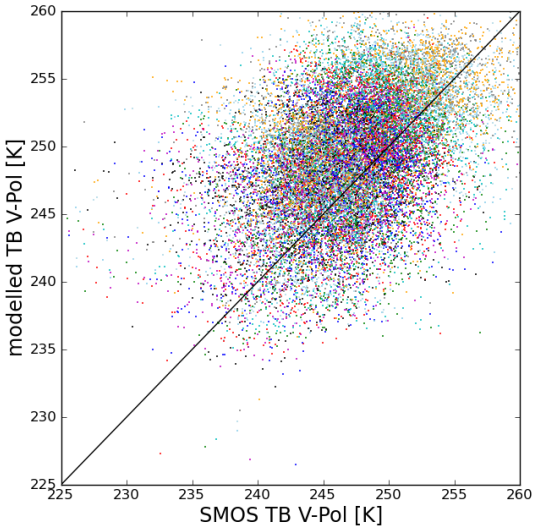

Figure 10.5: Vertically polarised brightness temperatures as measured by SMOS and as modelled for IceBridge **ice and snow thicknesses** using the model for **one ice and one snow layer**. The colors indicate the incidence angle increasing from 0° at the lower left corner to 60° at the upper right corner of the data cloud. The root mean square deviation between the brightness temperatures is 5.6 K, the correlation coefficient is r^2= 0.19 (for N= 22798).

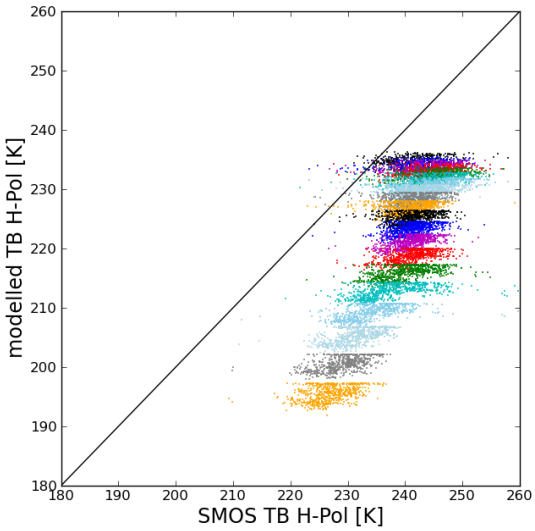

Figure 10.6: Horizontally polarised brightness temperatures as measured by SMOS and as modelled for IceBridge **ice thicknesses** using the model for **one ice layer**. The colors indicate the incidence angle increasing from 0° at the upper right corner to 60° at the lower left corner of the data cloud. Only data points with $c_{ice} \geq 95\%$ and -37.3°C< T_{surf} <-28.3°C are included. The root mean square deviation between the brightness temperatures is 20.0 K, the correlation coefficient is r^2= 0.58 (for N= 12084).

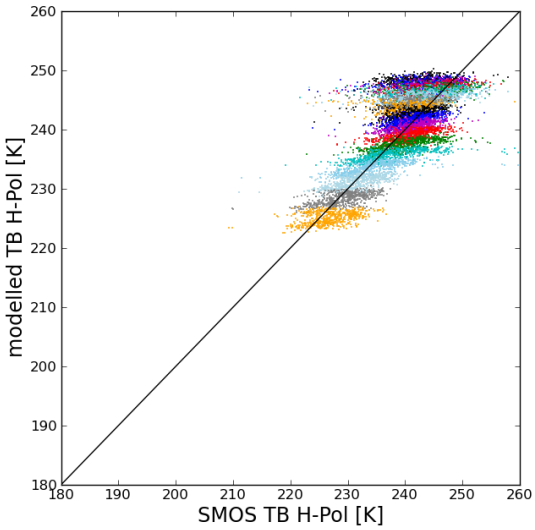

Figure 10.7: Horizontally polarised brightness temperatures as measured by SMOS and as modelled for IceBridge **ice and snow thicknesses** using the model for **one ice and one snow layer**. The colors indicate the incidence angle increasing from 0° at the upper right corner to 60° at the lower left corner of the data cloud. Only data points with $c_{ice} \geq 95\%$ and -37.3°C< T_{surf} <-28.3°C are included. The root mean square deviation between the brightness temperatures is 4.4 K, the correlation coefficient is r^2= 0.61 (for N= 12084).

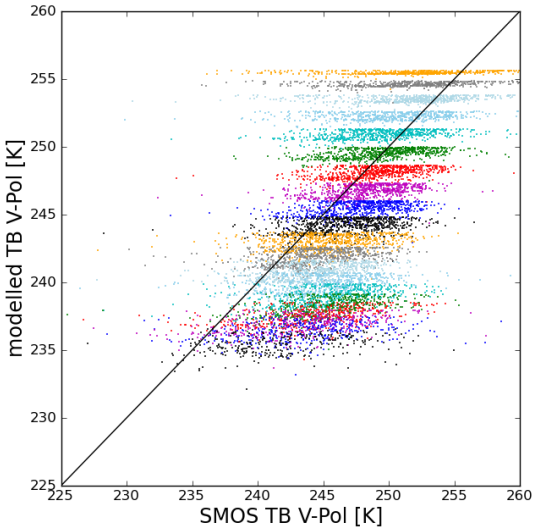

Figure 10.8: Vertically polarised brightness temperatures as measured by SMOS and as modelled for IceBridge **ice thicknesses** using the model for **one ice layer**. The colors indicate the incidence angle increasing from 0° at the lower left corner to 60° at the upper right corner of the data cloud. Only data points with $c_{ice} \geq 95\%$ and -37.3°C< T_{surf} <-28.3°C are included. The root mean square deviation between the brightness temperatures is 5.2 K, the correlation coefficient is r^2= 0.39 (for N= 12084).

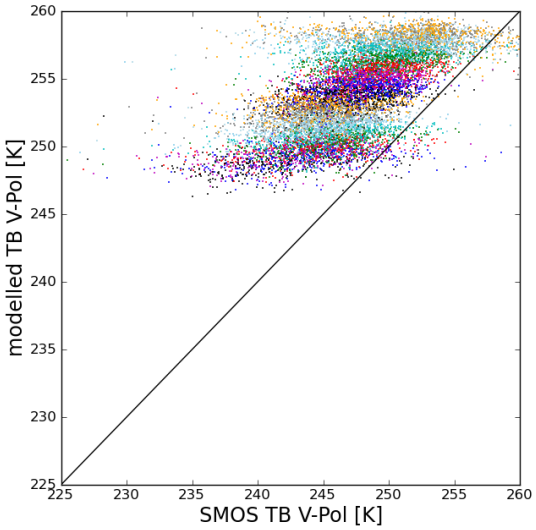

Figure 10.9: Vertically polarised brightness temperatures as measured by SMOS and as modelled for IceBridge **ice and snow thicknesses** using the model for **one ice and one snow layer**. The colors indicate the incidence angle increasing from 0° at the lower left corner to 60° at the upper right corner of the data cloud. Only data points with $c_{ice} \geq 95\%$ and -37.3°C< T_{surf} <-28.3°C are included. The root mean square deviation between the brightness temperatures is 7.4 K, the correlation coefficient is r^2= 0.39 (for N= 12084).

10.5 Summary and Discussion

In order to test the validity of our results from the theoretical investigations, we used snow and ice thickness measurements from the IceBridge flight campaign in spring 2012 in the Arctic to simulate brightness temperatures and compared these simulated brightness temperatures with brightness temperatures measured by SMOS. The IceBridge measurements were mainly taken over thick multi-year ice. Thus, they were not suitable for the validation of sea ice thickness retrieval from SMOS. However, the ice and snow thickness information was used here to validate the capability of the incoherent Burke model to realistically simulate brightness temperatures.
For the comparison of simulated and measured brightness temperatures, we calculated the root mean square deviations and the correlation coefficients between the brightness temperatures. The smaller the root mean square deviation, the better our model represents brightness temperatures as measured with SMOS. We should be careful, when we consider the correlation coefficient, because a high correlation between the brightness temperatures does not necessarily mean that the model and the observations agree well. A high correlation here means, that the brightness temperatures can be related to each other without large errors, when a certain linear function is used, which is not necessarily the identity function. Provided that there is a relationship between the two quantities, a high correlation and a contemporaneous high root mean square deviation would mean, that our model does not represent the observations well, even if the two independent data sets are highly related with each other.
For comparison with brightness temperatures observed with SMOS, we neglected the snow cover in one simulation and included the snow cover in the other simulation. At horizontal polarisation, brightness temperatures modelled for a snow cover on ice agreed considerably better with the observed SMOS brightness temperatures than the brightness temperatures modelled for snow-free sea ice. For the simulations with snow, the mean deviation and the root mean square deviation decreased, while the correlation remained approximately constant. At vertical polarisation, the difference between simulations without and with a snow cover was considerably smaller. A result that confirmed the findings from the previous sections.
The simulations were performed for different constraints concerning the ice concentration and the ice surface temperature of the included pixels. In one scenario we considered only pixels that were almost completely ice-covered ($c_{ice} \geq 95\%$) and that had a surface temperature within one standard deviation of the average surface temperature measured during the IceBridge campaign. For this scenario, ice concentration and ice surface temperature were set to constant values. At vertical polarisation, brightness temperatures were less affected by these constraints than at horizontal polarisation. At vertical polarisation, the mean deviation and the root mean square deviation between the SMOS observations and the snow simulations even increased slightly, when we constrained the compared data accordingly. The root mean square deviations between the simulated and the measured brightness temperatures at vertical polarisation ranged between 5.2 and 8.6 K. However, the correlation coefficient r^2 increased from 0.25 (without snow) and 0.19 (with snow) to 0.39, when we considered only pixels with high ice concentrations and certain surface temperatures.
At horizontal polarisation, the agreement between simulated and measured brightness temperatures improved considerably, when we excluded pixels with low ice concentrations and ice surface temperatures outside the defined range and used constant values instead. For both, the simulations that neglect a snow layer and the simulations that include a snow layer, the

mean deviation and the root mean square deviation decreased, while the correlation coefficient increased. For the simulations that include a snow layer, the mean deviation decreased from +4.4 to -0.9 K, the root mean square deviation decreased from 7.8 to 4.4 K, and the correlation coefficient r^2 increased from 0.38 to 0.61. For these constrained pixels, the root mean square deviation between simulated and measured brightness temperatures decreased from 20.0 K, when the snow layer was neglected, to 4.4 K, when the snow layer was included in the simulations. The mean deviation decreased from 18.5 K (without snow) to -0.9 K (with snow). The correlation coefficients were very similar for the simulations without snow (r^2= 0.58) and with snow (r^2= 0.61).

The reasons for the deviations between simulated and observed brightness temperatures are mainly the remaining uncertainties for the ice and snow thicknesses, the ice concentration, the ice temperature, and the ice salinity. While we had information on the former ice parameters, the ice salinity was only roughly estimated from the ice thickness using an empirical relationship between ice salinity and thickness. The IceBridge measurements were mainly taken over thick sea ice. The average value was 4 m and there were only very few measurements over sea ice with a thickness lower than 1 m. At these high ice thicknesses, ice thickness itself does not have a large impact on brightness temperature, whereas the salinity of thick sea ice is usually low, and, according to our studies in section 3.2, brightness temperature sensitivity to ice salinity variations is very high for sea ice with low salinities. Hence, knowledge on ice salinity is more crucial for thick multi-year ice with low salinities, as considered here, than for thin first-year ice with high salinities.

11 EM BALTIC

Nina Maaß

In order to validate the ice thickness retrieval based on SMOS brightness temperature measurements, we here compare ice thicknesses retrieved from SMOS with ice thicknesses as measured during an airborne EM ice thickness survey in March, 2011 in the Sea and Bay of Bothnia.

11.1 EM Bird ice thickness measurements

For the validation of SMOS ice thicknesses, we use ice thicknesses measured during an EU SafeWin project's winter field campaign in the northern Baltic Sea. Between 2nd and 7th March, 2011 a helicopter-towed EM Bird measured the ice thickness in the Bay of Bothnia and the northern Sea of Bothnia. All flight tracks of the 11 flights that were performed during the campaign are indicated in Figure 11.1.

The EM ice thickness sounding system consists of a laser altimeter and an assembly of coils that transmit and receive low-frequency EM fields. The transmitted and received EM fields give the sensor's height above the conductive seawater surface. The laser altimeter measures the sensor's altitude above the ice or snow surface. Over sea ice the difference between the sensor's height above the ice surface and its height above the seawater corresponds to the total ice thickness, i.e. the sum of the ice and snow thickness. (Haas et al., 2009)

The EM Bird used in the SafeWin field campaign operates at a frequency of 4.06 kHz. The sampling frequency is 10 Hz, corresponding to a spacing of approximately 3 – 4 m between subsequent measurements. The laser altimeter has a sampling frequency of 100 kHz. The EM Bird is flown 10 to 20 m above the ice surface. The strength of the measured EM field represents the average field of an area approximately 3.7 times the instrument's altitude above the ice surface, i.e. the footprint is approximately between 37 and 74 m. (Haas and Casey, 2012)

The accuracy of EM Bird ice thickness measurements over level ice is about 10 cm (Haas et al., 2009), whereas ice ridges can be underestimated by up to 50% (Haas and Jochmann, 2003). Therefore, sea ice thickness distributions obtained from EM Bird measurements are most accurate with respect to their modal thickness (Haas et al., 2010).

Because measuring ice thickness with the EM Bird is only possible due to the higher conductivity of seawater compared to sea ice, the brackish nature of the Baltic Sea provides challenging conditions for EM ice thickness measurements. Additionally, the accuracy of EM Bird ice thickness measurements in the Baltic Sea is further decreased by 1) shallow waters and by 2) freshwater layers under fast ice. 1) In brackish waters shallower than about 10 to 15 m ice thicknesses are overestimated by the EM Bird, because currents are induced in the seafloor, which is usually less conductive than seawater. 2) Freshwater layers can form under fast ice due to river runoff from land. These freshwater layers have very low conductivities. Both effects cause that the ice thickness measurements carried out over fast ice close

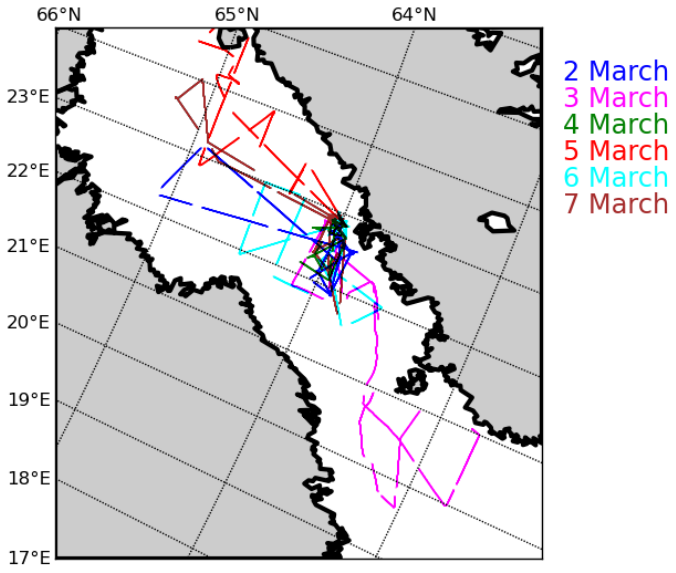

Figure 11.1: Overview of all EM Bird ice thickness flights performed during the SafeWin campaign in March, 2011. The colors indicate the date of the flights.

to the coast are less reliable. In this regard, the ice thickness measurements made in the region around the Hailuoto island (approximately at the geographical coordinates 65.0°N and 24.8°E) and along the shore west of Vaasa (approximately at 63.1°N and 21.6°E) are affected most for this flight campaign. (Haas and Casey, 2012)

11.2 Ice thickness retrieval with SMOS

For the retrieval of ice thickness, we here use horizontally and vertically polarised brightness temperatures with incidence angles $\theta \leq 50°$. We exclude all SMOS measurements that have a land fraction of more than 10% within a square area of 40 km $\times$ 40 km around the SMOS grid cell's centre point. The land-sea mask we use to determine the land fraction is the Global Self-consistent Hierarchical, High-resolution Shoreline Database (GSHHS) (Wessel and Smith, 1996).

Model assumptions

For the retrieval of ice thickness from SMOS brightness temperatures we use the incoherent Burke model with one ice and one snow layer. The retrieval requires information on 1. ice concentration, 2. ice temperature, 3. ice salinity, 4. water salinity, 5. water temperature, and 6. snow cover:

1. **Ice concentration**: Commonly, ice concentration is retrieved from passive microwave brightness temperatures using one of the available sea ice concentration algorithms. We considered using ice concentration maps obtained from the ASI algorithm applied to AMSR-E brightness temperature measurements (Kaleschke et al., 2001; Spreen et al., 2008) with tie-points adjusted to Baltic Sea conditions (Maaß and Kaleschke, 2010). However, these ice concentration maps showed lower ice concentrations than can be

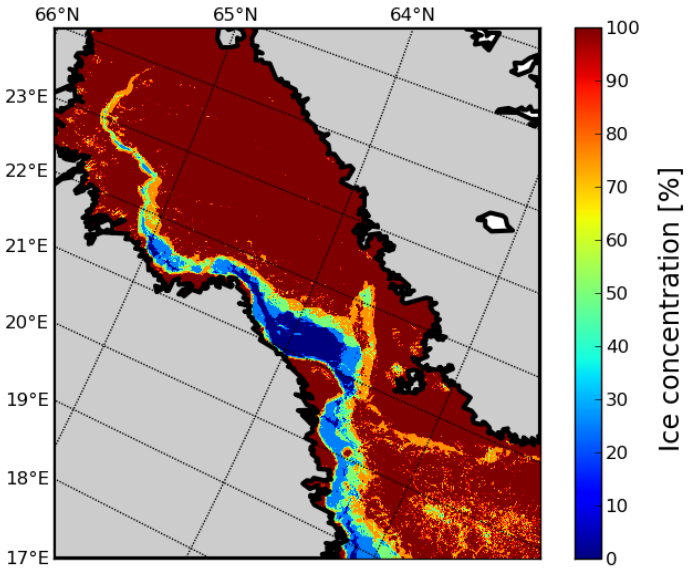

Figure 11.2: Mean ice concentration for 2nd – 7th March, 2011 obtained from averaging classified MODIS images from the 3rd, 5th, 6th, and 8th March. In the classification, each MODIS pixel (resolution 250 m x 250 m) is determined to be covered by water or ice.

visually inferred from the high-resolution optical MODIS images available for the area and time period considered here. The MODIS images taken over the Bay and Sea of Bothnia on the 3rd, 5th, 6th, and 8th March are cloud-free over large areas. Thus, in this case, these images with a resolution of 250 m $\times$ 250 m enable us to determine the ice coverage more reliably than the more coarsely resolved ice concentration maps based on passive microwave measurements. We produce ice concentration maps by applying a simple classification approach to the MODIS images at band 1, which measures at wavelengths λ= 620 – 670 nm. All MODIS pixels with reflectivities $r < 0.2$ are assigned to be open water pixels; all pixels with reflectivities $r \geq 0.2$ are assigned to be ice pixels. First, we classify each available MODIS image and then we average over all days. The resulting ice concentration field (Figure 11.2) is used as input for our radiation model.

2. **Ice surface temperature**: We use the MODIS IST MOD029 ice surface temperature product (Hall et al., 2004) to estimate the ice temperature of the ice in the Bay and Sea of Bothnia during the SafeWin field campaign. The average ice surface temperature of all MODIS pixels located within the area where the EM Bird measurements took place is T_{surf}= -3.4°C. Thus, this value is used as model input for the ice surface temperature.

3. **Ice salinity**: Sea ice salinity in the Baltic Sea typically takes values between 0.2 and 2 g/kg (Hallikainen, 1992). In the Bay and Sea of Bothnia ice salinities are generally lower than in the central Baltic Sea and its western parts. Due to desalination processes occuring in ice, we expect the ice salinity of older and thicker ice to be lower than the ice salinity of younger and thinner ice. According to Finnish ice charts, the campaign area south of approximately 63.5°N had been completely ice-covered for about one month before the EM Bird measurements were carried out from 2nd to 7th March, 2011. Most of the remaining area covered by the flight campaign had been almost

completely ice-covered for more than two months, when the campaign was carried out. The ice thicknesses measured during the flight campaign are mainly between 30 and 60 cm. Thus, we suppose that S_{ice}= 0.5 g/kg is a reasonable assumption for the average ice salinity of the ice in the area and for the time period considered here.

4. **Water salinity**: Water salinity is assumed to be S_{water}= 4 g/kg (Janssen et al., 1999).

5. **Water temperature**: Water is assumed to be at freezing temperature. For an ice salinity of S_{water}= 4 g/kg, the corresponding temperature of water at the freezing point is T_{water}= -0.2°C (Fofonoff and Millard, 1983).

6. **Snow cover:** We estimate the snow thickness from the empirical relationship between ice and snow thickness for Baltic Sea conditions given in equations (3.12) and (3.13). On the one hand, we thus account for the impact of a snow cover on brightness temperatures above snow-covered ice, as investigated in Chapter 3.4. On the other hand, the ice thicknesses measured by the EM Bird are total ice thicknesses (ice + snow thickness). In the following comparison, we thus retrieve total ice thicknesses from SMOS brightness temperatures and compare these to total ice thicknesses measured by the EM Bird. Snow is assumed to be dry and to have a density of ρ_{snow}= 360 kg/m^3, with ρ_{snow}= 360 kg/m^3 being a representative value for an average snow density between typical values for new snow (ρ_{snow}= 225 kg/m^3) and water-soaked snow (ρ_{snow}= 450 kg/m^3) in the Baltic Sea (Saloranta, 2000).

From brightness temperatures to total ice thicknesses
In order to retrieve ice thickness from brightness temperatures measured by SMOS, we use the incoherent Burke model for one ice and one snow layer to model brightness temperatures for a range of incidence angles and a range of total ice thicknesses. The considered range of incidence angles is θ= 5°, 12.5°, 17.5°, ..., 47.5° and the range of total ice thicknesses is d_{total}= 0 cm, 6 cm, 12 cm, 18 cm, 24 cm, ..., 90 cm.
For ice concentration, ice temperature and salinity, water temperature and salinity, and the snow cover we make the assumptions as given above. For the retrieval of ice thickness, we first collect all brightness temperatures measured by SMOS during the time period 2nd – 7th March, 2011. We average all brightness temperatures with incidence angles θ between 0° and 10°; for the remaining incidence angles brightness temperatures are averaged over 5° incidence angle intervals (i.e. for 10° – 15°, 15° – 20°, ..., 45° – 50°). In a second step, we calculate the root mean square deviations between these averaged SMOS brightness temperatures and the brightness temperatures modelled for θ= 5°, 12.5°, 17.5°, ..., 47.5°. The deviations are calculated for all model calculations with different total ice thicknesses (d_{total}= 0 cm, 6 cm, 12 cm, ..., 90 cm). The ice thickness for that the root mean square deviation between measured and modelled brightness temperatures over the considered incidence angle range is lowest is then the ice thickness we retrieve from SMOS. This ice thickness is retrieved separately for horizontal and for vertical polarisation, as well as for brightness temperature intensity.

11.3 Validation approach 1

Comparison of ice thicknesses measured by the EM Bird and ice thicknesses retrieved from SMOS is challenging, because every SMOS measurement represents an area of about 35 – 50 km × 35 – 50 km (depending on incidence angle), while single EM Bird measurements

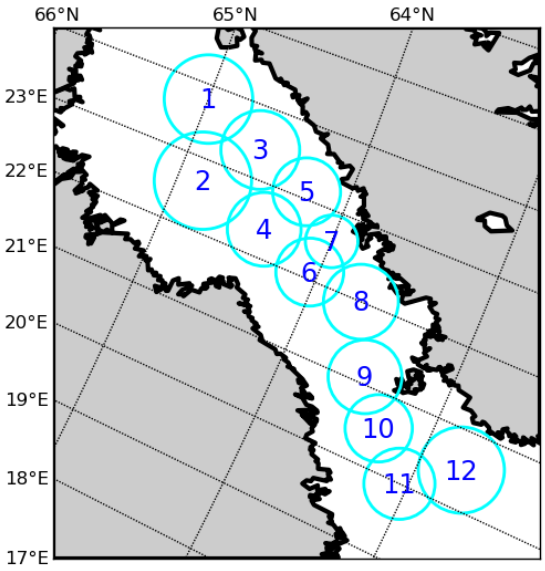

Figure 11.3: Numbering of the 12 circles used for the comparison of ice thicknesses as measured by the EM Bird and as retrieved from SMOS brightness temperatures.

have footprints in the order of 50 m $\times$ 50 m. In addition, SMOS measurements are located on a regular grid, while the EM Bird flight tracks are distributed irregularly. We choose to divide the area covered by the SafeWin campaign's flight tracks into 12 circular areas. We assign a number to each of the 12 circles (Figure 11.3) and assume that the ice thickness distribution within each of these circles is reasonably represented by the EM Bird ice thicknesses (Figures 11.4 and 11.5). For comparison, we show the results of a more traditional approach on the basis of a gridded field in section 11.4.

SMOS data selection

For each circle, we include all SMOS measurements whose centre points are located within a circular area defined by the corresponding validation circle's centre point and a radius of 0.75 times the radius of the corresponding circle (Figures 11.4 and 11.5). The factor 0.75 is chosen quite arbitrarily. It is a compromise between including as many measurements as possible and excluding SMOS measurements that represent large areas outside the circle.
The EM Bird flight tracks located within circle nos. 9 and 12 are single lines through the circles rather than covering representatively the defined circular areas. Thus, for circle no. 9 we exclude the SMOS measurements located north of 63.6°N, and for circle no. 12 we exclude the SMOS measurements located south of 62.65°N.

The ice conditions

The MODIS images for the 3rd March (Figure 11.4) and the 6th March (Figure 11.5) show the dynamical behaviour of ice in the Bay and Sea of Bothnia during the examined time period. In particular, within the circle nos. 8, 10, and 12 the ice cover changes within the three days from 3rd to 6th March. According to the MODIS images, in circle no. 8, there is a large open water area on 3rd March, whereas the circular area appears to be completely ice-covered on the 6th March. In contrast, the large linear opening in the sea ice cover within

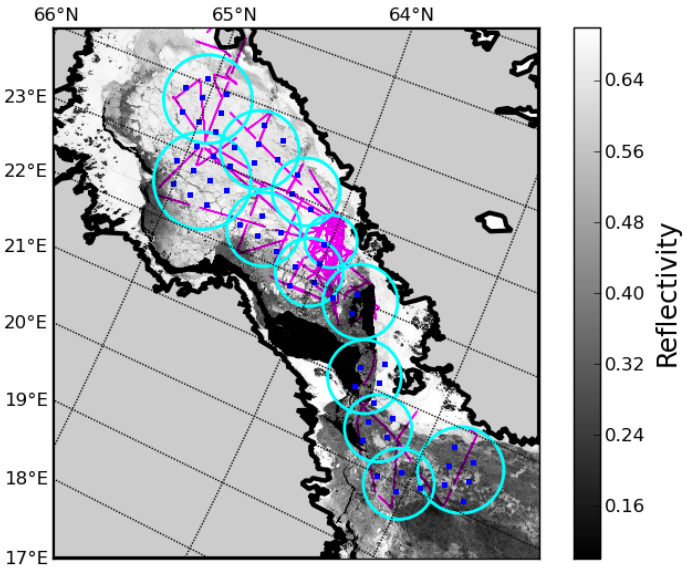

Figure 11.4: Distribution of EM Bird and SMOS measurements in the Bay and Sea of Bothnia and the 12 circular areas we choose for comparison of ice thicknesses. The pink lines indicate EM Bird flight tracks, the blue dots indicate the positions of SMOS measurements. These are overlaid on a MODIS image showing the reflectivities in band 1 (wavelength 620 – 670 nm) on 3rd March, 2011.

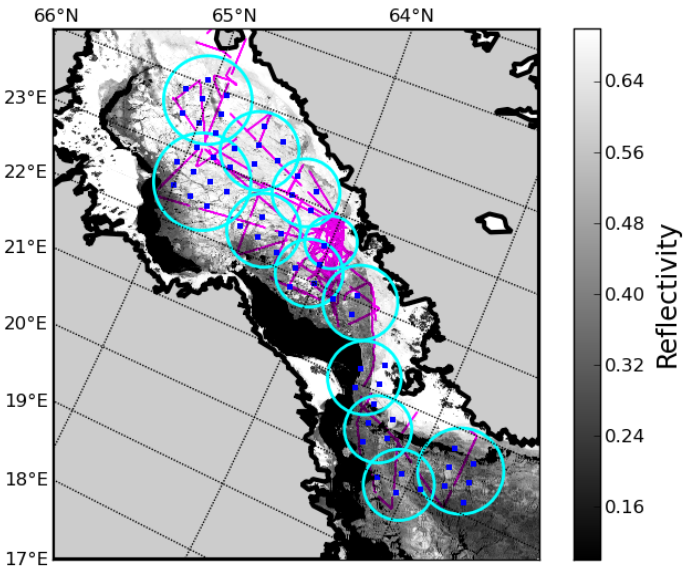

Figure 11.5: For figure description see caption of Figure 11.4, except that here the underlying MODIS image is from 6th March, 2011.

the circle nos. 10 and 12 that is visible on 6th March, had been a closed ice cover on 3rd March. Thus, in these areas (circle nos. 8, 10, and 12), the assumption of a constant ice cover for the duration of the campaign may cause more difficulties than in the other areas.

11.3.1 Results

First, we compare the ice thickness distributions as measured by the EM Bird with ice thicknesses retrieved from SMOS brightness temperature intensities for the 12 circles (Figures 11.6 and 11.7). Thereafter, we compare the modal ice thicknesses obtained from the EM ice thickness distributions with the ice thicknesses as retrieved from SMOS brightness temperatures at horizontal and at vertical polarisation, as well as from brightness temperature intensities. (Figures 11.8 to 11.11).

EM Bird ice thickness distributions
The ice thickness distributions as measured by the EM Bird for the 12 circles have quite similar shapes (Figures 11.6 and 11.7). For most of the circles, more than two-thirds of the measured ice thicknesses take values between 0 and 1 m. The distributions have quite long, exponential tails representing ice thicknesses of up to 5 m or even more (e.g. for circle nos. 9 and 10, but ice thicknesses $d_{ice}>$ 5 m not depicted here).
For eight out of the twelve circles, 69 – 85% of the measured ice thicknesses are below 1 m, and 13 – 21% of the ice thicknesses are between 1 and 2 m (circle nos. 1 – 6, 11, 12). For the remaining four circles, circle nos. 7, 8, 9, and 10, ice thicknesses below 1 m account for 58%, 69%, 54%, and 39%, respectively; and ice thicknesses between 1 and 2 m account for 25 – 29% of the measured ice thicknesses. These four circles with the highest ice thicknesses are the four circles that are closest to the Finnish coast west of Vaasa (approximately at 63.1°N and 21.6°E). Thus, their locations coincide with the region, where the EM Bird tends to overestimate ice thickness due to shallow waters and potential freshwater layers underneath the fast ice (as indicated in section 11.1). However, compared to the other circles, circle no. 7 contains the highest number of EM Bird measurements and thus contains also a lot of ice thickness measurements off the coast.

Comparison of EM Bird and SMOS ice thicknesses
For the comparison of ice thicknesses retrieved from SMOS brightness temperatures and ice thicknesses measured by the EM Bird, we here use the modal value of the EM ice thickness distributions. Firstly, the modal value is considered to be the most accurate value obtained from EM Bird measurements (Haas et al., 2010). Secondly, the maximum ice thickness value that is retrievable from L-band brightness temperatures under Baltic conditions is about 1 – 2 m (Kaleschke et al., 2010). Ice thicknesses higher than this maximum value do not change the brightness temperature signal observed over ice. Thus, we expect that the ice thickness that can be retrieved from SMOS is mainly the modal ice thickness.
For each circle, the ice thickness as retrieved from SMOS brightness temperature intensities is indicated in the figures that show the ice thickness distributions measured by the EM Bird (Figures 11.6 and 11.7). The ice thickness as retrieved from SMOS brightness temperature intensities coincides with the modal ice thickness from EM Bird measurements in five out of the twelve cases (circle nos. 1, 4, 7, 11, and 12). In two cases, the SMOS ice thickness is one bin (about 6 cm) too high (circle nos. 2 and 9), in one case, the SMOS ice thickness is one bin too low (circle no. 10). In two cases, the SMOS ice thickness is two bins (about 12 cm) too high (circle nos. 3 and 5), or two bins too low (circle nos. 6 and 8). Thus, with the cho-

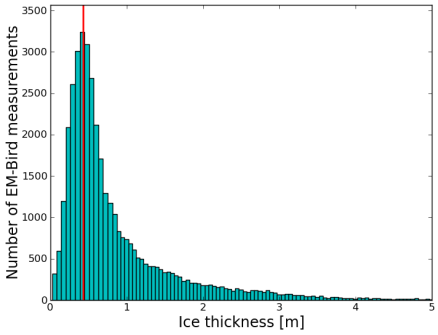

(a) Circle no. 1

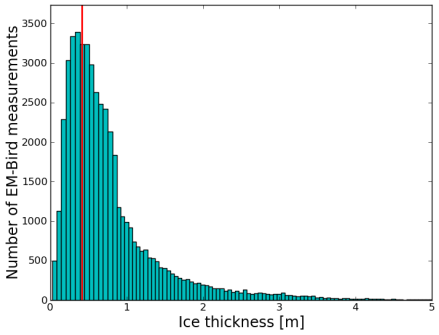

(b) Circle no. 2

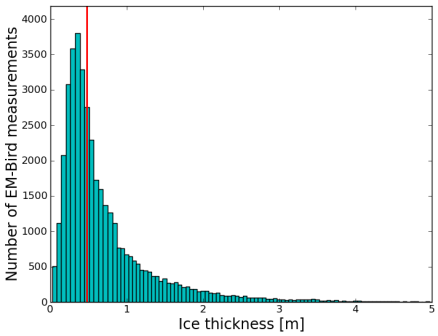

(c) Circle no. 3

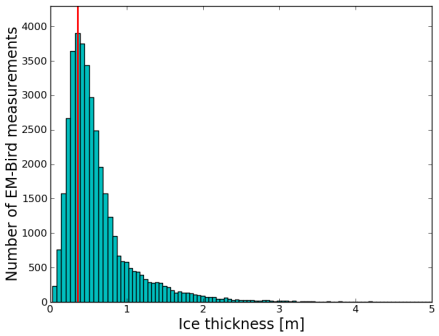

(d) Circle no. 4

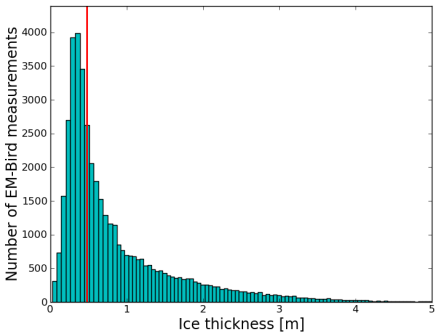

(e) Circle no. 5

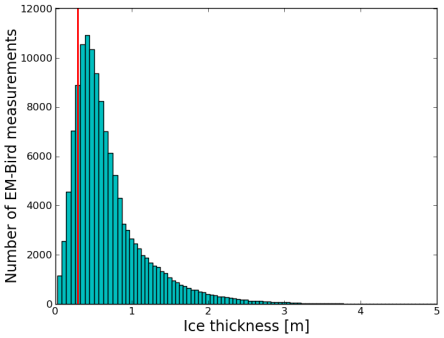

(f) Circle no. 6

Figure 11.6: Distribution of total ice thicknesses as measured by the EM Bird within the circular areas depicted in Figure 11.3. The red lines indicate ice thicknesses as retrieved from SMOS brightness temperature intensities (or vertically polarised brightness temperatures).

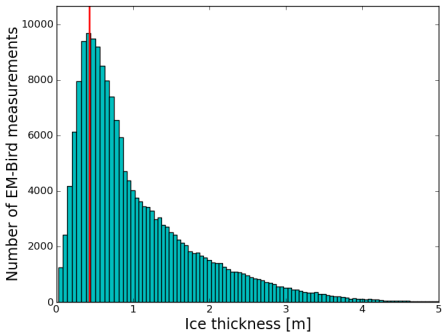

(a) Circle no. 7

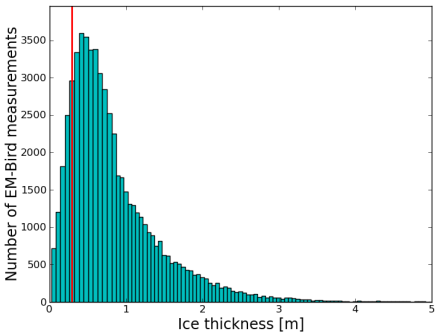

(b) Circle no. 8

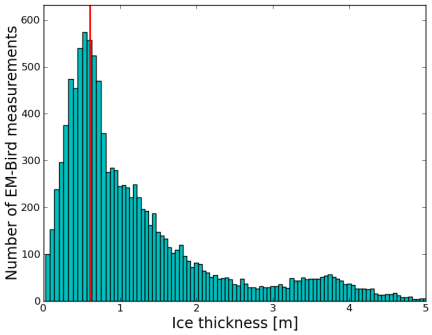

(c) Circle no. 9

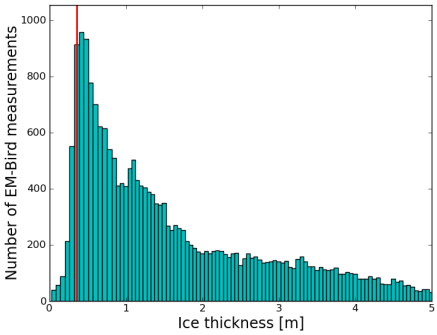

(d) Circle no. 10

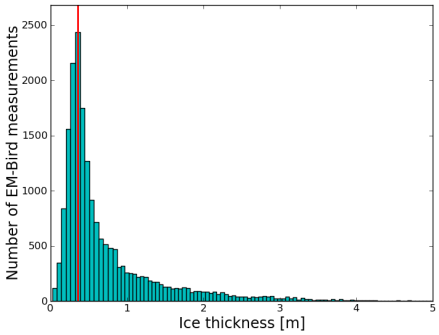

(e) Circle no. 11

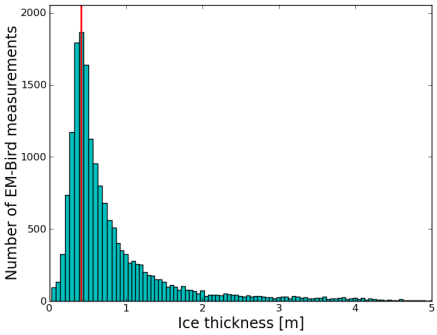

(f) Circle no. 12

Figure 11.7: For figure description see caption of Figure 11.6.

sen assumptions for the model, the deviations between SMOS and EM Bird ice thicknesses are evenly distributed, and we do not observe a systematic over- or underestimation of ice thickness by SMOS, when compared to the EM Bird measurements.
Figures 11.8 to 11.11 show the spatial distributions and scatter plots of the modal EM Bird ice thicknesses and the ice thicknesses retrieved from SMOS brightness temperatures. The SMOS ice thicknesses are retrieved from horizontally polarised brightness temperatures (Figures 11.8 and 11.9), and from vertically polarised brightness temperatures and brightness temperature intensities (Figures 11.10 and 11.11). Here, the ice thicknesses retrieved from vertical polarisation and from brightness temperature intensities are identical.
The ice thicknesses retrieved from horizontal and from vertical polarisation (or from intensities) differ only slightly. The spatial distribution of the compared ice thicknesses does not reveal any distinct pattern of regional differences. The ice thicknesses that fit best are found both in the northernmost and in the southernmost circles, as well as both in the eastern part and the western part of the Bay of Bothnia. What is striking is that the two circles with the highest positive deviation and the two circles with the highest negative deviation between SMOS and EM Bird ice thicknesses are located next to each other, respectively. For the adjacent circle nos. 3 and 5, the SMOS ice thickness is about 12 cm higher than the EM Bird modal ice thickness, while for the adjacent circle nos. 6 and 8, the SMOS ice thickness is about 12 cm lower than the EM Bird modal ice thickness.
The scatter plots for SMOS retrieved ice thicknesses and EM ice thicknesses reveal that the range of ice thicknesses that is obtained from SMOS measurements is somewhat broader than the range of ice thicknesses obtained from the modal values of the EM ice thicknesses. For example, for the SMOS retrieval based on brightness temperature intensity or on vertically polarised brightness temperatures (Figure 11.11), we obtain values between 29 and 61 cm ($2\times d_{ice}$= 29 cm, $3\times d_{ice}$= 35 cm, $4\times d_{ice}$= 41 cm, $2\times d_{ice}$= 48 cm, and $1\times d_{ice}$= 61 cm). Whereas, we obtain values between 35 and 54 cm from the EM Bird measurements ($5\times d_{ice}$= 35 cm, $6\times d_{ice}$= 41 cm, and $1\times d_{ice}$= 54 cm).
Considering all 12 circles, the root mean square deviations between EM Bird ice thicknesses and ice thicknesses retrieved from SMOS are 8.8 cm for horizontal polarisation, and 7.7 cm for vertical polarisation and for intensity. The mean ice thickness for all 12 modal values from the EM Bird ice thickness measurements is 39.9 $\pm$ 5.1 cm, compared to a mean ice thickness of 40.4 $\pm$ 8.2 cm for the SMOS ice thickness retrievals based on vertical polarisation and on intensity, and a mean ice thickness of 41.4 $\pm$ 10.0 cm for the SMOS retrieval based on horizontal polarisation.

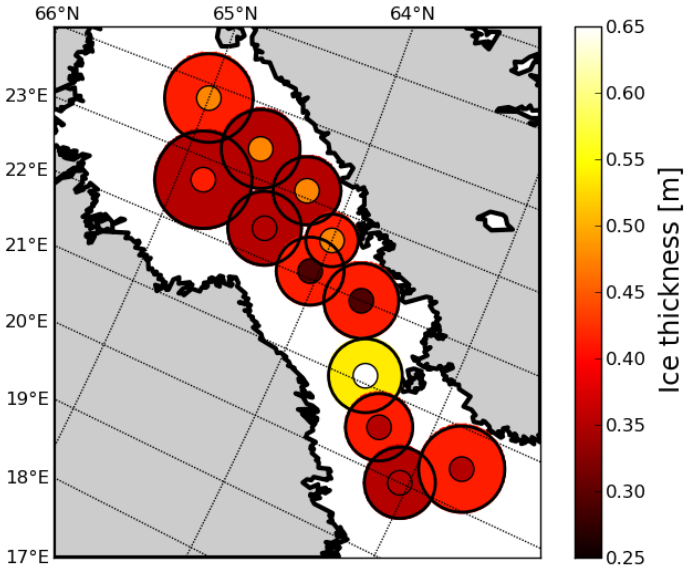

Figure 11.8: Total ice thicknesses as measured by the EM Bird and as retrieved from horizontally polarised SMOS brightness temperatures. The inner circles depict ice thicknesses as retrieved from SMOS, the outer circles depict the modal values of all ice thicknesses measured within the validation circles by the EM Bird.

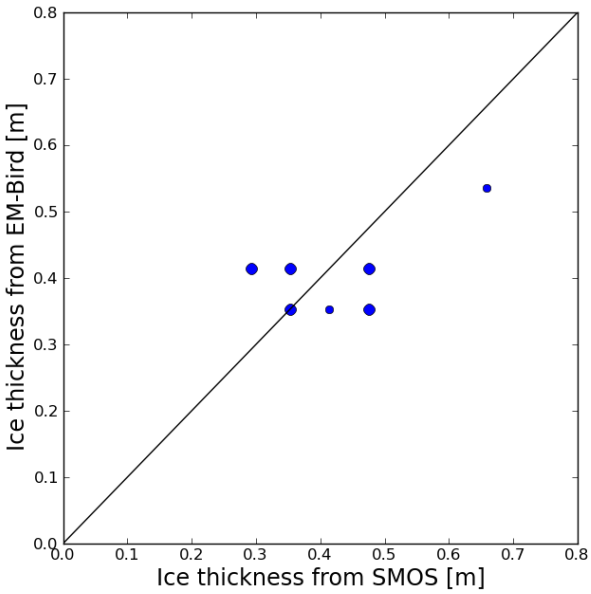

Figure 11.9: Modal ice thicknesses from the EM Bird versus ice thicknesses retrieved from horizontally polarised SMOS brightness temperatures for the 12 circles shown in Figure 11.8. The size of the points corresponds to the number of cases in that the given combination of ice thicknesses from EM Bird and SMOS coincide.

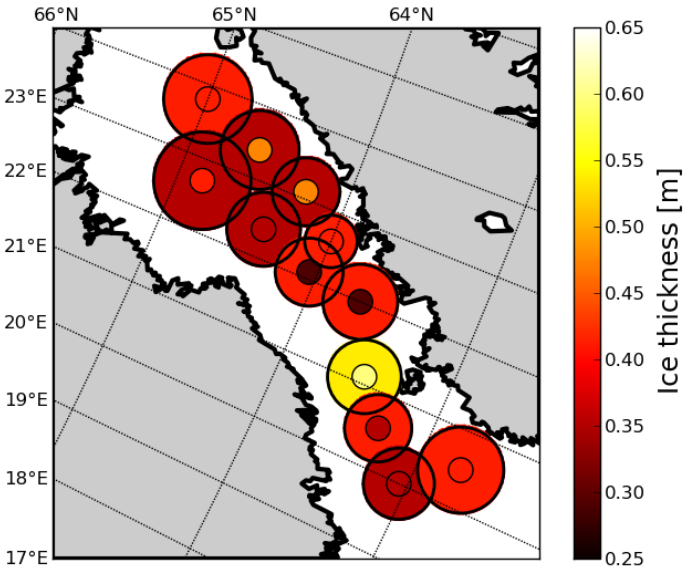

Figure 11.10: For figure description see caption of Fig.11.8, but here the SMOS ice thicknesses are retrieved from vertically polarised brightness temperatures or from brightness temperature intensities (giving the same retrieved ice thicknesses).

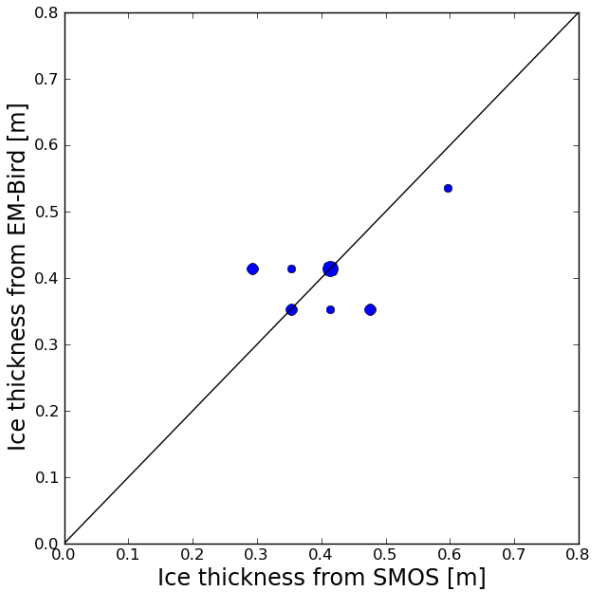

Figure 11.11: For figure description see caption of Fig.11.9, but here the SMOS ice thicknesses are retrieved from vertically polarised brightness temperatures or from brightness temperature intensities (giving the same retrieved ice thicknesses).

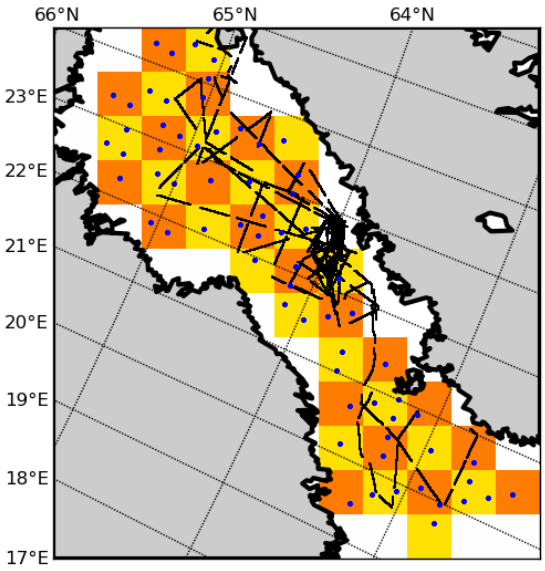

Figure 11.12: EM Bird flight tracks of the SafeWin field campaign from 2nd to 7th March, 2011 (black lines) and SMOS measurements (blue points) plotted over the 30 km × 30 km grid used in the validation approach 2 of section 11.4. Only the grid boxes that contain suitable SMOS brightness temperature data for a potential ice thickness retrieval are shown here. For the corresponding criteria see sections 11.4 and 11.2.

11.4 Validation approach 2

A common approach to compare two data sets is to define a regular grid, to select all data located within one grid cell from both data sets, and for each grid cell to compare the values obtained from one data set with the values obtained from the other data set. In this section, we show the results of such a comparison between SMOS retrieved ice thicknesses and EM Bird measurements.

Data selection

We divide the area of investigation into 12 × 11 grid cells with cell sizes of 30 km × 30 km (Figure 11.12). For the further analysis, we include all SMOS measurements whose centre points are located within an area of 0.75 times the grid cell size around the grid cell's centre point. As in section 11.3, the factor 0.75 is chosen quite arbitrarily and is a compromise between including as many measurements as possible and excluding SMOS measurements that represent large areas outside the grid cell. Thus, we include all SMOS measurements with their centre points being located within an area of 22.5 km × 22.5 km around the grid cell's centre point.

For the EM Bird ice thickness determination for each grid cell, we collect all EM Bird measurements located within an area of 1.25 times the grid cell size around the grid cell's centre point. Thus, for each grid cell we include all EM Bird measurements within an area of 37.5 km × 37.5 km around the grid cell's centre point. We include EM Bird measurements from a larger area (37.5 km × 37.5 km) than we do for SMOS measurements (22.5 km × 22.5 km) because the SMOS measurements have footprint sizes of 35 – 50 km × 35 – 50 km. Thus, even with the constricted selection of SMOS measurements for each grid cell, the in-

cluded SMOS measurements represent large areas outside the 22.5 km × 22.5 km area and cover at least the 37.5 km × 37.5 km area of included EM Bird measurements. As in section 11.3, we take the modal value of the corresponding ice thicknesses as the representative total ice thickness.
In order to avoid that we assign obviously unrepresentative values to grid cells that are only marginally covered by EM Bird measurements, we impose two requirements. These have to be fulfilled before we assign an EM ice thickness to a grid cell. Firstly, we only assign an EM ice thickness to grid cells that contain EM Bird measurements within their inner 22.5 km × 22.5 km area, i.e. in the area where the SMOS measurements' centre points have to be located in order to be included. Secondly, the grid cell has to contain more than 1000 single EM Bird measurements. According to the spacing of subsequent EM Bird measurements, 1000 single EM Bird measurements correspond to a flight track length of about 3 – 4 km.

11.4.1 Results

SMOS ice thickness
The ice thicknesses retrieved from SMOS show higher ice thicknesses of up to 50 - 60 cm close to the Finnish coast in the eastern part of the Bay of Bothnia (Figure 11.13). The SMOS ice thicknesses decrease further inwards the Bay of Bothnia (westward) and reach their minimum values of about 25 – 30 cm at the edge of the open water tongue that is indicated in the ice concentration map obtained from MODIS images (Figure 11.2). West of this open water tongue, close to the Swedish coast in the south-western part of the Bay of Bothnia and the Sea of Bothnia, SMOS ice thicknesses are thicker than 65 cm.

EM ice thickness
The modal ice thicknesses obtained from the EM Bird measurements show high ice thicknesses of more than 65 cm west of the coast of Vaasa (approximately at 63.1°N and 21.6°E) and ice thicknesses of about 60 cm near the island Hailuoto (Figure 11.13). These areas are expected to be areas, where the EM Bird tends to overestimate ice thicknesses, due to shallow waters and freshwater layers underneath the fast ice (see section 11.1). Additionally, EM ice thicknesses exceeding 65 cm are found in the north-western part of the Bay of Bothnia near the area with low ice concentrations indicated in MODIS images (Figure 11.2).

Comparison of EM and SMOS ice thicknesses
As in the validation approach 1 of the previous section, the ice thicknesses retrieved from horizontally polarised, from vertically polarised brightness temperatures, and from brightness temperature intensities are relatively similar. Thus, we here only show the results for the comparison of EM ice thicknesses and ice thicknesses retrieved from SMOS brightness temperature intensities (Figures 11.13 and 11.14).
As in the validation approach 1, we cannot identify any regions, where the EM and SMOS ice thicknesses agree particularly well or particularly poorly. The deviations between EM and SMOS ice thicknesses are distributed evenly over the considered area (Figure 11.13).
All SMOS ice thicknesses that are compared with EM ice thicknesses here take values between 29 and 48 cm. Thus, these SMOS ice thicknesses are in the same range as for the validation approach 1, where all except of one ice thickness had values in this ice thickness range. In contrast, the EM Bird modal values for the grid-based validation approach 2 are distributed over a broader range of ice thickness values than in the validation approach 1. Here, the EM modal ice thicknesses range between 29 and 95 cm and are thus more variable

than the corresponding SMOS ice thicknesses. In contrast, the range of EM ice thicknesses was 35 – 54 cm in the validation approach 1 and the EM ice thicknesses were distributed over a smaller range than the corresponding SMOS ice thicknesses.
When we average over all grid cells that contain both EM and SMOS ice thicknesses, the mean ice thickness from EM Bird measurements is 48.0 $\pm$ 16.2 cm, as compared to 38.4 $\pm$ 6.5 cm for the mean ice thickness retrieved from SMOS brightness temperature intensities. The root mean square deviation between EM Bird and SMOS ice thicknesses for the grid-based comparison here is 19.3 cm.

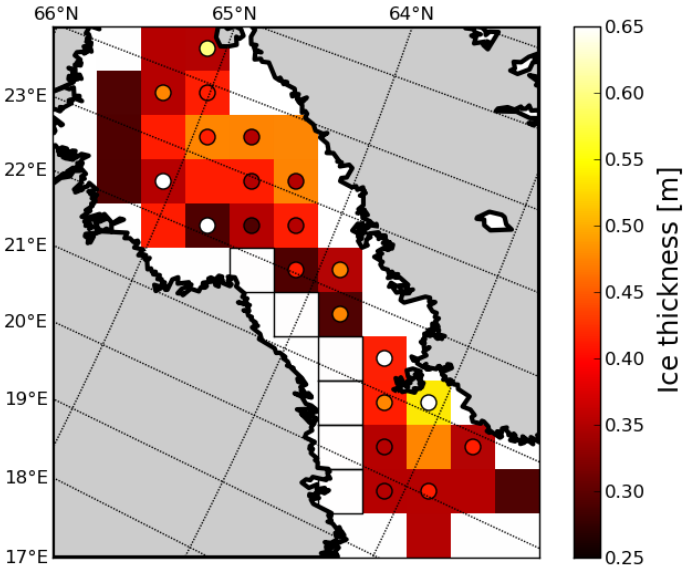

Figure 11.13: Total ice thicknesses as measured by the EM Bird and as retrieved from SMOS brightness temperature intensities. The square boxes depict ice thicknesses as retrieved from SMOS, the circles depict the modal values of all ice thicknesses measured within the square boxes by the EM Bird.

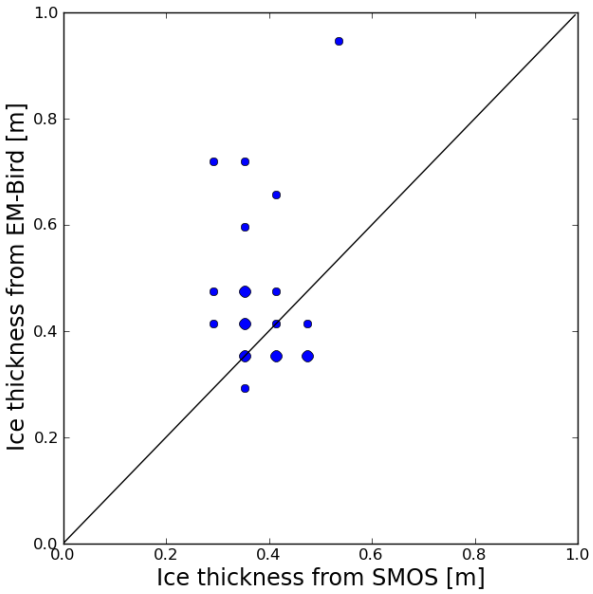

Figure 11.14: Modal ice thicknesses from the EM Bird versus ice thicknesses retrieved from SMOS brightness temperature intensities for the validation approach 2, which uses a gridded field (see Figures 11.12 and 11.13). The size of the points corresponds to the number of cases in that the given combination of ice thicknesses from EM Bird and SMOS coincide.

11.5 Summary and Discussion

In order to validate the sea ice thickness retrieval using SMOS, we compared ice thicknesses retrieved from SMOS brightness temperatures with ice thicknesses measured during an EM Bird flight campaign in the Bay and northern Sea of Bothnia in March, 2011. The Baltic Sea is a challenging area for the retrieval of ice thickness using SMOS. L-band brightness temperatures in the Baltic Sea region suffer from a quite high RFI contamination, and the land impact on measured brightness temperatures is relatively high in the land-enclosed Baltic Sea basin.
For the retrieval of ice thickness in the Baltic Sea, we simulated brightness temperatures for a range of incidence angles (θ= 0 – 50°). Therefore, we used the incoherent Burke model for one snow and one ice layer and assumed constant values for the model input parameters ice concentration, ice temperature and salinity, water temperature and salinity, and the density and thickness of a snow layer on top of the ice. Ice concentration was determined by the classification of MODIS reflectivities. In order to estimate the ice temperature for the model calculations, we averaged the ice surface temperatures obtained from MODIS measurements over the considered area and the time period. For ice and water salinity, water temperature, and snow density and thickness, we used typical values observed for sea ice in the Baltic Sea. While the above mentioned model parameters were set to constant values, the ice thickness was varied. We calculated the root mean square deviation between brightness temperatures observed by SMOS and brightness temperatures simulated for the different ice thicknesses. The retrieved ice thickness was then the ice thickness for that the brightness temperature simulations had the lowest deviation from the brightness temperature observations.
We showed the results for two different approaches to compare SMOS and EM Bird ice thicknesses. For the first approach (validation approach 1), we first manually defined 12 circular areas in the Bay and Sea of Bothnia. These circular areas were chosen in consideration of the EM Bird flight tracks such that we supposed every circle to be reasonably represented by the ice thicknesses measured by the EM Bird. In the next step, we then chose the matching SMOS measurements, applied our ice thickness retrieval method, and compared the resulting SMOS ice thicknesses with the EM Bird modal ice thicknesses for each of the 12 circles. The second validation approach (validation approach 2) was more governed by the distribution of the SMOS measurements. We defined a regular grid for the area of investigation. For each grid cell, we then chose the corresponding SMOS brightness temperatures and EM Bird ice thickness measurements. However, we expected the results of such a comparison to be less representative than the results of the comparison based on the circular areas (validation approach 1) for the measurements considered here. The reason is, that we here compared irregularly distributed field campaign data with satellite data distributed on a regular grid. Additionally, the footprint sizes of the two data sets were very different: single SMOS measurements have footprints of about 35 – 50 km $\times$ 35 – 50 km, while single EM Bird measurements have footprints in the order of 50 m $\times$ 50 m.
The results of our analysis confirmed that a comparison based on a gridded field is not necessarily representative for comparison of SMOS and EM Bird measurements. For this approach (validation approach 2), the mean ice thicknesses obtained from EM Bird measurements and from the SMOS retrieval differed by almost 10 cm for mean ice thicknesses of 40 – 50 cm, and the root mean square deviation was 19.3 cm.
In contrast, ice thicknesses from the EM Bird measurements and from the SMOS retrieval agreed considerably better for the validation approach that was more oriented on the availability of the EM Bird validation data (validation approach 1). The mean EM and SMOS

ice thicknesses agreed within 0.5 cm. The mean EM ice thickness, obtained from the 12 modal values, was 39.9 $\pm$ 5.1 cm. The mean SMOS ice thickness was determined to be 40.4 $\pm$ 8.2 cm for the retrieval from vertically polarised brightness temperatures and brightness temperature intensities. The corresponding root mean square deviation between EM and SMOS ice thicknesses for this validation approach was 7.7 cm. For ice thicknesses retrieved from SMOS brightness temperatures at horizontal polarisation, the agreement with EM ice thicknesses was slightly lower (the mean SMOS ice thickness being 1.5 cm higher than the EM ice thickness, and the root mean square deviation between the ice thicknesses being 8.8 cm).

Thus, we here showed that the retrieval of ice thickness from SMOS brightness temperatures is possible, even in a challenging region like the Baltic Sea. Furthermore, we demonstrated that it is important to choose an adequate approach to compare satellite-based data that are provided on a regular grid with flight campaign data that are provided along irregularly distributed flight tracks.

Part V

Validation data reports

12 MODIS THICKNESS

Marko Mäkynen

STSE-SMOS Sea Ice Retrieval Study
SMOSIce

WP 3 Assembly of the SMOSIce Data Base

SMOSIce-DAT user manual for the validation data
Deliverable D-6b

EUROPEAN SPACE AGENCY STUDY CONTRACT REPORT
UNDER ESTEC CONTRACT No. 4000101476/10/NL/CT

Prepared by

Marko Mäkynen
Finnish Meteorological Institute

Date: 24 May 2012

ESA STUDY CONTRACT REPORT

ESA Contract No:	SUBJECT:	CONTRACTOR:
4000101476/10/NL/CT	STSE-SMOS Sea Ice Retrieval Study (SMOSIce)	Univ. Hamburg
ESA CR( )No:	No. of Volumes: 1 This is Volume No: 1	CONTRACTOR'S REFERENCE: Deliverable D-6b

ABSTRACT:

This user manual is the reference document for the datasets provided by Finnish Meteorological Institute (FMI) for the validation of the SMOS sea ice thickness algorithms. The validation data consists of in-situ measurements (SMOSIce-DAT-CV), remote sensing data (SMOSIce-DAT-RS) and sea ice and near surface atmospheric model data (SMOSIce-DAT-MD). Together these datasets form the validation database (SMOSIce-DAT-DB) which is available on the SMOSIce ftp-server. The helicopter-borne EM-ice thickness data by AWI are not presented here.

Names of authors:

Marko Mäkynen

NAME OF ESA STUDY MANAGER: DIV: DIRECTORATE:	ESA BUDGET HEADING:

Table of Contents

1. INTRODUCTION

This user manual is the reference document for the datasets provided by Finnish Meteorological Institute (FMI) for the validation of the SMOS sea ice thickness algorithms. The validation data consists of in-situ measurements (SMOSIce-DAT-CV), remote sensing data (SMOSIce-DAT-RS) and sea ice and near surface atmospheric model data (SMOSIce-DAT-MD). Together these datasets form the validation database (SMOSIce-DAT-DB) which is available on the SMOSIce ftp-server. SMOS brightness temperature data is included in SMOSIce-DAT-RS, but it is described in separate user manual (deliverable D-6a). The helicopter-borne EM-ice thickness data by AWI are not presented here.

For the validation the SMOS sea ice thickness algorithms and products FMI provides data for two sea ice areas: 1) the Baltic Sea and 2) the Kara Sea, and the eastern part of the Barents Sea (called in the following as Kara Sea area). Validation datasets are for the winters of 2010 (1 Jan to 30 Apr) and 2010-2011 (1 Oct 2010 to 30 Apr 2011).

The in-situ data for the Baltic Sea includes coastal weather station data, snow and ice thickness measurements by Finnish icebreakers, and data from two field campaigns (March 2010 and Feb-March 2011). For the Kara Sea we have only coastal weather data at our disposal.

The main remote sensing validation data is the MODIS ice surface temperature based thin ice thickness charts for both the Baltic and Kara Seas. Other data are MODIS based ice surface temperature for cloud-free areas, daily ENVISAT SAR mosaic for the Kara Sea, ice charts, Polar View SAR ice thickness chart for the Baltic Sea, and experimental MODIS - ENVISAT SAR based ice thickness chart for the Kara Sea. The MODIS based thickness chart shows the level ice thickness accurately up to 50 cm in the Kara Sea and up to 40 cm in the Baltic Sea. The MODIS-SAR chart gives qualitative ice thickness estimates also for thicker ice areas. It is recommended that this product is only used for visual assessment of the SMOS thickness charts, e.g. to see if both charts show same locations for ice thicker than 0.5 m. In the construction of the MODIS-SAR thickness chart a level ice thickness field from a one dimensional high resolution snow and sea ice thermodynamic process model (HIGHTSI) (Launiainen and Cheng 1998) is used as a background field which constraints σ° based ice thickness range.

Modeled atmospheric boundary layer (ABL) data for the Kara and Baltic Seas validation areas is provided by the HIRLAM model. HIRLAM data is used for the MODIS ice surface temperature based ice thickness retrieval and as external forcing in the Kara Sea for the HIGHTSI model.

In the following the Baltic and Kara Seas validation areas are first presented in Section 2. This is followed by descriptions of the in-situ, remote sensing and numerical model datasets in Sections 3 to 5. The equations and procedures to derive MODIS and MODIS-SAR thickness charts are discussed in detail. The accuracy of the HIRLAM variables and the thickness charts are also studied. Section 6 presents the validation database (SMOSIce-DAT-DB) available on the SMOSIce ftp-server.

2. SMOS ICE THICKNESS VALIDATION SITES

2.1 Barents and Kara Seas

The main Eurasian Arctic validation area for the SMOS Sea Ice Retrieval Study is located over the Kara Sea and the eastern part of the Barents Sea, see Figures 1 and 2. In this document the validation are is referenced shortly as the Kara Sea area. The size of the validation area is 1500 by 1350 km. The coverage over the Barents and Kara Seas was limited in order to keep satellite data volumes at reasonable level. The study area includes large thin areas even in the middle of the winter due to many re-occurring polynyas.

Time periods for the validation data acquisition are 1 Jan – 30 Apr 2010 and 1 Oct 2010 – 30 Apr 2011. These time periods include a lot of cloud-free cold weather periods suitable for MODIS based ice thickness retrieval. After April sea ice and snow cover starts to melt and capability of MODIS and SAR data to classify different sea ice thickness categories is poor.

The following coordinate system is used for the validation area:

Polar stereographic projection

mid-longitude of 63 E and true-scale latitude of 70 N

WGS84 ellipsoid (datum)

upper left corner = [-800000, -1100000], lower right corner = [+700000, -2450000]

In this coordinate system north corresponds to image up-direction. The NSIDC's polar stereographic projection has mid-longitude of 45 W and uses Hughes ellipsoid.

For the Kara Sea validation area ENVISAT WSM images are acquired from the ESA's Rolling Archive through a FMI's CAT-1 project. In the winter 2010 typically three to four images were acquired for each day, but in winter 2010-2011 (ENVISAT Mission Extension period) the number of images was smaller, sometimes only one per day. The images have variable lengths in the along track direction. In Jan and Apr 2010 (six dates in total) 27 TerraSAR-X ScanSAR images were acquired over the Kara Sea through FMI's AO-project with DRL. In winter 2011 TerraSAR-X were not acquired (no quota left in the AO-project). Daily Terra MODIS data are available from NASA's WIST service.

The products derived from the ENVISAT and MODIS images are:

- ENVISAT SAR mosaic over the Barents and Kara Seas study area. Updated daily.
- MODIS based ice surface temperature for cloud-free areas.
- MODIS based thin ice thickness chart (accurate up to 0.5 m thickness).
- MODIS and ENVISAT SAR based ice thickness chart (experimental).

TerraSAR-X images can be used for fine scale validation of these products. Atmospheric forcing data for the MODIS based ice thickness retrieval is obtained from the HIRLAM model. HIRLAM is also used as external forcing data for a one dimensional high resolution snow and sea ice thermodynamic model (HIGHTSI) which gives estimates of snow and level ice thickness and surface temperatures (Launiainen and Cheng 1998).

Currently only in-situ data available are weather data from seven coastal weather stations (see Figure 1) and occasional in-situ fast ice thickness values in the Russian ice charts.

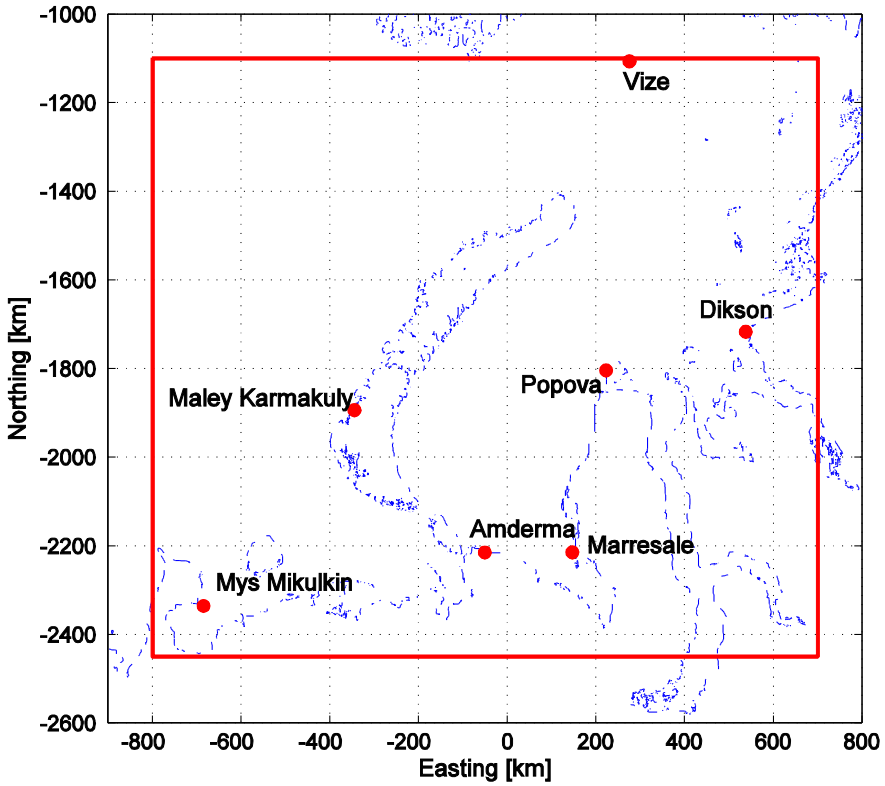

Figure 1. Barents and Kara Seas validation area. Red rectangle shows the validation area and red dots are weather stations. Polar stereographic coordinates with mid-longitude of 63 E.

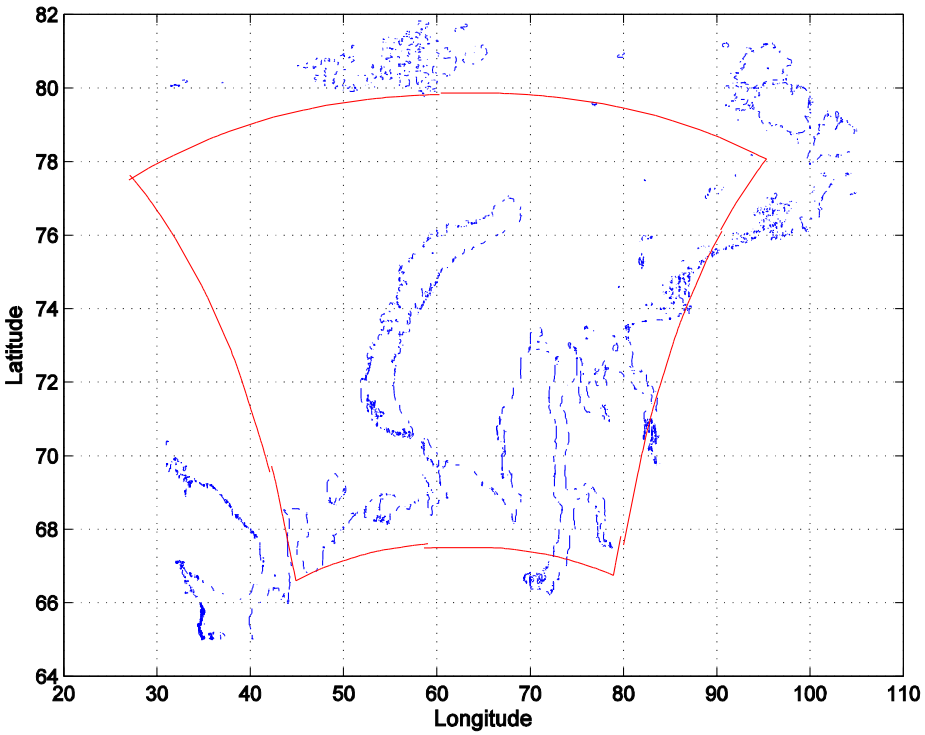

Figure 2. Barents and Kara Seas validation area in latitude-longitude coordinates. Red rectangle shows the validation area.

2.2 Baltic Sea

The Baltic Sea validation area is shown in Figure 3. It equals with the coverage of the Finnish Ice Service (FIS) ice chart. Time periods for the validation data acquisition are 1 Feb – 31 Mar 2010 and 1 Dec 2010 – 31 Mar 2011. During these time periods sea ice extent reaches its maximum (typically in March) and there are periods of cold weather suitable for the MODIS based ice thickness retrieval (air temperature should be less than -10ºC). After March sea ice and snow cover starts to melt and capability of MODIS and SAR data to classify different sea ice thickness categories is poor.

The following coordinate system is used for the Baltic Sea validation area:

Mercator projection

true-scale latitude of 61.667 N

WGS84 ellipsoid (datum)

upper left corner = [+480000, +4680000], lower right corner = [+1600000, +3350000]

[65.99 N, 9.06 E] [53.49 N, 30.21 E]

For this validation area ENVISAT WSM and RADARSAT-2 ScanSAR images are acquired within the EC MyOcean project. Daily Terra MODIS data are available from NASA's WIST service.

The products derived from the SAR and MODIS images are:

- Polar View ice thickness chart.
- MODIS based ice surface temperature for cloud-free areas.
- MODIS based thin ice thickness chart (accurate up to 0.4 m).

Polar View ice thickness chart is based on the FIS ice chart and ENVISAT or RADARSAT-2 SAR data. It is issued operationally for each SAR image acquired.

Atmospheric forcing data for the MODIS based ice thickness retrieval is obtained from the HIRLAM model. In-situ validation data include coastal weather station data, ice thickness measurements by Finnish ice-breakers, and helicopter-borne EM-ice thickness measurements conducted during the 2010 and 2011 Baltic Sea ice field campaigns. The EM-thickness data is provided by AWI and presented in a separate document.

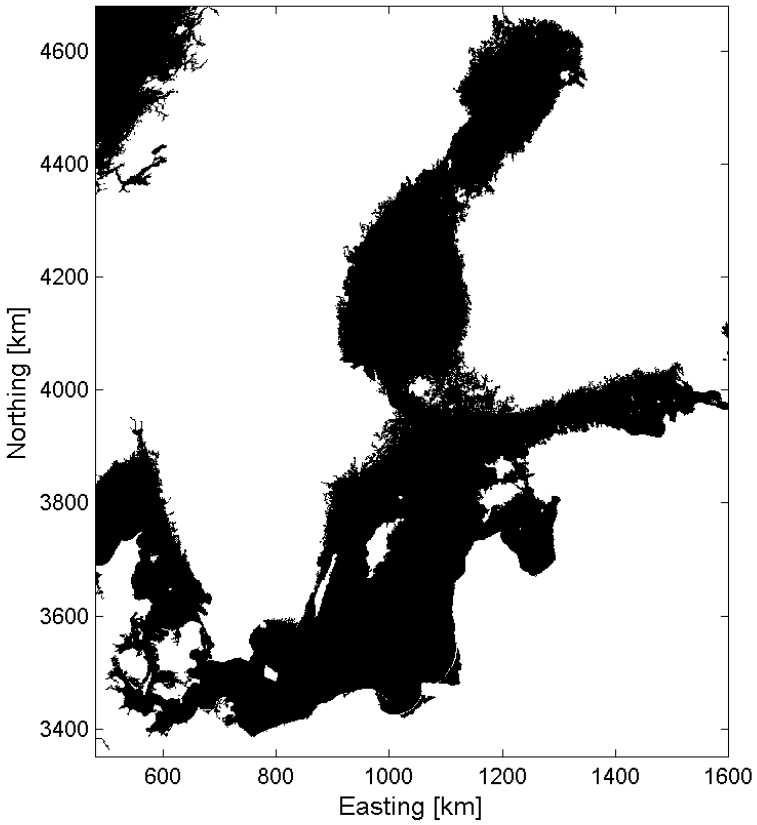

Figure 3. Baltic Sea validation area. Mercator projection.

3. IN-SITU CALIBRATION/VALIDATION DATA – SMOSIce-DAT-CV

3.1 Barents and Kara Seas

Currently only in-situ data available are weather data from seven coastal weather stations (see Figure 1) and occasional in-situ ice thickness values for fast ice found in the Russian ice charts.

3.1.1 Weather station data

Weather data are available from seven weather stations:

1. Ostrov Vize; 79.50 N, 76.98 E (Matlab-matrix *vize*)
2. IM. M.V. Popova; 73.33 N, 70.05 E (*popova*)
3. Dikson; 73.50 N, 80.40 E (*dikson*)
4. Malye Karmakuly; 72.37 N, 52.70 E (*karma*)
5. Amderma; 69.75 N, 61.70 E (*amderma*)
6. Marresale; 69.72 N, 66.80 E (*marre*)
7. Mys Mikulkin; 67.80 N, 46.67 E (*mikulkin*)

Weather observations were conducted at 0, 6, 12, 18 hours UTC. For the time period from 1 Oct 2005 to 30 Apr 2011 following weather parameters have been extracted from BUFR-files to Matlab-format:

- Air temperature at 2 m [K]; *ta*
- Wind speed at 10 m [m/s]; *ws*
- Wind direction at 10 m [deg]; *wd*
- Dew point temperature at 2 m; *dp*
- Pressure reduced to mean sea level [Pa]; *pres*
- Total cloud cover [%]; *cc*
- Cloud amount [oktas]; *ca*
- Present weather [code number]; *wcode*

From the Dikson and Vize stations also total precipitation [kg/m^2] during past 24 hours and snow thickness [m] are available; Matlab-variables *prec* and *hs*. Missing data is coded with -1. Weather codes can be found in the document "Code-FlagTables-11-2007.pdf".

Time is expressed as serial date number (*pvm*).

Matlab-file "KS_weatherdata.mat" has data matrices for all seven stations. The columns are:
[*pvm ta dp pres wd ws cc ca wcode hs prec*] for Dikson and Vize stations and
[*pvm ta dp pres wd ws cc ca wcode*] for other stations.

Matrix "lws" has latitudes and longitudes of the stations and matrix "mws" easting and northing coordinates.

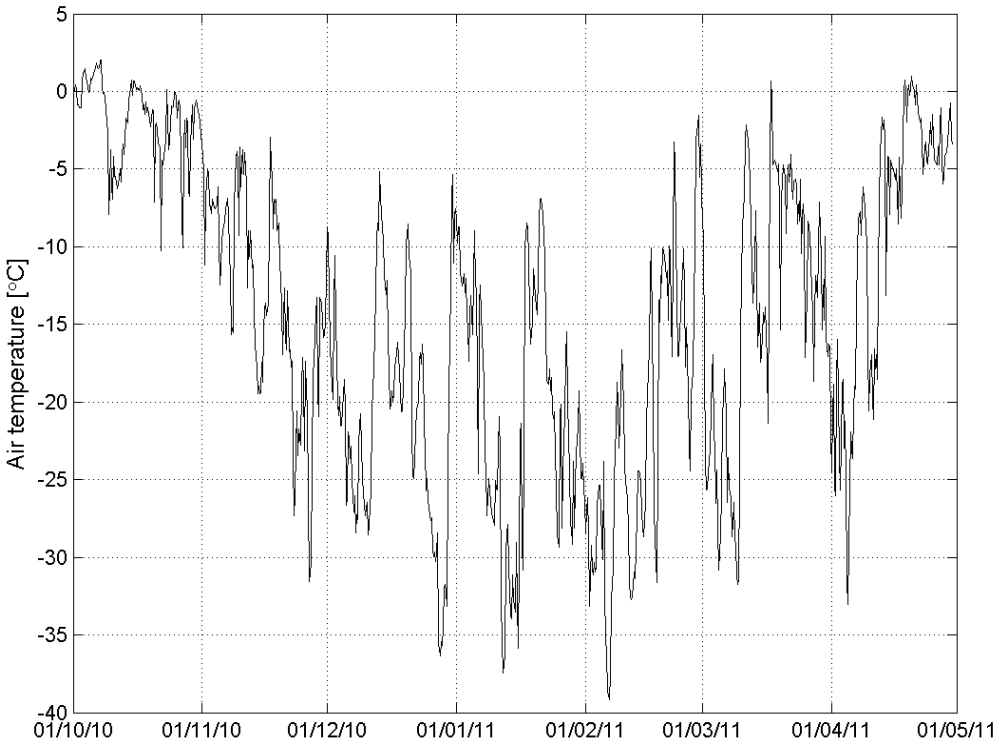

Figure 4. Air temperature measured by the Popova station during 1 Oct 2010 - 30 Apr 2011.

3.1.2 Russian ice charts

Ice charts covering parts of the Kara and Barents Sea are available from Scientific Research Center of Space Hydrometeorology "Planeta" in Russia; web-page:

http://planet.iitp.ru/english/index_eng.htm

The ice charts are available in a rolling archive. We started to collect ice charts on 15 March 2010. The ice charts have occasionally in-situ ice thickness values for fast ice.

The ice charts are in Russian, but an ICCWG 2009 presentation "Trenina_PLANETA_Ice_Cover_Analysis.pdf" has English translations for the ice chart codes (Trenina 2009).

3.2 Baltic Sea

Baltic Sea in-situ validation data include coastal weather station data, ice thickness measurements by Finnish ice-breakers and data from two Baltic Sea ice field campaigns; the first one was conducted on 8-18 March 2010 in the Gulf of Finland and the second one on 22 Feb - 7 Mar 2011 in the Bay of Bothnia. The main dataset from the field campaigns for the SMOSIce validation is the helicopter-borne EM-ice thickness data. Additional data from the field campaigns include e.g. snow and ice thickness (by EM-31 and drillings), and snow and ice medium characteristics.

The March 2010 field campaign is described in detail in a separate cruise report (Haapala et al. 2010) which is included in the SMOSIce database. In general, data from this field campaign is not very useful for sea ice remote sensing studies due to the small number of EM-flights and small amount of in-situ measurements on drift ice. EM-flights were conducted only before the campaign (5 and 7 March). During the field campaign the weather conditions (cloudiness) and ice conditions (helicopter cannot fly over open water areas; there was no interesting ice to measure) did not permit

further flights. In the evening of 11 March a severe storm broke up the ice field in the Gulf of Finland and ice floes drifted to the Russian side (R/V Aranda did not have permit to sail there). At the end of the field campaign there was a lot thin ice in the Gulf of Finland. Due to the prevailing cloud cover only a few usable MODIS images were acquired.

The field campaign in 2011 had one ice station near Kokkola Tankar lighthouse and weather station. An intensive EM-measurement flight campaign was conducted. Air temperature was close to 0 ºC and thus, snow cover was typically somewhat moist. The report for the 2011 field campaign is under preparation.

In the following sub-sections the Baltic Sea in-situ validation datasets are described.

3.2.1 Weather station data

Finnish coastal weather stations selected for the in-situ validation dataset are shown in Figure 5 (in total 22 stations). For the Bay of Bothnia and Sea of Bothnia the station list starting from northernmost one and going to the southernmost one are: Kemi Ajos (Matlab-matrix kemiajos), Kemi 1 (kemi1), Marjaniemi (mn), Nahkiainen (nahk), Ulkokalla (ulkok), Kokkola Tankar (ktankar), Pietarsaari Kallan (pkallan), Valassaaret (valas), Strömmingsbådan (sbadan), Kristiinankaupungin Majakka (kkm), Pori Tahkoluoto (ptahko), Rauma Kylmäpihjala (rauma), Kustavi Isokari (isokari) and Märket (market). For the Gulf of Finland the stations from the west to the east are: Kökar Bogskär (kokar), Utö (uto), Hanko Russarö (hanko), Kirkkonummi Mäkiluoto (mluoto), Helsingin Majakka (hki), Porvoo Kalbådagrund (kalba), Loviisa Orrengrund (orre) and Kotka Haapasaari (haapa).

The stations Kalbådagrund, Loviisa Orrengrund and Kotka Haapasaari are within the area of the Baltic Sea ice field campaign in March 2010. The Kokkola Tankar station is closest one for the 2011 field campaign.

Weather observations were conducted at 0, 3, 6, 9, 12, 15, 18 and 21 hours UTC. For the time periods from 1 Jan to 30 Apr 2010 and 1 Nov 2010 to 31 Mar 2011 following weather parameters were extracted from FMI's data archive:

- Air temperature at 2 m [K]; 2. column in the Matlab matrix
- Relative humidity [%]; 3. column
- Pressure reduced to mean sea level [Pa]; 4. column
- Wind direction at 10 m [deg]; 5. column
- Wind speed at 10 m [m/s]; 6. column

Time is expressed as serial date number (1. column in the Matlab matrix). The weather data are in Matlab-files “BS_wdata2010.mat” (1 Jan – 30 Apr 2010) and “BS_wdata2011.mat” (1 Nov 2010 – 31 Mar 2011). Vectors starting with “l” has latitudes and longitudes of the stations and those starting with “m” Mercator easting and northing coordinates.

3.2.2 In-situ sea ice thickness

Crew of Finnish icebreakers conduct occasionally in-situ snow and thickness measurements. The measurements are conducted either by drilling (around 80% of the cases) or estimating snow and ice thickness of ice breaking at the bow of the ship. Typically only one thickness value for snow and ice are given (70% of the cases), but sometimes minimum and maximum thickness for snow or ice or for both were measured. We utilize thickness data measured in 2006-2010 for determination of a statistical relationship between snow and ice thickness needed in the MODIS ice surface temperature based ice thickness retrieval. Thickness data measured in winters 2010 and 2011 can be used in the SMOS ice thickness validation and they are provided as ascii-files.

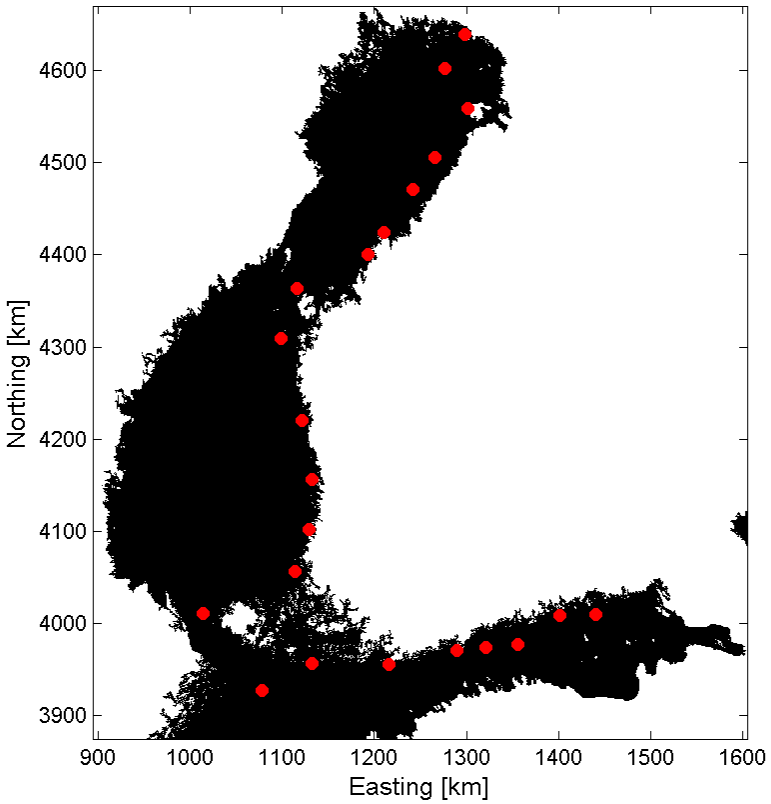

Figure 5. Finnish coastal weather stations selected for the Baltic Sea validation area.

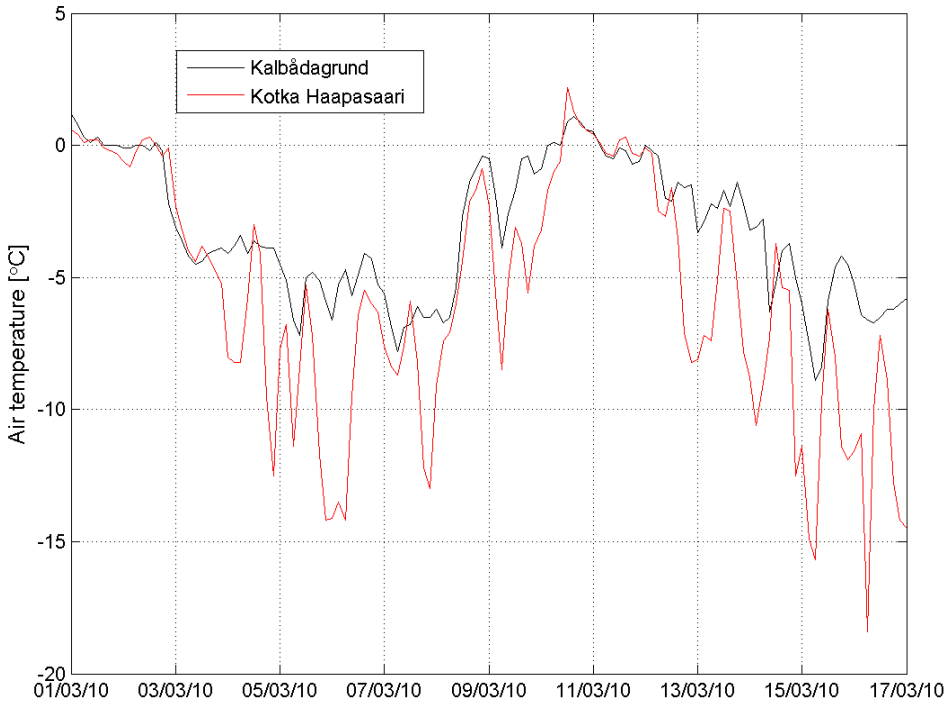

Figure 6. Air temperature during the Baltic Sea March 2010 field campaign measured by two coastal weather stations.

4. REMOTE SENSING DATA – SMOSIce-DAT-RS

In the following Kara and Baltic Seas products available for the SMOS ice thickness validation are described, including data models of the products, input data for the products, data formats, temporal coverage, accuracy estimates of the products, and known data problems. Spatial coverage of the products is typically smaller than the validation areas shown in Figures 1 and 3 due to the clouds in the MODIS images and limited SAR coverages.

4.1 Barents and Kara Seas

In the following satellite data and sea ice products for the Barents and Kara Seas validation area are described. The last sub-section contains the data format descriptions.

4.1.1 ENVISAT WSM images and SAR mosaic

FMI has an ESA Category-1 project for acquisition free of charge ENVISAT ASAR Wide Swath Mode (WSM) images through ESA's Rolling Archive. Typically three to four images are acquired for each day. The images have variable lengths in the along track direction.

Due to the ENVISAT mission extension operations (orbit change) there are no images for 22 Oct – 1 Nov 2010. In Jan-Apr 2011 images were mainly available in the Rolling Archive only from the ascending orbits (acquisition in afternoon), and the number of daily images was sometimes only one or two.

Typically the WSM images are acquired during 05-09:30 UTC (descending orbits) and 13:30-18:30 UTC (ascending orbits).

The rectification of the WSM images to our polar stereographic projection was performed using ESA's BEAM software. The pixel size of the rectified images is 100 m.

A 500 m pixel size mosaic of ENVISAT WSM images over the Barents and Kara Seas validation area was continuously updated with new image acquisitions. An ENVISAT mosaic image typically consists of 8-10 newest image strips. Backscatter intensity (in dB-scale) of the single image trips in the mosaic is linearly scaled to an incidence angle of 35 degrees. The scaling is based on an empirical investigation of backscattering coefficient (in dB scale) vs. incidence angle relationship. The mosaic pixel values are converted from dB-values to a 8-bit number (0-255).

ENVISAT mosaics in the SMOSIce-DAT-DB are for those days which have a MODIS ice thickness chart (mosaics for all days are available if needed). The SAR mosaic can be used mainly for visual investigation of the sea ice conditions. Individual rectified WSM image strips are also available for the project team, if needed.

4.1.2 TerraSAR-X ScanSAR images

TerraSAR-X ScanSAR images at HH-polarization have been acquired over the Kara Sea on the following dates: 20 Jan 2010 (5 images), 23 Jan (3 images), 30 Jan (5 images), 2 Apr (6 images), 5 Apr (5 images) and 9 Apr (3 images); in total 27 images. The size of one image is 100 by 150 km, pixel size is 8.25 m and the resolution is around 20 m. In winter 2011 TerraSAR-X images were not acquired. FMI does not have rights to deliver TerraSAR-X images to a third party.

TerraSAR-X images can be used for fine scale validation (visual and quantitative) of the ENVISAT and MODIS based sea ice products.

4.1.3 MODIS images and products

MODIS data (MOD02 and MOD03 product) are freely available from NASA's WIST service. We chose to use only Terra MODIS data as its acquisition times match those of ENVISAT WSM; MODIS data were acquired at 07:00-08:50 UTC (descending orbits) and 15:15-17:15 UTC

(ascending orbits). Only nighttime MODIS data is used in the ice thickness retrieval so that the uncertainties related to the effect of the solar shortwave radiation and surface albedo are excluded. After 15 March only the afternoon MODIS data is utilized as the morning data starts to has too low sun zenith angle.

For the winters 2010 and 2011 suitable Terra MODIS datasets (contain large cloud-free areas) for the ice temperature and thickness retrieval have been collected. There are 48 cloud masked ice surface temperature images (maximum one image per day) for the time period from 1 Jan to 30 Apr 2010, and 81 images for 1 Nov 2010 – 30 Apr 2011. For Oct 2010 there is no usable MODIS data due to the prevailing cloud cover over the Kara Sea.

After April air temperature starts to be high for accurate ice thickness retrieval and also the sun zenith angle for the afternoon data too low. The average time difference between two MODIS images in 2010 is 2.3 days, and the difference varies from 0.6 to 8.3 days. For 2011 the average time difference is 2.0 days and the variation is from 0.6 to 12.4 days.

The selection of the MODIS datasets was conducted using NASA's MOD29 product (MODIS/Terra Sea Ice Extent 5-Min L2 Swath 1km) and MODIS thermal RGB-images (see details below).

MODIS nighttime data were rectified to our polar stereographic coordinates using NASA's MODIS Swath Reprojection Tool (MRT Swath) with 1000 m pixel size.

Landmask for the MODIS data was derived from the NASA's MODIS 250 m land-water mask product (MOD44W). Coastline data was extracted from the landmask.

The MODIS datasets for the winters 2010 and 2010-2011 are listed together with the weather station data at the time of the MODIS acquisitions in Excel-files "KaraSea_MODIS2010.xls" and "KaraSea_MODIS2011.xls".

Below different MODIS images and products are described.

RGB-images

Two different RGB-images were calculated from MODIS data: 1) brightness temperature channels 20 (red), 31 (green) and 32 (blue) (3.750, 11.030 and 12.020 μm), and 2) channel difference 32-31, difference 31-22 and channel 31 (this combination is used for Meteosat SEVIRI-instrument and it is called as NightMicrophysical). Both images are used in the visual cloud-masking (see below), and the first-one can be also used in the visual investigation of the sea ice conditions. The RGB-images were constructed without any gamma-corrections, only lower and upper limits were set when the brightness temperatures were scaled to between 0-255. The RGB-images include coastline. These images are also available to the project team, if needed.

Cloudmask

We use the following method for the cloud masking of the nighttime MODIS images. Based on a study on MODIS cloud masking (Frey et al. 2008) and our visual analysis of different cloud tests for the nighttime data, we have selected the following three cloud tests: 1) 11-3.9 μm brightness temperature difference (BTD) for low clouds, 2) 3.9-12 μm BTD for high clouds, and 3) 6.7 μm brightness temperature (BT) for high clouds. The thresholds for the tests were determined using empirical BT and BTD data for clouds and cloud-free sea ice and open water. The cloud tests are performed using 10x10 pixel blocks (10 by 10 km). If 10% or 20% (depending of cloud test) of the block pixels are cloudy according to a cloud test then the block is labeled as cloudy. Next morphological operations are performed to remove small isolated block groups and to fill isolated small holes. The results of the individual cloud tests are combined so that if a block is cloudy according to any cloud test then it is cloudy also in the combined mask. Clear restoration is conducted using 11 μm brightness temperature (BT11) by reasoning that if under cold conditions

BT11 is over 272 K it must represent cloud-free open water or very thin ice. After that removal of the isolated block groups and filling of the small holes is again conducted. Next, following manual editing procedures can be conducted: filling holes, removing erroneous cloud mask elements, and masking arbitrary polygonal areas as cloudy or clear. The manual editing is conducted using the two RGB-images described above. Finally, ice surface temperature image is calculated and an another round of manual cloudmask editing is conducted using the ice temperature image and the two RGB-images.

Our approach for the MODIS cloud masking yields a mask that is much less 'grainy' than a typical pixel based mask, e.g. in the MOD29 product. In addition, in our cloud mask the mask errors due to the MODIS sensor striping effect are not present. However, discriminating clear-sky from clouds is nowhere more difficult than in winter nighttime conditions (Frey et al. 2008), and there are cases of unmasked thin clouds and fog in the images.

Cloudmasked RGB-image

The cloudmask is applied to the RGB-image from channels 20, 31 and 32 as semi-transparent layer. This image can be used for visual evaluation of the cloudmask quality, e.g. to find out areas with unmasked fog and thin clouds.

Ice surface temperature

The MODIS sea ice surface temperature (T_S) under clear sky condition is obtained with a split-window technique, where "split-window" refers to brightness temperature difference in the 11-12 μm atmospheric window (Hall et al. 2004). This technique allows for the correction of atmospheric effects primarily due to water vapor. The rms-accuracy of T_S is at the best 1.3 K (Hall et al. 2004). The T_S map is delivered as Matlab-file. Landmask has T_S value of 300 K, cloudmask 210 K and no-data areas over the ocean has 200 K. Pixel size of the T_S map is 1 km.

MODIS based thin ice thickness chart

Level ice thickness (less than 1 m) from T_S can be estimated on the basis of surface heat balance equation. Major assu§mptions here are that the heat flux through the ice and snow is equal to the atmospheric flux and temperature profiles are linear in ice and snow (Yu and Rothrock 1996). The heat balance equation at the top surface (whether sea ice or snow) during the nighttime is (Yu and Rothrock 1996):

$$(F_l^{up}+F_l^{dn}+F_s+F_e)+F_c=F_t+F_c=0 \qquad (1)$$

where F_l^{up} and F_l^{dn} are upward and downward longwave radiative fluxes, F_s and F_e are turbulent sensible and latent heat fluxes, and F_c is the conductive heat flux approximated as:

$$F_c=\gamma(T_W-T_S) \quad , \quad (2)$$

$$\gamma=\frac{k_i k_s}{k_s h_i+k_i h_s} \quad , \quad (3)$$

where γ is the thermal conductance of the snow/ice sheet, k_i and k_s are heat conductivities of ice and snow, h_i and h_s are ice and snow thickness, and T_W is the freezing temperature of seawater approximated as $T_W=-0.054S_W$, where S_W is the salinity of seawater. In (1) fluxes entering the top surface are positive (F_l^{dn} always), and fluxes leaving the surface are negative (F_l^{up} always).

Based on the known T_S , the surface heat fluxes and parametrized h_s , k_i and k_s the estimation of h_i can then be carried out. F_l^{up} is obtained on the basis of MODIS derived T_S

assuming constant sea ice thermal emissivity (ϵ) of 0.98, and F_l^{dn} from the HIRLAM data. F_s and F_e are calculated as in (Yu and Rothrock 1996) where the bulk transfer coefficients for heat and evaporation (C_s and C_e) are assumed to be 0.003 for very thin ice and 0.00175 for thick ice. For k_s we assume a constant climatological value of 0.3 W/m K^{-1} (Sturm et al. 1997). S_W has here constant value of 30 ppt. k_i is estimated using Untersteiner's (1964) equation and estimating ice bulk temperature (T_i) with T_S as was done in (Yu and Rothrock 1996). k_i depends also somewhat on bulked ice salinity (S_i). According to a following general expression that relates S_i to h_i (Kovacs 1996):

$$S_i = 4.606 + 91.603/h_i \qquad (4)$$

S_i decreases from 13.8 ppt to 6.4 ppt when h_i increases from 10 to 50 cm. To simplify the h_i retrieval and to take into account that S_i is in reality a complex function of sea water salinity, ice growth rate and desalination processes, we always use in the k_i calculation a S_i value for 30 cm thick ice (7.7 ppt). The variation of k_i as a function of S_i is very small (less than 10%) when $T_i < 268\,\mathrm{K}$ and $h_i > 10\,\mathrm{cm}$. When T_S is close to T_W then k_i decreases rapidly as a function of T_S . Thus, k_i is assumed to be constant when T_S >270 K.

For the ice thickness (h_i) retrieval a relationship between h_i and snow thickness (h_s) is needed. Yu and Rothrock (1996) used an empirical relationship between snow and ice thickness by Doronin (1971) in retrieval of ice thickness from AVHHR data:

$$\begin{aligned} h_s &= 0 \quad \text{, for} \quad h_i < 5 \text{ cm} \\ h_s &= 0.05 \cdot h_i \quad \text{, for} \quad 5 \text{ cm} \leqslant h_i \leqslant 20 \text{ cm} \\ h_s &= 0.10 \cdot h_i \quad , \quad h_i > 20 \text{ cm} \end{aligned} \qquad (5)$$

We use snow and ice thickness data from the Soviet Union's airborne Sever expeditions (NSIDC 2004) conducted in 1950-1989 to determine the relationship between snow and ice thickness for our test area. The Sever expeditions took place mainly from mid March to early May and the Sever data represent late winter conditions before the starting of the sea ice melt. For the estimating snow and ice thickness relationship we use only the so-called runway data, which represent level ice, from a geographical area extending 200 km from the borders of our test area (eastern limit is Vilkitsky Strait and northern is Franz Josef Land). Data acquired after the end of April is not used as this time period is not included in the MODIS datasets. Only ice thickness values up to 100 cm are used as we assume that the MODIS based h_i retrieval is not accurate enough for thicker ice. The total number of data points is 322. The amount data for h_i less than 40 cm is very small, only 23 data points. The scatter plot between the snow and ice thickness data with fitted linear regression line is shown in Figure 7. The linear regression fit to the data is:

$$h_s = 0.049 \cdot h_i + 3.3 \text{ cm} \qquad (6)$$

The coefficient of determination is very small, only 0.04 (p-value is 0.00), due to the large data scatter. Typically the snow thickness is below 10 cm regardless of the ice thickness. Using equation (6) h_s is 4.3 cm when h_i is 20 cm, whereas (5) yields h_s of only 1 cm. For ice thinner than 40 cm (6) gives likely too thick snow covers. Due to the small amount and large scatter of data points when $h_i \leqslant 35$ cm these data points could have a large effect on the regression coefficients. Thus, next the regression line is fitted to data points with $h_i > 35$ cm (number of data points is 310):

$$h_s = 0.054 \cdot h_i + 2.9 \text{ cm} \qquad (7)$$

The coefficient of determination is again only 0.04 (p-value is 0.00). The difference between (6) and (7) is insignificant indicating that (6) is robust fit to the data.

As (6) likely gives too thick snow covers for thin ice we combine the Sever data and Doronin's (1971) relationship of (5) in the following way: a) the Sever data are divided into 10 cm thickness bins centered from 30 cm to 90 cm (in the 30 cm bin one outlier datapoint was removed due its large effect on the mean h_s value) and the mean h_s and h_i are calculated, b) at h_i values of 0, 10 and 20 cm (4) is used, and c) linear regression is fitted to these datapoints, see Figure 8. The regression equation is:

$$h_s = 0.09 \cdot h_i + 0.1 \text{ cm} \qquad (8)$$

The constant term is so small that it can be dropped. When $h_i < 20$ cm this equation likely gives too thick snow cover, especially for polynyas. Thus, for this thickness range we chose to use (5) yielding the following final h_i vs. h_s relationship:

$$\begin{aligned} h_s &= 0 \text{ , for } h_i < 5 \text{ cm} \\ h_s &= 0.05 \cdot h_i \text{ , for } 5 \text{ cm} \leqslant h_i \leqslant 20 \text{ cm} \\ h_s &= 0.09 \cdot h_i \text{ , } h_i > 20 \text{ cm} \end{aligned} \qquad (9)$$

The only difference between (9) and (5) is 10% smaller slope term in (9) when h_i is larger than 20 cm.

Ice thickness is now estimated using:

$$h_i = \frac{k_s}{k_s + b_1 k_i} H \text{ , } \qquad (10)$$

where b_1 is the slope term in (9) and H is the thermal ice thickness (effect of snow cover excluded):

$$H = \frac{k_i (T_S - T_W)}{F_t} \text{ . } \qquad (11)$$

Distinctly, there are quite many simplifications/approximations in the approach above to minimize the difficulties in the retrieval of h_i . The h_i retrieval is highly sensitive with respect to the model parameterizations and the accuracy of the forcing data. In a previous study in the Arctic it was assessed that the uncertainty increases from 25% for thin ice (10-30 cm) up to 50% for h_i around 1 m (Yu and Rothrock 1996). The largest uncertainties came from downward longwave radiation flux and sensible heat flux. A more recent study utilizing the same method for the h_i retrieval as Yu and Rothrock (1996) with the Advanced Very High Resolution Radiometer (AVHRR) Polar Pathfinder extended (APP-x) product (25 km pixel size) showed h_i estimation capability up to approximately 2.8 m with an correct accuracy of over 80% (Wang et al. 2010). During the nighttime the largest error sources were snow thickness, cloud amount, and wind speed. Yu and Rothrock (1996) used uncertainty estimates of the heat fluxes in the h_i accuracy analysis, but Wang et al. (2010) used variables of the heat fluxes. Both studies did not use NWP model data in the h_i retrieval. Air temperature(T_a) was estimated as T_S average over a large area plus a climatological constant, and wind speed from the geostrophic wind. In summary, the h_i accuracy decreases as h_i increases, and the accuracy and the maximum retrievable h_i decreases as weather gets warmer as then T_S saturates at smaller h_i and the T_S contrast between different ice thicknesses decreases. It is noted that the above approach for T_S based h_i retrieval is basically only valid for smooth thermodynamically grown ice.

When calculating the MODIS h_i chart following restrictions and procedures are applied. 1) The MODIS sensor scan angle (max 55º) of the T_S data is limited to below 40º in order to restrict the effect of atmosphere and deterioration of spatial resolution in T_S . At scan angle of 40º

the across track resolution is around 2 km (at nadir it is 1 km). 2) The calculated h_i is rounded to 1-cm resolution. 3) The h_i retrieval yields sometimes erroneous negative h_i values for thick ice ($F_t > 0$ in (11) which is erroneous) due to the either errors in the HIRLAM data or in the model parameterizations. These erroneous h_i values are flagged in the h_i chart. 4) For very thin ice (few cm) negative h_i values are sometimes obtained, these are marked to 0 m (i.e. open water). 5) Using 10x10 km block averages of T_S and T_a following changes are made to the calculated h_i chart: a) If $T_a > -5$ ºC then the calculated h_i is masked away. It is assumed that at these warm air temperatures the sensitivity between T_S and h_i is too small for accurate h_i retrieval. b) If $T_a > -5$ ºC but $T_S - T_w$ >-1.0 ºC, then the block is flagged as open water. It is not possible to separate accurately open water and 0-3 cm thick ice due to the inaccuracies of the T_S (RMSE at best 1.3 K) and heat fluxes. 6) Finally, it is assumed that h_i values over 1.0 m are too unreliable and they are flagged away.

The MODIS based ice thickness chart is delivered as Matlab-file with 1-cm resolution. In the data landmask has value of 1.0 m, cloudmask has -0.2 m, areas with scan angle larger than 40º have also -0.2 m, no-data areas over the ocean have -0.3 m, areas with air temperature larger than -5 ºC have values of -0.15 m, but if block averaged T_S was larger than T_W -1.0 K then open water is instead indicated, and finally, ice thickness values over 1.0 m and erroneous negative thickness values are both flagged with -0.1 m. Figure 9 shows an example of the ice thickness chart.

Tiff-images showing daily ENVISAT WSM strip coverages over the MODIS ice thickness images are also processed. These were used to select the best image pairs for the MODIS-SAR based ice thickness chart calculation.

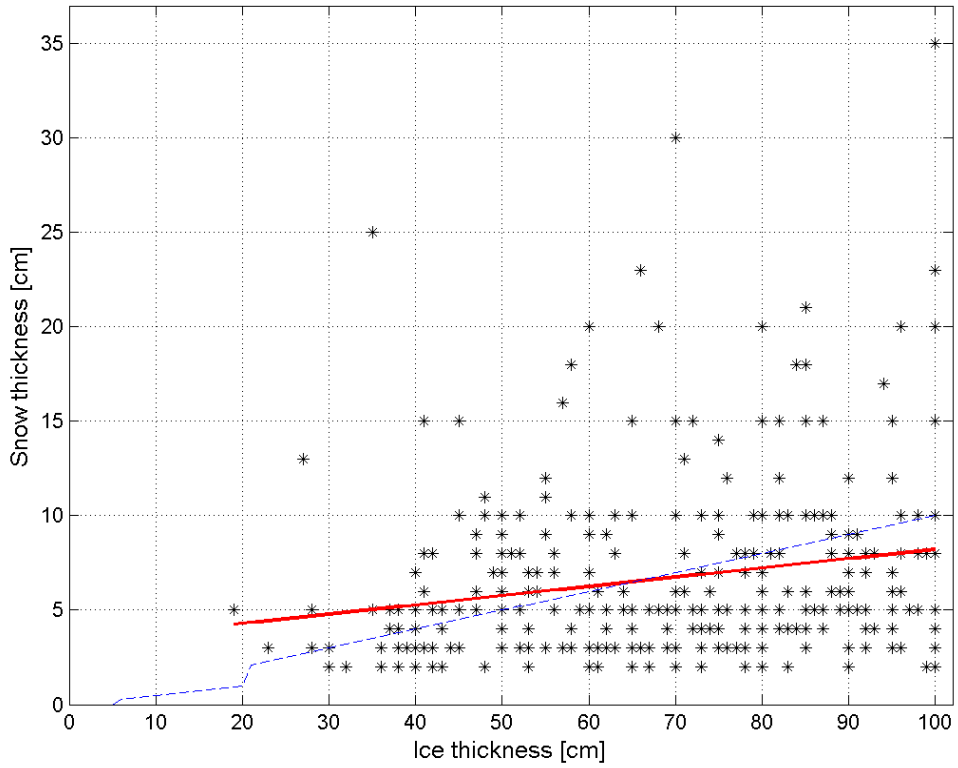

Figure 7. The relationship between snow and ice thickness for level ice from the Sever data acquired in 1950-1989 in the Kara Sea study area. Only ice thickness values less than 1 m. Red line is linear regression fit to the data. Blue dashed line is Doronin's (1971) empirical relationship.

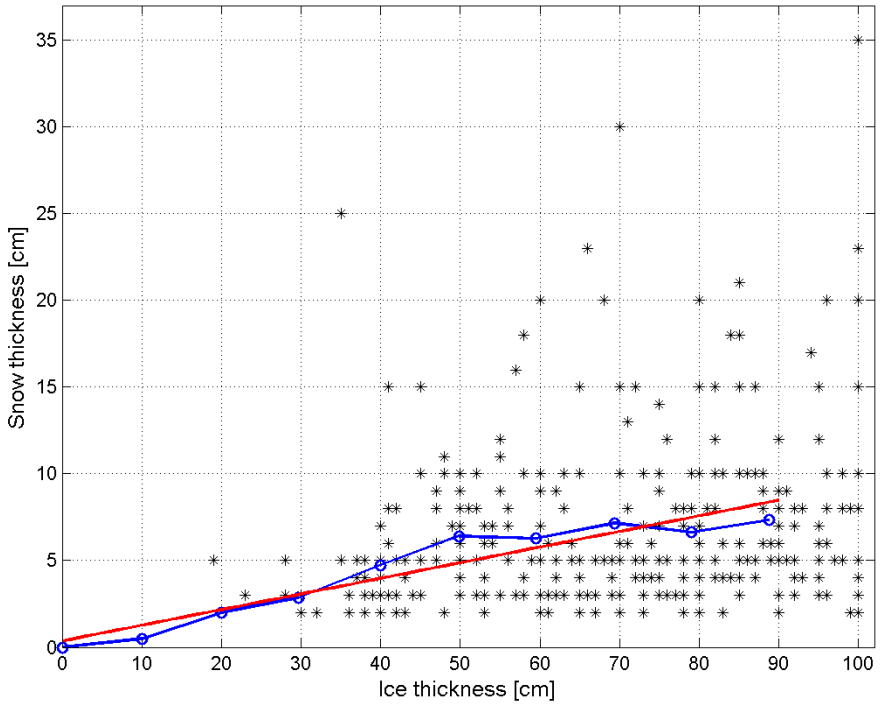

Figure 8. The relationship between snow and ice thickness for level ice from the Sever data acquired in 1950-1989 in the Kara Sea study area. The blue line is the average snow and ice thickness relationship using the Sever data for thickness range from 30 to 90 cm and Doronin's (1971) empirical equation for 0 to 20 cm range. Red line is linear regression fit to the average data.

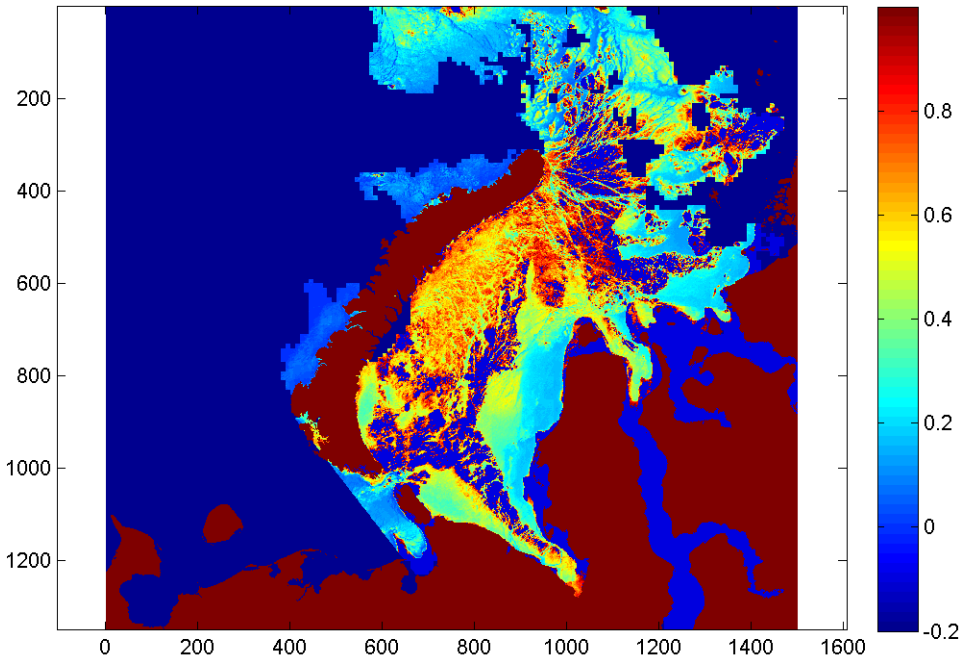

Figure 9. MODIS based ice thickness [m] chart for the Kara Sea validation area on 23 February 2010.

4.1.4 Accuracy and maximum value of the MODIS based ice thickness

The accuracy of the MODIS T_S based h_i is studied here in following two ways: 1) Using estimated or guessed standard deviations and correlations of the input variables to the h_i retrieval the h_i uncertainty is estimated with the Monte Carlo method. The uncertainty, or relative accuracy, is quantified with std(h_i)/mean(h_i) (coefficient of variation vc) of the sampled h_i values from (10). 2) MODIS h_i charts from consecutive days are compared to each other. Large differences are mainly due to the cloud masking errors and HIRLAM data inaccuracies. The comparison estimates repeatability of the h_i retrieval when the true h_i change is insignificant, but the forcing data and T_S may have large changes in short period of time. Currently we don't have any co-incident in-situ thickness data for the Kara Sea to accuracy studies.

The typical maximum retrievable h_i under different T_a ranges is determined using besides the results of the h_i accuracy analyses also empirical mean $T_a - T_S$ vs. h_i relationship which shows how rapidly h_i changes as a function of slight change of T_S or T_a .

In the above studies the Kara Sea MODIS h_i charts for the winter 2010-2011 are utilized.

Ice thickness uncertainty with the Monte Carlo method

The Monte Carlo sampling of h_i values is conducted only at the HIRLAM grid points to reduce computation burden. T_S is here 3 by 3 pixels average at the grid points to decrease T_S local variation. A grid point is included in the h_i sampling only if all pixels of a 3 by 3 block in the h_i chart have valid h_i values ($0 \leqslant h_i < 1$ m). In total there are 36549 grid point datasets for the h_i sampling. Table 1 shows the estimated or 'best guessed' standard deviations of the variables needed in the h_i sampling. Snow thickness uncertainty is characterized by std of b_1 . The chosen std of 0.02 for b_1 in (8) represents 40% vc for h_s when $h_i \leqslant 20$ cm and 22% when $h_i > 20$ cm . The stds for T_a , u and Rh are from the HIRLAM vs. weather station data comparison, see Section 5.1.1. For these variables stds, not RMSEs, from the comparison are used because the observed difference distributions are characterized by the mean bias and std. Only correlations between T_S and the HIRLAM T_a , F_l^{dn} , u and Rh are taken into account in the random sampling. These were estimated from the grid point data. The correlation is the largest, +0.89, between T_a and F_l^{dn} , and the second largest, +0.83, between T_S and T_a . For other variable combinations the absolute correlation varied from 0.23 to 0.79. T_S , T_a , u , Rh and F_l^{dn} were sampled from a 5-dimensional normal distribution. Also other variables were sampled from normal distributions. With each grid point dataset 1000 random h_i values were calculated. Before calculating mean and std for the sampled h_i values negative un-physical v h_i alues are rejected as are the upper 5% of the positive h_i values. Very large h_i values ($h_i \gg 1$ m) are due to the random F_t in (11) having a value very close to zero, and they would increase std(h_i) considerably if not excluded. Next, the h_i values are divided into 5 cm wide bins and the average and std of std(h_i)/mean(h_i) are calculated for the all data and for the 5 ºC wide T_a ranges and 2 m/s wide u ranges. The results of the Monte Carlo simulation are shown in Figures 10-12.

The mean vc using all the data is the smallest, 39-41%, for the h_i range from 10 to 30 cm and it increases slowly to 63% when h_i is 80 cm, see Figure 10. The mean vc is 46% when h_i is 5 cm and approaches 100% when h_i is only 1-2 cm. If the maximum allowable mean vc is set to 50% then the typical maximum h_i we can retrieve reliably from the MODIS T_S is around 50 cm, and the typical minimum is 3-4 cm.

Table 1. Standard deviations of the variables used in the Monte Carlo estimation of the MODIS based ice thickness uncertainty for the Barents and Kara Seas study area.

Variable	std	Variable	std
T_S	1.3 K	k_s	0.05 W m^{-1} K^{-1}
T_a	3.7 K	b_1	0.02
u	function of u 2.0 – 5.1 m/s	S_i	1 ppt
Rh	10%	ϵ	0.01
F_l^{dn}	20 W/m^2	C_s, C_e	10% of expected value

The large scatter of datapoints in Figure 10 is partly due to the dependence of the h_i uncertainty on T_a and u ; e.g. F_s is a function of $T_a - T_S$ and u . Figure 11 shows the mean vc as a function of T_a range. There are missing values in the curves due to insufficient amount data at some h_i bins and T_a ranges. The mean vc , i.e. the h_i uncertainty, clearly decreases with decreasing T_a when $h_i > 20$ cm . If we again take the vc limit of 50% for the reliable h_i then the maximum h_i is 60 cm when $T_a < -30$ ºC , but it is only 25 cm when $-20 < T_a < -15$ ºC . For all the 2010-2011 MODIS data the HIRLAM T_a is less than -20 ºC in 86% of the cases. The mean vc as function of u range is depicted in Figure 12. The mean vc increases considerably with the increasing u when $h_i > 10$ cm . With the 50% h_i uncertainty limit the maximum h_i is 65 cm when $u \leqslant 2$ m/s and only 20 cm when $7 \leqslant u \leqslant 8$ m/s . For the MODIS data the modal u is 3 m/s and 90% of the u values are below 6 m/s. Figures 11 and 12 show that the h_i uncertainty is the smallest under very cold calm wind conditions. As the h_i uncertainty depends considerably on T_a and u it is difficult to determine the typical maximum for reliable h_i , but under typical weather conditions for the MODIS data the maximum h_i is around 50 cm.

The h_i uncertainty figures obtained here are larger than those by Yu and Rothrock (1996). They assessed that the h_i uncertainty increases from around 25% for thin ice (10-30 cm) up to 50% for h_i around 1 m. However, they estimated much smaller stds for T_a and u , only 1.6 ºC and 0.7 m/s, respectively. If we decrease here stds of T_a and u to 1 ºC and 1 m/s then the h_i uncertainty is below 40% when h_i is 80 cm and in the h_i range of 10-30 cm it is only around 20%. Also the dependence of the h_i uncertainty on T_a and u decreases. When the std of b_1 is doubled to 0.04, corresponding 68% and 44% h_s uncertainty when $h_i \leqslant 20$ cm and $h_i > 20$ cm , respectively, the h_i uncertainty increases slightly; 50% limit is reached when h_i is 45 cm.

The contribution of different variables to the h_i uncertainty was studied by taking into account std of only one variable at the time in the h_i sampling. The largest h_i uncertainty comes from T_a . T_S and F_l^{dn} have somewhat smaller roughly equal contributions. When $h_i < 30$ cm then also u has significant contribution to the h_i uncertainty. The h_i uncertainty from snow thickness alone is around 10%. Direct comparison of our results to those by Yu and Rothrock (1996) and Wang et al. (2010) is not possible as they did not use NWP model data in the h_i retrieval, but in their results F_l^{dn} and u were among the largest error sources.

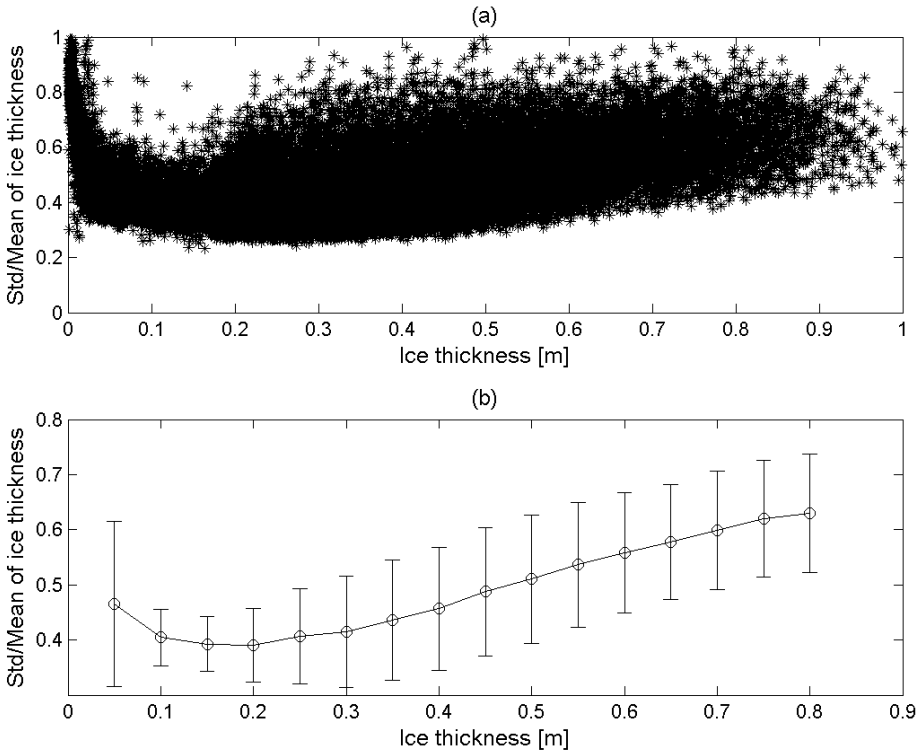

Figure 10. Uncertainty of the MODIS based ice thickness estimated with the Monte Carlo method for the Kara Sea validation area. (a) Mean and std/mean of the sampled thickness values. (b) The average thickness uncertainty as a function of thickness and the variation of the uncertainty characterized by std(std/mean).

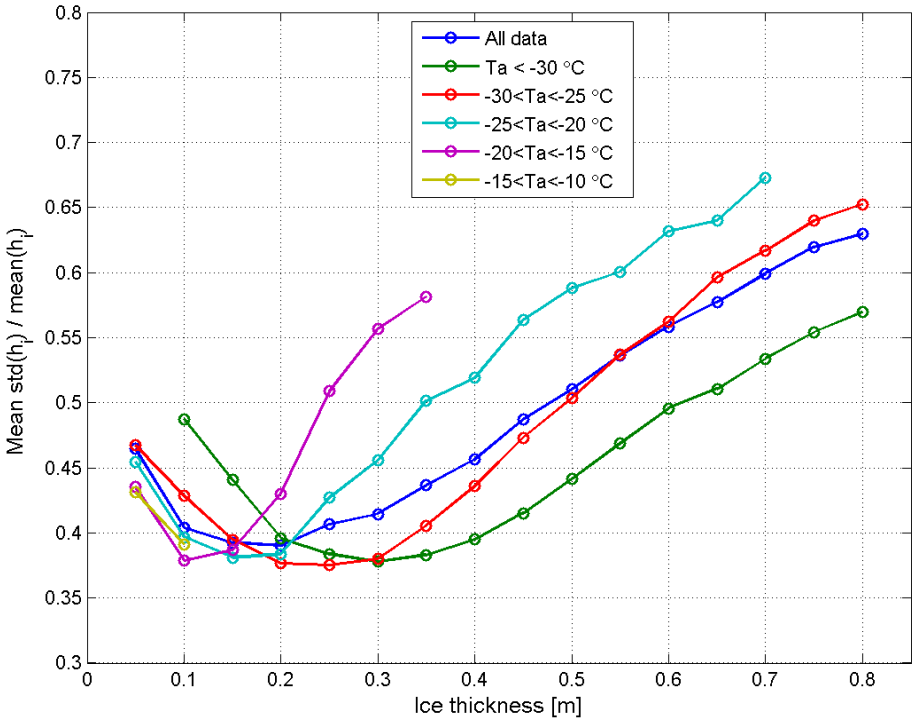

Figure 11. The average uncertainty of the MODIS based ice thickness as a function HIRLAM air temperature range.

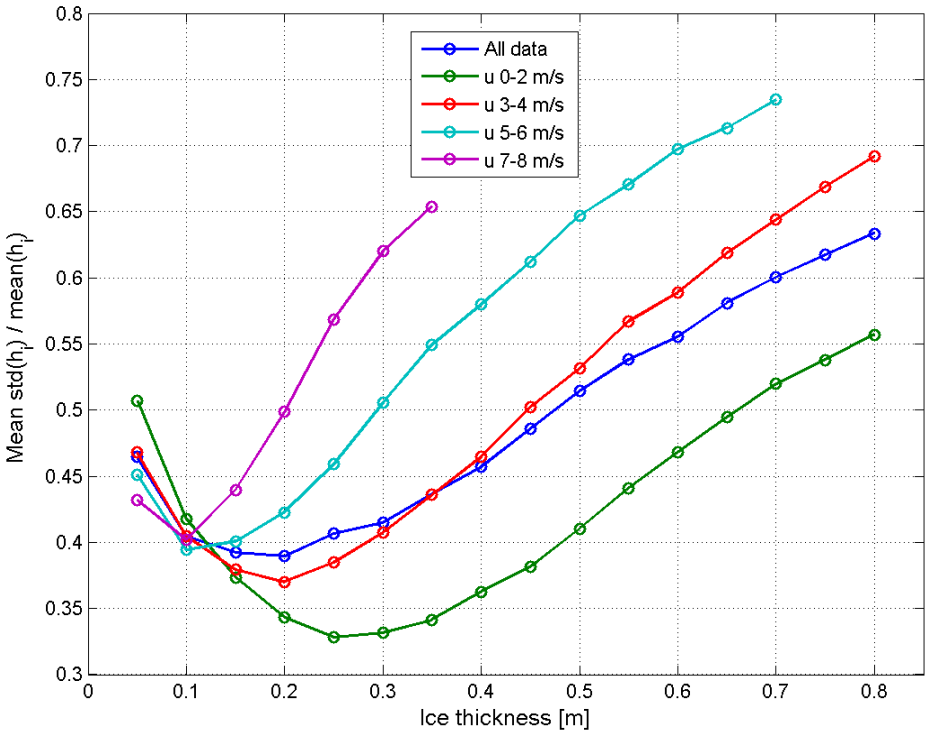

Figure 12. The average uncertainty of the MODIS based ice thickness as a function HIRLAM wind speed range.

Comparison of thickness charts from consecutive days

The comparison of the h_i charts from consecutive days estimates repeatability of the h_i retrieval when the true h_i change is insignificant, but the forcing data and T_S may have large changes in short period of time. Large h_i differences are mainly due to the cloud masking errors and HIRLAM data inaccuracies. Undetected high thin clouds results in a cold bias in T_S making the ice appear thicker than it actually is (Martin et al. 2004, Tamura et al. 2006). Ice fog generated by intense vapour from leads under cold conditions is warmer than surrounding fast or pack ice T_S and colder than T_S for thin ice leads. This leads to h_i underestimation for pack ice and overestimation for leads.

For this study there are 51 h_i chart pairs from the winter 2010-2011. The time difference between the h_i charts varied from 15 to 33 hours with the average of 24 hours. During these short time periods the ice growth is typically only few centimetres (Leppäranta 1993). h_i differences (earlier h_i chart minus later one) from the chart pairs were calculated using 10 by 10 km block averages in order to diminish the effect of ice movement. The coefficient of variation (std/mean) for each block with all h_i pixels valid ($0 \leqslant h_i < 1$ m) was required to be less than 20% to reject too heterogeneous ice areas (large h_i variation) in the comparison. In total there are 12632 h_i difference values from the charts pairs.

The overall RMSE for the h_i difference data is 7.7 cm, the mean absolute bias is 5.8 cm and 90% of the absolute h_i differences are below 12.3 cm. Within the h_i chart pairs RMSE varies from 2.8 to 20.4 cm and the average is 8.8 cm. There are no clear relationships between the T_a or u differences and the h_i differences, but the absolute T_a and u differences are typically small, below 2.5 ºC and 2.5 m/s, respectively. This suggests that cloud masking problems caused the large RMSE for some h_i chart pairs. For the h_i intervals of 0-10, 10-20, 20-30, 30-40, 40-50 and 50-60 cm RMSE is 4.8, 5.1, 6.6, 8.2, 10.0 and 10.1 cm, respectively. RMSE is from 18% to 34% of the

h_i bin centre value when the bin 0-10 cm is excluded. These statistics demonstrate rather good stability (or repeatability) of the MODIS and HIRLAM data based h_i charts.

Maximum reliable MODIS ice thickness

Next typical maximum reliable h_i under different T_a ranges (width 5 ºC) is studied using empirical mean $T_a - T_S$ vs. h_i curves which shows how rapidly h_i changes as a function of slight change of T_S or T_a . These curves were calculated from the MODIS T_S and h_i and HIRLAM T_a averages (3 by 3 pixel block) at the HIRLAM grid points. As $T_a - T_S$ vs. h_i depends also on the HIRLAM u it was required to be less than 6 m/s to include only the most common wind conditions of the MODIS data. The number of the grid point datasets is here 33420. The mean h_i in the curves was calculated inside 1 ºC wide $T_a - T_S$ bins with bin centers from -20 to +3 ºC. Figure 13 shows as an example $T_a - T_S$ vs. h_i scatterplot and the calculated average relationship for the T_a range of $-25 \leqslant T_a < -20$ ºC . Figure 14 shows the mean $T_a - T_S$ vs. h_i curves for six different T_a ranges.

When $T_a - T_S$ approaches 0 ºC then the sensitivity between $T_a - T_S$ and h_i increases, merely 1 ºC change in $T_a - T_S$ can cause over 10 cm change in h_i . Taking into account the rms-accuracies of T_S and T_a (and other variables in (10)) this sensitivity is too large for accurate h_i retrieval. Whereas when $T_a - T_S < -5$ ºC then a 1 ºC change leads at maximum to 4 cm change in h_i . Besides the maximum acceptable $T_a - T_S$ vs. h_i sensitivity also the $T_a - T_S$ difference itself could be a limiting factor when determining the maximum reliable h_i . When $T_a - T_S > 0$ ºC then due to the radiative surface cooling the snow/ice surface is colder than the air and the simple parametrizations of the turbulent sensible and latent heat fluxes may be liable to large errors, a common problem for stable boundary layer (Järvenoja 2004; Hanna and Yang, 2001). We suggest that the maximum allowed $T_a - T_S$ should be 0 ºC or only few degrees larger. Figure 14 indicates that at a fixed $T_a - T_S$ value the corresponding mean h_i decreases considerable with increasing T_a .

In summary, the maximum reliable h_i depends on 1) maximum acceptable $T_a - T_S$ vs. h_i sensitivity, 2) maximum allowed $T_a - T_S$, 3) acceptable h_i uncertainty based on the Monte Carlo simulation, and 4) T_a . If we set the maximum $T_a - T_S$ to 0 ºC and the $T_a - T_S$ vs. h_i sensitivity to be less 10 cm / 1 ºC then the maximum h_i varies from 49 cm when $T_a < -30$ ºC (max $T_a - T_S$ now -2 ºC due the sensitivity limit) to 36 cm when $-20 \leqslant T_a < -15$ ºC (max $T_a - T_S = 0$ ºC). For the first T_a range the h_i uncertainty is below 50%, but for the second one the 50% uncertainty limit decreases the maximum h_i to 25 cm. For all the MODIS data the HIRLAM T_a is less than -20 ºC in 86% of the cases. Combining the results of different accuracy analyses the typical maximum reliable h_i is here around 35-50 cm under typical weather conditions present in the MODIS data.

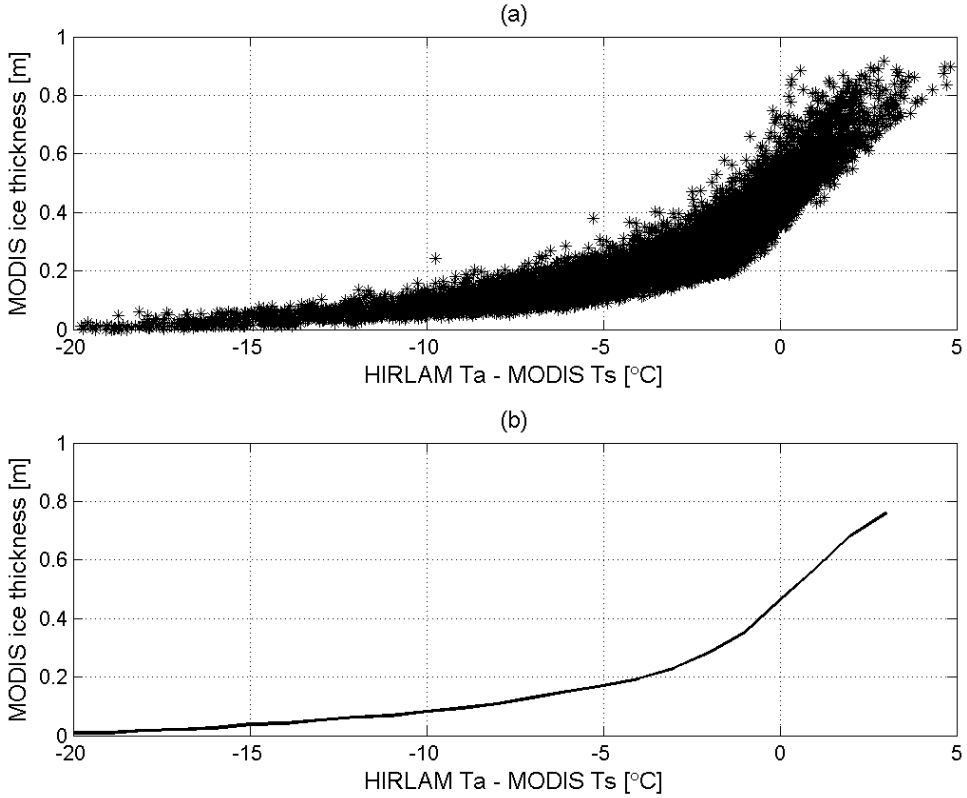

Figure 13. Empirical relationship between $T_a - T_S$ and h_i in the HIRLAM T_a range of $-25 \leqslant T_a < -20$ ºC . (a) scatterplot between the variables and (b) calculated average relationship.

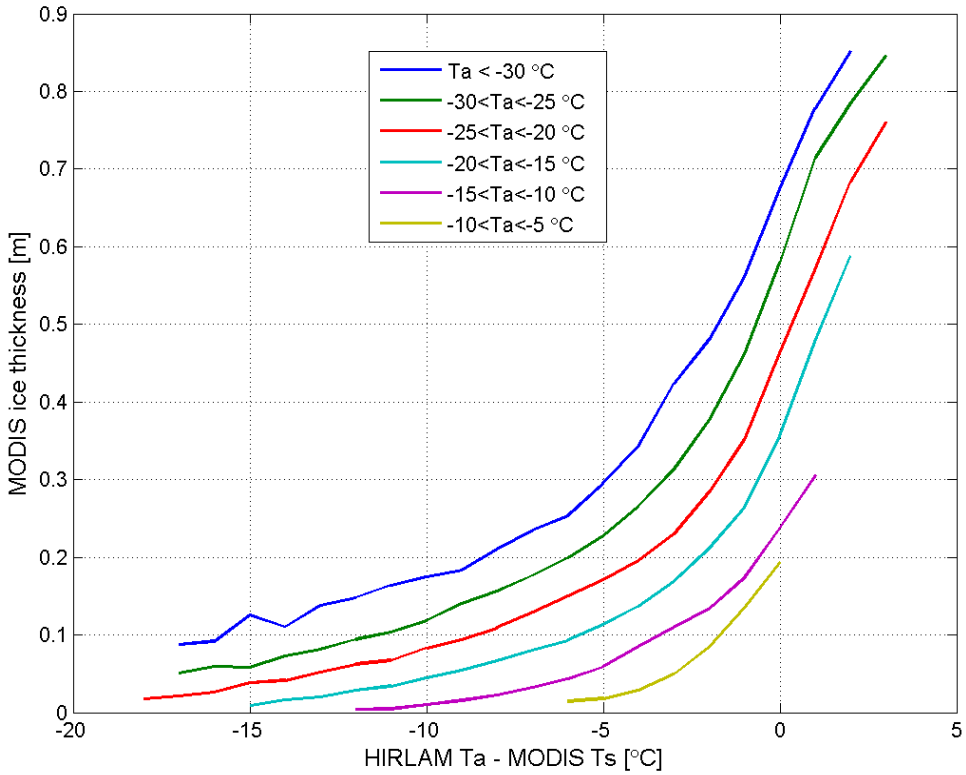

Figure 14. Empirical average relationship between $T_a - T_S$ and h_i for different T_a ranges.

4.1.5 MODIS and ENVISAT WSM based ice thickness chart

We introduce here a method to construct an ice thickness chart using three satellite sensors and one-dimensional high-resolution thermodynamic sea ice model HIGHTSI (see Section 5.2 for HIGHTSI details). In the chart the ice cover is divided into several ice thickness categories for level and deformed ice fields. The basic idea is to retrieve the thin (0-40 cm) and thick (>40 cm) ice thickness categories using different satellite sensors. The thin ice thickness h_i is retrieved from the MODIS h_i charts. h_i is assessed to be accurate up to 35-50 cm in the weather conditions typical for the Kara Sea in winter. When the MODIS h_i map indicates ice to be thicker than our threshold of 60 cm, the ice thickness is retrieved from a combination of ENVISAT WSM image and background level ice thickness chart H_i provided by the HIGHTSI model forced with HIRLAM data. When one examines the C-band backscattering coefficient (σ^o) statistics as a function of ice thickness in the cold conditions of the Kara Sea, the distribution of σ^o values for thin ice (<30 cm) covers the whole dynamic range of σ^o . However, now we are able to exclude thin ice regions with the MODIS h_i maps. This significantly reduces the ambivalence in the interpretation of σ^o in the SAR images. We use a feature which adds information on mesoscale ice dynamics into the static H_i . The dynamics are derived from AMSR-E ASI sea ice concentration maps. The modified background ice thickness field H_b is then combined with the SAR data to produce the ice thickness chart for thicker ice categories (> 60 cm). In the absence of in-situ data the algorithm is calibrated according to the Arctic and Antarctic Research Institute (AARI) ice charts for thicker ice categories.

Our primary objective is to locate the areas of thinnest ice among the drift ice. The resulting thickness charts do not attempt to estimate the total ice mass, only the spatial distribution of thin and thick ice. Our approach is effective especially during the freeze-up period but it is able provide information on the marginal ice zone and polynya dynamics also later in the winter.

Our approach is presented in detail in a paper submitted to Annals of Glaciology in May 2012 (Similä et al. 2012) (special issue for IGS 2012 conference). Here a summary is presented. In the paper we discuss the ice thickness chart construction method and the chart accuracy with Kara Sea data for the winter 2008-2009 which is previous to the SMOS data availability. However, the results there are also valid for the thickness charts of 2010-2011 available to the SMOSIce work. In the paper the assessment of the detection success of thin and thick ice areas was performed using the AARI charts and visually interpreted SAR images as reference data.

It is suggested that the MODIS-SAR based ice thickness chart is used only for visual qualitative comparison with the SMOS thickness chart, e.g. to check how areas of ice thicker than 0.5 m match each other in the charts.

The MODIS-SAR based ice thickness chart is delivered as Matlab-file with 10 cm thickness bins with bin centers of 0, 5, 15, 25 cm and so on. In the data landmask has value of 1.5 m and no-data areas are marked as -0.5 m. The pixel size of the chart is 400 m.

HIGHTSI ice thickness field

We used the HIGHTSI model to create a thermodynamically grown ice thickness field H_i . For details of the HIGHTSI model and its output parameters see Section 5.2. The HIGHTSI model run was forced by HIRLAM using a grid size of 20 km. At each grid cell, the ice/no ice condition is determined by AMSR-E ASI sea ice concentration (IC) map (Spreen et al. 2008). IC values less 15% were considered to represent open water. In the model run the occurrence of open water in a previously ice covered area was taken into account using the following procedure. The model run was stopped when the grid point situated in open water and the previous snow and ice parameters were resumed when the grid point in question is again ice covered. This gives reasonable results when we have a practically closed basin where the majority of pack ice moves back and forth between the nearest grid points. This is the case e.g. in the Bay of Bothnia in the Baltic Sea. In sea areas where the ice conditions are highly dynamic and the basin has a large open boundary, as in the Kara Sea, the adopted approach produces mixed results.

The static H_i field yielded too large ice thickness values in several instances. To gain insight into these errors, their magnitude and spatial location, we compared the monthly AARI ice charts to the H_i fields. The origin of these errors are typically in the ice situations where the ice edge has retreated and new ice is formed in opened sea. Then the activation of the HIGHTSI model run with previous ice and snow parameters produces erroneous results. The same argument applies for the large polynya areas. During December and January the H_i values were in the southern and northern Kara Sea 0-40 cm thicker compared to the AARI ice charts. Too large H_i values persisted through February and March in the southern Kara Sea. The difference between the H_i values and the dominant mean thickness according to the AARI ice charts began to reduce from February onwards in the northern Kara Sea basin. From mid-March the H_i values could be considered to be generally close to those shown in the AARI charts, with the exception of thin ice areas. In April the trend actually slightly reversed so that the H_i values stayed often below those in the AARI chart. However, the overestimation bias through three and half months period affected to our practice to utilize the H_i values because the majority of our images were acquired during that period.

In order to introduce some large scale ice dynamics into the H_i we utilize the changes in the daily IC's. We recorded the IC history in the test area during the previous 14 days prior the classification day to modify the H_i field. A set of rules were constructed to extract from the IC history information on mesoscale ice dynamics and occurrences of large polynyas. The goal of these rules was to locate ice areas in which significant divergent events have been occurring. As the end result we reduced H_i in these areas. Based on the IC statistics we construct a weight matrix W which

is applied to H_i field to obtain a modified background ice thickness H_b, see details in (Similä et al. 2012), which would correspond better the thickest mean ice present in the area of interest. Prior the classification H_b is interpolated to the same grid as the SAR data.

The proposed approach utilizing the W matrix is a very rough approximation for the ice dynamics on the mesoscale and works only for a part of the ice covered area. One fundamental problem is that it is not able to indicate anything about convergent areas. All information related to the ice deformation must be derived from MODIS h_i maps or from SAR σ^o level.

SAR based ice thickness chart

The backscattering at C-band HH-polarization is dominated by the ice surface scattering when the incidence angle is less than 45 degrees (Carlström and Ulander 1995; Dierking et al. 1999). The magnitude of σ^o is modulated by the small-scale (mm) and large-scale (cm to m) surface roughness. The σ^o values from level ice can in some rare cases rise up to those from deformed ice, but in most cases they are essentially smaller. In a Baltic Sea ice data set analyzed by Similä et al. (2010) the maximum measured σ^o from level ice was about -15 dB, most of the σ^o values being less than -17 dB. However, large scale surface roughness appear in many shapes and forms such as brash ice, pancake ice, rafted ice, hummocked and ridged ice. These first-year ice (FYI) types have largely different ice thickness categories from 5-15 cm (pancake ice) to a few meters (heavily ridged areas). However, all these ice types typically have large σ^o values. Some of the variability of the SAR σ^o signatures can be seen in Figure 15. There the ice cover was divided into four ice types: nilas (< 10 cm), young ice (10-30 cm), smooth FYI ice (totally or mostly undeformed ice) and rough FY pack ice where visible traces of deformation could be detected in the SAR imagery. The identification of the two first ice types was done using the MODIS h_i charts, and the last two visually in the SAR imagery.

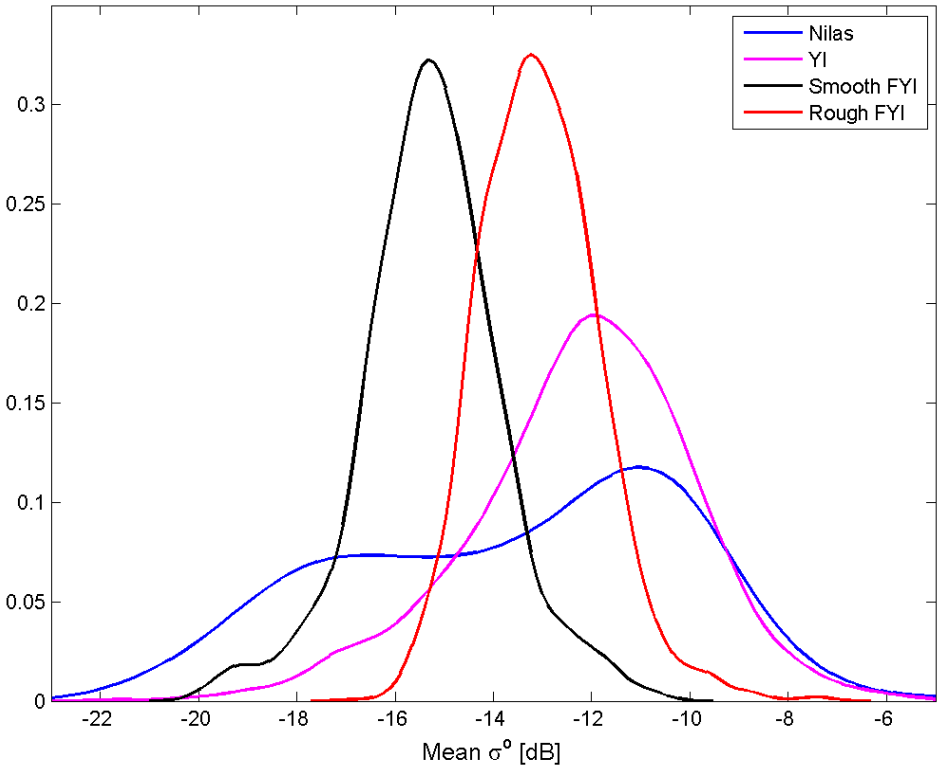

Figure 15. The distribution of the backscattering coefficients σ^o for four different ice types. The σ^o value is the average over 3.1 km by 3.1 km area. The incidence angle is 30 degrees. Nilas

(thickness less than 10 cm) and young ice (10-30 cm) were identified on the basis of MODIS based ice thickness charts.

The WSM images were rectified to a polar stereographic coordinate system (mid-longitude 63E, true-scale 60 latitude 70N) with 100 m pixel size and calibrated. Due to the large variation of the incidence angle in a single WSM scene a linear incidence angle correction proposed by Mäkynen et al. (2002) was performed. Using the same approach we determined empirically a correction factor for the Kara Sea, the value of the factor is -0.25 dB/deg. This is very close to the factor -0.23 dB/deg obtained for the Baltic Sea in (Mäkynen et al. 2002).

To translate the magnitude of the SAR σ^o to correspond a specific ice type in a meaningful way we use the results shown Figure 15 and the experience gained by visually interpreting a multitude of SAR images over the test area. We averaged the σ^o values to the resolution of 400 m. In our SAR data the dynamic σ^o range at this resolution is from -20 dB (smooth new ice) to -9 dB (pancake ice). Also larger σ^o values appear but they represent open water.

There exist several ice types simultaneously in the ice pack. In the ice charts this variability is typically denoted by assigning to each ice polygon the areal fractions of the three main ice types. Here we extract several ice types on the basis of the MODIS and SAR data. According to the MODIS h_i charts we locate thin ice areas. The rest of ice thickness chart estimates h_{ch} are determined according to the h_i and H_b values. We define h_{ch} as

$$h_{ch} = F \cdot H_b \quad . \qquad (12)$$

We let the factor F depend on the σ^o magnitude. The σ^o based sea ice typing rules, the F values and the expected ranges for h_{ch} are shown in (Similä et al. 2012). When we assign an ice type and a F value to a specific σ^o range we are aware of the unambiguous relationship between σ^o and ice type. We choose the ice type which on the basis of our subjective experience and knowledge is the most likely ice type for a given σ^o range. We are not able to say how much the σ^o values originating from different ice types overlap each other. We also experimented with some texture features, but we were not able to relate them to different ice types in a consistent manner.

Combined ice thickness chart

To produce the overall ice thickness chart we combine the different ice thickness charts at our disposal in the following two ways. The MODIS/SAR chart covers only the cloud-free MODIS area whereas in the AMSRE/MODIS/SAR chart the coverage is the whole SAR image area. The MODIS/SAR chart is constructed as follows:

$$h_{ch1} = h_i, \text{ if } h_i \leq 0.6 \text{ m} \qquad (13)$$
$$h_{ch1} = F \cdot H_b, \text{ if } h_i > 0.6 \text{ m}$$

The h_{ch1} chart covers the cloud-free area of the MODIS image. We regard it very likely that even in the range 50-60 cm the uncertainty of the h_i values is smaller than the uncertainty of the thickness estimates obtained by (12). The major problem in the MODIS/SAR chart is the cloud cover which prevents to calculate this chart regularly for a given area.

Our second approach is designed to overcome the cloud cover issue and to obtain ice thickness estimates also for clouded areas. Instrumental mean in this respect is the IC history based weight matrix W . The AMSRE/MODIS/SAR chart is constructed in the following manner:

$$h_{ch2} = h_i, \text{ if } h_i \text{ defined and } h_i < 0.4 \text{ m} \qquad (14)$$

$$h_{ch2} = F \cdot H_b, \text{ if } h_i > 0.4 \text{ m or } h_i \text{ undefined}$$

According to the definitions the major difference between h_{ch1} and h_{ch2} is that the latter one is defined for the whole SAR covered area regardless if MODIS based h_i is defined or not. The MODIS/SAR chart h_{ch1} requires that h_i is defined, i.e. the area in question is cloud-free. Thick ice estimates are always identical for the cloud-free areas. As the h_{ch2} chart also requires cloud-free MODIS data, it is not possible to monitor continuously the ice movement except the mesoscale dynamics coded into the W matrix. The major benefit of the h_{ch2} chart is that we obtain ice thickness chart for the whole SAR covered area. A disadvantage is that the uncertainties related to this approach are larger than those in the h_{ch1} chart.

On the basis of the AARI ice charts the h_{ch} charts usually give a realistic view of the ice mass distribution although the ice thickness values are only rough estimates. However, in the detection of thin ice areas our procedure usually gives good results although it is sometimes subject to error because of the underestimation bias in the MODIS h_i chart.

Figures 16-20 show an example of the input images to the ice chart construction and the resulting h_{ch1} and h_{ch2} charts.

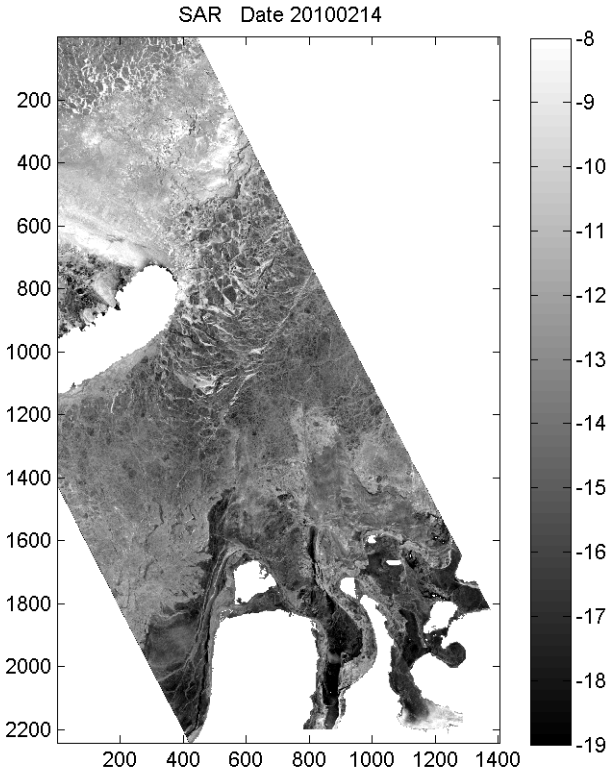

Figure 16. ENVISAT WSM image acquired on 21 Feb 2010.

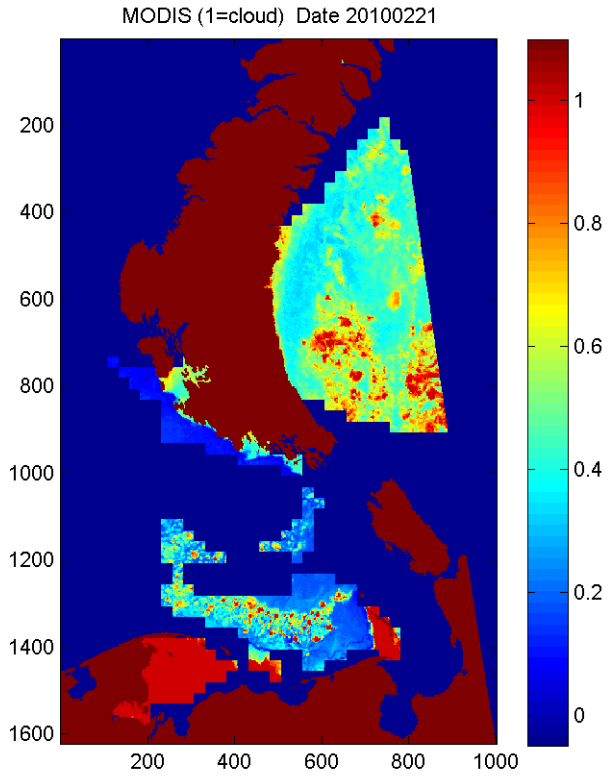

Figure 17. MODIS ice thickness chart on 21 Feb 2010.

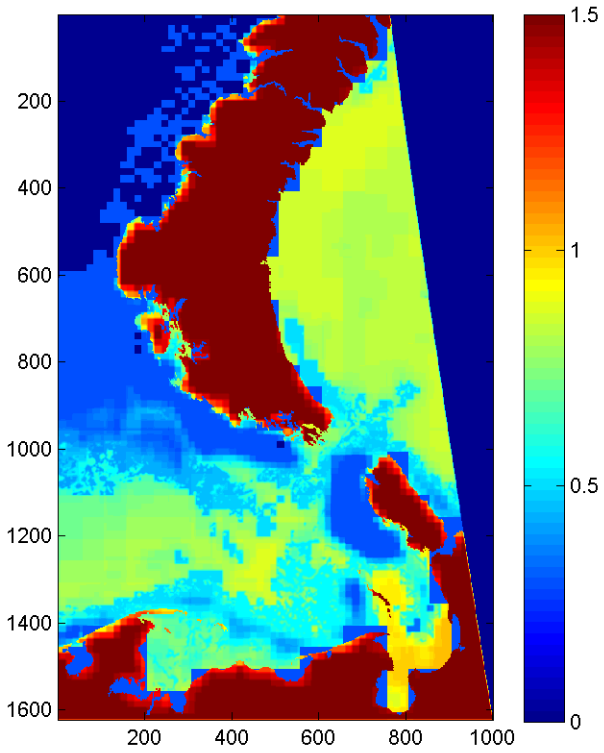

Figure 18. HIGHTSI ice thickness field on 21 Feb 2010 multiplied with the weight matrix W obtained from the ASI ice concentration data time series.

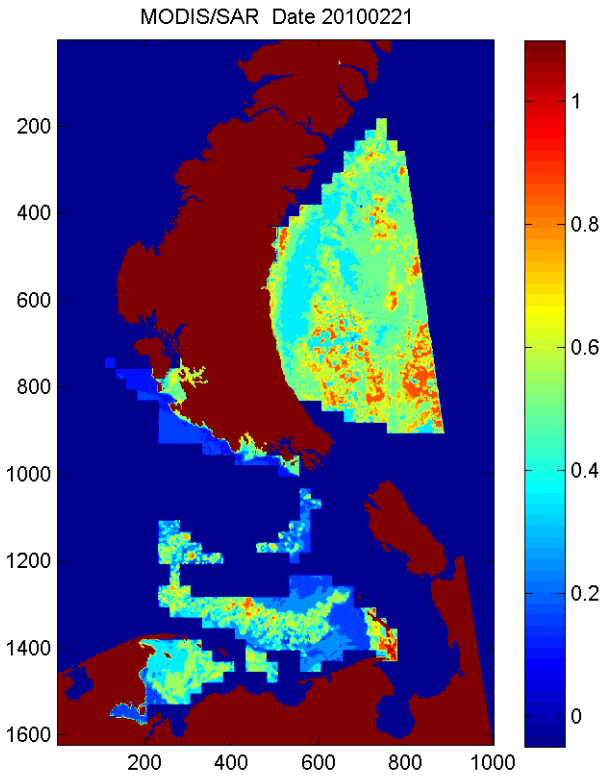

Figure 19. MODIS/SAR ice thickness chart on 21 Feb 2010.

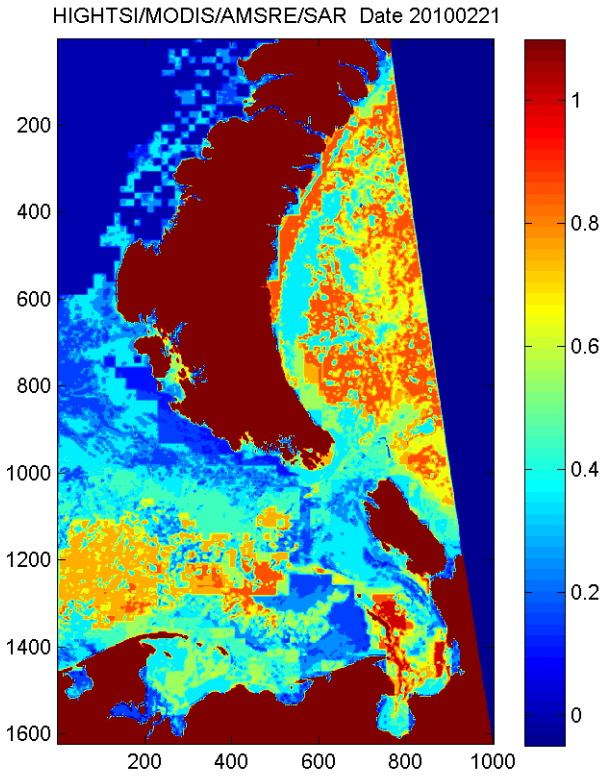

Figure 20. AMSR-E/MODIS/SAR ice thickness chart on 21 Feb 2010.

4.1.6 Data format

Table 2. Data format of the remote sensing images and products for the Barents and Kara Seas.

Dataset	File type	Format	Pixel size	Image size (rows x cols)	Corner coordinates (east, north)	Filename[1)]
ENVISAT WSM mosaic	pgm	uint8	500 m	2701 x 3001	ul = [-800000, -1100000] lr = [+700000, -2450000]	yyyymmddtime_mosa.pgm
MODIS ice surface temperature (IST)	Matlab	Matlab	1000 m	1350 x 1500	ul = [-799500, -1100500] lr = [+699500, -2449500]	ist_yyyymmdd_time.mat
MODIS ice surface temperature image	tiff-image of Matlab figure			-	-	yyyymmdd_time_ist.tif
MODIS based ice thickness map	Matlab	Matlab	1000 m	1350 x 1500	ul = [-799500, -1100500] lr = [+699500, -2449500]	modishi_yyyymmdd_time.mat
MODIS based ice thickness map	tiff-image of Matlab figure			-	-	yyyymmdd_time_modishi.tif
WSM daily coverage over the MODIS h_i images	tiff-image of Matlab figure			-	-	yyyymmdd.tif[1)]
MODIS-SAR based ice thickness map	Matlab	Matlab	400 m	variable	variable; ul and lr in the Matlab-file	modiswsm_yyyymmdd.mat[2)]
MODIS-SAR based ice thickness map	tiff-image of Matlab figure			-	-	modiswsm_yyyymmdd.tif

1) yyyymmdd = year-month-day; time = UTC time.

2) MODIS and SAR images are acquired at different times, thus only the date is given.

4.2 Baltic Sea

Below satellite data and sea ice products for the Baltic Sea are described. The last sub-section contains the data format descriptions.

4.2.1 Ice chart

A daily ice chart over the Baltic Sea is produced manually at the Finnish Ice Service (FIS) during the ice season. The ice chart production is performed mostly by subjective methods by updating previous chart with new input data (mainly SAR images). The mean level ice thickness estimates given in the ice chart are compiled by an ice analyst from multiple sources including drilling measurements near coastline, systematic field observations (including thickness), provided by the staff of icebreakers and other ships on sea, and ice growth estimates yielded by ice models.

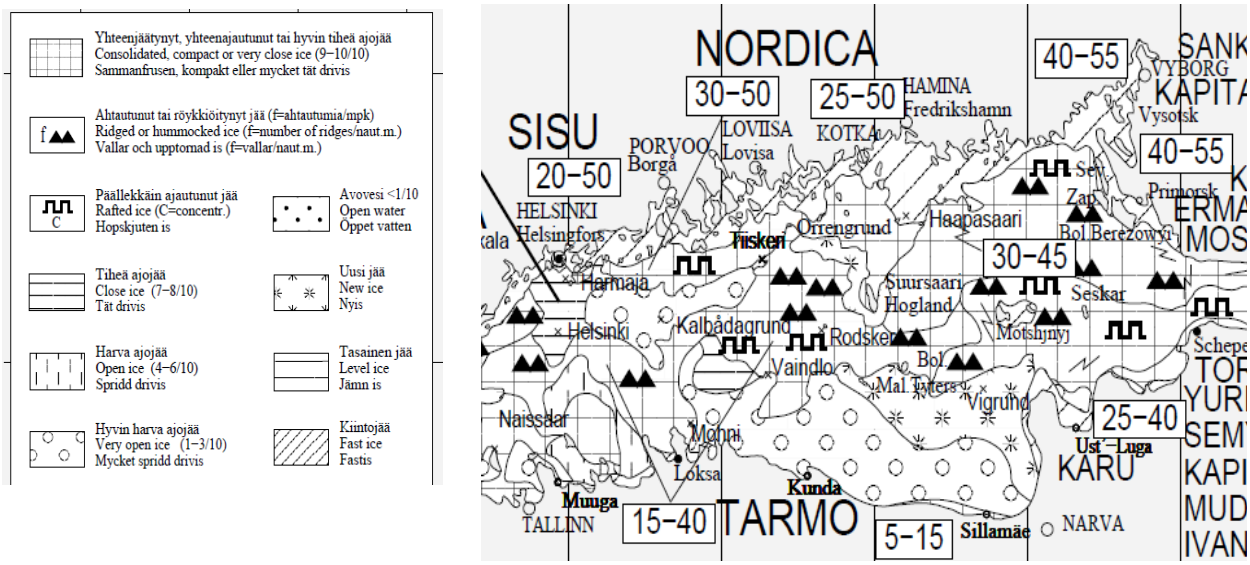

Figure 21. Part of the Finnish Ice Service ice chart showing sea ice conditions during the helicopter-borne EM-ice thickness measurements on 5 March 2010.

4.2.2 SAR images

For the Baltic Sea ice monitoring ENVISAT WSM and RADARSAT-2 ScanSAR images are acquired through the EC MyOcean project. In winter 2010 all RADARSAT-2 images were acquired only at HH-polarization, but in winter 2011 some dual-polarized images were acquired in March. During the ice season, from the end of November to the end of May, typically one or two images are acquired at each day by both SAR sensors. The images are rectified to our Mercator projection with 100 m pixel size (also FIS uses this projection). Typically the WSM images are acquired during 08:20-09:40 UTC (descending orbits) and 19:15-21:10 UTC (ascending orbits), and the RADARSAT-2 ones during 04:30-05:25 and 15:40-16:40 UTC.

The SAR images are used in the Polar View ice thickness chart construction.

4.2.3 Polar View SAR based ice thickness chart

RADARSAT-2 ScanSAR and Envisat ASAR WSM images are used to produce spatially more accurate level ice thickness charts (LITC) than given by the traditional ice charts (Karvonen et al. 2003, 2007). A SAR based LITC is operationally produced after a SAR image has been received, using the latest available digitized routine FIS ice chart (IC) as an initial input (either from the previous day or the same day, depending on the receiving time of the SAR image). The ice area

boundaries in the digitized IC are then relocated to correspond the area boundaries of the SAR image segments. Inside the generated segments, the thickness values are mapped to be between the segment minimum and maximum thickness values (given by the digitized IC) based on the SAR image segment backscattering mean (i.e. filtered SAR backscattering) values. The resulting ITC's are delivered to the end-users at 500 m x 500 m resolution in the Mercator projection. Typical minimum segment size is 20-30 pixels.

The spatial accuracy of the LITC charts as well as that of the routine ice charts have been analyzed using helicopter-borne EM-ice thickness measurements (Karvonen et al. 2004). The performed analysis showed more accurate results for the LITC charts. Karvonen et al. (2007) made also comparisons to ice thickness values measured by Finnish ice-breakers in winter 2005-2006. The mean error for the ice chart ice thickness was 10.8 cm and for the LITC chart it was 8.6 cm.

As the LITC charts are also used for studying the accuracy of the MODIS T_S based ice thickness they are interpolated with nearest neighbor sampling to our constant Baltic Sea MODIS grid (1330 by 1120 km, see Table 4) with 1000 m pixel size. The landmasks in the original LITCs are not equal, and thus they are substituted with the MODIS landmask. In the modified LITCs the land has value of -10, no-data areas over the sea have -5, and ice thickness in expressed in centimeter-scale. Due to the slight mismatches between the MODIS landmask and the landmasks of the original LITCs there are some 0 cm thickness pixels near the coast over landfast ice. These erroneous pixels do not cause problems for the MODIS and SMOS thickness validation as fast ice areas are not suitable for the validation; there are either too thick (MODIS) or too close to land (SMOS). An example of modified LITC is shown in Figure 22.

The LITC charts are also available through a MyOcean web-site myocean.met.no, e.g. in NetCDF format.

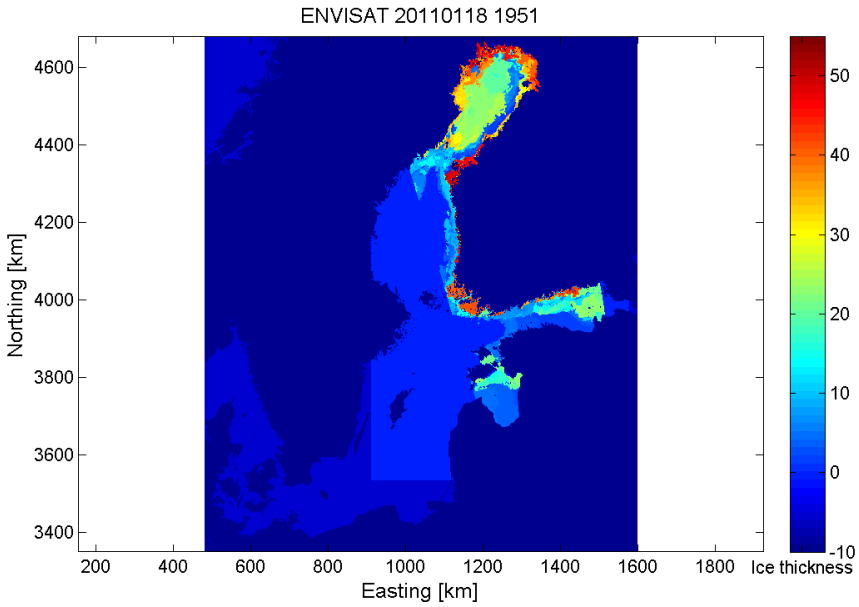

Figure 22. Polar View ENVISAT WSM based ice thickness chart on 18 Jan 2011. Mercator projection.

4.2.4 MODIS images and products

The MODIS images and products for the Baltic Sea are processed in same ways as for the Kara Sea validation area with the following exceptions: 1) In the cloud masking smaller window size is used, 5x5 km, due to the smaller size of the Baltic Sea validation area. 2) Sea ice is assumed to have bulk salinity of 1 ppt when calculating k_i . 3) Sea salinity varies from 3 ppt in the northern part of the Bay of Bothnia to 8 ppt in Kattegat. 4) A statistical snow vs. ice thickness relationship is derived from the icebreaker thickness data (see Section 3.2.2). Here icebreaker data acquired after the end of March is not used as this time period is not included in the MODIS datasets and it represents sea ice melting conditions.

A scatter plot between in-situ snow and ice thickness data (211 datapoints) acquired by Finnish icebreakers in 2006-2010 is shown Figure 23. Linear regression fit to the data is:

$$h_s = 0.29 \cdot h_i - 3.4 \text{ cm} \qquad (15)$$

The coefficient of determination (r^2) is small, only 0.40, due to the large data scatter. However, the *p*-value for the regression is nonetheless 0.00. As the thermodynamic thickness of level ice in drift ice areas is mostly below 50 cm the linear regression is next fit to data with $h_i < 50$ cm :

$$h_s = 0.22 \cdot h_i - 1.3 \text{ cm} \qquad (16)$$

The number of datapoints is now 172 and r^2 is only 0.21, but *p*-value is again 0.00. The standard error of the estimated h_s is 4.4 cm. Using (13) h_s is 0.9, 3.1 and 5.3 cm when h_i is 10, 20 and 30 cm, respectively. h_s is 0 cm when h_i below 6 cm.

As the constant term in (16) is significant the Baltic Sea ice thickness is estimated using:

$$h_i = \frac{k_s}{k_s + b_1 k_i} H - \frac{b_0 k_i}{k_s + b_1 k_i} \quad , \qquad (17)$$

where $h_s = b_1 h_i + b_0$.

For the ice season 2010, time period from 1 Feb to 31 Mar 2010, 18 MODIS images suitable for the ice temperature and thickness retrieval (images have large cloud-free areas) have been processed. Images were rectified to our Mercator projection. Again only Terra MODIS data is used as its acquisition times (19:00-20:40 UTC) match those of the ENVISAT and RADARSAT-2 afternoon images.

For the winter 2010-2011, from 1 Dec 2010 to 31 Mar 2011, 29 MODIS images have been processed. March 2011 was more cloudier and warmer than typically and, thus, there no images for the first half of March and only five MODIS images for the second half. The quality all March MODIS ice thickness data seems to be poor (large underestimation of ice thickness) due to warm and wet conditions, and their usage is not recommended. The best ice thickness data were acquired in Feb 2011 (13 images) with very cold conditions and large thin areas in the Sea of Bothnia.

The MODIS datasets for the winters 2010 and 2010-2011 and are listed together with the weather station data at the time of the MODIS acquisitions in Excel-files “BalticSea_MODIS2010.xls” and “BalticSea_MODIS2011.xls”.

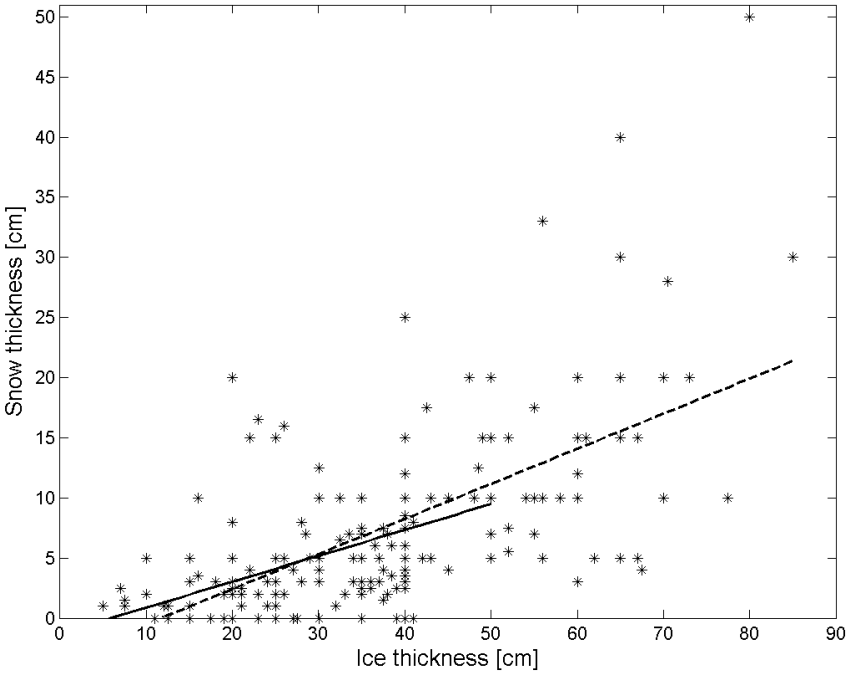

Figure 23. The relationship between snow and ice thickness from Finnish icebreaker data acquired in 2006-2010. The dotted line is linear regression fit to all data and the solid line is fit to data with ice thickness less than 50 cm.

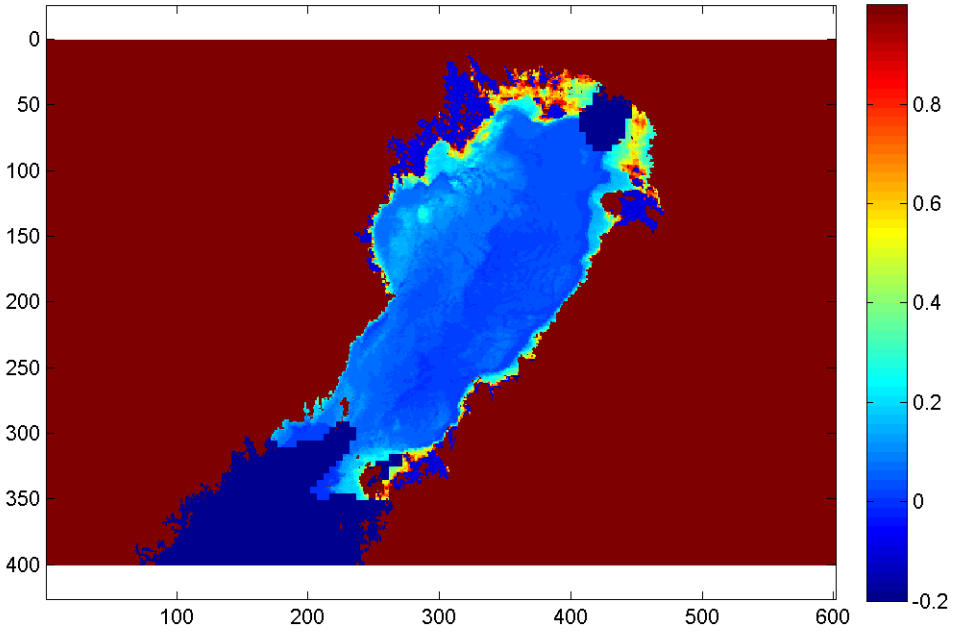

Figure 24. MODIS based ice thickness [m] chart for the Baltic Sea validation area on 28 Dec 2010.

4.2.5 Accuracy and maximum value of the MODIS based ice thickness

For the Baltic Sea validation area the accuracy of the MODIS T_S based h_i is studied in following three ways: 1) Using estimated or guessed standard deviations and correlations of the input variables to the h_i retrieval the h_i uncertainty is estimated with the Monte Carlo method. 2) MODIS h_i charts from consecutive days are compared to each other. The comparison estimates repeatability of the h_i retrieval when the true h_i change is insignificant. 3) The h_i charts are compared with the SAR based h_i charts. This shows how well the MODIS h_i charts compare with the FIS ice charts. It is noted that 3) does not give the 'true' absolute accuracy of the h_i charts as the SAR based h_i chart has its own inaccuracies.

The typical maximum retrievable h_i under different T_a ranges is determined using besides the results of the h_i accuracy analyses also the empirical mean $T_a - T_S$ vs. h_i relationship.

Ice thickness uncertainty with the Monte Carlo method

The Monte Carlo sampling of h_i values is conducted similarly as for the Kara Sea validation area. In total there are 13092 grid point datasets for the h_i sampling. Table 3 shows the estimated or 'best guessed' standard deviations of the variables needed in the h_i sampling. Snow thickness uncertainty is characterized by std of b_1 . The chosen std of 0.04 for b_1 in represents from 20% (h_i =50 cm) to 45% (h_i =10 cm) vc for h_s . Only correlations between T_S and the HIRLAM T_a , F_l^{dn} , u and Rh are taken into account in the random sampling. The correlation is the largest, +0.82, between T_a and T_S , and the second largest, -0.71, between T_a and Rh . For other variable combinations the absolute correlation varied from 0.40 to 0.66. With each grid point dataset 1000 random h_i values were calculated. Before calculating mean and std for the sampled h_i values negative un-physical h_i values are rejected as are the upper 5% of the positive h_i values. The h_i values are divided into 5 cm wide bins and the average and std of std(h_i)/mean(h_i) are calculated for the all data and for the 5 ºC wide T_a ranges and 2 m/s wide u ranges. The results of the Monte Carlo simulation are shown in Figures 25-27.

The mean vc with all the data is the smallest, 26%, for the h_i range from 10 to 15 cm and it increases to 60% when h_i is 50 cm, see Figure 19. The mean vc approaches 100% for very thin ice; 1-2 cm in thickness. If we set the maximum allowable mean vc to 50% then the maximum h_i we can retrieve reliably from the MODIS T_S is around 40 cm.

Figure 26 shows the mean vc as a function of T_a range. The mean vc decreases with decreasing T_a when $h_i \geqslant 20$ cm . With the vc limit of 50% the maximum reliable h_i is 45 cm when $T_a < -20$ ºC , but it is only around 25 cm when $-15 < T_a < -10$ ºC . The mean vc as function of u range is in Figure 27. There were enough data for the mean vc curves only at $u \leqslant 4$ m . The maximum reliable h_i is roughly 45 cm when $u \leqslant 2$ m/s and 35 cm when $3 \leqslant u \leqslant 4$ m/s . For all the winter 2010-2011 MODIS data the HIRLAM T_a is less than -15 ºC in 49% of the cases. The modal u is 3 m/s and 70% of the u values are below 4 m/s. In general, under cold conditions ($T_a < -15$ ºC) present for half the MODIS data the maximum reliable h_i is around 35-45 cm, but under warmer conditions (T_a around -10 ºC) it is only 20-25 cm. Unfortunately, there are no previous Baltic Sea ice studies for comparison.

Table 3. Standard deviations of the variables used in the Monte Carlo estimation of the MODIS based ice thickness uncertainty for the Baltic Sea study area.

Variable	std	Variable	std
T_S	1.3 K	k_s	0.05 W m^{-1} K^{-1}
T_a	2.9 K	b_1	0.04
u	function of u 2.1 −3.8 m/s	S_i	0.25 ppt
Rh	10%	ϵ	0.01
F_l^{dn}	20 W/m^2	C_s, C_e	10% of expected value

If we decrease stds of T_a and u to 1 ºC and 1 m/s then the h_i uncertainty reaches 50% when h_i is 55 cm and in the h_i range of 10-20 cm it is only around 20%. When the std of b_1 is doubled to 0.08, corresponding 40-50% h_s uncertainty when $20 \leqslant h_i \leqslant 50$ cm , the h_i uncertainty increases slightly; 50% limit is reached when h_i is 35 cm.

The contribution of different variables to the h_i uncertainty was studied by taking into account std of only one variable at the time in the h_i sampling. The largest h_i uncertainties come from T_a and F_l^{dn} . T_S has slightly smaller contribution. When $h_i < 20$ cm then also u has significant contribution to the h_i uncertainty. The h_i uncertainty from snow thickness alone is around 10%.

Comparison of thickness charts from consecutive days

The comparison of the h_i charts from consecutive days is conducted in the same way as for the Kara Sea. Due to the smaller size of the Baltic Sea a smaller block size, 5 by 5 km, is used here. There are 12 h_i chart pairs from the winter 2010-2011. The average time difference between the h_i charts is 24 hours. In total there are 4628 h_i difference values from the charts pairs.

The overall RMSE for the h_i difference data is 5.9 cm, the mean absolute bias is 3.5 cm and 90% of the absolute h_i differences are below 8.8 cm. Within the h_i chart pairs RMSE varies from 1.1 to 13.7 cm and the average is 5.6 cm. There are no clear relationships between the T_a or u differences and the h_i differences suggesting that cloud masking problems caused the large RMSE for some h_i chart pairs. For the h_i intervals of 0-10, 10-20, 20-30, 30-40, and 40-50 RMSE is 2.3, 4.1, 7.4, 10.2, and 13.8, respectively. RMSE is from 29% (20-30 cm bin) to 46% (0-10 cm bin) of the h_i bin centre value.

The repeatability of the MODIS and HIRLAM data based h_i charts for the Baltic Sea is somewhat better than for the Kara Sea. This difference may be due to the more diverse ice conditions in the Kara Sea, and larger amount of ice fog in the Kara Sea due to much colder prevailing air temperatures.

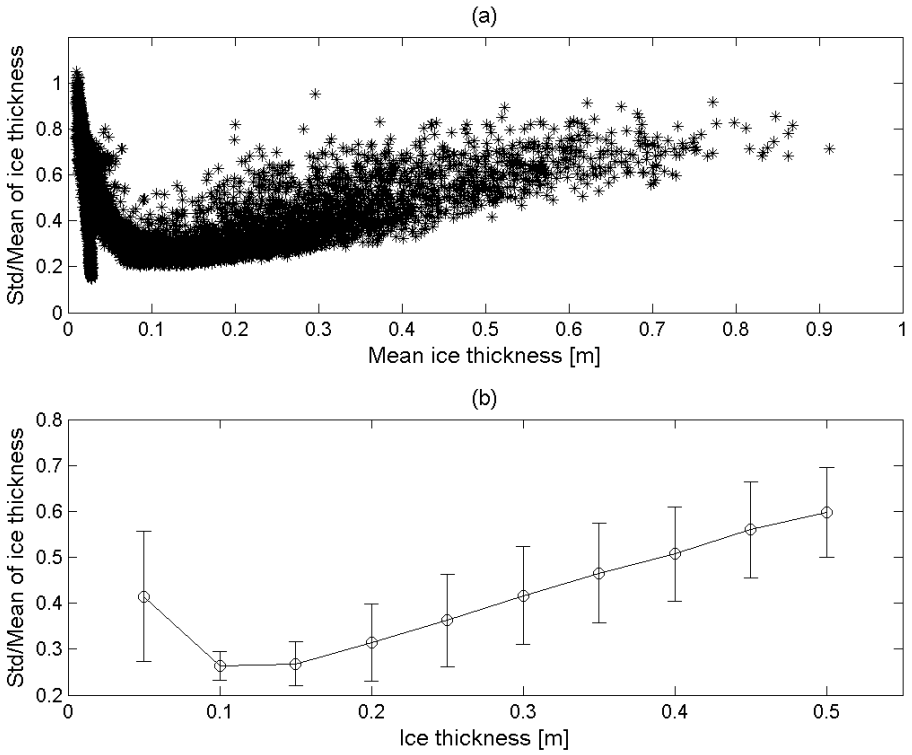

Figure 25. Uncertainty of the MODIS based ice thickness estimated with the Monte Carlo method for the Baltic Sea validation area. (a) Mean and std/mean of the sampled thickness values. (b) The average thickness uncertainty as a function of thickness and the variation of the uncertainty characterized by std(std/mean).

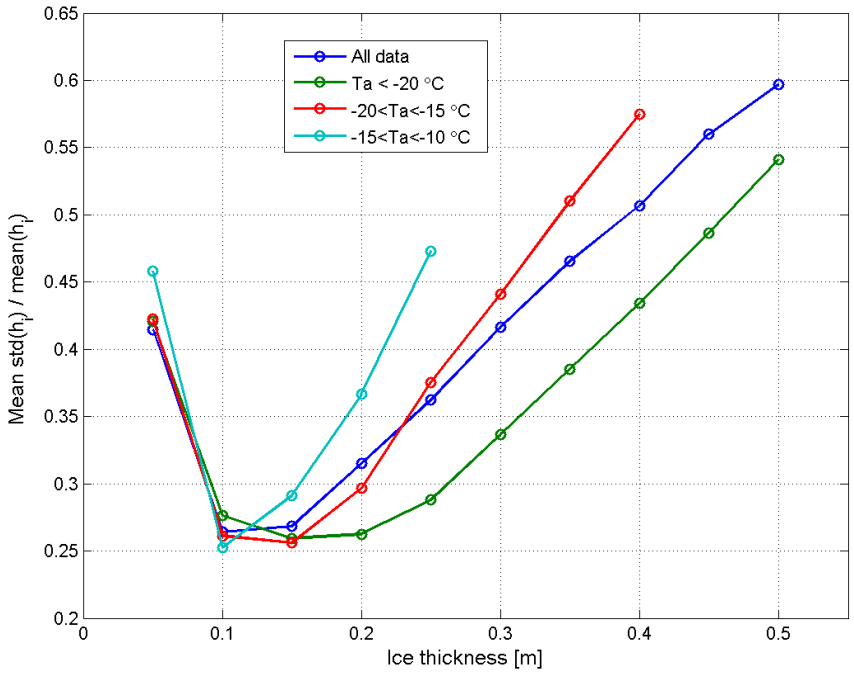

Figure 26. The average uncertainty of the MODIS based ice thickness as a function HIRLAM air temperature range.

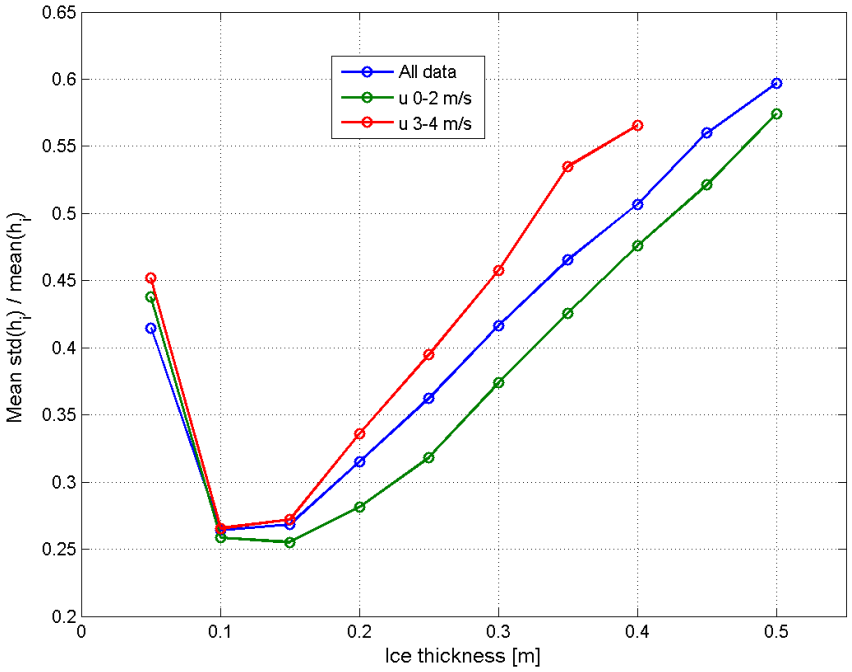

Figure 27. The average uncertainty of the MODIS based ice thickness as a function HIRLAM wind speed range.

Comparison with the SAR based thickness charts

Correspondence of the MODIS h_i charts with the FIS ice chart thickness information is studied by comparing them to the Polar View SAR based ice thickness charts. For the comparison 18 chart pairs were selected. An example of the SAR based h_i charts is shown in Figure 22. The SAR h_i chart shows the typical thickness of level ice, but the MODIS h_i is a weighted average of thicknesses of various ice types present. Thus, it is meaningful to do the chart comparison only over homogeneous level ice areas. Based on this reasoning h_i differences between the two charts (MODIS h_i chart minus SAR one) are calculated using 10 by 10 km block averages, the mean MODIS h_i is required to be less than 40 cm, and the coefficient of variation (std/mean) for each block in both h_i charts is required to be less than 20%.

Based on a scatterplot between the SAR h_i and the MODIS-SAR h_i difference (in total 1731 datapoints) showing a dependence between these two variables, the mean h_i difference is calculated for the following SAR h_i bins: 0-10, 10-15, 15-20, 20-25, 25-30, 30-35 and 35-40 cm. The mean biases for these h_i bins are: +0.1, -3.1, -7.4, -10.6, -15.2, -17.1 and and -16.9 cm, respectively. Excluding snow cover by using thermal ice thickness (11) in the comparison decreases the mean h_i bias, e.g. in the SAR bin of 20-25 cm the mean bias is now -3.8 cm. This demonstrates the need for accurate h_s estimation in the h_i retrieval.

In general, when the SAR h_i is less than 15 cm then on the average the MODIS h_i corresponds well with it, but in the SAR h_i range of 15-40 cm the MODIS h_i is clearly smaller leading overestimation of amount of thin ice in the MODIS h_i chart. This can be explained, at least partly, by the observed HIRLAM underestimation of T_a (see Section 5.1.1) which decreases the $T_a - T_S$ difference. For very thin ice h_i increases slowly as a function of $T_a - T_S$ and, thus, a

bias error in T_a does not change the MODIS h_i considerably, but for thicker ice (over 15 cm in here) even a slight decrease in $T_a - T_S$ can cause significant decrease in the MODIS h_i .

Despite the h_i underestimation problem the MODIS h_i chart has the advantage of better spatial resolution than the SAR h_i chart; 1 km pixel size in the MODIS chart vs. 2-3 km minimum segment size in the SAR chart. The MODIS chart shows better the spatial fine scale variation of h_i . Larger leads are identified in the MODIS chart, but not in the SAR chart. In addition, the MODIS h_i chart is based on a physical relationship between measured T_S and h_i , whereas the SAR h_i chart is a result of statistical spatial refinement of the FIS ice chart h_i information (Karvonen et al. 2003).

Maximum reliable MODIS ice thickness

The typical maximum reliable h_i under different T_a ranges is studied likewise as for the Kara Sea data. Mean $T_a - T_S$ vs. h_i curves were calculated for four T_a ranges, see Figure 28. HIRLAM u was required to be again less than 6 m/s to include only the most common wind conditions of the MODIS data. The number of the HIRLAM grid point datasets (3 by 3 block pixel averages) is 13137.

We again suggest that the maximum reliable h_i here depends on 1) maximum acceptable $T_a - T_S$ vs. h_i sensitivity, 2) maximum allowed $T_a - T_S$, 3) acceptable h_i uncertainty based on the Monte Carlo simulation, and 4) T_a . The maximum allowed $T_a - T_S$ should likely be 0 ºC or only few degrees larger due to inaccuracy problems that radiative surface cooling may cause to the calculated turbulent fluxes. If we set the maximum $T_a - T_S$ to 0 ºC, the $T_a - T_S$ vs. h_i sensitivity to be less 10 cm / 1 ºC and maximum h_i uncertainty to 50% then the maximum h_i varies from 38 cm when $T_a < -20$ ºC to only 15 cm when $-10 \leqslant T_a < -5$ ºC .

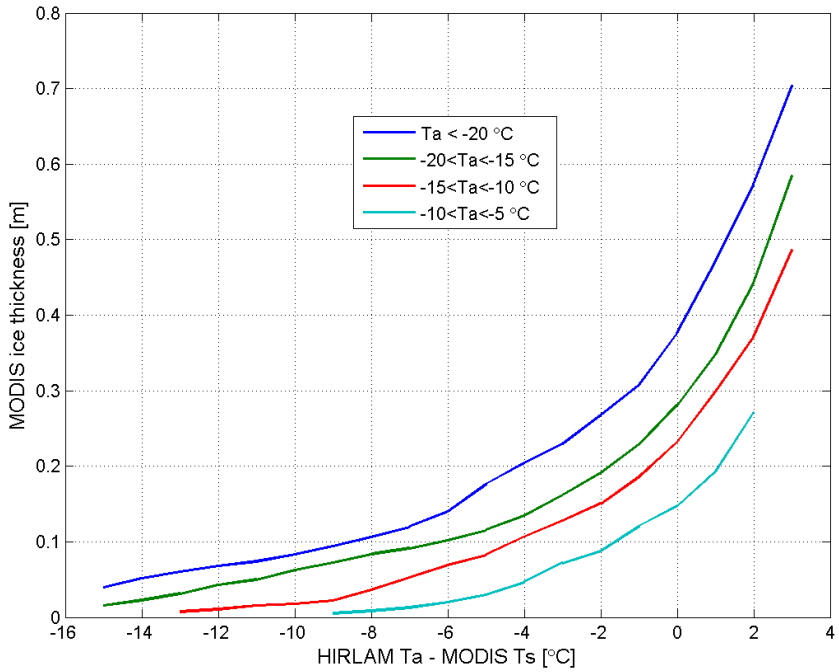

Figure 28. Empirical average relationship between $T_a - T_S$ and h_i for different T_a ranges.

4.2.6 Data format

Table 4. Data format of the remote sensing images and products for the Baltic Sea.

Dataset	File type	Format	Pixel size	Image size (rows x cols)	Corner coordinates (east, north)	Filename[1)]
Polar View SAR based ice thickness chart	Matlab	Matlab	1000 m	1330 x 1120	ul = [480500, 4679500] lr = [1599500, 3350500]	rs2hi_yyyymmdd_time.mat wsmhi_yyyymmdd_time.mat
Polar View SAR based ice thickness chart	tiff-image of Matlab figure			-	-	yyyymmdd_time_rs2.tif yyyymmdd_time_wsm.tif
MODIS ice surface temperature (IST)	Matlab	Matlab	1000 m	1330 x 1120	ul = [480500, 4679500] lr = [1599500, 3350500]	ist_yyyymmdd_time.mat
MODIS ice surface temperature image	tiff-image of Matlab figure			-	-	yyyymmdd_time_ist.tif
MODIS based ice thickness map	Matlab	Matlab	1000 m	1330 x 1120	ul = [480500, 4679500] lr = [1599500, 3350500]	modishi_yyyymmdd_time.mat
MODIS based ice thickness map	tiff-image of Matlab figure			-	-	yyyymmdd_time_modishi.tif

yyyymmdd = year-month-day; time = UTC time

5. MODEL DATA – SMOSIce-DAT-MD

Modeled atmospheric boundary layer (ABL) data for the Kara and Baltic Seas validation areas is provided by the HIRLAM model. HIRLAM data is used as external forcing for a one dimensional high resolution snow and sea ice thermodynamic process model (HIGHTSI) (Launiainen and Cheng 1998) in the Kara Sea, and for MODIS ice surface temperature based ice thickness retrieval. Below both models are described, including model output parameters. In addition, HIRLAM accuracy is estimated using weather station data.

5.1 HIRLAM model

HIRLAM (HIgh-Resolution Limited Area Model) is a numerical short-range weather forecasting system for operational use within the international HIRLAM program partners of 11 European countries (http://hirlam.org). HIRLAM is based on the hydrostatic primitive equations; the dependent variables are temperature, wind component, humidity, surface pressure, cloud water content and turbulent kinetic energy (Källen 1996; Unden et al. 2002). We applied the HIRLAM version 7.3, which contains an improved surface and lake parametrization.

As a limited area model, HIRLAM requires lateral boundary conditions from global/hemispheric model, normally provided by the European Centre for Medium Range Weather Forecasting (ECMWF). For Kara Sea and Baltic Sea cases, the lateral boundary conditions are taken from ECMWF analysis.

In the present study, the initial state for the cycles starting at 00, 06, 12, 18 UTC of each day, was provided by combining the ECMWF upper air analysis with HIRLAM surface analysis. In particular, for the Kara sea the ice concentration was based on the ECMWF operational sea surface temperature (SST) analysis. For the Baltic Sea, Ice Chart from Finnish Ice Service provided the ice concentration. The HIRLAM spatial resolutions were 0.15 degrees for the Kara sea and 0.068 degrees for the Baltic Sea in the HIRLAM rotated coordinate system. The time step of HIRLAM model run was 3 minutes. At each UTC step (00, 06, 12, 18), the HIRLAM model runs continuously for the next 9-54 hrs. We applied the first 6 hrs forecasts to create daily time series of HIRLAM weather data with 1 hour time step.

HIRLAM data are used as atmospheric forcing data for the MODIS based ice thickness retrieval and as external forcing for the HIGHTSI model runs.

HIRLAM model domains for the Barents and Kara Seas and for the Baltic Sea are shown in Figures 29 and 30. For the Barents and Kara Seas model grid point spacing is 20 km both in the easting and northing direction. For the Baltic Sea the grid spacing is 10.6 km in the easting and 8.8-13 km in the northing. For the Barents and Kara Seas the model domain is defined in our polar stereographic projection, but for the Baltic Sea in the latitude-longitude coordinates. In the Baltic Sea model domain HIRLAM is run only for the grid points over the sea, but in the Barents and Kara Seas domain it is run for both land and sea grid points. Table 5 shows the details of the two model domains.

For each grid point the following HIRLAM model parameters are provided:

- air temperature at 2 m height [ºC]
- wind speed at 10 m [m/s]
- relative humidity at 2 m [%]
- downward longwave radiation [W/m^2]
- downward shortwave radiation [W/m^2] (not needed in the MODIS h_i retrieval)

- total precipitation [kg/m^2]; accumulated during last 1 hour
- snow precipitation [kg/m^2]; water equivalent, accumulated during last 1 hour

The parameters at 2 and 10 m heights are diagnostic variables obtained from the HIRLAM lowest level (around 32 m) prognostic variables. For the h_i retrieval the HIRLAM parameters are interpolated to the MODIS 1 km pixels using nearest neighbour sampling.

Table 5. HIRLAM and HIGHTSI (only Kara Sea) model domains and data time periods for the Kara and Baltic Seas validation areas.

Domain	Corner coordinates	Grid spacing	Grid points over sea	Time period
Kara Sea	ul=[-799500, -1100500] lr=[+700500, -2440500]	20 x 20 km	3841	1 Oct – 31 Mar
Baltic Sea	ul=[9 E, 66 N] lr=[31 E, 53 N]	0.2º lon 0.1º lat	3582	1 Dec 2009 – 30 Apr 2010 1 Nov 2010 – 31 Mar 2011

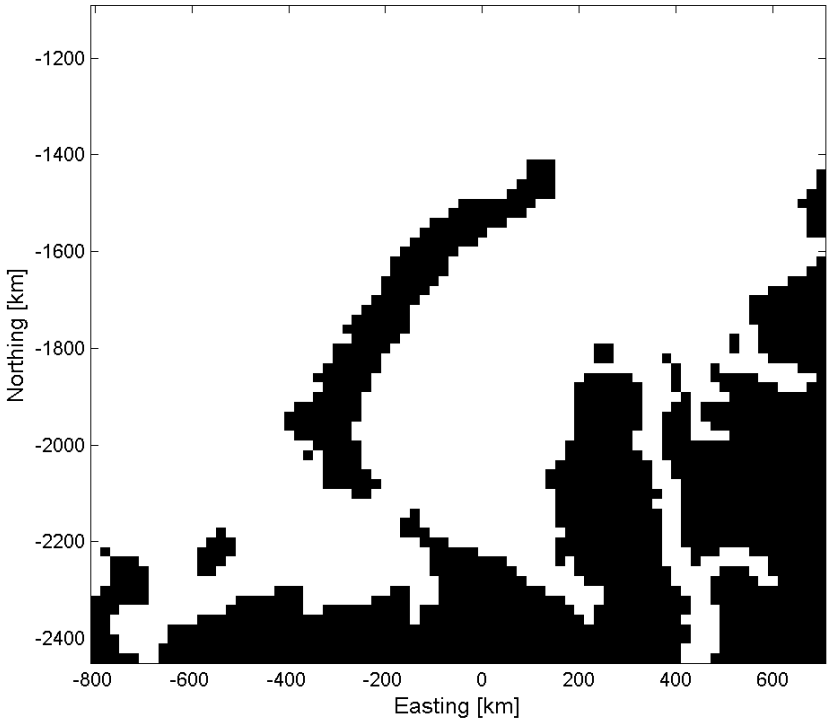

Figure 29. The HIRLAM/HIGHTSI model grid for the Kara Sea validation area in polar stereographic projection (mid-longitude of 63 E). The grid spacing is 20 km. Both HIRLAM and HIGHTSI models are run for both land and sea grid points, but the HIGHTSI results for the land points are not meaningful.

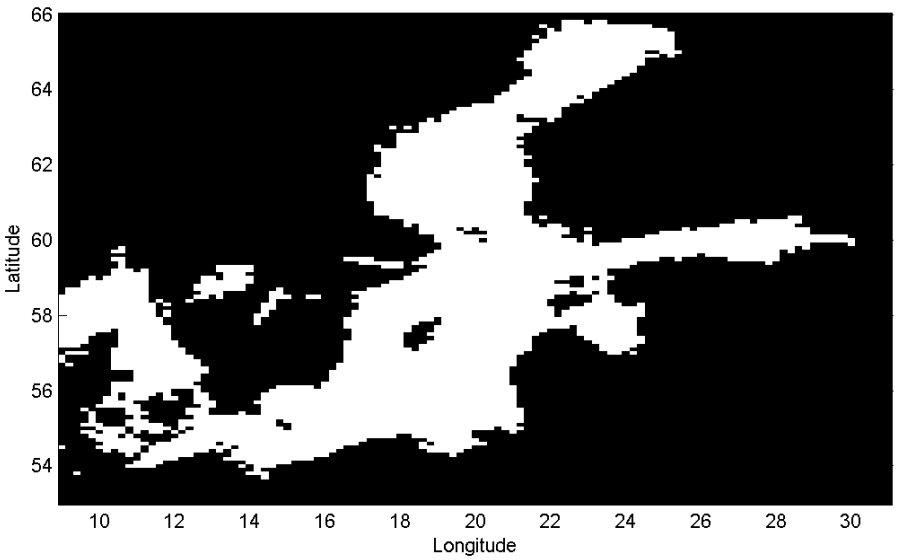

Figure 30. The HIRLAM model grid for the Baltic Sea validation area. The grid spacing is 0.2º in longitude and 0.1º in latitude. Both models are run for the sea grid points only.

5.1.1 HIRLAM accuracy

The accuracy of the HIRLAM air temperature (T_a^H), wind speed (u^H) and relative humidity (Rh^H) are studied by comparing them to the coastal weather station data (T_a^W , u^W , Rh^W) There are seven stations in the Barents and Kara Seas validation area (see Figure 1), and of the 22 Finnish stations in the Baltic Sea (see Figure 5) 12 stations were selected for the comparison. In the comparison the HIRLAM data (one hour time step) from the grid points over the ocean closest to the weather stations and co-incident with the weather station data (3 h time step for the Baltic Sea and 6 h step for the Barents and Kara Seas) are used. The comparison is conducted using HIRLAM and weather station datasets for the winter 2010-2011. Statistical difference (HIRLAM minus weather station data) between the two datasets is described with the mean bias, root mean square error (RMSE), standard deviation (std) and their variation from station to station, and the correlation coefficient. Stds are used in studying the MODIS h_i uncertainty with the Monte Carlo method.

We dont have any in-situ data to do comparison for the HIRLAM downward longwave radiative flux (F_l^{dn}). For the std of the HIRLAM F_l^{dn} we assume a figure of 20 W/m^2 based on a study where different F_l^{dn} schemes were compared to in-situ F_l^{dn} measurements on the Baltic Sea ice (Zhang et al. 2006).

In the following the comparison results for the Baltic and the Kara Seas study areas are presented.

Baltic Sea

Table 6 shows the comparison results for three HIRLAM variables. Figures 31 and 32 show comparisons between the weather station and HIRLAM data. The overal mean bias of T_a^H is -0.9 ºC (T_a^H is on the average 0.9 ºC smaller than T_a^W). The negative mean $T_a^H - T_a^W$ difference is evident in Figure 31. The overall RMSE and std are rather high, 3.0 and 2.9 ºC, but the correlation between the two T_a datasets is nonetheless 0.92. The variation of the mean bias and RMSE from station to station is quite large, e.g. from 2.2 to 4.3 ºC for RMSE. Thus, a large number of stations as used here are needed to get reliable overall difference statistics. The mean bias and RMSE increase with decreasing T_a^H , for the T_a^H ranges of -10 – -5 ºC and -25 – -20 ºC the mean bias is -0.9 ºC and -4.0 ºC, respectively, and RMSE is 2.9 ºC and 5.3 ºC. Thus, the accuracy of T_a^H degrades with decreasing T_a . This typical HIRLAM underestimation of T_a leads to underestimation of h_i from the MODIS T_S as now the $T_a - T_S$ difference resembles that of a thinner ice.

These differences between the two T_a datasets could be partly due to the sea ice mask used in the HIRLAM model. The mask only shows either open water or thick sea ice and, thus, the atmosphere over the sea ice is always insulated from the ocean regardless of the ice thickness. In addition, a modelling study by Lüpkes et al. (2008) demonstrated that for sea ice concentrations > 90% small changes in the sea ice fraction have a strong increasing effect on the near-surface T_a over thick ice under clear-sky conditions during polar night.

The correlation between the u datasets is much lower than for the T_a ones, only 0.65. The overall mean bias of u^W is -1.8 m/s, std is 3.1 m/s and RMSE is 3.6 m/s. This overall RMSE indicates over 100% uncertainty (std(u^H)/ u^H) for u^H at lower wind speeds. Thus, RMSE of $u^H - u^W$ is also studied as a function of u^H , see Figure 32. RMSE varies between 3.2 and 3.9 m/s when u^H increases from 1 m/s to 15 m/s, but the u^H uncertainty decreases from over 100% to 25%. The u^H uncertainty is over 100% when $u^H \leqslant 3$ m/s . The mean bias is -2.4 to -2.0 m/s when $u^H \leqslant 6$ m/s . During the acquisitions of the MODIS datasets u^H was typically small; the average was 4 m/s. The HIRLAM underestimation of u leads to underestimation of absolute values of F_s and F_e which are linear functions of u . This in turn leads to either h_i overestimation if $F_s + F_e < 0$, or underestimation if $F_s + F_e > 0$.

Table 6. Comparison between the Baltic Sea weather station and HIRLAM data (HIRLAM minus station) for air temperature (T_a [ºC]), wind speed (u [m/s]) and relative humidity (Rh [%]). The time period is from 1 Nov 2010 to 31 Mar 2011.

Parameter	Mean bias		RMSE		STD		Correlation
	Overall	Variation	Overall	Variation	Overall	Variation	
T_a	-0.9	-1.8 – -0.2	3.0	2.2 – 4.3	2.9	2.2 – 4.0	+0.92
u	-1.8	-5.3 – -0.3	3.6	2.6 – 6.0	3.1	2.4 – 2.9	+0.65
Rh	+4	-2 – +8	10	9 – 12	10	8 – 11	+0.39

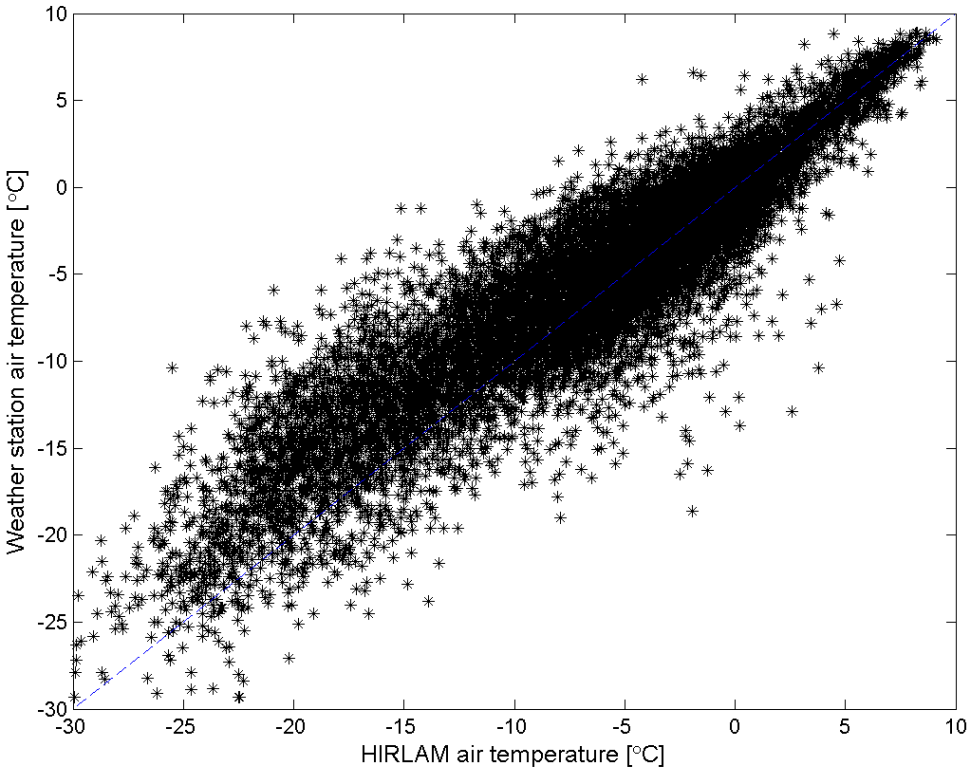

Figure 31. Scatterplot between air temperatures from the HIRLAM model for the Baltic Sea and 12 Finnish coastal weather stations during 1 Nov 2010 – 31 Mar 2011.

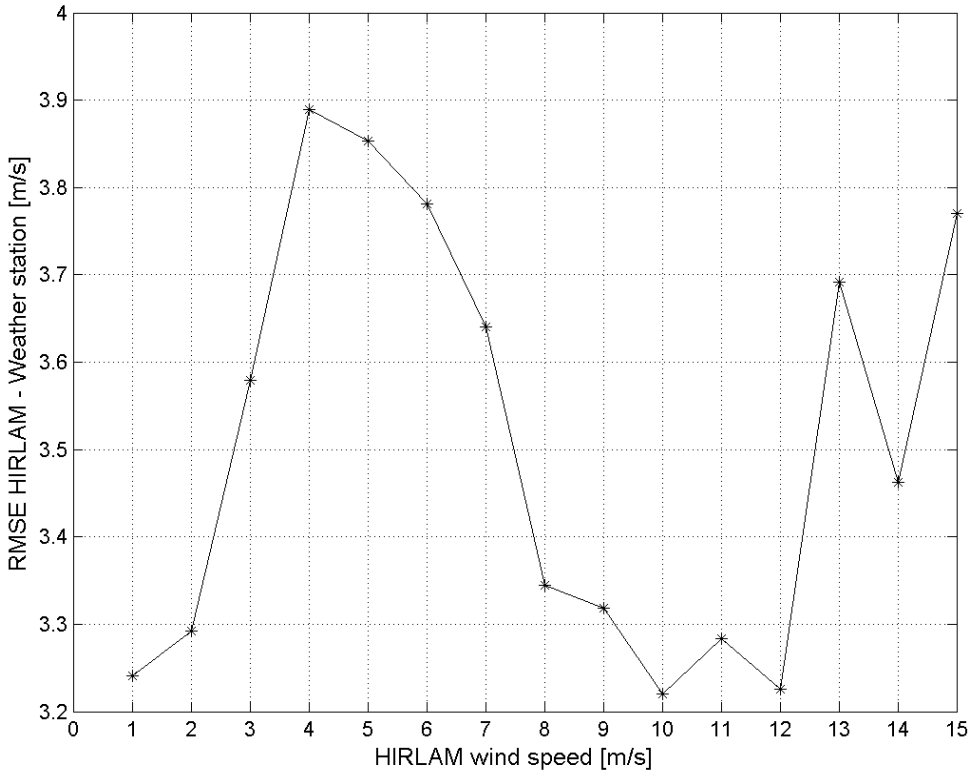

Figure 32. RMSE between the Baltic Sea weather station and HIRLAM wind speeds as a function of HIRLAM wind speed on 1 Nov 2010 – 31 Mar 2011.

The overall mean bias and RMSE for $Rh^H - Rh^W$ is +4% and 10%, respectively. HIRLAM significantly overestimates Rh when $Rh^W < 70\%$. In addition, the correlation between the weather station and HIRLAM Rh datasets is very small. Rh is the input parameter only for the turbulent latent flux (F_e) which contribution to the heat balance equation (1) is the smallest. In many previous T_S based ice thickness retrieval studies Rh has been simply assumed to be constant, e.g. 90% in (Yu and Rothrock 1996; Wang et al. 2010).

Kara Sea

The comparison results are shown in Table 7 and Figures 33 and 34. In the winter 2010-2011 the overal mean bias of T_a^H is -0.9 ºC. The overall RMSE and std are large, 3.8 and 3.7 ºC, respectively, but the correlation between the T_a datasets is high, 0.94. The mean bias increases somewhat with decreasing T_a^H ; for the T_a^H ranges of -10 – -5 ºC and -25 – -20 ºC it is -0.1 ºC and -2.3 ºC, respectively. This was also the case with the Baltic Sea data. Both RMSE and std again increases with decreasing T_a^H (see Figure 33); e.g. in the above mentioned T_a^H ranges RMSE is 3.0 and 4.8 ºC. The effect of the HIRLAM T_a underestimation on the retrieved h_i and possible reason for it were discussed above within the Baltic Sea results.

The correlation between the u datasets is also here much lower than for the T_a ones, only 0.67. The overal u^W statistics are: mean bias is -1.2 m/s, std is 3.1 m/s and RMSE is 3.3 m/s. RMSE as a function of u^W is shown in Figure 34. RMSE increases up to u^W is 12 m/s, but at the same time the u^W uncertainty decreases from over 100% when $u^H \leqslant 2$ m/s to around 40%. When u^W is larger than 9 m/s then HIRLAM mostly underestimates u . At low u^W (less than 3 m/s) HIRLAM on the contrary slightly overestimates u .

The overall mean bias and RMSE for Rh^H is +9% and 15%, respectively. There is no correlation between the Rh datasets. HIRLAM significantly overestimates Rh when $Rh^W < 80\%$.

Table 7. Comparison between the Barents and Kara Seas weather station and HIRLAM data (HIRLAM minus station) for air temperature (T_a [ºC]), wind speed (u [m/s]) and relative humidity (Rh [%]). The time period is from 1 Oct 2010 to 30 Apr 2011.

Parameter	Mean bias		RMSE		STD		Correlation
	Overall	Variation	Overall	Variation	Overall	Variation	
T_a	-0.9	-2.1 – +0.8	3.8	3.1 – 4.7	3.7	2.9 – 4.2	+0.94
u	-1.2	-2.4 – +0.7	3.3	2.4 – 4.6	3.1	2.2 – 3.9	+0.67
Rh	+9	+1 – +15	15	11 – 18	12	9 – 13	-0.02

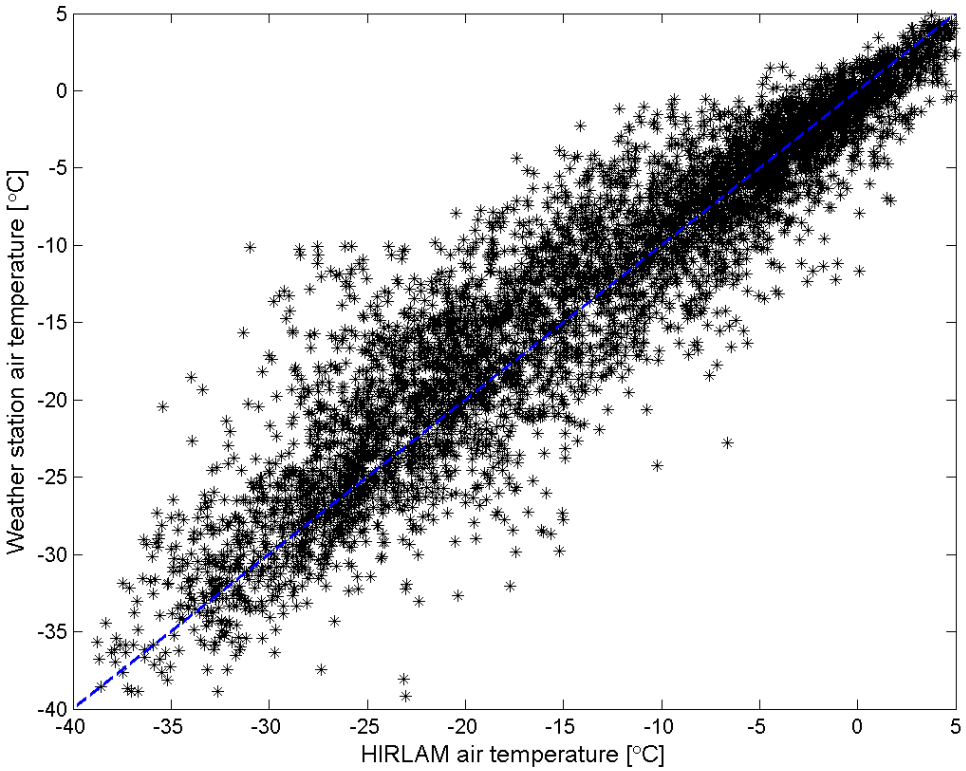

Figure 33. Scatterplot between air temperatures from the HIRLAM model and seven weather stations in the Barents and Kara Seas validation area during 1 Oct 2010 – 30 Apr 2011.

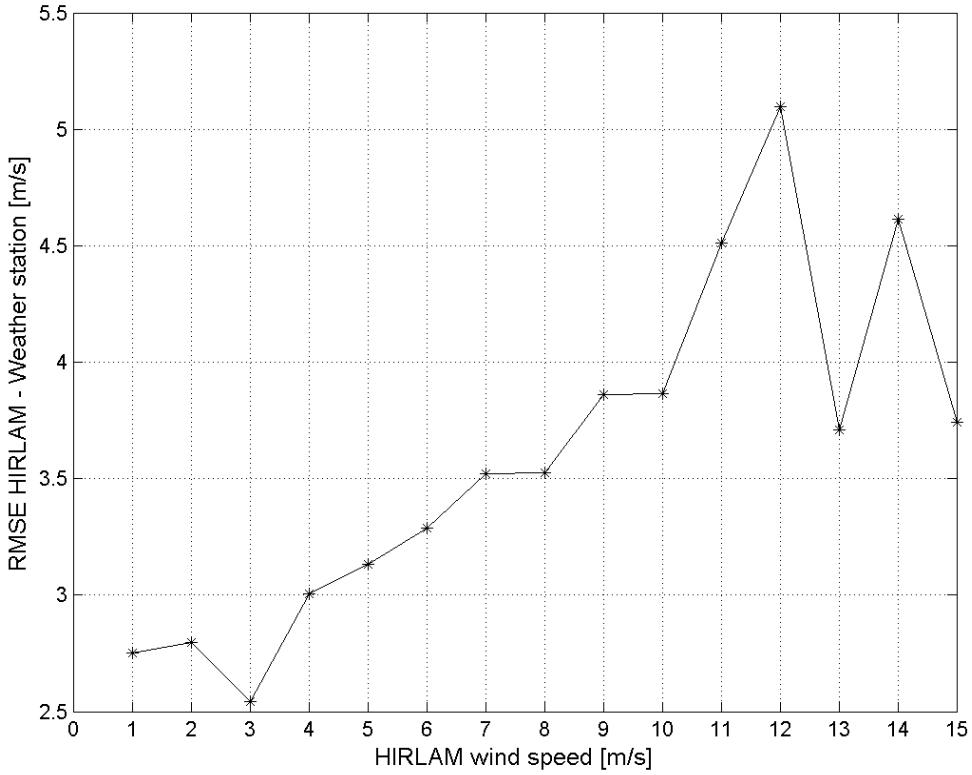

Figure 34. RMSE between the Barents and Kara Seas weather station and HIRLAM wind speeds as a function of HIRLAM wind speed on 1 Oct 2010 – 30 Apr 2011.

5.2 HIGHTSI model

The HIGHTSI is a one dimensional high resolution snow and sea ice thermodynamic process model (Launiainen and Cheng 1998). The model solves the partial-differential heat conduction equation of the snow and ice layer, respectively. The turbulent surface fluxes are parametrized taking the thermal stratification into account. The radiative fluxes are parametrized based on, e.g. (Zillman 1972), (Key at al. 1996). The surface temperature is solved from a detailed surface heat/mass balance equation, which is defined as the upper boundary condition and also used to determine whether surface melting occurs. The global radiation penetrating through the surface layer is parametrized, making the model capable of calculating sub-surface melting quantitatively. A heat and mass balance at the ice bottom serves as the lower boundary condition of the model. The snow to ice transformation is calculated by heat flux divergence at the snow/ice interface. The results of the formation of snow-ice (re-freezing of flooded snow) and superimposed ice (re-freezing of snow melt or wet snowfall) are finally integrated into the total ice thickness calculation. Slush formation from ocean flooding is considered as well. Snow evolution is determined by precipitation (snowfall), snow melt, slush formation and refreezing. The simple parameterizations of snow metamorphism, such as snow compaction, densification and change of heat conductivity were calculated according to (Anderson 1976) and (Yen 1981). The model has been validated successfully against field data from several ice covered oceans (Cheng et al. 2006; 2008). The modeled snow and sea ice thermodynamics have also been used to interpret time series of C-band backscattering coefficient (Mäkynen et al. 2007).

Altogether HIGHTSI is capable to calculate snow thickness based on snow precipitation and snow melting process and typically, the results compares well against field measurements. However, for the Barents and Kara Seas validation area the snow thickness is parametrized according to (5), because we think that in drift ice areas snow thickness based in the precipation yields too high values as the snow drifting and compacting due to the wind is not taken into account in the HIGHTSI model.

The HIGHTSI model is run in the HIRLAM grid shown in Figure 29. The weather forcing data are from the HIRLAM model. For the Barents and Kara Seas open water mask is derived from the AMSR-E based sea ice concentration map with spatial resolution of 6.25 km (ASI algorithm) (Spreen et al. 2008). The concentration map is rectified to our polar stereographic projection (mid-longitude of 63 E; original map has 45 W). For each HIRLAM grid point (grid spacing is 20 km) the sea ice concentration is an average value over 3x3 block in the ASI concentration map. Avarage ice concentration values less 30% are considered to represent open water. When a grid point becomes open water due to the ice drifting/opening of leads then the HIGHTSI run for that point is suspended and the latest HIGHTSI data for that point are stored. After the grid point becomes again covered by sea ice the HIGHTSI run continues from the stored values. This procedure estimate the maximum level ice thickness for each grid point. This maximum thickness estimates the real ice thickness only in fast ice areas where sea ice cover has been continuous since the time of its forming. The HIGHTSI level ice thickness chart is utilized in the MODIS-SAR based ice thickness algorithm for the Kara Sea, see Section 4.1.5.

For each model grid point the HIGHTSI model yields the following parameters: snow thickness, ice thickness, surface temperature, and snow-ice interface temperature. The model time step is 1 hour.

5.3 HIRLAM and HIGHTSI data format

The HIRLAM model domain for the Baltic Sea is described by the following variables in Matlab file "BS_hirlamgrid.mat":

- hlon, hlat – vectors having the longitude-latitude coordinates of the grid points over sea; from west to east and north to south order (in total 3582 points)
- hx, hy – Mercator coordinates of the grid points; hx=easting, hy=northing
- hgp – vector showing the running number of the grid points; from west to east and north to south order (in total 3582 points)
- hmask – model domain mask matrix; 0=land, 1=sea

For the Barents and Kara Seas validation area Matlab-file "KS_hirlamgrid.mat" has the following variables:

- hx, hy – matrices having Polar stereographic coordinates of the grid points (grids with equal spacing, see details in Table 4)
- hlon, hlat – matrices of the longitude-latitude coordinates of the grid points
- hgp – matrix showing the running numbers of the grid points (both land and sea); from west to east and north to south order (in total 5168 points of which 3841 are over sea)
- hmask – model domain mask matrix; 0=land, 1=sea

Each HIRLAM and HIGHTSI variable is provided as Matlab-matrix where each column has time series data for a grid point. The number of columns is 3582 for the Baltic Sea and 5168 for the Kara Sea. A seperate time vector has the time in serial date number format. The HIRLAM variables are: air temperature *TA*, wind speed *VA*, relative humidity *RH*, downward longwave radiation *QL*, downward short wave radiation *QS*, total precipitation *TP*, and snow precipitation *SP*. The HIGHTSI variables are: snow thickness *hs*, ice thickness *hi*, surface temperature *ts*, and snow-ice interface temperature *tsi*. The time vector is *htime*.

The HIRLAM and HIGHTSI (only for Kara Sea) data are in Matlab files "XX_hirlamYYYYZ.mat" and "XX_hightsiYYYY.mat" where XX is BS for the Baltic Sea and KS for the Kara Sea, YYYY is 2010 and 2011 for the winters 2009-2010 and 2010-2011, respectively, and Z is null for a file that contains variables *TA*, *VA*, *RH* and *QL* and 'b' for a file having *QS*, *TP*, and *SP* (having all variables in a single file takes too much Matlab-workspace memory).

In order to construct a map of some parameter at a given time following Matlab-code can be used for the Baltic Sea case:

```
hta=zeros(size(hmask));  %air temperature
[y I]=min(abs(htime-gtime)); %given time in serial date number format
datestr(gtime)
datestr(htime(I))
tmp1=TA(I,:);
l=1;
for g=1:length(hta(:,1))
  for f=1:length(hta(1,:))
    if hmask(g,f)==1
      hta(g,f)=tmp1(l);
      l=l+1;
    end
  end
end
hta=hta+273.15; %to kelvins
i=find(hmask==0);hta(i)=-1; %land masked to value of -1
```

For the Kara Sea following code can be utilized:

```
hta=zeros(size(hmask));  %air temperature
[y I]=min(abs(htime-gtime)); %given time in serial date number format
datestr(gtime)
datestr(htime(I))
tmp1=TA(I,:);
l=1;
for g=1:length(hta(:,1))
  for f=1:length(hta(1,:))
    hta(g,f)=tmp1(l);
    l=l+1;
  end
end
hta=hta+273.15; %to kelvins
i=find(hmask==0);hta(i)=-1; %land masked to value of -1
```

Figures 35 and 36 show examples of the HIRLAM air temperature maps.

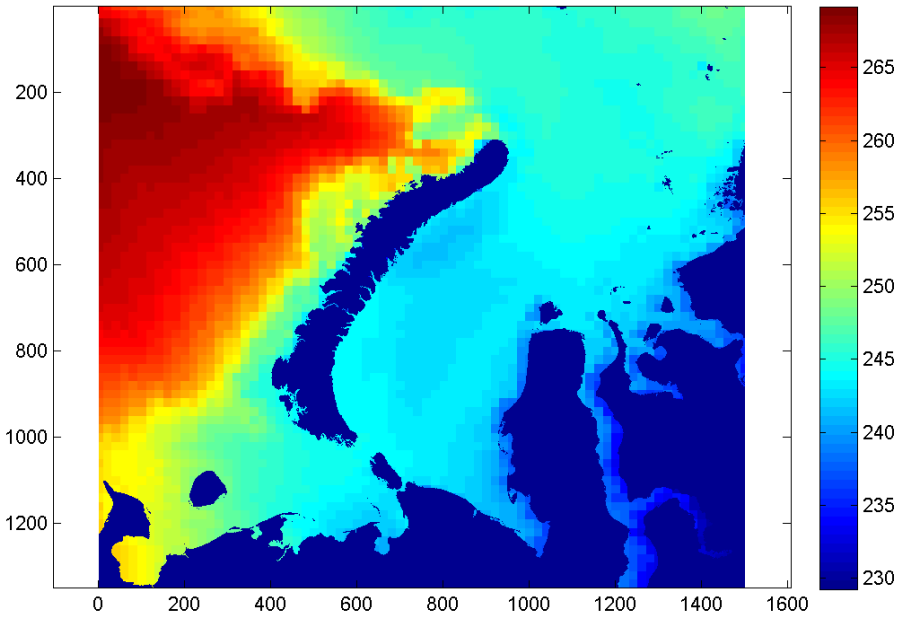

Figure 35. HIRLAM air temperature over the and Kara Sea validation area on 23 Feb 2010 16:00 UTC.

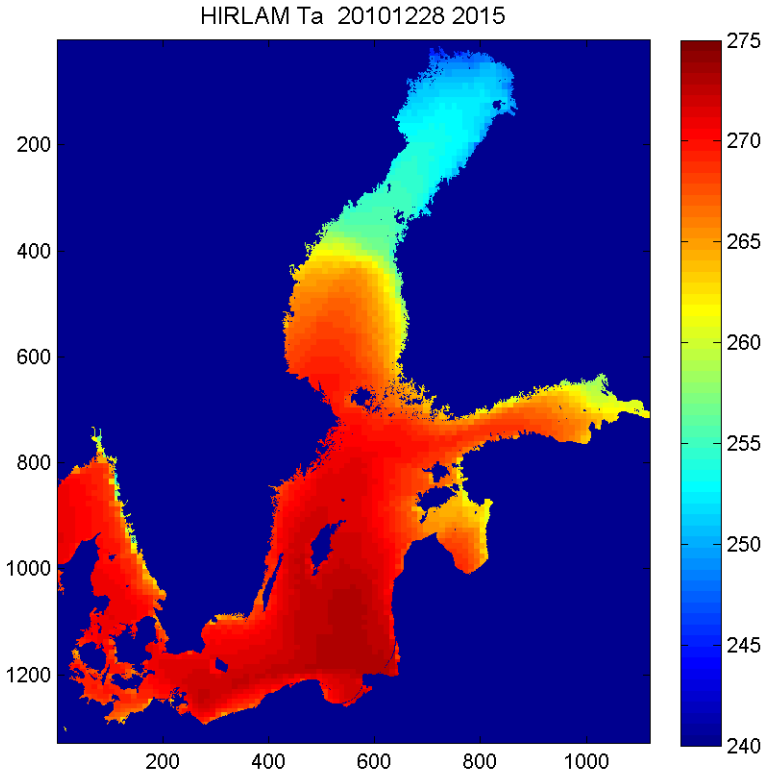

Figure 36. HIRLAM air temperature over the Baltic Sea on 28 Dec 2010 20:00 UTC.

6. DATABASE - SMOSIce-DAT-DB

6.1 Directory structure in the SMOSIce ftp-server

6.1.1 Baltic Sea data

Below is the directory structure for the Baltic Sea validation data.

BalticSea – *main directory for all data*

- Insitu – *main directory for in-situ cal/val data, SMOSIce-DAT-CV*
  - Icebreaker – *Finnish ice-breaker thickness measurements;winters 2010 and 2011*
  - Weatherdata – *Finnish coastal weather station data*
  - Fieldcampaigns – *In-situ data from the Baltic Sea ice field campaigns*
- Model – *main directory for model data, SMOSIce-DAT-MD*
  - HIRLAM – *HIRLAM model data and HIRLAM grid data; 2009-2010, 2010-2011*
- RemoteSensing – *main directory for remote sensing data and products, SMOSIce-DAT-RS*
  - Icecharts – *Finnish Ice Service ice charts*
    - 2010 – *Charts for winter 2010; 1 Feb – 31 Mar*
    - 2011 – *Charts for winter 2010-2011; 1 Dec 2010 – 31 Mar 2011*
  - PolarView – *Polar View SAR (ENVISAT and RS-2) based ice thickness charts*
    - 2010 – *Charts for winter 2010; 1 Jan – 31 Mar*
    - 2011 – *Charts for winter 2010-2011; 1 Dec 2010 – 31 Mar 2011*
  - MODIS – *main directory for all MODIS data and products*
    - IST – *Ice surface temperature data in Matlab-files and tiff-images*
      - 2010 – *Data for winter 2010*
      - 2011 – *Data for winter 2010-2011*
    - Icethickness – *MODIS thin ice thickness maps; Matlab-files and tiff-images*
      - 2010 – *Data for winter 2010*
      - 2011 – *Data for winter 2010-2011*

6.1.2 Kara Sea data

Below is the directory structure for the Kara Sea validation data.

KaraSea – *main directory for all data*

- Insitu – *main directory for in-situ cal/val data, SMOSIce-DAT-CV*
  - Icecharts – *SRC Planeta (Russia) ice charts*
    - 2010 – *Charts for winter 2010; 15 Mar – 30 Apr (FMI has only these)*
    - 2011 – *Charts for winter 2010-2011; 1 Oct 2010 – 30 Apr 2011*
  - Weatherdata – *Russian coastal weather station data*
- Model – *main directory for model data, SMOSIce-DAT-MD*
  - HIRLAM – *HIRLAM model data and HIRLAM grid data; 2009-2010, 2010-2011*
  - HIGHTSI – *HIGHTSI model data; 2009-2010, 2010-2011*
- RemoteSensing – *main directory for remote sensing data and products, SMOSIce-DAT-RS*
  - ENVISAT – *main directory for ENVISAT data*
    - SARmosaic – *Daily SAR mosaics*
      - 2010 – *Mosaics for winter 2010; 1 Jan – 30 Apr*
      - 2011 – *Mosaics for winter 2010-2011; 1 Nov 2010 – 30 Apr 2011*
    - Coverages - *WSM daily coverage over the MODIS thickness images*
      - 2010 – *Images for winter 2010; 1 Jan – 30 Apr*
      - 2011 – *Images for winter 2010-2011; 1 Nov 2010 – 30 Apr 2011*
  - MODIS – *main directory for all MODIS data and products*
    - IST – *Ice surface temperature data in Matlab-files and tiff-images*
      - 2010 – *Data for winter 2010*
      - 2011 – *Data for winter 2010-2011*
    - Icethickness – *MODIS thin ice thickness maps; Matlab-files and tiff-images*
      - 2010 – *Data for winter 2010*
      - 2011 – *Data for winter 2010-2011*
  - MODIS-SAR – *MODIS and SAR based ice thickness maps; Matlab-files and tiff-images*
    - 2010 – *Data for winter 2010*
    - 2011 – *Data for winter 2010-2011*

6.2 Usage restrictions

There are no usage restrictions for the Baltic and Kara Seas validation data available in the SMOSIce ftp-server, but notify the author if the data is used outside the SMOSIce project.

6.3 Demonstration of SMOSIce-DAT-DB use

The validation data (part of SMOSIce-DAT-DB) are available at the SMOSIce ftp-site. Using directory structures shown in Section 6.1 and file formats described in Tables 2 and 4 a wanted validation dataset can be easily found, downloaded and used in the SMOS thickness validation. Thus, there is no need for a database query system.

7. REFERENCES

Anderson, E.A. A point energy and mass balance model of a snow cover. *NOAA Tech. Rep. NWS/19*, Off. of Hydrol., Natl. Weather Serv., Silver Spring, Md. 150 pp., 1976.

Carlström, A., and L.M.H. Ulander, "Validation of backscatter models for level and deformed sea ice in ERS-1 SAR images," *Int. J. Remote Sens.*, 16(7), 3245-3266, 1995.

Cheng, B., T. Vihma, R. Pirazzini, and M. Granskog, "Modeling of superimposed ice formation during spring snow-melt period in the Baltic Sea," *Ann. Glaciol.* 44, pp. 139-145, 2006.

Cheng, B., Z. Zhang, T. Vihma, M. Johansson, L. Bian, Z. Li and H. Wu, H. "Model experiments on snow and ice thermodynamics in the Arctic Ocean with CHINARE 2003 data," *J. Geophys. Res.* 113(C09020), doi:10.1029/2007JC004654, 2008.

Dierking, W., M. I. Pettersson, and J. Askne, "Multifrequency scatterometer measurements of Baltic Sea ice during EMAC-95," *Int. J. Remote Sens.*, 20(2), 349-372, 1999.

Doronin, Y. P. Thermal Interaction of the Atmosphere and Hydrosphere in the Arctic, 85 pp., Isr. Program for Sci. Transl, Jerusalem, 1971.

Frey, R.A. et al., "Cloud detection with MODIS. Part I: Improvements in the MODIS Cloud Mask for Collection 5," *J. Atmos. Oceanic Technol.*, 25, pp. 1057-1072, 2008.

Haapala, J., et al., "Cruise Report SeaIce10 2/2010", Finnish Meteorological Institute, 2010.

Hall, D.K., J.R. Key, K.A. Casey, G.A Riggs, and D.J. Cavalieri, "Sea ice surface temperature product from MODIS," *IEEE Trans. GeoSci. Remote Sens.*, 42(5), pp. 1076-1087, 2004.

Hanna, S. R. and R. Yang, "Evaluation of mesoscale numerical models' simulations of near surface wind, Temperature Gradients and Mixing depth," *J. Appl. Meteor.*, 40, 1095-1104, 2001.

Järvenoja, S., "Problems in predicted HIRLAM T2m in winter, spring and summer," *Proc. SRNWP/HIRLAM Workshop on Surface Processes and Turbulence*, SMHI, Norrköping, 15-17 September 2004, 14-26, 2004.

Karvonen, J., M. Similä, J. Haapala, C. Haas, and M. Mäkynen, "Comparison of SAR Data and Operational Sea Ice Products to EM Ice Thickness Measurements in the Baltic Sea," *Proc. IGARSS'04*, pp. 3021–3024, 2004.

Karvonen, J., J. Haapala, J. Lehtiranta, and A. Seinä, "Polarview@FIMR: WWW-based Delivery of Baltic Sea Ice Products to End-Users," *Proc. IGARSS'07*, 4 pp., 2007.

Key, J.R., R.A. Silcox, and R.S. Stone, "Evaluation of surface radiative flux parameterizations for use in sea ice model." *J. Geophys. Res.* C101(C2), pp. 3839-3849, 1996.

Kovacs, A. Sea ice: Part I. Bulk salinity versus ice floe thickness. *CRREL Report 96-7*, U.S. Army Cold Reg. Res. and Eng. Lab., Hanover, N. H.

Launiainen, J., and B. Cheng, "Modelling of ice thermodynamics in natural water bodies," *Cold Reg. Sci. Technol.*, 27(3), pp. 153-178, 1998.

Leppäranta, M., “A review of analytical models of sea-ice growth,” *Atmosphere-Ocean*, 31 (1), 123-138, 1993.

Lüpkes, C., T. Vihma, G. Birnbaum, and U. Wacker, “Influence of leads in sea ice on the temperature of the atmospheric boundary layer during polar night,” *Geophys. Res. Letters*, 35, L03805, doi:10.1029/2007gl032461, 2008.

Martin, S., R. Drucker, R. Kwok and B. Holt ”Estimation of the thin ice thickness and heat flux for the Chukchi Sea Alaskan coast polynya from Special Sensor Microwave/Imager data, 1990–2001,” *Journal of Geophysical Research*, 109, C10012, doi:10.1029/2004JC002428, 2004.

Mäkynen, M., T. Manninen, M. Similä, J. Karvonen, and M. Hallikainen, ”Incidence Angle Dependence of the Statistical Properties of the C-Band HH-Polarization Backscattering Signatures of the Baltic Sea Ice,” *IEEE Trans. GeoSci. Remote Sens.*, 40(12), 2593-2605, 2002.

Mäkynen, M., B. Cheng, M. Similä, T. Vihma and M. Hallikainen, ”Comparisons between SAR backscattering coefficient and results of a thermodynamic snow/ice model for the Baltic Sea land-fast sea ice,” *IEEE Trans. GeoSci. Remote Sens.* 45(5), pp. 1131-1141, 2007.

National Snow and Ice Data Center. *Morphometric characteristics of ice and snow in the Arctic Basin: aircraft landing observations from the Former Soviet Union, 1928-1989*. Compiled by I.P. Romanov. Boulder, CO: National Snow and Ice Data Center. Digital media, 2004.

Similä, M., M. Mäkynen, and I. Heiler, ”Comparison between C band synthetic aperture radar and 3-D laser scanner statistics for the Baltic Sea ice,” *J. Geophys. Res*, 115, C10056, doi:10.1029/2009JC005970, 2010.

Similä, M., M. Mäkynen, B. Cheng, and E. Rinne, “Multisensor and thermodynamic sea ice model based sea ice thickness charts over the Kara and Barents Seas in wintertime,” submitted to *Annals of Glaciology*, 2012.

Spreen, G., L. Kaleschke, and G. Heygster, “Sea ice remote sensing using AMSR-E 89 GHz channels,” *J. Geophys. Res.*, doi:10.1029/ 2005JC003384, 2008.

Sturm, M., J. Holmgren, M. König and K. Morris, “The thermal conductivity of seasonal snow,” *J. Glaciol.*, 43(143), 26-41, 1997.

Tamura, T., K. I. Ohshima, H. Enomoto, K. Tateyama, A. Muto, S. Ushio and R. A. Massom,. ”Estimation of thin sea-ice thickness from NOAA AVHRR data in a polynya off the Wilkes Land coast, East Antarctica,” *Annals of Glaciology*, 44, 269-274, 2006.

Trenina, I., “Planeta ice cover analysis based on real-time satellite data and time-series of satellite data processing,” *Presentation at 10th meeting of the International Ice Charting Working Group*, Geneva, October 12-16, 2009.

Yen, Y.-C. Review of thermal properties of snow, ice and sea ice. *CRREL Report 81-10*, Hanover, N.H., 26 pp., 1981.

Untersteiner, N., “Calculations of temperature regime and heat budget of sea ice in the central Arctic, “*Journal of Geophysical Research*, 69, 4755-4766, 1964.

Wang, X., J. R. Key, and Y. Liu, “A thermodynamic model for estimating sea and lake ice thickness with optical satellite data,” *Journal of Geophysical Research*, 115, C12035, doi:10.1029/2009JC005857, 2010.

Zhang Z., B. Cheng, J. Launiainen, H. Wu, and Y. Liu, “Inter-comparisons of thermodynamic sea-ice modeling results using various parameterizations of radiative flux,” *Acta Oceanologica Sinica*, 25(l), 2l-31, 2006.

Zillman, Z. A study of some aspects of the radiation and heat budgets of the southern hemisphere oceans. *Meteorol. Stud. Rep. 26*, Bur. Of Meteorol., Dep. of the Inter., Canberra, A.C.T., 1972.

13 EM THICKNESS

Thomas Krumpen, Stefan Hendricks, Christian Haas

Data report on EM-Bird ice thickness measurements for SMOSIce validation obtained during Transdrift XX, ARK XXVII/3 and SafeWin 2011 campaigns

Thomas Krumpen &
Stefan Hendricks
Alfred Wegener Institute
for Polar and Marine Research
Busse Str. 24, 2770
Bremerhaven
Germany
Email: tkrumpen@awi.de &
stefan.hendricks@awi.de

Christian Haas
Department of Earth and Space
Science and Engineering
105 Petrie Science Building
York University, 4700 Keele St.
Tronto, ON, M3J 1P3, Canada
Email: haasc@yorku.ca

29. January 2012

Table of Contents

Figures

1. Introduction

In this report we summarize ice thickness information obtained for a validation of SMOS derived thin ice thickness estimates over thin ice areas during three field campaigns: The Transdrift (TD) XX (Laptev Sea), the *Polarstern* cruise ARK XXVII/3 (central Arctic Ocean), and SafeWin 2011 (Baltic Sea). The data is provided by the Alfred Wegener Institute and the University of Alberta. The ice thickness data obtained in the Baltic Sea during SafeWin 2011 can be archieved via Mikko Lensu (Finnsih Meteorolocial Institute, mikko.lensu@fmi.fi).

Below an introduction to electromagnetic (EM) ice thickness measurements and other instrumentation is given as well as a description of associated uncertainties and errors if applied over thin ice and in areas of low and variable surface salinities. We further outline the objectives of the three campaigns and provide a short summary on the data itself.

2. EM sea ice thickness sounding

Ice thickness measurements for SMOS thin ice thickness (SMOSIce) validation were obtained during helicopter-borne ice thickness surveys performed in the Laptev Sea (TD XX), in the central Arctic Ocean (ARK XXVII/3) and in the Baltic Sea (SafeWin 2011). Measurements were made with a so called electromagnetic (EM)-Bird, an airborne system with a single-frequency of 4.08 kHz (Haas et al. 2009). The instrument is towed by a helicopter 10-15 meters above the ice surface (Fig. 1). The method utilizes the contrast of electrical conductivity between sea water and sea ice to determine the distance to the ice-water interface. An additional laser altimeter yields the distance to the uppermost reflecting surface, hence the ice thickness is obtained as the ice- plus snow thickness from the difference between the laser range and the EM derived distance. Since the laser beam is always reflected at the uppermost surface, the thickness of the snow layer, if present, is included in the ice thickness estimates. The measurements were taken with point spacing of 3 to 4 m depending on the speed of the helicopter. Comparison with drill-hole data shows that within the footprint of a single measurement (40-50 meter) the accuracy over level sea ice is on the order of ± 10 cm (Pfaffling et al. 2007). However, the accuracy is worse over ridges. Because the low-frequency EM field is diffusive, its strength represents the average thickness of an area of approximately 3.7 times the instruments altitude above the ice surface. Due to this footprint, the maximum ridge thickness can be underestimated by as

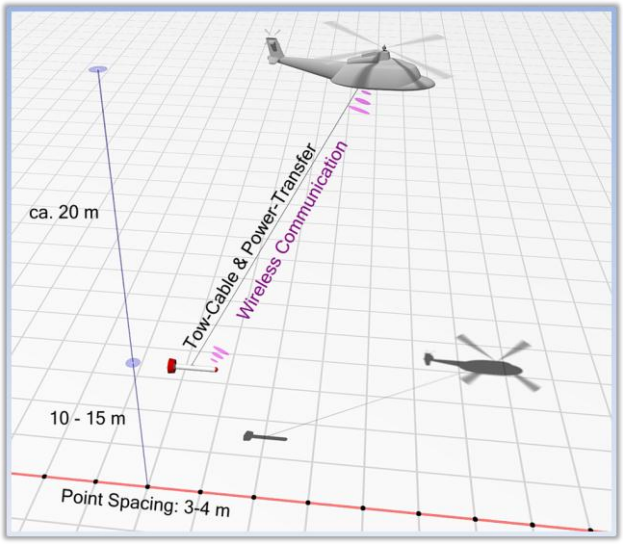

Figure 1: Schematic drawing of the EM Bird towed by a helicopter 10-15 m above the ice surface.

much as 50% in the worst cases, depending on the geometry and consolidation of the ridge keel. More information about the sensor and procedures can be found in Haas et al. (2009).

2.1 Additional sea ice information

During the TD XX campaign, a nadir-looking camera mounted inside the helicopter on a gimbal was taking pictures at a 30 second interval. All aerial pictures were taken with a GPS-compatible Ricoh© Caplio camera (Fig. 2). The external GPS antenna was mounted outside the helicopter, approximately 1.8 m away from image center point. The GPS position was taken every second. GPS-heights (hGPS) were corrected using the BIRD Laser altimeter plus rope length (approx. 29 m). The used zoom focal length was 5.8mm. The 35mm equivalent is 28mm with a view angle of 46.4° (β - vertical) x 65.5° (α - horizontal). After defining image corner coordinates, photographs were georeferenced to a stereographic coordinate system using a cubic convolution methodology. A detailed description of processing steps and associated errors is given in Krumpen et al. (2011a).

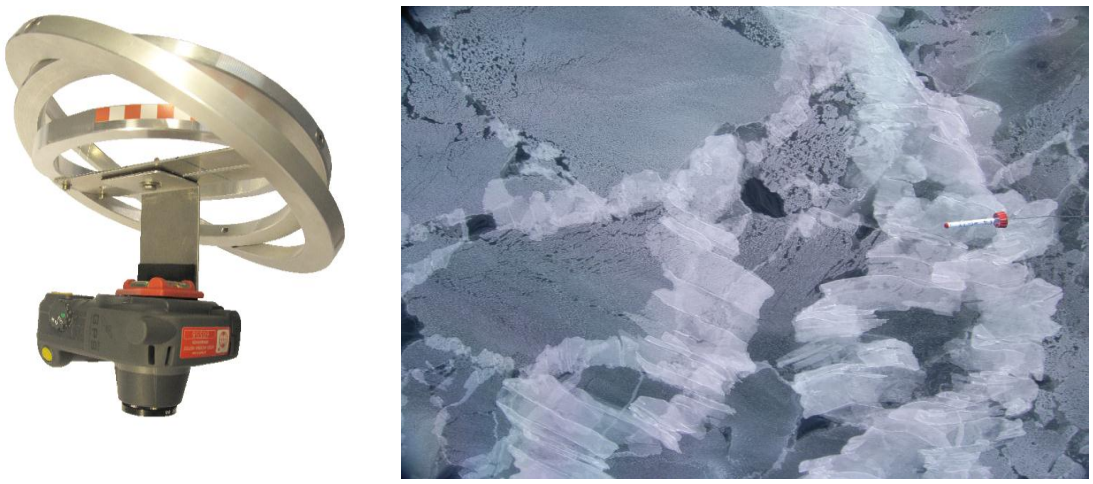

Figure 2: Camera system mounted on a gimbal (left) and aerial picture taken over thin ice during flight on April 20, 2012 (right).

3. Field campaigns

3.1 Transdrift XX, Laptev Sea

Two EM ice thickness survey flights were made during the Transdrift (TD) XX campaign in the Laptev in April, 2012. The campaign was carried out in the framework of a Russian – German research cooperation called 'Laptev Sea System'.

The first survey flight (April 16, 2012) covered a fast ice area north of the Lena delta. A second flight was performed 4 days later (April 20, 2012) over pack ice offshore the fast ice edge. Given the importance of the Laptev Sea for the Arctic Ocean sea ice budget, aim of the second EM survey flight was to determine ice thickness and production rates in the vicinity of the West New Siberian (WNS) polynya and the Anabar-Lena (AL) polynya. The retrieved ice information on pack ice were used to a) calibrate and validate new satellite algorithms for the determination of thin sea ice and b) as an input for model based ice production estimates.

The survey flight made across the polynya on April 20 covers mostly thin ice being formed in the WNS and AL polynya. A period of strong and consistent offshore winds led to the development of an extensive thin ice zone extending several hundred kilometres offshore. The flight started from a fuel deposit at the fast ice edge towards a pre-defined point of return and back. The point of return and length of the flight track were chosen according to available fuel capacity, weather condition and ice conditions.

Because the EM-Bird requires instrument drift correction, flight tracks are divided into profiles with a length of 10 to 25 minutes. Note that the EM-Bird internal GPS was not working. Therefore, data was synchronized afterwards to a handheld GARMIN GPS.

During the TD XX campaign the EM-Bird was operated by Thomas Krumpen (AWI) and Valeria Selyuzhenok (AWI).

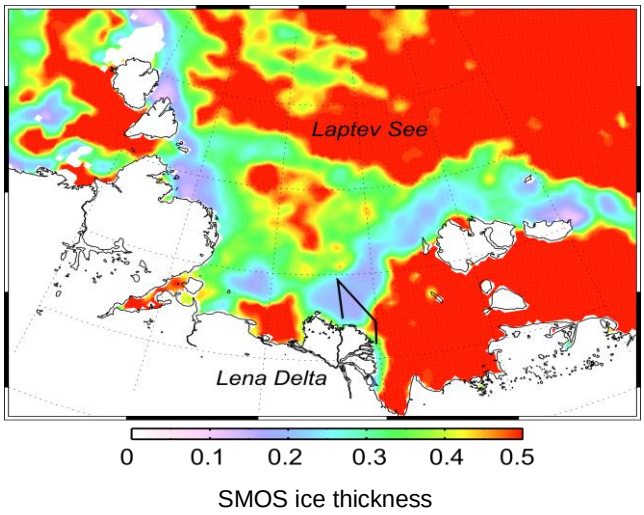

Figure 3: EM survey track over the WNS and AL polynya on April 20, 2012 in the Laptev Sea (*SMOSIce data source: University Hamburg*).

3.2 ARK XXVII/3, central Arctic Ocean

The objective of the EM airborne survey performed during ARK XXVII/3 was to continue a time series of sea ice thickness data obtained during *Polarstern* cruises between 1991 and 2011. Unfortunately, flight operations were significantly hampered by weather conditions with low cloud and fog in the first half the cruise. However, in the second part of the cruise colder temperatures led to better flying conditions and the majority of sea ice thickness data along the 60°E transect to the central Arctic.

Two flights covering extensive thin ice areas at the ice margin were obtained on September 27, 2012 (morning and afternoon). The large thin ice areas were formed during freeze-up and consisted mainly of nilas and pancake ice (see Fig. 4). Unfortunately, no nadir-looking aerial pictures were taken owing to a failure of the central data acquisition system of the primary EM sensor, which had to be replaced with a backup system.

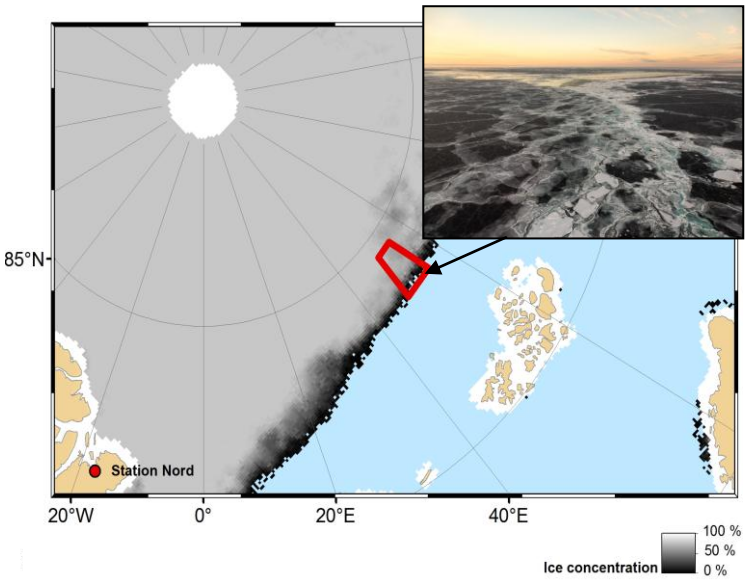

Figure 4: Surveyed freeze up area (red) during ARK XXVII/3 on September 27, 2012. The photo (upper right panel) taken on flight shows thin ice formed during freeze up.

EM survey flights during ARK XXVII/3 were performed by Stefan Hendricks (AWI) and Thomas Krumpen (AWI).

3.3 SafeWin 2011, Baltic Sea

The Baltic EM thickness campaign and analysis was conducted within the EU-funded project 'Safety of winter navigation in dynamic ice' (contract SCP8-GA-2009-233884 - SAFEWIN). The partners in this project are Aalto University, Arctic and Antarctic Research Institute, Finnish Meteorological Institute, Finnish Transport Agency, ILS Oy, Stena Rederi AB, Swedish Maritime Administration, Swedish Meteorological and Hydrological Institute, Tallinn University of Technology and AS Tallink Group.

As part of the latter, two winter field campaigns have been performed to provide data for the development and improvement of models and ship-in-ice studies, and for their validation. Ice thickness is one of the key parameters governing navigation in ice. Therefore, extensive ground-based, ship-borne, underwater, and airborne ice thickness surveys have been performed.

Surveys were flown during and after the RV Aranda sea ice cruise in the Sea and Bay of Bothnia, between March 2 and 7, 2011. Due to sever ice conditions, RV Aranda arrived late at her final destination in the Bay of Bothnia. Therefore, and due to further delays related to technical problems with the helicopter and contaminated fuel, surveys from the ship could only be performed on two days, before the ship had to return south. However, we decided to keep the EM Bird on land in Kokkola, and after some careful training by Alec Casey, Mikko Lensu was able to perform surveys on four more days.

In total, 11 flights were performed, covering large parts of the Bay of Bothnia, the Quarken, and the northern Sea of Bothnia (Figure 1). While some flights were designed to provide the best overview of the regional ice thickness distribution, several flights were performed over the buoy array in the region surrounding the ship, to observe thickness changes resulting from changes in ice deformation.

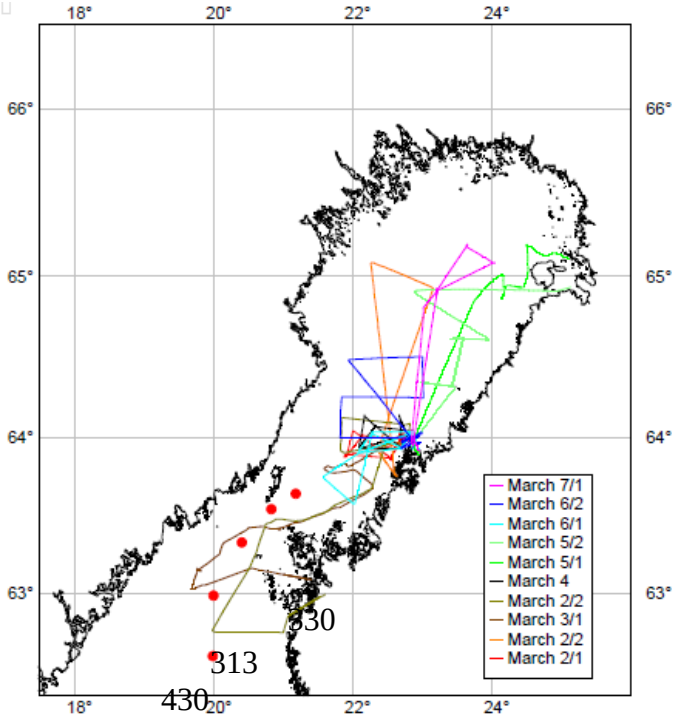

Figure 5: Overview of all EM ice thickness flights performed during SafeWin 2011. Red circles show locations of CTD profiles and respective surface seawater conductivities in mS/m.

The University of Alberta participants in the SafeWin 2011 sea ice cruise were Alec Casey, John Lobach, and Christian Haas. Data can be archieved via

Mikko Lensu

Finnish Meteorological Institute
Erik Palmenin Aukio 1
P.O. Box 503
FI-00101 Helsinki, Finland
(mikko.lensu@fmi.fi)

4. Uncertainties in ice thickness estimates

Comparison with drill-hole data shows that within the footprint of a single measurement (40-50 meter) the accuracy over level sea ice is on the order of ± 10 cm (Pfaffling et al. 2007). However, additional uncertainties in ice thickness measurements may arise from the assumption that sea ice can be regarded as a non-conductive medium. However, over thin ice, this assumption may be invalid because the conductivity of saline young ice can be significantly higher than that of older first-year or multi-year ice. This can lead to an underestimation of the ice thickness. Therefore, all thin ice thickness data have to be interpreted as minimum ice thicknesses.

Moreover, measurements made in the Baltic Sea (SafeWin 2011) are challenging due to the brackish nature of the sea water, with salinities of only around 5 ppt in the Sea of Bothnia and 3 ppt in the Bay of Bothnia, with a sharp salinity gradient in the Quarken region (Fig. 5). However, surveys have successfully been performed by a team from the Finish Geological Survey in the 1990s, and during the EU IRIS project between 2003 and 2005 (Haas, 2004), during PolIce in 2006, and during SafeWin 2010. Note that with such low salinities/conductivities, the Quadrature component Q of the secondary EM field is larger than the Inphase I. Therefore, Q also has a better signal-to-noise ratio, and all thickness retrievals have been based on this component. This is different from measurements over ocean sea water, where the Inphase component is mostly used.

The accuracy of the EM measurements obtained during SafeWin 2011 is further compromised by the existence of shallow water and the formation of a freshwater layer under fast ice fed by river runoff from land. Haas (2006) has shown that ice thicknesses will be overestimated in brackish water shallower than 10 to 15 m, because currents are induced in the seafloor, which typically has a lower conductivity than the seawater. Similarly, the freshwater layer under the fast ice has negligible conductivity and cannot be distinguished from the ice. These two effects strongly influenced the results obtained during flights over fast ice, which resided near the coasts, most notably in the region around Hailuoto and along the shores west of Vasa, and east of the Quarken.

For processing of the TD XX data, assumptions on the unknown surface conductivity had to be made. The surveyed area is characterized by large interannual variations, being the consequence of an enormous freshwater input from the Lena river and ice formation and salt rejection processes taking place in polynyas offshore the fast ice edge. Following e.g. Dmitrenko et al. 2008, distribution of the freshwater, and as such the surface salinity in winter, is controlled by the atmospheric circulation during summer months. Anticyclonic wind conditions force the riverine water northwards and result in a stronger density stratification in the eastern Laptev sea during winter. Cyclonic atmospheric circulation deflects the freshwater plume of the Lena river eastward towards the East Siberian Sea, thus causing higher salinities in the eastern Laptev Sea and the area around the WNS polynya. The sommer of 2011 was characterized by an anticyclonic wind regime (comparatively

strongly stratified water column with low surface salinity). Based on hydrographic observations carried out in March and April by the Soviet Sever expeditions (1979-2010, Krumpen et al. 2011b), we calculated an average surface water conductivity for winters pre-conditioned by summers with an anticyclonic atmospheric circulation regime (2000 mS/m). The surface conductivity was then used to compute the distance of the EM-Bird to the ice water interface (see Haas et al. 2009 for details on EM processing). The error associated to the conductivity assumptions are thought to be within the range of the instrument error, because during processing manually identified regions of open waters are used to constantly calibrate the EM-signal.

4.1 EM-Bird data structure

Data for a single survey flight are stored in an ASCII file. The file name consists of the date (e.g.20110719), an abbreviation for the campaign (e.g. SW11 for SafeWin2011) and an "_allfinal.dat" extension.

A single data take (row) includes the year (1st column), the month (2nd column), the day (3rd column), the FID (4th column), latitude (5th column), longitude (6th column), distance from FID 0 (7th column), ice thickness (8th column) and instrument height above ice (9th column).

5. References

Dmitrenko, I. A., Kirillov, S. A., Tremblay, L. B., Bauch, D., Willmes, S. (2009). Sea-ice production over the Laptev Sea shelf inferred from historical summer-to-winter hydrographic observations of 1960s-1990s, *Geophysical Research Letters, 36*

Haas, C. (2004). Airborne EM sea-ice thickness profiling over brackish Baltic sea water, *Proceedings of the 17th international IAHR symposium on ice*, June 21-25, 2004, St. Petersburg, Russia, All-Russian Research Institute of Hydraulic Engineering (VNIIG), Saint Petersburg, Russia,2,12-17.

Haas, C. (2006). Airborne electromagnetic sea ice thickness sounding in shallow, brackish water environments of the Caspian and Baltic Seas, *Proceedings of OMAE2006 25th International Conference on Offshore Mechanics and Arctic Engineering*, June 4-9, 2006, Hamburg, Germany, 6pp.

Haas, C., Lobach, J., Hendricks, S., Rabenstein, L., Pfaffling, A. (2009). Helicopter-borne measurements of sea ice thickness, using a small and lightweight, digital EM system, *Journal of Applied Geophysics*, 67(3), 234-241., doi:10.1016/j.jappgeo.2008.05.005.

Krumpen, T., Haas, C., Hendricks, S., Hoelemann, J., Gerdes, R., Kalmbach, D. (2011a). HELIOS, a nadir-looking sea ice monitoring camera. *Cold Region Science and Technology, 65*, 308-313

Krumpen, T., Hoelemann, J. A., Willmes, S., Maqueda, M. A. M., Busche, T., Dmitrenko, I. A., Gerdes, R., Haas, C., Hendricks, S., Kirillov, S., Rabenstein, L., Schroeder, D. (2011b). Sea ice production and water mass modification in the eastern Laptev Sea, *Journal of Geophysical Research, 116*.

Pfaffling, A., Haas, C., Reid, J. E. (2007). A direct helicopter EM sea ice thickness inversion, assessed with synthetic and field data, *Geophysics,* F127-F137.

Appendix: EM-Bird data

On the following pages, details of ice thicknesses along the individual flight tracks are given by means of EM thickness profiles. In addition, a frequency histogram of ice thickness data is presented (bin-width 0.1 m) together with information on flight date and track length as well as mean and modal thicknesses. A map shows the location of the ice survey.

A.1 Data obtained during TD XX

A.1.1 Flight, April 20, 2012, 05.01 UTC

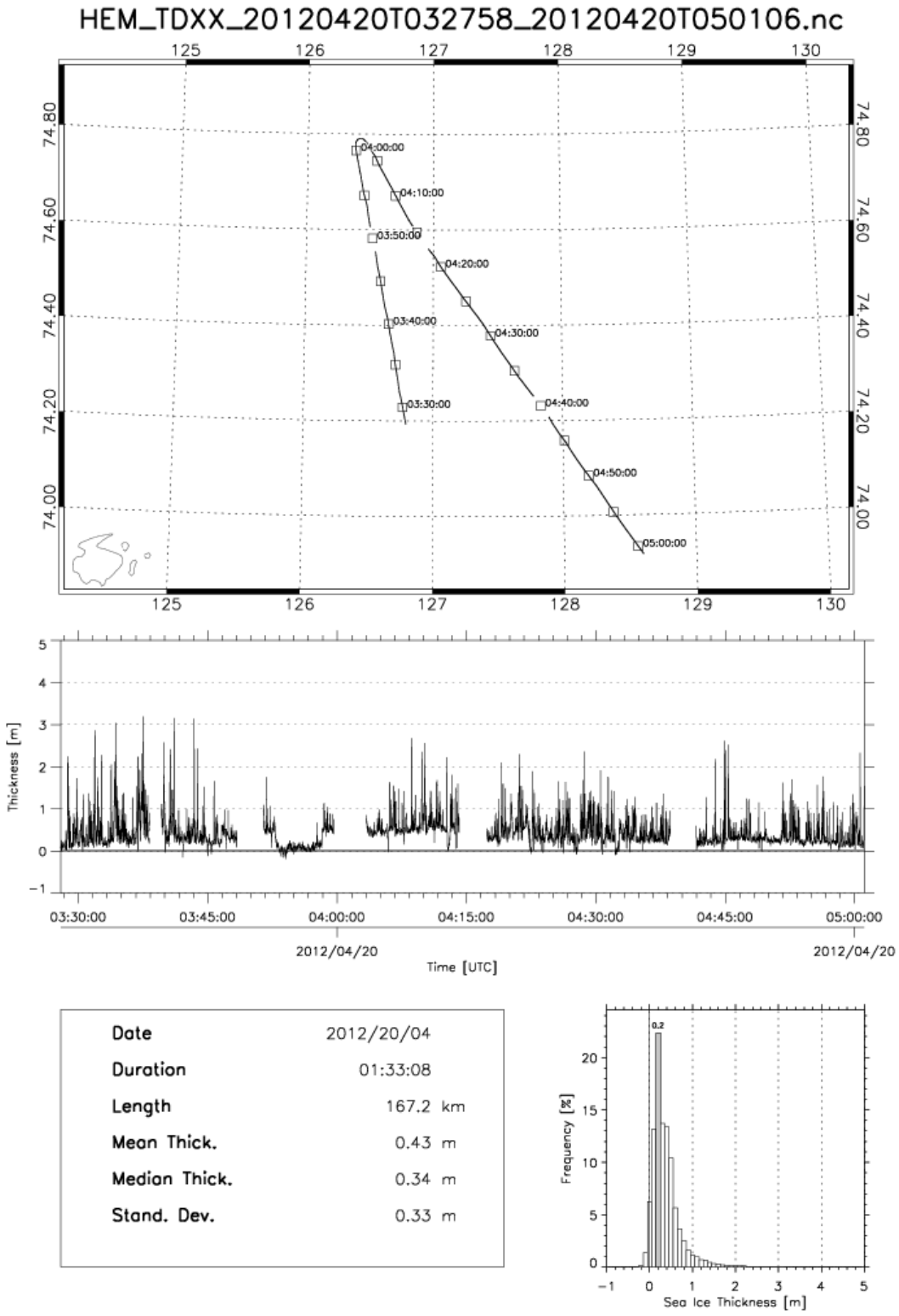

A.2 Data obtained during ARK XXVII/3

A.2.1 Flight, September 27, 2012, 11.39 UTC

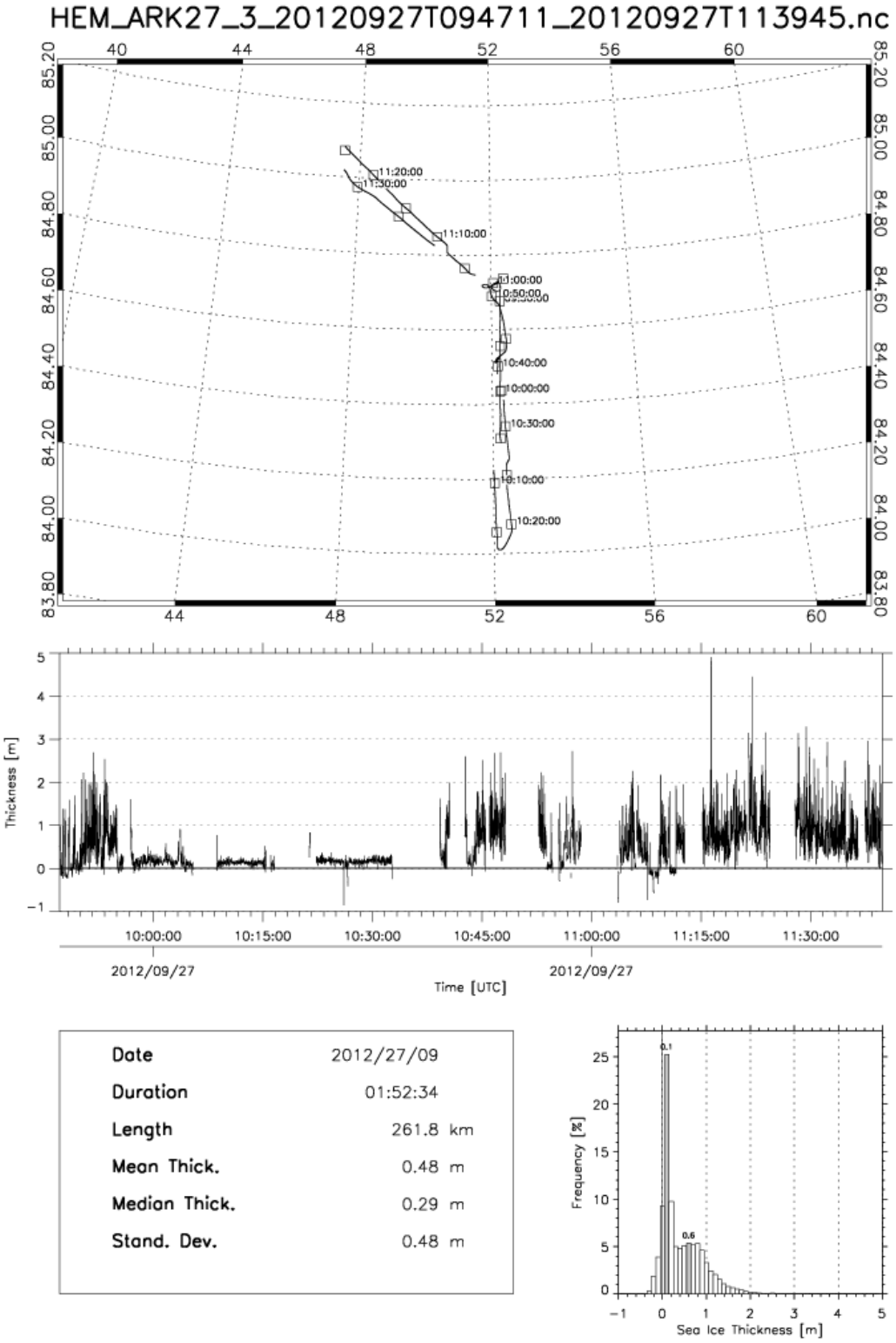

A.2.2 Flight, September 29, 2012, 08.55 UTC

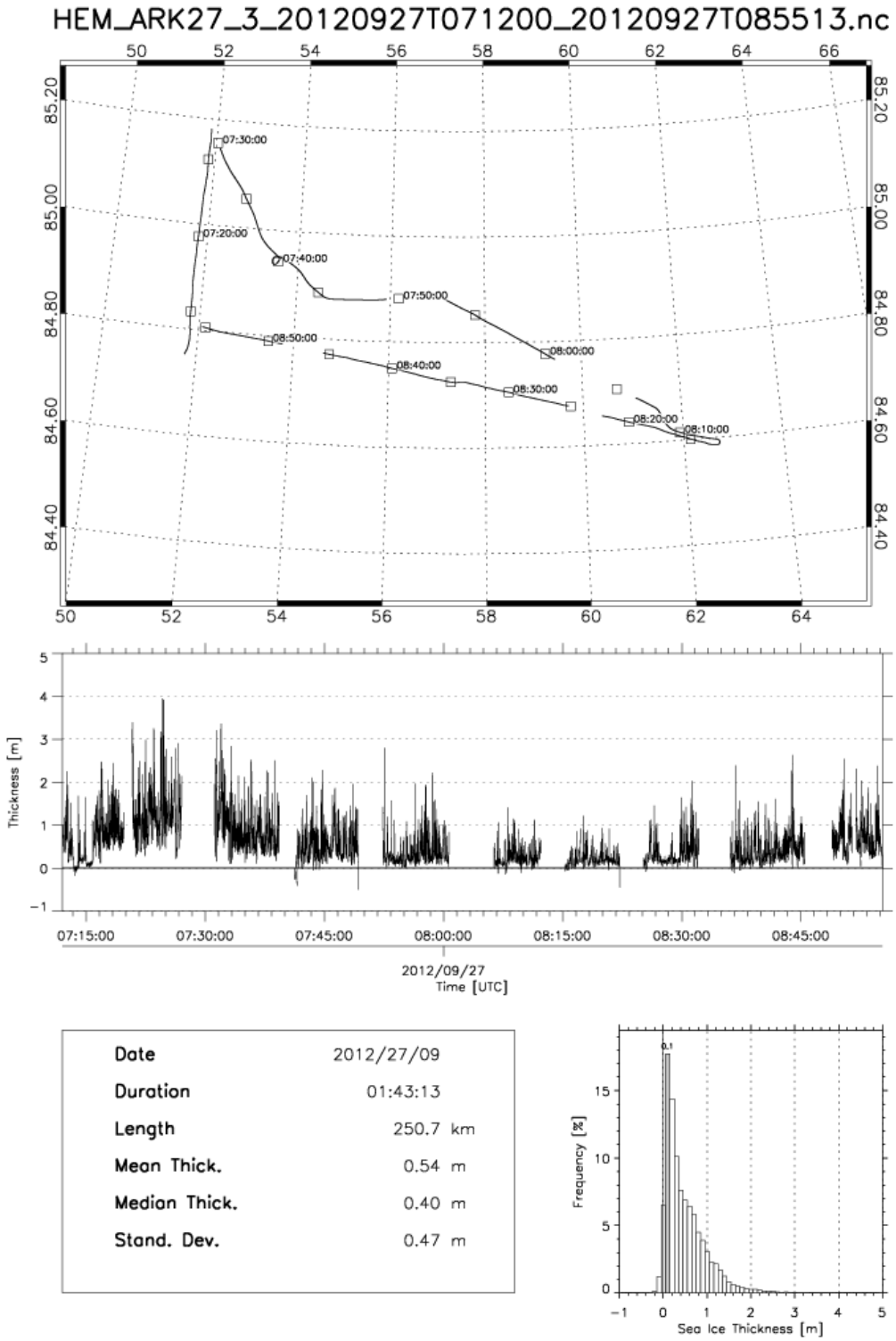

A.3 Data obtained during SafeWin 2011

A.3.1 Flight, March 02, 2011, 07.49 UTC

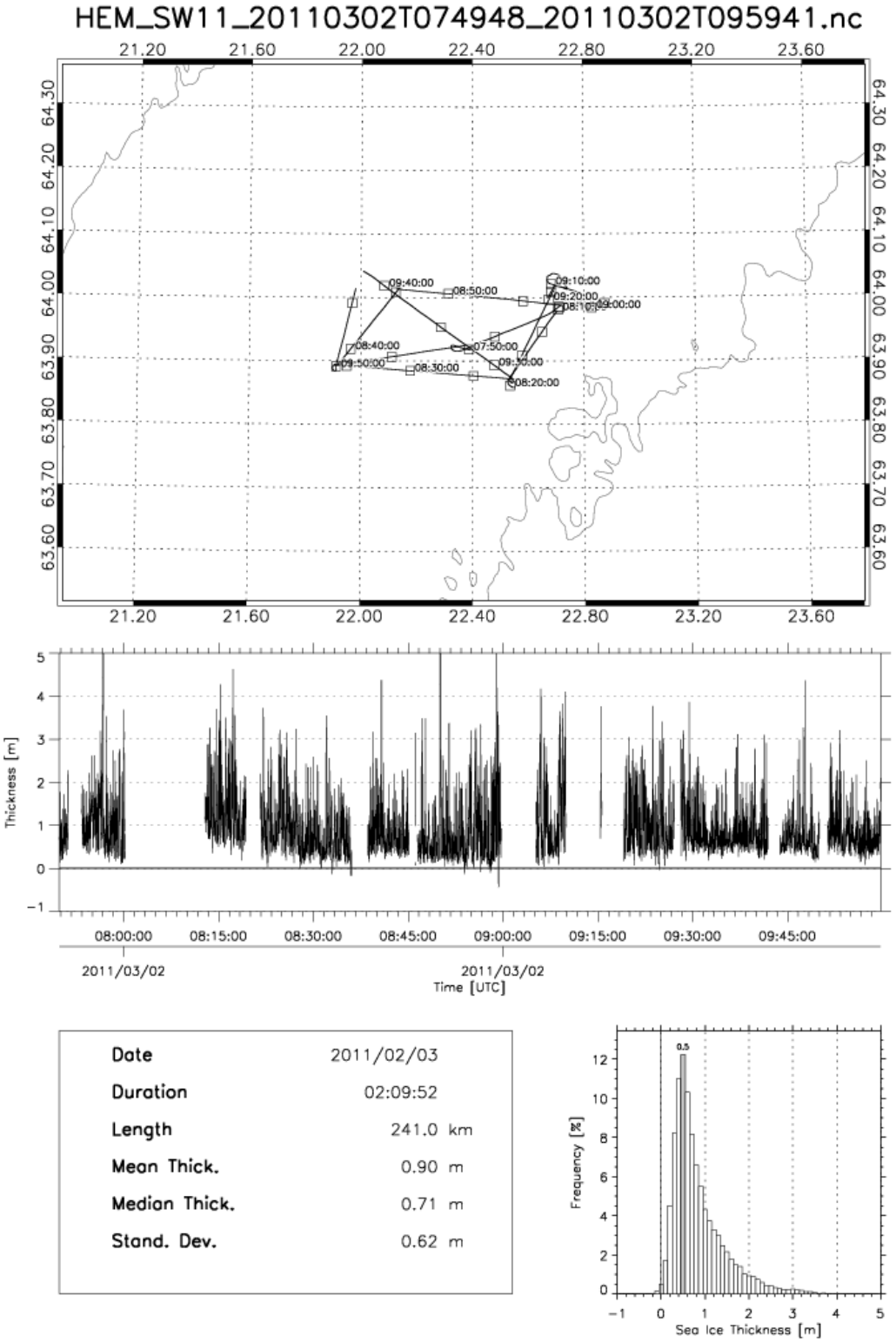

A.3.2 Flight, March 02, 2011, 11.50 UTC

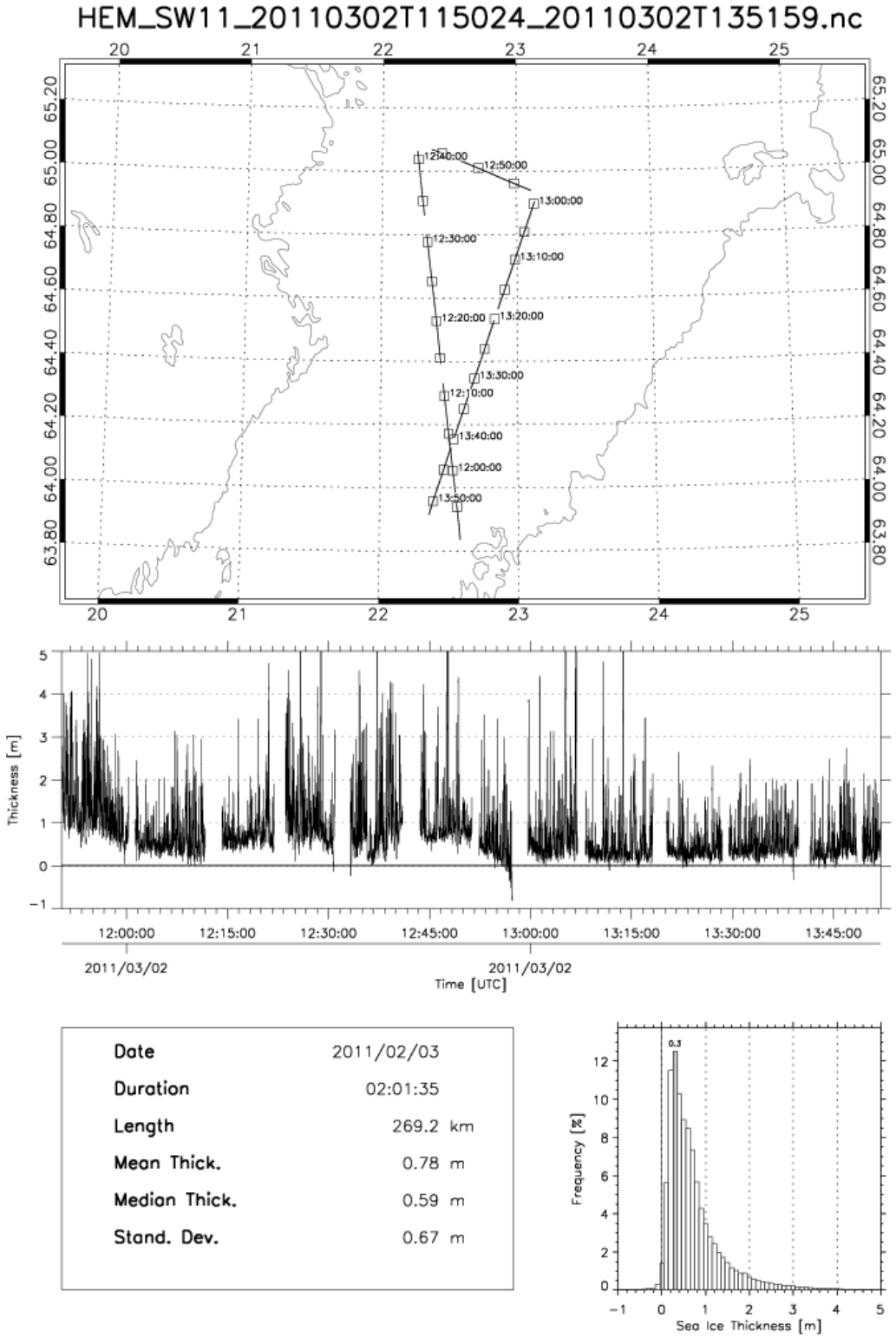

A.3.3 Flight, March 03, 2011, 07.56 UTC

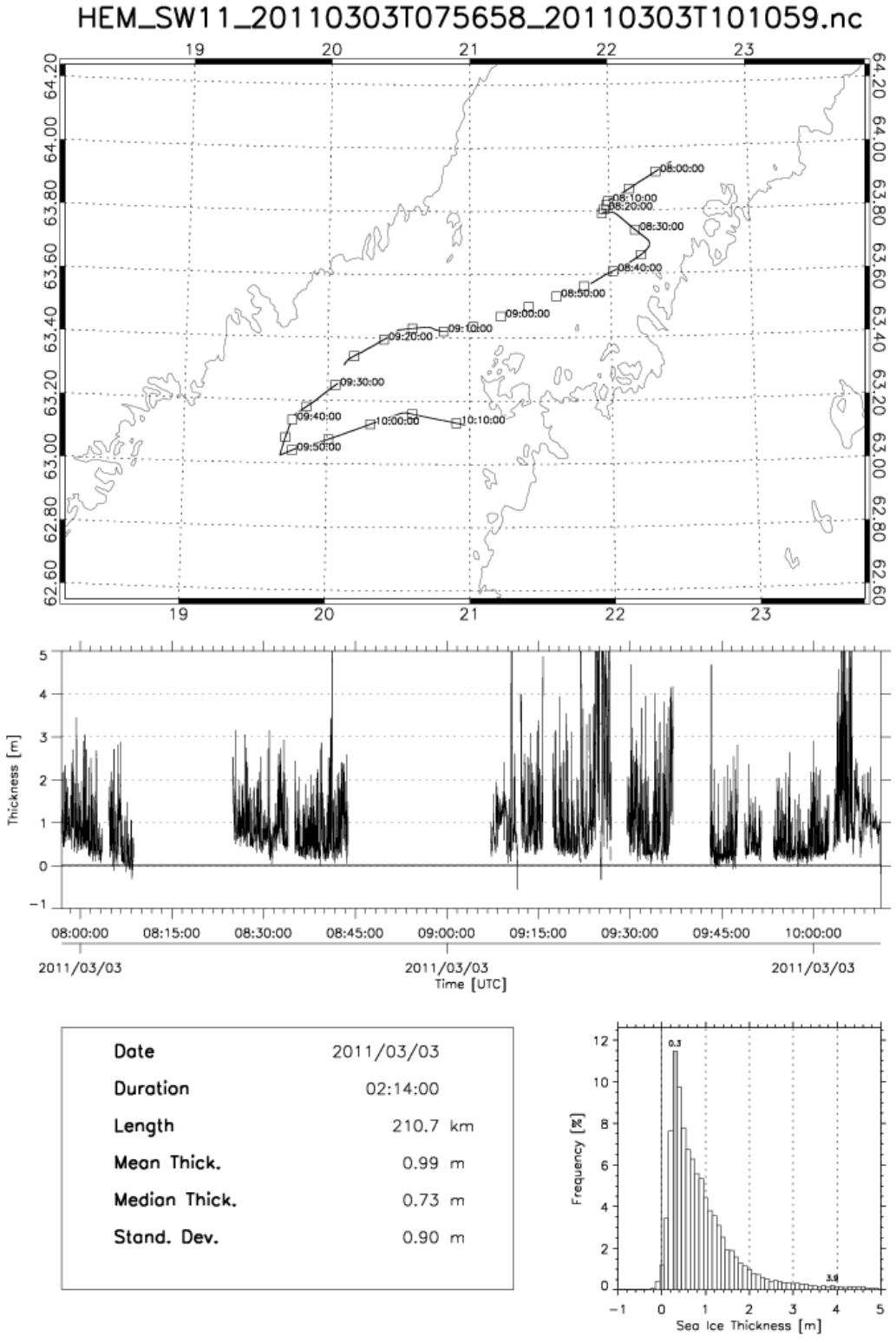

A.3.4 Flight, March 03, 2011, 12.19 UTC

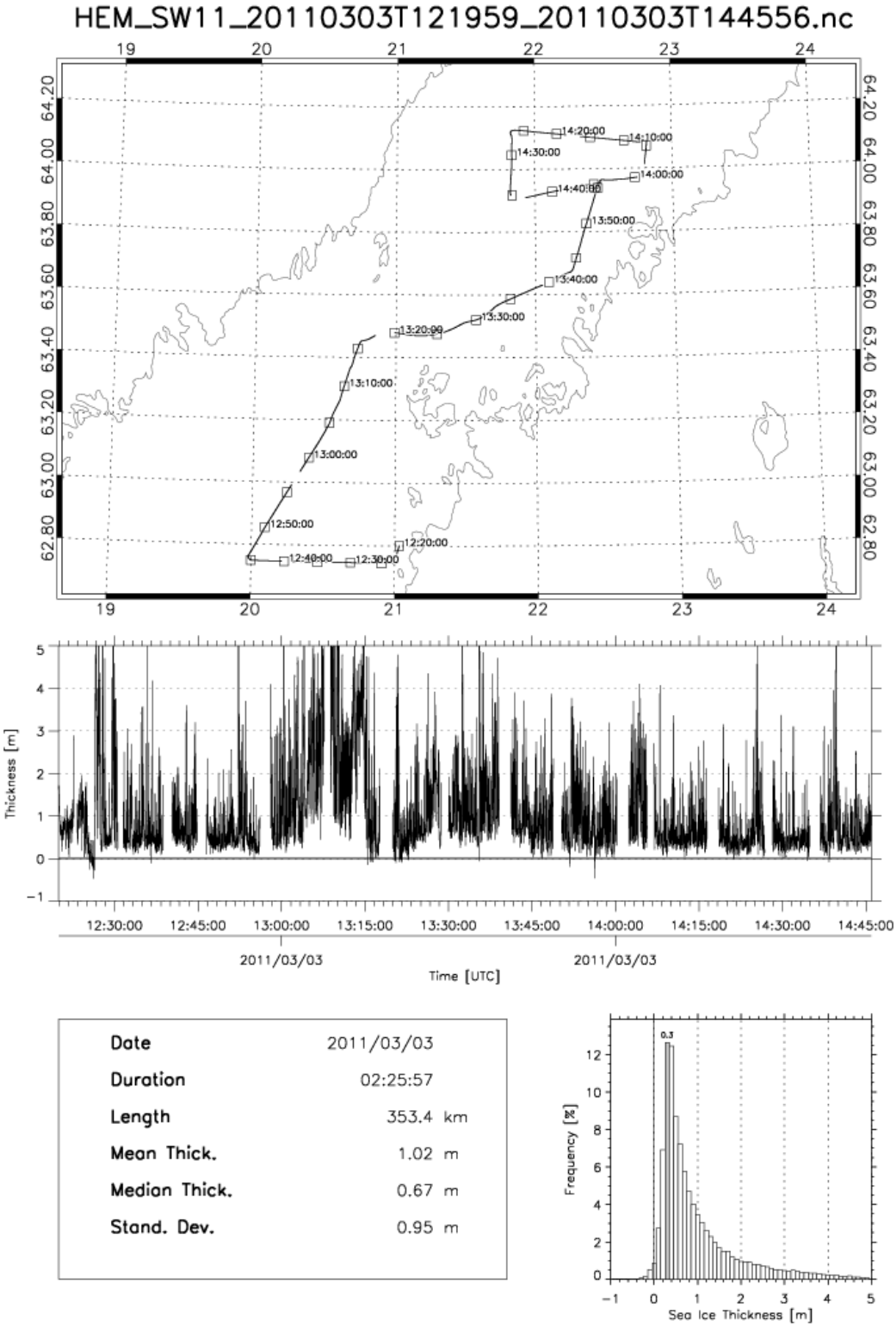

A.3.5 Flight, March 04, 2011, 12.43 UTC

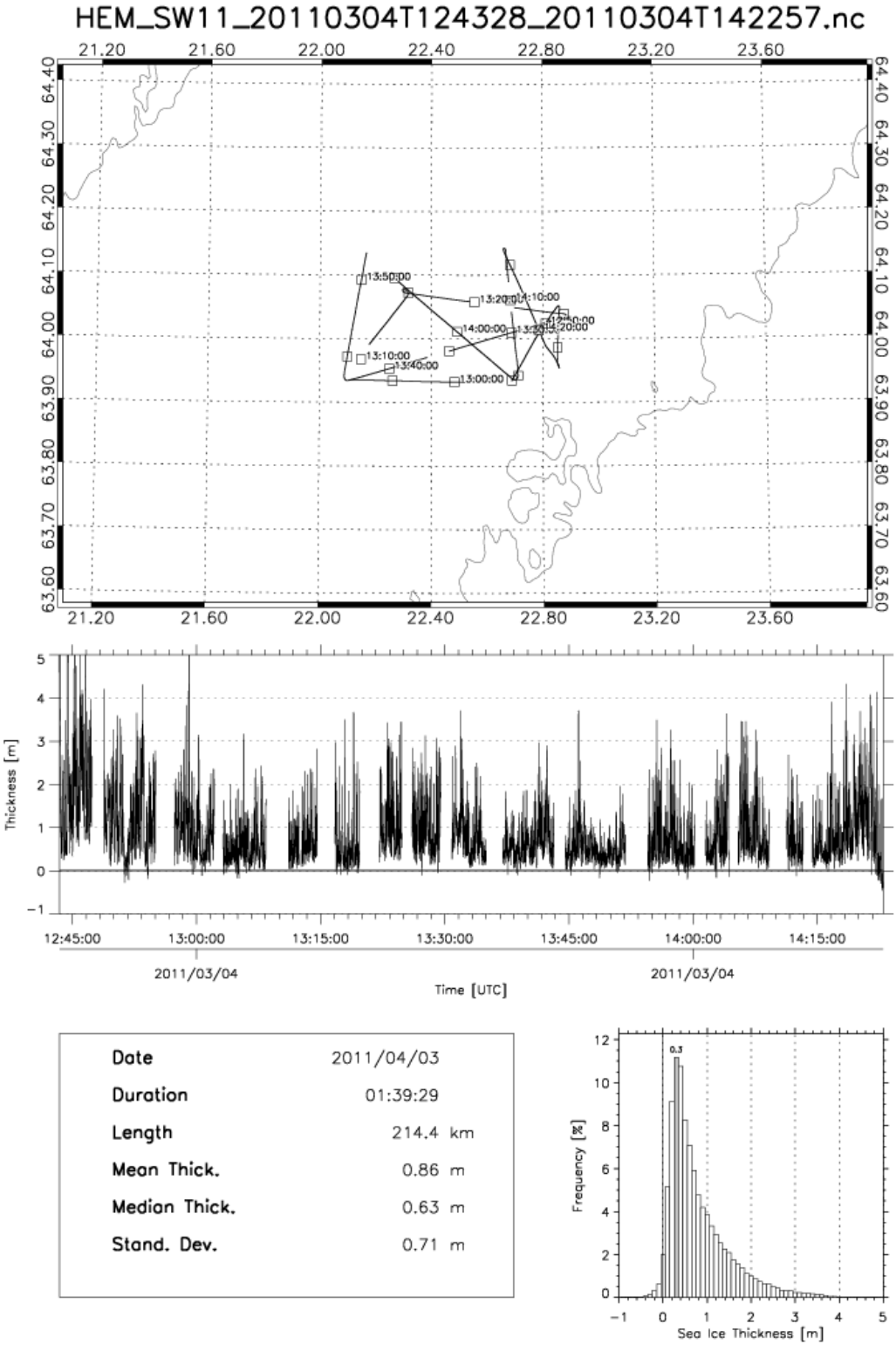

A.3.6 Flight, March 05, 2011, 07.16 UTC

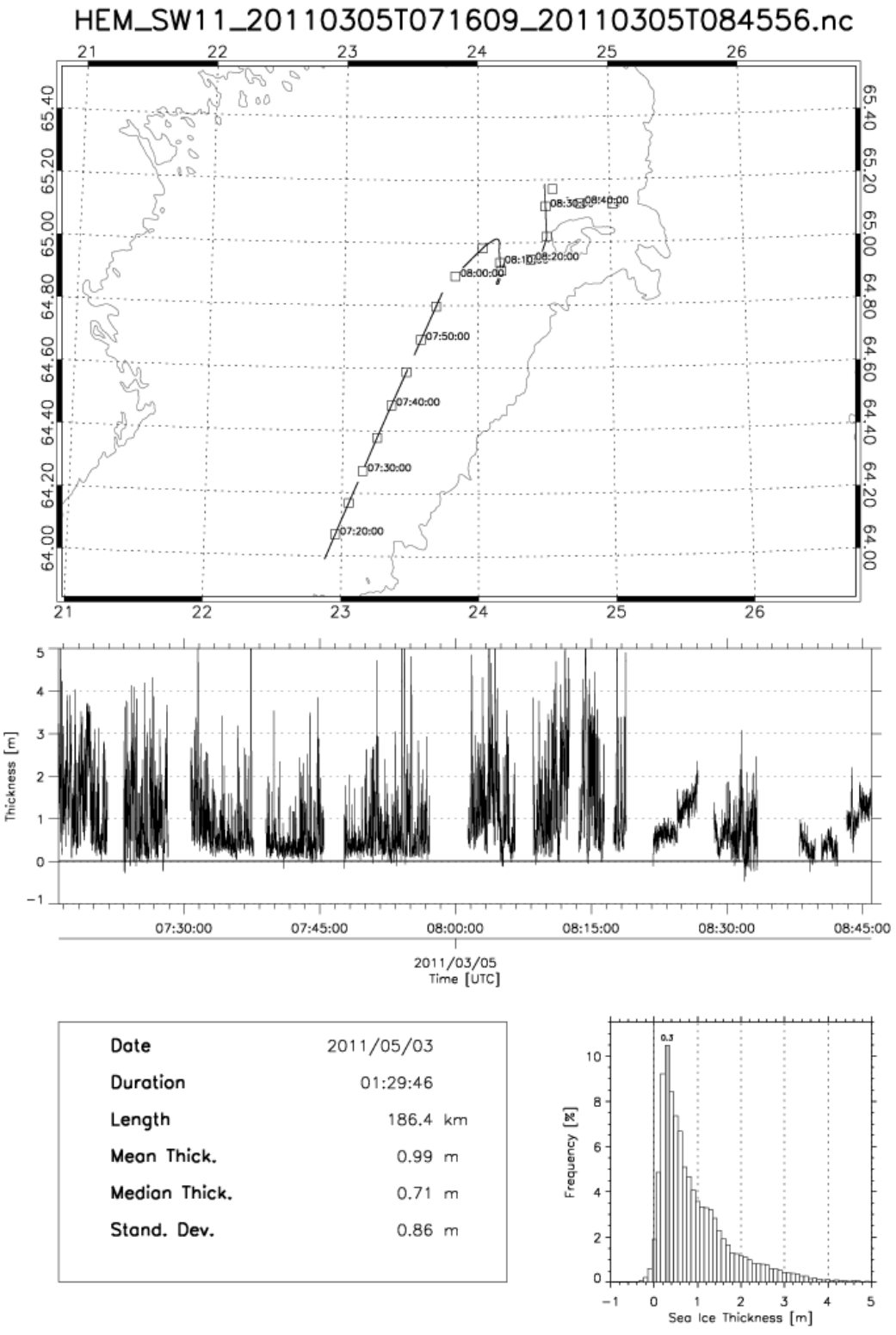

A.3.7 Flight, March 05, 2011, 10.47 UTC

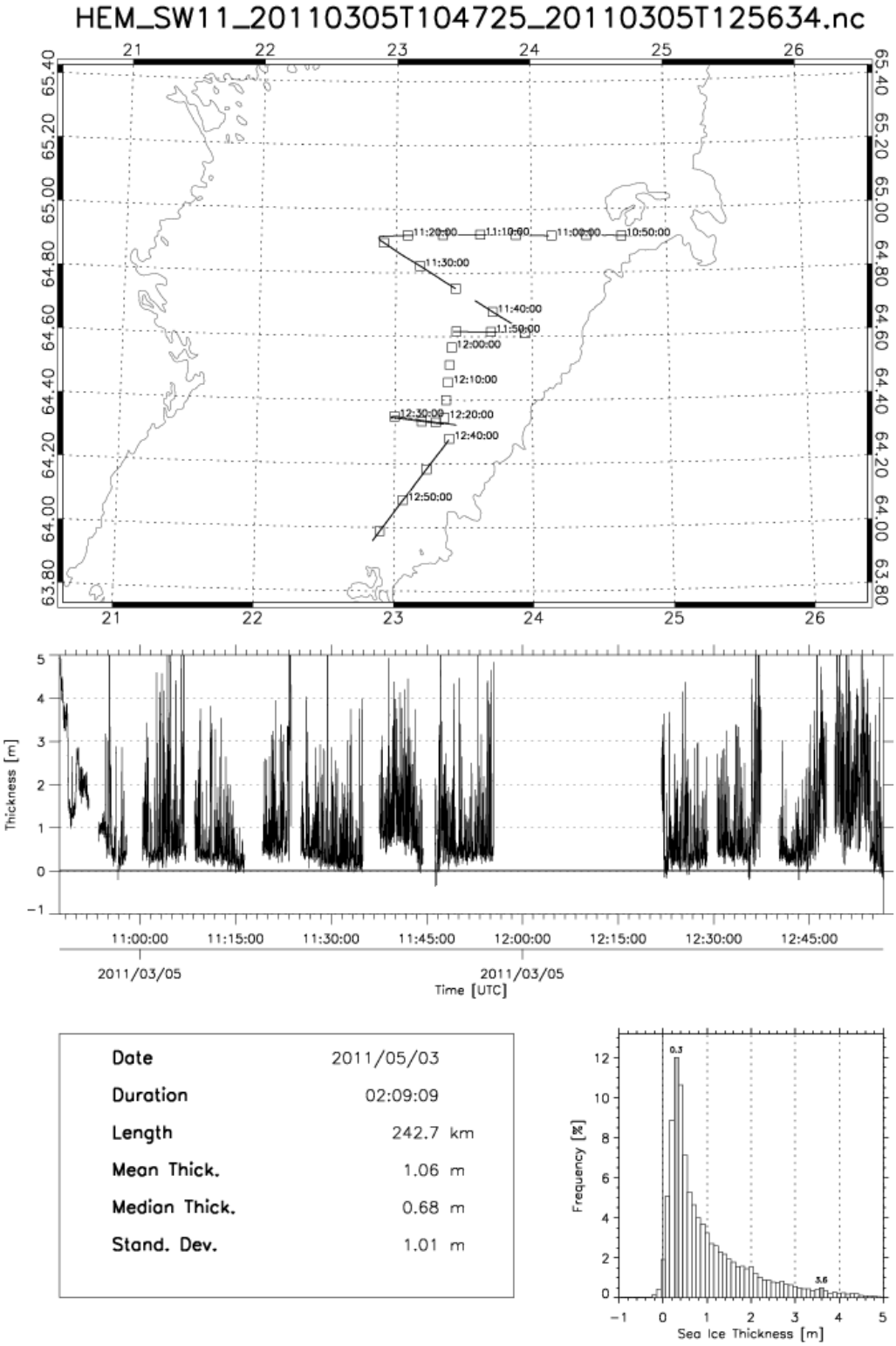

A.3.8 Flight, March 06, 2011, 08.19 UTC

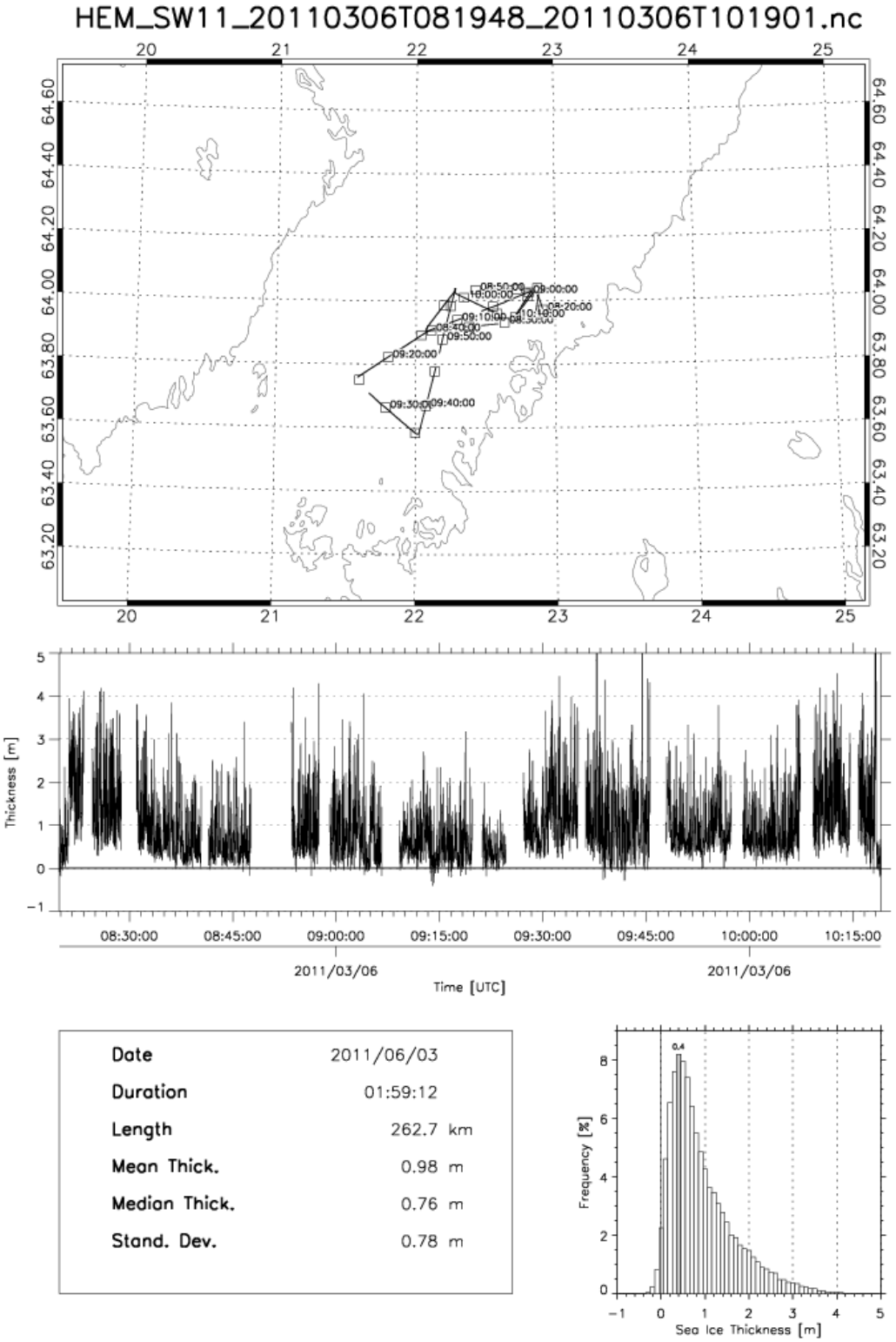

A.3.9 Flight, March 06, 2011, 12.04 UTC

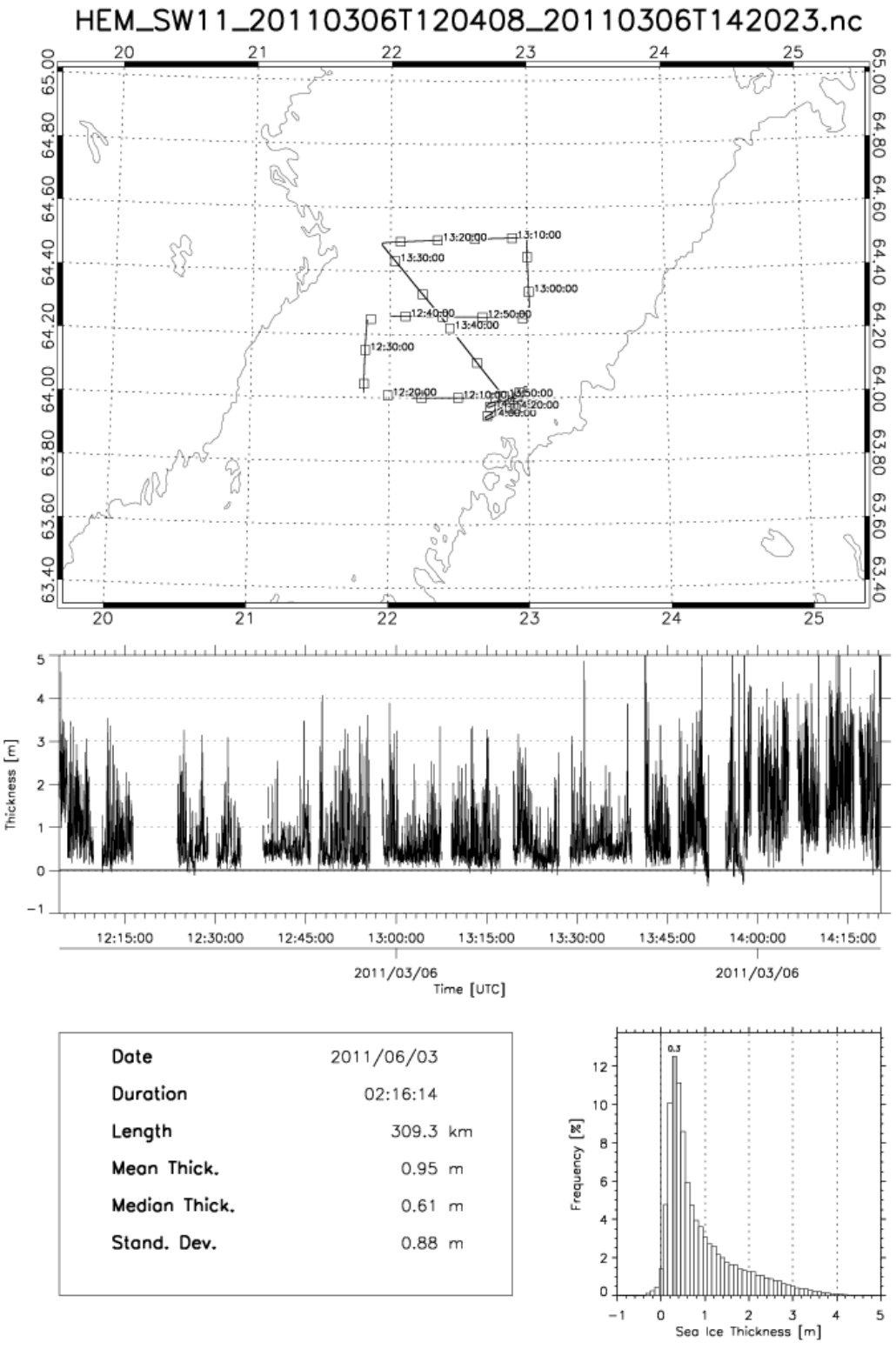

A.3.10 Flight, March 07, 2011, 07.10 UTC

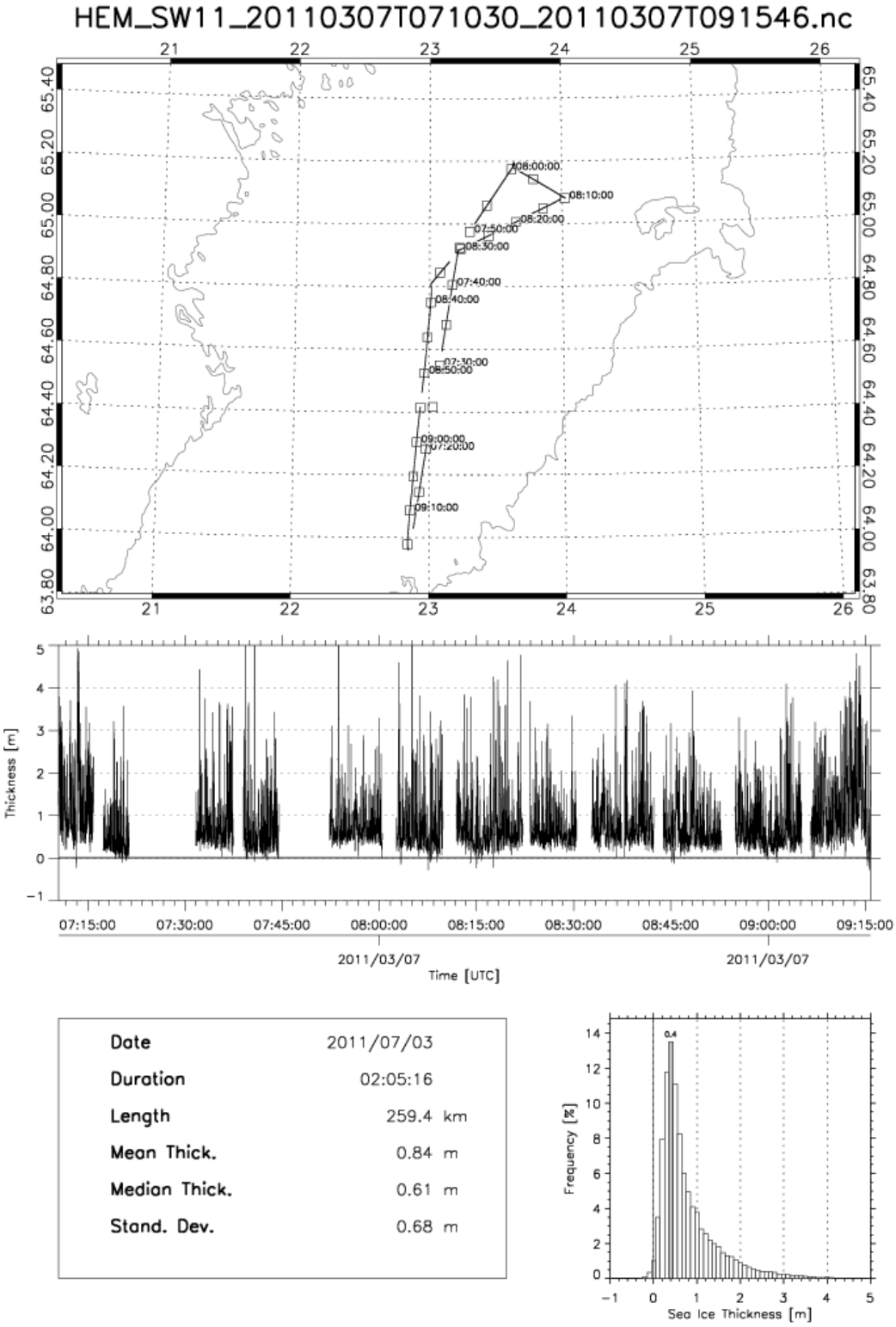

A.3.11 Flight, March 07, 2011, 11.37 UTC

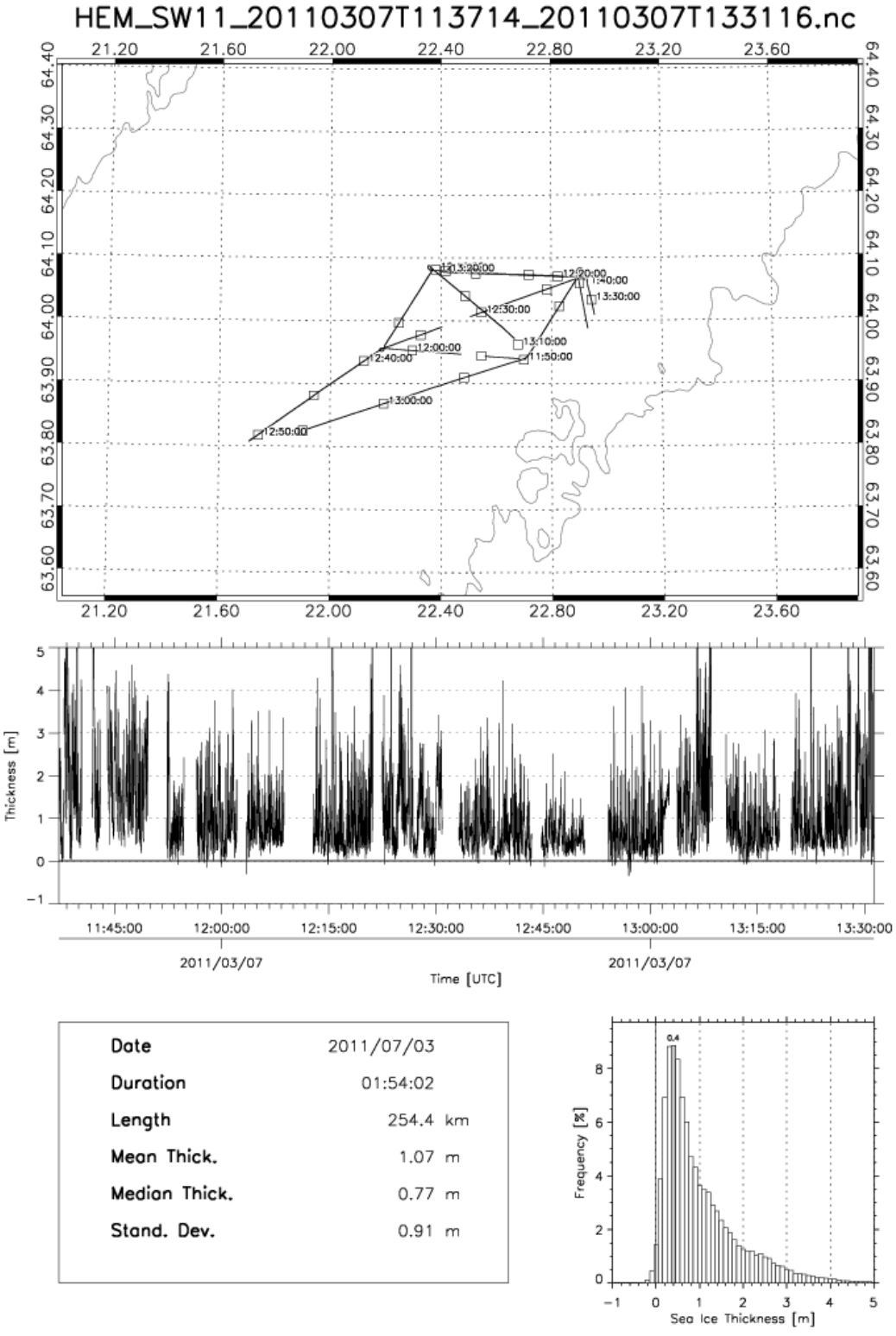

Part VI

References

BIBLIOGRAPHY

Andersen, S., Tonboe, R., Kaleschke, L., Heygster, G., and Pedersen, L.: Intercomparison of passive microwave sea ice concentration retrievals over the high-concentration Arctic sea ice, J. Geophys. Res, 112, C08, 2007.

Bertino, L. and Lisæter, K. A.: The TOPAZ monitoring and prediction system for the Atlantic and Arctic Oceans, Journal of Operational Oceanography, 1, 15–19, 2008.

Brath, M., Scharffenberg, M. G., Serra, N., and Stammer, D.: Altimeter-based estimates of eddy variability and eddy transports in the subpolar North Atlantic, Marine Geodesy, 33, 472–503, 2010.

Burke, W., Schmugge, T., and Paris, J.: Comparison of 2.8- and 21-cm microwave radiometer observations over soils with emission model calculations, Journal of Geophysical Research, 84, 287 – 294, 1979.

Camps, A., Vall-llossera, N., Duffo, N., Torres, F., and Corbella, I.: Performance of sea surface salinity and soil moisture retrieval algorithms with different auxiliary datasets in 2-D L-band aperture synthesis interferometric radiometers, IEEE TRANSACTIONS ON GEOSCIENCE AND REMOTE SENSING, 43, 1189–1200, doi:{10.1109/TGRS.2004.842096}, 2005.

Camps, A., Gourrion, J., Tarongi, J., Gutierrez, A., Barbosa, J., and Castro, R.: RFI Analysis in SMOS Imagery, in: Geoscience and Remote Sensing Symposium (IGRASS proceedings 2010, pp. 2007–2010, 2010.

Cavalieri, D., Gloersen, P., and Campbell, W.: Determination of sea ice parameters with the Nimbus 7 SMMR, Journal of Geophysical Research, 89, 5355–5369, 1984.

Cavalieri, D., Markus, T., and Comiso, J.: AMSR-E/Aqua daily L3 12.5 km brightness temperature, sea ice concentration, and snow depth polar grids V002, 2004.

Cox, G. and Weeks, W.: Salinity variations in sea ice, Journal of Glaciology, 13, 109–120, 1974.

Cox, G. and Weeks, W.: Equations for determining the gas and brine volumes in sea ice samples, Journal of Glaciology, 29, 306 – 316, 1983.

Dee, D. P., Uppala, S. M., Simmons, A. J., Berrisford, P., Poli, P., Kobayashi, S., Andrae, U., Balmaseda, M. A., Balsamo, G., Bauer, P., Bechtold, P., Beljaars, A. C. M., van de Berg, L., Bidlot, J., Bormann, N., Delsol, C., Dragani, R., Fuentes, M., Geer, A. J., Haimberger, L., Healy, S. B., Hersbach, H., Hólm, E. V., Isaksen, L., Kållberg, P., Köhler, M., Matricardi, M., McNally, A. P., Monge-Sanz, B. M., Morcrette, J.-J., Park, B.-K., Peubey, C., de Rosnay, P., Tavolato, C., Thépaut, J.-N., and Vitart, F.: The ERA-Interim reanalysis:

configuration and performance of the data assimilation system, Quarterly Journal of the Royal Meteorological Society, 137, 553–597, doi:10.1002/qj.828, 2011.

Dmitrenko, I. A., Kirillov, S. A., Ivanov, V. V., Rudels, B., Serra, N., and Koldunov, N. V.: Modified Halocline Water over the Laptev Sea Continental Margin: Historical Data Analysis, Journal of Climate, 25, 5556–5565, 2012.

Doronin, Y.: Thermal interaction of the atmosphere and the hydrosphere in the Arctic, CoronetBooks, Philadelphia, 1971.

Eppler, D. T., Farmer, L. D., Lohanick, A. W., Anderson, M. R., Cavalieri, D. J., Comiso, J., Gloersen, P., Garrity, C., Grenfell, T. C., Hallikainen, M., Maslanik, J. A., Mätzler, C., Melloh, R. A., Rubinstein, I., and Swift, C. T.: Passive Microwave Signatures of Sea Ice, pp. 47–71, American Geophysical Union, doi:10.1029/GM068p0047, http://dx.doi.org/10.1029/GM068p0047, 2013.

Erlingsson, B.: Two-dimensional deformation patterns in sea ice, J. Glaciol, 34, 301–308, 1988.

Ezraty, R.: Detection and monitoring of new-ice in the East Greenland Sea using the SeaWinds scatterometer, Journal of Ocean University of Qingdao, 1, 109–118, doi:10.1007/s11802-002-0002-z, http://dx.doi.org/10.1007/s11802-002-0002-z, 2002.

Farrell, S., Kurtz, N., Connor, L., Elder, B., Leuschen, C., Markus, T., McAdoo, D., Panzer, B., Richter-Menge, J., and Sonntag, J.: A first assessment of IceBridge snow and ice thickness data over Arctic sea ice, IEEE Transactions on Geoscience and Remote Sensing, 50, 2098–2111, 2012.

Fofonoff, N. and Millard, R.: Algorithms for computation of fundamental properties of seawater, Tech. Rep. 44, UNESCO, Technical Papers in Marine Science., 1983.

Font, J., Camps, A., Borges, A., Martin-Neira, M., Boutin, J., Reul, N., Kerr, Y. H., Hahne, A., and Mecklenburg, S.: SMOS: The Challenging Sea Surface Salinity Measurement From Space, PROCEEDINGS OF THE IEEE, 98, 649–665, doi:{10.1109/JPROC.2009.2033096}, 2010.

Frey, R. A., Ackerman, S. A., Liu, Y., Strabala, K. I., Zhang, H., Key, J. R., and Wang, X.: Cloud detection with MODIS. Part I: Improvements in the MODIS cloud mask for collection 5, Journal of Atmospheric and Oceanic Technology, 25, 1057–1072, 2008.

Godlovitch, D., Monahan, A., and Flato, G.: An idealised stochastic model of sea ice thickness dynamics, Cold Regions Science and Technology, 78, 14–30, 2012.

Goodberlet, M. and Mead, J.: Improved Models of Soil Emission for Use in Remote Sensing of Soil Moisture, IEEE Transactions on Geoscience and Remote Sensing, 50, 3991 – 3999, 2012.

Granskog, M., LeppÃ¯Â¿Â½ranta, M., Kawamura, T., Ehn, J., and Shirasawa, K.: Seasonal development of the properties and composition of landfast sea ice in the Gulf of Finland, the Baltic Sea, Journal of geophysical research, 109, C02 020, 2004.

Haas, C. and Casey, A.: Helicopterborne EM ice thickness surveys during SafeWin 2011 field campaign, Tech. rep., University of Alberta, 2012.

Haas, C. and Jochmann, P.: Continuous EM and ULS thickness profiling in support of ice force measurements, in: Proceedings of the 17th International Conference on Port and Ocean Engineering under Arctic Conditions, POAC Â´03, edited by Loeset, S., Bonnemaire, B., and Bjerkas, M., Department of Civil and Transport Engineering, Norwegian University of Sci., trondheim, Norway., 2003.

Haas, C., Lobach, J., Hendricks, S., Rabenstein, L., and Pfaffling, A.: Helicopter-borne measurements of sea ice thickness, using a small and lightweight, digital EM system, Journal of Applied Geophysics, 67, 234–241, 2009.

Haas, C., Hendricks, S., Eicken, H., and Herber, A.: Synoptic airborne thickness surveys reveal state of Arctic sea ice cover, Geophysical Research Letters, 37, L09 501, 2010.

Hall, D., Key, J., Casey, K., Riggs, G., and Cavalieri, D.: Sea ice surface temperature product from MODIS, IEEE Transactions on Geoscience and Remote Sensing, 42, 1076 – 1087, 2004.

Hall, Dorothy, K.: Remote sensing applications to hydrology: imaging radar, Hydrological Sciences, 41, 609 – 624, 1996.

Hallikainen, M.: Microwave Remote Sensing of Sea Ice, chap. Microwave remote sensing of low-salinity sea ice, pp. 361 – 373, Washington, DC: AGU, 1992.

Hallikainen, M. and Winebrenner, D.: The physical basis for sea ice remote sensing, Microwave remote sensing of sea ice, 68, 29–46, 1992.

Heygster, G., Hendricks, S., Kaleschke, L., Maass, N., Mills, P., Stammer, D., Tonboe, R., and Haas, C.: L-Band Radiometry for Sea-Ice Applications. Final Report for ESA ESTEC Contract 21130, 2009.

Heygster, G., Huntemann, M., and Wang, H.: Polarization-based SMOS sea ice thickness retrieval algorithm (Algorithm II), Algorithm Theoretical Basis Document (ATBD), STSE SMOSICE, 2012.

Huntemann, M., Heygster, G., Kaleschke, L., Krumpen, T., Mäkynen, M., and Drusch, M.: Empirical sea ice thickness retrieval during the freeze up period from SMOS high incident angle observations, The Cryosphere Discussions, 7, 4379–4405, doi:10.5194/tcd-7-4379-2013, http://www.the-cryosphere-discuss.net/7/4379/2013/, 2013.

Indra: SMOS DPGS: SMOS Level 1 and Auxiliary Data Products Specifications, Ref. SO-TN-IDR-GS-0005, 2010.

Jackson, T. and O'Neill, P.: Microwave dielectric model for aggregated soils, IEEE Transactions on Geoscience and Remote Sensing, 24, 920 – 929, 1986.

Janssen, F., Schrum, C., and Backhaus, J.: A climatological data set of temperature and salinity for the Baltic Sea and the North Sea, Deutsche Hydrographische Zeitschrift, 51, 5 – 245, 1999.

Kaellen, E.: HIRLAM Documentation Manual, System 2.5. Swed. Meteorol. and Hydrol. Inst., Norrkoeping, Sweden, 1996, 1996.

Kaleschke, L. and Rickert, R.: Sea Ice Outlook 2013-Sea Ice Thickness from CryoSat-2 and SMOS, 2013.

Kaleschke, L., Lüpkes, C., Vihma, T., Haarpaintner, J., Bochert, A., Hartmann, J., and Heygster, G.: SSM/I sea ice remote sensing for mesoscale ocean-atmosphere interaction analysis, Canadian Journal of Remote Sensing/Journal Canadien de Teledetection, 27, 526 – 537, 2001.

Kaleschke, L., Maaß, N., Haas, C., Hendricks, S., Heygster, G., and Tonboe, R.: A sea-ice thickness retrieval model for 1.4 GHz radiometry and application to airborne measurements over low salinity sea-ice, The Cryosphere, 4, 583 – 592, 2010.

Kaleschke, L., Tian-Kunze, X., Maaß, N., Mäkynen, M., and Drusch, M.: Sea ice thickness retrieval from SMOS brightness temperatures during the Arctic freeze-up period, Geophysical Research Letters, 39, doi:10.129/2012GL050916, 2012.

Kalnay, E., Kanamitsu, M., Kistler, R., Collins, W., Deaven, D., Gandin, L., Iredell, M., Sana, S., White, G., Woollen, J., et al.: The NCEP/NCAR 40-Year Reanalysis Project, Bull. Am. Meteorol. Soc., 77, 437 – 471, 1996.

Kerr, Y., Waldteufel, P., Wigneron, J., Martinuzzi, J., Font, J., and Berger, M.: Soil moisture retrieval from space: The Soil Moisture and Ocean Salinity (SMOS) mission, IEEE Transactions on Geoscience and Remote Sensing, 39, 1729 – 1735, 2001.

Key, J. and McLaren, A.: Fractal nature of the sea ice draft profile, Geophysical Research Letters, 18, 1437–1440, 1991.

Klein, L. and Swift, C.: An improved model for the dielectric constant of sea water at microwave frequencies, IEEE Transactions on Antennas and Propagation, 25, 104 – 111, 1977.

Kong, J.: Theory of electromagnetic waves, vol. 1, New York, Wiley-Interscience, 1975.

Kovacs, A.: Sea Ice. Part 1. Bulk Salinity Versus Ice Floe Thickness, Tech. rep., DTIC Document, 1996.

Krabill, W. B.: IceBridge KT19 IR Surface Temperature, online, boulder, Colorado USA: NASA DAAC at NSIDC, 2012.

Kurtz, N.: IceBridge quick look sea ice freeboard, snow depth, and thickness product manual, 2012.

Kurtz, N. and Farrell, S.: Large-scale surveys of snow depth on Arctic sea ice from operation IceBridge, Geophysical Research Letters, 38, L20 505, 2011.

Kurtz, N., Studinger, M., Harbeck, J., Onana, V., and Farrell, S.: IceBridge Sea Ice Freeboard, Snow Depth, and Thickness., online, boulder, Colorado USA: NASA DAAC at NSIDC, 2012.

Kurtz, N. T., Farrell, S. L., Studinger, M., Galin, N., Harbeck, J. P., Lindsay, R., Onana, V. D., Panzer, B., and Sonntag, J. G.: Sea ice thickness, freeboard, and snow depth products from Operation IceBridge airborne data, The Cryosphere, 7, 1035–1056, doi:10.5194/tc-7-1035-2013, http://www.the-cryosphere.net/7/1035/2013/, 2013.

Laxon, S. W., Giles, K. A., Ridout, A. L., Wingham, D. J., Willatt, R., Cullen, R., Kwok, R., Schweiger, A., Zhang, J., Haas, C., et al.: CryoSat-2 estimates of Arctic sea ice thickness and volume, Geophysical Research Letters, 2013.

Le Vine, D. and Abraham, S.: Galactic noise and passive microwave remote sensing from space at L-band, IEEE Transactions on Geoscience and Remote Sensing, 42, 119 – 129, 2004.

Le Vine, D., Abraham, S., Kerr, Y., Wilson, W., Skou, N., and Sobjaerg, S.: Comparison of model prediction with measurements of galactic background noise at L-band, IEEE Transactions on Geoscience and Remote Sensing, 43, 2018 – 2023, 2005.

Lebedev, V. V.: Rost l'do v arkticheskikh rekakh I moriakb v zavisimosti ot otrisatel' nykh temperatur vozdukha, Problemi Arktiki, 5, 9–25, 1938.

Leppäranta, M. and Manninen, T.: The brine and gas content of sea ice with attention to low salinities and high temperatures, Internal Rep. 88-2, Finnish Institute of Marine Research, Helsinki, 1988.

Liebe, H., Hufford, G., and Cotton, M.: Propagation modeling of moist air and suspended water/ice particles at frequencies below 1000 GHz, in: Proceedings of the AGARD 52nd Specialists' Meeting of the Electromagnetic Wave Propagation Panel, 1993.

Maaß, N.: Remote sensing of sea ice thickness using SMOS data, Reports on Earth System Science, http://www.mpimet.mpg.de/fileadmin/publikationen/Reports/WEB_BzE_131.pdf, 2013a.

Maaß N. and Kaleschke, L.: Improving passive microwave sea ice concentration algorithms for coastal areas: applications to the Baltic Sea, Tellus A, 62, 393 – 410, doi:10.1111/j.1600-0870.2010.00452.x, 2010.

Maaß, N., Kaleschke, L., Tian-Kunze, X., and Drusch, M.: Snow thickness retrieval over thick Arctic sea ice using SMOS satellite data, The Cryosphere Discuss., 7, 3627–3674, doi:10.5194/tcd-7-3627-2013, 2013b.

Maekynen, M., Cheng, B., and Similae, M.: On the accuracy of thin-ice thickness retrieval using MODIS thermal imagery over Arctic first-year ice, Annals of Glaciology, 62, doi:10.3189/2013AoG62A166, 2013.

Mäkynen, M.: SMOSIce-DAT user manual for the validation data, STSE-SMOS Sea Ice Retrieval Study SMOSIce contract report, European Space Agency, 2012.

Marshall, J., Adcroft, A., Hill, C., Perelman, L., and Heisey, C.: A finite-volume, incompressible Navier Stokes model for studies of the ocean on parallel computers, J. Geophys. Res., 102, 5753–5766, 1997.

Maykut, G. and Untersteiner, N.: Some results from a time-dependent thermodynamic model of sea ice, Journal of Geophysical Research, 76, 1550 – 1575, 1971.

Maykut, G. A.: Geophysics of Sea Ice, chap. The surface heat and mass balance, pp. 395 – 463, Plenum, New York, 1986.

Mecklenburg, S., Drusch, M., Kerr, Y. H., Font, J., Martin-Neira, M., Delwart, S., Buenadicha, G., Reul, N., Daganzo-Eusebio, E., Oliva, R., et al.: ESA's soil moisture and ocean salinity mission: mission performance and operations, IEEE Tansactions on Geoscience and Remote Sensing, 50, 1354–1366, 2012.

Menashi, J., Germain, K., Swift, C., Comiso, J., and Lohanick, A.: Low-frequency passive-microwave observations of sea ice in the Weddell Sea, Journal of Geophysical Research, 98, 22 569 – 22 577, 1993.

Mills, P. and Heygster, G.: Retrieving Ice Concentration From SMOS, Geoscience and Remote Sensing Letters, IEEE, pp. 283–287, 2011a.

Mills, P. and Heygster, G.: Sea Ice Emissivity Modeling at L-Band and Application to 2007 Pol-Ice Campaign Field Data, Geoscience and Remote Sensing, IEEE Transactions on, 49, 612–627, 2011b.

Murray, F.: On the computation of saturation vapor pressure, Journal of Applied Meteorology, 6, 203 – 204, 1967.

NOAA, U. and Force, U.: US standard atmosphere, 1976, Washington, DC, 1976.

Notz, D. and Worster, M. G.: Desalination processes of sea ice revisited, Journal of Geophysical Research: Oceans (1978–2012), 114, 2009.

NSIDC: Morphometric characteristics of ice and snow in the Arctic Basin: aircraft landing observations from the Former Soviet Union, 1928-1989. Compiled by I.P. Romanov. Boulder, CO: National Snow and Ice Data Center. Digital media., 2004.

Onogi, K., Tslttsui, J., Koide, H., Sakamoto, M., Kobayashi, S., Hatsushika, H., Matsumoto, T., Yamazaki, N., Kaalhori, H., Takahashi, K., Kadokura, S., Wada, K., Kato, K., Oyama, R., Ose, T., Mannoji, N., and Taira, R.: The JRA-25 reanalysis, Journal of the Meteorological Society of Japan, 85, 369–432, 2007.

Pfaffling, A., Haas, C., and Reid, J. E.: Direct helicopter EM-Sea-ice thickness inversion assessed with synthetic and field data, Geophysics, 72, F127–F137, 2007.

Pounder, E.: The physics of ice, Oxford, Pergamon Press, the Commonwealth and International Library, Geophysics Division., 1965.

Rosenkranz, P.: Water vapor microwave continuum absorption: A comparison of measurements and models, Radio Science, 33, 919 – 928, 1998.

Rott, H. and Mätzler, C.: Possibilities and limits of synthetic aperture radar for snow and glacier surveying, Annals of Glaciology, 9, 195 – 199, 1987.

Ryvlin, A. I.: Method of forecasting flexural strength of an ice cover, Probl. Arct. Antarct, 45, 79–86, 1974.

Saloranta, T.: Modeling the evolution of snow, snow ice and ice in the Baltic Sea, Tellus A, 52, 93 – 108, 2000.

Serra, N., Käse, R. H., Köhl, A., Stammer, D., and Quadfasel, D.: On the low-frequency phase relation between the Denmark Strait and the Faroe-Bank Channel overflows, Tellus A, 62, 530–550, doi:10.1111/j.1600-0870.2010.00445.x, 2010.

Spreen, G., Kaleschke, L., and Heygster, G.: Sea ice remote sensing using AMSR-E 89 GHz channels, Journal of Geophysical Research, 113, 2008.

SWIFT, C.: PASSIVE MICROWAVE REMOTE-SENSING OF THE OCEAN - REVIEW, BOUNDARY-LAYER METEOROLOGY, 18, 25–54, 1980.

Tan, B., Li, Z.-j., Lu, P., Haas, C., and Nicolaus, M.: Morphology of sea ice pressure ridges in the northwestern Weddell Sea in winter, Journal of Geophysical Research: Oceans (1978–2012), 117, 2012.

Thorndike, A.: Estimates of sea ice thickness distribution using observations and theory, Journal of Geophysical Research, 97, 12 601–12, 1992.

Thorndike, A., Rothrock, D., Maykut, G., and Colony, R.: The thickness distribution of sea ice, Journal of Geophysical Research, 80, 4501–4513, 1975.

Tian-Kunze, X., Kaleschke, L., Maaß, N., Mäkynen, M., Serra, N., Drusch, M., and Krumpen, T.: SMOS derived sea ice thickness: algorithm baseline, product specifications and initial verification, The Cryosphere Discussions, 7, 5735–5792, doi:10.5194/tcd-7-5735-2013, http://www.the-cryosphere-discuss.net/7/5735/2013/, 2013.

Tian-Kunze, X., Kaleschke, L., and MaaÃ¯Â¿Â½, N.: Detection and mitigation of RFI influence within SMOS application for high latitudes, in: Geophysical Research Abstracts, pp. Vol. 13, EGU2011–3108–1, EGU General Assembly 2011 , 2011.

Tiuri, M., Sihvola, A., Nyfors, E., and Hallikainen, M.: The complex dielectric constant of snow at microwave frequencies, IEEE Journal of Oceanic Engineering, 9, 377 – 382, 1984.

Tonboe, R., Dybkjær, G., and Høyer, J.: Simulations of the snow covered sea ice surface temperature and microwave effective temperature, Tellus A, 63, 1028 – 1037, 2011.

Tsang, L., Kong, J., and Ding, K.: Theory of Microwave Remote Sensing, Wiley-Interscience, New York, 2000.

Ulaby, F., Moore, R., and Fung, A.: Microwave remote sensing: Active and passive, vol. 1 - Microwave remote sensing fundamentals and radiometry, Addison-Wesley, 1981.

Unden, P. e. a.: HIRLAM-5 scientific documentation. Swed. Meteorol. and Hydrol. Inst., Norrkoeping, Sweden, 2002, 2002.

Untersteiner, N.: Calculations of temperature regime and heat budget of sea ice in the Central Arctic, Journal of Geophysical Research, 69, 4755 – 4766, 1964.

Vancoppenolle, M., Fichefet, T., and Bitz, C. M.: Modeling the salinity profile of undeformed Arctic sea ice, Geophysical Research Letters, 33, L21 501, 2006.

Vancoppenolle, M., Bitz, C. M., and Fichefet, T.: Summer landfast sea ice desalination at Point Barrow, Alaska: Modeling and observations, JOURNAL OF GEOPHYSICAL RESEARCH-OCEANS, 112, doi:{10.1029/2006JC003493}, 2007.

Vancoppenolle, M., Fichefet, T., and Goosse, H.: Simulating the mass balance and salinity of Arctic and Antarctic sea ice. 2. Importance of sea ice salinity variations, OCEAN MODELLING, 27, 54–69, doi:{10.1016/j.ocemod.2008.11.003}, 2009a.

Vancoppenolle, M., Fichefet, T., Goosse, H., Bouillon, S., Madec, G., and Maqueda, M. A. M.: Simulating the mass balance and salinity of Arctic and Antarctic sea ice. 1. Model description and validation, OCEAN MODELLING, 27, 33–53, doi:{10.1016/j.ocemod.2008.10.005}, 2009b.

Vant, M., Ramseier, R., and Makios, V.: The complex-dielectric constant of sea ice at frequencies in the range 0.1–40 GHz, Journal of Applied Physics, 49, 1264 – 1280, 1978.

Warren, S., Rigor, I., Untersteiner, N., Radionov, V., Bryazgin, N., Aleksandrov, Y., and Colony, R.: Snow depth on Arctic sea ice, Journal of Climate, 12, 1814 – 1829, 1999.

Weeks, W. and Lee, O.: The salinity distribution in young sea-ice, Arctic, 15, 92 – 108, 1962.

Wessel, P. and Smith, W.: A global, self-consistent, hierarchical, high-resolution shoreline database, Journal of Geophysical Research – Solid Earth, 101, 1996.

Yu, Y. and Rothrock, D.: Thin ice thickness from satellite thermal imagery, Journal of Geophysical Research, 101, 25 753 – 25 766, 1996.

Zhang, J. and Rothrock, D.: Modeling global sea ice with a thickness and enthalpy distribution model in generalized curvilinear coordinates, Monthly weather review, 131, 845–861, 2003.

Zine, S., Boutin, J., Font, J., Reul, N., Waldteufel, P., Gabarró, C., Tenerelli, J., Petitcolin, F., Vergely, J., Talone, M., et al.: Overview of the SMOS sea surface salinity prototype processor, IEEE Transactions on Geoscience and Remote Sensing, 46, 621 – 645, 2008.